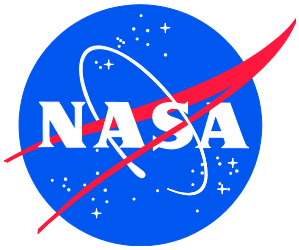
NASA/CR-2019-220284



An Evaluation and Recommendations for Further CFD Research Based on the NASA Common Research Model (CRM) Analysis from the AIAA Drag Prediction Workshop (DPW) Series

Edward N. Tinoco
Drag Prediction Workshop Organizing Committee
Retired, Boeing Technical Fellow, Boeing Commercial Airplanes

June 2019

NASA STI Program . . . in Profile

Since its founding, NASA has been dedicated to the advancement of aeronautics and space science. The NASA scientific and technical information (STI) program plays a key part in helping NASA maintain this important role.

The NASA STI program operates under the auspices of the Agency Chief Information Officer. It collects, organizes, provides for archiving, and disseminates NASA's STI. The NASA STI program provides access to the NTRS Registered and its public interface, the NASA Technical Reports Server, thus providing one of the largest collections of aeronautical and space science STI in the world. Results are published in both non-NASA channels and by NASA in the NASA STI Report Series, which includes the following report types:

- TECHNICAL PUBLICATION. Reports of completed research or a major significant phase of research that present the results of NASA Programs and include extensive data or theoretical analysis. Includes compilations of significant scientific and technical data and information deemed to be of continuing reference value. NASA counter-part of peer-reviewed formal professional papers but has less stringent limitations on manuscript length and extent of graphic presentations.

- TECHNICAL MEMORANDUM. Scientific and technical findings that are preliminary or of specialized interest, e.g., quick release reports, working papers, and bibliographies that contain minimal annotation. Does not contain extensive analysis.

- CONTRACTOR REPORT. Scientific and technical findings by NASA-sponsored contractors and grantees.

- CONFERENCE PUBLICATION. Collected papers from scientific and technical conferences, symposia, seminars, or other meetings sponsored or co-sponsored by NASA.

- SPECIAL PUBLICATION. Scientific, technical, or historical information from NASA programs, projects, and missions, often concerned with subjects having substantial public interest.

- TECHNICAL TRANSLATION. English-language translations of foreign scientific and technical material pertinent to NASA's mission.

Specialized services also include organizing and publishing research results, distributing specialized research announcements and feeds, providing information desk and personal search support, and enabling data exchange services.

For more information about the NASA STI program, see the following:

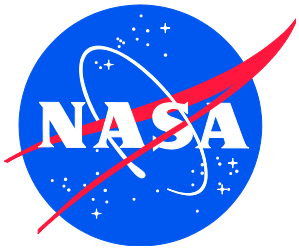
- Access the NASA STI program home page at http://www.sti.nasa.gov

- E-mail your question to help@sti.nasa.gov

- Phone the NASA STI Information Desk at 757-864-9658

- Write to:
  NASA STI Information Desk
  Mail Stop 148
  NASA Langley Research Center
  Hampton, VA 23681-2199

NASA/CR-2019-220284



An Evaluation and Recommendations for Further CFD Research Based on the NASA Common Research Model (CRM) Analysis from the AIAA Drag Prediction Workshop (DPW) Series

Edward N. Tinoco
Drag Prediction Workshop Organizing Committee
Retired, Boeing Technical Fellow, Boeing Commercial Airplanes

National Aeronautics and
Space Administration

Langley Research Center
Hampton, Virginia
23681-2199

Prepared for Langley Research Center under
Cooperative Agreement NNL09AA00A

June 2019

Table of Contents

Executive Summary and Recommendations 1

Section I: Introduction and DPW history 6

Section II: Geometry 10

Section III: Experimental Data Description 14

Section IV: Gridding Guidelines and Description of Common Grids 19

Section V: Test Case Descriptions 20

Section VI: Participant Descriptions 23

Section VII: Grid Convergence Study 29

A. Drag; CRM Wing-Body and Wing-Body-Tail: DPW-IV, -V, and -VI. 29

B. Drag; CRM Wing-Body-Nacelle-Pylon: DPW-VI. 37

C. Drag Increment: CRM Wing-Body and Wing-Body-Nacelle-Pylon; DPW-VI. 39

D. Pressure Distributions: DPW-IV, -V, and -VI. 41

Section VIII: Drag Rise Study 49

Section IX: Reynolds Number Study 51

Section X: Angle-of-Attack Sweep/Buffet Study 57

A. DPW-IV Results 57

B. DPW-V Results 60

C. DPW-VI Results 70

Section XI: Trim Drag and Stabilizer Effectiveness 84

A. Trimmed Lift and Drag 84

B. Stabilizer Effectiveness 88

Section XII: WB Grid Adaptation Study 91

Section XIII: WB Coupled Aerostructural Simulation 96

Section XIV: Emerging Technologies 100

A. Finite Element Solvers 100

B. Solution/Grid Adaptive Methods 100

C. Lattice-Boltzmann Method (LBM) 101

Section XV: Questions and Issues 101

A. Premature Side-of-Body Separation 101

B. Excessive Aft-Loading 105

C. Solution Spread 107

D. Inadequate Test Data 117

Section XVI: Observations, Recommendations, and Concluding Remarks 118

A. Observations 118

1. Single Point Solutions 118

2. Angle-of-Attack Sweep/Buffet Study 119
3. One-of-a-Kind Studies 120
4. Emerging Technologies 120
5. Experimental Data 121
6. Workshops and CFD Validation 121

B. Specific Recommendations 122

C. Concluding Remarks 122

Section XVII: Acknowledgments 123

Section XVIII: References 124

Appendix A. Enhanced Experimental Pressure Distributions 130

Appendix B. Grids 149

B-A. Expanded Section IV: Description of Common Grids 149

B-B. DPW-IV Grids 150

B-C. DPW-V Grids 151

B-D. DPW-VI Grids 153
B-D-1. Baseline Overset Grid Families for DPW-VI 153
B-D-2. Baseline NASA GeoLab Unstructured Meshes for DPW-VI 156
B-D-3. DLR SOLAR Unstructured Meshes for DPW-VI 157
B-D-4. Additional Available Meshes for DPW-VI 158

Appendix C. Participants 159

C-A. Tables used in Section VI – Participant Descriptions 159

C-B. Tables used in Appendix D - Grid Convergence 164

C-C. Tables used in Section XV – Questions and Issues 168

Appendix D. Convergence 171

D-A. Richardson Extrapolation 171

D-B. DPW-IV Grid Convergence (WBT IH = 0°) 172

D-C. DPW-V Grid Convergence (WB "As -Built") 182

D-D. DPW-VI Grid Convergence 192
D-D-1. DPW-VI Grid Convergence: Wing-Body (WB) 192
D-D-2. DPW-VI Grid Convergence: Wing-Body-Nacelle-Pylon (WBNP) 206
D-D-3. DPW-VI Grid Convergence: WBNP minus WB Drag Increment 215

Appendix E. Angle-of-Attack Sweep Forces and Moments 219

E-A. DPW-IV: CRM Wing-Body (As-Built) 219

E-B. DPW-V: CRM Wing-Body (As-Built) 223

E-C. DPW-VI: CRM Wing-Body (Aeroelastic) 244

Appendix F. Downwash Study 258

Appendix G. CFD Wing Pressure Distributions 268

G-A DPW-VI Comparisons 268

G-B DPW-V Comparisons 283

G-C DPW-IV Results – Experimental data were not yet available for comparison 287

Table of Figures

Figure S-I-1. DLR-F6 Model in ONERA S2MA Wind Tunnel....8
Figure S-I-2. FX2B Wing-Body....8
Figure S-II-1. NASA Common Research Model....11
Figure S-II-2. CRM Wing and Horizontal Planform....11
Figure S-II-3. Static Aeroelastic Wing Twist Distribution Derived from Wind Tunnel Measurements....13
Figure S-II-4. Impact of Aeroelastic Deformation on WB Lift and Moment; M = 0.85, Re_c = 5 Million....13
Figure S-II-5. Impact of Aeroelastic Deformation on WB Outboard Wing Pressure Distribution; M = 0.85, Re_c = 5 Million....14
Figure S-III-1. WBT Forces and Moments from NTF, Ames, and ETW Wind Tunnels; M = 0.85, Re_c = 5 million....16
Figure S-III-2. WBT Forces and Moments from NTF and ETW Wind Tunnels; M = 0.85, Re_c = 5 and 20 million....16
Figure S-III-3. Enhancement of Wind Tunnel Pressure Distributions....18
Figure S-IV-1. Block Topology for the CRM Wing-Body MB Grid Family....19
Figure S-V-1. CRM Wing-Body-Tail and Wing-Body (As-Built)....21
Figure S-V-2. CRM Wing-Body (As-Built)....21
Figure S-V-3. CRM Wing-Body and Wing-Body-Nacelle-Pylon (Aeroelastic)....22
Figure S-VII-1. Richardson Extrapolation Example; Drag....29
Figure S-VII-2. Grid Convergence; C_{D_TOT}, C_{D_PR}, C_{D_SF}....30
Figure S-VII-3. Grid Convergence; Grid Type; Total Drag C_{D_TOT}....31
Figure S-VII-4. Grid Convergence; Grid Type; Pitching Moment C_{M_TOT}....31
Figure S-VII-5. Grid Convergence; Grid Type; Angle of Attack....32
Figure S-VII-6. Grid Convergence; Unstructured Grids; Drag C_{D_TOT}....33
Figure S-VII-7. Grid Convergence; Geolab and Boeing Unstructured Grids; Total Drag C_{D_TOT}....34
....34
Figure S-VII-8. Grid Convergence; Custom Mixed and All–Tetrahedra Grids; Total Drag C_{D_TOT}....34
Figure S-VII-9. Grid Convergence; Overset and Structured Multiblock Grids; Total Drag C_{D_TOT}....35
Figure S-VII-10. DPW-IV WBT Total Drag Grid Convergence Sensitivity....36
Figure S-VII-11. DPW-V WB (As-Built) Total Drag Grid Convergence Sensitivity....36
Figure S-VII-12. DPW-VI WB (Aeroelastic) Total Drag Grid Convergence Sensitivity....37
Figure S-VII-13. Grid Convergence; Wing-Body-Nacelle-Pylon; Drag C_{D_TOT}, CD_{PR}, C_{D_SF}....38
Figure S-VII-14. Grid Convergence; Wing-Body-Nacelle-Pylon: Drag by Grid and Turbulence Model....38
Figure S-VII-15. WBNP (Aeroelastic) Total Drag Grid Convergence Sensitivity....39
Figure S-VII-16. Grid Convergence; Nacelle-Pylon Drag Increment by Grid Type and Turbulence Model.
....40
Figure S-VII-17. Potential Impact of Grid Drag Convergence Slope on Drag Increment....40
Figure S-VII-18. Nacelle-Pylon Drag Increment Sensitivity on Grid Convergence....41
Figure S-VII-19. DPW-IV: WBT Wing Pressure Distribution; Grid Convergence; WBL133, $\eta = 0.115$....42
Figure S-VII-20. DPW-IV: WBT Wing Pressure Distribution; Grid Convergence; WBL878, $\eta = 0.846$....42
Figure S-VII-21. DPW-V: WB (As-Built) Wing Pressure Distribution; Grid Convergence: $\eta = 0.502$....43
Figure S-VII-22. DPW-V: WB (As-Built) Wing Pressure Distribution; Convergence: $\eta = 0727$; Select Solutions....44
Figure S-VII-23. DPW-VI: WB (Aeroelastic) Wing Pressure Distributions; Grid Convergence: $\eta = 0.131$, 0.502, and 0.846; Solutions P1 and K4....45
Figure S-VII-24. DPW-VI WB (Aeroelastic) Wing Pressure Distributions; Grid Convergence: $\eta = 0.131$, 0.502, and 0.846; Solutions G1 and H2....45
Figure S-VII-25. DPW-VI: WB (Aeroelastic) Wing Pressure Distributions; Finest Grid; All Solutions....46
Figure S-VII-26. DPW-VI: WBNP (Aeroelastic) Wing Pressure Distributions; Finest Grid: All....47
Figure S-VII-27. DPW-VI: WBNP (Aeroelastic) Nacelle Pressure Distributions; Finest Grid; All Solutions.
....47
Figure S-VII-28. CRM WBNP and WB Wing Section Lift and Moment; M = 0.85, C_L = 0.50....48
Figure S-VIII-1. Drag Rise CRM Wing-Body-Tail; iH = 0, C_L = 0.50....49
Figure S-VIII-2. Drag Rise CRM Wing-Body-Tail; iH = 0, C_L = 0.45....50

Figure S-VIII-3. Drag Rise CRM Wing-Body-Tail; iH = 0, C_L = 0.40. 50
Figure S-IX-1. WBT Drag Polar; 5 and 20 Million chord Reynolds Number. 52
Figure S-IX-2. WBT Lift and Pitching Moment: 5 and 20 Million chord Reynolds Number. 52
Figure S-IX-3. WBT Reynolds Number Effect on Total, Pressure, and Skin Friction Drag Increment (Re20M – Re5M). 53
Figure S-IX-4. WBT Reynolds Number Effect on Total Drag, Pitching Moment, and Angle of Attack Increment (Re20M – Re5M). 54
Figure S-IX-5. WBT Wing Pressure Distributions; Effect of Reynolds Number; CFD vs. Test. 55
Figure S-IX-6. WBT Wing Trailing Edge Pressure Distributions: Effect of Reynolds Number; CFD vs. Test. 56
Figure S-IX-7 WBT Aft Loading Delta Cp; Effect of Reynolds Number; CFD vs. Test. 56
Figure S-IX-8. WBT Aft Loading Delta C_p vs. Span Fraction; Effect of Reynolds Number; CFD vs. Test.57
Figure S-X-1. DPW-IV: WB (As-Built) Lift and Pitching Moment; All Solutions, M=0.85. 58
Figure S-X-2. DPW-IV: WB (As-Built) Lift; Grid Type - All Solutions, M=0.85. 59
Figure S-X-3. DPW-IV: WB (As-Built) Pitching Moment; Grid Type - All Solutions, M=0.85. 59
Figure S-X-4. DPW-IV: WB (As-Built) “Profile” Drag Polar; All Solutions, M=0.85 60
Figure S-X-5. “Pseudo” Wind Tunnel Test Data, M=0.85. 61
Figure S-X-6. DPW-V: WB (As-Built) Lift and Pitching Moment; All Solutions, M=0.85 62
Figure S-X-7. DPW-V: WB (As-Built) “Profile” Drag Polar; All Solutions, M=0.85. 62
Figure S-X-8. DPW-V: WB (As-Built) Overset and Multiblock Grid Solutions, M=0.85. 63
Figure S-X-9. DPW-V: WB (As-Built) Hex and Hybrid Unstructured Grid Solutions, M=0.85. 64
Figure S-X-10. DPW-V: WB (As-Built) Prism and Custom Unstructured Grid Solutions, M=0.85. 64
Figure S-X-11. DPW-V: WB (As-Built) Lift and Pitching Moment; All Solutions minus Outliers, M=0.85. 65
Figure S-X-12. DPW-V: WB (As-Built) “Profile” Drag Polar: All Solutions minus Outliers, M=0.85 66
Figure S-X-13. DPW-V: WB (As-Built) Side-of-Body Separation Bubble, M=0.85 67
Figure S-X-14. DPW-V: WB (As-Built) Wing Trailing Edge Separation at 2.5° Angle of Attack, M=0.85. 68
Figure S-X-15. DPW-V: WB (As-Built) Wing Trailing Edge Separation at 3.0° Angle of Attack, M=0.85. 68
Figure S-X-16. DPW-V: WB (As-Built) Wing Trailing Edge Separation at 4.0° Angle of Attack, M=0.85. 69
Figure S-X-17. DPW-V: WB (As-Built) Pressure Distributions and Lift Characteristics of Select Solutions, M=0.85. 70
Figure S-X-18. DPW-VI: WB (Aeroelastic) Lift and Pitching Moment; All Solution. M=0.85. 71
Figure S-X-19. DPW-VI: WB (Aeroelastic) “Idealized Profile” Drag Polar; All Solutions. , M=0.85 71
Figure S-X-20. DPW-VI: WB (Aeroelastic) Side-of-Body Separation Bubble Comparison with DPW-V WB (As-Built), M=0.85. 72
Figure S-X-21. DPW-VI: WB (Aeroelastic) Side-of-Body Separation with Angle of Attack, M=0.85. 72
Figure S-X-22. DPW-VI: WB (Aeroelastic) Wing Pressure Distributions - All Solutions - AOA = 3.0°, M=0.85. 73
Figure S-X-25. WB Wing Trailing Edge Separation Comparison Between DPW-V and DPW-VI, M=0.85. 75
Figure S-X-26. DPW-VI: WB (Aeroelastic) Wing Section Lift Coefficient, M=0.85. 76
Figure S-X-27. WB (Aeroelastic) Wing Section Pitching Moment Coefficient, M=0.85. 76
Figure S-X-28. DPW-VI: WB (Aeroelastic) Forces and Moments; Overset and Multiblock Grids, M=0.85. 77
Figure S-X-29. DPW-VI: WB (Aeroelastic) Forces and Moments; Geolab and Custom Unstructured Grids, M=0.85. 78
Figure S-X-30. DPW-VI: WB (Aeroelastic) Forces and Moments; Boeing Unstructured and Custom Cartesian Grids, M=0.85. 78
Figure S-X-31. DPW-VI: WB (Aeroelastic) Solution Outliers, M=0.85 79
Figure S-X-32. DPW-VI: WB (Aeroelastic) Lift and Moment Characteristics; All Solutions minus Outliers, M=0.85. 79
Figure S-X-34. DPW-VI: WB (Aeroelastic) Wing Pressure Distribution; All Solutions minus Outliers, C_L = 0.50, M=0.85. 81

Figure S-X-36. DPW-VI: WB (Aeroelastic) Wing Pressure Distributions; All Solutions minus Outliers, AOA = 3.5°, M=0.85.....82
Figure S-X-37. DPW-VI: WB (Aeroelastic) Wing Pressure Distributions; All Solutions minus Outliers, AOA = 4.0°, M=0.85.....83
Figure S-XI-1. DPW-IV: Lift vs. Angle of Attack; Wing-Body-Tail iH = –2°, 0°, 2°, M=0.85.....84
Figure S-XI-2. DPW-IV: Pitching Moment: Wing-Body and Wing-Body-Tail iH = –2°, 0°, 2°, M=0.85...85
Figure S-XI-3. DPW-IV: Pitching Moment Components; Wing-Body-Tail iH = –2°, M=0.85. 85
Figure S-XI-4. DPW-IV: Wing-Body-Tail Trimmed Drag Polars and iH to Trim, M=0.85. 86
Figure S-XI-5. DPW-IV: Pitching Moment Corrected for Mounting System and Aeroelastics; WB and WBT iH = –2°, 0°, 2°, M=0.85. 87
Figure S-XI-6. DPW-IV: WBT "Corrected" Trimmed Lift and Drag, M=0.85.....88
Figure S-XI-7. Change of Pitching Moment vs. Tail Angle, M=0.85. 89
Figure S-XI-8. Stabilizer Effectiveness: Grid Type, M=0.85. 89
Figure S-XI-9. Stabilizer Effectiveness: Turbulence Model, M=0.85.....90
Figure S-XI-10. Effect of Dynamic Pressure on Change in Pitching Moment due to Tail Angle, M=0.85..90
Figure S-XII-1. WB (As-Built) Grid Effect on Solutions, M=0.85.....91
Figure S-XII-2. EPIC Adaptive Grid Tool.....92
Figure S-XII-3. DPW-VI: WB (Aeroelastic) Lift and Drag - Adapted Solutions, M=0.85. 93
Figure S-XII-4. DPW-VI: WB (Aeroelastic) Adapted and Fixed Grid Drag Convergence, M=0.85.....93
Figure S-XII-5. WB (Aeroelastic) Total Drag Convergence with Solution A1, M=0.85. 94
Figure S-XII-6. WB (Aeroelastic) Effect of Adaption on Wing Tip Pressures, M=0.85.....94
Figure S-XII-7. Adapted Grid and Solution Sequence for WBNP (Aeroelastic) Configuration, M=0.85....95
Figure S-XIII-1. Numerical Simulation Procedure for Coupled Aerostructural Analysis. 97
Figure S-XIII-2. WB Wing Pressure Distributions: Coupled Aerostructural Analysis, M=0.85. 98
Figure S-XIII-3. WB Wing Deflection and Twist: Coupled Aerostructural Analysis, M=0.85. 99
Figure S-XIII-4. WB Force and Moment Data: Coupled Aerostructural Analysis, M=0.85. 99
Figure S-XV-1. DPW-VI Side-of-Body Separation Bubble Comparison with DPW-V, M=0.85.....102
Figure S-XV-2. DPW-VI: WB (Aeroelastic) Wing Trailing Edge Pressures; All solutions; C_L = 0.50, M=0.85. 105
Figure S-XV-3. DPW-VI: WB (Aeroelastic) Wing Trailing Edge Pressures; AOA = 2.5° to 4.0°, M=0.85. 106
Figure S-XV-4. DPW-VI: WB (Aeroelastic) Wing Section Lift and Pitching Moment; Outboard Wing, M=0.85.....106
Figure S-XV-5. DPW-VI: WB (Aeroelastic) Lift, Pitching Moment, and Pressure Distributions; SA Turbulence Model, M=0.85.....108
Figure S-XV-6. DPW-VI: WB (Aeroelastic) Lift, Pitching Moment, and Pressure Distributions; SA-QCR Turbulence Model.....109
Figure S-XV-7. DPW-VI: WB (Aeroelastic) Lift, Pitching Moment, and Pressure Distributions; Non-SA Turbulence Models.....109
Figure S-XV-8. DPW-VI: WB (Aeroelastic) Lift and Pitching Moment Shifted to Match Experiment at C_L = 0.53. 110
Figure S-XV-9. DPW-VI: WB (Aeroelastic) "Selected" Lift and Pitching Moment Solutions; Shifted to Match Experiment at C_L = 0.53. 111
Figure S-XV-10. DPW-VI: WB (Aeroelastic) Wing Pressure Distributions: "Selected" Solutions; AOA = 3.0°.....112
Figure S-XV-11. DPW-VI: WB (Aeroelastic) Wing Pressure Distributions: "Selected" Solutions; AOA = 3.5°.....112
Figure S-XV-12. DPW-VI: WB (Aeroelastic) Wing Pressure Distributions: "Selected" Solutions; AOA = 3.75°.....113
Figure S-XV-13. DPW-VI: WB (Aeroelastic) Wing Pressure Distributions: "Selected" Solutions; AOA = 4.0°.....113
Figure S-XV-14. DPW-VI: WB (Aeroelastic) "Selected" Lift and Pitching Moment Solutions: USS Corrections Only.....114
Figure S-XV-15. WB (Aeroelastic) Lift and Pitching Moment: SA Solution That Do Not Match Experiment. 116

Figure S-XV-16. WB (Aeroelastic) Lift and Pitching Moment: SA-QCR Solution That Do Not Match Experiment. 116
Figure S-XV-17. WB (Aeroelastic) Lift and Pitching Moment: 2-Eq. TM Solutions That Do Not Match Experiment. 117
Figure A-A-1.Wing Pressure Distribution, Eta = 0.131, M = 0.85, AoA = –3.00° to 0.98°. 131
Figure A-A-2. Wing Pressure Distribution, Eta = 0.131, M = 0.85, AoA = 2.06° to 3.10°. 131
Figure A-A-3. Wing Pressure Distribution, Eta = 0.131, M = 0.85, AoA = 3.36° to 4.37°. 132
Figure A-A-4. Wing Pressure Distribution, Eta = 0.131, M = 0.85, AoA = 4.61° to 6.64°. 132
Figure A-A-5. Wing Pressure Distribution, Eta = 0.201, M = 0.85, AoA = –3.00° to 0.98°. 133
Figure A-A-6. Wing Pressure Distribution, Eta = 0.201, M = 0.85, AoA = 2.06° to 3.10°. 133
Figure A-A-7. Wing Pressure Distribution, Eta = 0.201, M = 0.85, AoA = 3.36° to 4.37°. 134
Figure A-A-8. Wing Pressure Distribution, Eta = 0.201, M = 0.85, AoA = 4.61° to 6.64°. 134
Figure A-A-9. Wing Pressure Distribution, Eta = 0.283, M = 0.85, AoA = –3.00° to 0.98°. 135
Figure A-A-10. Wing Pressure Distribution, Eta = 0.283, M = 0.85, AoA = 2.06° to 3.10°. 135
Figure A-A-11. Wing Pressure Distribution, Eta = 0.283, M = 0.85, AoA = 3.36° to 4.37°. 136
Figure A-A-12. Wing Pressure Distribution, Eta = 0.283, M = 0.85, AoA = 4.61° to 6.64°. 136
Figure A-A-13 Wing Pressure Distribution, Eta = 0.397, M = 0.85, AoA = –3.00° to 0.98°. 137
Figure A-A-14. Wing Pressure Distribution, Eta = 0. 397, M = 0.85, AoA = 2.06° to 3.10°. 137
Figure A-A-15. Wing Pressure Distribution, Eta = 0. 397, M = 0.85, AoA = 3.36° to 4.37°. 138
Figure A-A-16. Wing Pressure Distribution, Eta = 0. 397, M = 0.85, AoA = 4.61° to 6.64°. 138
Figure A-A-17. Wing Pressure Distribution, Eta = 0.502, M = 0.85, AoA = –3.00° to 0.98°. 139
Figure A-A-18. Wing Pressure Distribution, Eta = 0. 502, M = 0.85, AoA = 2.06° to 3.10°. 139
Figure A-A-19. Wing Pressure Distribution, Eta = 0. 502, M= 0 .85, AoA = 3.36° to 4.37°. 140
Figure A-A-20. Wing Pressure Distribution, Eta = 0. 502, M = 0.85, AoA = 4.61° to 6.64°. 140
Figure A-A-21. Wing Pressure Distribution, Eta = 0.603, M = 0.85, AoA = –3.00° to 0.98°. 141
Figure A-A-22. Wing Pressure Distribution, Eta = 0. 603, M = 0.85, AoA = 2.06° to 3.10°. 141
Figure A-A-23. Wing Pressure Distribution, Eta = 0. 603, M = 0.85, AoA = 3.36° to 4.37°. 142
Figure A-A-24. Wing Pressure Distribution, Eta = 0. 603, M = 0.85, AoA = 4.61° to 6.64°. 142
Figure A-A-25. Wing Pressure Distribution, Eta = 0.727, M = 0.85, AoA = –3.00° to 0.98°. 143
Figure A-A-26. Wing Pressure Distribution, Eta = 0. 727, M = 0.85, AoA = 2.06° to 3.10°. 143
Figure A-A-27. Wing Pressure Distribution, Eta = 0. 727, M = 0.85, AoA = 3.36° to 4.37°. 144
Figure A-A-28. Wing Pressure Distribution, Eta = 0. 727, M = 0.85, AoA = 4.61° to 6.64°. 144
Figure A-A-29. Wing Pressure Distribution, Eta = 0.846, M = 0.85, AoA = –3.00° to 0.98°. 145
Figure A-A-30. Wing Pressure Distribution, Eta = 0. 846, M = 0.85, AoA = 2.06° to 3.10°. 145
Figure A-A-31. Wing Pressure Distribution, Eta = 0. 846, M = 0.85, AoA = 3.36° to 4.37°. 146
Figure A-A-32. Wing Pressure Distribution, Eta = 0. 846, M = 0.85, AoA = 4.61° to 6.64°. 146
Figure A-A-33. Wing Pressure Distribution, Eta = 0. 846, M = 0.85, AoA = –3.00° to 0.98°. 147
Figure A-A-34. Wing Pressure Distribution, Eta = 0.950, M = 0.85, AoA = 2.06° to 3.10°. 147
Figure A-A-35. Wing Pressure Distribution, Eta = 0.950, M = 0.85, AoA = 3.36° to 4.37°. 148
Figure A-A-36. Wing Pressure Distribution, Eta = 0. 950, M = 0.85, AoA = 4.61° to 6.64°. 148
Figure A-B-1. Block Topology for the CRM Wing-Body Multiblock (MB) Grid Family (Figure-S-IV-1). 152
Figure A-B-2. Overset Patch Grids Derived from the Multiblock Structured Grid. 152
Figure A-B-3. Unstructured Grids Derived from Multiblock Structured Grid 153
Figure A-B-4. Topology of Overset Near-Field Grid Blocks and Nacelle-Pylon Grid Blocks. 154
Figure A-B-5. Close-Up of WBNP Surface and Nacelle/Pylon Surface Grids for the Medium Overset Mesh. 155
Figure A-B-6. Close-Up of Overset Features for Medium Overset Mesh. 155
Figure A-B-7. Close-Up of NASA GeoLab Unstructured Surface Meshes. 156
Figure A-B-8. Close-Up of DLR Solar Unstructured Surface Mesh. 157
Figure A-D-1. Richardson Extrapolation Example; Drag (Figure S-VII-1 in Section VII). 171
Figure A-D-2. DPW-IV: Total Drag Grid Convergence Sensitivity: Drag Ordered; TM (Figure S-VII-10). 173
Figure A-D-3. DPW-IV: Total Drag Grid Convergence Sensitivity, M=0.85: Drag Ordered; TM. 173
Figure A-D-4. DPW-IV: Total Drag Grid Convergence Sensitivity, M=0.85: Sensitivity Ordered; Grid. 174
Figure A-D-5. DPW-IV: Total Drag Grid Convergence Sensitivity, M=0.85: Delta Drag Ordered; Grid. 174

Figure A-D-6. DPW-IV: Total Drag Grid Convergence Sensitivity, M=0.85: Sensitivity Ordered; TM. ..175
Figure A-D-7. DPW-IV: Total Drag Grid Convergence Sensitivity, M=0.85: Delta Drag Ordered; TM...175
Figure A-D-8. DPW-IV: Grid Convergence; Total Drag C_{D_TOT}, M=0.85: All Solutions. 176
Figure A-D-9. DPW-IV: Grid Convergence; Total Drag C_{D_TOT}, M=0.85: Structured Grid Solutions. 176
Figure A-D-10. DPW-IV: Grid Convergence; Total Drag C_{D_TOT}, M=0.85: Unstructured Grid Solutions.....177
Figure A-D-11. DPW-IV: Grid Convergence; Total Drag C_{D_TOT}, M=0.85: BCA Zeus Structured Grid Solutions. 177
Figure A-D-12. DPW-IV: Grid Convergence; Total Drag C_{D_TOT}, M=0.85: Overflow and Cartesian/Oct-Tree Grid Solutions.....178
Figure A-D-13. DPW-IV: Grid Convergence; Total Drag C_{D_TOT}, M=0.85: Miscellaneous Structured Grid Solutions.....178
Figure A-D-14. DPW-IV: Grid Convergence; Total Drag C_{D_TOT}, M=0.85: All Unstructured Grid Solutions. 179
Figure A-D-15. DPW-IV: Grid Convergence; Total Drag C_{D_TOT}, M=0.85: SOLAR Unstructured Grid Solutions.....179
Figure A-D-16. DPW-IV: Grid Convergence; Total Drag C_{D_TOT}, M=0.85: VGRID Unstructured Grid Solutions.....180
Figure A-D-17. DPW-IV: Grid Convergence; Total Drag C_{D_TOT}, M=0.85: AFLR3 and MIME Unstructured Grid Solutions.....180
Figure A-D-18. DPW-IV: Grid Convergence; Total Drag C_{D_TOT}, M=0.85: Miscellaneous Unstructured Grid Solutions.....181
Figure A-D-19. DPW-V: Total Drag Grid Convergence Sensitivity, M=0.85: Drag Ordered; TM (Figure S-VII-11).....183
Figure A-D-20. DPW-V: Total Drag Grid Convergence Sensitivity, M=0.85: Drag Ordered; TM. 184
Figure A-D-21. DPW-V: Total Drag Grid Convergence Sensitivity, M=0.85: Sensitivity Ordered; Grid. 184
Figure A-D-22. DPW-V: Total Drag Grid Convergence Sensitivity, M=0.85: Delta Drag Ordered; Grid. 185
Figure A-D-23. DPW-V: Total Drag Grid Convergence Sensitivity, M=0.85: Sensitivity Ordered; TM. .185
Figure A-D-24. DPW-V: Total Drag Grid Convergence Sensitivity, M=0.85: Delta Drag Ordered; Grid. 186
Figure A-D-25. DPW-V: Grid Convergence; Total, Pressure, and Skin Friction Drag, M=0.85: All Solutions. 186
Figure A-D-26. DPW-V: Grid Convergence; Total Drag C_{D_TOT}, M=0.85: All Solutions.....187
Figure A-D-27. DPW-V: Grid Convergence; Total Drag C_{D_TOT}, M=0.85: All Structured Grid Solutions. ...187
Figure A-D-28. DPW-V: Grid Convergence; Total Drag C_{D_TOT}, M=0.85: Common Overset Grid Solutions. 188
Figure A-D-29. DPW-V: Grid Convergence; Total Drag C_{D_TOT}, M=0.85: Common Mutliblock Grid Solutions. 188
Figure A-D-30. DPW-V: Grid Convergence; Total Drag C_{D_TOT}, M=0.85Custom Structured Grid Solutions. 189
Figure A-D-31. DPW-V: Grid Convergence; Total Drag C_{D_TOT}, M=0.85: All Unstructured Grid Solutions. 189
Figure A-D-32. DPW-V: Grid Convergence; Total Drag C_{D_TOT}, M=0.85: Common Hex Unstructured Grid Solutions.....190
Figure A-D-33. DPW-V: Grid Convergence; Total Drag C_{D_TOT}, M=0.85: Common Hybrid Unstructured Grid Solutions.....190
Figure A-D-34. DPW-V: Grid Convergence; Total Drag C_{D_TOT}, M=0.85: Common Prism Unstructured Grid Solutions.....191
Figure A-D-35. DPW-V: Grid Convergence; Total Drag C_{D_TOT}, M=0.85: Custom Unstructured Grid Solutions. 191
Figure A-D-36. DPW-VI: Total Drag Grid Convergence Sensitivity, M=0.85 (Figure S-VII-12). 193
Figure A-D-37. DPW-VI: Total Drag Grid Convergence Sensitivity, M=0.85: Drag Ordered; TM.....193
Figure A-D-38. DPW-VI: Total Drag Grid Convergence Sensitivity, M=0.85: Sensitivity Ordered; Grid. 194
Figure A-D-39. DPW-VI: Total Drag Grid Convergence Sensitivity, M=0.85: Delta Drag Ordered; Grid. 194
Figure A-D-40. DPW-VI: Total Drag Grid Convergence Sensitivity, M=0.85: Sensitivity Ordered; TM. 195

Figure A-D-41. DPW-VI: Total Drag Grid Convergence Sensitivity, M=0.85: Delta Drag Ordered; Grid. 195
Figure A-D-42. DPW-VI: Grid Convergence; Total, Pressure, and Skin Friction Drag, M=0.85: All Solutions. 196
Figure A-D-43. DPW-VI: Grid Convergence; Total Drag C_{D_TOT}, M=0.85: All Solutions. 196
Figure A-D-44. DPW-VI: Grid Convergence; Total Drag C_{D_TOT}, M=0.85: All Structured Grid Solutions. 197
Figure A-D-45. DPW-VI: Grid Convergence; Total Drag C_{D_TOT}, M=0.85: All Unstructured Grid Solutions. 197
Figure A-D-46. DPW-VI: Grid Convergence; Total Drag C_{D_TOT}, M=0.85: Overflow Structured Grid Solutions. 198
Figure A-D-47. DPW-VI: Grid Convergence; Total Drag C_{D_TOT}, M=0.85: NASA/Overflow Structured Grid Solutions 198
Figure A-D-48. DPW-VI: Grid Convergence; Total Drag C_{D_TOT}, M=0.85: Multiblock Structured Grid Solutions 199
Figure A-D-49. DPW-VI: Grid Convergence; Total Drag C_{D_TOT}, M=0.85: Cartesian/Oct-Tree Grid Solutions. 199
Figure A-D-50. DPW-VI: Grid Convergence; Total Drag C_{D_TOT}, M=0.85: Geolab Unstructured Grid Solutions. 200
Figure A-D-51. DPW-VI: Grid Convergence; Total Drag C_{D_TOT}, M=0.85: Boeing Unstructured Grid Solutions. 200
Figure A-D-52. DPW-VI: Grid Convergence; Total Drag C_{D_TOT}, M=0.85: Custom Unstructured Grid Solutions. 201
Figure A-D-53. DPW-VI: Grid Convergence; Total Drag C_{D_TOT}, M=0.85: FUN3D/Geolab Unstructured Grid Solutions 201
Figure A-D-54. DPW-VI: Grid Convergence; Total Drag C_{D_TOT}, M=0.85: MDOlab ADflow Solutions. 202
Figure A-D-55. DPW-VI: Grid Convergence; Total Drag C_{D_TOT}, M=0.85TAS Solver Solutions. 202
Figure A-D-56. DPW-VI: Grid Convergence; Total Drag C_{D_TOT}, M=0.85: CFD++ Solver Solutions..... 203
Figure A-D-57. DPW-VI: Grid Convergence; Total Drag C_{D_TOT}, M=0.85: Cflow Solver Solutions..... 203
Figure A-D-58. DPW-VI: Grid Convergence; Total Drag C_{D_TOT}, M=0.85: CARDC, Mflow Solver Solutions. 204
Figure A-D-59. DPW-VI: Grid Convergence; Total Drag C_{D_TOT}, M=0.85: Boeing Unstructured Grid Solutions with SA TM. 204
Figure A-D-60. DPW-VI: Grid Convergence; Total Drag C_{D_TOT}, M=0.85: All-Tests Unstructured Grid Solutions with Finite Element Solver. 205
Figure A-D-61. DPW-VI: Grid Convergence; Total Drag C_{D_TOT}, M=0.85: Unstructured Grid Solutions with TAS and EDGE Solvers. 205
Figure A-D-62. DPW-VI WBNP Total Drag Grid Convergence Sensitivity, M=0.85 (Figure S-VII-15). 207
Figure A-D-63. DPW-VI: WBNP Total Drag Grid Convergence Sensitivity, M=0.85: TM. 207
Figure A-D-64. DPW-VI: WBNP Total Drag Grid Convergence Sensitivity, M=0.85: Ordered by Sensitivity; Grid. 208
Figure A-D-65. DPW-VI: WBNP Total Drag Grid Convergence Sensitivity, M=0.85: Ordered by Delta Drag; Grid. 208
Figure A-D-66. DPW-VI: WBNP Total Drag Grid Convergence Sensitivity, M=0.85: Ordered by Sensitivity; TM. 209
Figure A-D-67. DPW-VI: WBNP Total Drag Grid Convergence Sensitivity, M=0.85: Ordered by Delta Drag; TM. 209
Figure A-D-68. DPW-VI: WBNP Grid Convergence; Total, Pressure, and Skin Friction Drag, M=0.85: All Solutions 210
Figure A-D-69. DPW-VI: WBNP Grid Convergence; Total Drag, M=0.85: All Solutions. 210
Figure A-D-70. DPW-VI: WBNP Grid Convergence; Total Drag, M=0.85: All Solutions Parsed by Grid Type and Turbulence Model 211
Figure A-D-71. DPW-VI: WBNP Grid Convergence; Total Drag, M=0.85: Overset Grid Solutions..... 211
Figure A-D-72. DPW-VI: WBNP Grid Convergence; Total Drag, M=0.85: Multiblock Structured Grid Solutions 212

Figure A-D-73. DPW-VI: WBNP Grid Convergence; Total Drag, M=0.85: Geolab Unstructured Grid Solutions.....212
Figure A-D-74. DPW-VI: WBNP Grid Convergence; Total Drag, M=0.85: Boeing Unstructured Grid Solutions.....213
Figure A-D-75. DPW-VI: WBNP Grid Convergence; Total Drag, M=0.85: Custom Unstructured Grid Solutions.....213
Figure A-D-76. DPW-VI: WBNP Grid Convergence; Total Drag, M=0.85: Cartesian/Oct-tree Grid Solutions.....214
Figure A-D-77. DPW-VI: WBNP Drag Increment Grid Convergence Sensitivity, M=0.85. (Figure S-VII-18).....215
Figure A-D-78. DPW-VI: Impact of Grid Drag Convergence Slope on Drag Increment, M=0.85 (Figure S-VII-18).....215
Figure A-D-79. DPW-VI: WBNP Drag Increment Grid Convergence Sensitivity, M=0.85: Ordered by Drag Increment.....216
Figure A-D-80. DPW-VI: WBNP Drag Increment Grid Convergence Sensitivity, M=0.85: Ordered by Drag Sensitivity; Grid.....216
Figure A-D-81. DPW-VI: WBNP Drag Increment Grid Convergence Sensitivity, M=0.85: Ordered by Drag Increment; TM.....217
Figure A-D-82. DPW-VI: WBNP Drag Increment Grid Convergence Sensitivity, M=0.85: Ordered by Drag Sensitivity; TM.....217
Figure A-D-83. DPW-VI: WBNP Grid Convergence; Drag Increment Compared to Test, M=0.85: All Solutions Parsed by Grid Type and Turbulence Model.....218
Figure A-E-1. DPW-IV: Lift and Pitching Moment, M=0.85; All Solutions.....219
Figure A-E-2. DPW-IV: Lift and Pitching Moment; Structured Grid Solutions, M=0.85 (See Figure A-E-8 for Pseudo WT).....220
Figure A-E-3. DPW-IV: Lift and Pitching Moment; Unstructured Grid Solutions, M=0.85 (See Figure A-E-8 for Pseudo WT).....220
Figure A-E-4. DPW-IV: Lift; Structured and Unstructured Grid Solutions, M=0.85. 221
Figure A-E-5. DPW-IV: Pitching Moment; Structured and Unstructured Grid Solutions, M=0.85.....221
Figure A-E-6. DPW-IV: Drag Polar; All Solutions, M=0.85.....222
Figure A-E-7. DPW-IV: “Profile” Drag Polar; All Solutions, M=0.85.....222
Figure A-E-8. DPW-V: “Pseudo” Wind Tunnel Test Data.....223
Figure A-E-9. DPW-V: Lift and Pitching Moment; All Solutions, M=0.85.....224
Figure A-E-10. DPW-V: Lift and Pitching Moment; All Unstructured Grid Solutions, M=0.85. 224
Figure A-E-11. DPW-V: Lift and Pitching Moment; All Structured Grid Solutions, M=0.85. 225
Figure A-E-12. DPW-V: “Profile” Drag Polar; All Solutions, M=0.85. 225
Figure A-E-13. DPW-V: Overset and Multiblock Grid Solutions, M=0.85. 226
Figure A-E-14. DPW-V: Hex and Hybrid Unstructured Grid Solutions, M=0.85. 226
Figure A-E-15. DPW-V: Prism and Custom Unstructured Grid Solutions, M=0.85.....227
Figure A-E-16. DPW-V: Lift and Pitching Moment, M=0.85; Solutions with Lift Break AoA = 3.0° or Lower. 227
Figure A-E-17. DPW-V: Lift and Pitching Moment, M=0.85; Solutions with Lift Break between AoA = 3.25° to 3.50°.....228
Figure A-E-18. DPW-V: Lift and Pitching Moment; Solutions with Lift Break, M=0.85, AoA = 3.75°…228
Figure A-E-19. DPW-V: Lift and Pitching Moment, M=0.85; DLR TAU Solver Results.....229
Figure A-E-20. DPW-V: Lift and Pitching Moment, M=0.85; Embraer CFD++ Solver with SST Results. 229
Figure A-E-20. DPW-V: Lift and Pitching Moment, M=0.85; FOI EDGE Solver Results.....230
Figure A-E-21. DPW-V: Lift and Pitching Moment, M=0.85; Gulfstream FUN3D and USM3D Solver Results.....230
Figure A-E-22. DPW-V: Lift and Pitching Moment, M=0.85; JAXA FaSTAR and UPACS Solver Results. 231
Figure A-E-23. DPW-V: Lift and Pitching Moment, M=0.85; NASA OVERFLOW, FUN3D, and CFL3D Solver Results.....232
Figure A-E-24. DPW-V: Lift and Pitching Moment, M=0.85; Unstructured Custom Grid Solutions. 232
Figure A-E-25. DPW-V: “Profile” Drag Polar, M=0.85; Unstructured Custom Grid Solutions.....233

Figure A-E-26. DPW-V: Lift and Pitching Moment, M=0.85; Unstructured Hex Grid Solutions. 233
Figure A-E-27. DPW-V: "Profile" Drag Polar, M=0.85; Unstructured Hex Grid Solutions. 234
Figure A-E-28. DPW-V: Lift and Pitching Moment, M=0.85; Unstructured Hybrid Grid Solutions..... 234
Figure A-E-29. DPW-V: "Profile" Drag Polar, M=0.85; Unstructured Hybrid Grid Solutions. 235
Figure A-E-30. DPW-V: Lift and Pitching Moment, M=0.85; Unstructured Prism Grid Solutions. 235
Figure A-E-31. DPW-V: "Profile" Drag Polar, M=0.85; Unstructured Prism Grid Solutions..... 236
Figure A-E-32. DPW-V: Lift and Pitching Moment, M=0.85; Structured OVERFLOW Grid Solutions. . 236
Figure A-E-33. DPW-V: "Profile" Drag Polar, M=0.85; Structured OVERFLOW Grid Solutions. 237
Figure A-E-34. DPW-V: Lift and Pitching Moment, M=0.85; Structured Multiblock Grid Solutions. 237
Figure A-E-35. DPW-V: "Profile" Drag Polar, M=0.85; Structured Multiblock Grid Solutions..... 238
Figure A-E-36. DPW-V: Lift and Wing Pressure Distributions, M=0.85: Selected SA Turbulence Model Solutions AoA = 4.0°. 238
Figure A-E-37. DPW-V: Lift and Wing Pressure Distributions, M=0.85: Selected SST Turbulence Model Solutions AoA = 4.0°. 239
Figure A-E-38. DPW-V: Pitching Moment and Wing Pressure Distributions, M=0.85: Selected SST Turbulence Model Solutions AoA = 4.0°. 239
Figure A-E-39. DPW-V: Lift and Wing Pressure Distributions, M=0.85: Selected Turbulence Model Solutions: AoA = 4.0°. 240
Figure A-E-40. DPW-V: Lift and Wing Pressure Distributions, M=0.85: Selected Turbulence Model Solutions: AoA = 3.5°. 240
Figure A-E-41. DPW-V: Lift and Wing Pressure Distributions, M=0.85: Selected Turbulence Model Solutions: AoA = 3.0 241
Figure A-E-42. DPW-V: Lift and Pitching Moment, M=0.85; All Solutions minus Outliers 241
Figure A-E-43. DPW-V: "Profile" Drag Polar, M=0.85: All Solutions minus Outliers. 242
Figure A-E-44. DPW-V: Wing Pressure Distributions, M=0.85: Selected HEX Unstructured Grid Solutions: AoA = 4.0°. 242
Figure A-E-45. DPW-V: Wing Pressure Distributions, M=0.85: Selected HEX Unstructured Grid Solutions: AoA = 3.5°. 243
Figure A-E-46. DPW-V: Wing Pressure Distributions, M=0.85: Selected HEX Unstructured Grid Solutions: AoA = 3.0°. 243
Figure A-E-47. Static Aeroelastic Twist Distribution Derived from Wind Tunnel Measurements, M=0.85. 244
Figure A-E-48. Impact of Aeroelastic Deformation on Lift and Moment; M = 0.85, Re = 5 Million. 244
Figure A-E-49. Impact of Aeroelastic Deformation on "Profile" Drag Polar; M = 0.85, Re = 5 Million... 245
Figure A-E-50. DPW-VI: Lift and Pitching Moment, M=0.85; All Solutions. 245
Figure A-E-51. DPW-VI: "Idealized Profile" Drag Polar, M=0.85; All Solutions. 246
Figure A-E-52. DPW-VI: Lift and Pitching Moment, M=0.85; All Structured Grid Solutions. 246
Figure A-E-53. DPW-VI: Lift and Pitching Moment, M=0.85; All Unstructured Grid Solutions. 247
Figure A-E-54. DPW-VI: Forces and Moments, M=0.85; Boeing Unstructured and Custom Cartesian Grids. 247
Figure A-E-55. DPW-VI: Forces and Moments, M=0.85; Geolab and Custom Unstructured Grids. 248
Figure A-E-56. DPW-VI: Forces and Moments, M=0.85; Overset and Multiblock Grids. 248
Figure A-E-57. DPW-VI: Solution Outliers, M=0.85. 249
Figure A-E-58. DPW-VI: Solutions minus Outliers Parsed by Grid and Turbulence Model, M=0.85..... 249
Figure A-E-59. DPW-VI: Multiblock and Cartesian Grid Solutions minus Outliers, M=0.85. 250
Figure A-E-60. DPW-VI: Overset Grid Solutions minus Outliers, M=0.85. 250
Figure A-E-61. DPW-VI: Geolab Unstructured Grid Solutions minus Outliers, M=0.85. 251
Figure A-E-62. DPW-VI: Custom Unstructured Grid Solutions minus Outliers, M=0.85. 251
Figure A-E-63. DPW-VI: Parsed Lift and Pitching Moment Solutions Corrected for USS minus Outliers, M=0.85. 252
Figure A-E-64. DPW-VI: Lift and Pitching Moment Solutions Corrected for USS minus Outliers, M=0.85. 252
Figure A-E-65. DPW-VI: "Profile" Drag Solutions Corrected for USS minus Outliers, M=0.85. 253
Figure A-E-66. DPW-VI: Shifted Lift and Pitching Moment Solutions minus Outliers, M=0.85. 253
Figure A-E-67. DPW-VI: Shifted Lift and Pitching Moment Solutions minus Outliers minus Solutions that do not Match Experimental trends, M=0.85. 254

Figure A-E-68. DPW-VI: Shifted Lift and Pitching Moment SA Solutions minus Outliers, M=0.85.....254
Figure A-E-69. DPW-VI: Shifted Lift and Pitching Moment SA-QCR Solutions minus Outliers, M=0.85. 255
Figure A-E-70. DPW-VI: Shifted Lift and Pitching Moment Non-SA Solutions minus Outliers, M=0.85. 255
Figure A-E-71. DPW-VI: Wing Section Lift Coefficient; All Solutions, M=0.85.....256
Figure A-E-72. DPW-VI: Wing Section Pitching Moment Coefficient; All Solutions, M=0.85. 256
Figure A-E-73. DPW-VI: Wing Section Lift and Pitching Moment Coefficient on Outboard Wing, M=0.85; All Solutions.....257
Figure A-F-1. DPW-IV: Pitching Moment, M=0.85: Wing-Body and Wing-Body-Tail iH = –2°, 0°, 2° (Figure S-XI-2). 258
Figure A-F-2. DPW-IV: Pitching Moment Corrected for CFD based Mounting System USS, M=0.85: Wing-Body and Wing-Body-Tail iH = –2°, 0°, 2°.....259
Figure A-F-3. DPW-IV: Pitching Moment Corrected for CFD based Mounting System USS and Aeroelastics, M=0.85: Wing-Body and Wing-Body-Tail iH = –2°, 0°, 2° (Figure S-XI-5).....259
Figure A-F-4. DPW-IV: Pitching Moment Components, M=0.85; Wing-Body-Tail iH = –2° (Figure S-XI-3). 260
Figure A-F-5. DPW-IV: Pitching Moment Components: Boeing CFL3D Solver, M=0.85; Wing-Body-Tail iH = –2°.....261
Figure A-F-6. DPW-IV: Trimmed Drag Polars and iH to Trim, M=0.85 (Figure S-XI-4).....261
Figure A-F-7. DPW-IV: “Corrected” Trimmed Lift and Drag, M=0.85 (Figure S-XI-6).....262
Figure A-F-8. DPW-IV: Tail Drag Increment shown by Grid Type, M=0.85: iH = –2°, 0°, 2°.....262
Figure A-F-9. DPW-IV: Tail Drag Increment shown by Turbulence Model, M=0.85: iH = –2°, 0°, 2°. ...263
Figure A-F-10. DPW-IV: Experimental Stabilizer Effectiveness with CFD based Corrections for Mounting System USS, M=0.85.....263
Figure A-F-11. DPW-IV: Experimental Pitching Moment vs. Stabilizer Angle with CFD based Corrections for Mounting System USS Compared to CFD, M=0.85 (Figure S-XI-7).....264
Figure A-F-12. DPW-IV: Corrected and Rigidized Experimental Stabilizer Effectiveness Compared to CFD at AoA = 2.5° shown by Turbulence Model, M=0.85.....264
Figure A-F-13. DPW-IV: Corrected and Rigidized Experimental Stabilizer Effectiveness Compared to CFD at AoA = 2.5° shown by Grid Type, M=0.85.....265
Figure A-F-14. DPW-IV: Corrected and Rigidized Experimental Stabilizer Effectiveness Compared to CFD at AoA = 3.0° shown by Turbulence Model, M=0.85 (Figure S-XI-9). 265
Figure A-F-15. DPW-IV: Corrected and Rigidized Experimental Stabilizer Effectiveness Compared to CFD at AoA = 3.0° shown by Grid Type, M=0.85 (Figure S-XI-8).....266
Figure A-F-16. DPW-IV: Corrected and Rigidized Experimental Stabilizer Effectiveness Compared to CFD at AoA = 2.5° shown by Turbulence Model, M=0.85 (Note origin set to zero).....266
Figure A-F-17. NTF 197 Test Data for Wing-Body and Wing-Body-Tail iH = –2°, 0°, 2°, M = 0.85. 267
Figure A-F-18. Ames 11-Foot T216 Test Data for Wing-Body and Wing-Body-Tail iH = –2°, 0°, 2°, M = 0.85.....267
Figure A-G-1. DPW-VI: Wing Pressure Distribution; All Solutions; Finest Grid, C_L = 0.50, M = 0.85. ...268
Figure A-G-2. DPW-VI: Wing Pressure Distribution; All Solutions, AoA = 3.0°, M = 0.85.....269
Figure A-G-3. DPW-VI: Wing Pressure Distribution; All Solutions, AoA = 3.5°, M = 0.85.....269
Figure A-G-4. DPW-VI: Wing Pressure Distribution; All Solutions, AoA = 4.0°, M = 0.85.....270
Figure A-G-5. DPW-VI: Wing Pressure Distribution; All Solutions minus Outliers, C_L = 0.50, M = 0.85. 270
Figure A-G-6. DPW-VI: Wing Pressure Distribution; All Solutions minus Outliers, AoA = 3.0°, M = 0.85. 271
Figure A-G-7. DPW-VI: Wing Pressure Distribution; All Solutions minus Outliers, AoA = 3.5°, M = 0.85. 271
Figure A-G-8. DPW-VI: Wing Pressure Distribution; All Solutions minus Outliers, AoA = 4.0°, M = 0.85. 272
Figure A-G-9. DPW-VI: Wing Pressure Distribution; All Solutions minus Outliers, AoA = 2.75°, M = 0.85, Eta = 0.131 to 0.603. 273
Figure A-G-10. DPW-VI: Wing Pressure Distribution; All Solutions minus Outliers, AoA = 2.75°, M = 0.85, Eta = 0.727 to 0.950. 273

Figure A-G-11. DPW-VI: Wing Pressure Distribution; All Solutions minus Outliers, AoA = 3.50°, M = 0.85, Eta = 0.131 to 0.603. 274
Figure A-G-12. DPW-VI: Wing Pressure Distribution; All Solutions minus Outliers, AoA = 3.50°, M = 0.85, Eta = 0.727 to 0.950. 274
Figure A-G-13. DPW-VI: Wing Pressure Distribution; Geolab Unstructured Grid Solutions minus Outliers, AoA = 2.75°, M = 0.85, Eta = 0.131 to 0.603 275
Figure A-G-14. DPW-VI: Wing Pressure Distribution; Geolab Unstructured Grid Solutions minus Outliers, AoA = 2.75°, M = 0.85, Eta = 0.727 to 0.950 275
Figure A-G-15. DPW-VI: Wing Pressure Distribution; Geolab Unstructured Grid Solution minus Outliers, AoA = 3.0°, M = 0.85, Eta = 0.131 to 0.603 276
Figure A-G-16 DPW-VI: Wing Pressure Distribution; Geolab Unstructured Grid Solutions minus Outliers, AoA = 3.0°, M = 0.85, Eta = 0.727 to 0.950 276
Figure A-G-17. DPW-VI: Wing Pressure Distribution; Geolab Unstructured Grid Solutions minus Outliers, AoA = 3.25°, M = 0.85, Eta = 0.131 to 0.603 277
Figure A-G-18. DPW-VI: Wing Pressure Distribution; Geolab Unstructured Grid Solutions minus Outliers, AoA = 3.25°, M = 0.85, Eta = 0.727 to 0.950 277
Figure A-G-19. DPW-VI: Wing Pressure Distribution; Geolab Unstructured Grid Solutions minus Outliers, AoA = 3.50°, M = 0.85, Eta = 0.131 to 0.603 278
Figure A-G-20. DPW-VI: Wing Pressure Distribution; Geolab Unstructured Grid Solutions minus Outliers, AoA = 3.50°, M = 0.85, Eta = 0.727 to 0.950 278
Figure A-G-21. DPW-VI: Wing Pressure Distribution; Geolab Unstructured Grid Solution minus Outliers, AoA = 3.75°, M = 0.85, Eta = 0.131 to 0.603 279
Figure A-G-22. DPW-VI: Wing Pressure Distribution; Geolab Unstructured Grid Solutions minus Outliers, AoA = 3.75°, M = 0.85, Eta = 0.727 to 0.950 279
Figure A-G-23. DPW-VI: Wing Pressure Distribution; Geolab Unstructured Grid Solutions minus Outliers, AoA = 4.0°, M = 0.85, Eta = 0.131 to 0.603 280
Figure A-G-24. DPW-VI: Wing Pressure Distribution; Geolab Unstructured Grid Solutions minus Outliers, AoA = 4.0°, M = 0.85, Eta = 0.727 to 0.950 280
Figure A-G-25. DPW-VI: Wing Pressure Distribution; Matched “Selected” Solutions minus Outliers, AoA = 3.0°, M = 0.85. 281
Figure A-G-26. DPW-VI: Wing Pressure Distribution; Matched “Selected” Solutions minus Outliers, AoA = 3.5°, M = 0.85. 281
Figure A-G-27. DPW-VI: Wing Pressure Distribution; Matched “Selected” Solutions minus Outliers, AoA = 3.75°, M = 0.85 282
Figure A-G-28. DPW-VI: Wing Pressure Distribution; Matched “Selected” Solutions minus Outliers, AoA = 4.0°, M = 0.85. 282
Figure A-G-29. DPW-V: Wing Pressure Distribution; All Solutions Medium Grid, C_L = 0.50, M = 0.85. 283
Figure A-G-30. DPW-V: Wing Pressure Distribution; All Solutions, Grid Refinement, Eta = 0.502, C_L = 0.50, M = 0.85. 284
Figure A-G-31. DPW-V: Wing Pressure Distribution; All Solutions, Medium Grid, Eta = 0.502, AoA Sweep = 2.75° to 4.0°, M = 0.85. 284
Figure A-G-32. DPW-V: Wing Pressure Distribution; Embraer Solutions with SST, AoA = 2.5° M = 0.85 285
Figure A-G-33. DPW-V: Wing Pressure Distribution; Embraer Solutions with SST, AoA = 3.5°, M = 0.85. 285
Figure A-G-34. DPW-V: Wing Pressure Distribution; Embraer Solutions with SST, AoA = 4.0°, M = 0.85. 286
Figure A-G-35. DPW-V: Wing Pressure Distribution; 3 Solutions with SA, Different Grids, AoA = 4.0°, M = 0.85. 286
Figure A-G-36. DPW-IV: Wing Pressure Distribution; Grid Convergence, Eta=0.131, C_L=0.50, M = 0.85. 287
Figure A-G-37. DPW-IV: Wing Pressure Distribution; Grid Convergence, Eta=0.846, C_L =0.50, M = 0.85. 287
Figure A-G-38. DPW-IV: Wing Pressure Distribution; SA Turbulence Model, C_L =0.50, M = 0.85. 288
Figure A-G-39. DPW-IV: Wing Pressure Distribution; SA Turbulence Model, Aft loading at Eta=131, Shock location at Eta=0.846, C_L =0.50, M = 0.85. 288

Table of Tables

Table S-I 1 Drag Prediction Workshop 7
Table S-II-1. Reference Quantities for the CRM (Full Scale).....12
Table S-III-1. Corrections for Aeroelastic Twist and USS, ...17
Table S-VI-1. DPW-IV Submissions and Participant Data Key. 25
Table S-VI-1. (Concluded) DPW-IV Submissions and Participant Data Key. 26
Table S-VI-2. DPW-V Submissions and Participant Data Key 26
Table S-VI-2. (Concluded) DPW-V Submissions and Participant Data Key.....27
Table S-VI-3. DPW-VI Submissions and Participant Data Key. 27
Table S-VI-3. (Concluded) DPW-VI Submissions and Participant Data Key. 28
Table S-XIII-1. Aerostructural Analysis Participants.....96
Table S-XIII-2. Overview of Aerostructural Simulation Methods Used in DPW-VI.....96
Table S-XV-1. DPW-V: Detailed Side-of-Body Separation by Participant.....103
Table S-XV-2. DPW-VI: Detailed Side-of-Body Separation by Participant. 104
Table S-XV-1. DPW-VI: Solutions Minus Outliers Comparison to Test Data. 115
Table A-B-1. Gridding guidelines for DPW-IV and DPW-V. 149
Table A-B-2. Gridding Guidelines for DPW-VI. 150
Table A-B-3. DPW-IV CRM Grids: Size in Millions. 151
Table A-B-4 DPW-V Metric Parameters for the Common Grids (Counts in Millions). 153
Table A-B-5. Overset Grid Family Statistics. 156
Table A-B-6. NASA GeoLab Wing-Body Grid Refinement Family Statistics. 156
Table A-B-7. NASA GeoLab Wing-Body-Nacelle-Pylon Grid Refinement Family Statistics. 157
Table A-B-8. NASA GeoLab Wing-Body Aeroelastic Sweep Grid Family Statistics. 157
Table A-B-9. Grid Resolution DLR Solar Grids (GG: Gridding Guidelines). 158
Table A-C-1. DPW-IV Submissions and Participant Data Key. 159
Table A-C-1. (Cont.) DPW-IV Submissions and Participant Data Key. 160
Table A-C-2. DPW-V Submissions and Participant Data Key. 160
Table A-C-2. (Cont.) DPW-V Submissions and Participant Data Key.....161
Table A-C-3. DPW-VI Submissions and Participant Data Key. 162
Table A-C-3. (Cont.) DPW-VI Submissions and Participant Data Key. 163
Table A-C-4. DPW-IV Participants and Data Set Characteristics-Convergence Slope and Drag in the Continuum: Wing-Body-Tail.....164
Table A-C-5. DPW-V Participants and Data Set Characteristics-Convergence Slope and Drag in the Continuum: Wing-Body (As-Built).....165
Table A-C-6. DPW-VI Participants and Data Set Characteristics-Convergence Slope and Drag in the Continuum: Wing-Body (Aeroelastic). 166
Table A-C-7. DPW6 Participants and Data Set Characteristics-Convergence Slope and Drag in the Continuum: Wing-Body-Nacelle-Pylon (Aeroelastic). 167
Table A-C-8. DPW5: Participants Detail on Side-of-Body Separation. 168
Table A-C-9. DPW6: Participants Detail on Side-of-Body Separation. 169
Table A-C-10. DPW6: Solutions minus Outliers Comparison to Test Data. 170
Table A-D-1. DPW-IV Participants and Data Set Characteristics; Wing-Body-Tail. 172
Table A-D-2. DPW-V Participants and Data Set Characteristics: Wing-Body (As-Built). 182
Table A-D-3. DPW-VI Participants and Data Set Characteristics: Wing-Body (Aeroelastic).....192
Table A-D-4. DPW6 Participants and Data Set Characteristics: Wing-Body-Nacelle-Pylon (Aeroelastic). 206

Executive Summary and Recommendations

The six Drag Prediction Workshops (DPW) have drawn a total of 125 participants submitting 225 data entries. Over half of these occurred in the last three workshops dealing with the NASA Common Research Model (CRM). Participants have ranged from North America, Europe, Asia, and South America, representing Government, Industry, Academia, and Commercial/Vendors. The DPW Series has generated a tremendous amount of CFD data, freely available to the public domain. A continuous improvement of the results as measured by: the reduction of the spread of drag predictions for the specified "nominal" cruise point, accuracy of drag increment, and the angle-of-attack sweep behavior, has been noted. Although it has been difficult separating out the parts and pieces that contribute to errors in CFD drag predictions, part of the improvements over the years can be attributed to grid resolution. The scatter in predicted drag in the continuum has been reduced dramatically from ±50 counts in DPW-I to around ±5 counts for DPW-V and -VI. During the six workshops, the grid size has grown dramatically. The average size of the medium wing-body meshes in DPW-I through DPW-IV have been 3.2, 5.4, 7.8 and 10.9 million, respectively. This represents a growth rate of ~17% per year during the eight years between DPW-I and DPW-IV. For DPW-VI, this number has grown from 25 to 50M points for the various families of grids available. The finest level grids have increased steadily, from just over 3 million grid points in DPW-I to 225 million for the WBNP in DPW-VI. While progress has been made, persistent problems with grid generation and separated flow prediction continue. The experiences and recommendations presented here are consistent with those espoused in the "CFD Vision 2030 Study: A Path to Revolutionary Computational Aerosciences," NASA/CR-2014-218178.

Results from grid/convergence studies are clearly dependent on the combination of solver, grid, turbulence model, etc. Same solver and turbulence model on different grid families show different grid convergent rates and force and moment values in the continuum (infinite grid size). Same solver and grid but different turbulence model can also show very different convergence rates, and values in the continuum. No determination can be made as to which combination of solver, grid, and turbulence model produces the "best" drag, only which do not.

Of significant importance to industry design processes is the prediction of the drag increment between two similar configurations. A well-crafted wind tunnel campaign can yield very accurate drag increments. CFD also can and does do a very credible job at calculating drag increments if done carefully. The CFD drag increment predictions between the Wing-Body and the Wing-Body-Nacelle-Pylon configurations in DPW-VI were within or very close to the experimental values for many cases. Most (24 out of 36) solution pairs submitted yielded drag increments calculated in the continuum within the experimental 1-sigma tolerance. But only 8 out of those 36 solution pairs yielded increments within the experimental 1-sigma tolerance by just differencing the medium grid results (which is the most common practice). Those 8 solution pairs were all characterized by a low drag/grid convergence (dCDT/dGRIDFAC) rate; that is a small change in drag over a range of grid sizes.

Angle-of-attack sweeps resulted in many outliers due to premature side-of-body separation seen in over half the submitted solutions. While we now know of some "fixes", we do not know the reason for the sensitivity of premature side-of-body separation to solver, turbulence model, and grid, nor the implications this might have for other geometries, and/or, flow conditions. The CFD solutions minus the outliers show an increasing spread of lift and pitching moment with increasing angle of attack. This appears to be largely due to predicted shock location on the wing. An examination of CFD results revealed only 5 solutions (two turbulence models) that matched the experimental variation with angle of attack out of 41 data sets submitted. Turbulence models appeared to be the biggest discriminator between the five solutions that matched the test data well, and those that did not.

One-of-a-kind CFD studies of drag rise, Reynolds number increments, stabilizer effectiveness, and coupled aerostructural modeling did relatively well compared to test data.

Grid generation is easy; good consistent grid generation has proven not to be. Even with extensive experience, the DPW community struggled to deliver good consistent grid families in every workshop on a relatively simple configuration. All too often solution differences could be attributed to grids. Transonic and separated flow solutions are very sensitive to grid details. Solution adaptive grids can be generated without need for best-practice guidelines, and hence utilized in applications where historical data may not be available. They may also yield more consistent and superior results for cases blessed with a large body of experience. Having adequate gridding in the right places reduces uncertainty in the analysis. It is expected that combining an output-based error-estimate that is optimized for the analysis along with adaptive meshing will provide significant advantages in grid convergence and solution accuracy. Much work remains to be done to bring this technology to a "production" capability for 3D RANS. This is a technology that must be matured.

There is a certain stagnation of CFD development due to the lack of experimental data in the public domain (and maybe even privately held). CFD can do a very credible job in the attached flow regime as demonstrated in DPW. It is in the expansion of the flight envelope, where significant flow separation is present, that significant issues arise. CFD is just not cutting it in these flow regimes as evidenced by the extensive "extra" flight testing that every new configuration undergoes in dealing with unexpected flow related problems. Detailed experimental data, beyond simple force and moment, and pressure distribution, is needed to guide the further development of CFD technology.

Getting new CFD technology into the product is a long and arduous task. Not only is significant progress needed in CFD development to deal with issues of adaptive grid generation, separated and unsteady flows, etc., but a substantial level of "validation" is also needed to assess their worth. Individual groups will do their own assessment to determine if the new CFD technology is "good-enough" for their proprietary engineering processes. But first, they must be given the confidence that the new technology is worth the time, money, and effort to carry out those evaluations. Findings are likely to remain proprietary. An open forum with an agglomeration of comparisons at multiple conditions, code-to-code comparisons, an understanding of the wind tunnel corrections, etc., leads to a better understanding of the CFD progress and needs, and spurs further development. The Drag Prediction Workshop has helped to give us a view of new technologies, affirming the practices that have done well, and hopefully a wake-up call for those practices that have not. These open forum workshops provide an avenue for needed government labs and academia involvement and must continue.

The following specific recommendations are made for further action:

1. A new CFD study of the CRM wind tunnel mounting system effects is needed. This study should be based on the aeroelastically deflected geometries created for DPW-VI and include the effects on the CRM Wing-Body, Wing-Body-Tail, and Wing-Body-Nacelle-Pylon configurations. This will provide a better basis for using CRM wind tunnel data in future validation studies.

2. The 20 million Reynolds number data from the NTF are significantly different from that from ETW and CFD. More research should be done to better understand the consistency and accuracy of both the computational and experimental data.

3. CFD pressure distributions around the wing trailing edge with significant aft camber reveal an excessive "aft-loading" compared to test data. This contributes to excessive lift and flap/aileron hinge moments. The lack of modeling the "trip strip" on the wind tunnel model is one suspect for the excess; turbulence modeling is also a possibility. Further CFD studies are needed to resolve this issue.

4. Premature side-of-body separation plagued many of the submitted solutions. While we now know of some "fixes", we do not know the reason for the sensitivity of premature side-of-body separation to solver, turbulence model, and grid, nor the implications this might have for other geometries, and/or, flow conditions. This type of 3D corner flow separation continues to need more attention in turbulence model development and CFD application.

5. CFD solutions over a sweep of angle of attack show an increasing spread of lift and pitching moment. An examination of CFD results revealed only 5 solutions (two turbulence models) that matched the experimental variation with angle of attack. Further CFD studies are needed to better understand this trend, and its implications as to the validity of different turbulence models.

6. Solution adaptive grids will provide significant advantages in grid convergence and solution accuracy, while significantly reducing the expert human labor currently required for grid generation. Much work remains to be done to bring this technology to a "production" capability for 3D RANS. This is a technology that must be matured.

7. The Lattice-Boltzmann Method (LBM) provides an alternative technology that might overcome many of the limitations of the current classical finite volume/finite element methods dealing with grid generation and separated and unsteady flows. Initial results presented in DPW-VI were encouraging, but extensive verification/validation will be necessary to prove its worth. This is a technology that must be watched.

8. Further detailed experimental measurements that adequately capture the flow separation and unsteadiness on these types of configurations at "off-design" conditions are needed. NASA, DLR, ONERA, JAXA, and other organizations/groups have ongoing research programs that address fundamental questions related to turbulence models, unsteady flows, etc. The NASA Juncture Flow Model test is of this type. A working group should be convened to define experimental needs, identify existing relevant data, ongoing research programs, and better openly disseminate this type of fundamental information.

9. DPW has highlighted CFD and experimental issues dealing with "off-design" conditions involving significant separation and unsteady flows. An open forum with an agglomeration of comparisons at multiple conditions, code-to-code comparisons, an understanding of the wind tunnel corrections, etc., leads to a better understanding of the CFD progress and needs. A new workshop addressing these needs must be organized.

The Drag Prediction Workshop series is coming to an end. The tremendous amount of CFD data collected (and available) coupled with the public domain wind tunnel data should spawn further studies beyond what has been covered in this report, and by these past workshops. It is hoped that this vast openly available set of CFD and related experimental data can serve as a catalyst for further work. This should be of particular value to the academic community, which frequently has not had access to quality industry relevant data. The CFD and experimental issues highlighted by this workshop series are still there and in need of further resolution. This is particularly so for the "off-design" conditions involving significant separation and unsteady flows. Hopefully, a new Workshop addressing these needs will be organized.

Nomenclature

AIAA	American Institute of Aeronautics and Astronautics
AR	Wing Aspect Ratio
b	Wing Span
BL	Butt Line Coordinate (y)
C_D	Drag Coefficient (CD_TOT)
C_{DP}	Idealized Profile Drag = $C_D - C_L^2/\pi AR$
C_{Dpr}	Pressure Drag Coefficient (CD_PR)
C_{Dsf}	Skin-Friction Drag Coefficient (CD_SF)
C_L	Lift Coefficient (CL)
C_{Ls}	Section Lift Coefficient
C_m	Pitching Moment Coefficient (CM, CM_TOT)
C_{ms}	Section Pitching Moment Coefficient
C_P	Pressure Coefficient (CP) = $(P-P_\infty)/q_\infty$
c_{ref}	Wing Reference Chord ~ MAC
C_f	Local Coefficient of Skin Friction
CFD	Computational Fluid Dynamics
CFL	Courant–Friedrichs–Lewy (CFL) condition
count	drag count (0.0001)
CRM	Common Research Model
dCDT/dGRIDFAC	drag/grid convergence slope
DLR	DLR Institute of Aerodynamics and Flow Technology
DPW	Drag Prediction Workshop
EPIC	Edge Primitive Insertion Collapse
ETW	European Transonic Wind Tunnel Facility
FSI	Fluid-Structure Interaction
GRIDFAC	$GRIDSIZE^{-2}$
iH	Horizontal Tail Incidence
LBM	Lattice-Boltzmann Method
MAC	Mean Aerodynamic Chord
MB	Multiblock (grid)
N	Number of solution points (GRIDSIZE)
NTF	National Transonic Facility
p	pressure
q_∞	dynamic pressure = $\frac{1}{2}\ \rho V^2$
QCR	Quadratic Constitutive Relation
RANS	Reynolds-Averaged Navier-Stokes
Re_c	Chord Reynolds Number
S_{ref}	Reference Area
S_{trap}	Trapezoidal Wing Area
SFW	Subsonic Fixed Wing
SOB	Side-of-Body
SUPG	Streamline/Upwind Petrov-Galerkin finite element method
TWG	Aerodynamics Technical Working Group (TWG)
UN	Unstructured (grid)
USS	Upper-Swept Strut (mounting system)
V	Velocity
WB	Wing-Body
WBL	Wing Butt Line Coordinate
WBNP	Wing-Body-Nacelle-Pylon
WBT	Wing-Body-Tail
w	Wing Section Bending Deflection (ω)
x/c	Wing Chord Fraction
y^+	Normalized Wall Distance

α	Angle of attack (AoA, alpha), degrees
δ	difference, also used as solution identifier
Δ	Difference
ε	Wing Section Twist Deflection
η	Fraction of Wing Semi-Span; eta
$\Lambda_{c/4}$	Quarter Chord Sweep
λ	Wing Taper Ratio
ρ	density

Section I: Introduction and DPW history

This study is based on the NASA Common Research Model (CRM) analysis from the American Institute of Aeronautics and Astronautics (AIAA) Drag Prediction Workshop (DPW) series. This report will primarily delve into the computational data reported during the last three Drag Prediction Workshops that dealt with the Common Research Model. Comparisons with wind tunnel data from the National Transonic Facility (NTF), the Ames 11-foot Transonic Wind Tunnel Facility, and the European Transonic Wind Tunnel Facility (ETW) will guide the evaluation of some of these results. By looking at CRM related data across the three workshops, related results reported in the literature, and new analysis, there is hope to provide a more complete picture of the state of computational analysis than was possible from a single workshop. In order to provide a better context of this study, a history of the AIAA Drag Prediction Workshop series is provided.

The AIAA Computational Fluid Dynamics (CFD) Drag Prediction Workshop Series was initiated by a working group of members from the Applied Aerodynamics Technical Committee of the AIAA. The primary goal of the workshop series was to assess the state-of-the-art of modern computational fluid dynamics methods using geometries and conditions relevant to commercial aircraft. From the onset, the DPW organizing committee has adhered to a primary set of guidelines and objectives for the DPW series:

- Assess state-of-the-art CFD methods as practical aerodynamic tools for the prediction of forces and moments on industry-relevant geometries, with a focus on absolute drag
- Provide an impartial international forum for evaluating the effectiveness of CFD Navier-Stokes solvers
- Promote balanced participation across academia, government labs, and industry
- Use common public-domain subject geometries, simple enough to permit high-fidelity computations
- Provide baseline grids to encourage participation and help reduce variability of CFD results
- Openly discuss and identify areas needing additional research and development
- Conduct rigorous statistical analyses of CFD results to establish confidence levels in predictions
- Schedule open-forum sessions to further engage interaction among all interested parties
- Maintain a public-domain accessible database of geometries, grids, and results
- Document workshop findings; disseminate this information through publications and presentations

Six workshops have been held prior to this present study, all held in conjunction with the AIAA Applied Aerodynamics Conference for that year.

Table S-I 1 Drag Prediction Workshop.

Year	Location	Configuration	Case Descriptions
2001	Anaheim, CA	DLR-F4 Wing-Body	Single Point Drag Prediction Drag Polar Drag Rise Curves at Constant C_L*
2003	Orlando, FL	DLR-F6 Wing-Body Wing-Body-Nacelle	Single Point Grid Convergence Study Drag Polar Boundary Layer Trip Study* Drag Rise Curves at Constant C_L*
2006	San Francisco, CA	DLR-F6 Wing-Body with and without FX2B fairing; W1/W2 Wing Alone	Single Point Grid Convergence Study Drag Polar Grid Convergence Study Drag Polar
2009	San Antonio, TX	NASA Common Research Model Wing-Body and Wing-Body-Tail	Grid Convergence Study Downwash Study Mach Sweep Study* Reynolds Number Study*
2012	New Orleans, LA	NASA Common Research Model Wing-Body 2-D Flat Plate* 2-D Bump-in-channel* 2-D NACA 0012 Airfoil*	Grid Convergence Study Alpha Sweep Buffet Study Turbulence Model Verification*
2016	Washington DC	NASA Common Research Model Wing-Body and Wing-Body-Nacelle-Pylon 2-D NACA 0012 Airfoil	Grid Convergence Study Nacelle-Pylon Drag Increment Study Alpha Sweep Buffet Study Solution Adaption Grid Study* Coupled Aerostructural Analysis Study* Turbulence Model Verification

*Optional Cases

While there have been some variations, the workshops have typically used subjects based on commercial transport Wing-Body configurations—a consensus of the organizing committee based on a reasonable compromise between simplicity and industry relevance. The vast majority of the participants submit results generated with Reynolds Averaged Navier-Stokes (RANS) codes, although the organizing committee does not restrict the methodology.

The first Drag Prediction Workshop [1] used the DLR-F4 geometry for the above reasons and because of the availability of publicly released geometry and wind tunnel results [2]. The focus of the workshop was to compare absolute drag predictions, including the variation due to grid type and turbulence model type. The results were also compared directly to the available wind tunnel data. The workshop committee provided a standard set of multiblock structured, overset, and unstructured grids for the DLR-F4 geometry to encourage participation in the workshop and reduce variability in the CFD results. The average baseline grid size was approximately 2.5 million control volumes. However, participants were also encouraged to construct their own grids using their best practices so that learned knowledge concerning grid generation and drag prediction might be shared among workshop attendees. The test cases were chosen to reflect the interests of industry and included a fixed-C_L single point solution, drag polar, and constant-C_L drag rise data sets. To help encourage wide participation, a formal paper documenting results was not required at the workshop. Eighteen participants submitted results, using 14 different CFD codes; many submitted multiple sets of data exercising different options in their codes, e.g., turbulence models and/or different grids. A summary of these results was documented by the DPW-I organizing committee [3]. Because of strong participation, DPW-I successfully amassed a CFD data set suitable for statistical analysis [4]. However, the results of that analysis were rather disappointing, showing a 270-drag-count (drag count, $C_D = 0.0001$) spread in the fixed-C_L data, with a 100:1 confidence interval of more than ±50 drag counts.

Despite the somewhat disappointing results, the consensus of the participants and organizers was that DPW-I was a definitive success. First and foremost, it was initiated as a "grass roots" effort by CFD developers, researchers, and practitioners to focus on a common problem of interest to the aerospace industry. There was open and honest exchange of common practices and issues that identified areas for further research and scrutiny. The workshop framework was tested successfully on high fidelity 3D RANS methods using a common geometry, grids, and test cases. Finally, it reminded the CFD community that CFD is not a fully mature discipline.

The interest generated from the workshop was continued and resulted in several individual efforts documenting results more formally [5–8], presented at a special session of the 2002 AIAA Aerospace Sciences Meeting and Exhibit in Reno, NV. The interest generated by DPW-I naturally led to the planning and organization of the second AIAA Drag Prediction Workshop, DPW-II. The DPW-II organizing committee, recognizing the success of DPW-I, maintained the format and objectives for DPW-II.

The second workshop [9] used the DLR-F6, shown in Figure S-I-1, as the subject geometry in both wing-body (WB, similar to DLR-F4) and wing-body-nacelle-pylon (WBNP) form. The average WB grid size was about 4.8 million control volumes with a maximum of 10 million for the WB and 13.7 million for the WBNP. The DPW-II organizing committee worked with DLR and ONERA to make pertinent experimental data available to the public domain. One specific objective of DPW-II was the prediction of the incremental drag associated with nacelle/pylon installation. The F6 geometry contained known pockets of flow separation more severe than the F4, occurring predominantly at the wing/body and wing/pylon juncture regions. The results from the workshop were documented with a summary paper [10], a statistical analysis [11], an invited reflections paper [12] on the workshop series, and numerous participant papers [13–21] in two special sessions of the 2004 AIAA Aerospace Sciences Meeting in Reno, NV. A conclusion of DPW-II was that the separated flow regions made it difficult to draw meaningful conclusions with respect to grid convergence and drag prediction. During the follow-up open-forum discussions, the CFD community voiced the desire for the organizing committee to include blind test cases, and simpler geometries in the third workshop. The request for blind test cases is motivated by an earnest attempt to better establish a measure of the CFD community's capability to predict absolute drag, rather than match it after-the-fact. The request for simpler geometries allows more extensive research in studies of asymptotic grid convergence.



Figure S-I-1. DLR-F6 Model in ONERA S2MA Wind Tunnel.

The third workshop [22] retained the DLR-F6 WB from DPW-II as a baseline configuration to provide a bridge to the previous workshop. However, to test the hypothesis that the grid-convergence issues of DPW-II were the direct result of the large pockets of flow separation, a new wing-body fairing was designed to eliminate the side-of-body separation. Details of the FX2B fairing design, shown in Figure S-I-2, are documented by Vassberg [23]. In addition, to help reduce the wing upper-surface trailing-edge flow separation, a higher Reynolds number was introduced for the WB test cases. These changes in both geometry and flow condition also provided the DPW-III participants a blind test since no test data would be available prior to the workshop. A total of 70 grids were provided by 12 participating organizations for the two Wing-Body configurations in a three-member family of coarse, medium, and fine grid levels. The nominal sizes of these grids were 2.7, 8.0, and 24 million control volumes. Furthermore, two wing-alone geometries were created to provide workshop participants with simpler configurations on which more extensive grid-convergence studies could be conducted; these wings were designed to exhibit no appreciable separation at their design conditions. The DPW-III was heavily documented with summary papers [24, 25], a statistical analysis paper [26], participant papers [27–30], and a special section of the AIAA *Journal of Aircraft*, edited by Vassberg [31–36]. After three workshops, the

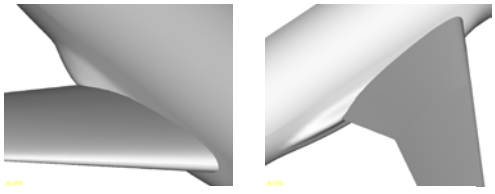


Figure S-I-2. FX2B Wing-Body.

organizing committee recognized that a recurring theme of the workshop series was related to grid quality and resolution (see Mavriplis et al. [37]).

For the fourth workshop [38], a completely new geometry was developed, called the Common Research Model. The NASA Subsonic Fixed Wing (SFW) Aerodynamics Technical Working Group (TWG), in collaboration with the DPW Organizing Committee, developed the CRM. This Wing-Body (with and without nacelle-pylons and horizontal tail) configuration is representative of a contemporary high-performance transonic transport. A detailed description of its development is given by Vassberg et al. [39].

One aspect of DPW-IV that is different from the other workshops was in the timing of the availability of wind-tunnel test data on the subject geometries. In DPW-IV, the workshop was held before any experimental data were collected and is a set of blind tests. Due to past observations of grid dependence on the solutions, a greater emphasis was placed on establishing a comprehensive set of meshing guidelines for the generation of baseline grid families. With these guidelines in place, grids were requested from several organizations for structured multiblock, overset, and unstructured types. Each grid family was required to include a coarse (C), medium (M), and fine (F) grid; adding an optional extra-fine (X) grid was also encouraged. Target sizes for these grids were 3.5, 10, 35, and 100 million mesh (grid) points, respectively. Note that mesh size is not necessarily the same as the number of computed unknown locations. For example, in a tetrahedral unstructured mesh, if the flow solver is cell centered, the number of tetrahedral cells is about six times the number of mesh points. If the unstructured mesh is comprised of a mixture of tetrahedral, prisms, pyramids, and hexahedra, then the relationship between number of cells and number of points varies between one and six, depending on the distribution of each. The DPW Organizing Committee asked each participant to provide the appropriate metric for grid size which is consistent with their flow solver when we plot the grid-convergence trend lines.

The medium mesh was intended to be representative of current engineering applications of CFD being used to estimate absolute drag levels on similar configurations. A total of 74 meshes of 18 families were provided and made available to participants for use.

The fourth workshop requested grid convergence and Mach sweep computations as in the previous workshops, plus downwash and Reynolds Number studies. Data were submitted from 19 organizations totaling 29 individual data sets. For the grid refinement study, a Richardson Extrapolation methodology was employed to estimate a continuum value for the total drag coefficient. Excluding a single outlier, the scatter band for DPW-IV reduces dramatically to 41 counts, which is a definite improvement over DPW-I (with one outlier, the range for the total drag coefficient spanned 152 counts). While this improvement was quite significant, the confidence level was not down to a low enough level to compete with experimental methods. Documentation for these results can be found in summary papers [40, 41] and in individual contributing papers [42–56] from two special sessions held at the 28th Applied Aerodynamics Conference in June 2010.

Despite the emphasis placed on grid generation with the intent of reducing the associated errors, the variation in the DPW-IV results was still disappointing. For the fifth workshop [57], which was held in conjunction with the 30th AIAA Applied Aerodynamics conference in June 2012, a new approach was taken with the goal of reducing grid-related errors even further. As with the fourth workshop, the NASA Common Research Model wing body configuration was used for the geometry (without tail). For the grids, a unified baseline [58] family of multiblock structured meshes was developed with six different levels ranging in size from 0.64×10^6 (tiny) to 136×10^6 (superfine) mesh points. Each successive coarse level was derived directly from the finest mesh. Only five blocks were used. Once the cloud of points was defined for this series of grids, then overset and unstructured grids were derived. The unstructured grids were defined in hexahedral, and prismatic elements, plus a hybrid grid with prismatic boundary layer and tetrahedral field elements was defined.

The test cases included a grid refinement study using the common grids or user-supplied custom grids if desired. The second case focused on buffet prediction, with a finely spaced alpha sweep spanning the range where flow separation on the wing was observed in the wind tunnel data and the results in DPW-IV. This was a change from previous workshops, where angle-of-attack sweeps from 0° to 4° were calculated for the purpose of determining trimmed drag polars. For a commercial transport like the CRM, high-speed lines development is undoubtedly very important, as it would contribute to whether speed and range goals are met. However, it usually comprises less than 25 percent of the total aerodynamics-related airplane development effort. Significant effort must also be paid to loads,

handling qualities, and other constraints that are required to meet structural and certification requirements. Many of these high-speed flight concerns occur at the edges of the flight envelope, which are characterized by large regions of separated flows. For the fifth Drag Prediction Workshop, the buffet study was included to assess CFD prediction in this regime. The optional third test case used geometries, grids, and conditions from the Turbulence Model Resource website [59] prepared by the Turbulence Model Benchmarking Working Group. Three verification cases were selected: (1) 2D Zero Pressure Gradient Flat Plate, (2) 2D Bump-in-channel, and (3) 2D NACA 0012 Airfoil. These test cases were designed to discriminate between turbulence model implementations through rigorous grid convergence studies. Documentation for these results can be found in summary papers [60, 61]and in individual contributing papers [62–70] from two special sessions held at the 51st Aerospace Sciences Meeting, January 2013, the 52nd Aerospace Sciences Meeting, January 2014, and a special collection in the AIAA *Journal of Aircraft* [71].

The Sixth Drag Prediction Workshop [72] was held in conjunction with AIAA Aviation 2016 and included 25 participant teams from 4 continents representing government, industry, academic, and commercial CFD organizations. The workshop again focused on the CRM model and the NACA 0012 airfoil. Five cases were specified. Case 1 featured detailed grid convergence studies for drag and skin friction coefficient for the Turbulence Modeling results based on the NACA 0012 airfoil [73]. Cases 2–5 involved the CRM model. An overview of the computational results, geometry, and grid definitions used for the CRM cases are presented in Ref. 74. For the CRM, four case studies were specified, two of which were optional. The required cases included a grid refinement study using the common grids or user-supplied custom grids for both the Wing-Body and Wing-Body-Nacelle-Pylon configurations (Case 2), and a WB angle-of-attack sweep with a finely spaced alpha sweep spanning the range where flow separation on the wing was observed in the wind tunnel data similar to that in DPW-V (Case 3). New for DPW-VI was the inclusion of the static aeroelastic deformation in the definition of the CRM models for each angle-of-attack/C_L condition specified in the test cases. This makes comparisons to force, moment, and pressure data from the related wind tunnel tests more meaningful in that the geometry of the computational model better represents that of the wind tunnel model at the specified flow condition. The Case 2 grid refinement study consisted of up to seven levels of grid sizes ranging from 7.4 to 225 million control volumes. Richardson extrapolation was used to estimate the continuum force levels and the drag increment between the two configurations. This showed the scatter band of results in the continuum to be further reduced from that seen in previous workshops. Results of a statistical analysis of Case 2 are presented in Ref. 75. Analysis of the Case 3 static aeroelastic/buffet study including force/moment and pressure predictions with comparisons to wind tunnel test data was similar to that seen in DPW-V, but with fewer outliers. Few participants submitted results for the two optional cases: Case 4 grid adaptation, and Case 5 coupled aerostructural simulation. A detailed description of Case 5 results can be found in Ref. 76. Documentation of many of the individual contributing papers can found and a special collection in the AIAA *Journal of Aircraft* [77].

An in-depth look at the results from the last three Drag Prediction Workshops dealing with the CRM will follow.

Section II: Geometry

The subject “airplane” geometry for DPW-IV, -V, and -VI was the CRM [39] developed jointly by the NASA SFW TWG and the DPW Organizing Committee. The CRM represents a modern transonic commercial transport airplane and was designed as a full configuration with a low wing, body, horizontal tail, and engine nacelles mounted below the wing. The Wing-Body configuration was used in all three workshops, the Wing-Body-Nacelle-Pylon was also used in DPW-VI, and a Wing-Body-Tail configuration was used in DPW-IV. The Wing-Body-Tail configuration featured three different tail incidence settings. A rendering of the Wing-Body-Nacelle-Pylon configuration geometry is shown in Figure S-II-1, along with a photo of the 0.027 scale wing-body wind tunnel model (with horizontal tail) installed in the NASA Ames Research Center Unitary Plan Wind Tunnel 11-Foot Transonic Wind Tunnel (Ames). The wing and horizontal planforms are shown in Figure S-II-2. Also shown in this figure are the buttline (WBL) stations along which CFD pressure distributions were requested. Note that 9 of the stations on the wing correspond to stations along which experimental data were gathered.



Figure S-II-1. NASA Common Research Model.

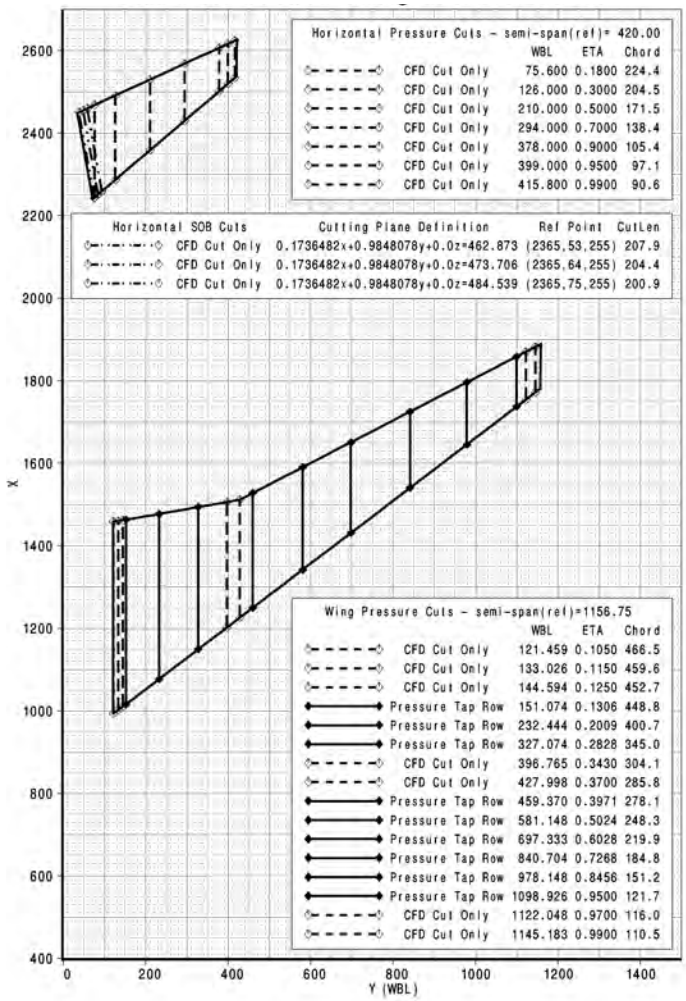


Figure S-II-2. CRM Wing and Horizontal Planform.

The wing was designed for a nominal condition of Mach = 0.85, C_L = 0.50, and Reynolds Number 40 × 10^6 based on c_{ref} which is typical for a full-size commercial transport. Pertinent geometric parameters are listed in Table S-II-1. The Boeing Company took the lead on the aerodynamic design featuring a supercritical wing. Certain features were designed into the wing profile for the purposes of research and development. For example, the upper-surface pressure

recovery over the outboard wing was intentionally made aggressively adverse over the last 10–15 percent local chord. This promotes separation of the upper-surface boundary layer in close proximity to the wing trailing edge at lift conditions slightly above the design point. The strong adverse pressure gradient will likely amplify the differences in various turbulence models that may be employed by DPW participants. Another feature is that the span loading was designed to be very nearly elliptical as compared to a more practical design that would use a compromise distribution (more triangular) to reduce structural loads and decrease airframe weight. This feature was included to provide a challenge for possible future workshops on aerodynamic shape optimization that might explore structure and fuel weight trade-offs.

Table S-II-1. Reference Quantities for the CRM (Full Scale).

Parameter		Units of Measure		Parameter	Units of Measure	
S_{ref}	594,720.0 in^2	= 4,130 ft^2	[458.89 m^2]	x_{ref}	1,325.9 in	[33.68 m]
S_{trap}	576,000.0 in^2	= 4,000 ft^2	[444.44 m^2]	y_{ref}	468.75 in	[11.91 m]
b	2,313.5 in	= 192.8 ft	[58.765 m]	z_{ref}	177.95 in	[4.520 m]
c_{ref}	275.800 in	= 16.07 ft	[4.8978 m]	$\Lambda_{c/4}$	35.0°	
AR	9.0	λ	0.275			

The fuselage is representative of a wide/body commercial transport aircraft; it includes a wing-body fairing, as well as a scrubbing seal for the horizontal tail. The wing-body fairing was designed to provide a fully-attached junction flow at flight Reynolds number. The nacelle is a single-cowl, high bypass-ratio, flow-through design with an exit area sized to achieve a natural unforced mass-flow ratio typical of commercial aircraft engines at cruise. The simplicity of this unbifurcated nacelle geometry will facilitate grid generation efforts of subsequent CFD validation exercises. The horizontal tail was designed for dive Mach number conditions and is suitably sized for typical stability and control requirements.

The wing geometry defined for DPW-IV and -V was intended to represent the shape the wing would deflect to under load at the nominal $M = 0.85$, $C_L = 0.50$, 5 million Reynolds number condition. After the initial wind tunnel tests, which took place between those two workshops, it became apparent that this was not the case. The wing geometry used in those two workshops was the "as-built" geometry. Under the aerodynamic loads in the wind tunnel, the wing deflected to a different shape. New for DPW-VI was the inclusion of the static aeroelastic deformation in the definition of the CRM models for each angle-of-attack/C_L condition specified in the test cases. The wing static aeroelastic bending and twist deflection were derived using a videogrammetry technique in which the position of markers on the wing was optically measured during the test. The bending and twist deflection used to define the geometries for DPW-VI were based on data measured in the ETW test in 2014. While the test results from the ETW test and those from the NASA NTF and 11-foot TWT tests were quite similar, it was decided to use the ETW results. These data were interpolated to the angles of attack required in test cases 2–4 to define the various geometries [78]. Static aeroelastic wing twist for various angles of attack is shown in Figure S-II-3. Note that the resulting aeroelastic twist is small, amounting to only a little over one degree near the wing tip. However, at transonic flow conditions, this small amount of aeroelastic wing twist has a significant effect on the resulting pressure distributions as well as the computed lift, drag, and pitching moments, as shown in Figures S-II-4 and -5 using a representative CFD solver. Figure S-II-4. shows the impact on lift and pitching moment. The aeroelastic deformation reduces the lift and makes the pitching moment more positive as load (angle of attack) is increased. The impact on pressure distribution, shown in Figure S-II-5, is most dominant on the outboard part of the wing. The suction peak (rooftop) is reduced and the shock moves forward, reducing the section lift. Inclusion of the aeroelastic deformation makes comparisons to force, moment, and pressure data from the related wind tunnel tests more meaningful in that the geometry of the computational model better represents that of the wind tunnel model at the specified flow condition.

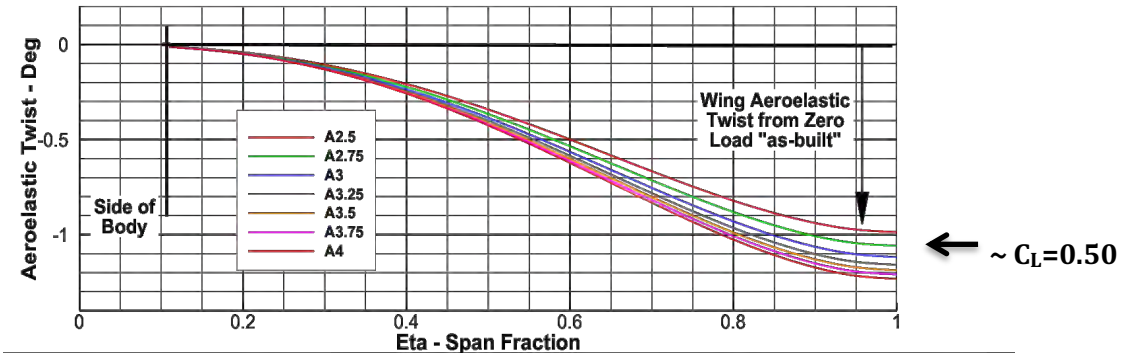


Figure S-II-3. Static Aeroelastic Wing Twist Distribution Derived from Wind Tunnel Measurements.

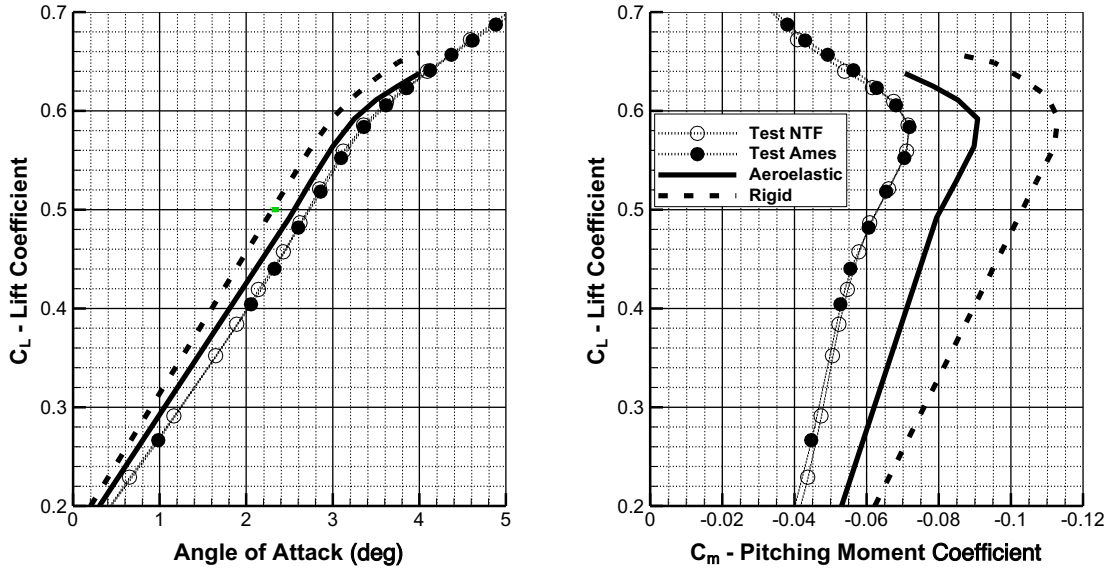


Figure S-II-4. Impact of Aeroelastic Deformation on WB Lift and Moment; M = 0.85, Re_c = 5 Million.

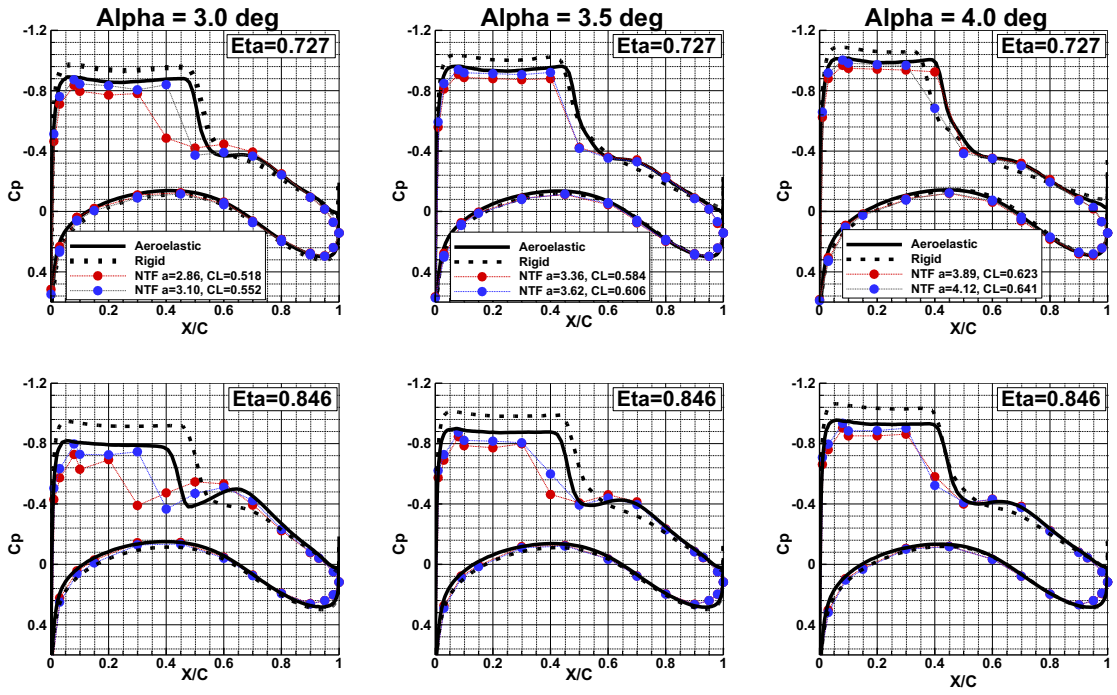


Figure S-II-5. Impact of Aeroelastic Deformation on WB Outboard Wing Pressure Distribution; M = 0.85, Re_c = 5 Million.

Section III: Experimental Data Description

An advantageous outcome of the collaborative endeavor sponsored by the NASA TWG has been that the CRM has now been tested in several facilities thus far, and the data from several of these tests are now publicly available. The National Transonic Facility at NASA Langley tested the CRM during January and February 2010, followed by a test at the NASA Ames 11-Foot TWT (Unitary Plan Wind Tunnel 11-Foot Transonic Wind Tunnel) during March and April 2010. Data from the Langley and Ames tests have been released to the public domain by Rivers and Dittberner [79,80,81]. The CRM Wing-Body configuration was tested at the European Transonic Wind Tunnel facility in February 2014 [82]. These data have also been released to the public domain [83]. These three tests all used the same physical wind tunnel model. A slightly larger version of the CRM Wing-Body-Tail was more recently built by ONERA and tested in the ONERA S1MA wind tunnel [84]. In 2012, an 80 percent scale model of the NASA CRM built by JAXA was tested in the JAXA 2 × 2 m Transonic Wind Tunnel [85].

A particular discriminator of the DPW-IV relative to the first three workshops was in the timing of the availability of wind-tunnel test data on the subject geometries. In DPW-IV, the workshop was held (and all finalized CFD solution sets were provided) several months before any experimental data were collected. Hence, the totality of this workshop is undeniably a set of blind tests.

In assessing the accuracy of CFD, wind tunnel results are frequently used as the "gold standard." However, even if we had the perfect CFD code, we would not, nor should we, get perfect agreement with wind tunnel results, because the wind tunnel is also imperfect. Each wind tunnel experiment has its own imperfections, which must be understood or at least recognized in order to assess or validate the CFD. Differences in the "test" setup between Wind Tunnel and CFD are well known, and a few are listed below:

Wind Tunnel	CFD
Walls	Free Air
Support System (Sting)	Free Air
Laminar/Turbulent (Tripped @ 10% chord)	"Fully" Turbulent Specified (usually)
Aeroelastic Deformation	Specified Shape
Measurement Uncertainty	Numerical Uncertainty and Error
Corrections for known effects	No Corrections

With this approach, physical experiments are adjusted/corrected to approximate free air conditions and the CFD also simulates free-air conditions. Free-air conditions are conducive to the numerical assessments of DPW. For comparisons with experiment, it is becoming a common practice to simulate more of the test environment with CFD (e.g., support system, static aeroelastics) and incorporate correspondingly less corrections in the data. Support system simulations [86,87] and static aeroelastic deformation effects (DPW-VI) are two examples of this trend.

Clearly there are potentially significant differences between what the wind tunnel and CFD are measuring/computing. Effective CFD assessment requires intimate knowledge of both the CFD and the experimental data being compared. CFD assessment cannot consist of the comparison of the results of one code to those of one experiment. Rather, it is the agglomeration of comparisons at multiple conditions, code-to-code comparisons, an understanding of the wind tunnel corrections, etc., that leads to the understanding of the CFD for use as an engineering tool. The Drag Prediction Workshop series has given us the opportunity to conduct such comparisons and assessments.

Force and moment data from the different wind tunnels for the same model will differ. These differences are mainly due to small flow variations, and the corrections applied to the "raw" measured data to account for wind tunnel walls, mounting system, nonuniform flow (buoyancy, upflow, etc.), Mach blockage, lift interference, etc. Each wind tunnel facility tries very hard to determine the "best" set of corrections to its data to simulate "free air." Both the NTF and the Ames 11-foot wind tunnels use the Transonic Wall Interference Correction System to provide blockage and incidence corrections due to the presence of the test section boundary [80]. A similar process is used to correct the ETW data. For comparison purposes, test data from the NASA 11-Foot TWT (Ames), the NTF, and the ETW tests will be used. The Wing-Body, Wing-Body-Nacelle-Pylon, and the Wing-Body-Tail configurations of the same physical model were tested at Ames and Langley at 5 million chord Reynolds number. The same physical Wing-Body-Tail configuration was tested at both the NTF and ETW at several Reynolds numbers. Figure S-III-1 presents force and moment data from NTF, Ames 11-Foot, and ETW for the CRM Wing-Body-Tail iH = 0 at Mach = 0.85, Reynolds number = 5 million. Other than a shift in drag, the data are almost indistinguishable between the tunnels. Figure S-III-2 shows force and moment data from NTF and ETW at both 5 million and 20 million Reynolds number. The NTF 20 million Reynolds number lift and moment data appear suspect. We would expect that lift would increase and pitching moment become more negative with increasing Reynolds number in this range, just as is seen for the ETW data. The NTF data do not show this behavior. Both NTF and ETW drag data decrease, but by different amounts. These data will be compared to CFD results from DPW-IV. Perhaps CFD will shed light on the Reynolds number effect in Section VIII Reynolds Number Study.

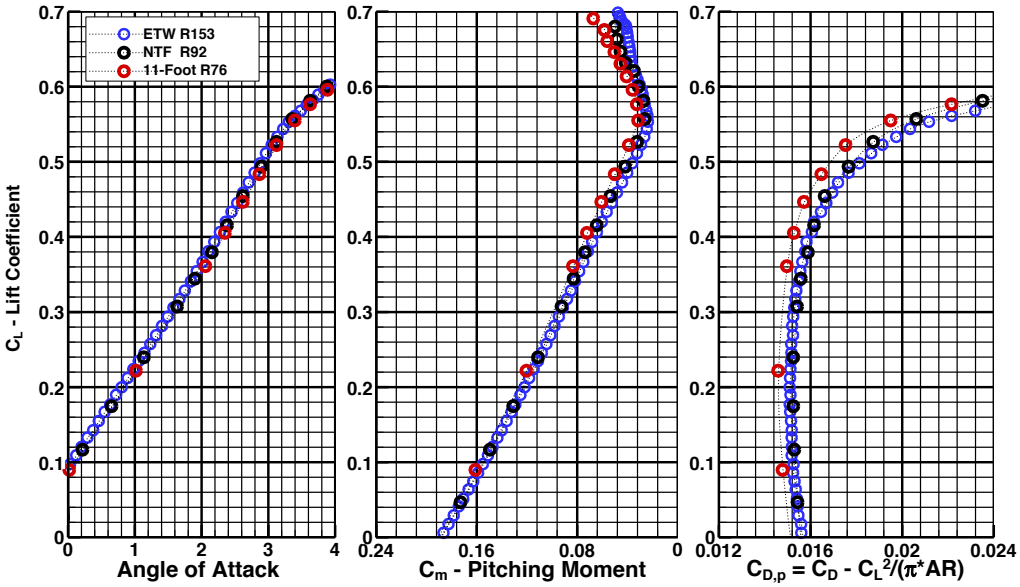


Figure S-III-1. WBT Forces and Moments from NTF, Ames, and ETW Wind Tunnels; M = 0.85, Re_c = 5 million.

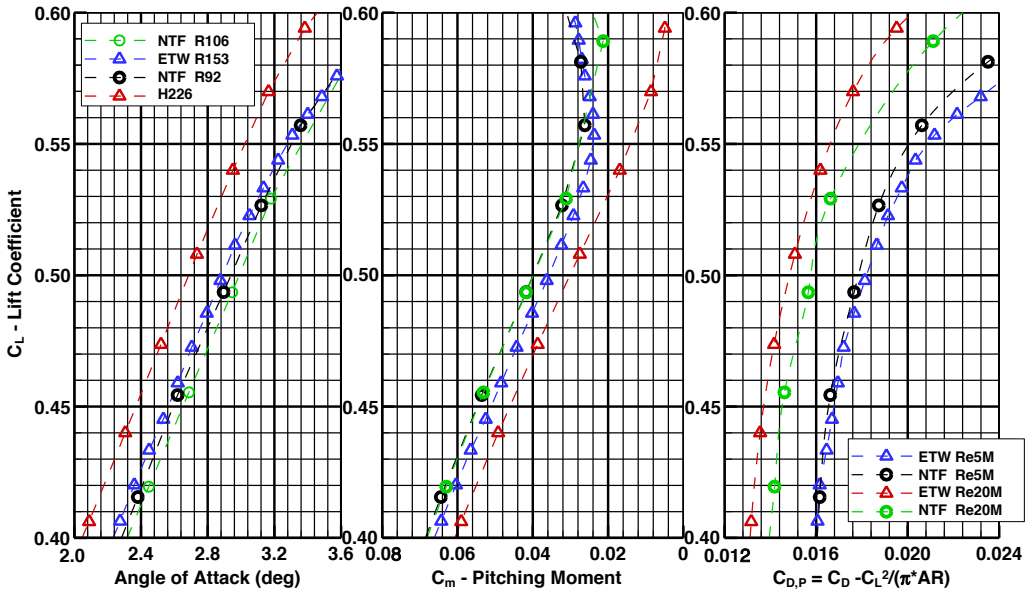


Figure S-III-2. WBT Forces and Moments from NTF and ETW Wind Tunnels; M = 0.85, Re_c = 5 and 20 million.

Wind tunnel test data typically do not include detailed mounting system corrections beyond the classical corrections already mentioned. These additional corrections require an additional set of alternate mounting techniques to determine. Alternate mounting techniques were not performed on the CRM. Computational studies by Rivers, Hunter, and Campbell [86,87] and discussion by Pfeiffer [12] illustrate the magnitude of the mounting system influence on the CRM Wing-Body-Tail configuration. In the NTF, Ames 11-foot, and ETW wind-tunnel tests, the CRM model is supported by an upper-swept strut/sting combination (USS). The upper-swept strut (blade) resembles a vertical fin. The presence of this mounting system primarily affects the flow over the aft end of the fuselage, which

can significantly affect the absolute value of pitching moment, drag level, and lift to some extent. This is particularly true when the model includes a horizontal tail. The blade-sting induces a downward flow on the horizontal, which increases the nose-up pitching moment. Furthermore, an increase in downwash affects the drag of a lifting tail. The presence of the USS also applies a buoyancy to the model thereby reducing its drag.

A set of "nominal" corrections to add to the CFD results to account for the lack of static aeroelastic deformation in the DPW-IV and -V models, and the lack of upper-swept strut in all sets of three workshop results was recently developed by this author to support further data analyses for this report. These corrections are based on the work of Rivers, Hunter, and Campbell [87]. A "nominal" lift, $\delta C_{L_{AERO}} = -0.0360$, pitching moment, $\delta C_{M_{AERO}} = 0.0300$, and drag, $\delta C_{D_{AERO}} = 0.0$ correction increments can be added to CFD results from DPW-IV and -V to account for the lack of static aeroelastic deformation in the "as-built" computational models. This lift and pitching moment correction applies to both the WB and WBT configurations. "Nominal" lift and pitching moment increments ($\delta C_{L_{WBT-USS}} = -0.0270$, $\delta C_{M_{WBT-USS}} = 0.0457$) were also derived to be added to the WBT computational data to account for the presence of the upper-swept strut. Effects of the upper-swept strut on the WB configuration were not carried out in that study. A "nominal" correction for the WB configuration was derived by applying the ratio of horizontal tail planform area covered by the fuselage to that of the complete planform area to the WBT increment. The resulting WB configuration corrections are $\delta C_{L_{WB-USS}} = -0.0030$ for lift, and $\delta C_{M_{WB-USS}} = 0.0050$ for pitching moment. For both the WB and WBT configurations, the "nominal" drag corrections to be added to the CFD results are $\delta C_{D_{USS}}$ and $\delta C_{D_P USS} = -0.0025$. Corrections to the WBNP are the same as for the WB. These corrections to be added to the computational data are summarized in Table S-III-1.

Table S-III-1. Corrections for Aeroelastic Twist and USS.

Correction for	δCL	δCD	δCM	Add to
Aeroelastic Twist	−0.0360	0.0	0.0300	WB; DPW-IV, -V WBT; DPW-IV
USS	−0.0030	−0.0025	0.0050	WB; All DPWs
USS	−0.0270	−0.0025	0.0457	WBT; DPW-IV
USS	−0.0030	−0.0025	0.0050	WBNP; DPW-VI

A comparison of data from the various wind tunnels shows that the wing pressure distributions are virtually indistinguishable at the conditions specified for the DPW series. Whether this is true for other conditions has not been checked in detail. Limitations in the total number of pressure taps that can be built into the wind tunnel model and subsequent plugged and/or "slow" taps may result in inadequate definition of the experimental pressure distributions at the various span stations. This is particularly the case in defining the wing shock location in transonic flow and adequately defining the aft loading near the wing trailing edge. For attached flow conditions, there is very little change in the pressures near the wing trailing edge with angle-of-attack changes. In order to calculate section lift and moment characteristics, it was necessary to get a complete distribution from trailing edge around the section cut back to the trailing edge. This was accomplished by "enhancing" the experimental pressure distributions as necessary. The "enhancement" to the pressures near the wing trailing edge was based on a combination of interpolation/extrapolation guided by experience with test data and CFD. At three midspan stations, missing or very "slow" taps required a further "enhancement." These "enhanced pressures" were based on pressure measurements from the JAXA 80 percent CRM model, which did not suffer the same pressure tap manufacturing deficiencies found in the original model. An example of these enhancements is shown in Figure S-III-3 for two spanwise stations. The original pressure data are shown by the open symbols, the enhanced distributions, which include the original data points, are shown by the solid symbols. A more complete set of the enhanced pressure distributions for all nine spanwise stations and covering the specified

DPW conditions of $C_L = 0.50$, $\alpha = 2.75°$, 3.00°, 3.25°, 3.50°, 3.75°, 4.00°, (α = –3.00° to 6.64°) can be found in Appendix A.

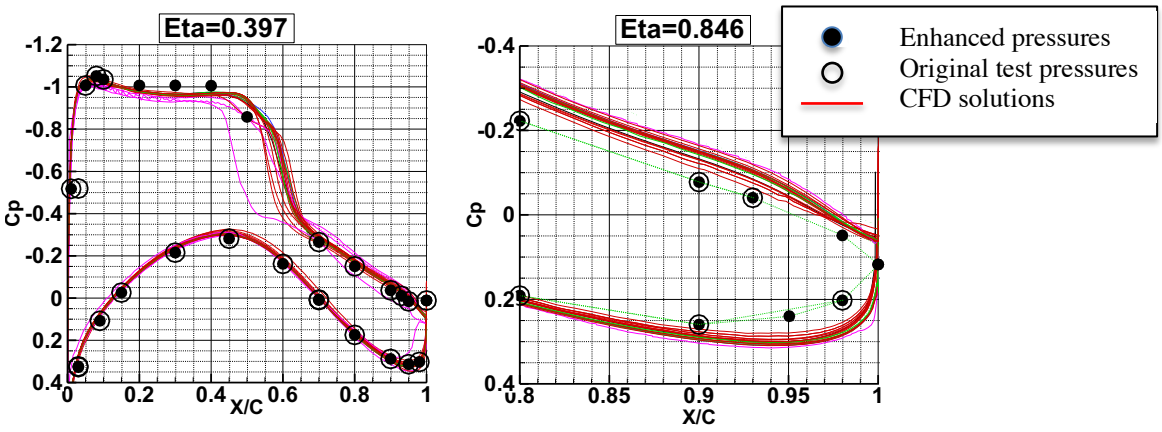


Figure S-III-3. Enhancement of Wind Tunnel Pressure Distributions.

In assessing the "accuracy" of DPW CRM computational predictions the following should be considered:

1. Because of the flow anomalies present in every wind tunnel and the approximate nature of the corrections applied to account for these irregularities, the absolute measurement of forces and moments corresponding to "free air" is impractical if not impossible. It is not unusual that the drag levels will differ between wind tunnels. However, the calculation or measurement of increments between two similar configurations should certainly be feasible with carefully executed wind tunnel test programs and CFD.

2. The close agreement of force and moment data between NTF, the 11-Foot, and ETW wind tunnels, shown in Figure S-III-1, is a good indication that these measurements are representative of the configuration and should be used as a basis of comparison with CFD data. Just remember that absolute levels may differ, but increments, including those with angle of attack, should merit a higher degree of confidence.

3. Close agreement of the wing pressure distribution data between the three wind tunnels has also been seen for the M = 0.85, Reynolds number = 5 million condition. However, limitations of the number of "working" pressure taps did require the "enhancing" of pressure data shown in the comparisons in this report. A complete set of the "enhanced" pressures compared to the original can be found in Appendix A. In many cases, the location and density of pressure taps in the model is not sufficient to adequately define shock locations.

4. Above 3.5° angle of attack, the wind tunnel model experienced a significant amount of buffet. The force and moment data were heavily filtered, and the pressure transducers were incapable of responding to high frequency variations. The degree of flow unsteadiness is not known. However, the general agreement of the forces, moments, and pressure distributions between the three wind tunnel data sets at 4° angle of attack is an indication that these data are not largely impacted by the flow unsteadiness, but without detailed experimental measurements that adequately capture the flow separation and unsteadiness on these types of configurations, recommendations as to the level of "unsteady" modeling necessary to adequately model these flows cannot be made.

Perhaps when direct numerical simulation of the Navier-Stokes equations is possible for complex configurations at high Reynolds number, the calculation of absolute forces and moments will be possible. Until that time, in order to expand CFD into buffet and the edges of the flight envelope, better and more detailed experimental measurements that adequately capture the flow separation and unsteadiness on these types of configurations will be necessary to guide further CFD development.

Section IV: Gridding Guidelines and Description of Common Grids

A common theme and discussion topic in the DPW series has been the effect of the computational grid on the results. Gridding guidelines have been developed over the course of the DPW series and did not change much for the last three workshops except for the target sizes and as dictated by the geometries. The gridding guidelines were provided in an attempt to maintain some level of uniformity across all types of meshes. A more detailed description of the grids and the gridding guidelines for DPW-IV and DPW-V are given in Table A-B-1, and those for DPW-VI in Table A-B-2, found in Appendix B. This appendix contains further details on all the grids beyond what is included in this section.

For DPW-IV, the individual participants following the published guidelines generated most of the grids for their own use. However, a few grid families were used by more than one participant. Each grid family was required to include coarse (C), medium (M), and fine (F) grids; adding an optional extra-fine (X) grid was also encouraged. The medium mesh was to represent the current engineering applications of CFD being used to estimate drag levels on similar configurations. For unstructured meshes, the size of the medium mesh is also a function of the intended flow solver. For example, a cell-centered scheme has about 5.5 times the numbers of unknowns as that of a nodal scheme for a given unstructured tetrahedral mesh, with the ratio being closer to 3.5 for typical hybrid meshes.

Table A-B-3 in Appendix B provides the grid size for each grid family, configuration, and resolution in DPW-IV. The types of meshes included multiblock (MB), overset (OS), and unstructured (UN). This table also indicates whether the associated flow solver is based on a nodal (N) or cell (C) centered scheme. These grids range in size from 2.8–189.4 million. The average medium grid sizes for the WBT and WB configurations are 13.3 million and 10.9 million, respectively. Details of the individual grid families can be found in Refs. 42–56.

A substantial effort was made in DPW-IV to address the effect of computational grid on the results, yet there was still significant variation in the results among the different grid types. The DPW Organizing Committee recognized that for DPW-V a relatively simple structured multiblock grid could be created for the CRM wing-body geometry that conformed to the desired gridding guidelines. From this baseline grid the remaining grid types could be generated, thereby guaranteeing a high degree of commonality. The grid topology for the baseline MB grid is shown in Figure S-IV-1. Starting with the finest grid (L6), the smaller grids were derived by combining cells, keeping even the smallest grid (L1) "multigrid friendly" for up to three levels. Once the MB series was developed, then a set of unified grids for other types were derived. These included OS and three types of UN grids: hexahedral, prismatic, and hybrid tetrahedral (prismatic in the boundary layer and tetrahedral in the field). Details of the individual grid families can be found in Ref 58 and in Appendix B. A summary comparison of the grid sizes for all levels and types is listed in Table A-B-4 shown in Appendix B. Note that suitable grid refinement sequences are available for unstructured cell- or node-based schemes.

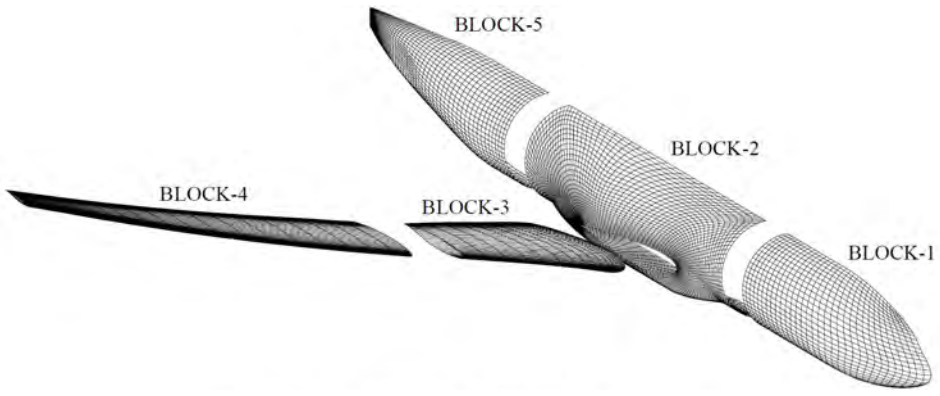


Figure S-IV-1. Block Topology for the CRM Wing-Body MB Grid Family.

For DPW-VI, grid families were required for Wing-Body and Wing-Body-Nacelle-Pylon grid convergence studies, and a set of medium Wing-Body grids, each at a different aeroelastic deflection, for the angle-of-attack series.

Some grid sets were provided by members of the DPW-VI Organizing committee, others by some of the participants. Grids provided by members of the Organizing committee included an OS grid family by Boeing, a UN mesh family by NASA, and a UN mesh family by DLR. Additional information of these baseline grid families is provided in the section below. An MB grid family for the Wing-Body configuration was provided by Embraer, an MB set for the Wing-Body-Nacelle-Pylon by CFS Engineering, a UN grid family by the China Aerodynamics Research and Development Center, and a UN grid set by Boeing. Since these grids were developed by several different people from different institutions, a set of gridding guidelines (Table A-B-2) was developed beforehand, in order to maintain some level of consistency between the baseline grid families of the various types of grid systems. These gridding guidelines were then used by the various grid developers as a target end state of their grid systems and families. We note that while these gridding guidelines are fairly comprehensive, the resulting grid systems do not strictly conform to them. The reasons for this vary but are usually the result of being difficult to implement. Hence, the baseline grid families closely, but not necessarily exactly, conform to most of the gridding guidelines. A more detailed description of the DPW-VI grid families is given in Appendix B.

Section V: Test Case Descriptions

The success of the DPW Series is due in large part to the significant amount of personal time and computing resources invested by the participants of the workshops. In order to keep these individual investments from growing out of control, the organizing committee made optional some of the test cases for the individual workshops. Each of the workshops considered in this study had cases with similar objectives though different in detail. The Wing-Body in DPW-VI differed from that in DPW-IV and -V in that it included the aeroelastic deflections under load at each specified condition analyzed. Nevertheless, it is possible to look across the three CRM related workshops to discern significant findings. Each of the workshops included a single-point grid-sensitivity/convergence study, and an alpha-sweep on medium-size grids. The single-point grid-sensitivity studies specified a fixed lift coefficient that requires convergence on angle of attack, α; this in turn adds additional effort. The required and optional test cases for the three workshops are listed below. Note that the case numbering is different for each workshop.

The required and optional test cases for DPW-IV are listed below (see Figure S-V-1):

Case 1a: NASA CRM Wing-Body-Tail (iH = 0) Common Grid Study

- Required Grid Convergence study at Mach = 0.85, C_L = 0.500 (±0.001), Re_c = 5 million
- Grid refinement series from the Common Grid Sequence consisting of at least four grid levels
- Coarse, medium, fine, and extra-fine grids (extra-fine is optional)

Case 1b: NASA CRM Downwash Study

- Angle-of-attack (alpha) sweep on both WB and WBT
- Mach = 0.85, Re_c = 5 million, α = [0.0°,1.0°,1.5°,2.0°,2.5°3.0°,4.0°], Horizontal Tail: Off and On with iH = [–2°, 0°, +2°]
- Trimmed WBT Polar and Lift curves, Downwash Variation, Delta Drag Polar: Trimmed WBT; WB

Case 2 (Optional): NASA CRM Wing-Body-Tail (iH = 0) Mach-Sweep Study

- Drag Rise on medium WBT grid
- C_L = [0.40,0.45,0.50], Mach = [0.70,0.75,0.80,0.83,0.85,0.86,0.87], Re_c = 5 million, iH = 0°, Extracted from Polars or with C_L converged to ±0.001

Case 3 (Optional): NASA CRM Wing-Body-Tail (iH = 0) Reynolds number Study

- Fixed-C_L Single-Point Solutions on medium WBT grid, Re_c = [5 and 20] million
- Mach = 0.85, C_L = 0.5±0.001, iH = 0°

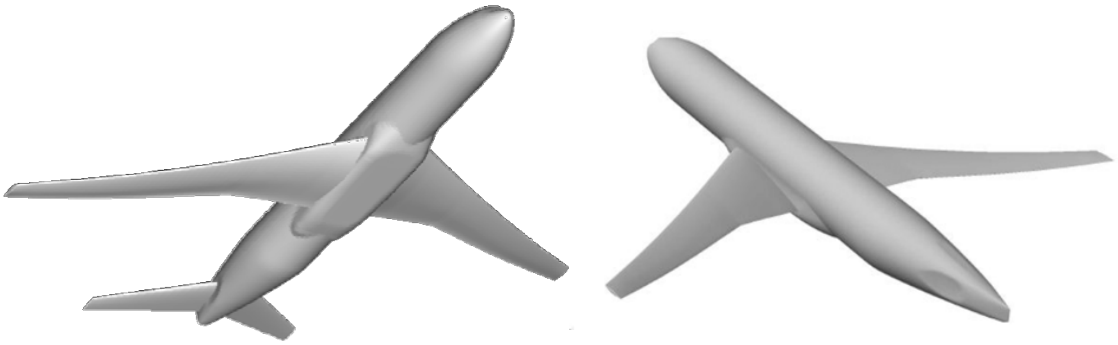


Figure S-V-1. CRM Wing-Body-Tail and Wing-Body (As-Built).

The required and optional test cases for DPW-V are listed below (see Figure S-V-2):

Case 1: NASA (CRM Wing-Body Common Grid Study:

- Required Grid Convergence study at Mach = 0.85, C_L = 0.500 (±0.001), Re_c = 5 million
  - Grid refinement series from the Common Grid Sequence consisting of at least four grid levels
  - Coarse, medium, fine, and extra-fine grids (extra-fine is optional)
- Optional Grid Convergence study using participant developed grids:
  - All participants are encouraged to build their own grids using "best practice" techniques

Case 2: NASA CRM Wing-Body Buffet Study:

- Mach = 0.85, Re_c = 5 million
- Drag Polar for alpha = 2.50°, 2.75°, 3.00°, 3.25°, 3.50°, 3.75°, 4.00°
- Medium grid used in Case 1 from the Common Grid Sequence or participant developed grids

Case 3 (Optional, Not CRM): Turbulence Model Verification:

- 2D Zero Pressure Gradient Flat Plate: M = 0.20; $Re_L = 5 \times 10^6$; T_{ref} = 540°R
- 2D Bump-in-channel: M = 0.20; $Re_L = 3 \times 10^6$; T_{ref} = 540°R
- 2D NACA 0012 Airfoil: M = 0.15; $Re_c = 6 \times 10^6$; T_{ref} = 540°R

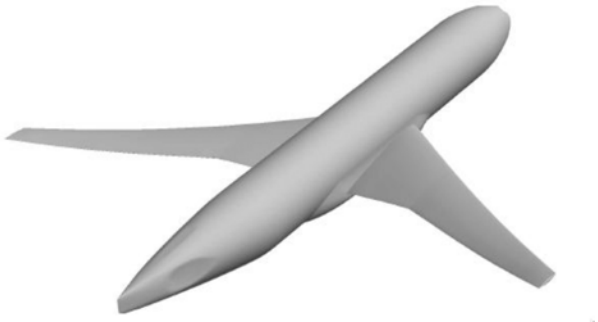


Figure S-V-2. CRM Wing-Body (As-Built).

The required and optional test cases for DPW-VI are listed below (see Figure S-V-3):

Case 1 (Optional: Not CRM) Turbulence Model Verification from the Turbulence Modeling Resource:

- 2D NACA 0012 Airfoil: M = 0.15; $Re_c = 6 \times 10^6$; $T_{ref} = 540°R$

Case 2: NASA CRM Wing-Body/Wing-Body-Nacelle-Pylon Grid Study/Nacelle-Pylon Drag Increment:

- Required Grid Convergence study at Mach = 0.85, $C_L = 0.500$ (±0.001), $Re_c = 5$ million
  - Grid refinement series from both WB and WBNP Grid Sequence consisting of at least four grid levels
  - Coarse, medium, fine, and extra-fine grids (extra-fine is optional)
- Calculate the drag increment between the CRM WBNP and the CRM WB configurations.

Case 3: NASA CRM Wing-Body Static Aeroelastic Buffet Study:

- Mach = 0.85, Re_c = 5 million
- Drag Polar for alpha = 2.50°, 2.75°, 3.00°, 3.25°, 3.50°, 3.75°, 4.00°
- Medium grids defined for each angle of attack [7 solutions on 7 grids]
  - Aeroelastic deflections measured in the ETW Wind Tunnel Test

Case 4 (Optional): NASA CRM Wing-Body Static Grid Adaption Study:

- Mach = 0.85, $Re_c = 5$ million, fixed $C_L = 0.5 \pm 0.0001$
- Using an adapted grid family provided by the participant.

Case 5 (Optional): NASA CRM Wing-Body Coupled Aerostructural Simulation:

- Mach = 0.85, $Re_c = 5$ million, fixed $C_L = 0.5 \pm 0.0001$
- Fixed lift condition for the CRM Wing-Body coupled with computational structural analysis.
- Start with the undeformed medium baseline grid.
- A structural FEM supplied by NASA via the CRM Website. Modal shapes are also available.

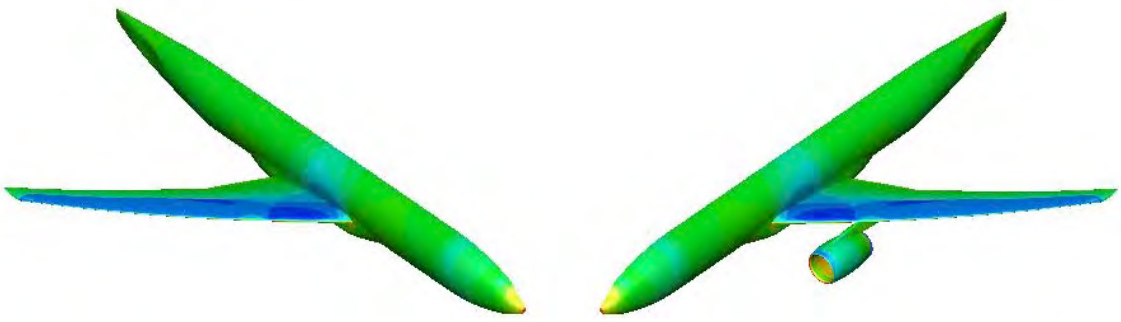


Figure S-V-3. CRM Wing-Body and Wing-Body-Nacelle-Pylon (Aeroelastic).

All CRM simulations are "free air" with no wind tunnel walls or support system. The boundary layer is to be modeled as "fully turbulent" for all cases. No free or fixed laminar to turbulent transition is to be specified. With the exception of the Reynolds number study in DPW-IV, all CFD results and test data are for a $Re_c = 5$ million.

To collect a consistent set of data from each participant, template data sets were supplied. These templates request lift, drag (broken down into skin friction and pressure components), pitching moment, pressure distributions at specified span stations, trailing-edge separation locations, dimensions of the side-of-body separation bubble, grid

family and sizes, turbulence model, computing platform and code performance, number of processors used, number of iterations required, etc. For DPW-VI Case 5, values of the calculated wing twist and bending deflections were also requested. These workshops capture an extensive amount of information that serves as a snapshot of the industry capabilities of the time. For example, in the six workshops held thus far, one obvious trend is that the grid size has grown dramatically. The average size of the medium WB meshes in DPW-I through DPW-IV were 3.2, 5.4, 7.8, and 10.9 million, respectively. This represents a growth rate of ~17 percent per year during the eight years between DPW-I and DPW-IV. For DPW-VI, this number has grown from 25 to 50 million points for the various families of grids available. The finest level grids have increased steadily, from just over 3 million grid points in DPW-I to 225 million for the WBNP in DPW-VI.

Section VI: Participant Descriptions

The Drag Prediction Workshop welcomed any individual, group or organization that wished to perform the calculations according to the specifications set out by the organizing committee. Tables detailing names, organizations, codes, grid types, and turbulence models of each data set submitted for each of the three CRM related workshops are listed below and in Appendix C**.** Each data set was assigned an alphanumeric (including Greek) symbol type in order received. This symbol type is unique to the specific workshop and is not consistent between workshops. In all, 10 organizations attended all three of these workshops, 6 attended two, and 20 attended only a single workshop.

DPW-IV had a total of 19 participants submit 29 solution sets for the CRM cases. Balance of participation achieved at this workshop is shown below by the demographics of the DPW-IV:

- 7 North America, 9 Europe, 3 Asia
- 5 Industry, 7 Government Labs, 2 Academia, 5 Commercial

The presentations by each participant can be found at the DPW-IV website[38] and contain a description of the computational method used and results presented. Characterization of the 29 sets is given in Table S-VI-1.

Grid Types:

1	Overset
11	Structured Multiblock (8 Teams)
7	Common Unstructured (2 Teams)
10	Custom User Generated (8 Teams)

Turbulence Models:

18	SA (all types)
7	SST (all types)
1	Goldberg RT
2	EARSM
1	SSG/LRR-ω

The response for DPW-V increased somewhat from the previous workshop, following a trend of gradually increasing participation. A total of 57 data sets were submitted from 22 different teams or organizations. Of these teams, they are broken down by location and type as follows:

- 10 North America, 5 Europe, 6 Asia, 1 South America
- 9 Government, 5 Industry, 6 Academia, 2 Commercial

The presentations by each participant can be found at the DPW-V website[57] and contain a description of the computational method used and results presented. Characterization of the 57 sets is given in Table S-VI-2. Note that one team submitted data for the non-CRM turbulence modeling Case 3 only. For Cases 1 and 2, the grid type and turbulence model breakdown follow:

Grid Types:

5	Common Overset (4 Teams)
7	Common Structured Multiblock (5 Teams)
25	Common Unstructured (13 Teams: 14 Hex, 7 Hybrid, 4 Prism)
20	Custom User Generated (7 Teams: 6 Overset, 2 MB, 2 Hex, 8 Hybrid, 2 Tet)

Turbulence Models:

38	SA (all types)
13	SST (all types)
4	Goldberg RT
1	EARSM
1	Lag-RST

The response for DPW-VI again increased somewhat from the previous workshop, following a trend of gradually increasing participation. A total of 55 data sets were submitted from 25 different teams or organizations. These teams were broken down by location and type as follows:

- 12 North America, 6 Europe, 6 Asia, 1 South America
- 8 Government, 5 Industry, 7 Academia, 5 Commercial

The presentations by each participant can be found at the DPW-VI website[72] and contain a description of the computational method used and results presented. Characterization of the 55 sets is given in Table S-VI-3. For DPW-VI Cases 2–5, the grid type and turbulence model breakdown included:

Grid Types:

7	Common Overset (4 Teams)
4	Common Structured Multiblock (3 Teams)
21	Common Unstructured (12 Teams)
15	Custom Unstructured (12 Teams)
7	Custom Cartesian (4 Teams)

Turbulence Models:

21	SA (many variants)
15	SA-QCR (many variants)
8	SST (many variants)
2	k-kLe-MEAH2015
3	k-ε Lam Bremhorst
1	EARSM
1	RSM-ω
1	Realizable k-ε
1	k-ε
1	LBM-VLES

Solvers:

23	Finite Volume
2	Finite Element
1	Lattice-Boltzmann Method

DPW-VI had a new type of solution based on the Lattice-Boltzmann Method [89] that is totally different from the classical finite volume/finite element methods used to date. Two sets of solutions were based on finite element Streamline/Upwind Petrov-Galerkin (SUPG) solvers [90,91], one more than DPW-V.

Tables detailing names, organizations, codes, grid types, and turbulence models of each data set submitted for each of the three CRM related workshops are also listed in Appendix C**.**

Table S-VI-1. DPW-IV Submissions and Participant Data Key.

Team	ID	SYM	SYM	Name	Organization	Code	Algorithm	Grid Generator	Grid	Turbulence Model
1	A	A		Jan B. Vos	RUAG Aerospace	NSMB	4th order Central Scheme, LU-SGS time integration	ICEMCFD HEXA	Multiblock Structured	Menter k-w SST
2	B	B		O.Brodersen	DLR, Institute of Aerodynamics and Flow Technology	TAU	cell-vertex, finite volume, hybrid, unstructured mesh	Centaur 8.1	Hybrid	SA
	C	C					cell-vertex, finite volume, hybrid, unstructured mesh	SOLAR 13.0	Hybrid	SA
3	D	D		Peter Eliasson	FOI	EDGE	Unstructured node-centered, Finite-volume	SOLAR 13.0	Hybrid	EARSM (Explicit Algebraic Reynolds Stress
4	E	E		Prof N. Balakrishnan	Indian Inst. Science	HIFUN	Upwind, cell-centered	Gambit and Tgrid	Hybrid	SA
5	F	F		Kazuomi YAMAMOTO	JAXA	TAS_Flow code	Upwind, cell-vertex finite volume, Hybrid(Mixed Elm.) unstructured	TAS_Mesh code	hybrid	Spalart-Allmaras model with a modification (SA_mod)
	G	G					Upwind, cell-vertex finite volume, Hybrid(Mixed Elm.) unstructured	TAS_Mesh code	Hex	Spalart-Allmaras model with a modification (SA_mod)
5	H	H				UPACS Ver.2.0	Upwind, cell-centered finite volume, Multi-Block structured	Gridgen (V15.10)	Multiblock Structured	Spalart-Allmaras model with a modification (SA_mod)
6	I	I		Elizabeth Lee-Rausch & Christopher L.	NASA LaRC	FUN3D	Node-Based UMUSCL	VGrid-4.1	Unstructured_ Larc/NodeBase grids)	SA
7	J	J		Mark Chaffin	Cessna	NSU3D	TLNS Node-centered, central diff	VGRID 4.2	Unstructured, Cessna spacing	SA
	K	K					TLNS Node-centered, central diff	VGRID 4.2	Unstructured, Mods by	SA
8	L	L		Ben Rider	Boeing Commercial Airplanes, Seattle	CFL3D	Full NS, finite volume	BCA Zeus	Multiblock Structured	SA
	M	M					Full NS, finite volume	BCA Zeus	Multiblock Structured	Menter k-w SST
	N	N					thin-layer N-S, finite volume	BCA Zeus	Multiblock Structured	SA
	O	O					thin-layer N-S, finite volume	BCA Zeus	Multiblock Structured	Menter k-w SST
9	P	P		Tony Sclafani	Boeing (Huntington)	OVERFLOW	Thin-layer Overset Roe Upwind	MADCAP/ HYPGEN	Overset	SA
10	R	R		Marco Oswald	ANSYS	ANSYS	Density based, FDS Roe Upwind	ICEM Hexa	Multiblock Structured	Menter k-w SST
2	S	S		O.Brodersen	DLR, Institute of Aerodynamics and Flow Technology	TAU	cell-vertex, finite volume, hybrid, unstructured mesh	SOLAR 13.0	Hybrid	Reynolds stress SSG/LRR-omega
	T	T					cell-vertex, finite volume, hybrid, unstructured mesh	SOLAR 13.0	Hybrid	Menter k-w SST
11	U	U		Basant Kumar Gupta	Zeus Numerix Private Ltd.	HLLC	Explicit Time Marching	GridZ	Multiblock Structured	SA
12	V	V		Simon TRAPIER	Airbus	elsA	cell centered finite volume solver, Jameson type scheme	ICEM Hexa	Multiblock Structured	Menter k-w SST
13	W	W		Uriel Goldberg	Metacomp	CFD++	Finite volume unstructured mixed-element cell-based	MIME	Unstr/Hybrid	Realizable k-epsilon
	X	X					Finite volume unstructured mixed-element cell-based	MIME	Unstr/Hybrid	SA

Table S-VI-1. (Concluded) DPW-IV Submissions and Participant Data Key.

14	Y	Y		Sebastien ESQUIEU	ONERA	elsA	cell centered finite volume solver, Jameson type	BCA Zeus	Multiblock Structured	SA
15	Z	Z		Dimitri Mavriplis and	U Wyoming	NSU3D	Unstructured, mixed elements, multigrid	VGRID	LaRC Node-Based	SA
	2	2		C. Winkler, A. Dorgan, A. Cary, and M. Mani	Boeing - St. Louis	BCFD	Unstructured, finite volume	AFLR3	mixed-element	SA
16	3	3					Unstructured, finite volume	AFLR3	mixed-element	Menter k-w SST
17	4	4		Lionel Temmerman	NUMECA International	FINE/ Open	Jameson-Schmidt-Turkel Scheme with scalar		Multiblock Structured	SA
3	5	5		Peter Eliasson	FOI	EDGE	Unstructured node-centered, Finite-volume	Tritet	Hybrid	EARSM (Explicit Algebraic Reynolds Stress

Table S-VI-2. DPW-V Submissions and Participant Data Key.

Team	ID	SYM	SYM	Name	Organization	Code	Algorithm	Grid Generator	Grid	Turbulence Model
	A			Sclafani	Boeing (Huntington)	OVERFLOW v2.2c	Full NS Central Diff, cell-centered	Common Grid	Overset	SA-Ia
	B							Common Grid	Overset	SA-Ia w/ RC
	C								Custom (Overset)	SA-Ia
	D								Custom (Overset)	SA-Ia QCR
	E								Custom (Overset)	SA-Ia w/ RC
	F								Custom (Overset)	SA-Ia w/ RC QCR
	G								Custom (Overset)	SA-Ia w/ RC
1	H								Custom (Overset)	SA-Ia w/ RC QCR
	I			Chen	CADRC	MFlow	ROE scheme cell-centered upwind	Common Grid	Hex	SA
2	J							Common Grid	Hybrid	SA
	K			GariÈpy	EcolePolytech Montreal	Fluent V13	Density based solver, ROE scheme, cell-centered, upwind diff	Common Grid	Prism	SA
3	L								Custom (Hex)	SA
	M			Scalabrin	Embraer	CFD++	Finite volume unstructured mixed-element cell-centered, upwind	Common Grid	Hex	k-e-RT
	N							Common Grid	Hex	Menter k-w SST
	O							Common Grid	Hybrid	k-e-RT
	P							Common Grid	Hybrid	Menter k-w SST
	Q							Common Grid	Prism	k-e-RT
	R							Common Grid	Prism	Menter k-w SST
	S							ICEM TGRID	Custom (Hybrid)	k-e-RT
4	T							ICEM TGRID	Custom (Hybrid)	Menter k-w SST
	U			Eliasson	FOI	EDGE	Unstructured node-centered, Finite-volume	Common Grid	Hex	EARSM (Explicit Algebraic Reynolds Stress Model)
	V							Common Grid	Hex	SA
5	W							Common Grid	Hex	Menter k-w SST
6	X			Powell	Gulfstream	FUN3D	Node-centered UMUSCL	Common Grid	Hybrid	SA
7	Y			Balakrishnan	Indian Inst.	HiFUN	Upwind, cell-centered	Common Grid	Hex	SA
	Z			Hashimoto	JAXA	FaSTAR	Upwind, cell-centered	Common Grid	Hex	SA-noft2-R
8	2						Upwind, cell-centered	Custom Hex Hexabri oct-	Custom (Hex)	SA-noft2-R

Table S-VI-2. (Concluded) DPW-V Submissions and Participant Data Key.

9	3			Yamamoto	JAXA	UPACS	Upwind, cell-vertex finite volume	Common Grid	Multiblock Structured	SA-noft2-R (Crot=1)
	4					UPACS		Common Grid	Multiblock Structured	Menter k-w SST-V
10	5			Olson	NASA Ames	overflow 2.2e_LRS	Full NS Matrix, cell-centered	Common Grid	Overset	Lag RST
11	6			Park	NASA Langley	FUN3D	Node-centered UMUSCL	Common Grid	Hybrid	SA
	7					CFL3D v6.6	Full NS, finite volume, cell centered	Common Grid	Multiblock Structured	SA
12	8			Cai	NPU China	ExStream	Full NS Upwind Diff, cell-centered	Common Grid	Overset	Menter k-w SST-V
13	9			Hue	ONERA	elsA	Full NS Central Diff, cell-centered	Common Grid	Multiblock Structured	SA
14	a			Coder	Penn St. U	OVERFLOW 2.2c	Full NS Upwind Diff, cell-centered	Common Grid	Overset	SA-fv3
15	b			Osusky	U. Toronto	Diablo	Newton-Krylov-Schur with SBP-SAT discretization, matrix diss	Common Grid	Multiblock Structured	SA
	d							Common Grid	Multiblock Structured	SA
16	e			Levy	Cessna Aircraft Co.	NSU3D	TLNS Node-centered, central diff	Common Grid	Hybrid	SA
	f					FUN3D	Node-centered UMUSCL upwind	Common Grid	Hybrid	SA
17	g			Crippa	DLR	TAU	Node-centered, matrix	Common Grid	Hex	SA
	h							Common Grid	Hex	Menter k-w SST-
18	k			Moitra	CRL_INDIA	CFD++	Finite volume unstructured mixed-element cell-centered, upwind	Common Grid	Prism	SA-RC
19	m			Winkler	Boeing (St. Louis)	BCFD	cell-centered	Common Grid	Hex	SA
	n							Common Grid	Hex	Menter k-w SST-
	q							Common Grid	Hex	SA
	r							Common Grid	Hex	Menter k-w SST-
20	t			Temmerman	NUMECA	FINE/	Cell-centereed, scalar diss	Common Grid	Multiblock	SA
21	α			Brodersen	DLR	TAU	Node-centered, matrix diss 1	Custom1-no hexa wake	Custom (Hybrid)	SA
	β							Custom1-no hexa wake	Custom (Hybrid)	SA
	δ							Custom2-hexa wake block	Custom (Hyb w/ Hex-Wake)	SA
	γ							Custom2-hexa wake block	Custom (Hyb w/ Hex-Wake)	SA
	λ							Custom2-hexa wake block	Custom (Hyb w/ Hex-Wake)	Menter k-w SST-V
	π							Custom2-hexa wake block	Custom (Hyb w/ Hex-Wake)	Menter k-w SST-V

Table S-VI-3. DPW-VI Submissions and Participant Data Key.

Team	ID	SYM	SYM	Name	Organization	Code	Algorithm	Grid Generator	Grid	Turbulence Model
1	A1	A	A	Tony Sclafani	Boeing, BCA Advanced Concepts, Long Beach CA	Overflow v2	Full NS Central Diff, cell-centered		Overset	SA-RC
	A2	a	a						Overset	SA-RC w/QCR on
2	B1	B	B	Khaled Abdol-H	NASA Langley Research Center	FUN3D 12.8	Node-centered UMUSCL upwind		Unst-Geolab	MEAH2015 w/Lim
	B2	b	b						Unst-Geolab	MEAH2015 no-lim
	B3	α	a						Unst-Geolab	SA no-limiter
3	D1	D	D	Jiangtao Chen	CARDC	Mflow	ROE scheme cell-centered upwind		Unst-Geolab	SA
	D2	d	d						Unst-custom	SA

Table S-VI-3. (Concluded) DPW-VI Submissions and Participant Data Key.

4	E1	E	E	Atsushi Hashim	JAXA, Ryoyu Syst	FaSTAR	Upwind, cell-centered		Unst-Geolab	-noft2-R w/QCR20
5	F1	F	F	Krishna Zore	Ansys	Fluent	Density based solver, ROE scheme, cell-centered, upwind diff		Unst-custom	Menter k-w SST-V
6	G1	G	G	Benedikt König	EXA Powerflow	PowerFLOW	LBM	Internal Grid Ger	Custom Cart	LBM-VLES
7	H1	H	H	Ales Prachar/ Peter Eliasson	Aerospace Research and Test Establishment,	Edge	Unstructured node-centered, Finite-volume		Unst-Geolab	SA
	H2	h	h						Unst-Geolab	EARSM (Explicit Algebraic
8	I1	I	I	Anna Rubekinak	Mentor Graphics	FloEFD	cell-centered	FloEFD Mesh	Custom Cart	ult k-e Lam-Bremh
	I2	β	b					FloEFD Mesh	Custom Cart	rid k-e Lam-Breml
	I3	χ	c					FloEFD Mesh	Custom Cart-B	ult k-e Lam-Bremh
9	J1	J	J	Brian Edge	Metacomp	CFD++	cell-centered, upwind		Unst-Boeing	SA
	J2	ϑ	J						Unst-Boeing	Menter k-w SST-
	J3	φ	j						Unst-Geolab	SA
	J4	Ω	W						Unst-custom	tealizable k-epsilo
10	K1	K	K	Taku Nagata	Kawasaki Heavy Industries	Cflow	Cell-centered, MUSCL		Unst-Boeing	SA-noft2
	K2	k	k						Unst-Boeing	A-noft2 w/QCR20
	K3	γ	g					Internal Grid Ger	Custom Cart	SA-noft2
	K4	Γ	G					Internal Grid Ger	Custom Cart	A-noft2 w/QCR20
11	L1	L	L	Stefan Keye / Vamshi Togiti	DLR	TAU	Node-centered, matrix		Unst-custom	RSM-ω
	L2	λ	l						Unst-custom	SA-neg
12	M1	M	M	Ryan S. Glasby	Tennessee, Pointwise, NASA Langley	COFFE/KCF	Node-centered, Finite eleme	Pointwise Tets	Unst-custom	SA-neg
	M2	m	m					Pointwise Tets	Unst-custom	SA-neg w/QCR200
13	N1	N	N	N. Balakrishnan	CAd Lab, Indian Institute of Sci	HiFun	Upwind, cell-centered		Unst-custom	SA
14	O1	O	O	David Hue	ONERA	elsA	Full NS Central Diff, cell-centered		Overset	SA
	O2	ϕ	f						Overset	SA-QCR2000
15	P1	P	P	Todd Michal	Boeing, St. Louis	BCFD	cell-centered		Unst-Boeing	SA-RC
	P2	π	p			GGNS	Node-centered, Finite element		All Tets	SA-RC
16	Q1	Q	Q	Gaetan Kenway	MDOlab, University of Michigan	ADflow	Full NS Central Diff, cell-centered		Embraer MB	SA 1stOrder
	Q2	q	q						Cust-Overset	SA 1stOrder
	Q3	θ	q						Embraer MB	SA-QCR2000
17	R1	R	R	Andrei Cimpoer	CFMS, Zenotech,	ZCFD			Unst-custom	Menter k-w SST-
18	S1	S	S	Kelly Laflin	Textron Aviation (Cessna)	FUN3D	Node-centered UMUSCL upwind		Unst-Geolab	SA-RC
19	T1	T	T	Yuntao Wang	CARDC	TRIP	Upwind Roe cell-centered		CommonMB	Menter k-w
20	U1	U	U	Jim Coder	Applied Research Lab, Penn State	Overflow 2.21 3rd	Full NS Upwind Diff, cell-centered		Overset	SA-RC W/QCF2000
	U2	u	u			Overflow 2.21 5TH	Full NS Upwind Diff, cell-centered		Overset	SA-RC W/QCF2000
21	V1	V	V	Rodrigo Felix de	Embraer S/A	CFD++	Node-centered, upwind		Unst-Geolab	Menter k-w SST-
	V2	ς	V						Embraer MB	Menter k-w SST-
	V3	Ξ	X						Unst-custom-A	Menter k-w SST-
	V4	Ψ	Y						Unst-custom-I	Menter k-w SST-
	V5					CMS AERO-F			Unst-custom	SA-QCR2013
22	W1	W	W	Dominic Chand	Institute of High Performance	μSICS	Node-based	Internal Grid Gen	Unst-custom	SA
23	X1	X	X	Patrick Hanley	Hanley Innovatio	Stallion3D			Custom Cart	k-e
24	Y1	Y	Y	Neil Ashton	University of Oxford,	OpenFOAM	Pressure, Density based solver, cell-centered	SnappyHexMes h	Unst-custom	SA
25	Z1	Z	Z	Yasushi Ito	JAXA, Ryoyu Syst	TAS limiter	Node-based		Unst-Geolab	-noft2-R w/QCR20
	Z2	ζ	z			TAS limiter	Node-based		Unst-Geolab	-noft2-R w/QCR20
	Z3	Δ	D			TAS limiter	Node-based		Unst-Geolab	-noft2-R w/QCR20
	Z4	ε	e			TAS limiter	Node-based		Unst-custom	-noft2-R w/QCR20
	Z5	η	h			TAS limiter	Node-based		Unst-Geolab	SA-noft2-R
	Z6	Π	P			TAS limiter	Node-based		Unst-Boeing	SA-noft2-R
	Z7	Υ	U			TAS limiter	Node-based		Unst-Boeing	-noft2-R w/QCR20

Section VII: Grid Convergence Study

A recurring case in all of the Drag Prediction Workshops had been the grid convergence study. A standard technique in grid convergence studies is to use Richardson extrapolation [40]. Solutions are obtained on a parametric family of three-dimensional meshes that have been "uniformly" refined in all three coordinate directions. Computational results are plotted versus grid factor, $N^{-2/3}$ (called GRIDFAC in the figures), where N is the number of unknowns. For second order codes, a linear fit should be observed with decreasing error as long as the refinement is in the asymptotic region. The *y*-intercept then estimates the theoretical infinite resolution (continuum) result. An example is shown in Figure S-VII-1. The slope of the linear fit (dCDT/dGRIDFAC) denotes the change in drag for a change in the GRIDFAC parameter. This can be thought of as the sensitivity of the solver/grid/turbulence model to grid size as long grid is in the asymptotic region. As discussed in Section IV, Gridding Guidelines and Description of Common Grids, the pragmatic approach to grid generation has been to define guidelines that result in grid families that feature some level of uniformity and consistency.

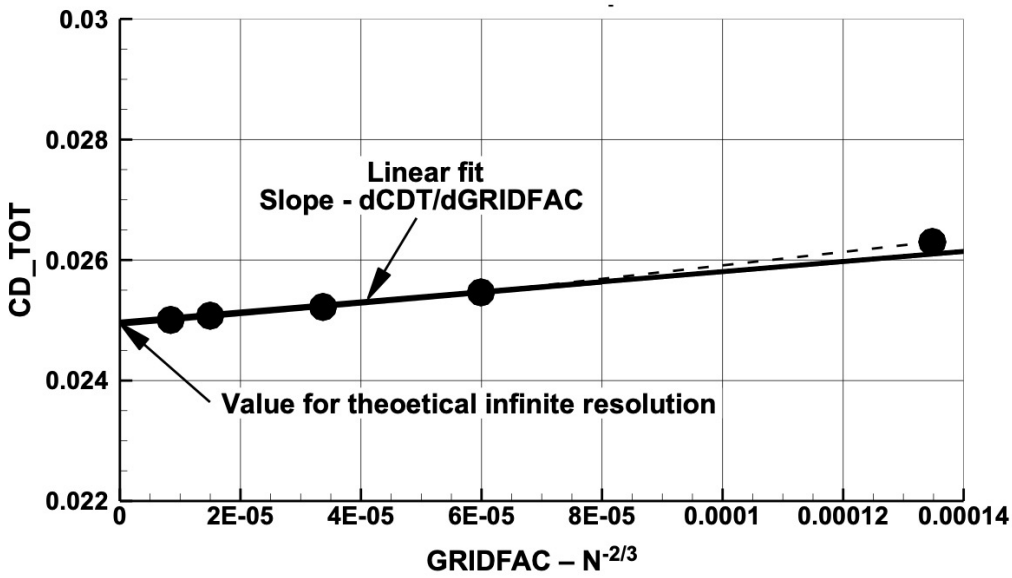


Figure S-VII-1. Richardson Extrapolation Example; Drag.

A. Drag; CRM Wing-Body and Wing-Body-Tail: DPW-IV, -V, and -VI

Grid convergence plots for total drag (C_{D_TOT}), pressure drag (C_{D_PR}), and skin friction drag (C_{D_SF}) are shown in Figure S-VII-2 for the three CRM workshops. Results are shown for the CRM Wing-Body-Tail iH = 0, featured in DPW-IV, and for the Wing-Body featured in DPW-V and -VI. Note however that the wing geometry in DPW-IV and -V was the "as-built" geometry, while that in DPW-VI included the aeroelastic deflection. The increase in grid size (smaller GRIDFAC) is immediately obvious in this figure, as well as a reduction of the spread of the solutions as the workshops progressed, i.e., between the years 2009 to 2016. We see the biggest variation in the pressure drag. The grid convergence charts are broken out into far greater detail in Appendix D.

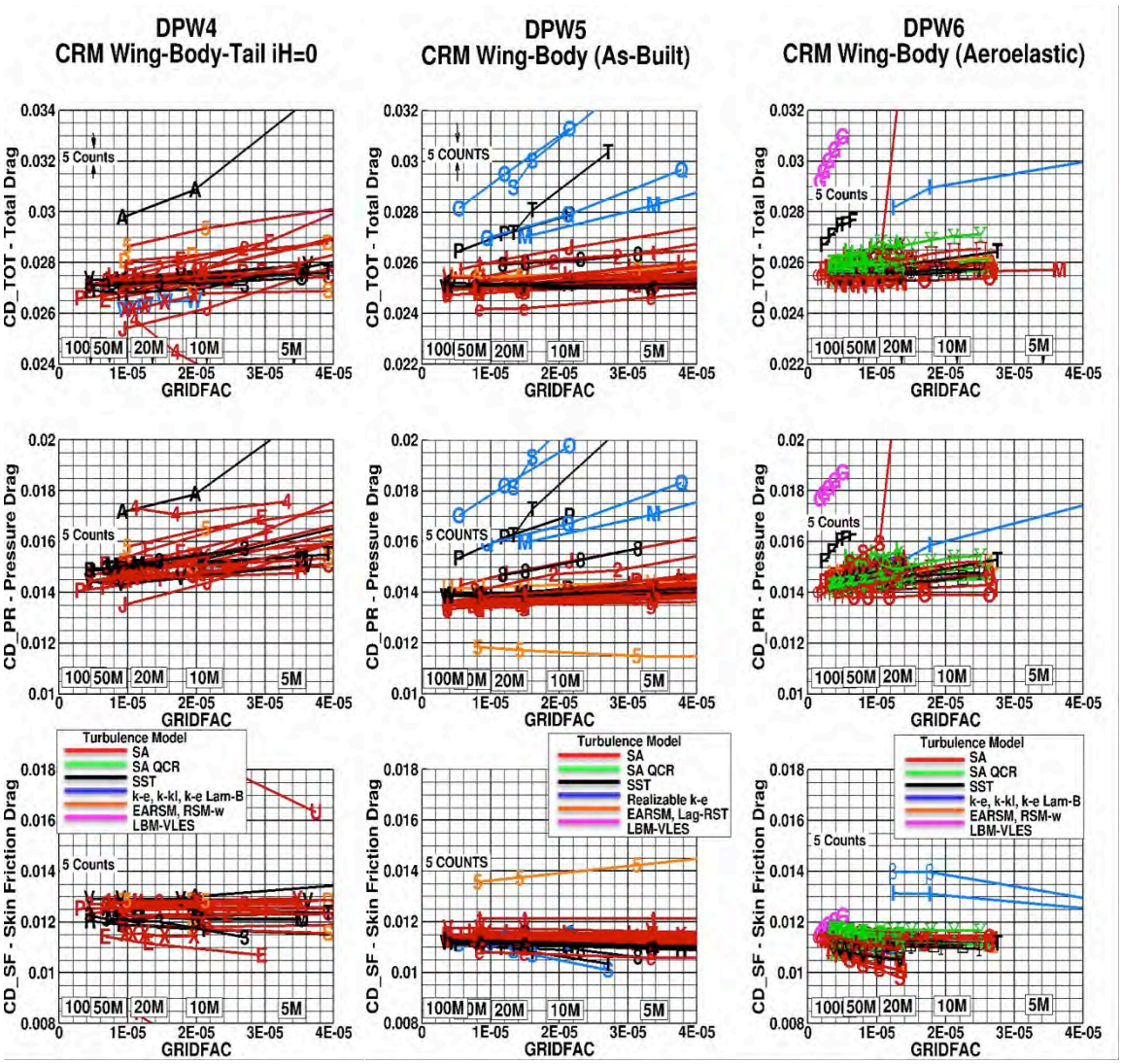


Figure S-VII-2. Grid Convergence; $C_{D,TOT}$, $C_{D,PR}$, $C_{D,SF}$.

With so many total-drag solutions on a single chart it is difficult to distinguish many (or any) trends. Grid type total-drag trends are shown in Figure S-VII-3. Here plots of total-drag are shown for structured (multiblock and overset), unstructured, and Cartesian grids for the three workshops. Here the trend is more obvious. With the exception of two outliers in DPW-IV there is a much smaller spread of results with structured grid solutions compared to those using unstructured grids. This is so even if the four unstructured grid solutions in DPW-V using the Realizable k-ε turbulence model were deleted. There are not enough Cartesian grid solutions to draw any firm conclusions, although two of the solutions in DPW-VI are from the same family of solvers used in DPW-VI and -V, and their convergence levels are similar to most other solutions. Similar grid convergence plots are shown for total pitching moment, Figure S-VII-4, and for angle of attack in Figure S-VII-5. Here any significant trends between grid type or workshop are less obvious.

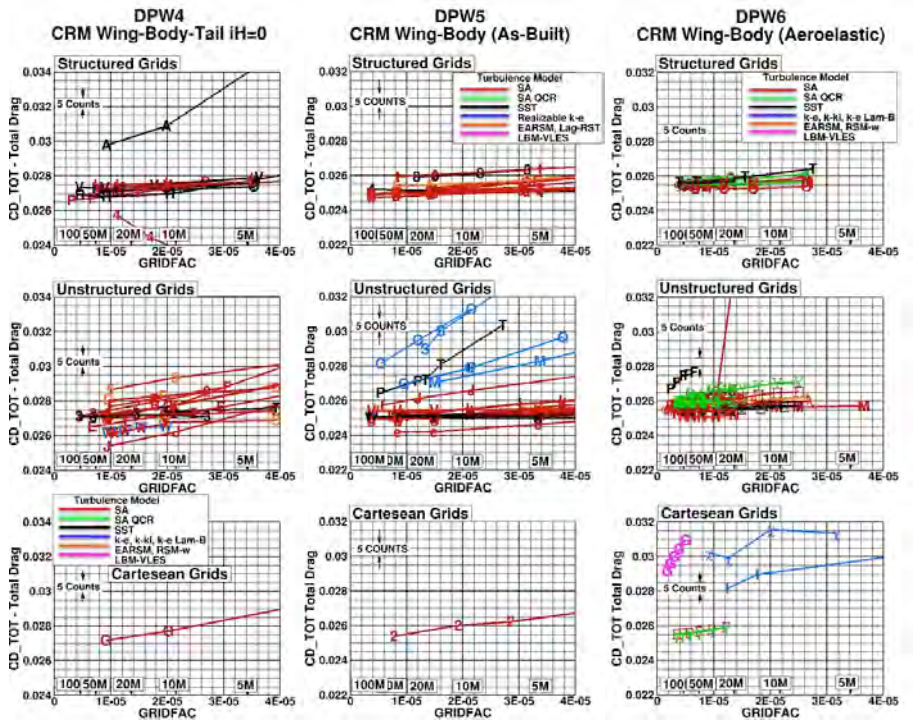


Figure S-VII-3. Grid Convergence; Grid Type; Total Drag C_{D_TOT}.

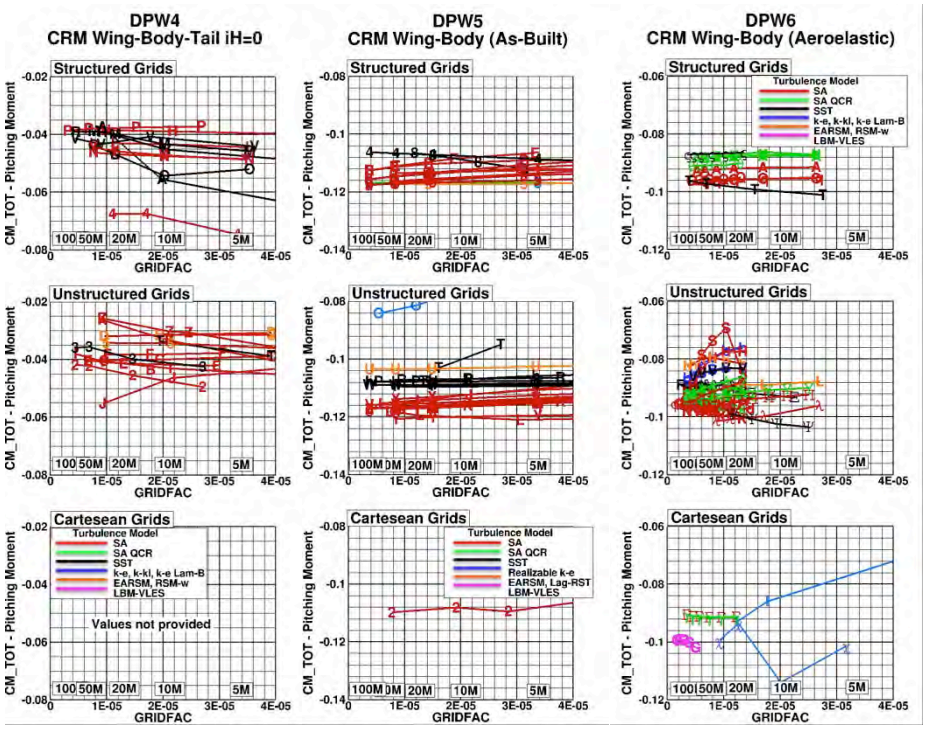


Figure S-VII-4. Grid Convergence; Grid Type; Pitching Moment C_{M_TOT}.

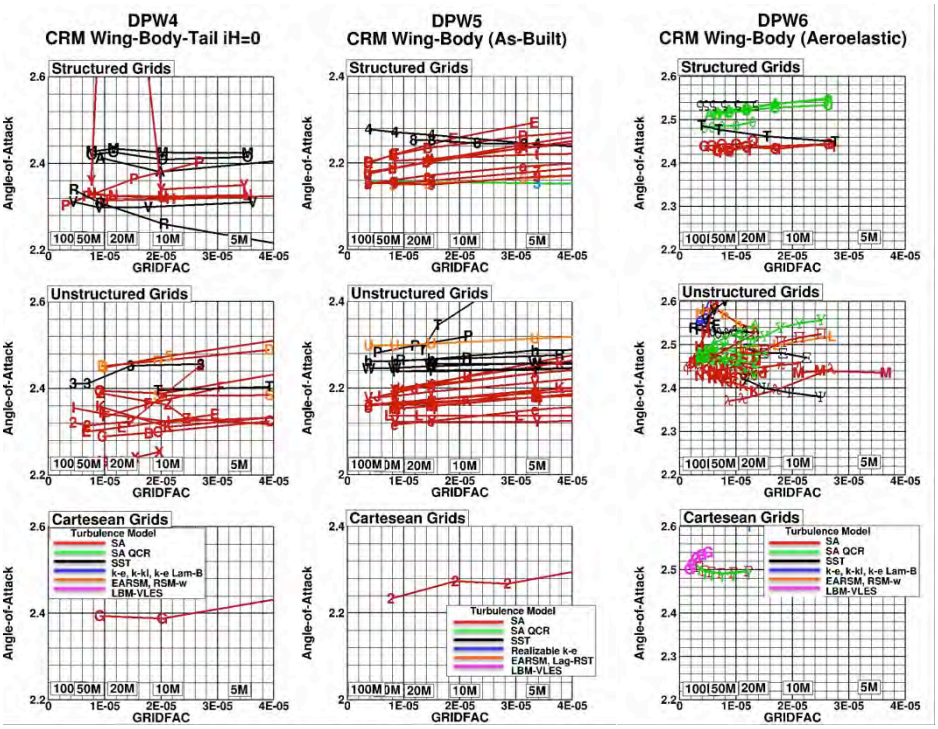


Figure S-VII-5. Grid Convergence; Grid Type; Angle of Attack.

Since the unstructured grids in Figure S-VII-3 for total drag showed the greatest variation, we will further parse those results by considering the unstructured grid solutions from DPW-V and -VI. These represented the same basic configuration. DPW-V featured three sets of DPW Committee supplied common grids plus user generated custom grids. DPW-VI featured two major sets of common mixed-type unstructured grids plus custom grids that were either mixed-type or all tetrahedral. Results from this parsing are shown in Figure S-VII-6. Again, neglecting the solutions based on the Realizable k-ε turbulence model, we see very little total drag spread in the DPW-V hex and prism unstructured grid solutions. This should not be a surprise since these types of grids are most similar to a structured grid, and the fact that these grids were actually derived from a multiblock structured grid [58].

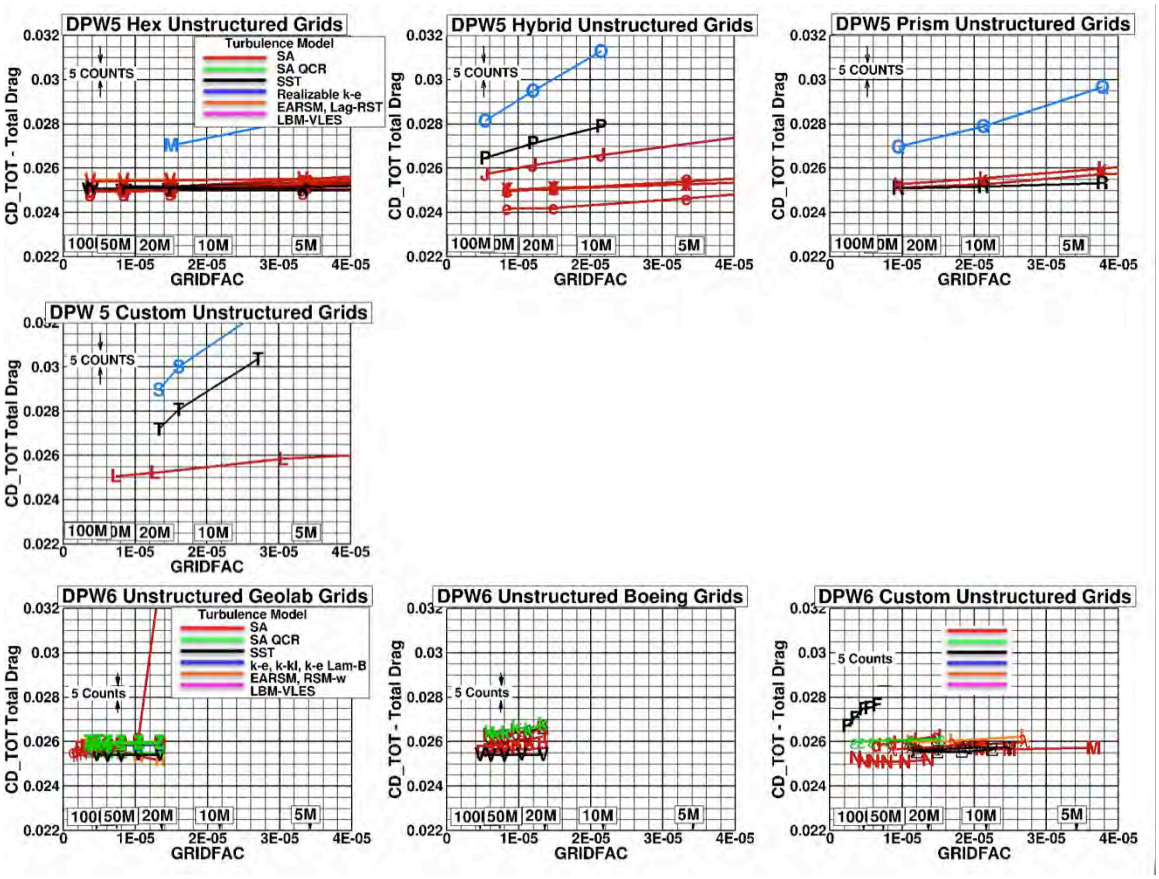


Figure S-VII-6. Grid Convergence; Unstructured Grids; Drag C_{D_TOT}.

The DPW-VI unstructured grids were either mixed-element or all-tetrahedra. A closer look at the solutions from these grids is shown in Figures S-VII-7 and -8. Figure S-VII-7 shows results using the Geolab and Boeing unstructured grids. These two accounted for the majority of the unstructured grid solutions in DPW-VI. From the Geolab grid series, we see that the convergence characteristics are not necessarily consistent between different codes, turbulence models, or turbulence models on the same code. Solutions H1 and H2 are from the FOI EDGE code with the same grid but show convergence rate slopes (dCDT/dGRIDFAC) of opposite sign depending on the turbulence model used. From the Boeing grid series, all but solution P1 show an "oscillatory" characteristic about the linear fit. Solution P1 is from the BCFD solver that Boeing used to check the family of grids before releasing them. Solutions with the Boeing grid set using the BCFD solver produced a fairly linear convergence. Three other codes using the same grid set did not. Drag using the Boeing grids was about six counts higher than that from the Geolab grids. Figure S-VII-8 shows results using the custom mixed-type and all-tetrahedra unstructured grids. Neglecting solutions F1 and N1 the solutions using the custom mixed-type elements are very similar to those using the Geolab grids in both level and grid-convergence characteristics. The all-tetrahedra grid solutions also gave similar drag levels. Note that solution P2 grid-convergence characteristic (shape) is very similar to those from solutions Z6 and Z7 using the Boeing mixed-element grids. The all-tetrahedra grid used in P2 was derived from the mixed-element Boeing grid. The P2 solution was from GGNS, a finite-element code. Z6 and Z7 were from TAS, a more conventional finite volume solver. For completeness, results from the overset and structured multiblock grids are shown in Figure S-VII-9. One other standout from the DPW-VI results is that drag from solutions with the SA-QCR turbulence model tended to be a few counts higher than those SA solutions without QCR.

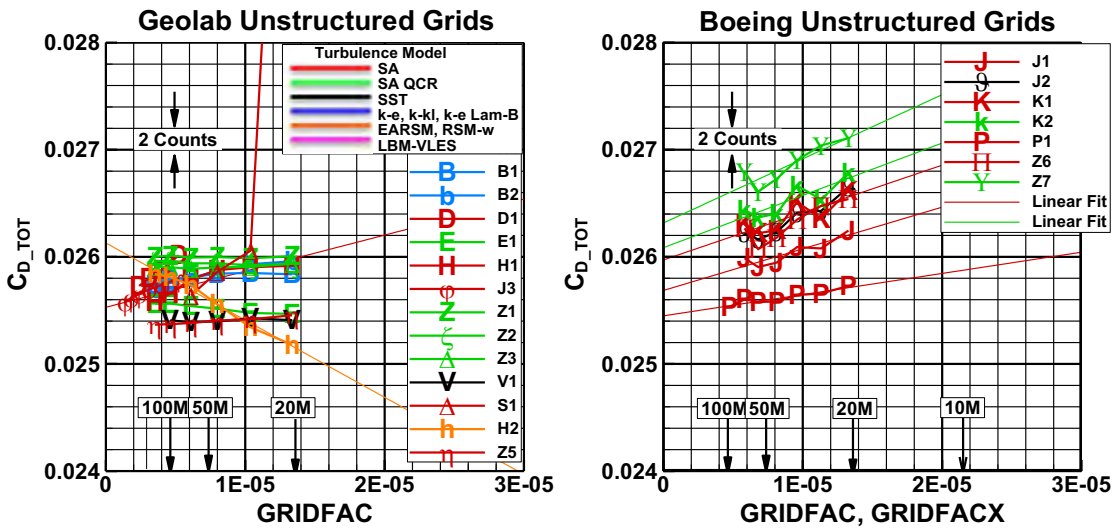


Figure S-**VII**-7. Grid Convergence**; Geolab and Boeing Unstructured Grids; Total Drag C_{D_TOT}.**

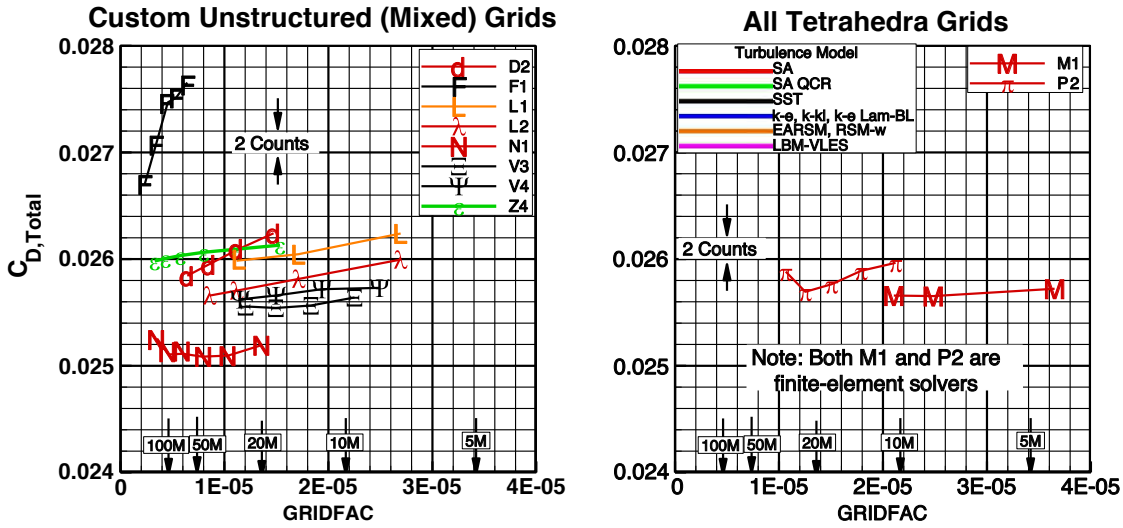


Figure S-VII-8. Grid Convergence; Custom Mixed and All–Tetrahedra Grids; Total Drag C_{D_TOT}.

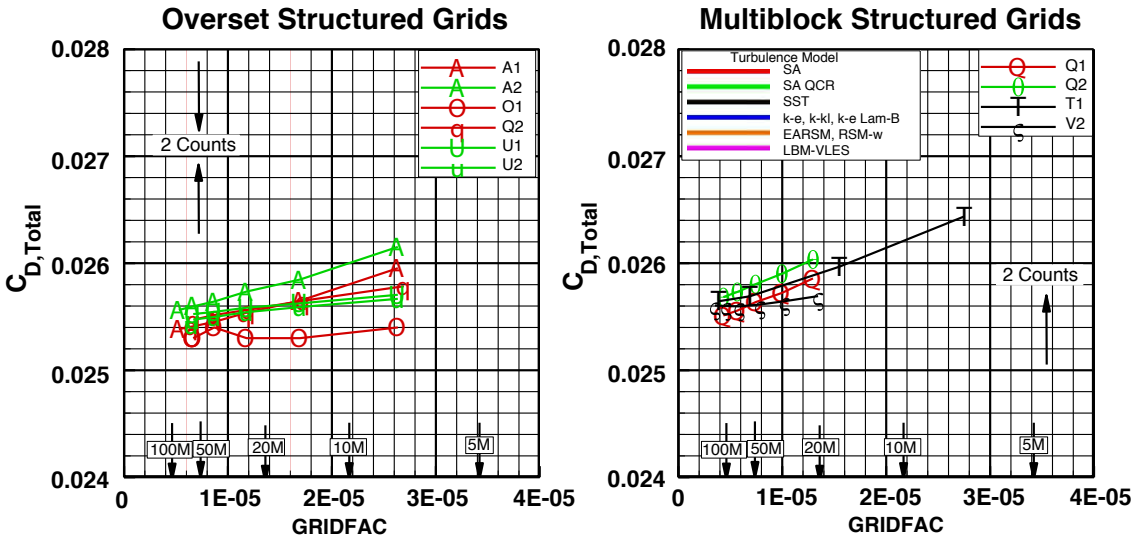


Figure S-VII-9. Grid Convergence; Overset and Structured Multiblock Grids; Total Drag $C_{D,TOT}$.

As illustrated in Figure S-VII-6, the value of drag at infinite grid resolution, C_D at GRIDFAC = 0, can be significantly different from that calculated on a finite grid. This would depend on the rate of drag change with decreasing GRIDFAC. This drag-grid convergence rate depends on the combination of code, grid, and turbulence model, and possibly other solver knobs. As we saw in Figure S-VII-7, the same code and grid (H1 and H2 EDGE code on Geolab grids) gave very different convergence rates depending on the turbulence model. Figures S-VII-10, -11, and -12 show convergence rate, dCDT/dGRIDFAC, the drag at infinite resolution, and the drag on a medium size grid. The medium size grid was the same size as that used for the angle-of-attack sweep and is typical of what might be used for general calculations. These values are shown for each data entry and are ordered by drag at infinite resolutions. Results are identified by the alphanumeric symbol assigned to each data entry and by the turbulence model used. Results for the Wing-Body-Tail from DPW-IV are shown in Figure S-VII-10, for the Wing-Body (as-built) from DPW-V in Figure S-VII-11, and for the Wing-Body (Aeroelastic) from DPW-VI in Figure S-VII-12. These values are listed in the tables in Appendix D. Note that these drag values may differ slightly from those previously published due to differences in the range of GRIDFAC used for calculating the linear slope.

The average of the drag at infinite resolution for the Wing-Body-Tail, shown in Figure S-VII-10, was 269.59 counts with a sigma of 8.09 counts. This average was for all solutions minus the solution U outlier. The omitted solution was so far removed from the others that it was not considered credible. Basing the drag on that obtained on the medium grid changes the average and sigma to 272.70 counts with a sigma of 8.54 counts. The changes in drag for each data entry correlate well with the convergence sensitivity. Solutions A and 4 have large values of convergence sensitivity and show the largest changes from the values at infinite resolution. Note that the drag value at infinite resolution of solution 4 was close to the average but was 30 counts lower on the medium grid.

For the Wing-Body (as-built), shown in Figure S-VII-11, the average of the drag at infinite resolution was 251.41 counts with a sigma of 5.25 counts. Considering the drag from the medium grid the average jumps to 258.75 counts with a sigma of 12.16 counts. This change is largely due to the large convergence sensitivity of solutions M, O, Q, and S that used the k-ε RT turbulence model. Solutions N, P, and R that used the same code and grids but used the Menter k-ω SST turbulence model had very low convergence sensitivity. Solution T used the same code and grid as solution S but with the SST turbulence model and also exhibited a large sensitivity similar to S.

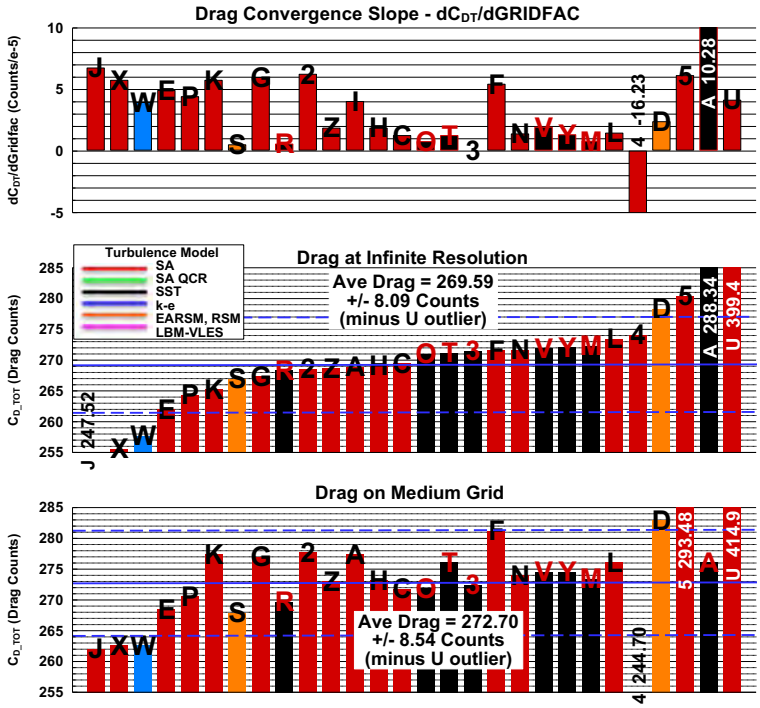


Figure S-VII-10. DPW-IV WBT Total Drag Grid Convergence Sensitivity.

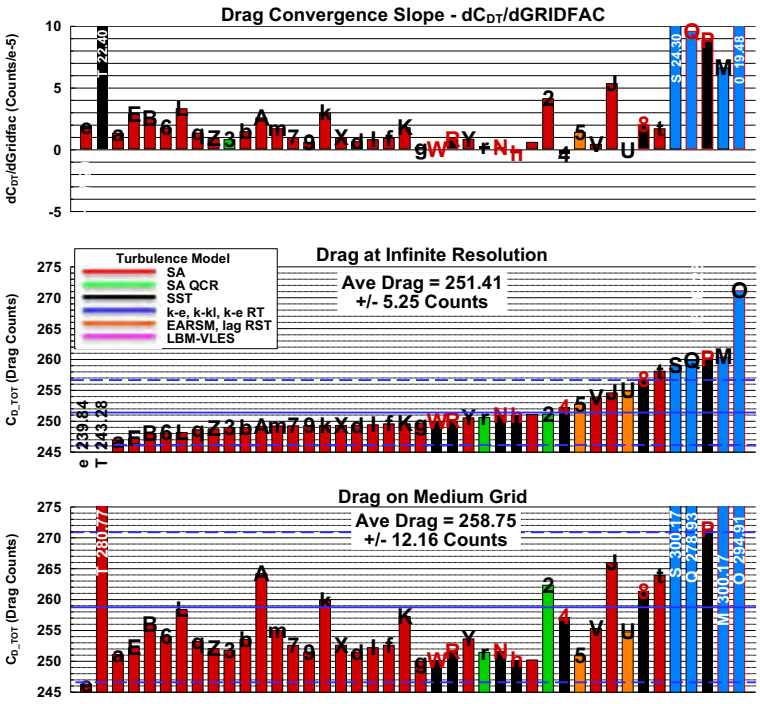


Figure S-VII-11. DPW-V WB (As-Built) Total Drag Grid Convergence Sensitivity.

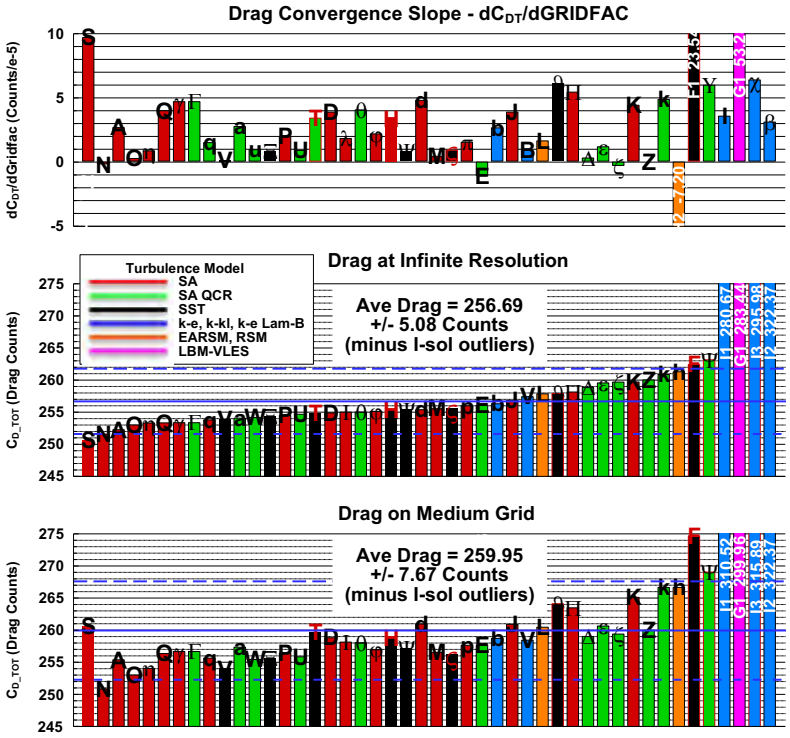


Figure S-VII-12. DPW-VI WB (Aeroelastic) Total Drag Grid Convergence Sensitivity.

The average of the drag at infinite resolution for the Wing-Body (aeroelastic) shown in Figure S-VII-12, was 256.69 counts with a sigma of 5.98 counts. Here the I-solutions were considered outliers due to the lack of convergence linearity. Considering the drag from just the medium grid the average jumps to 259.95 counts with a sigma of 7.67 counts. Obviously these average and sigma values are somewhat dependent on which solutions are considered outliers and ignored.

The differences between the drag values for the medium grids and at infinite resolution were of the order of three to four drag counts or less. These differences might be important depending on the application. The reality is that these types of convergence studies are rarely, if ever, performed and can give significantly different results depending on the choice of turbulence model, grid, and solver. The calculation of absolute drag is, for the most part, an illusion. How would we know if our calculations were correct? We can't measure absolute drag for a comparison basis. Every experiment has many uncontrolled variables and corrections. We account for all of these in either the wind tunnel or in flight by conducted a detailed uncertainty quantification or assessment. An uncertainty bound (which includes identified errors and estimates of possible unidentified error sources) is applied to all the data. The more important question is "can we predict, and measure increments accurately enough?"

B. Drag; CRM Wing-Body-Nacelle-Pylon: DPW-VI

DPW-VI Case 2 focused on computing the drag increment between the CRM Wing-Body-Nacelle Pylon and the CRM Wing-Body configurations. This included a grid refinement study for both configurations at $M = 0.85$, $C_L = 0.500$, and a Reynolds number of 5 million. Grid convergence plots for total drag (C_{D_TOT}), pressure drag (C_{D_PR}), and skin friction drag (C_{D_SF}) are shown in Figure S-VII-13 for the Wing-Body-Nacelle-Pylon configuration. The results are very similar to those seen in Figure S-VII-2 for the DPW-VI Wing-Body. A closer look is shown in Figure S-VII-14 for total drag broken out by grid and turbulence model. Again, fortunately, the results are very similar to those for the Wing-Body shown in Figures S-VII-7, -8, and -9.

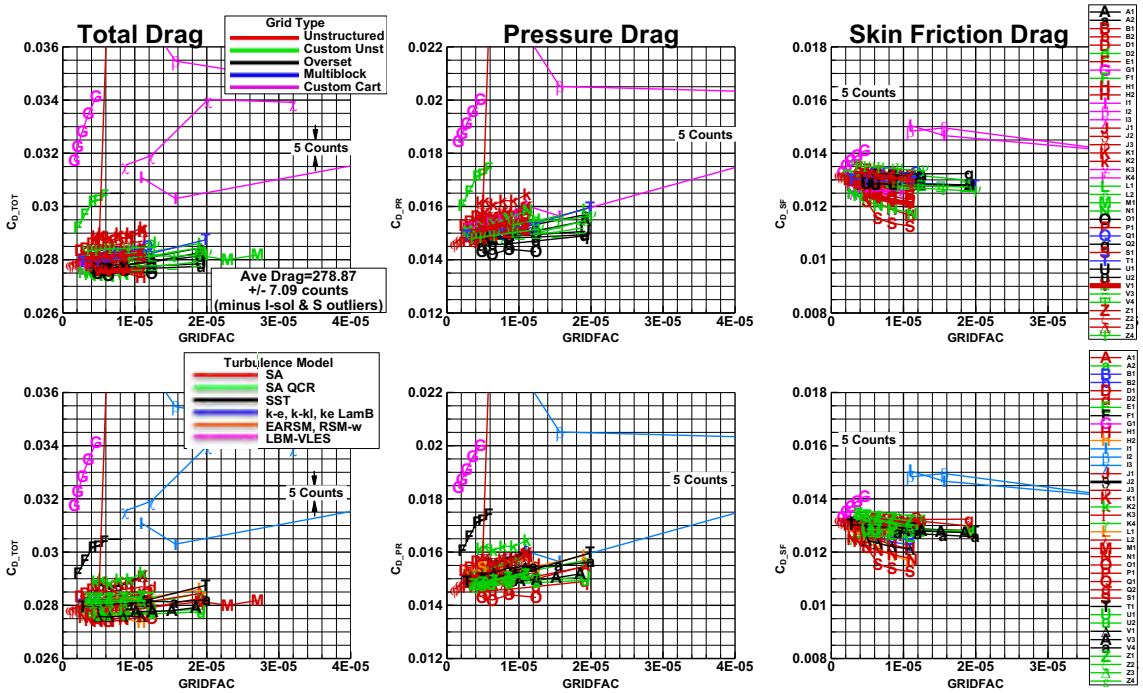


Figure S-VII-13. Grid Convergence; Wing-Body-Nacelle-Pylon; Drag C_{D_TOT}, CD_{PR}, C_{D_SF}.

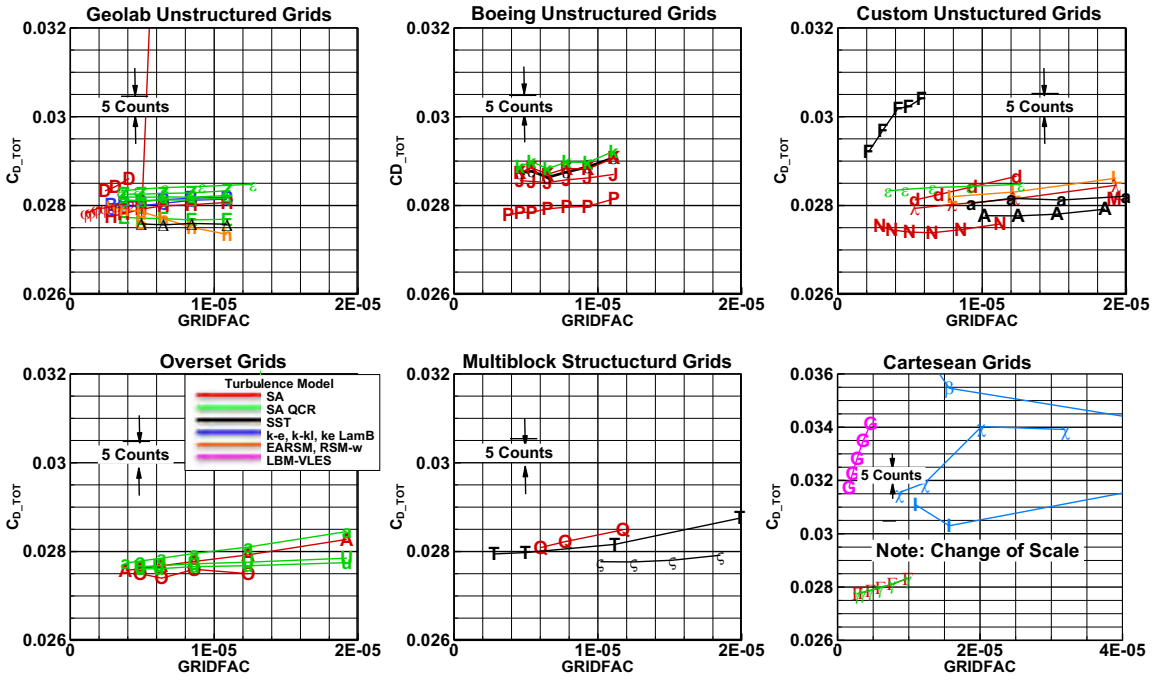


Figure S-VII-14. Grid Convergence; Wing-Body-Nacelle-Pylon: Drag by Grid and Turbulence Model.

Similar to Figure S-VII-12 for the Wing-Body, Figure S-VII-15 shows convergence rate, dCDT/dGRIDFAC, the drag at infinite resolution, and the drag on a medium size grid for the Wing-Body-Nacelle-Pylon. The average of the

drag at infinite resolution for the Wing-Body-Nacelle-Pylon (aeroelastic) was 279.50 counts with a sigma of 5.76 counts. Here the S- and I-solutions were considered outliers due to the lack of convergence linearity. Considering the drag from just the medium grid the average jumps to 282.70 counts with a sigma of 9.27 counts.

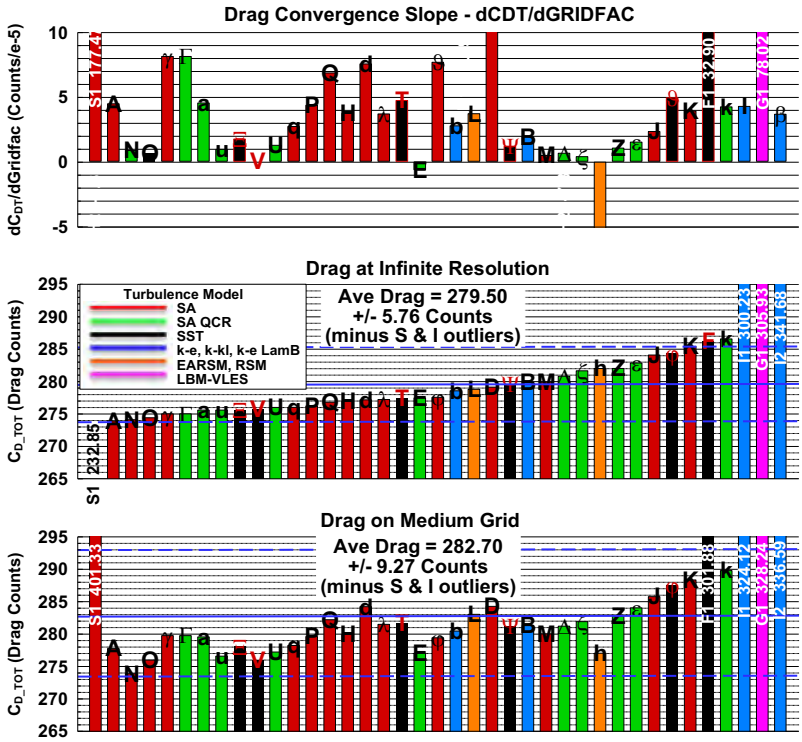


Figure S-VII-15. WBNP (Aeroelastic) Total Drag Grid Convergence Sensitivity.

C. Drag Increment: CRM Wing-Body and Wing-Body-Nacelle-Pylon; DPW-VI.

The objective here is to see how accurately CFD can compute the difference between two configurations of interest. In this case, it is the drag increment between the CRM Wing-Body-Nacelle-Pylon and the CRM Wing-Body. While measuring absolute values of drag may not be feasible, decades of wind tunnel experience have shown that with a carefully crafted wind tunnel test campaign, drag increments between similar configurations can be accurately measured. Both CRM configurations were tested in the National Transonic Facility and at the Ames 11-foot Transonic Tunnel at the same flow conditions. Taking data from three repeat runs for each configuration in each wind tunnel led to 18 sets of increments that were combined to yield the experimentally determined drag increment of 22.8 counts with a sigma of 1.2 counts.

For the CFD increment we will take for each data entry the results for the two configurations and differ them. The gridding guidelines were designed to minimize the gridding differences between the two configurations other than the geometric differences. Drag differences were taken three different ways. Scheme I took drag from entry pairs interpolated to mutually common values of GRIDFAC. The resulting increments are shown in Figure S-VII-16 for the different grid and turbulence model types. This shows many of the solutions converging to the wind tunnel estimate. Scheme II differs the drag at infinite resolution between entry pairs, and Scheme III differs the drag on a medium grid. These last two schemes are illustrated in Figure S-VII-17. Because of the added complexity of the Wing-Body-Nacelle-Pylon compared to the Wing-Body, its medium grid will be larger and at a smaller GRIDFAC

value. In practice, Scheme III represents how drag increments are calculated in CFD. Figure S-VII-18 shows convergence rate, dCDT/dGRIDFAC, the drag increment at infinite resolution using Scheme II, and the drag increment on a medium size grid using Scheme III. The values of dCDT/dGRIDFAC are for the Wing-Body configuration and are very similar to those of the Wing-Body-Nacelle-Pylon values. The average of the drag increment at infinite resolution for the difference between the Wing-Body-Nacelle-Pylon and the Wing-Body was 22.7 counts with a sigma of 1.6 counts. This is almost identical to the experimental value. Considering the drag from just the medium grid, Scheme III, the increment jumps to 25.9 counts with a sigma of 5.0 counts. Solutions with large convergence values yielded drag on the medium grids quite different than that at infinite resolution. The range of the experimental drag increment is also shown on the plots. The CFD drag increment predictions were within or very close to the experimental values for many cases. Most (24 out of 36) of the drag increments calculated in the continuum were within the experimental 1-sigma tolerance. Only 8 out of 36 made it by just differencing the medium grid results. Those were all characterized by a low drag/grid convergence (dCDT/dGRIDFAC) rate. CFD can and does do a very credible job at calculating drag increments if done carefully; it helps if the drag/grid convergence rate is low.

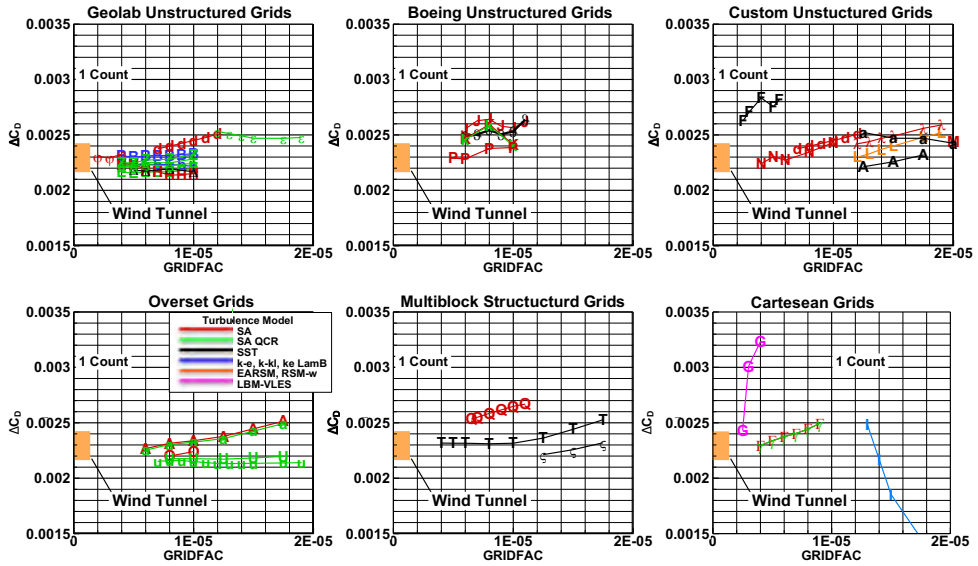


Figure S-VII-16. Grid Convergence; Nacelle-Pylon Drag Increment by Grid Type and Turbulence Model.

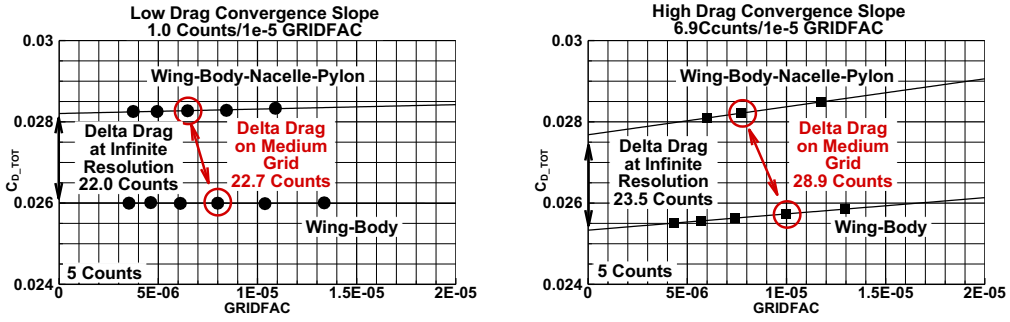


Figure S-VII-17. Potential Impact of Grid Drag Convergence Slope on Drag Increment.

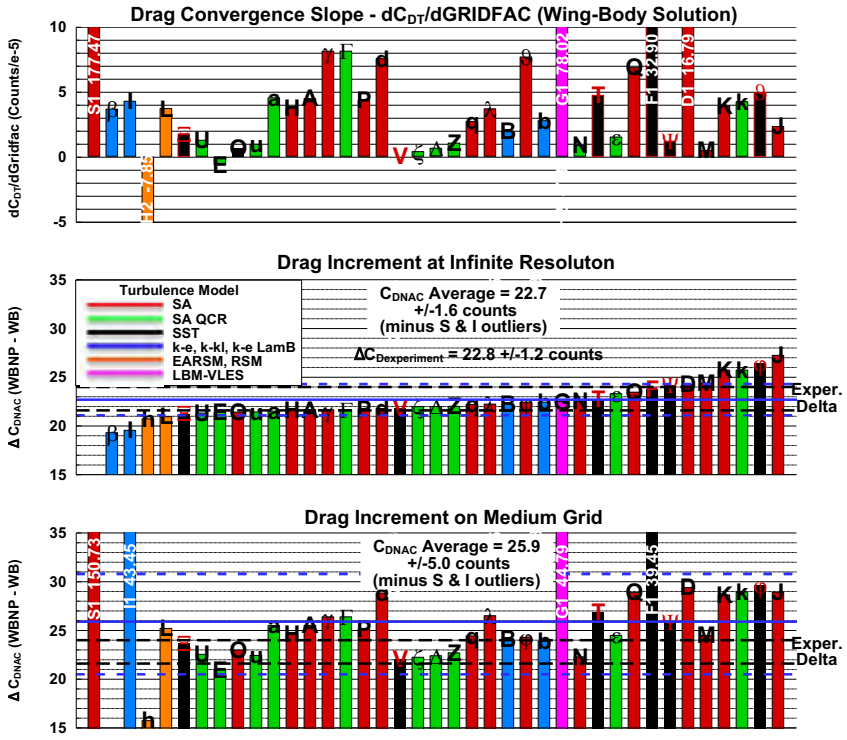


Figure S-VII-18. Nacelle-Pylon Drag Increment Sensitivity on Grid Convergence.

Again, as a reminder, the grid convergence charts are broken out into far greater detail in Appendix D. Plots are broken out by grid type, turbulence model, and in some cases by solver.

D. Pressure Distributions: DPW-IV, -V, and -VI.

In addition to looking at the grid convergence characteristics of forces and moments, it is useful to also look at pressure distributions. Figures S-VII-19 and -20 show wing pressure distributions at two span stations on the CRM Wing-Body-Tail from DPW-IV. Shown are distributions on each of the four different grid sizes used in study. Note that as the grid size increases, the shock sharpens up. The difference between solutions also appears to decrease going from the coarse to the fine grid. Fewer solutions were submitted for the extra fine grid, so it cannot be determined if this trend would have continued. With the exception of one entry, the shock position at wing station 13, $\eta = 0.846$, seems to have settled at one of two locations depending on the turbulence model used: SA or SST. (Note that this distinction cannot be determined from this figure but is based on prior knowledge of the solution turbulence models. The shocks from the SST model are further forward.)

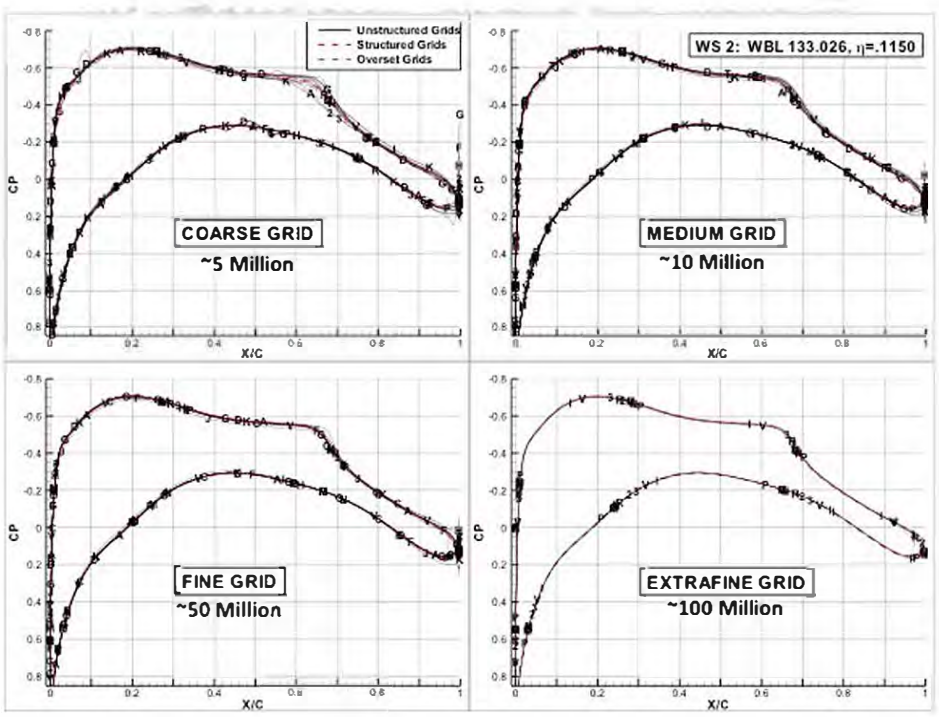


Figure S-VII-19. DPW-IV: WBT Wing Pressure Distribution; Grid Convergence; WBL133, η = 0.115.

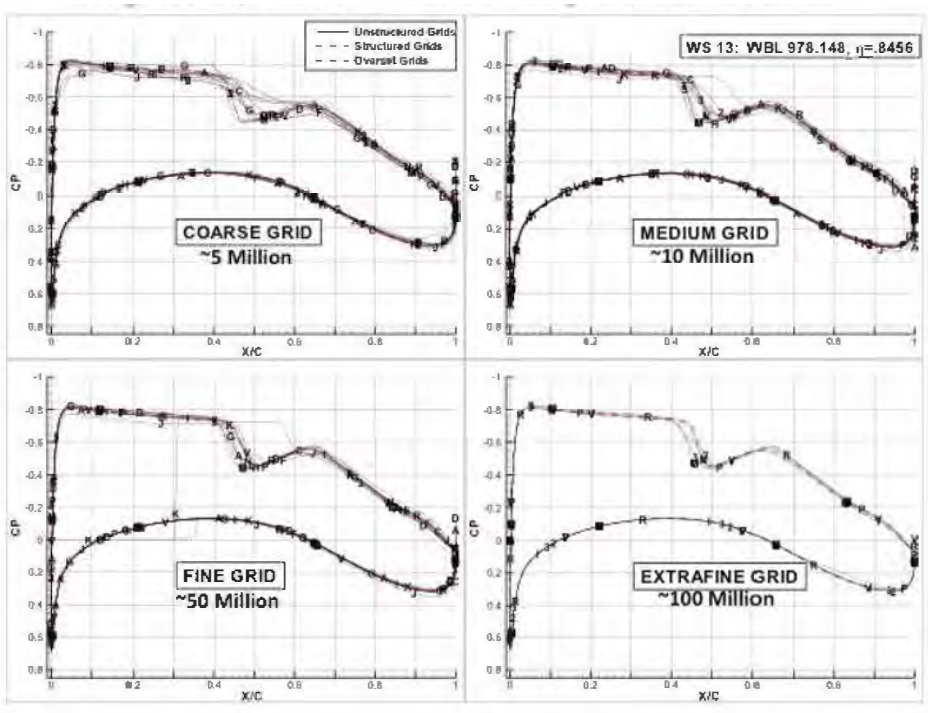


Figure S-VII-20. DPW-IV: WBT Wing Pressure Distribution; Grid Convergence; WBL878, η = 0.846.

Effects of grid refinement are shown in Figure S-VII-21 for a midspan station ($\eta = 0.502$) on the CRM Wing-Body (as-built) in DPW-V. Note that fewer pressure data sets were provided for Levels 1, 5, and 6; that should be

taken into account as it magnifies the decrease in scatter at higher grid resolutions. There is no fundamental change in shock location with the finer grids. There are no observable trends with grid type in the pressure distributions. (The data for entry "k" is correct as submitted; there is no explanation for the apparent shift in pressure.) A closer look is taken for four solutions at a further outboard station ($\eta = 0.727$) shown in Figure S-VII-22. Solutions N, U, and 4 show little change going from the coarsest grid (L1) to the finest. These solution sets also exhibited a low grid convergence rate, dCDT/dGRIDFAC. Solution M showed a significant change in shock location with grid level and also exhibited a higher grid convergence rate. Note that solutions M and N used the same solver and grid family but differed in turbulence model. The behavior of solution M and others using the k-ε RT turbulence model are not necessarily representative of other solver/grid/turbulence model sets with "higher" grid convergence rates.

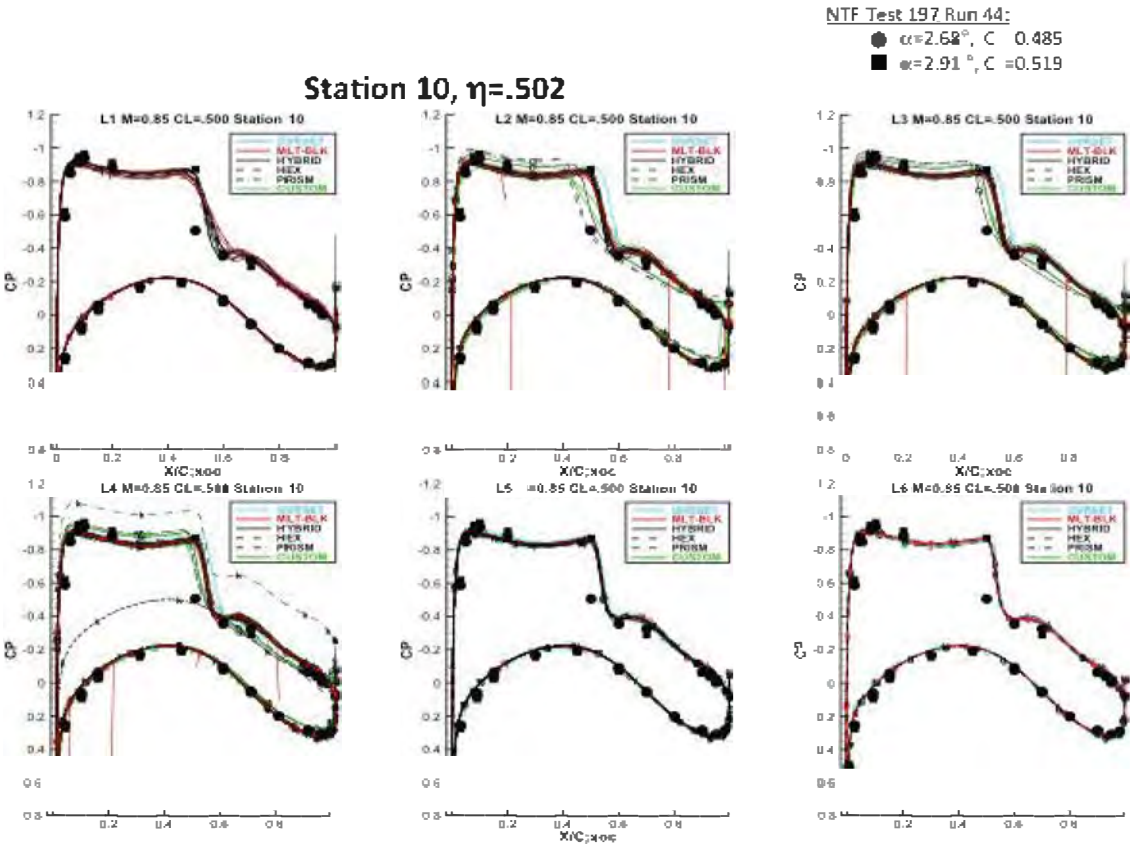


Figure S-VII-21. DPW-V: WB (As-Built) Wing Pressure Distribution; Grid Convergence: η = 0.502.

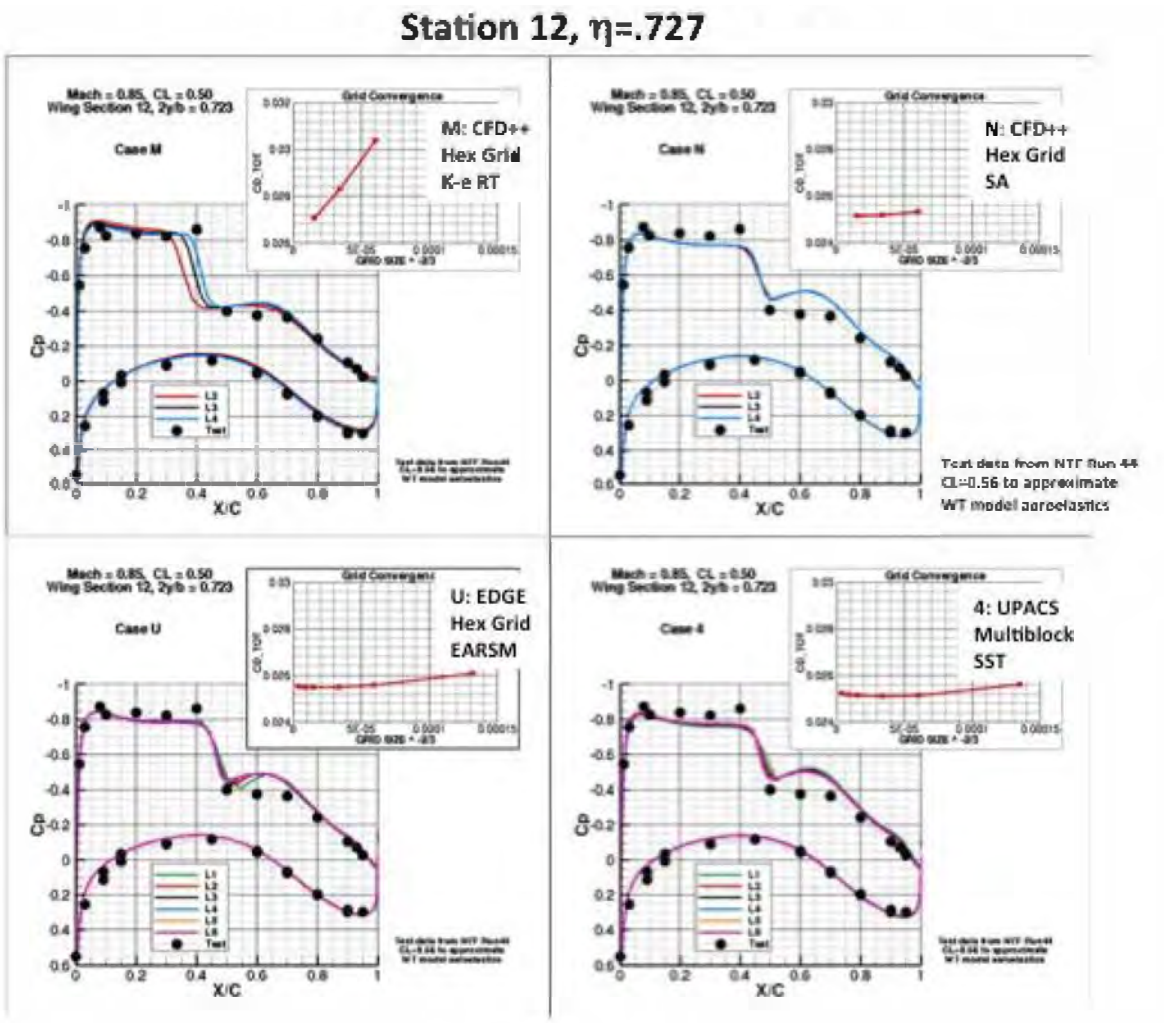


Figure S-VII-22. DPW-V: WB (As-Built) Wing Pressure Distribution; Convergence: η = 0727; Select Solutions.

Wing pressure distributions at three wing stations from four data sets for the Wing-Body (Aeroelastic) configuration from DPW-VI are shown in Figures S-VII-23 and -24. The pressure distributions are from three grid sizes, L1, the smallest, to L7, the largest. In these comparisons, experimental data from the Ames 11-foot TWT test are shown for two different lift coefficient, C_L, values that bracketed the computational value of $C_L = 0.50$. Figure S-VII-23 shows the results for P1 (BCFD) using the Boeing unstructured grid family and the SA-RC turbulence model, and K4 using a custom Cartesian grid family along with an SA-noft2 with a QCR2000 turbulence model. Figure S-VII-24 shows results from G1, a Lattice-Boltzmann method with its own Cartesian grid and its own VLES turbulence model [89]. Figure S-VII-24 also shows results from H2, a conventional finite volume code (EDGE), using the Geolab unstructured grid family and an EARSM turbulence model. There is very little difference in the distributions due to grid size from the four solutions. Similar comparisons from other data sets showed similar variation. This is an indication that even the smallest grids were already quite adequate for predictions of pressure distributions.

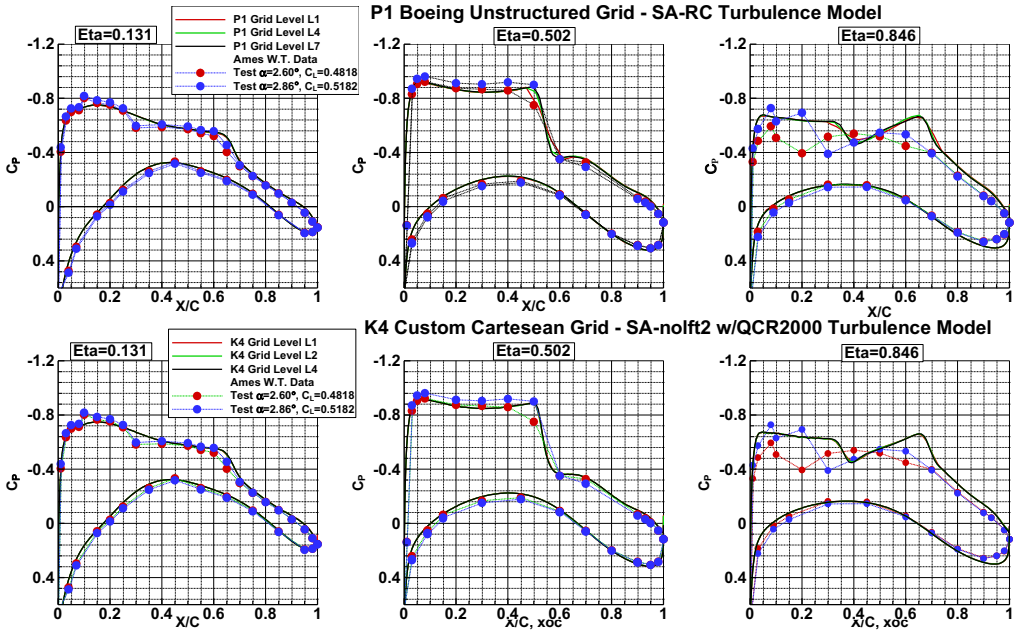


Figure S-VII-23. DPW-VI: WB (Aeroelastic) Wing Pressure Distributions; Grid Convergence: η = 0.131, 0.502, and 0.846; Solutions P1 and K4.

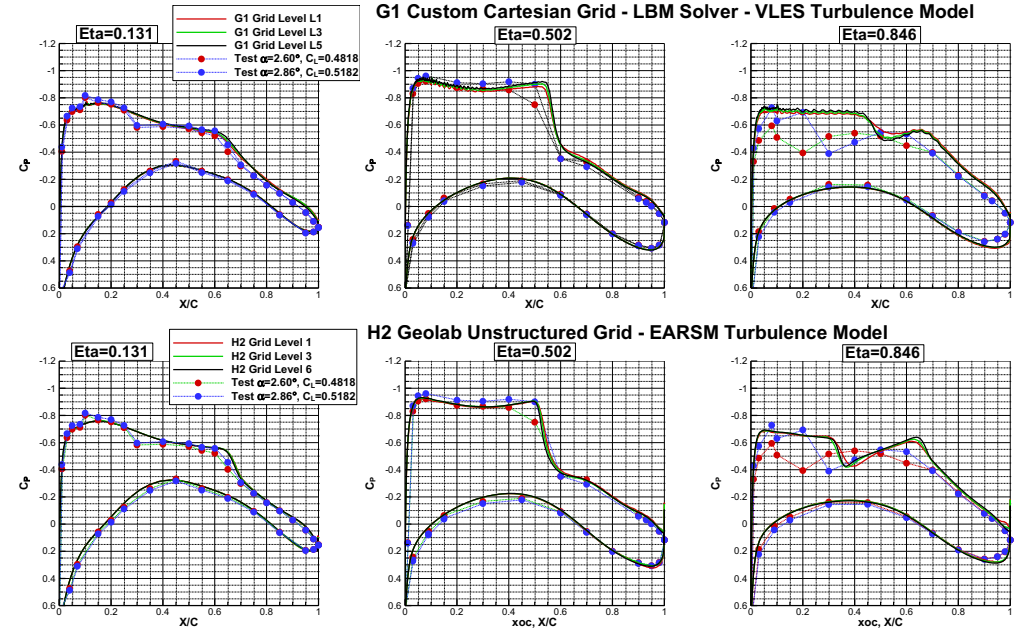


Figure S-VII-24. DPW-VI WB (Aeroelastic) Wing Pressure Distributions; Grid Convergence: η = 0.131, 0.502, and 0.846; Solutions G1 and H2.

Pressure distributions from the finest grid for the Wing-Body from each solution set submitted for DPW-VI are shown in Figure S-VII-25. It should not be too surprising that, with the exception of distributions for the solution I2, there is little difference between all the solutions. The differences between the remaining solutions are seen mainly in the shock location with the differences increasing on the outboard wing stations. Wing and nacelle pressure distributions from the finest grid for the Wing-Body-Nacelle-Pylon configuration from each solution set submitted are shown in Figures S-VII-26 and -27. Similar to that of the Wing-Body, very little difference is seen between wing pressures for the Wing-Body-Nacelle-Pylon sets. Nacelle pressure distributions were submitted by less than half of the participants. These were practically indistinguishable from one another.

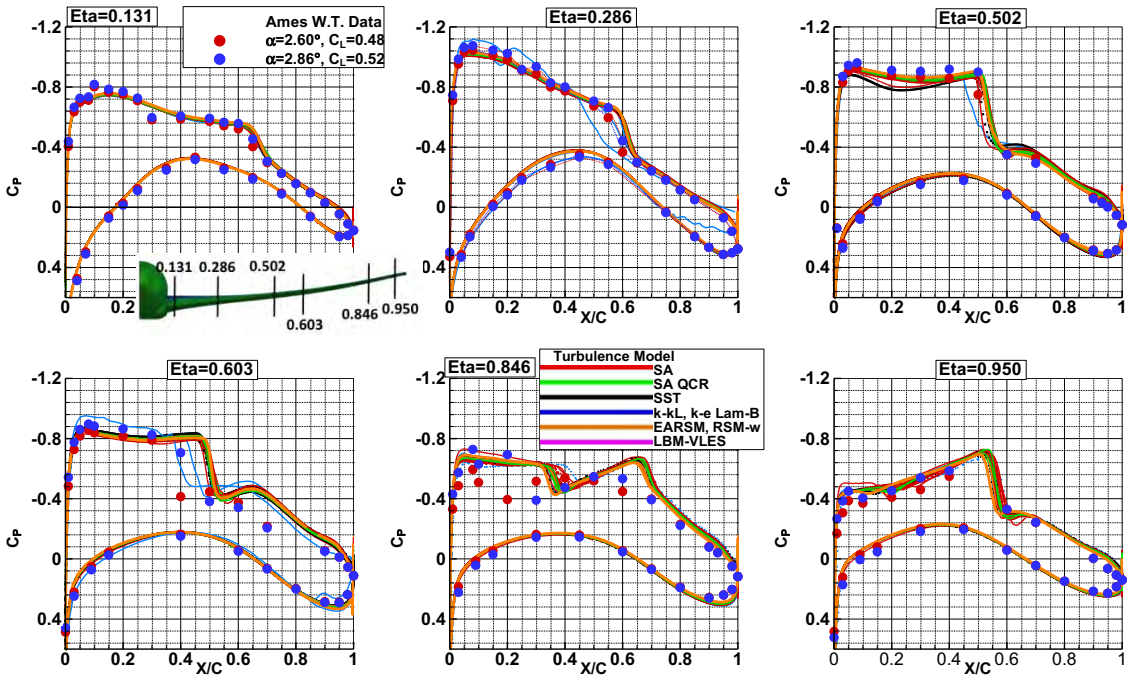


Figure S-VII-25. DPW-VI: WB (Aeroelastic) Wing Pressure Distributions; Finest Grid; All Solutions.

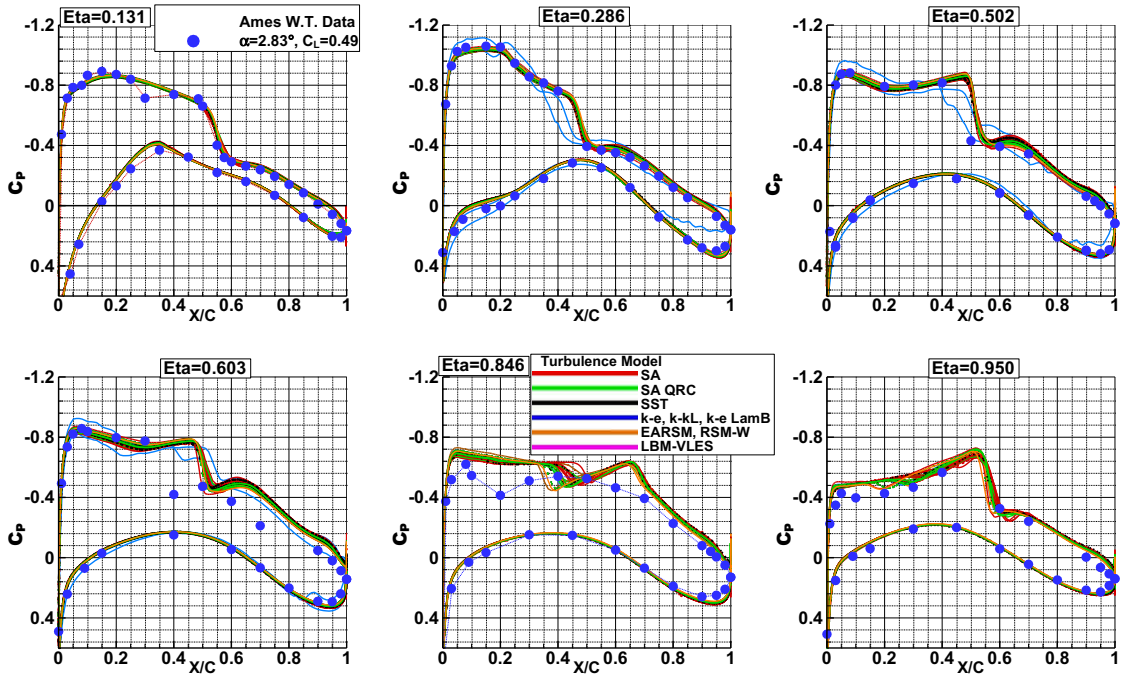


Figure S-VII-26. DPW-VI: WBNP (Aeroelastic) Wing Pressure Distributions; Finest Grid: All.

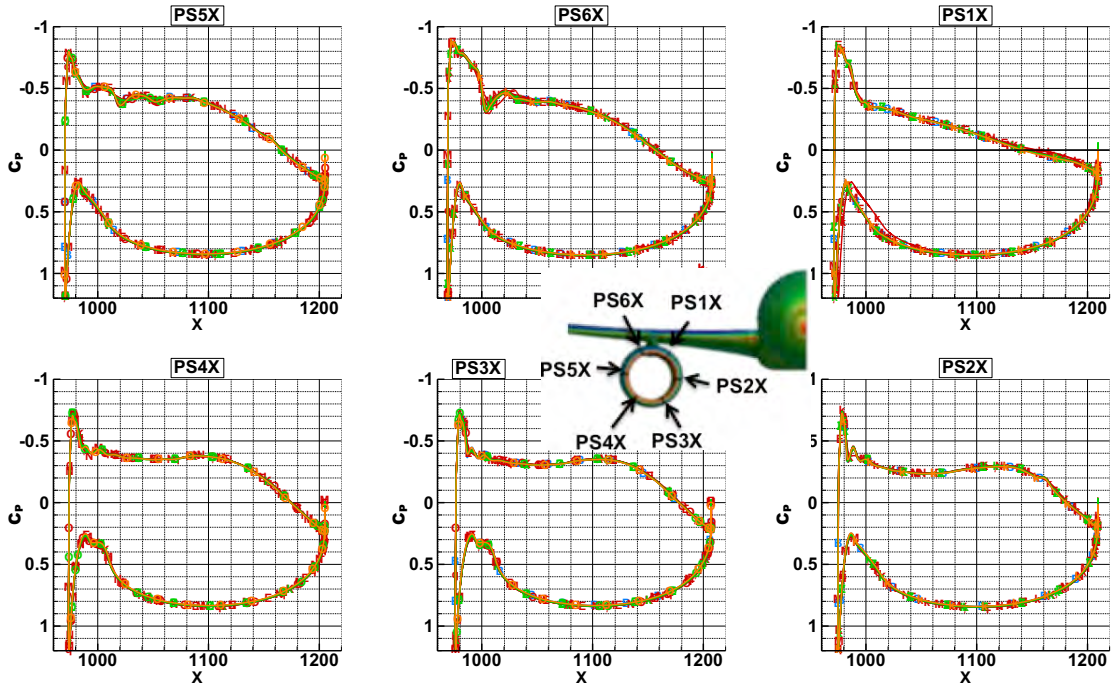


Figure S-VII-27. DPW-VI: WBNP (Aeroelastic) Nacelle Pressure Distributions; Finest Grid; All Solutions.

New for DPW-VI, wing section characteristics, lift (normal force) and pitching moment coefficients were requested. These are obtained by integrating pressure coefficient, Cp, vs. chord fraction, x/c. Less than half of the participants submitted these data sets. Figure S-VII-28 shows a comparison of wing section characteristics as a function of span fraction, η, for both the Wing-Body and Wing-Body-Nacelle-Pylon configurations. Given that there is little difference in wing pressures between data sets for the two configurations, it is not surprising that the resulting section lift (normal force) and pitching moment characteristics are nearly identical at the scale plotted in this figure. It is interesting to note that there is little difference in the section characteristics between the two configurations from either the computational or experimental results. The differences in either the CFD or test between the two configurations are mainly just outboard of the nacelle. However, there is a very significant difference between the CFD and the experimental section characteristics on the outboard part of the wing. These differences will be discussed in more detail in Sections X and XV.

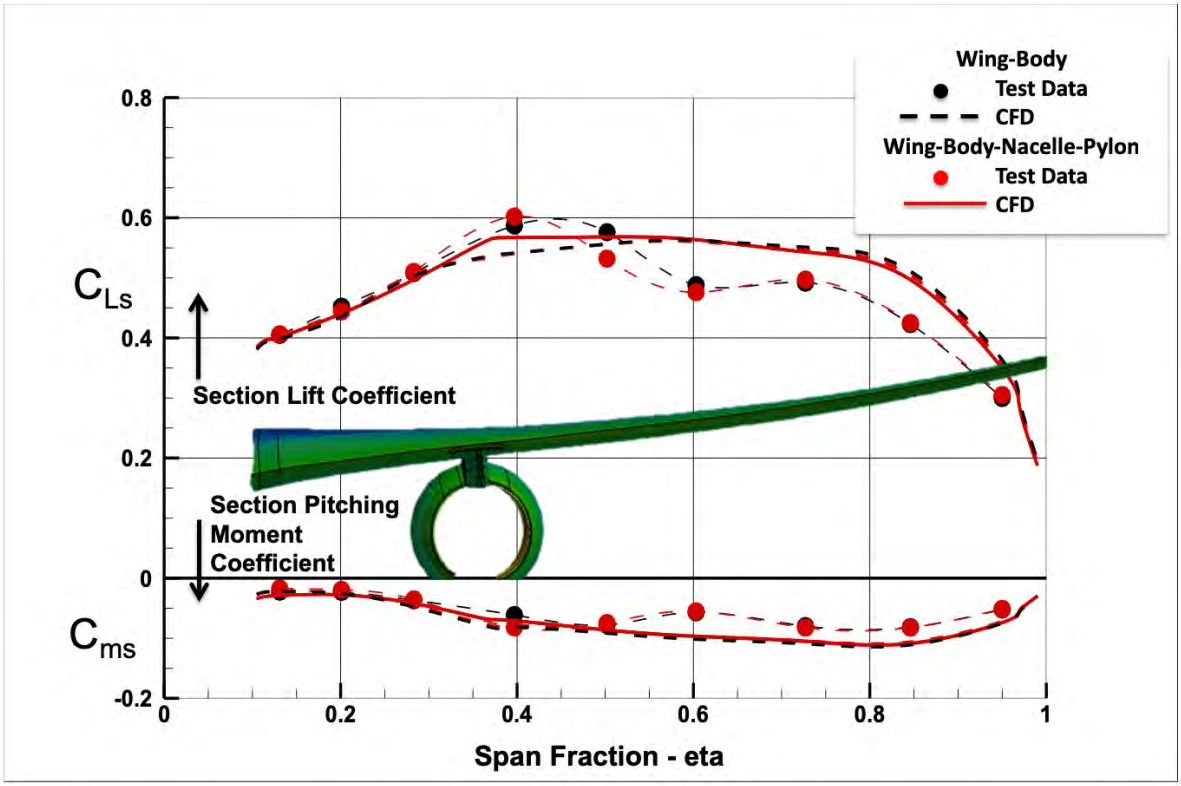


Figure S-VII-28. CRM WBNP and WB Wing Section Lift and Moment; M = 0.85, C_L = 0.50.

The Wing-Body grid convergence study in DPW-VI showed a steady improvement over the similar study in DPW-V, especially with respect to unstructured grids. As a whole, the solutions exhibited a "tighter" convergence of total-drag to the continuum with a spread of less than 10 drag counts. The grid convergence study for the Wing-Body-Nacelle-Pylon showed a somewhat greater spread. Only four entries would be considered to be significant outliers. The prediction of the drag increment between the two configurations is significantly important to industry design processes. Here we found that most participants were able to predict the drag increment within the uncertainty of the test data. With the exception of one case, there was very little difference seen in the wing or nacelle pressure distributions, or in wing section lift and pitching moments, due to grid type, turbulence model, convergence level, or solver. Results of a statistical analysis of DPW-VI Case 2 are presented in Ref. 75.

Section VIII: Drag Rise Study

It is important to be able to predict the drag rise characteristics of an aircraft, as this will establish the nominal cruise point. Failure to meet the predicted drag rise characteristics in flight test can lead to a very expensive "fix-it" program, and eventual failure of the commercial program [9292]. An optional case in DPW-IV was a Mach sweep or drag rise study. Solutions at fixed C_Ls of 0.40, 0.45, and 0.50 were requested for a range of Mach numbers from 0.70 to 0.87 at a chord Reynolds number of 5 million. No wind tunnel data had been acquired at that time, but it has since been made available and will be presented here.

Drag solutions are shown compared to NTF and 11-Foot data in Figures S-VIII-1, -2, and -3 for fixed lift coefficients, C_L, of 0.50, 0.45, and 0.40. Drag levels between the two tunnels differed by about 0.00077. This amount was arbitrarily added to the 11-Foot data to raise it to the same level as the NTF data. The result shows approximately the same drag rise shape from the two facilities. To further facilitate comparing the drag rise shape with the CFD results, an arbitrary 0.0010 (ten drag counts) was added to the NTF data in the curve labeled Drag Rise Shape. With the exception of one obvious outlier and two near outliers the solutions lie within a 10-count band and reasonably match the drag rise shape. The experimental drag rise at a $C_L = 0.50$, shown in Figure S-VIII-1, appears slightly steeper above Mach = 0.83 than the CFD results. The shape is better matched at the lower lift coefficients. In all, the drag rise shape is well predicted.

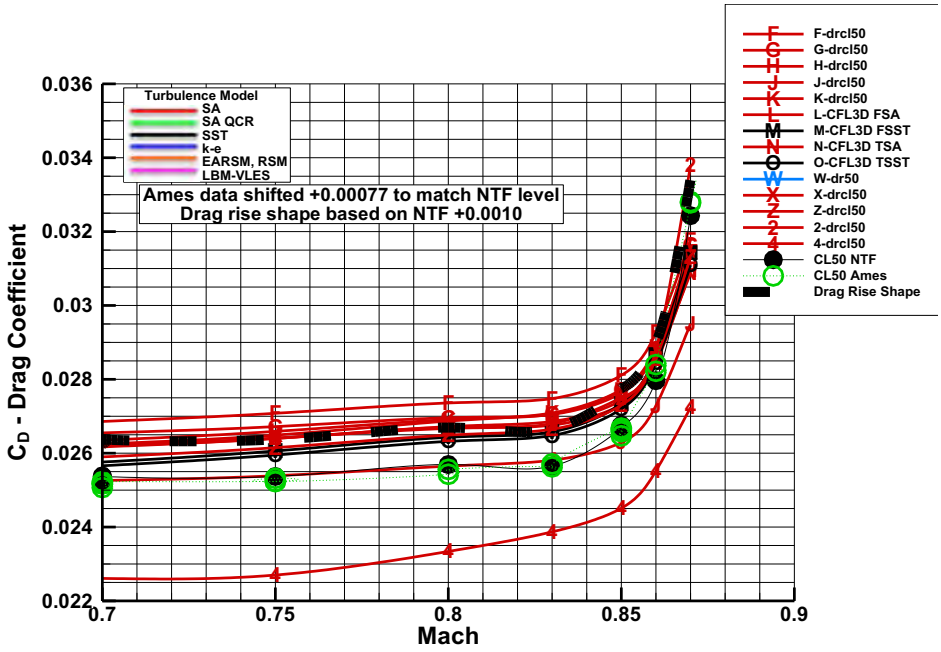


Figure S-VIII-1. Drag Rise CRM Wing-Body-Tail; iH = 0, C_L = 0.50.

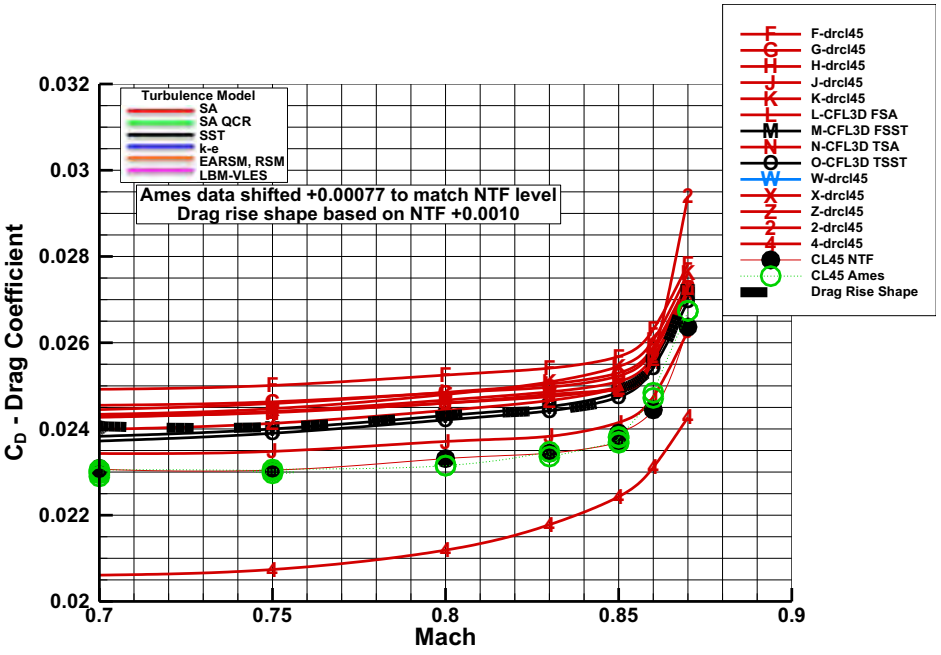


Figure S-VIII-2. Drag Rise CRM Wing-Body-Tail; iH = 0, C_L = 0.45.

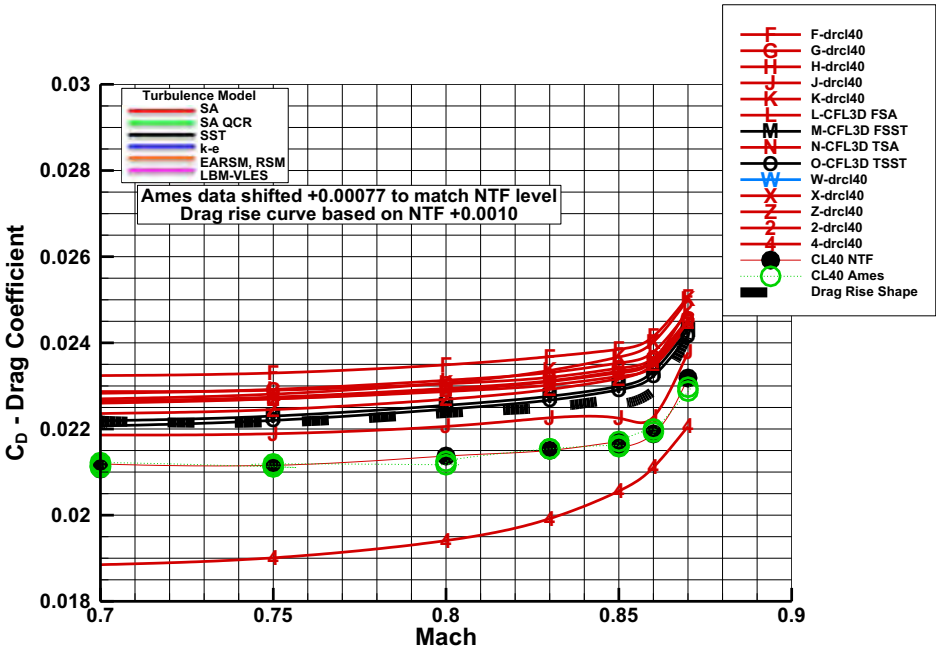


Figure S-VIII-3. Drag Rise CRM Wing-Body-Tail; iH = 0, C_L = 0.40.

Section IX: Reynolds Number Study

The ability to adequately predict flight characteristics of a design, whether it be an all new airplane, or a modification to an existing airplane is of the utmost importance. Failure to meet performance guarantees can lead to expensive "fix-it" programs as noted in the previous section. Likewise, failures to meet regulatory requirements can also result in very expensive "fix-it" programs. In addition to added expense, either failure can lead to significant delays in delivering the aircraft to the customer, and eventual financial failure of the program. A new airplane program involves tens of thousands of aerodynamic data points to define the performance, loads, stability and control, and handling characteristics. Most of these data are acquired in low Reynolds number wind tunnels. In more recent years, these data are being augmented by high Reynolds number (cryogenic) wind tunnel testing, and by CFD. Failure to "scale" data from low Reynolds number to flight values can take the form of missing drag levels and/or changes of the pressure distribution and flow separation characteristics affecting loads, stability and control characteristics, etc. [93].

Unique to DPW-IV was a Reynolds number study that called for a fixed-C_L ($C_L = 0.50$) single point solution for two Reynolds numbers on a medium grid for the CRM Wing-Body-Tail iH = 0°. configuration. For the 5 million chord Reynolds number solution, the same medium grid used for other cases in DPW-IV was used. For the 20 million chord Reynolds number solution a new grid of similar or identical size was developed to ensure that equivalent y^+ spacing at the viscous surfaces were maintained between Reynolds number solutions. Wind tunnel test data on the configuration is available from both the National Transonic Facility and the European Transonic Wind Tunnel facility. Note that these data were obtained after the DPW-IV workshop. Drag polars from the two wind tunnels are shown in Figure S-IX-1. The test data are from several runs at the two Reynolds numbers. Similar corrections to the test data were applied by their respective facilities. At the 5 million chord Reynolds number, the drag polars from the two facilities are almost identical. This is not the case at 20 million Reynolds number. The data from the ETW facility show a lower drag over most of the lift coefficient range shown. At a $C_L = 0.50$, the drag increment between the two Reynolds numbers was 21.6 counts with a sigma of 1.0 count from the NTF, and 33.3 counts with a sigma of 0.6 counts from ETW. Note that the sigma from ETW may have been smaller just because there were few runs to differ. Lift and pitching moment data are shown for the two Reynolds numbers in Figure S-IX-2. Note that the ETW data show the anticipated effect of increasing Reynolds number, i.e., lift increases at a fixed angle of attack and pitching moment becomes more negative. The NTF data do not show this trend.

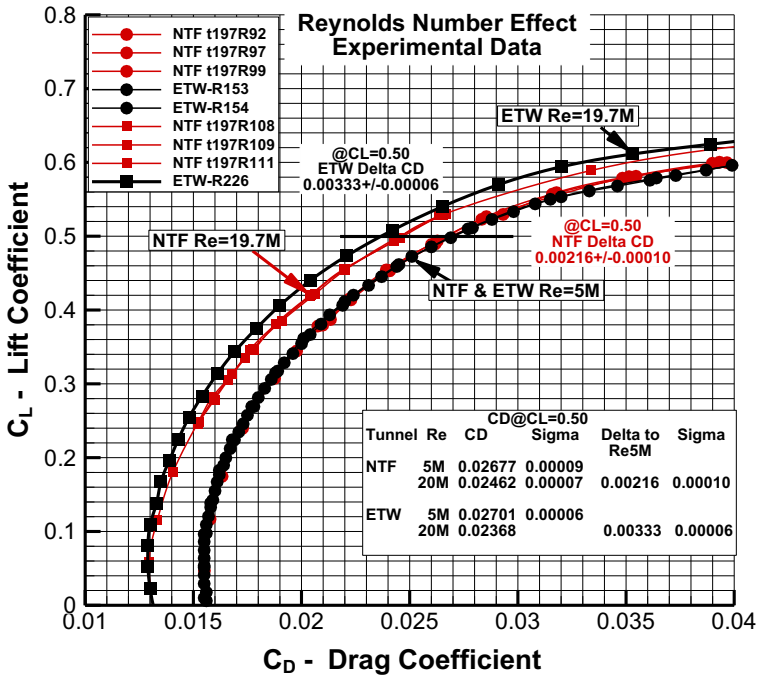


Figure S-IX-1. WBT Drag Polar; 5 and 20 Million chord Reynolds Number.

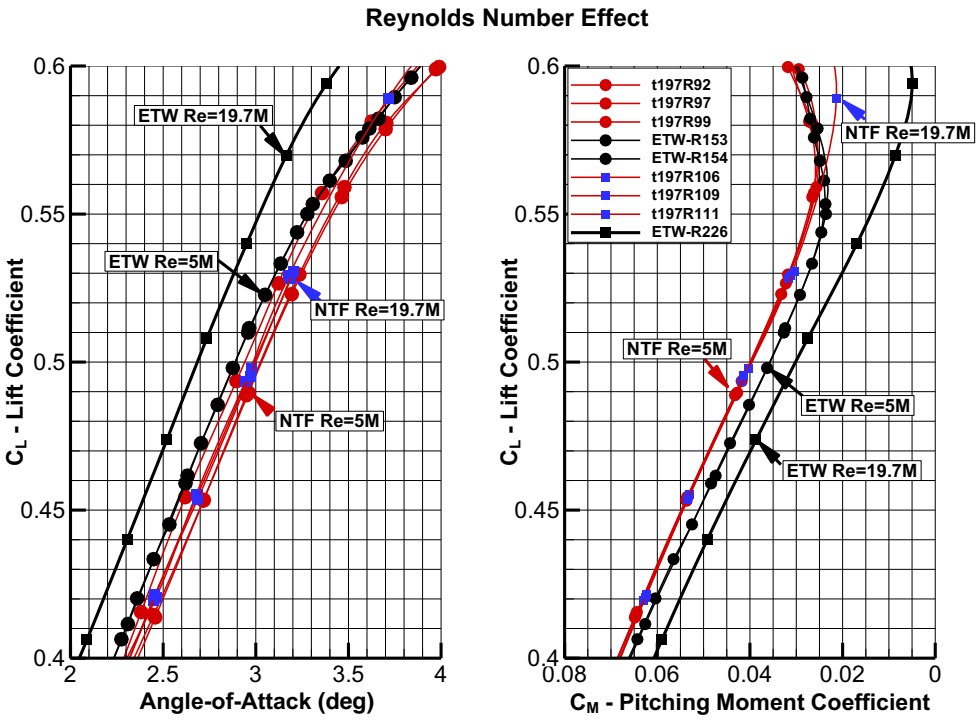


Figure S-IX-2. WBT Lift and Pitching Moment: 5 and 20 Million chord Reynolds Number.

Figure S-IX-3 shows the Reynolds number increments from the DPW-IV data entries and the experimental data. Increments are shown for total, pressure, and skin friction drag at a lift coefficient of $C_L = 0.50$. The CFD results are

identified by the alphanumeric symbol assigned to each data entry and are segregated by turbulence-model type: SA or SST. The data entry/identifiers are listed in Appendix C. Entry data were not received for other turbulence models. Typical "Reynolds number scaling" for drag will try to account for the difference in skin friction drag between the two Reynolds numbers. Here we see that the change in skin friction drag accounts for 2/3 of the change of total drag. The rest is due to changes in pressure drag. More surprisingly, the choice of turbulence model has little effect on the skin friction drag on the increment. It is the pressure drag increment that sees the bigger influence of turbulence model. This could be related to the differences in shock location between the two turbulence models.

Figure S-IX-4 shows the Reynolds number increments for drag, pitching moment, and angle of attack at a lift coefficient of $C_L = 0.50$ compared to experimental data. The first thing that strikes the eye is that all of the CFD data are clustered around the ETW increments and away from the NTF. This could be a case of CFD data validating the experimental results. The SA results yield a drag increment of approximately 31 to 33 counts while the SST results are around 35 counts. The ETW increment is in between the two. Most of the CFD results are within 1 to 2 counts of the ETW increment. Similarly, the pitching moment and angle of attack increments are also reasonably close to the corresponding ETW increment. More research should be done to better understand the consistency and accuracy of both the computational and experimental data.

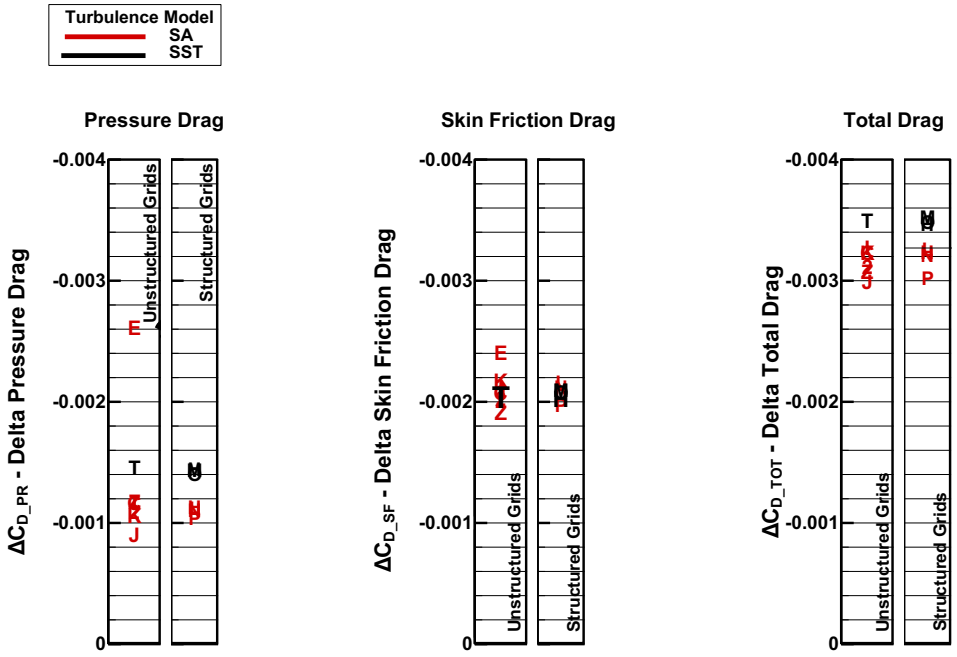


Figure S-IX-3. WBT Reynolds Number Effect on Total, Pressure, and Skin Friction Drag Increment (Re20M – Re5M).

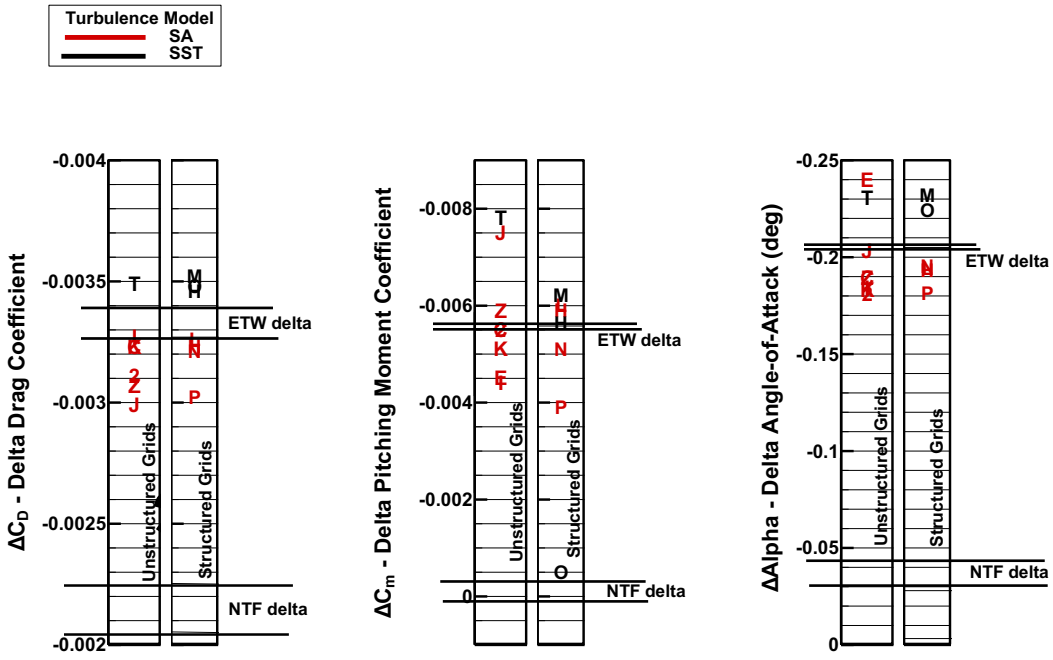


Figure S-IX-4. WBT Reynolds Number Effect on Total Drag, Pitching Moment, and Angle of Attack Increment (Re20M – Re5M).

Wing pressure distributions for the 20 million chord Reynolds number solutions were not asked for in DPW-IV. Fortunately, a set of pressure distributions from the 20 million chord Reynolds number solution from data set P of DPW-IV was recently acquired. This set was provided by Tony Sclafani from the Boeing Advanced Concepts group. Figure S-IX-5 shows pressure distributions from solution P at 5 and 20 million chord Reynolds number compared to test data from the NTF. The solution P data are for a fixed $C_L = 0.50$. The test data are for the closest available lift coefficient. The differences due to Reynolds number become more apparent the further outboard the comparisons are made. The higher Reynolds number results in a lower "roof top" (less negative C_p's on the wing upper surface) and an aft movement of the shock wave. This resultant reduction in shock strength reduces the pressure drag for the CFD data as indicated in Figure S-IX-3. Outboard on the wing, the CFD "roof top" is higher (more negative) than was seen for the experimental data. This is expected since the computational model did not include the aeroelastic deformation experienced at this flight condition.

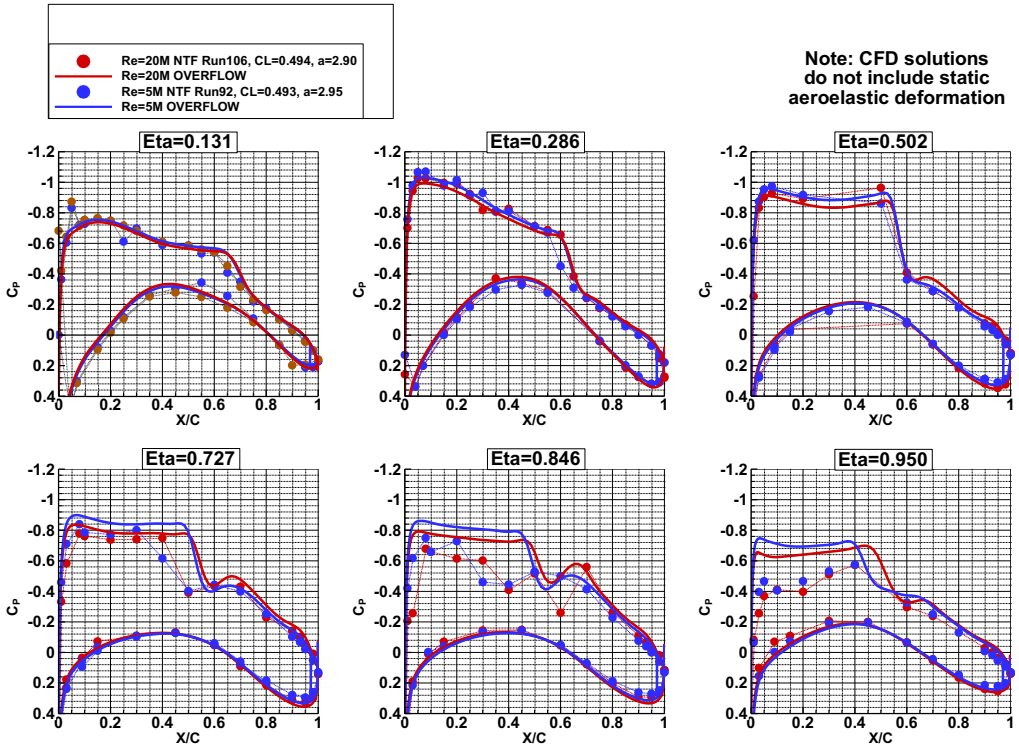


Figure S-IX-5. WBT Wing Pressure Distributions; Effect of Reynolds Number; CFD vs. Test.

Figure S-IX-6 shows the comparison over the last 20 percent of the chord. The aft loading (delta between upper and lower surface pressure) increases with increased Reynolds number, and for both Reynolds numbers, the computational aft loading is greater than seen in the experimental results. Another way to look at the aft loading is to compare the C_p difference between upper and lower surface pressures at a chord fraction of 85 percent. Values of the delta C_p at 85 percent chord at various span locations as a function of Reynolds number are shown in Figure S-IX-7. Values are from both solution P and from NTF test data. Also shown is the delta C_p from a Boeing 777-200 model that was previously tested in the NTF [94]. These data show a very similar trend to that of the CRM with CFD predicting higher aft loading than experiment. However, the delta C_p on the 777-200 measured in the NTF and the CFD prediction at 40 million Reynolds number was very close to that measured in flight on the airplane.

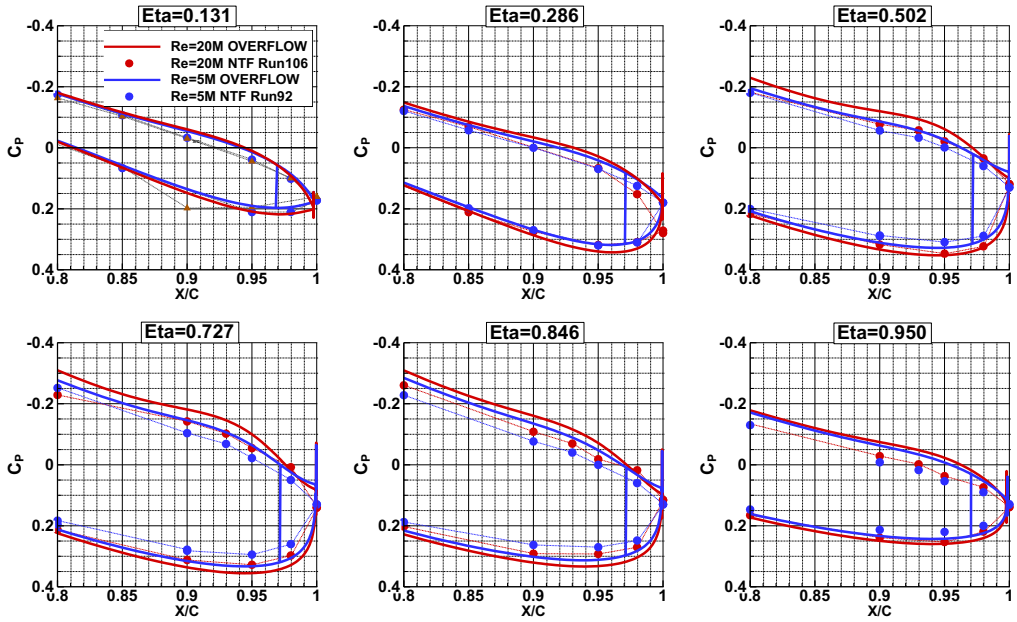


Figure S-IX-6. WBT Wing Trailing Edge Pressure Distributions: Effect of Reynolds Number; CFD vs. Test.

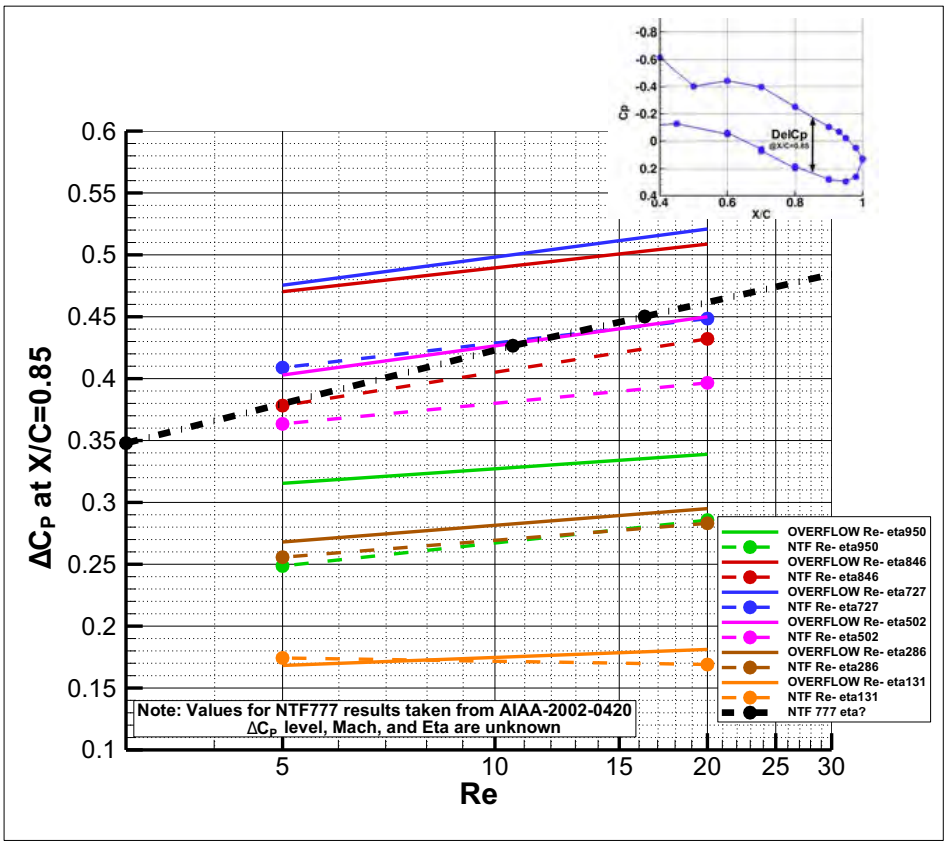


Figure S-IX-7 WBT Aft Loading Delta Cp; Effect of Reynolds Number; CFD vs. Test.

Delta C_p as a function of span fraction, η, for the two Reynolds numbers is shown in Figure S-IX-8. Again, values are shown for both solution P and NTF test data. This clearly shows the maximum delta C_p and the maximum difference between CFD and test occurring on the outboard part of the wing at around 80 percent span fraction. There is little deviation near the side of the body.

The question of excessive aft loading in CFD is certainly an issue that needs further attention.

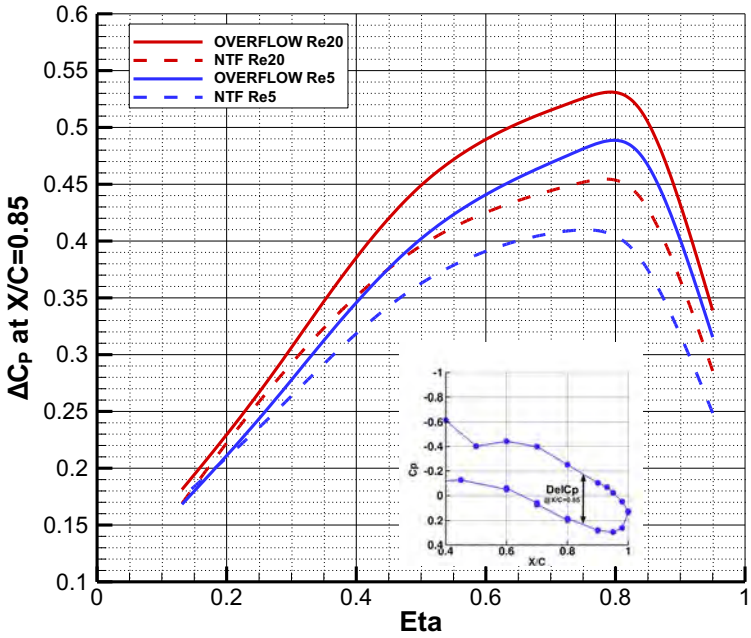


Figure S-IX-8. WBT Aft Loading Delta C_p vs. Span Fraction; Effect of Reynolds Number; CFD vs. Test.

Section X: Angle-of-Attack Sweep/Buffet Study

Another important recurring case in all the Drag Prediction Workshops has been the angle-of-attack sweep. This allows a look at the lift, drag, and pitching moment characteristics over a range of angle of attack of the computational results, and their comparison with experimental data as appropriate. Usually this has involved an angle-of-attack sweep of the Wing-Body configuration using the medium size grid from the grid convergence sweep. Exceptions to wing-body only have included a sweep of the F6 Wing-Body-Nacelle-Pylon configuration in DPW-II, the F6 Wing-Body with the FX2B fairing in DPW-III, and the CRM Wing-Body-Tail with three different tail deflections in DPW-IV. The CRM Wing-Body-Tail results will be discussed in the following section. Only the CRM Wing-Body results from DPW-IV, -V, and -VI will be considered in this section. The participant data-set key for each Workshop is found in Appendix C.

A. DPW-IV Results

Lift and pitching moment are shown in Figure S-X-1 from the DPW-IV solutions for the CRM Wing-Body "As-Built" configuration. These are compared to experimental data from both the NTF and 11-Foot wind tunnels. The CFD solutions were obtained at 0°, 1°, 2°, 3°, and 4° angle of attack. There were three immediate observations: (1) the significant off-set between the solutions and the experimental data; (2) the spread of the values at each angle of attack; and (3) the break from the linearity of the solutions and experiment between 3° and 4°. Note that the spread

of the solutions is still significant even after throwing out the two obvious outliers (solutions J and 4). The significant offset between the solutions and experimental data is largely due the lack of accounting in the computational model for the aeroelastic deformation the wind tunnel model undergoes, and the effect of the upper-swept strut/sting mounting system on the test data [86,87]. The aeroelastic deformation of the wind tunnel model under load was measured and was incorporated into the computational models in DPW-VI. The spread of the computational values at each angle of attack is an ongoing attribute of all the DPWs and will be discussed in greater detail later in this report. The break in linearity between 3° and 4° (and also seen in the test data) is due to shock-induced flow separation. This feature is investigated in greater detail in DPW-V and -VI.

Figures S-X-2 and -3 show the lift and moment data broken out by grid type: structured and unstructured. The only thing to be learned here is the greater spread of results from the unstructured grid solutions compared to those from the structured grids. However, some of this might just be due to the greater number of unstructured grid solutions.

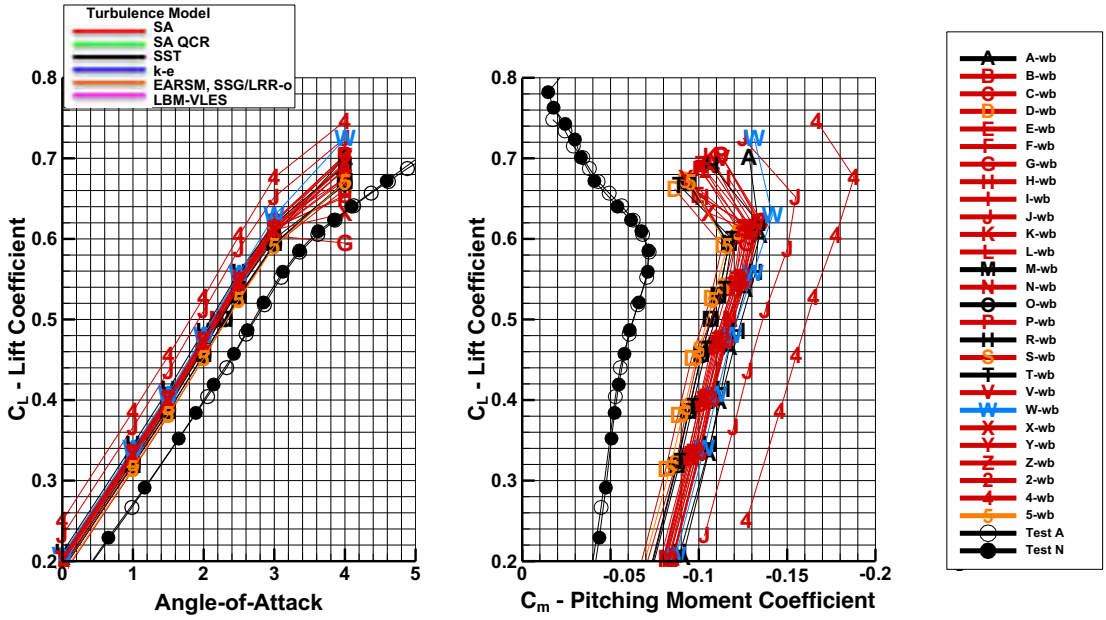


Figure S-X-1. DPW-IV: WB (As-Built) Lift and Pitching Moment; All Solutions, M=0.85.

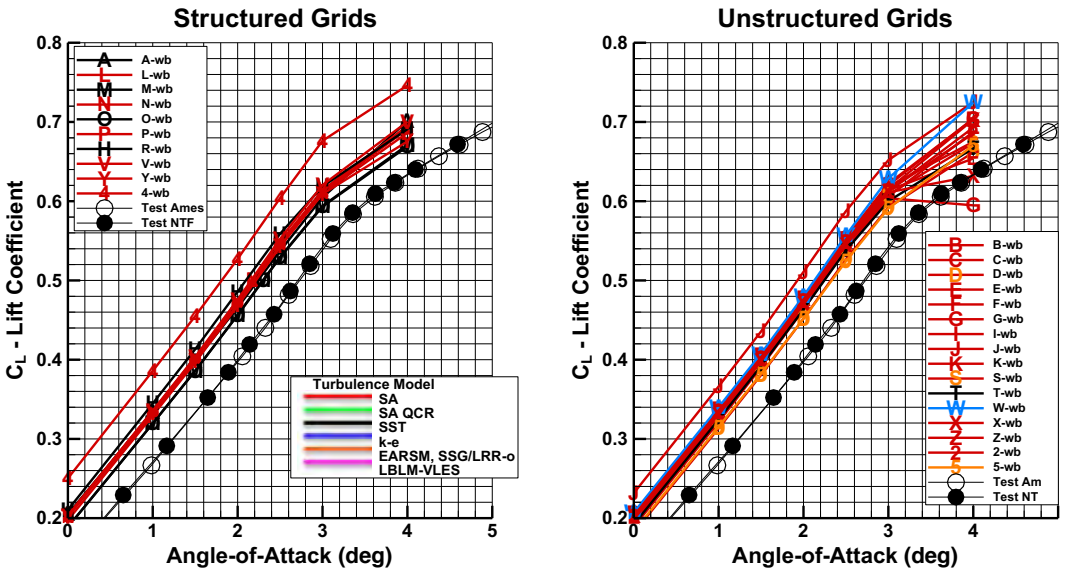


Figure S-X-2. DPW-IV: WB (As-Built) Lift; Grid Type - All Solutions, M=0.85.

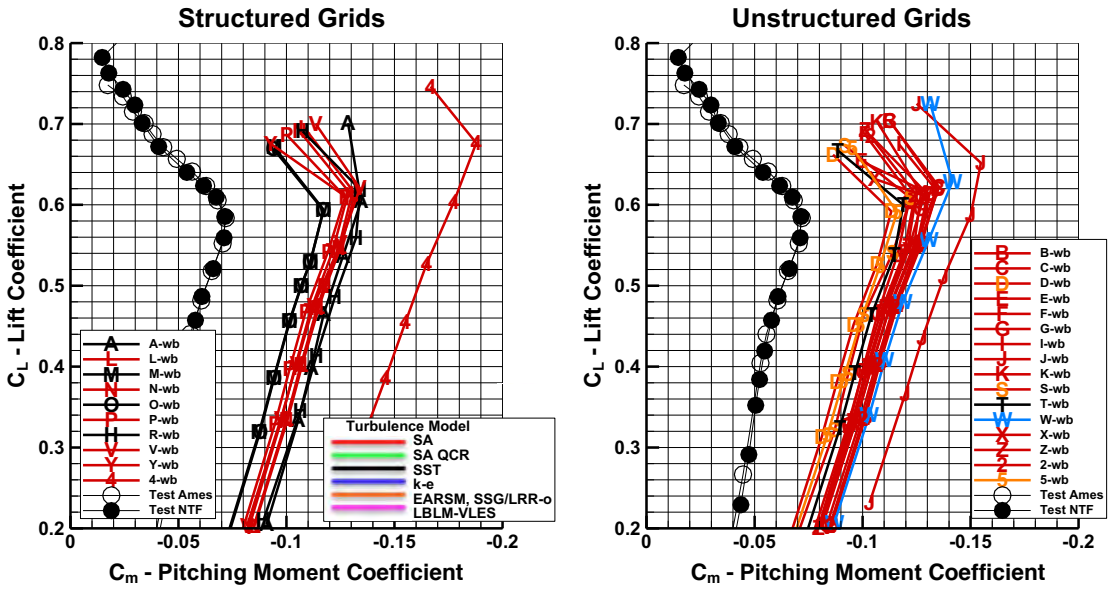


Figure S-X-3. DPW-IV: WB (As-Built) Pitching Moment; Grid Type - All Solutions, M=0.85.

Figure S-X-4 shows the idealized profile drag polar from DPW-IV. Idealized profile drag is defined as

$$C_{Dp} = C_D - C_L^2/\pi AR.$$

Plotting CD_p instead of CD can be very useful as its variation with CL is significantly diminished, and therefore, the scale of the plot can be greatly increased. In addition to the computational results, experimental results from both the NTF and Ames are provided. Notice that 0.00077 (7.7 drag counts) was added to the Ames data to match the level of the NTF results. The two experimental polar shapes are essentially identical. Again, we see that even after eliminating two outliers we are still left with a band of results. This is consistent with the range of drag results obtained by the grid convergence study in Section VII.

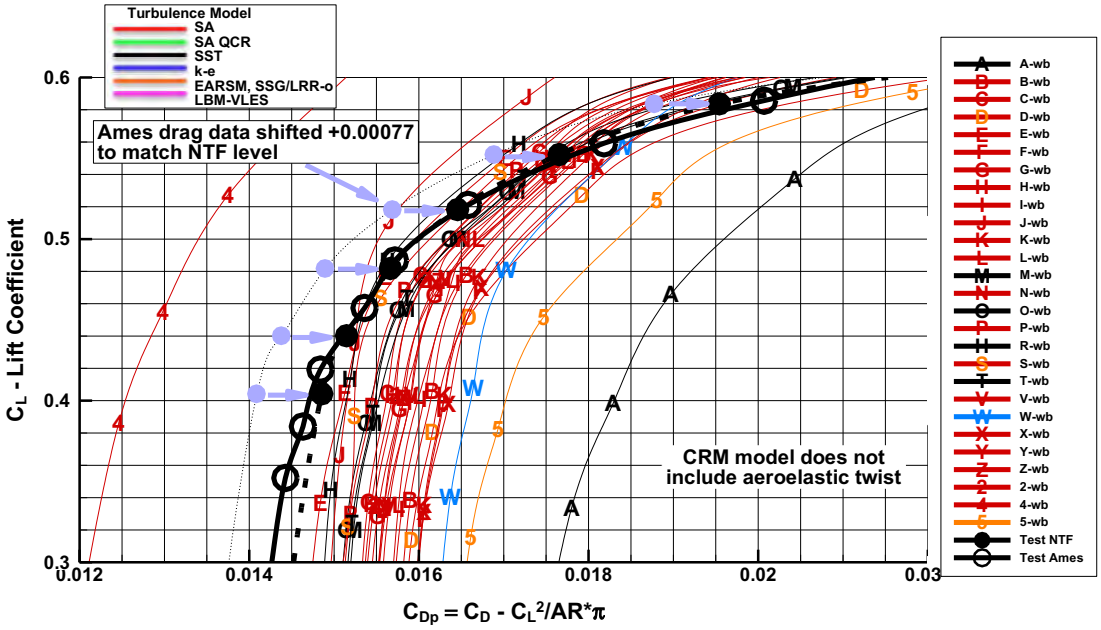


Figure S-X-4. DPW-IV: WB (As-Built) "Profile" Drag Polar; All Solutions, M=0.85.

B. DPW-V Results

For DPW-V, there was the added interest in better defining the solution behavior between 2.5° and 4.0° angle of attack, the availability of wind tunnel data, and a significant increase in the number of data entries. The angle-of-attack sweep was renamed the buffet study whose objective was to investigate the CFD predictions in an angle-of-attack range where significant flow separation is expected. This flight regime is of particular importance to determine aerodynamic loads and stability and control characteristics. Seven angles of attack were specified between 2.5° and 4.0° at 0.25° increments. Over 50 data sets were provided by the Workshop participants for this study.

The existence of the wind tunnel data led to the realization that the CRM model defined for the workshop did not represent the nominal M = 0.85, C_L = 0.50, 5 million Reynolds number cruise shape as had been desired, but instead represented the wind-off as-built shape. The CRM wing geometry used for both the Fourth and Fifth Drag Prediction Workshops was defined prior to the building and testing of the CRM wind tunnel model. Ideally the computational geometry should include the aeroelastic deformation of the experimental subject under the actual test conditions. This is not generally done at each test condition but should be if the best possible correlation is desired. Based on in-tunnel aeroelastic deformation measurements, computational model geometries were defined for each specified flight condition for DPW-VI (see Section II). The CRM geometry and grids used in DPW-IV and -V are the wind-off "as-built" shape.

To provide some measure for comparison in DPW-V, a set of "pseudo" wind tunnel data were created to represent "experimental" results corresponding to the shape used in the CFD analysis. These pseudo data are based on NTF

data for the Wing-Body configuration and computational results from Ref. 87 for a Wing-Body-Tail configuration. The Ref. 87 results were from solutions using the Workshop geometry, and solutions using a wing shape derived from the model deformation data from the NTF at the "cruise" M = 0.85, C_L = 0.50 condition. NTF test data, "pseudo" test data, and computational results for the original geometry, and the geometry with the measured twist are shown in Figure S-X-5. The difference between the two computational solutions was applied to the NTF experimental results to generate the "pseudo" test data. For lift, the computational results with the measured twist are in reasonable agreement with the NTF data while the computational results using the Workshop geometry agrees well with the "pseudo" test data. The pitching moment data is significantly different in that the available computational results were for a Wing-Body-Tail configuration while the test data is for a Wing-Body configuration. Nevertheless, to first order, the pitching moment increment due to twist should be applicable. Based on results from Ref. 87, it is anticipated that corrections for the effect of the wind tunnel model mounting system (if they have been available for the Wing-Body configuration) would have further increased the lift slightly and made the pitching moment more negative in the "pseudo" data. These "pseudo" data should provide some reference to what would have been measured if the wind tunnel model had assumed the "design" shape at the "cruise" condition. For purposes of the buffet study the drag differences were too small to warrant creating pseudo drag data.

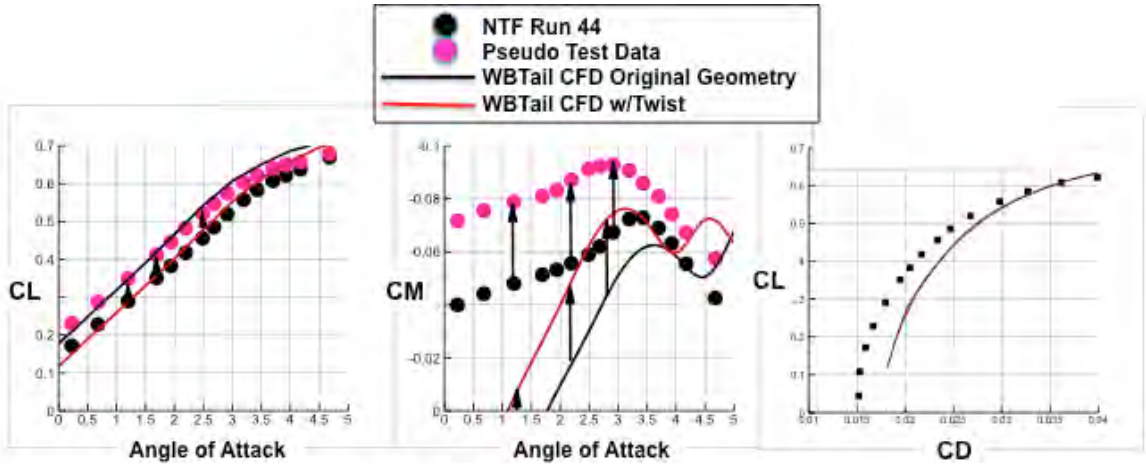


Figure S-X-5. "Pseudo" Wind Tunnel Test Data, M=0.85.

Lift and pitching moment results from all the DPW-V submittals, along with the "pseudo," NTF, and Ames test data are shown in Figure S-X-6. Most of the solutions are clustered within a "fan" that gets progressively wider with increasing angle of attack. The exceptions are a group of solutions based on the Goldberg R_T turbulence model, and other outliers that suffered an early massive flow separation.

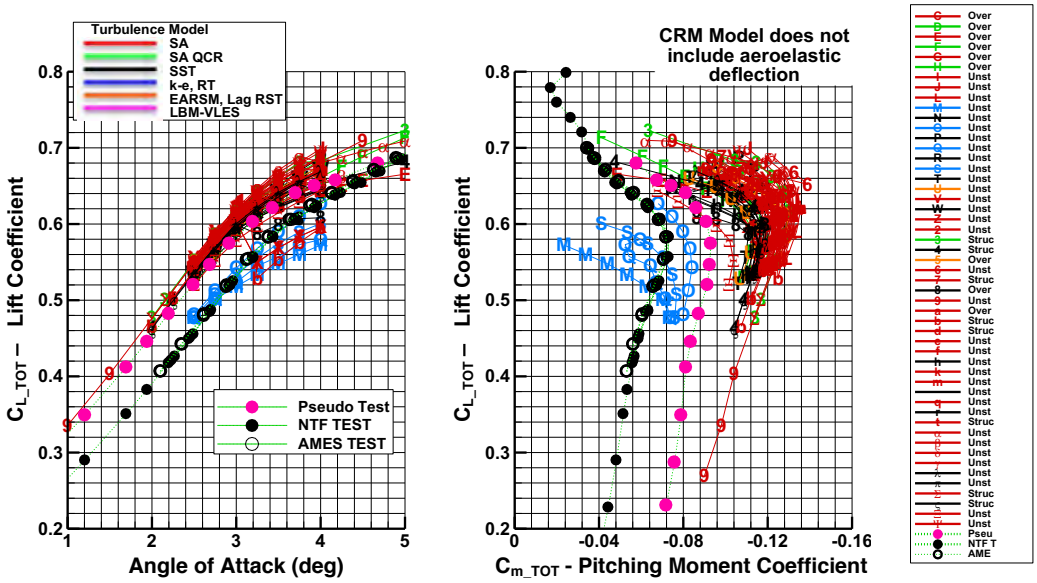


Figure S-X-6. DPW-V: WB (As-Built) Lift and Pitching Moment; All Solutions, M=0.85.

Figure S-X-7 shows the "profile" drag polar from all the entries of DPW-V. Wind tunnel data from the NTF and Ames wind tunnels are also shown. For the most part, the computational data lies within a fan shaped grouping with the exception of several significant outliers.

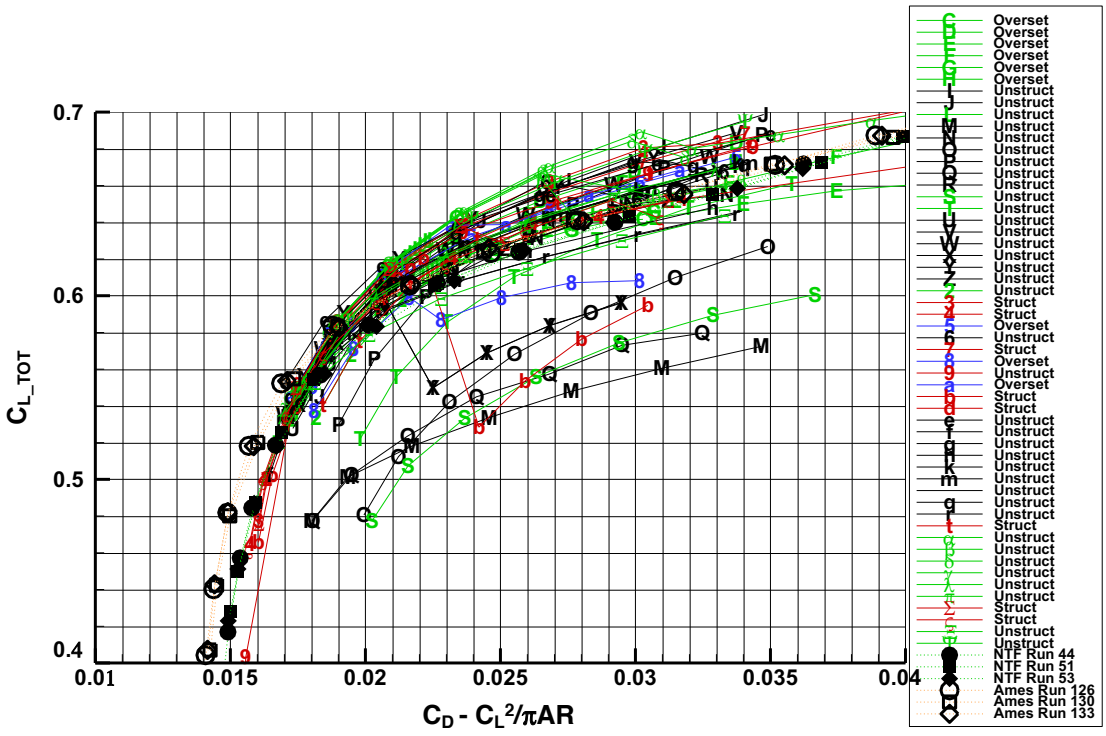
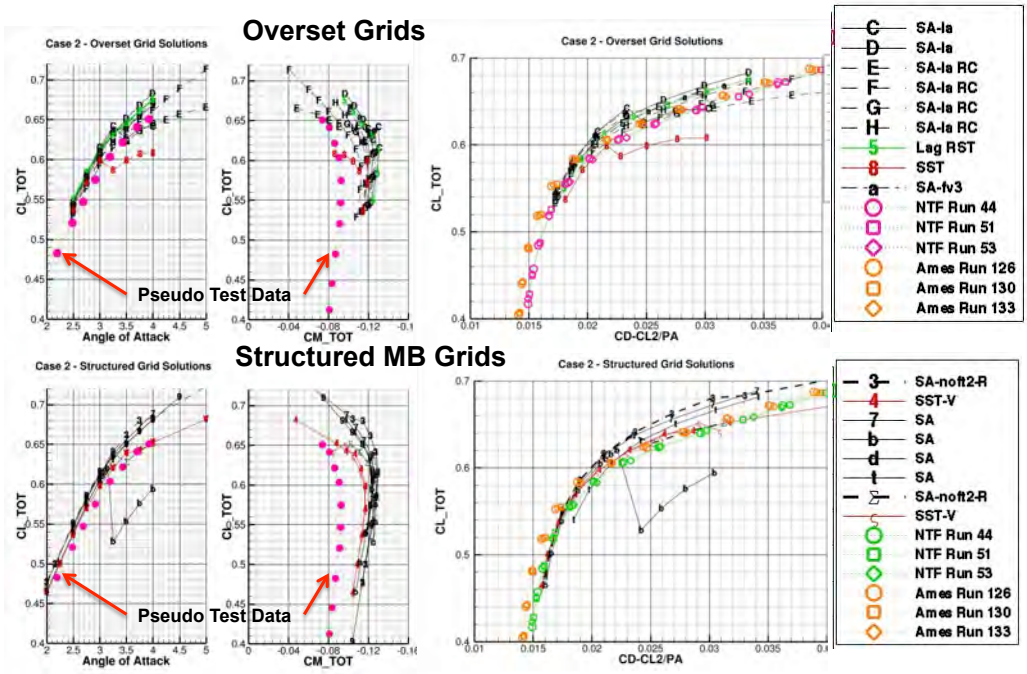


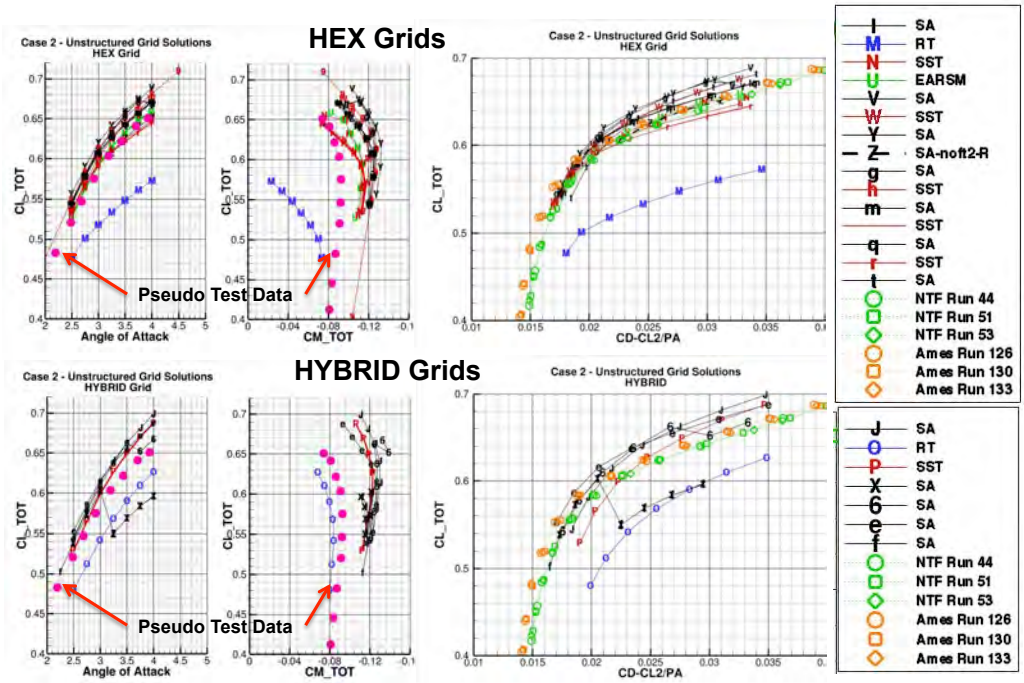
Figure S-X-7. DPW-V: WB (As-Built) "Profile" Drag Polar; All Solutions, M=0.85.

With so many solutions, the challenge is to decipher any useful information from so many entries. Figures S-X-8, -9, and -10 show lift, drag, and pitching moment parsed by grid and turbulence model. For the overset grids, solution 8 is immediately identified as an outlier; for the Multblock grids, solution b; for the hex unstructured grids, solution M; for the hybrid unstructured grids, solutions O, X, and 6; for the prism unstructured grids, solution Q; and for the custom unstructured grids, solutions S, T, α, β, δ, and γ were identified as outliers. The outliers were defined as solutions that exhibited a break in lift prior to $\alpha = 4°$ (relative to the linear lift curve slope, $C_{l\alpha}$) or exhibited lift and/or drag considerably outside the norm of the other solutions. Outliers were seen in solutions from all grid families, and from SA, SST, and Goldberg RT turbulence models.



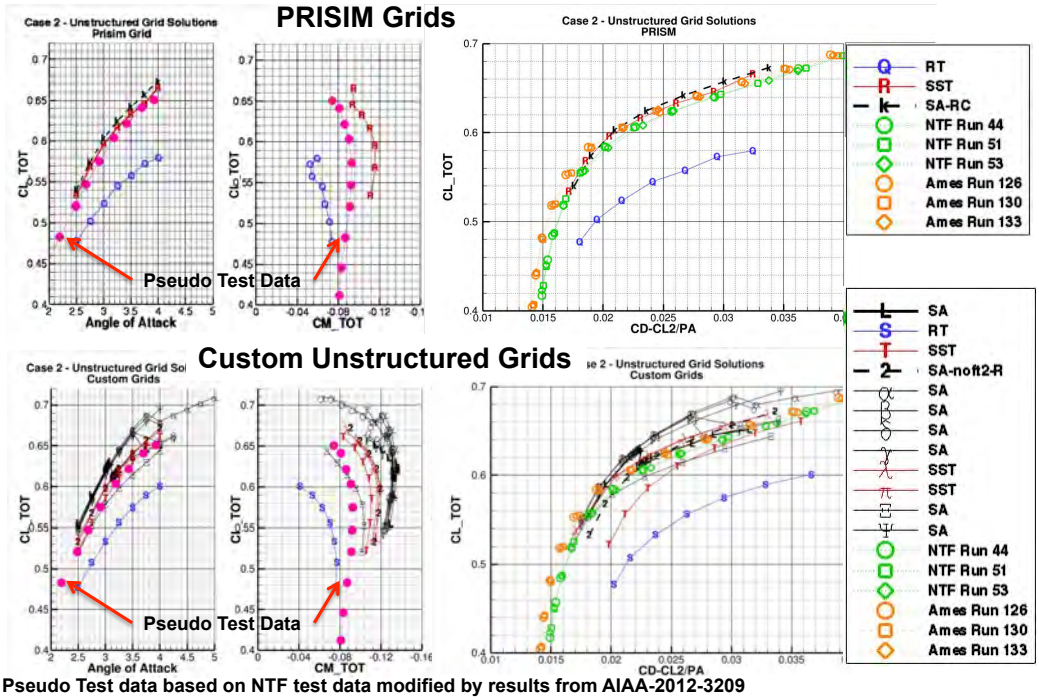
Pseudo Test data based on NTF test data modified by results from AIAA-2012-3209

Figure S-X-8. DPW-V: WB (As-Built) Overset and Multiblock Grid Solutions, M=0.85.



Pseudo Test data based on NTF test data modified by results from AIAA-2012-3209

Figure S-X-9. DPW-V: WB (As-Built) Hex and Hybrid Unstructured Grid Solutions, M=0.85.



Pseudo Test data based on NTF test data modified by results from AIAA-2012-3209

Figure S-X-10. DPW-V: WB (As-Built) Prism and Custom Unstructured Grid Solutions, M=0.85.

A closer examination of the solution lift characteristics identified a few more solutions that exhibited a lift break prior to 4.0° angle-of-attack. Lift break, which is indicative of a large increase in flow separation, occurred as early as 3° angle of attack in five solutions. Seven solutions exhibited a lift break between 3.25° and 3.5°, and a further

nine solutions at 3.75° angle of attack. Flow separation is expected at these higher angles of attack but is not sufficient to cause a sudden break in lift. Excluding these additional solutions leaves 26 solutions that did not exhibit any obvious shortcomings. Figures S-X-11 and -12 present the lift and pitching moment characteristics, and the "idealized profile" polar of the remaining solutions. In Figure S-X-11, we still see an expanding "fan" of this group as angle of attack is increased. At 4.0° angle of attack the spread in lift coefficient, ΔC_L, is 0.055, the spread of pitching moment, ΔC_M, is 0.043. Each one of these solutions on its own is a valid solution, yet as angle of attack increases and the resulting degree of flow separation increases, the variation between solutions increases. Further inspection could identify and remove more outliers based on additional criteria, but the spread may remain. This raises the question as to how we a priori define "correct," or assess the accuracy of our CFD solutions. There will be further discussion of this question and a proposed scheme to identify the "select" solutions in Section XV, Issues. However, that scheme requires that the CFD solutions include the aeroelastic deformation as angle of attack increases.

The drag characteristics of the remaining 26 solutions are shown in Figure S-X-12. Test results from three repeat runs at both the NTF and Ames wind tunnels are also shown. The drag characteristics are plotted in terms of the idealized profile drag, C_{DP}. The spread of the drag values is largely driven by the increasing spread of lift with increasing angle of attack.

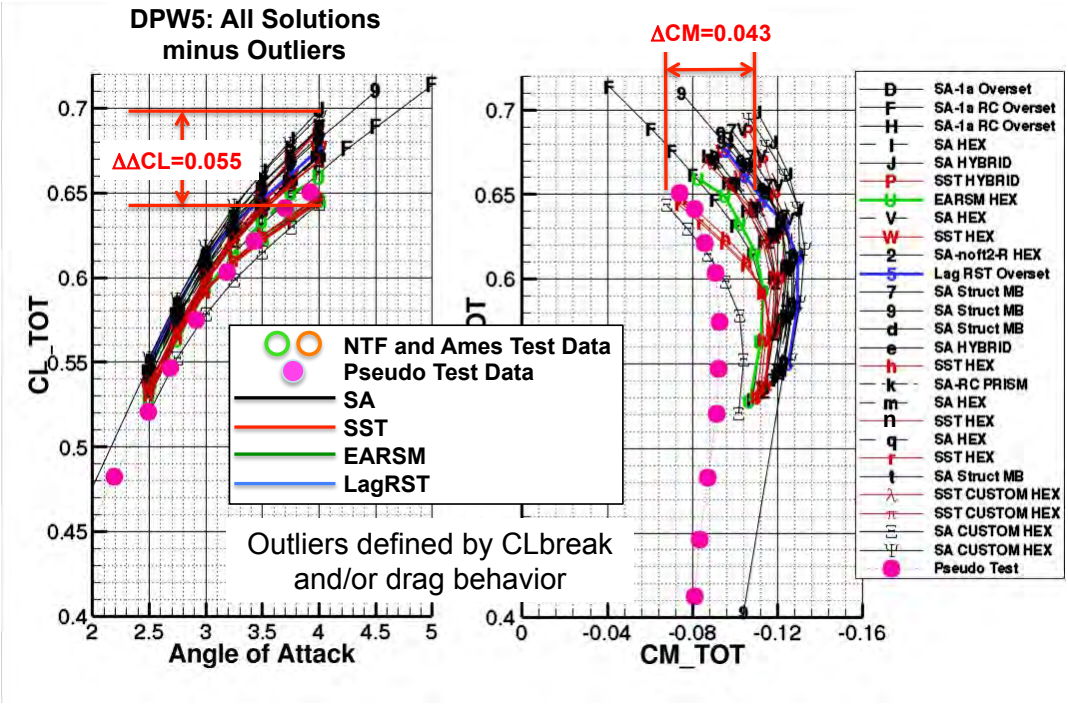


Figure S-X-11. DPW-V: WB (As-Built) Lift and Pitching Moment; All Solutions minus Outliers, M=0.85.

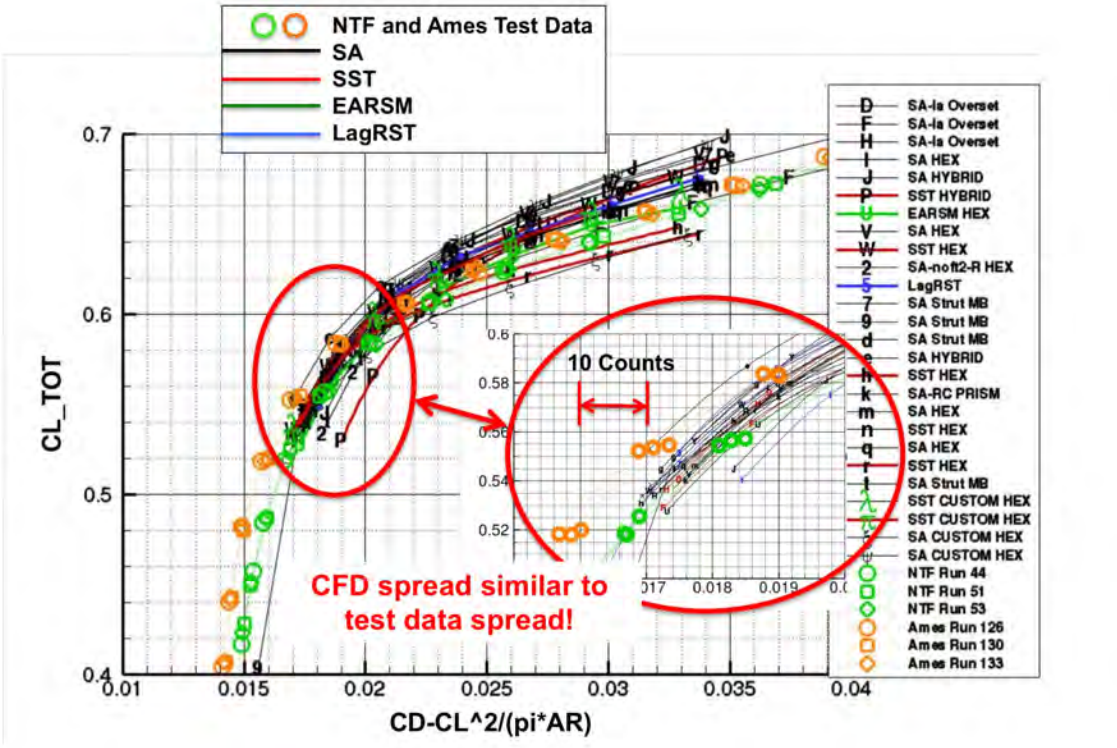


Figure S-X-12. DPW-V: WB (As-Built) "Profile" Drag Polar: All Solutions minus Outliers, M=0.85.

Force and moment data alone are not enough to get a better understanding of the computational results. We know that as the angle of attack is increased, flow separation will play a dominant role in the aerodynamic characteristics of the configuration. Among the data collected from the workshop participants were flow separation parameters describing the extent of the side-of-body separation bubble (if any), and the extent of separation on the wing. There is a tendency for some codes to predict a large separation bubble at the wing root trailing edge by the side of body (SOB), shown in Figure S-X-13, while others preserved smooth flow virtually all of the way to the trailing edge. The predicted SOB separation bubble extends forward up to 100 inches (25 percent root chord) and outward beyond BL = 250 (dimensions are full-scale inches) in some cases. This extent is large enough to be seen in the force and moment and pressure results. However, the wind tunnel data do not exhibit any evidence of flow separation of this order at the first row of pressures located at BL = 151, nor does it show an early lift break. A recent wind tunnel test by ONERA [84] measured the side-of-body separation bubble to be about 21 to 26 cm (full scale) wide, which corresponds to an extent to BL~128-131. All of the solutions identified with a separation bubble size greater than BL = 151 also exhibited a lift break well below 4° angle of attack and have been identified as outliers. This type of 3D corner flow separation continues to need more attention in turbulence model development. Spalart's Quadratic Constitutive Relation (QCR) model [95,96], which was used in some entries, appears to eliminate the tendency to predict too large a side-of-body separation.

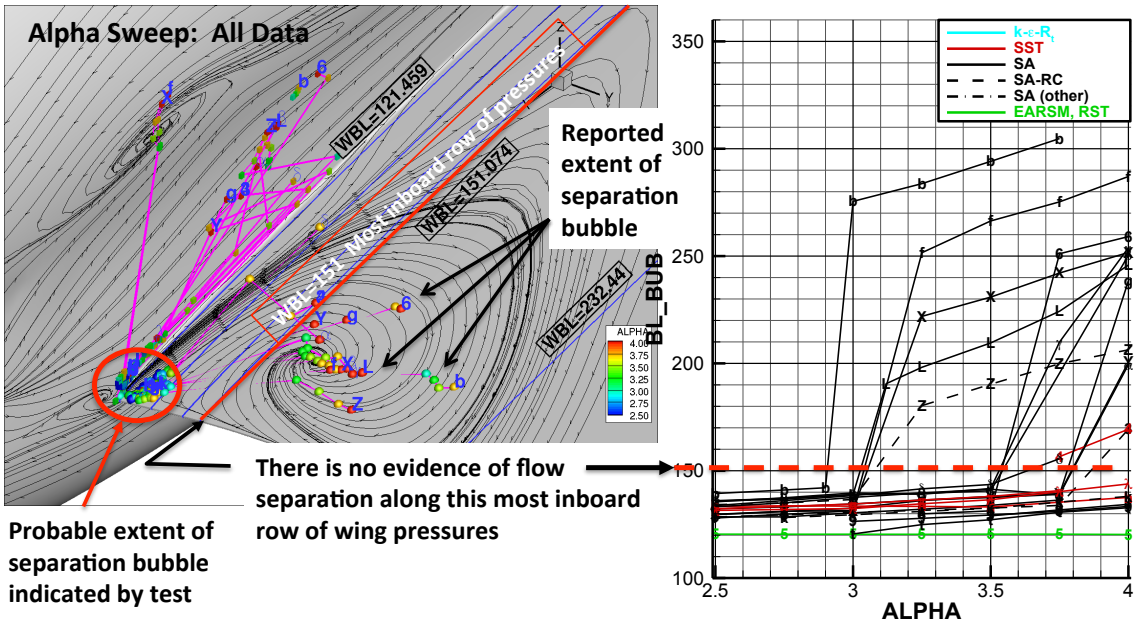


Figure S-X-13. DPW-V: WB (As-Built) Side-of-Body Separation Bubble, M=0.85.

The significant variations in lift and pitching moment seen in the various solutions at each angle of attack are driven largely by shock location, and by the amount of trailing edge separation. Figures S-X-14 to -16 show the variation of flow separation on the wing upper surface from the wing trailing edge along the span. The span locations are identified in terms of the data reporting stations, which ranged from 1 at BL = 121.5 ($\eta = 0.105$) to 16 at BL = 1145.1 ($\eta = 0.99$). At 2.50° angle of attack (Figure S-X-14), very little trailing edge separation exists (less than 2 percent chord except for solutions based on the Goldberg R_t turbulence model). The lift and pitching moment variations here are mainly driven by differences in shock location. By 3.0° angle of attack, as seen in Figure S-X-15, there is a significant amount of trailing edge separation for most solutions except for the one based on the EARSM turbulence model: somewhat more separation for the SST solutions, more variation among the various versions of the SA turbulence model. By 4.0° angle of attack, as seen in Figure S-X-16, there is a massive amount of trailing edge separation with significantly different patterns between solutions. There does not appear to be any single clear pattern. It would be extremely beneficial to have experimental flow visualization to better define the extent of the flow separation at these angles of attack.

Pressure distributions and the resulting lift characteristics are shown for several entries in Figure S-X-17. The pressure distributions are for 4.0° angle of attack. Four of the solutions are for the same hex unstructured grid, from two solvers, with different turbulence models. Two solutions used the SA turbulence model but different grids and solvers. One solution (f) with the SA turbulence model exhibited massive SOB separation at a relatively low angle of attack, the other (V) did not. The EDGE solver used in solution V has demonstrated a resistance to premature separation in cases presented in all the workshops. The Goldberg RT turbulence model used in solution M did no better with other unstructured grids (solutions O, Q, and S). This and other comparisons (not shown here) clearly illustrate the solution dependence on the combination of solver, grid, and turbulence model (and other details not tracked in the workshop).

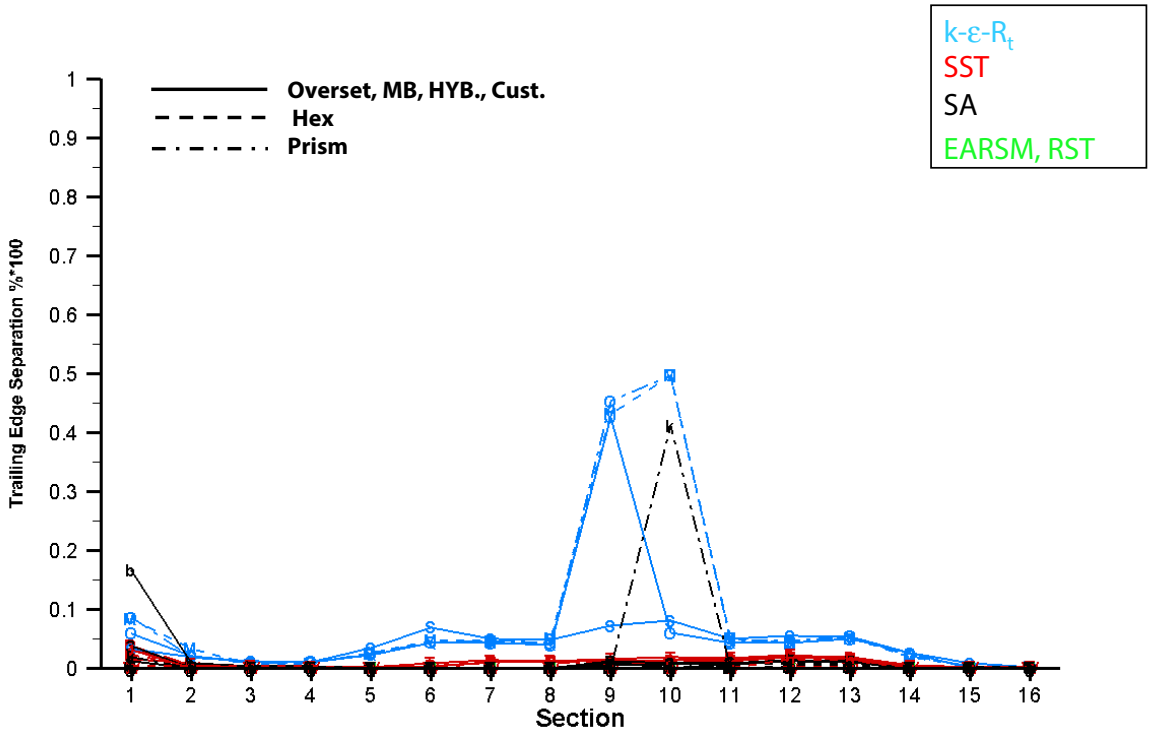


Figure S-X-14. DPW-V: WB (As-Built) Wing Trailing Edge Separation at 2.5° Angle of Attack, M=0.85.

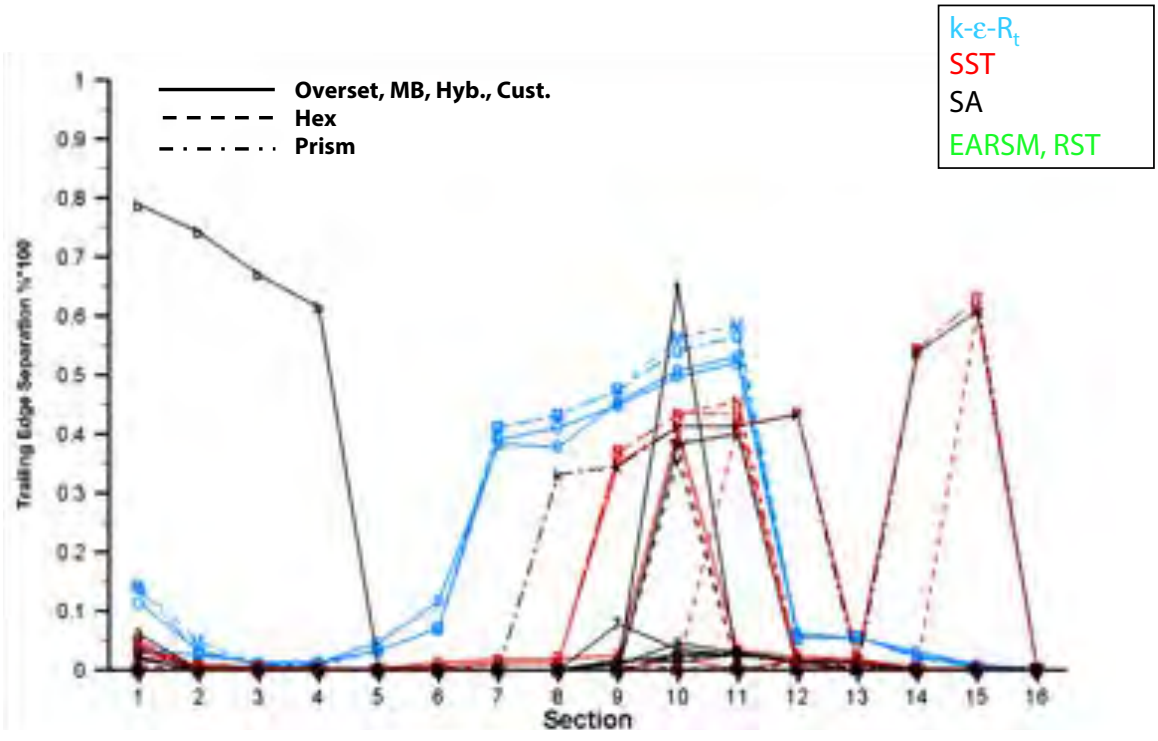


Figure S-X-15. DPW-V: WB (As-Built) Wing Trailing Edge Separation at 3.0° Angle of Attack, M=0.85.

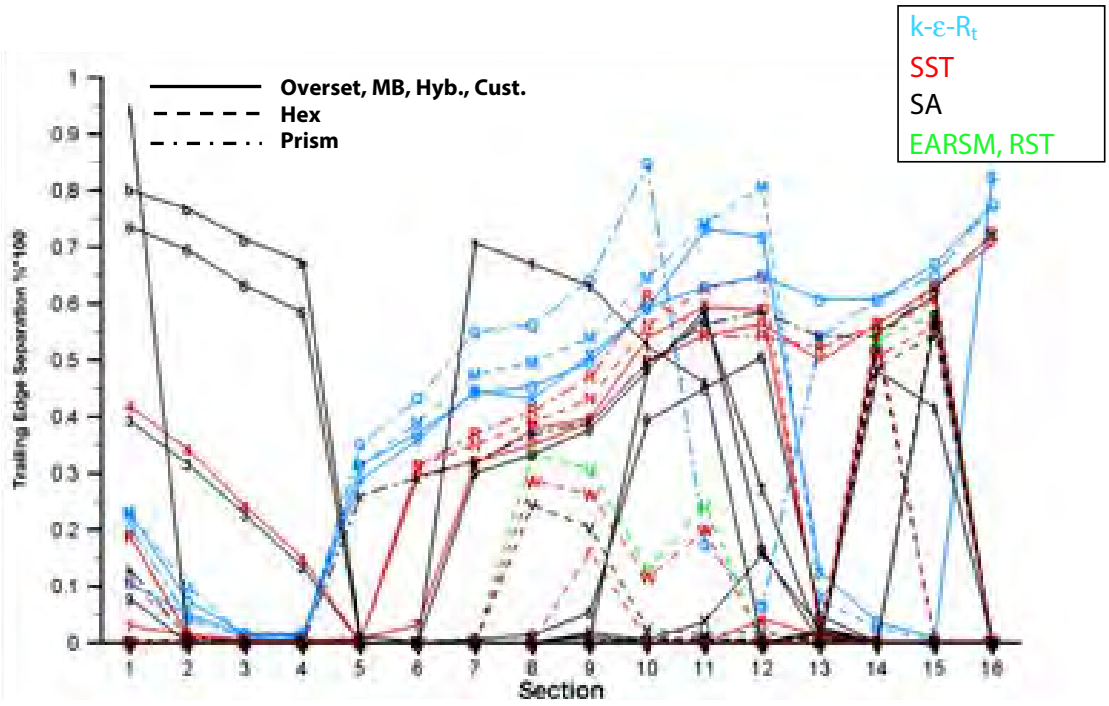


Figure S-X-16. DPW-V: WB (As-Built) Wing Trailing Edge Separation at 4.0° Angle of Attack, M=0.85.

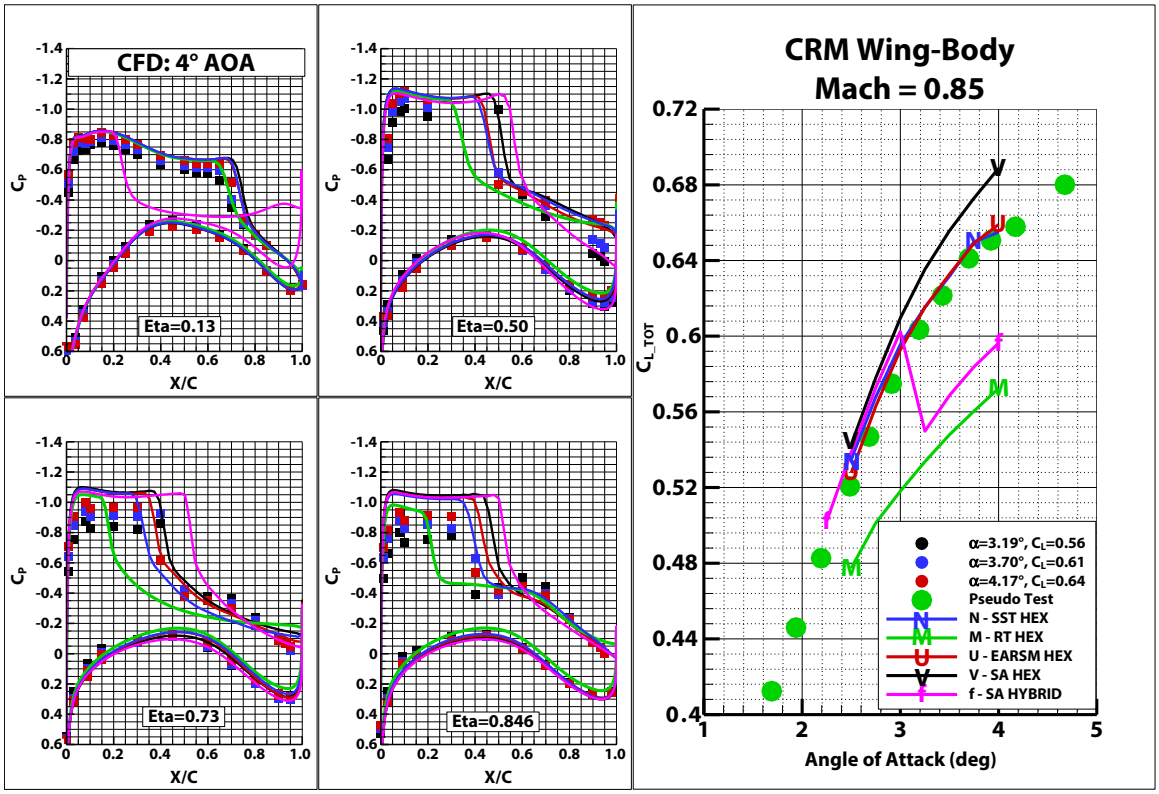


Figure S-X-17. DPW-V: WB (As-Built) Pressure Distributions and Lift Characteristics of Select Solutions, M=0.85.

C. DPW-VI Results

DPW-VI again called for a Wing-Body angle-of-attack sweep/buffet study similar to the one in DPW-V. However, this time the CRM geometries included the measured aeroelastic deflection at each specified angle of attack. The aeroelastic twist will unload the outboard part of the wing, which reduces the resulting shock induced separation at the higher angles of attack. The resulting computational results should agree better with the corresponding experimental results. 41 data sets were provided for this study.

Figure S-X-18 presents lift and pitching moment results from all the participants who submitted angle-of-attack data. These show the same fan shaped distribution of results seen for DPW-V. Several solutions continue to show evidence of massive premature separation with the attendant loss of lift. On the plus side, the computational results now are in much closer agreement to the test data without having to resort to that fictitious "pseudo" data in DPW-V. Figure S-X-19 presents an idealized profile drag polar. Several obvious outliers along with the widening fan distribution of the remaining solutions are seen.

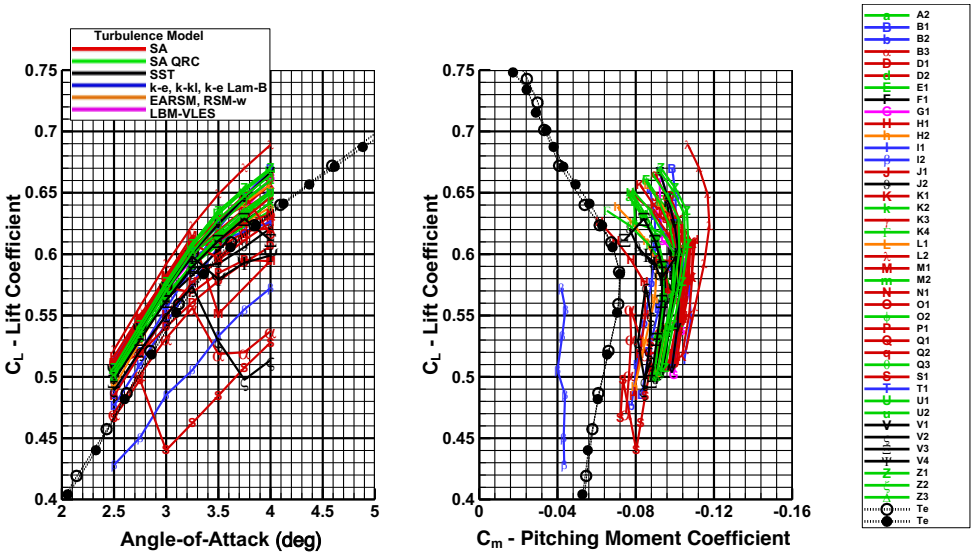


Figure S-X-18. DPW-VI: WB (Aeroelastic) Lift and Pitching Moment; All Solution. M=0.85.

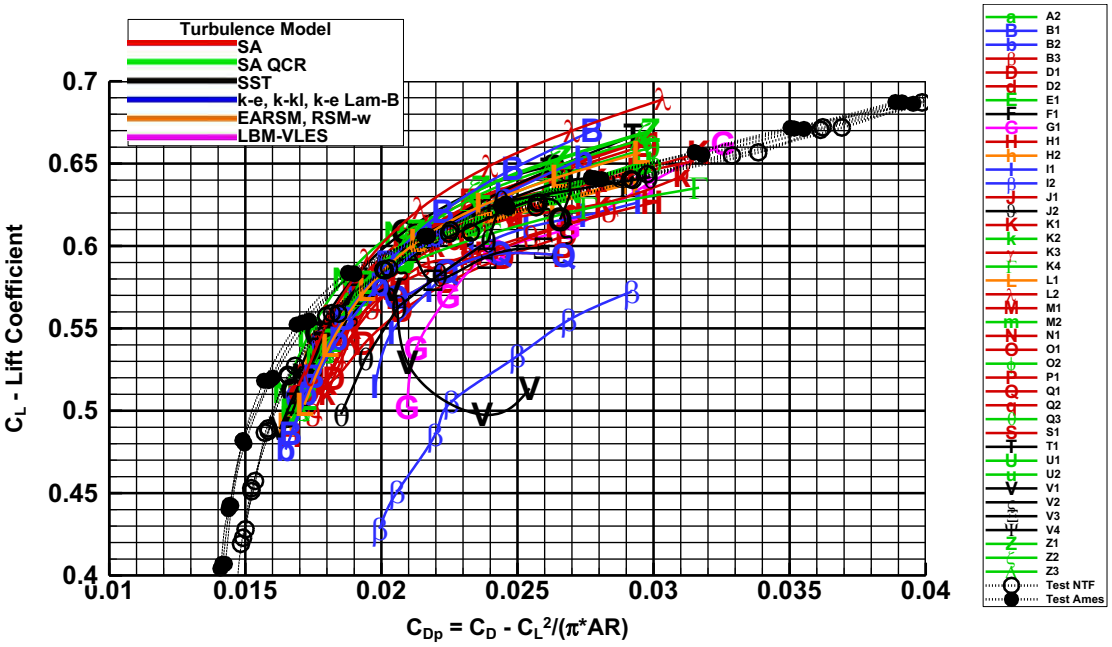


Figure S-X-19. DPW-VI: WB (Aeroelastic) "Idealized Profile" Drag Polar; All Solutions. M=0.85

We can again look at the SOB separation bubble characteristics and see how they behave with increasing angle of attack. Figure S-X-20 compares the bubble behavior from the DPW-VI results with those from DPW-V. There were fewer entries that reported an excessive SOB separation in DPW-VI, which is an improvement, but there were still too many. However, it should be recognized that most participants reporting an entry with excessive separation using the SA turbulence model, also did a comparison by submitting an entry using SA with Spalart's QCR model. SA with QCR eliminates the excessive separation as shown in Figure S-X-21. It should also be noted that several entries using SA did not suffer excessive SOB separation. Using SA does not guarantee excessive SOB separation, it is just more sensitive to details of the gridding and the solver.

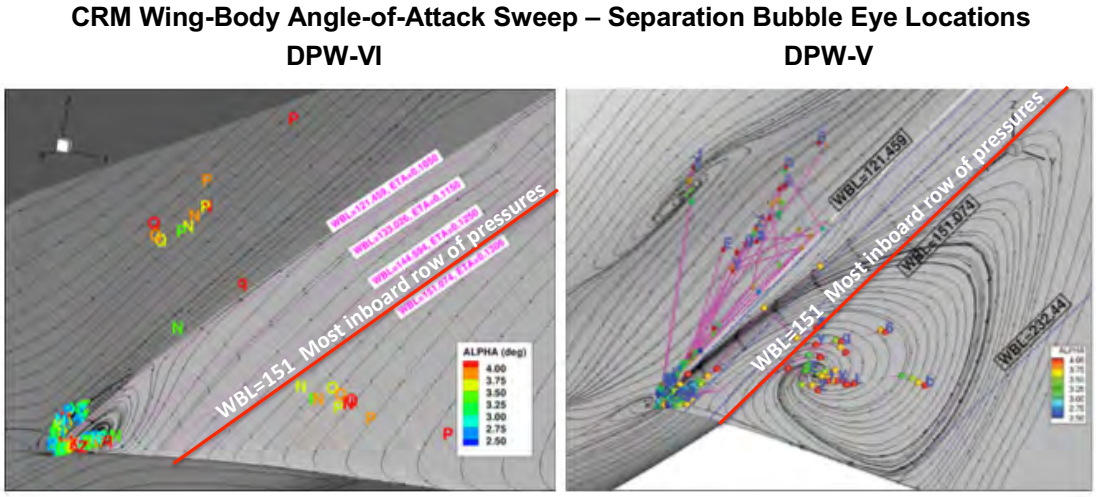


Figure S-X-20. DPW-VI: WB (Aeroelastic) Side-of-Body Separation Bubble Comparison with DPW-V WB (As-Built), M=0.85.

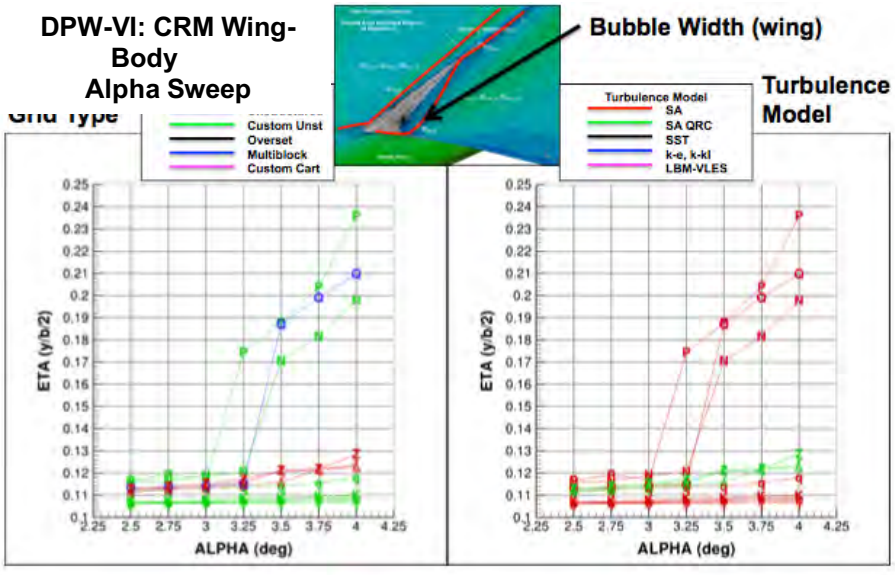


Figure S-X-21. DPW-VI: WB (Aeroelastic) Side-of-Body Separation with Angle of Attack, M=0.85.

The effect of premature SOB separation is clearly seen in the wing pressure distributions shown in Figures S-X-22, -23, and -24, for angles of attack of 3.0°, 3.5°, and 4.0°, respectively. The disruption of the pressure distribution is seen to impact more solutions with increasing angle of attack. This increased disruption is also being felt further outboard. The presence of trailing edge separation is harder to assess from the pressure distributions alone. A comparison of the reported trailing edge separation from DPW-V and -VI at 3.0 and 4.0 angles of attack is shown in Figure S-X-25. Much fewer entries were submitted for the trailing edge separation in DPW-VI. The only conclusion that can be drawn from this comparison is that the region of peak separation has moved further inboard in DPW-VI. This is consistent with the incorporation of the aeroelastic twist in the computational model, which will tend to unload the outboard part of the wing. The inclusion of the wind tunnel model aeroelastic deformation in the DPW-VI

computational models should have improved the accuracy of the separation prediction with increasing angle of attack. Unfortunately, without a more direct source of test data, i.e., flow visualization, this is very difficult to assess.

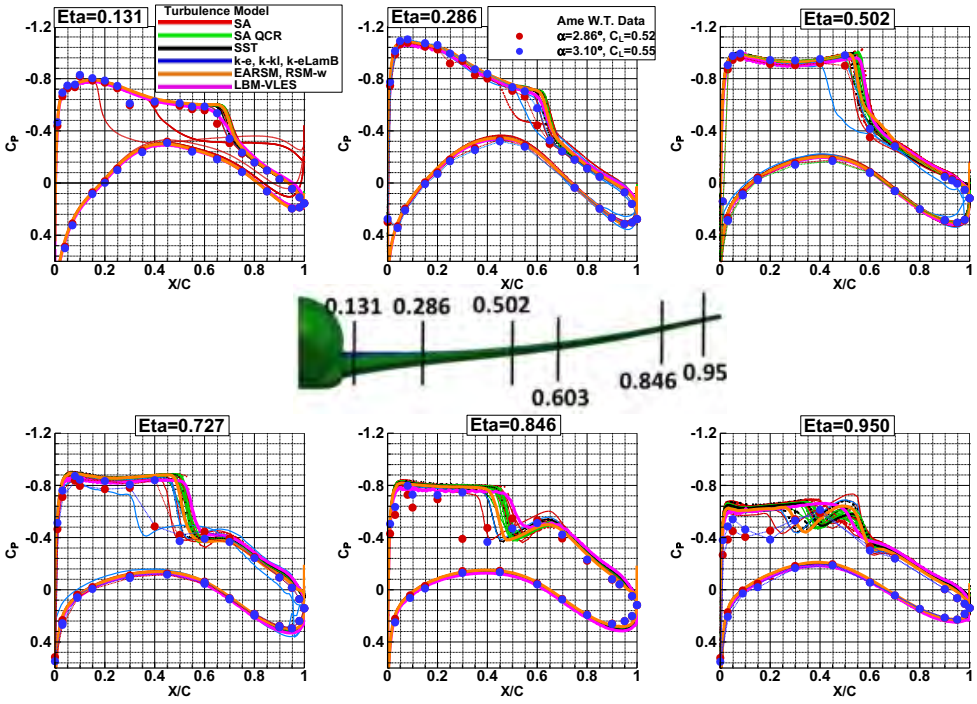


Figure S-X-22. DPW-VI: WB (Aeroelastic) Wing Pressure Distributions - All Solutions - AOA = 3.0°, M=0.85.

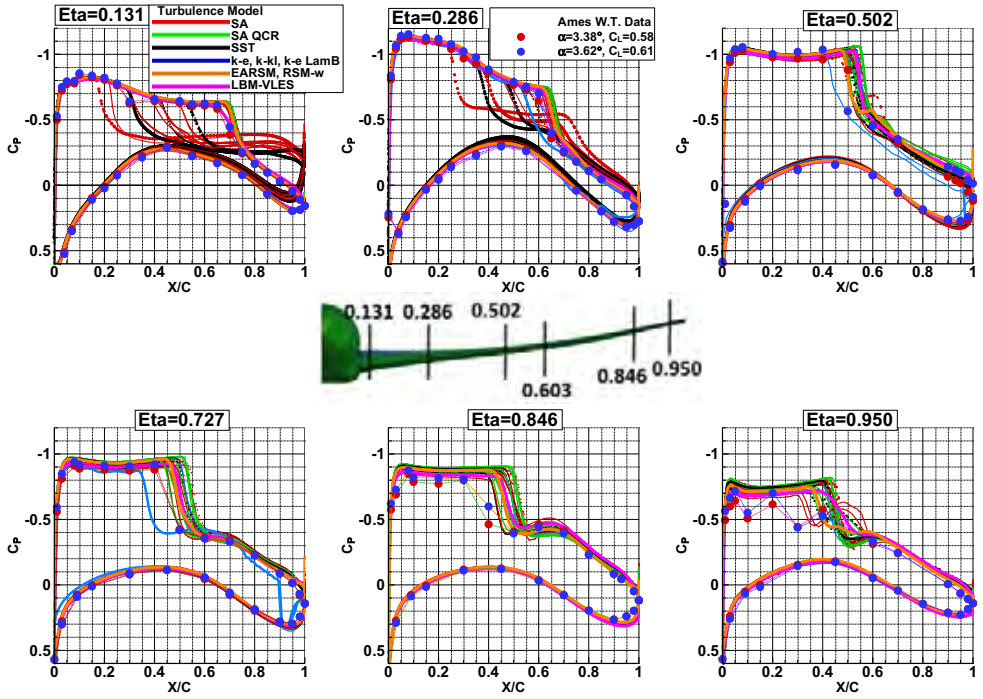


Figure S-X-23. DPW-VI: WB (Aeroelastic) Wing Pressure Distributions; All Solutions, AOA = 3.5°, M=0.85.

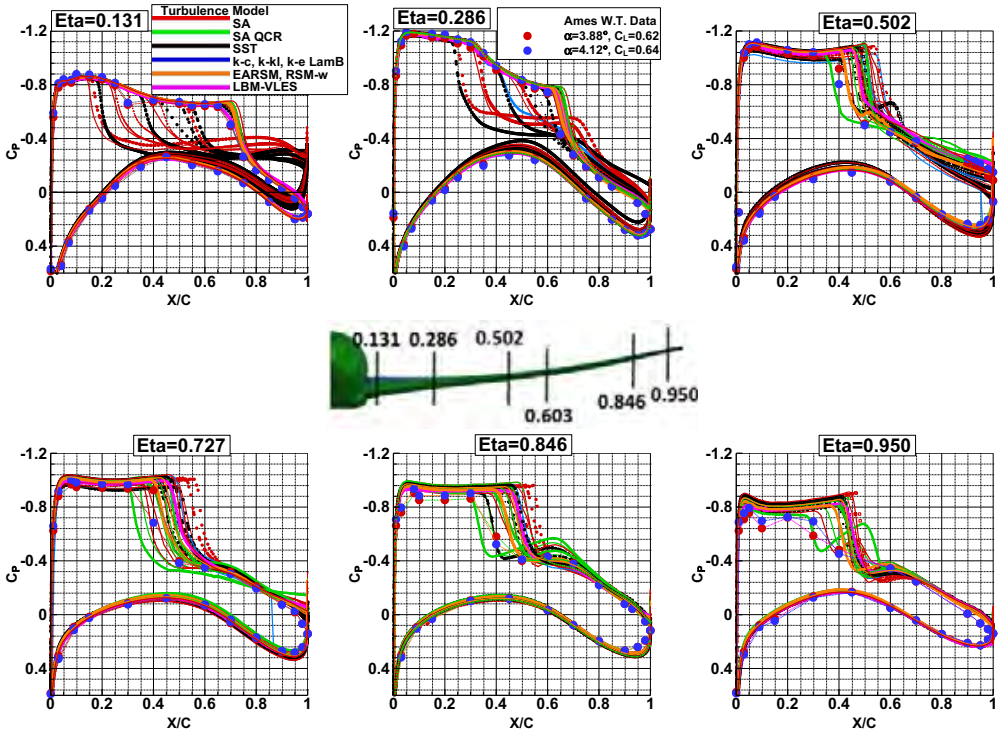


Figure S-X-24. DPW-VI: WB (Aeroelastic) Wing Pressure Distributions; All Solutions, AOA = 4.0°, M=0.85.

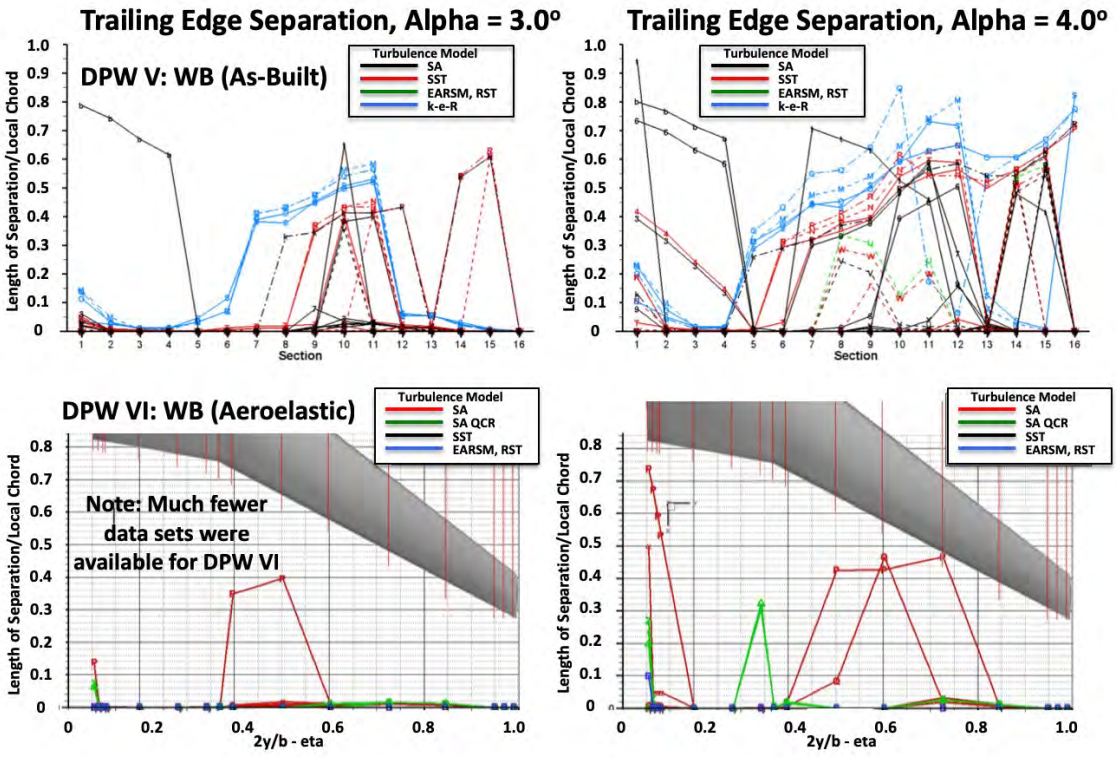


Figure S-X-25. WB Wing Trailing Edge Separation Comparison Between DPW-V and DPW-VI, M=0.85.

Another look at the wing section characteristics can be taken by integrating the pressure coefficients (C_p) vs. chord fraction (x/c) to derive the section lift (normal force) and pitching moment characteristics shown in Figures S-X-26 and -27. The section pitching moment coefficients are taken about the quarter chord (0.25 x/c) of each section. Unfortunately, these data were provided for less than half of the solutions submitted. Of the solution sets provided, some had obvious errors and had to be discarded. These figures clearly show the overprediction of section lift and the magnitude of the negative section pitching moment compared to the test data. This is also reflected in the total forces and moments shown in Figure S-X-18. The early lift loss on the inboard part of the wing is clearly shown for two of the solutions. The additional piece of information that is provided by these section characteristics is that the degree of disagreement between the computed and test results is increasing the further outboard the section is located on the wing.

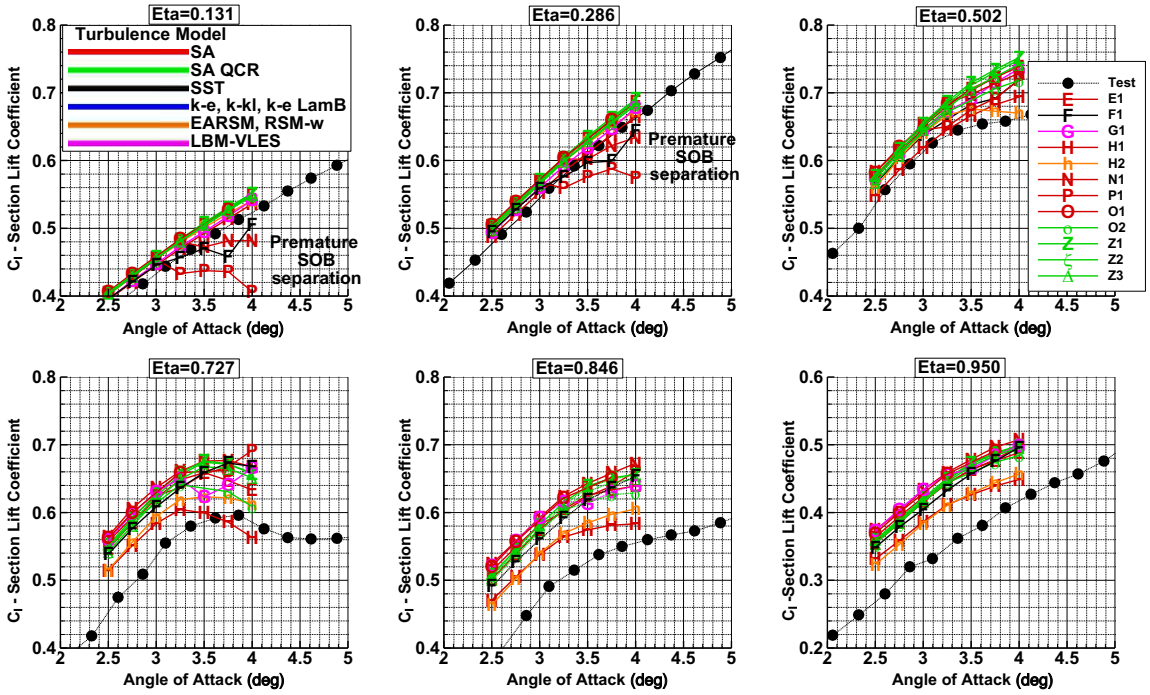


Figure S-X-26. DPW-VI: WB (Aeroelastic) Wing Section Lift Coefficient, M=0.85.

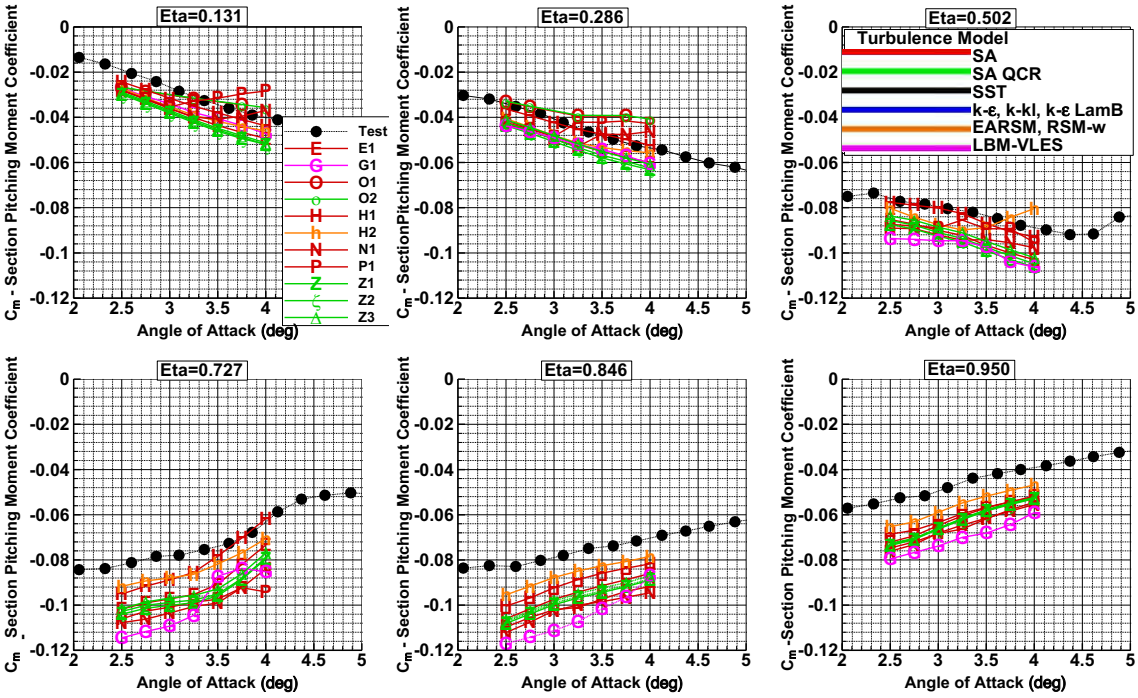


Figure S-X-27. WB (Aeroelastic) Wing Section Pitching Moment Coefficient, M=0.85.

Again, with so many solutions, the challenge is to decipher any useful information from the many entries. Figures S-X-28, -29, and -30 show lift, drag, and pitching moment parsed by grid and turbulence model. The solutions shown in these figures have been corrected for the presence of the wind tunnel upper-swept strut. The corrections represent nominal incremental values of lift, drag, and pitching moment based on the work of Ref. 87, and are listed in Table S-III-1 in Section III. Note that these corrections do not impact the wing section pressures, nor the section lift and pitching moment characteristics. Suspect solutions are identified by premature lift breaks, unusual pitching moment behavior, drag behavior, etc. The overset and multiblock grid solutions are shown in Figure S-X-28. Here three solutions (O1, Q1, and V2) show obvious premature lift breaks and are deemed outliers. Geolab and Custom unstructured grid solutions are shown in Figure S-X-29. Here solutions B3, M1, S1, V1, V3, and V4 standout as outliers. Boeing unstructured grid and Custom Cartesian solutions are shown in Figure S-X-30. Here G1, I2, J2, K2, and P1 are the standouts. While some more solutions are outliers, it is difficult to identify all of them in these crowded charts. Careful examination of the lift characteristics and pressure distributions identified all the solutions that exhibited premature lift breaks or other anomalies as shown in Figure S-X-31.

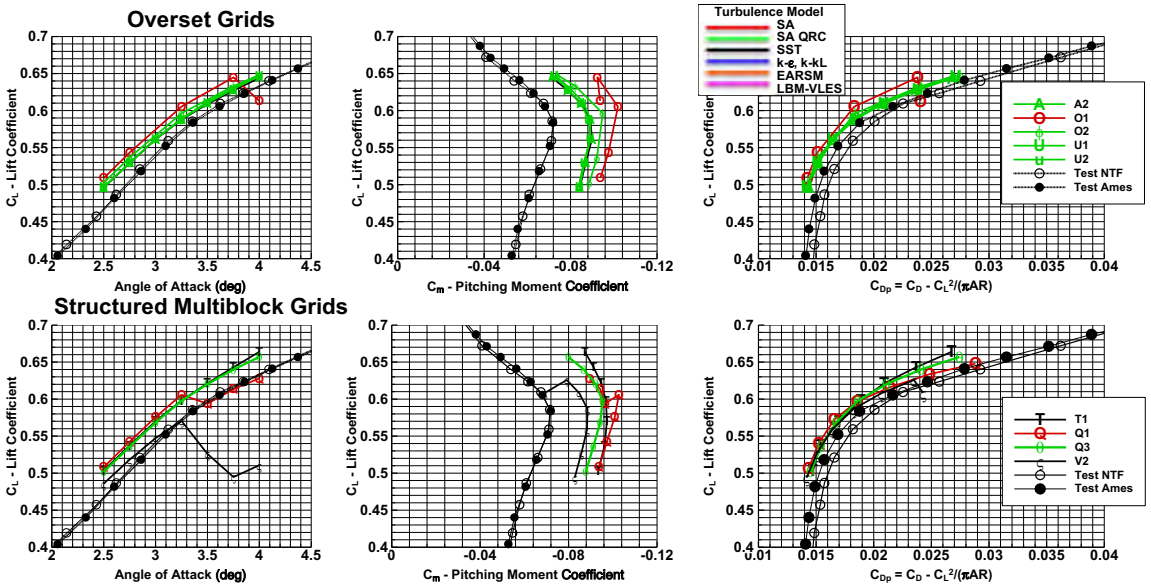


Figure S-X-28. DPW-VI: WB (Aeroelastic) Forces and Moments; Overset and Multiblock Grids, M=0.85.

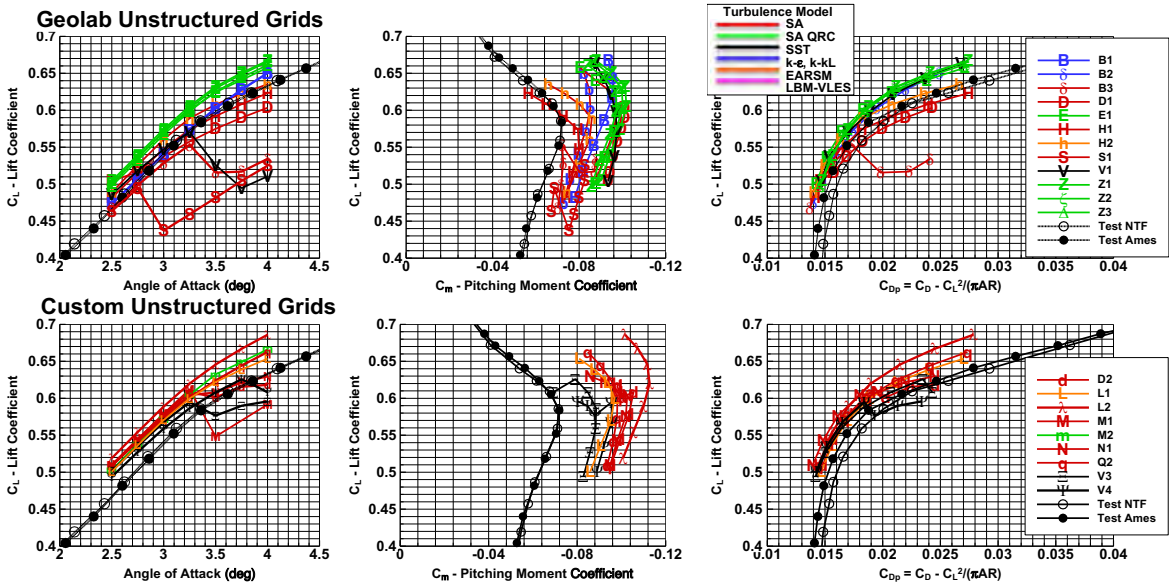


Figure S-X-29. DPW-VI: WB (Aeroelastic) Forces and Moments; Geolab and Custom Unstructured Grids, M=0.85.

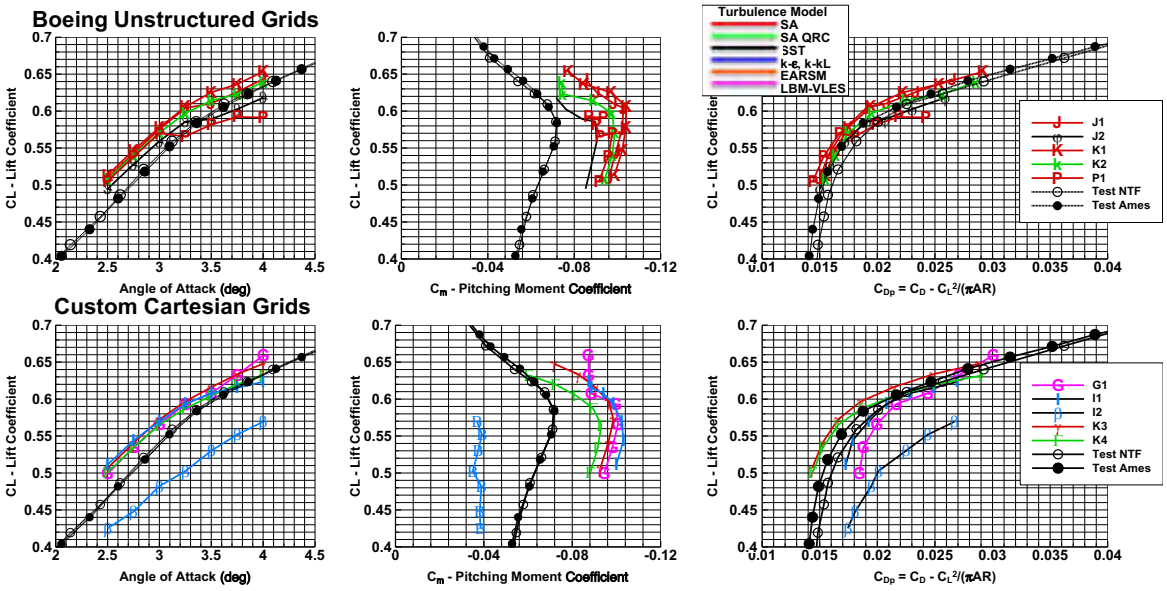


Figure S-X-30. DPW-VI: WB (Aeroelastic) Forces and Moments; Boeing Unstructured and Custom Cartesian Grids, M=0.85.

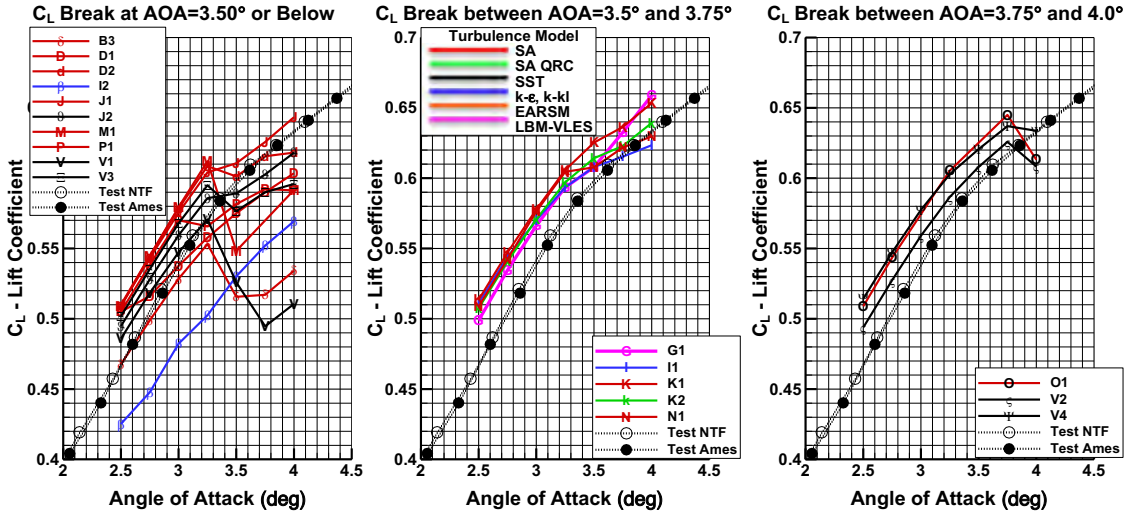


Figure S-X-31. DPW-VI: WB (Aeroelastic) Solution Outliers, M=0.85.

The lift and moments characteristics of the remaining 20 solutions are presented in Figure S-X-32. Even with all the outliers removed there is still an increasing spread of the lift and pitching moment with increasing angle of attack. At 4° angle of attack, the value of lift coefficient varies by 0.063 and the spread in pitching moment coefficient is 0.045. This is a bigger spread than we saw for DPW-V. Each one of these solutions on its own is a valid solution, yet as angle of attack increases the variation between solutions also increases. The drag characteristics of the remaining solutions are shown in Figure S-X-33. Also shown are test results from three repeat runs at both the LaRC NTF and the ARC 11-Foot TWT wind tunnels. As before, the drag characteristics are plotted in terms of the idealized profile. The spread of the drag values is largely driven by the increasing spread of lift with increasing angle of attack.

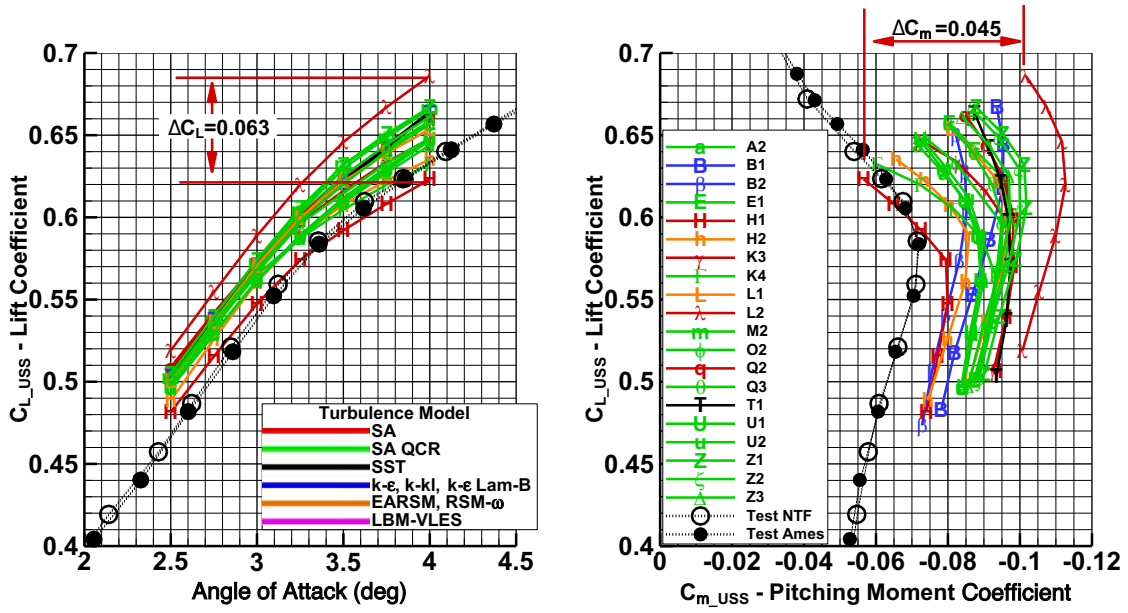


Figure S-X-32. DPW-VI: WB (Aeroelastic) Lift and Moment Characteristics; All Solutions minus Outliers, M=0.85.

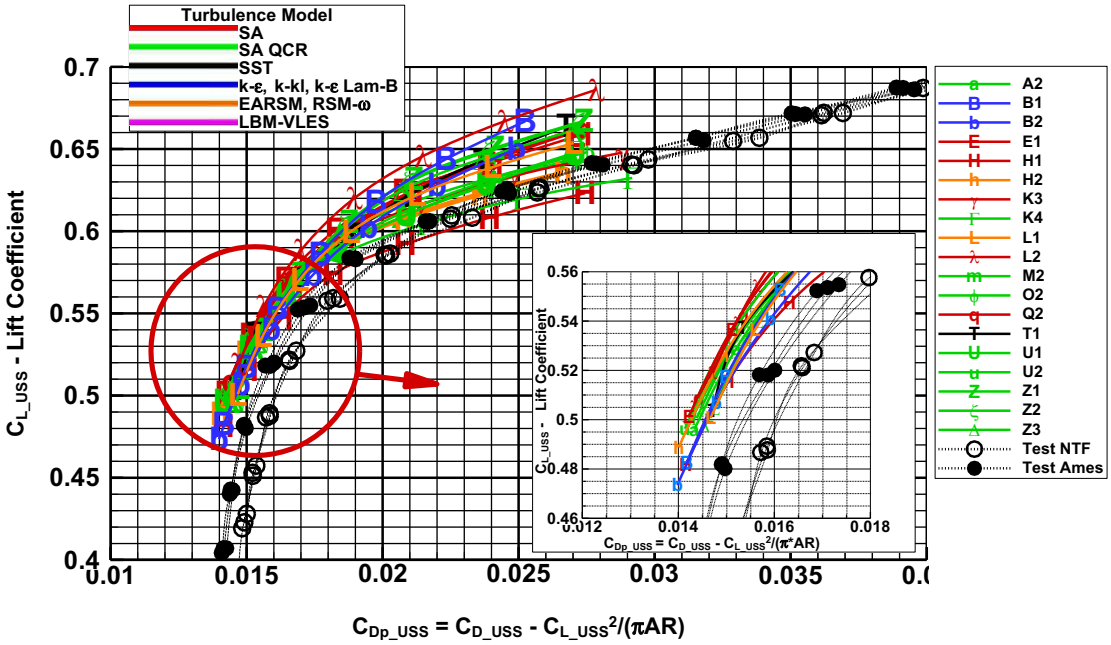


Figure S-X-33. DPW-VI: WB (Aeroelastic) "Idealized Profile" Drag Polar; All Solutions minus Outliers, M=0.85.

The pressure distributions of the remaining 20 solutions (minus the outliers) are shown in Figures S-X-34 to -37 for $C_L = 0.50$, and angles of attack of 3.0°, 3.5°, and 4.0°, respectively. Pressure distributions shown in Figure S-X-34 for $C_L = 0.50$ show very little variation between solutions. What little variation there is, is seen at the shock location on the outboard part of the wing. However, as the angle of attack is increased, we see increasing variation of the shock location across the span of the wing. At 4° angle of attack (Figure S-X-37), the shock location varies by as much as 20%' chord. This variation of shock location is consistent with the increasing spread of lift and moment seen in Figure S-X-32. Which solutions are most representative of the test data? Clearly there are issues that warrant further discussion later in this report (Section XV).

Additional plots showing lift break and further parsing of forces and moments by grid and turbulence model can be found in Appendix E**.**

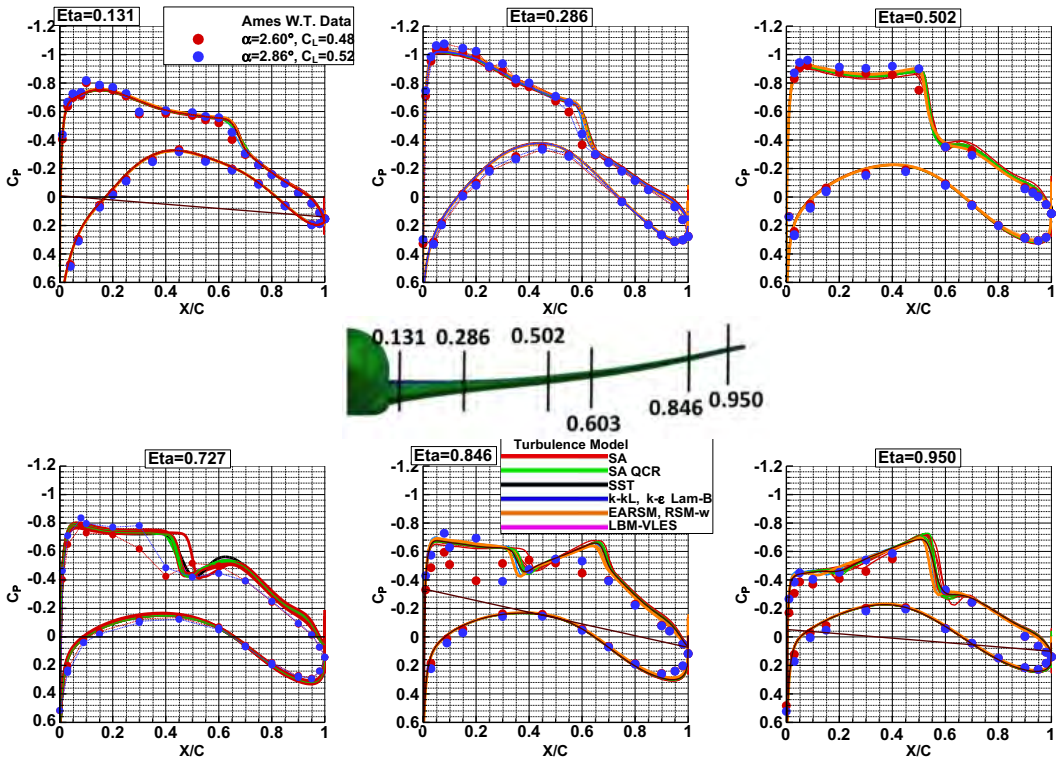


Figure S-X-34. DPW-VI: WB (Aeroelastic) Wing Pressure Distribution; All Solutions minus Outliers, C_L = 0.50, M=0.85.

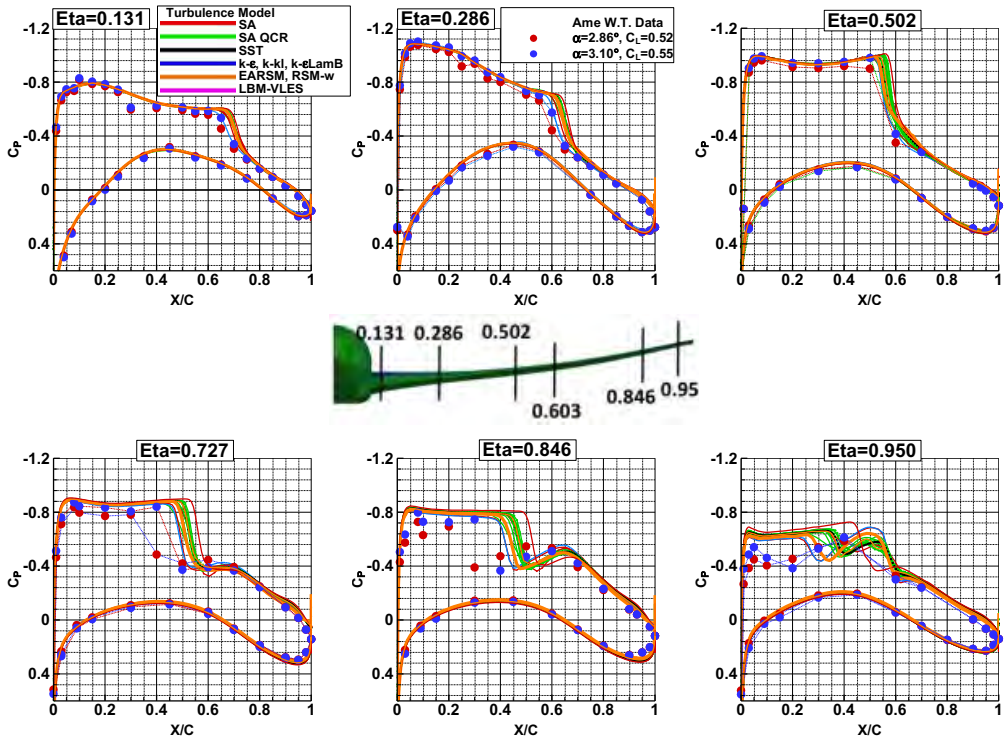


Figure S-X-35. DPW-VI: WB (Aeroelastic) Wing Pressure Distributions; All Solutions minus Outliers, AOA = 3.0°, M=0.85.

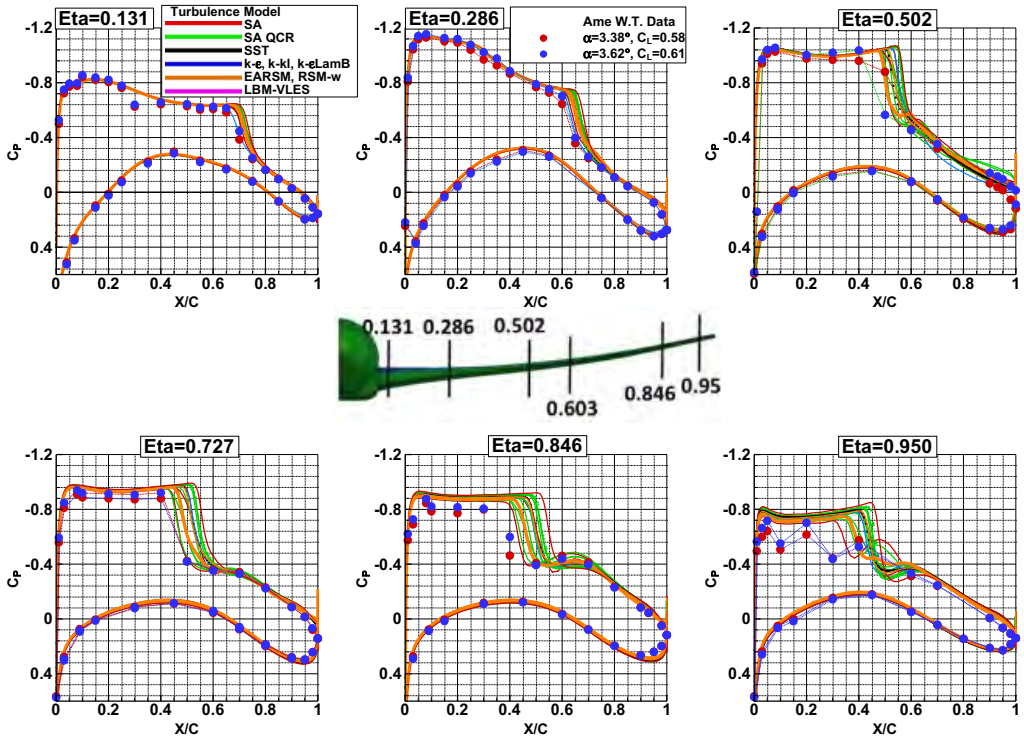


Figure S-X-36. DPW-VI: WB (Aeroelastic) Wing Pressure Distributions; All Solutions minus Outliers, AOA = 3.5°, M=0.85.

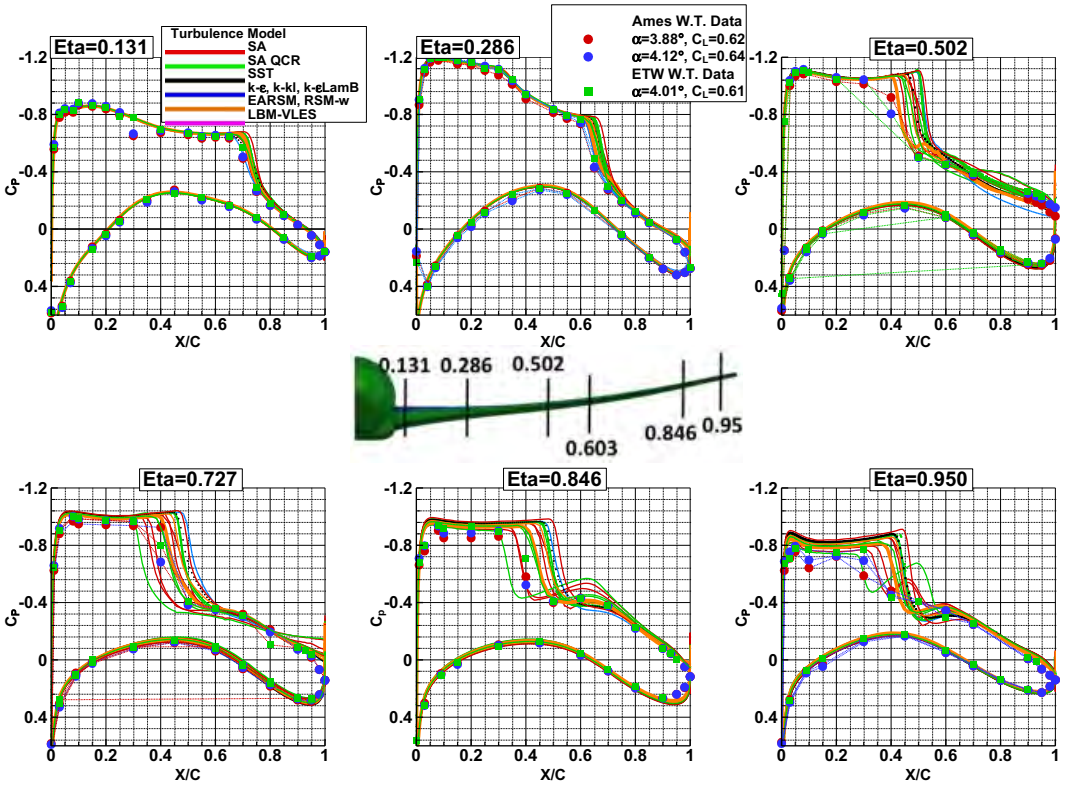


Figure S-X-37. DPW-VI: WB (Aeroelastic) Wing Pressure Distributions; All Solutions minus Outliers, AOA = 4.0°, M=0.85.

Section XI: Trim Drag and Stabilizer Effectiveness

The downwash study was unique to DPW-IV. Here, four angle-of-attack sweeps of the CRM were performed, three on the Wing-Body-Tail configuration at different horizontal-tail settings, and one without the tail on the Wing-Body configuration. The tail settings were iH = [–2°, 0°, +2°]. The three WBT polars provide sufficient information to reconstruct a trimmed drag polar, and trimmed lift curve, which was the stated purpose of this study. In addition, these computational results provide sufficient data to calculate stabilizer effectiveness. The data set identifiers for DPW-IV are found in Table S-VI-1 and in Appendix C**.**

A. Trimmed Lift and Drag

In this study, the CRM WBT is being trimmed at its pitching moment reference location (x_{ref}= 1,325.9). This means that the tail angle (stabilizer setting) iH must be determined to ensure pitching moment, C_{M_TOT}, equal to zero at all lifting conditions. A sample Excel spreadsheet detailing the process for calculating a trimmed lift curve, drag polar, and iH-to-trim can be found on the DPW-IV website [38]. These data are also used to develop trim-drag impact by comparing trimmed-WBT and WB polars.

Figure S-XI-1 shows lift vs. angle of attack for the WBT with the three different tail settings. The results have been broken out by grid type: structured or unstructured. The unstructured grid solutions show a greater spread in lift compared to those from structured grids. Both sets of results show the expected change of lift with changing tail settings. Both sets show the same lift break between an angle of attack of 3° and 4° also seen for the WB in Section X.

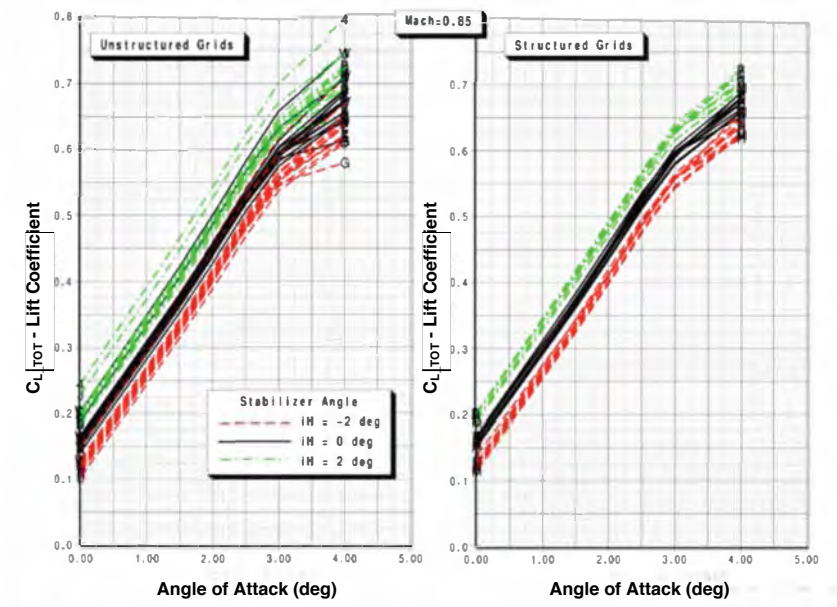


Figure S-XI-1. DPW-IV: Lift vs. Angle of Attack; Wing-Body-Tail iH = –2°, 0°, 2°, M=0.85.

Pitching moment for the WBT at the three tail settings, as well as for the WB configuration, and corresponding test data is shown in Figure S-XI-2. The test data are from both the NTF and 11-Foot wind tunnels. Note that there is little difference between the test data from the two tunnels. However, there is a significant shift between the computational results and test data. For the WBT configuration, the pitching moment increment from the computational results to experiment is about 0.10 more negative (nose down), less so for the WB. This difference is largely due to the influence of the USS mounting system, and the lack of consideration of the wind tunnel model aeroelastics in the computational model. The magnitude of these effects was not known at the time of DPW-IV, the Workshop having occurred before the wind tunnel tests. Note the spread of pitching moment for the computational results at each tail angle. This pitching moment spread has been typical of all DPW results. All solutions show a break in pitching moment between 3° and 4° angle of attack, most were less stable (more positive C_M), and a few were

more stable (more negative C_M). This tendency toward a more positive pitching moment with increasing lift (angle of attack) is referred to as "pitch-up" and represents a reduction of longitudinal stability. Figure S-XI-3 shows a breakdown of total pitching moment into components due to the wing, tail, and fuselage. Note that the reduction in stability between 3° and 4° angle of attack is always due to the wing. The contribution of the tail in this C_L range is to always increase negative pitching moment with increasing angle of attack.

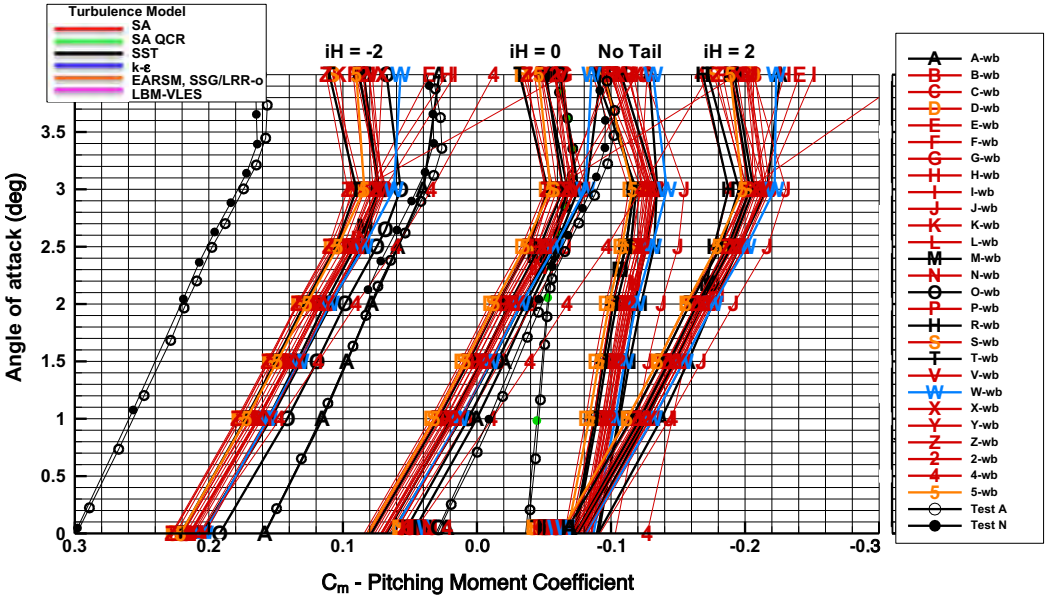


Figure S-XI-2. DPW-IV: Pitching Moment: Wing-Body and Wing-Body-Tail iH = –2°, 0°, 2°, M=0.85.

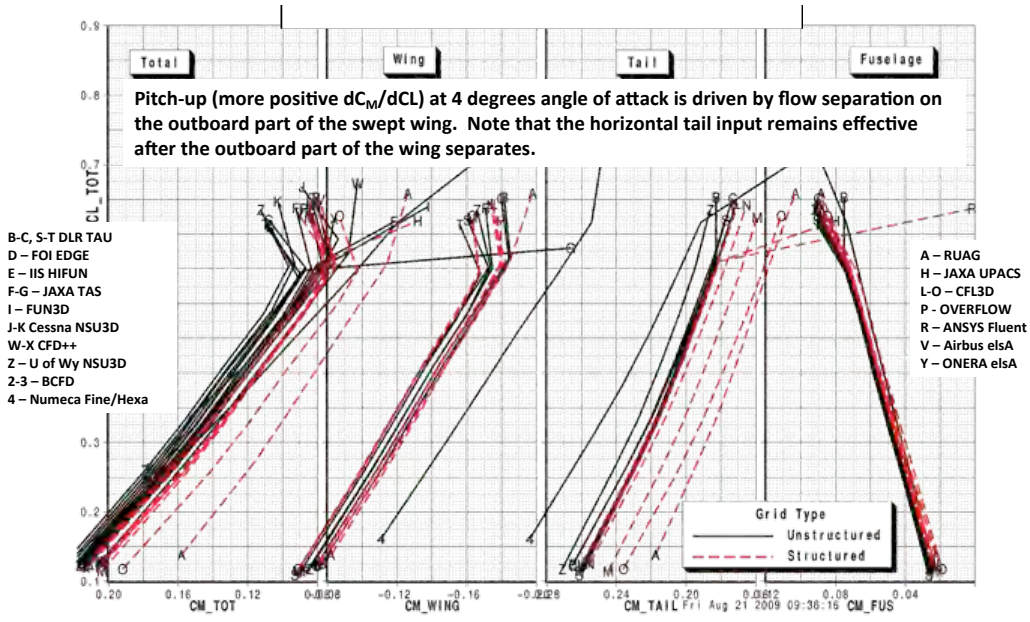


Figure S-XI-3. DPW-IV: Pitching Moment Components; Wing-Body-Tail iH = –2°, M=0.85.

Using the process provided by the Excel spreadsheet [38], or a similar process, trimmed drag polars and tail settings to trim to zero pitching moment were calculated and are seen in Figure S-XI-4. Most of the trimmed polars fall within a 20 drag count band. The spread of iH required to trim is about 0.5°.

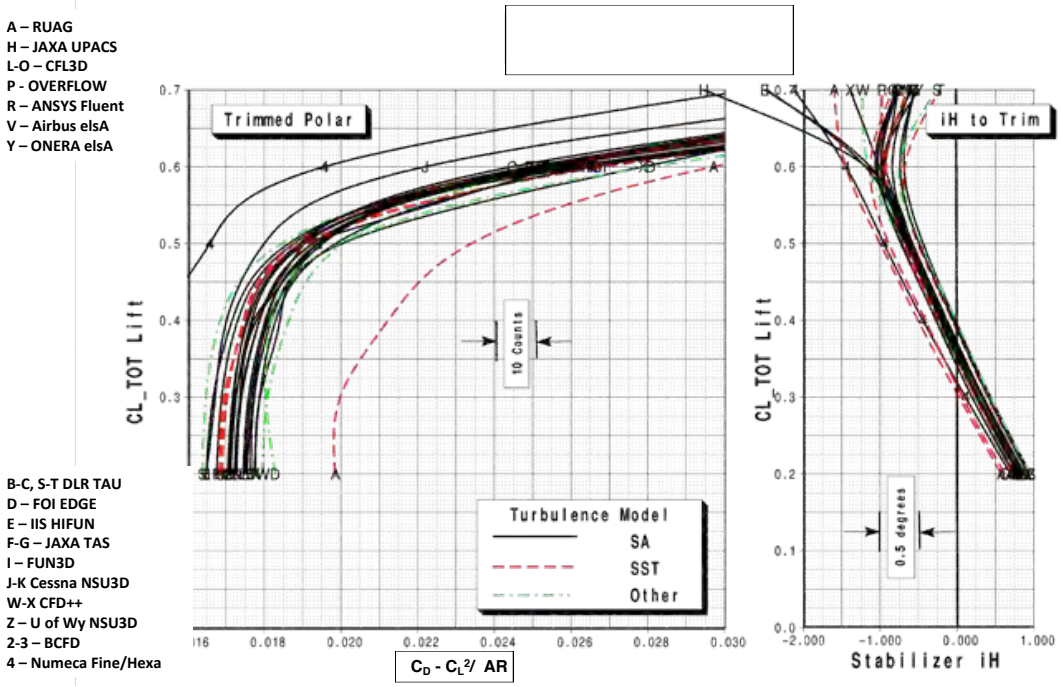


Figure S-XI-4. DPW-IV: Wing-Body-Tail Trimmed Drag Polars and iH to Trim, M=0.85.

In both the NTF and 11-foot wind-tunnel tests, the CRM model is supported by an upper-swept strut/sting combination. The presence of this mounting system primarily affects the flow over the aft end of the fuselage, which can significantly affect the absolute value of the forces and moments on the model. This is particularly true when the model includes a horizontal tail. The blade-sting induces a downward flow on the horizontal tail, which increases the nose-up pitching moment. Furthermore, an increase in downwash affects the drag of a lifting tail. To accurately correct for these effects, alternate mounting techniques (such as post or blade support on the belly of the fuselage or wing tip support) are required, which was not done due to budget and time considerations. Reference 87 details a computational study that modeled the presence of the model support system in the wind tunnel on the WBT configuration. From this study, corrections to the CFD results for average lift and pitching moment increments were derived and are listed in Table S-III-1. The aeroelastic and upper-swept strut corrections were combined and applied to the original submitted results. A comparison of these "corrected" pitching moment, C_{M_TOT}, results to wind tunnel data is shown in Figure S-XI-5. Note how these corrections have significantly reduced the differences between CFD and experiment. The CFD pitching moment is still more negative than from wind tunnel but much less so compared to Figure S-XI-2.

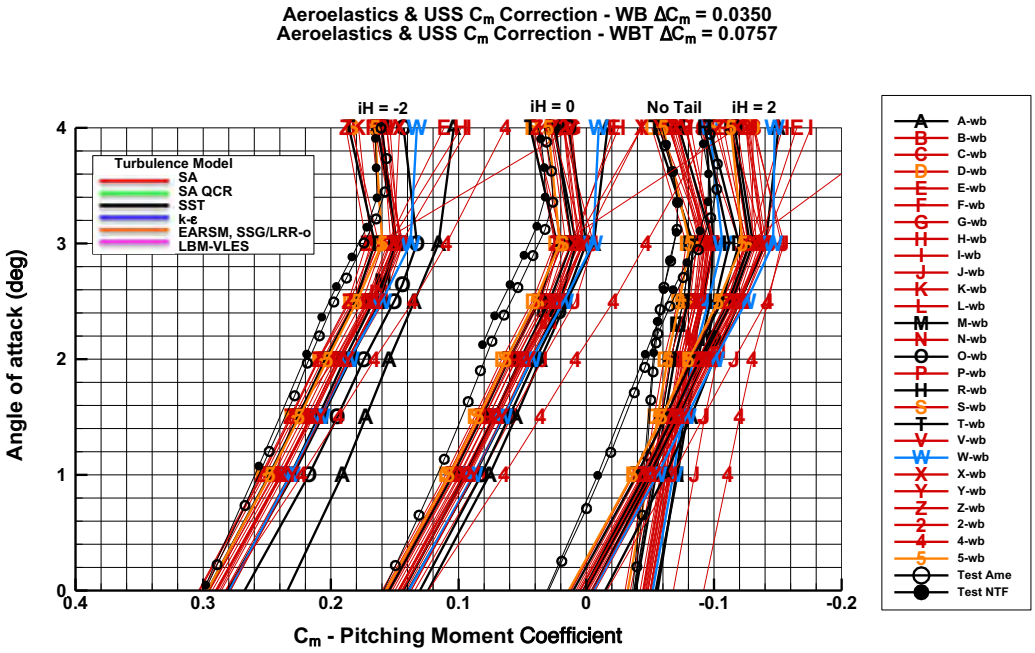


Figure S-XI-5. DPW-IV: Pitching Moment Corrected for Mounting System and Aeroelastics; WB and WBT iH = –2°, 0°, 2°, M=0.85.

It was not practical to recalculate the trimmed lift, drag, and iH-to-trim for all the DPW-IV data sets with the Ref. 87-based aeroelastic and USS corrections. These corrections were applied to one solution (O) in order to get an idea of the magnitude of the resulting changes. Trimmed lift, "profile" drag, and iH to trim results are shown in Figure S-XI-6. Results are shown for the NTF test, the original DPW-IV case, the same case with the USS corrections alone, and with the USS plus model aeroelastic corrections. The inclusion of the USS significantly changes the results with respect to the original DPW-IV solution. Note that the inclusion of the USS corrections results in very good agreement of trimmed lift with NTF, but not of trimmed drag. The additional inclusion of the model aeroelastics makes very little difference in the trimmed lift and drag but does change iH-to-trim. Just remember that the original DPW-IV calculations are actually more representative of a free-air solution.

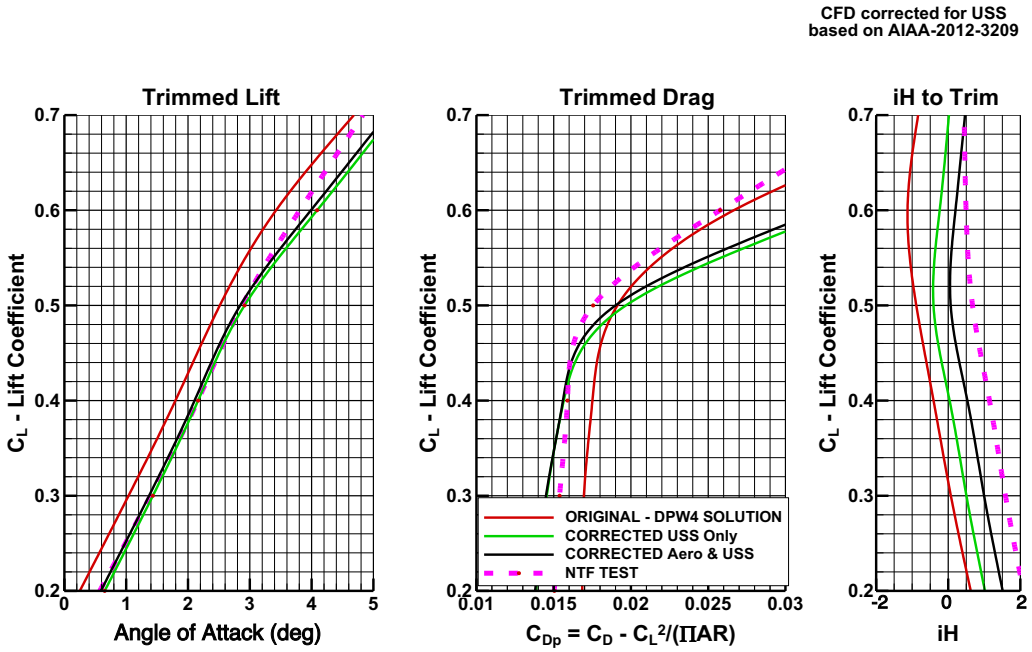


Figure S-XI-6. DPW-IV: WBT "Corrected" Trimmed Lift and Drag, M=0.85.

B. Stabilizer Effectiveness

Stabilizer effectiveness can be defined in terms of the change of total pitching moment due to change in stabilizer (or horizontal tail in this case) setting. Stabilizer effectiveness plays a key role in determining trimmed lift and drag, as well as iH-to-trim and other stability and control parameters. Change in pitching moment vs. tail angle is shown in Figure S-XI-7. Results from all the DPW-IV solutions and test data from LaRC NTF and ARC 11-Foot are shown. The computational data incorporated the corrections for the USS. The computational data agree quite well with the test both in level and slope. The effectiveness slope, $dC_m/Tail$ is shown in Figures S-XI-8 and -9 for all the solutions. These slopes were taken from the results shown in Figure S-XI-7 and have been ordered in terms of magnitude. Figure S-XI-8 identifies the individual solutions in terms of grid type; Figure S-XI-9 identifies them in terms of turbulence model. Also shown is the average for the solutions ±1 sigma. For reference the ±1 sigma range for the experimental results are also given from both the NTF and 11-Foot tunnels. The 1 sigma spread is quite small because of the very limited number of wind tunnel runs to draw on. A source of experimental error not considered was the actual value of iH, the tail (stabilizer) deflection. All that was available were the nominal values of iH. In practice, there is usually a small deviation from nominal that can vary every time the model is built up. In addition, the wind tunnel model is not infinitely rigid. The model fuselage and tail does experience some aeroelastic bending. This aeroelastic effect will reduce the effectiveness slope compared to the rigid geometry. The process of removing the aeroelastic effects in test data is referred to as "rigidizing" the data. The "rigidizing" of the stabilizer effectiveness was provided by Dave Bogue, Boom Supersonic. The "rigidizing" process is based on the tail on and off stability changes at two different dynamic pressures and extrapolating that back to zero dynamic pressure. These data were available from the NTF at 19 million chord Reynolds number. The change in pitching moment due to tail angle is shown in Figure S-XI-10. Granted the differences between the two dynamic pressures are small but become significant when extrapolated back to zero dynamic pressures. As expected, the "rigidization" process increases the experimental effectiveness slope, and that now lies within the lower 1 sigma limit of the CFD data.

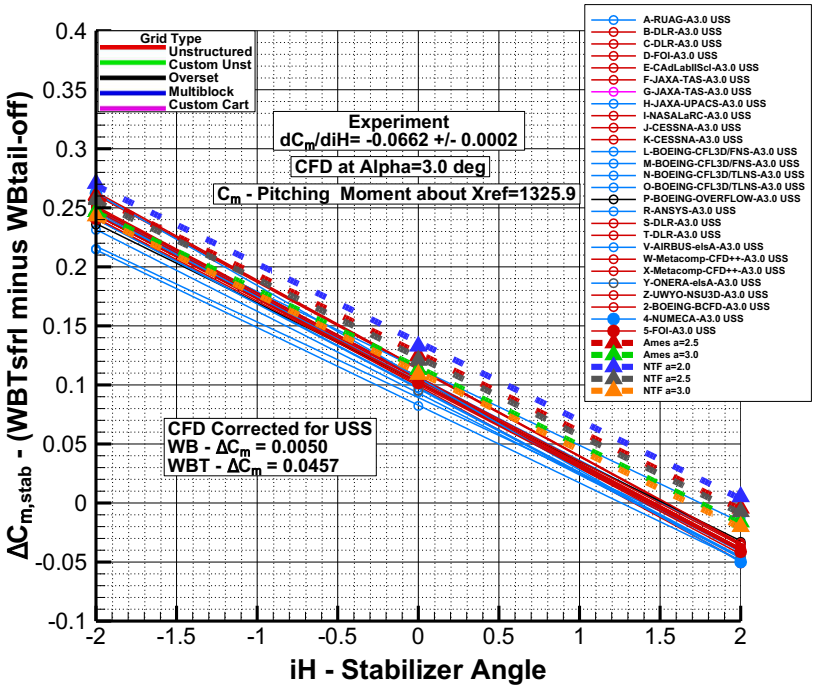


Figure S-XI-7. Change of Pitching Moment vs. Tail Angle, M=0.85.

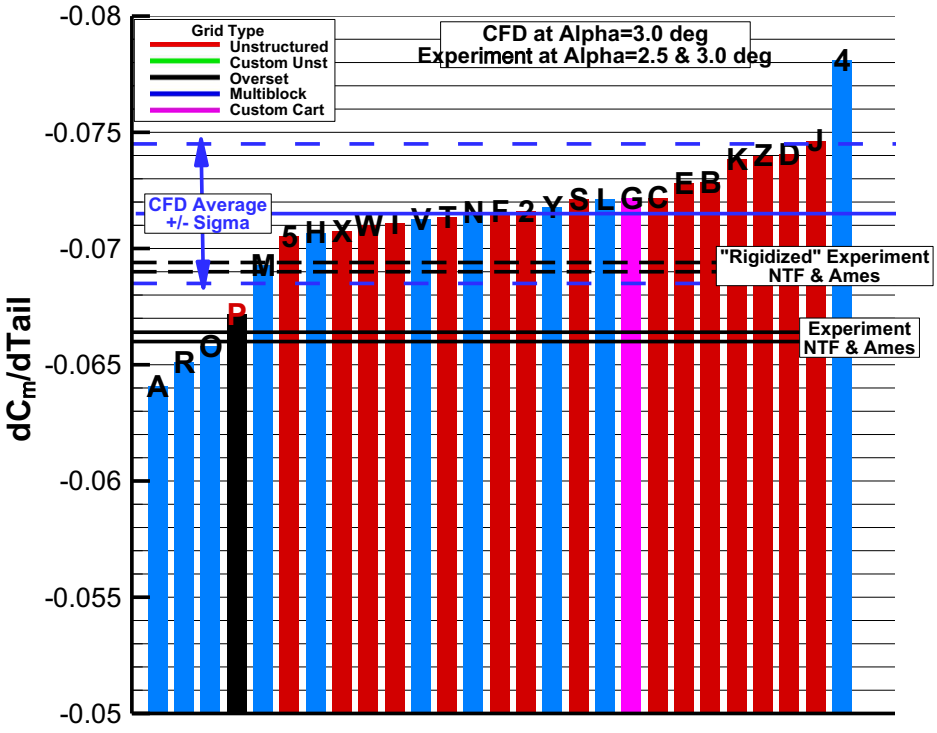


Figure S-XI-8. Stabilizer Effectiveness: Grid Type, M=0.85.

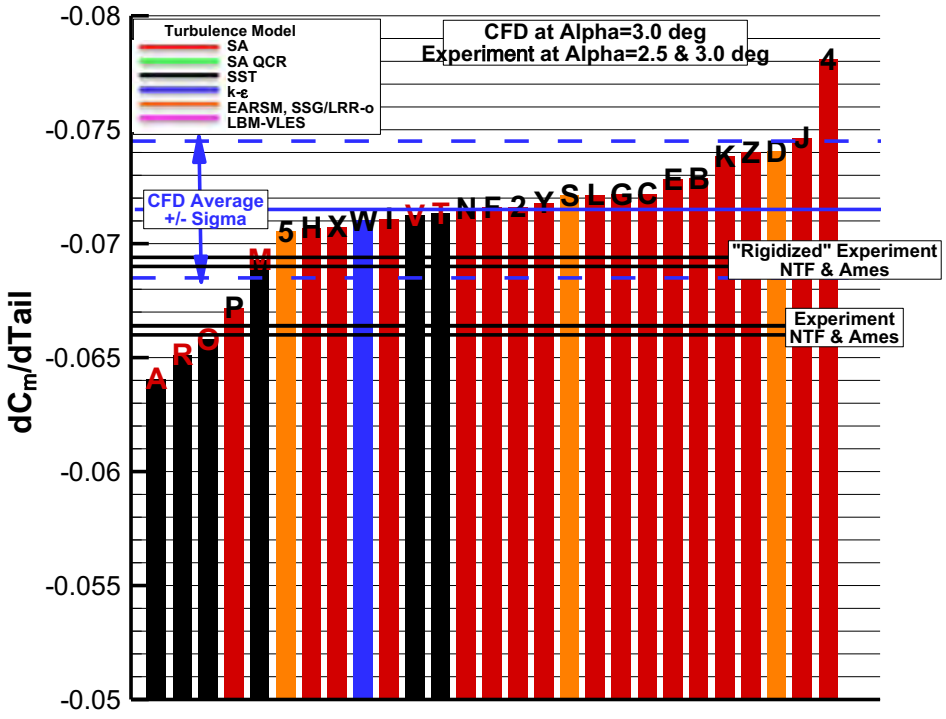


Figure S-XI-9. Stabilizer Effectiveness: Turbulence Model, M=0.85.

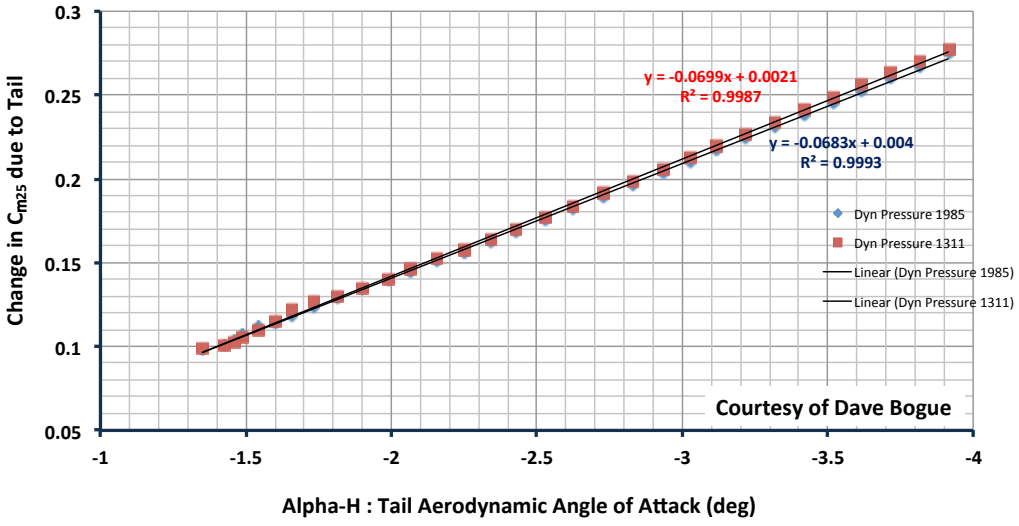


Figure S-XI-10. Effect of Dynamic Pressure on Change in Pitching Moment due to Tail Angle, M=0.85.

Additional plots related to these downwash studies can be found in Appendix F, including trim drag, stabilizer effectiveness plots, and plots comparing stabilizer drag for the three stabilizer deflection angles tested. However, without extensive corrections to account for the USS, the comparisons with experimental data are of limited value and are not included here.

Section XII: WB Grid Adaptation Study

A new request was made for DPW-VI for grid adaptation solutions of the CRM Wing-Body configuration as an optional case. This consists of a series of fixed lift, $C_L = 0.50$, solutions using an adapted grid family provided by the participant. Accurate prediction of drag (and other aerodynamic parameters) on a transport aircraft has proven to be very challenging, as we have seen in the previous sections of this report. There are many factors that make this problem challenging, but one of the most common is controlling and reducing discretization error resulting from inadequate grid resolution. Achieving adequate resolution is difficult because the grid requirements vary throughout the domain depending on factors such as the flow solution, discretization scheme, and physical models, etc. As we have seen, studies with the same solver, same turbulence model, but different grids, can give significantly different results as shown in Figure S-XII-1 from DPW-V. In fact, in DPW-V, most solver/turbulence model combinations yielded different results using identical grids as was shown in Figures S-X-8, -9, and -10. And remember, the "common" grids in DPW-V were carefully crafted for this specific geometry, Mach number, and design lift coefficient. The fixed grid process can be very labor intensive requiring many days or weeks of an expert user's effort to arrive at a family of fixed grids. Grid convergence studies along with Richardson extrapolations are really not very practical and are rarely done in practice for every configuration. Instead, users depend on a good set of gridding guidelines, and lots of experience with the type of configuration, and expected flow characteristics.

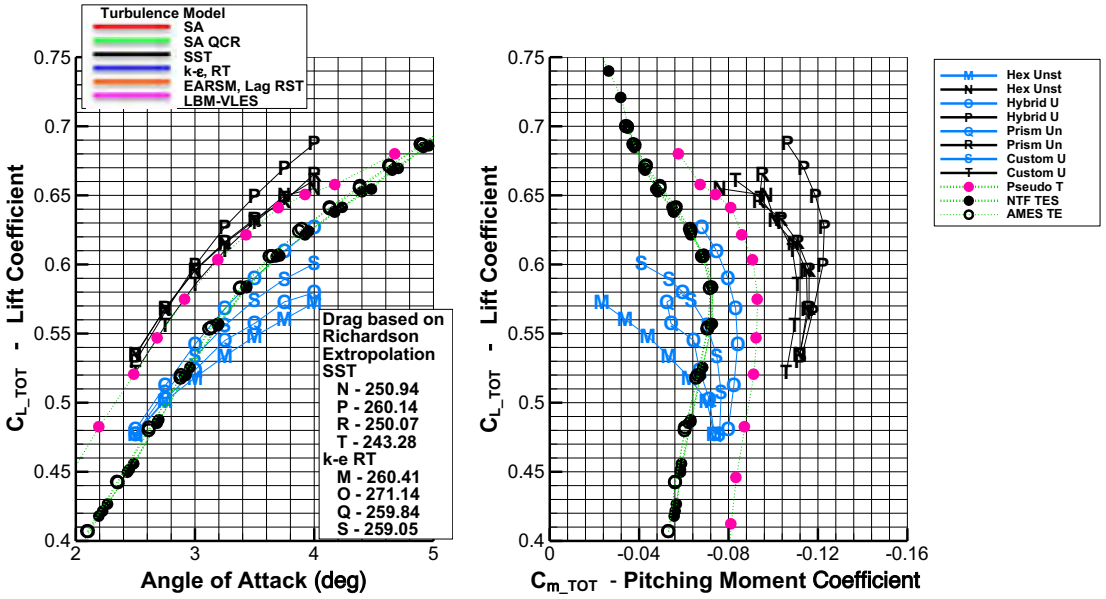


Figure S-XII-1. WB (As-Built) Grid Effect on Solutions, M=0.85.

Recently adaptive meshing techniques for unstructured grids have matured to the point that adaptive RANS solutions on full aircraft configurations now seem practical [97-100]. These methods automatically adapt the mesh to minimize solution error for a given number of degrees of freedom such as nodes or cells. The grid size can then be increased until a desired level of accuracy is achieved. It is expected that by directly targeting the discretization error, these methods can achieve a given level of accuracy more efficiently than with the fixed grid refinement approach. Another potential benefit of the adaptive approach is that it may remove the need for gridding guidelines and/or the need for an expert user to guide the mesh generation process.

As this is an active area of CFD research, it was time to take a measure of the progress. Unfortunately, only six solution sets were provided by three organizations. Three solutions, I1, I2 and I3, were based on the same solver, using a similar adaptation technique, but differed in two different treatments of the boundary layer. These employed a Cartesian mesh that can be successively refined to fit geometrical and flow features. Their solver employs a Favre-averaged, cell-center finite volume method. Indicator functions drive the refinement or coarsening as the solution progresses. The difference between the three solutions is the wall-function treatment of the boundary layer. I1 and I3 featured a more complete "thick" wall-function treatment. I2 employs the original "thin" layer subgrid model. The

other three solutions, A1, P1 and P2, were based on different solvers. Solution A1, Overflow, employs an implicit second-order cell centered finite volume solver, and employed a feature-based adaption scheme [101]. The sensor function is the undivided second difference of flow variables (truncation error in flow gradient regions). Isentropic grid refinement is in all directions where neighboring grids differ by 2x. P1, BCFD, employs an implicit second-order cell centered finite volume solver. P2, GGNS, employs a second-order node centered SUPG finite-element discretization with a strong solver that achieves machine precision residual convergence [90,102]. Both P1 and P2 employ the Edge Primitive Insertion Collapse (EPIC) adaptive grid tool [100] focusing on a sizing metric derived from the Mach Hessian or Entropy Adjoint error. The EPIC adaptive grid tool process is illustrated in Figure S-XII-2.

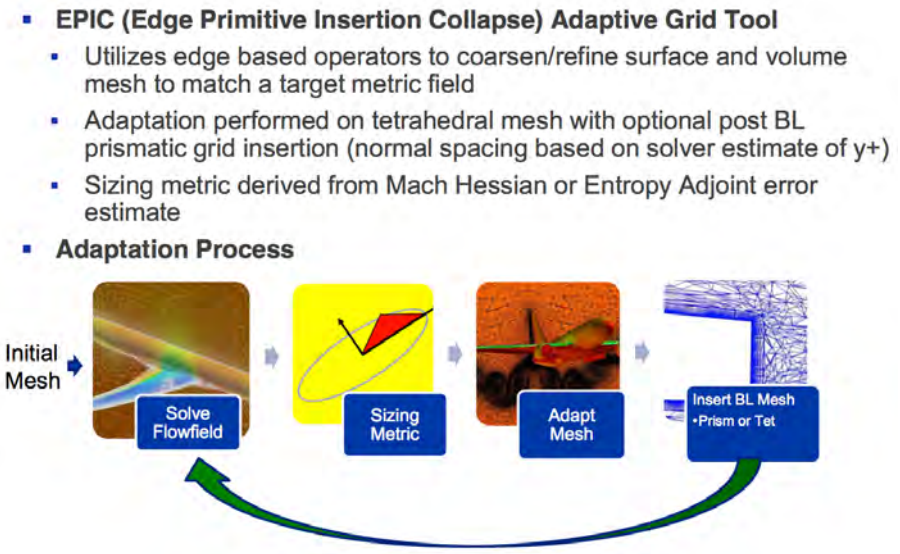


Figure S-XII-2. EPIC Adaptive Grid Tool.

Total lift and drag as a function of the grid factor (GRIDFAC) for the six adapted grid solutions are shown on the left side of Figure S-XII-3. Note that the GRIDFAC scale has been greatly expanded compared to those shown in Section-VII. It is immediately obvious that solutions I1, I2, and I3 were not at a constant $C_L = 0.50$. These cases were run at a constant angle of attack, resulting in varying values of lift and incompatible drag convergence characteristics. Since no firm conclusions can be drawn about these I solutions, further discussion will just focus on the remaining three solutions. Figure S-XII-4 shows the acceptable adapted grid solutions as well as all the fixed grid solutions, with just the adapted solutions on the left side of the plot and all the fixed grid solutions plus the adapted solutions on the right side of the plot. The fixed grid solutions from DPW-VI Case 2, previously shown in Figures S-VII-7, -8, and -9, have been included and are shown by dashed lines. Note that the drag scale on the right side is much tighter. This figure suggests that the three adaptive grid solutions are converging to the continuum similar to the fixed grid solutions. The fixed grid average was 256.64 counts with a sigma of 5.06. The average for the three adapted grid solutions was 253.43 counts.

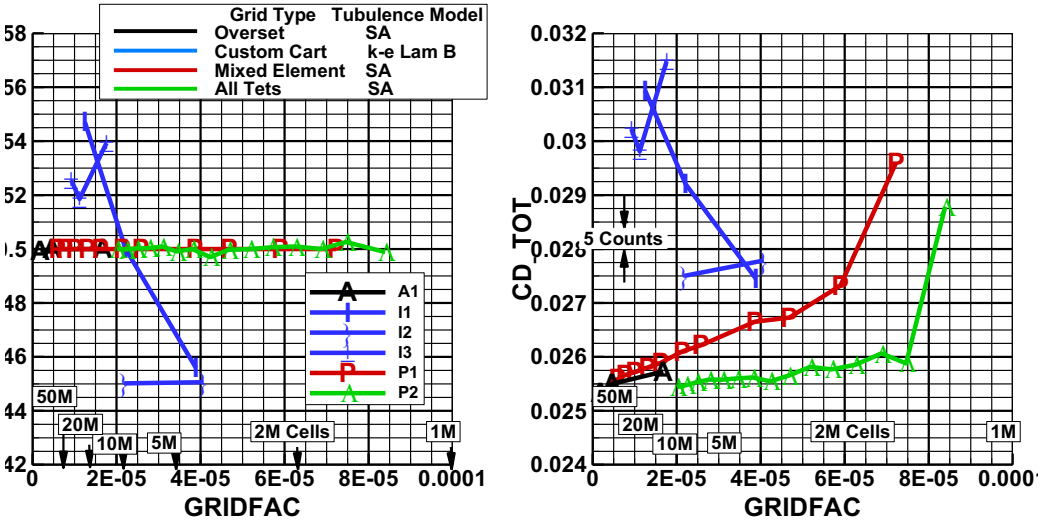


Figure S-XII-3. DPW-VI: WB (Aeroelastic) Lift and Drag - Adapted Solutions, M=0.85.

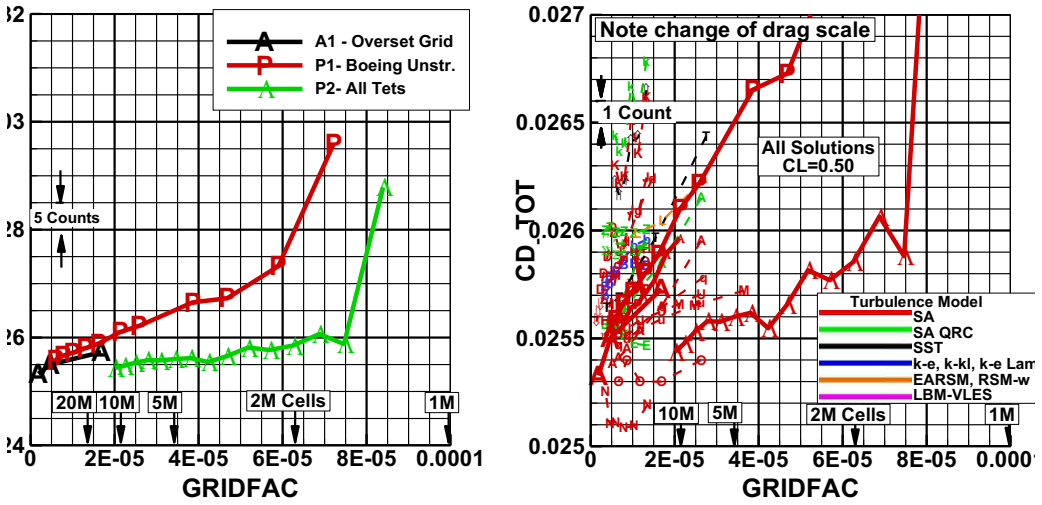


Figure S-XII-4. DPW-VI: WB (Aeroelastic) Adapted and Fixed Grid Drag Convergence, M=0.85.

The A1 solution (Overflow) refinement path is shown in Figure S-XII-5. Here drag has been plotted versus a function of the number of grid points on the wing, not the more conventional GRIDFAC. The fixed grid/uniform refinement path sequence (from DPW-VI Case2) is shown ending with point A representing the ultra-fine grid result. The A1 adaption began from the modification of the existing coarse grid from the existing fixed grid convergence sequence, point B. Two cycles of adaptive refinement resulted in solutions at points C and D on the plot. The resulting pressure distributions (not shown) are little changed from those of the fixed grid convergence set shown in Section VII. The main effect is to further sharpen the shocks. This can better be seen in Figure S-XII-6, which shows grid resolution and pressure contours for the four cases. Note that the wing tip shock structure characterized by a forward swept lambda shock in the adaption sequence was not captured as well by the ultrafine uniformly refined grid. This suggests that without adaption some flow features may not be adequately captured with fixed grids. This is particularly a risk with geometries/flow environments for which there is not extensive experience. A further description of this method and ensuing results may be found in Ref.103.

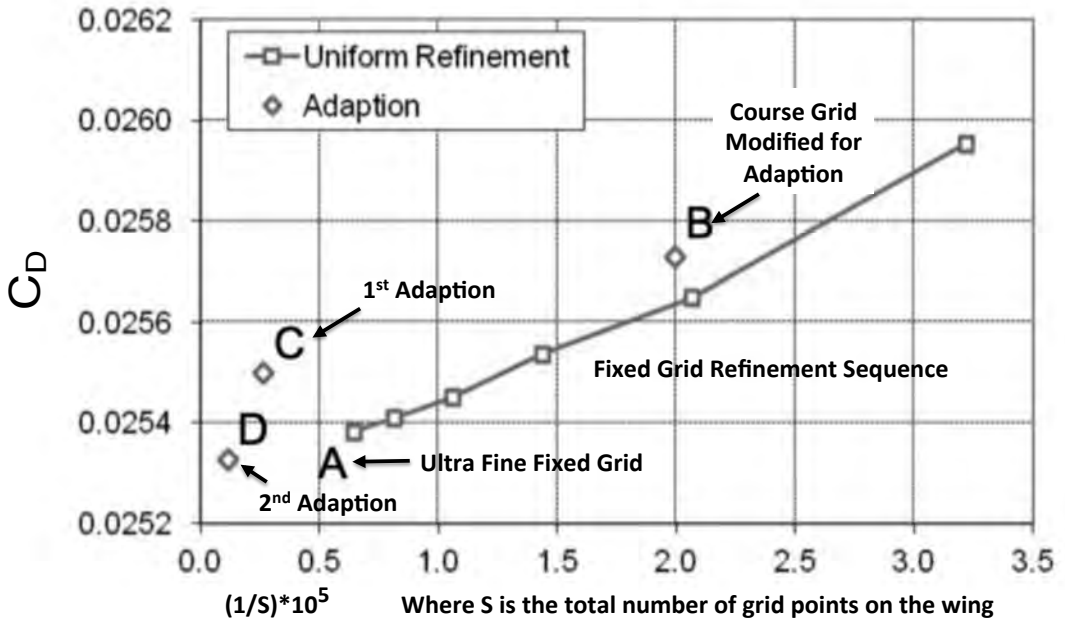


Figure S-XII-5. WB (Aeroelastic) Total Drag Convergence with Solution A1, M=0.85.

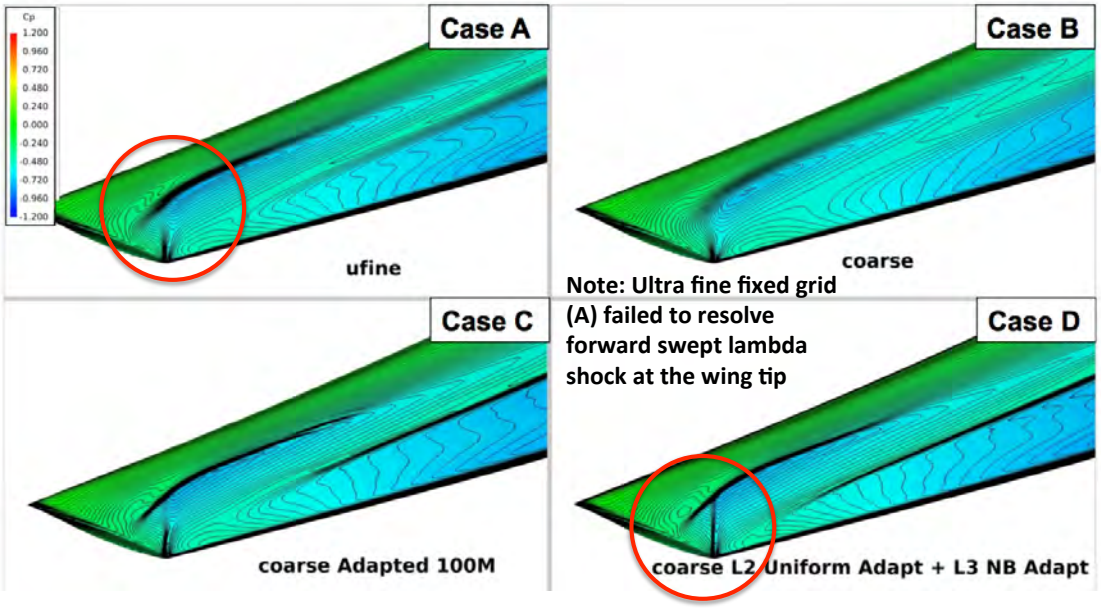


Figure S-XII-6. WB (Aeroelastic) Effect of Adaption on Wing Tip Pressures, M=0.85.

Both the P1 (BCFD), and P2 (GGNS) solutions shown in Figure S-XII-4 started with a relatively small grid of less than 2 million cells. Both show a rapid drop of drag with the first grid adaption followed by a steady convergence toward the continuum and ended up with solutions at moderate grid sizes that rivaled the carefully crafted "fixed" grids. The P1 and P2 adaption shown here was based on Mach Hessian. The behavior of P2 is particularly noteworthy. The combination of a strong solver, solid residual convergence, and grid adaption results in a rapid convergence to the continuum drag value with a very low grid convergence (dCDT/dGRIDFAC) rate. Although results for the WBNP were neither asked for, nor submitted prior to the DPW-IV workshop, the two solvers using EPIC generated adaptive solutions for both the WB and the WBNP [104]. Once started, the adaptation process was found to be very stable,

requiring little or no intervention from the user. The adaptive solutions were continued for 15 to 20 adaptation cycles using the specified grid growth rate of 20% between adaptation cycles.

An example of the progression of the adapted grids and solutions for the GGNS WBNP solution is shown in Figure S-XII-7. The displayed grids (taken from Ref. 104) correspond to adaptation cycles 1, 4, 7, and 14. Over the first 4 grid levels, the grid redistributes nodes and reorients elements from a predominantly isotropic mesh to an anisotropic mesh. By cycle 4, the main shock on the upper wing surface starts to become visible in the mesh. As the adaptation continues, the shock moves aft and the adapted grids resolve a secondary lambda shock near the wing tip and a shock on the upper surface of the nacelle. The shear layers and wing tip vortices are also well captured in the volume grid. The placement of nodes in the adapted grids was drastically different than for the fixed grids. The adapted grids generally achieved much better resolution of shock waves and off body flow field features such as wakes and vortices, though this extra resolution did not significantly improve the accuracy in the drag prediction. A method for limiting the resolution of these feature-based flow features away from the configuration where they don't contribute to the accuracy of the solution could reduce the cost of adaptation.

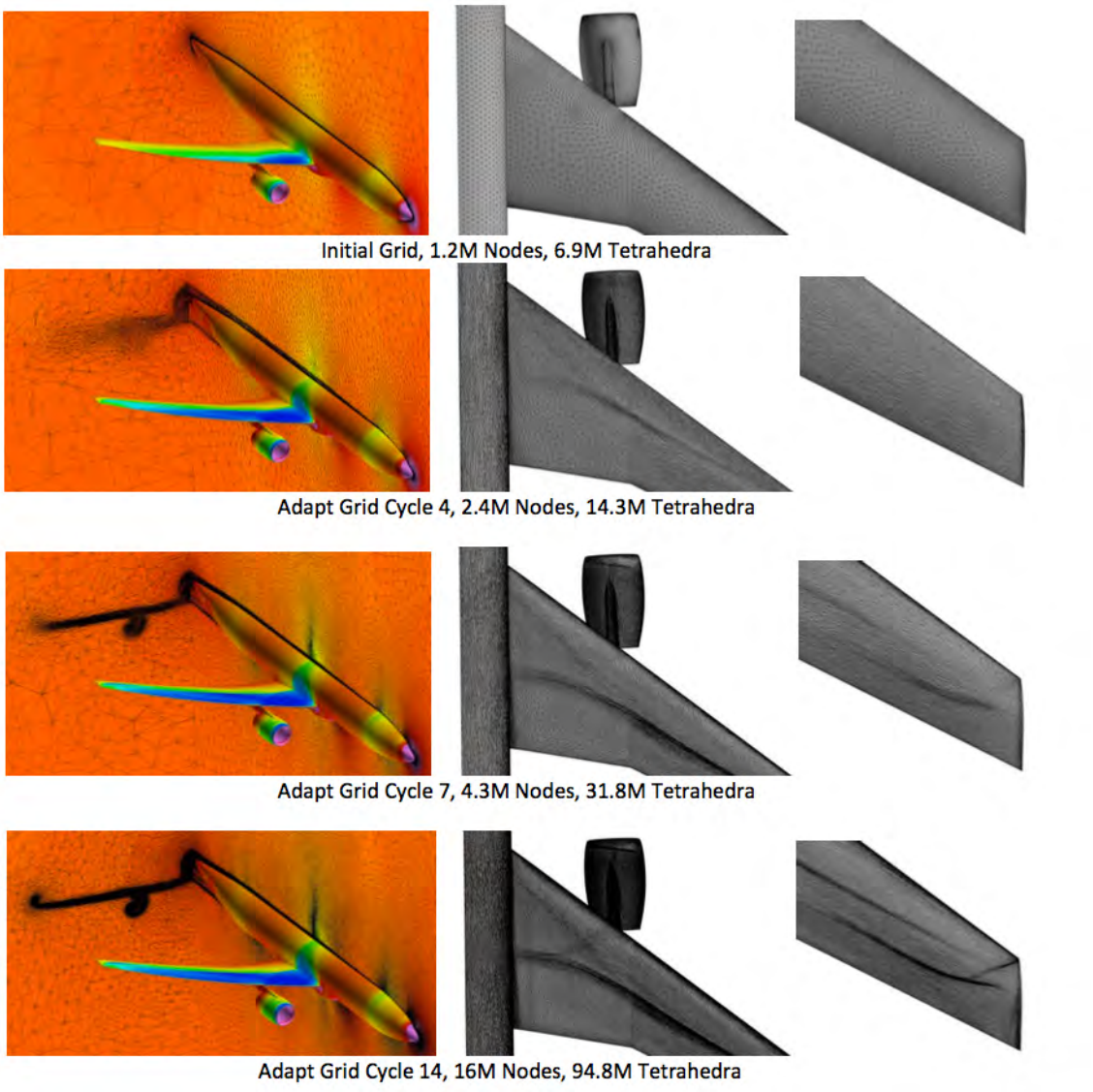


Figure S-XII-7. Adapted Grid and Solution Sequence for WBNP (Aeroelastic) Configuration, M=0.85.

The promise that solution adaptive grids bring is that they should be able to deliver a consistent set of solutions for configurations, and/or conditions for which prior gridding experience may not be available. Even for this configuration, the "optimum" grid distribution may change dramatically for a drag rise series ranging from Mach = 0.70 to 0.90 or over a wide angle-of-attack range. Much work remains to be done to bring this technology to a "production" capability for 3D RANS. It is expected that combining an output-based error-estimate that is optimized for the analysis along with adaptive meshing, will provide significant advantages in grid convergence for future adaptive grid applications, in addition to the user and uncertainty benefits demonstrated to date. It is a technology that needs to be matured.

Section XIII: WB Coupled Aerostructural Simulation

Another case new to DPW-VI was the request for a coupled aerostructural simulation. The effects of static aeroelastic twist and deflection can be very significant at transonic flow conditions. The inclusion of static aeroelastic deformation of the CRM wind tunnel model in DPW-VI attests to their importance. These deformations were based on "after the fact" wind tunnel measurements. Unlike a wind tunnel model, the deformations of a full-scale airplane wing can be as much as an order of magnitude greater. An accurate CFD prediction of the flight characteristics of a full-scale airplane (or even a wind tunnel model) requires that the actual static aeroelastic deformation be included in the computational model. A coupled aerostructural simulation is one approach in achieving this. A NASTRAN® finite element model was provided for structural analyses and coupling with an aerodynamic CFD flow solver for analysis of the CRM Wing-Body configuration at a fixed Mach and lift condition.

Data for the CRM Wing-Body Coupled Aerostructural Simulation (DPW-VI Case 5) were submitted by a total of four teams. The participating teams are listed in Table S-XIII-1. The data set key is that from DPW-VI, Table S-VI-3 and in Appendix C. Table S-XIII-2 gives an overview of the numerical methods used by the participants for CFD, computational structural mechanics, interpolation of aerodynamic forces, and mesh deformation. A detailed description of the results for DPW-VI Case 5 is given in Ref. 105.

Table S-XIII-1. Aerostructural Analysis Participants.

Team	Dataset Key	Organization	Country	Type
9	J4	Metacomp Technologies Inc.	USA	Commercial
11	L2	DLR e.V.	Germany	Government
19	T1	CARDC	China	Government
21	V5	Embraer S.A.	Brasil	Industry

Table S-XIII-2. Overview of Aerostructural Simulation Methods Used in DPW-VI.

	Dataset Key			
	J4	**L2**	**T1**	**V5**
Coupling Approach	linear static	linear static	linear static	linear modal
Flow Solver	Finite-Volume	Finite-Volume	Finite-Volume	Finite-Volume
Solver Name	CFD++	TAU	TRIP	CMS AERO-F
Turbulence Model	realizable k-ε	SA-neg	SST-2003	SA-QCR2013
Structural Solver	Finite-Element	Finite-Element	Finite-Element	Finite-Element
Model Suspension	Wing Root	Balance Interface	Wing Root	Center of Gravity
Force Interpolation Algorithm	Nearest-Neighbor Search	Nearest-Neighbor Search	Thin Plate Spline	Nearest-Neighbor Search
Mesh Deformation Method	Radial Basis Functions	Radial Basis Functions	Radial Basis Functions	linear Torsional Spring Analogy

An example of a typical coupled aerostructural simulation is illustrated in Figure S-XIII-1. Regarding the basic fluid-structure interaction (FSI) method, three participants, J4, L2, and T1, applied a linear static coupling approach, where the structural system equations are solved within each coupling loop. Team V5 used a linear modal approach. Here, a set of normal modes is computed prior to starting the actual FSI simulation and the static deflections are assembled through a superposition of modes in each coupling loop. All participants used different finite-volume flow solvers and turbulence models. T1 used the common multiblock CFD mesh, all others used custom unstructured (J4, L2) or structured (V5) meshes. Interpolation of aerodynamic forces between the CFD surface mesh and the structural model surface was performed using a nearest-neighbor search algorithm (teams J4, L2, and V5) or a thin plate spline (team T1). The model suspension in the structural analysis is located at the intersection line between wing root and belly fairing for teams J4 and T1 and at the balance interface for team L2. The boundary conditions in the modal analysis (team V5) are equivalent to a suspension at the model's center of gravity. Mesh deformation algorithms used include radial basis functions (RBF, teams J4, L2, and T1) and linear torsional springs analogy (LTSA, team V5).

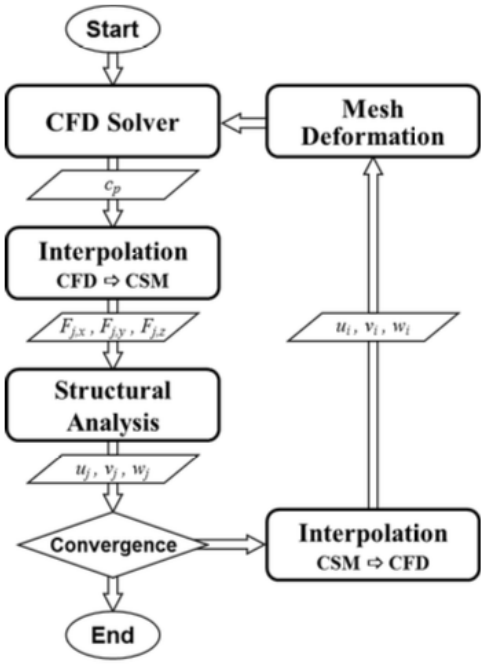


Figure S-XIII-1. Numerical Simulation Procedure for Coupled Aerostructural Analysis.

Unfortunately, the NASTRAN® bulk data file provided on the CRM website [81] did not include any definition of boundary conditions for the system matrices, leaving the structural analysis problem statically undetermined. As a result, the teams used differing locations for the model suspension, cf. Table S-XIII-2. The correct suspension, i.e., the one corresponding to the actual model attachment in the wind tunnel, is inside the fuselage at the inner cylindrical surface of the balance interface. At this location, the model is mounted to the internal wind tunnel balance during the test. With the wing root suspension used by two participants, zero deflection is prescribed along the junction line between wing and belly fairing. This suspension results in neglecting the compliancy of the structural components located between balance interface and wing root, leading to smaller deformations. Generally, the different model suspensions used in the structural analysis cause minor differences in the computed wing deformations, as will be discussed subsequently.

In Figure S-XIII-2, the chordwise static pressure coefficient is presented at six spanwise sections between $\eta = 0.131$ and $\eta = 0.950$. Sectional static pressure data were submitted by teams J4, L2, and T1. Experimental validation data has been taken from the Ames 11-foot wind tunnel [80], and from the 2014 ETW wind tunnel test campaign [83] to ensure consistency between pressure and deformation data. A generally good agreement is found between the different participants and measured data. All three teams predicted the shock location somewhat downstream of the experimental location. Shock location for teams J4 and T1 is predicted more upstream compared to L2. This is believed to be due to the one-equation turbulence model used by L2, whereas J4 and T1 used a two-

equation model. Although minor differences are also observed in the pressure distributions on the upper wing surface, the aeroelastic effects appear to be correctly captured by all participants. The resulting wing pressure distributions were essentially identical to those from Section VII.

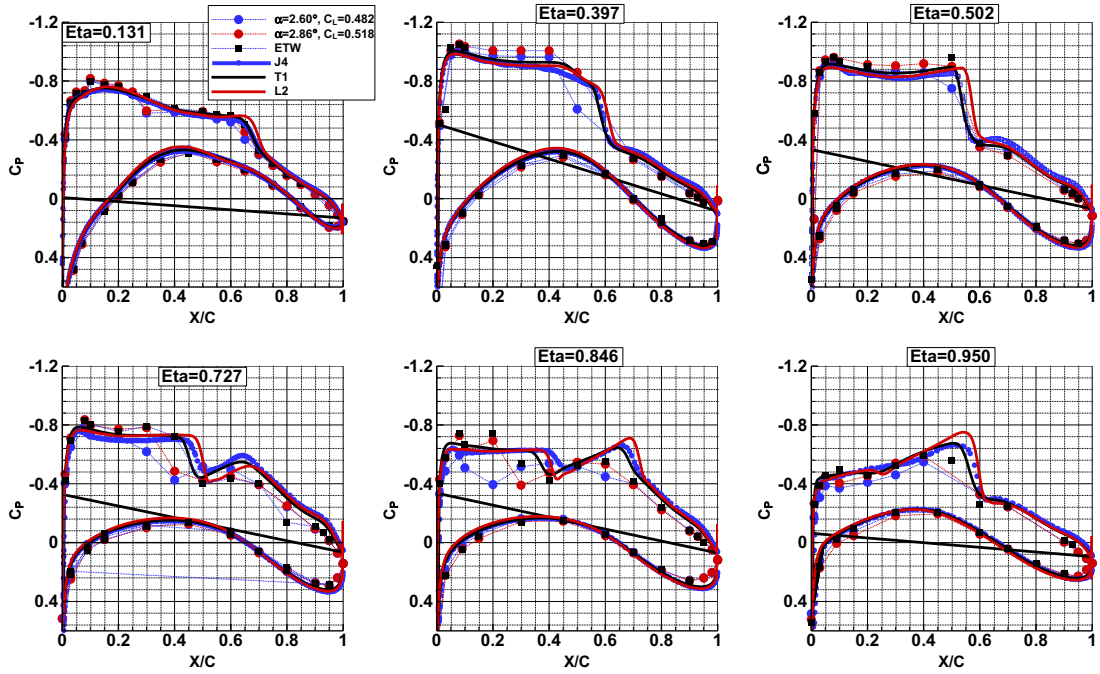


Figure S-XIII-2. WB Wing Pressure Distributions: Coupled Aerostructural Analysis, M=0.85.

Figure S-XIII-3 shows the spanwise wing bending and twist distributions. Numerical results are compared to ETW deformation data from Run 182, data point 531 ($\alpha = 2.99°$, $C_L = 0.514$). Bending deflections are given in millimeters and refer to the 0.027% scale NTF wind tunnel model. For bending, the best agreement is found for team V5. Here, the maximum deflection deviation at the wing tip is $\Delta w = -0.19$mm, followed by teams J4 ($\Delta w = -1.80$ mm) and L2 ($\Delta w = -2.18$ mm). The largest deviation occurs for team T1 at $\Delta w = -4.11$ mm. Apart from that, the deflection curve progression over span is very close to measured data for all participants, indicating that the spanwise lift distributions between the different teams match very well.

The aerodynamically more relevant twist deformation is plotted in Figure S-XIII-3(b). Here, the differences between the finite-element model suspensions become more apparent than for bending. For teams J4 and T1, who used the model suspension at the wing root, the twist deflection and spanwise deflection gradient at the innermost wing station are very close to zero, whereas the measurements show a small deflection and nonzero gradient caused by the compliance of the wind tunnel model structure.

Twist deflection results for participants T1 and V5 show a steeper gradient over most of the span compared to the experimental data. It is assumed that these differences are caused by differences in the structural analysis methods used. Team T1 performed a reduction of the stiffness matrix and computed the deflections outside NASTRAN®. Team V5 used a modal coupling approach where the deflections are calculated from a set of normal modes of the system matrices, which, in contradiction to the static coupling approaches, also take into account the model's mass distribution. The level differences at the tip are also more impacted by the finite-element model suspension. Unfortunately, no sectional lift and moment data, which would enable a more detailed deformation results analysis, has been submitted by the participants.

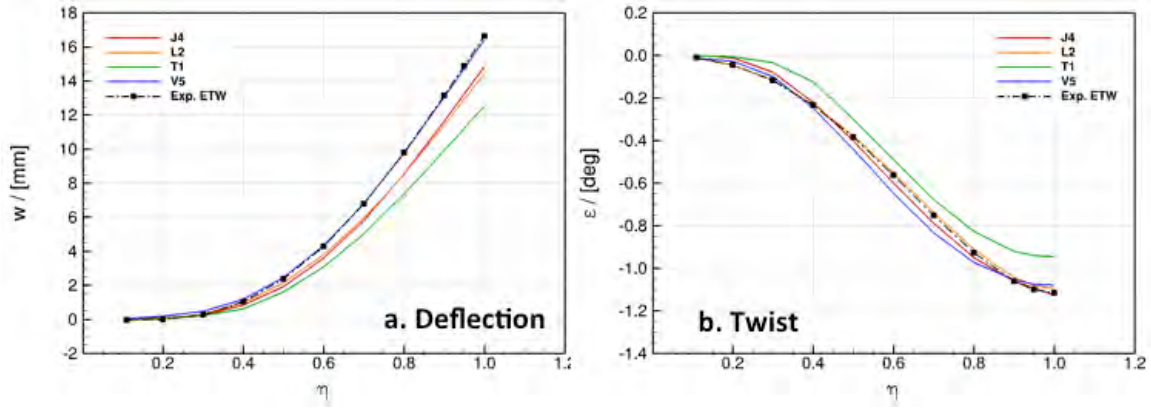


Figure S-XIII-3. WB Wing Deflection and Twist: Coupled Aerostructural Analysis, M=0.85.

Figure S-XIII-4 shows the computed lift, drag, and pitching moment, as well as the incidence obtained with the prescribed C_L condition for the four coupled aerostructural elastic data sets. Keeping in mind that these results are obtained on meshes representative of the medium workshop meshes, the mean and the spread of the results compare relatively well with the aggregate results obtained using the predetermined aeroelastically deflected grids used in DPW-VI Cases 2 and 3 for the workshop. Of these, only the pitching moments for two data sets (out of only three provided) appear to be at the edge of the range (more negative) of those reported in Case 2. Given the range of grid types and turbulence models used in this sparse data set, it should not be surprising that the spread is slightly larger when the additional effect of aeroelastic deflection is included in the simulations. In order to draw meaningful conclusions, a larger data set involving more participants including subsets using the same turbulence models and grid types would be needed.

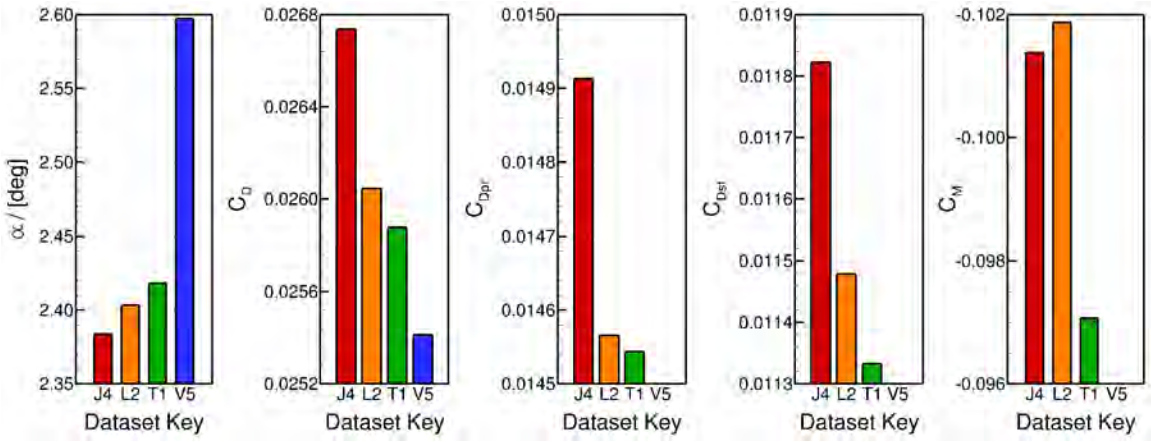


Figure S-XIII-4. WB Force and Moment Data: Coupled Aerostructural Analysis, M=0.85.

Although aeroelastic simulations are increasing in importance, the fact that only 4 out of 25 participants chose to perform the optional Case 5 in DPW-VI indicates that coupled static aeroelastic computations remain the exception rather than the norm in the current state of the practice.

Section XIV: Emerging Technologies

Three new technologies were seen in DPW-IV that merit watching and hopefully seeing further development. A brief discussion of each will follow.

A. Finite Element Solvers

Solutions from two finite element solvers were submitted in DPW-VI. Both feature strong solvers that facilitate machine precision residual convergence. Reliable convergence to machine accuracy removes one source error where solutions just stagnate, which can be mistaken as meaning convergence. Reliable convergence is essential to solution adaptive methods.

Solutions M1 and M2 were based on the COFFE solver [106]. COFFE utilizes the Streamline/Upwind Petrov-Galerkin finite element method (SUPG). COFFE uses a complex nonlinear solver to push flow solutions to a steady state in pseudotime with an inexact Newton's method. At each pseudotime step, an update to the solution vector is solved for with a preconditioned GMRES solver. This update is then checked for realizability and for unsteady residual decrease. If either of these constraints is violated, a fraction of the update is taken, and the global CFL number (Courant Friedrichs Lewy condition relates space discretization to time step necessary for convergence) is decreased. However, if the update is "healthy," the CFL number is increased. The grid refinement study exhibited a nearly flat grid convergence and featured some of the smallest grids.

Solution P2 was based on the GGNS solver [107]. Like COFFE, it is built upon the stabilized finite element discretization SUPG. The discrete non-linear solver in the GGNS code implements a variant of Newton-Krylov-Schwartz algorithm. Time stepping to the steady state algorithm is implemented using GMRES with drop-tolerance based preconditioner (locally on subdomains) implemented in the context of the additive Schwartz method. As in the COFFE method, CFL number is manipulated up and down to speed convergence. GGNS exhibited good convergence characteristics and was used in the grid adaption study.

It is not known if these finite element methods will do better on cases where the finite volume methods already do well. The opinion is that they will really be conducive to strong reliable solution adaptive methods.

B. Solution/Grid Adaptive Methods

The fixed grid approach to CFD is based on gridding guidelines developed over many years of CFD application experience on similar applications, and sometimes required several weeks of an expert user's effort to develop a grid family conforming to the guidelines. This is not conducive to CFD usage in a fast-paced airplane development program. Accurate prediction of drag (and other aerodynamic parameters) on a transport aircraft has proven to be very challenging, as we have seen in the previous sections of this report. There are many factors that make this problem challenging, but one of the most common is controlling and reducing discretization error resulting from inadequate grid resolution. Achieving adequate resolution is difficult because the grid requirements vary throughout the domain depending on factors such as the flow solution, discretization scheme, and physical models. In contrast, an adaptive grid approach is automatic, relying on an estimate of solution discretization error to guide the grid construction.

This suggests that without adaption some flow features may not be adequately captured with fixed grids. This is particularly a risk with geometries/flow environments for which there is not extensive experience. It is expected that by directly targeting the discretization error, these methods can achieve a given level of accuracy more efficiently than with the fixed grid refinement approach. Another benefit of the adaptive approach is that it removes the need for gridding guidelines or the need for an expert user to guide the mesh generation process. The result should be more reliable and accurate CFD solutions, particularly for calculating increments between solutions or addressing new and different configurations. Recently adaptive meshing techniques for unstructured grids have matured to the point that adaptive RANS solutions on full aircraft configurations now seem practical [97-100]. Results presented in DPW-VI (Section XII) and reported in further detail [103,104] are very encouraging. Much work remains to be done to bring this technology to a "production" capability for 3D RANS. It is expected that combining an output-based error

estimate that is optimized for the analysis along with adaptive meshing will provide significant advantages in grid convergence for future adaptive grid applications in addition to the user and uncertainty benefits demonstrated to date. It is a technology that needs to be matured.

C. Lattice-Boltzmann Method (LBM)

Unlike the traditional CFD methods, which solve the conservation equations of macroscopic properties (i.e., mass, momentum, and energy) numerically, the Lattice-Boltzmann Method (LBM) models the fluid consisting of fictive particles, and such particles perform consecutive propagation and collision processes over a discrete lattice mesh. Due to its particulate nature and local dynamics, LBM can easily deal with complex geometries. LBM has long been restricted to the low compressible isothermal flow regime. Recent developments [108] enabled the extension of the local Mach number regime up to $M \approx 2.0$, including shock discontinuities and consistent compressible gas dynamics. LBM, being inherently unsteady, might be more efficient than other unsteady scale-resolving methods due to its explicit and local nature. The unsteady nature of the solution makes the code especially well-suited for problems involving separated flows, shock movements and shock boundary layer interaction, i.e., buffet [109] and high lift problems [110].

Solution G1, based on LBM, was submitted to DPW-VI. Although, the drag levels were high, the predicted pressure distributions were in as good agreement with tests as those of most of the other entries. The predicted drag increment (in the continuum) between the WBNP and WB configurations was within the experimental results. The DPW-VI application is discussed in greater detail in Ref. 111. This technology should be followed.

Section XV: Questions and Issues

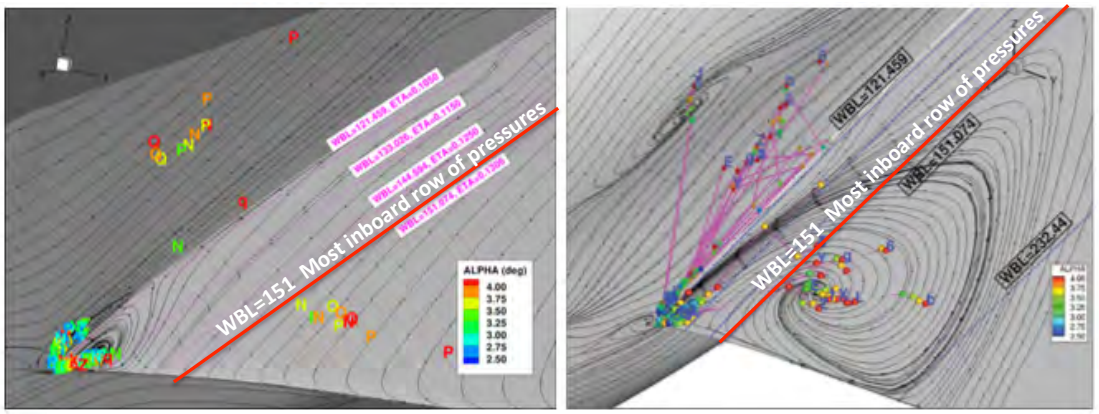
An important goal of the DPW series of workshops is to identify significant issues/shortfalls in need of further CFD development. DPW-VI highlights continuing issues that, while seeing some progress over the years, continue to plague the state of CFD and experiment. This section will delve deeper into these issues that drive (or should drive) the thinking of the community. More detailed information about how the experimental data were generated is needed to better validate the CFD, and to provide the detailed information necessary to improve the turbulence models, unsteady simulations, etc. Unquestionable grid convergence and knowledge of the aeroelastic deformations are also essential.

A. Premature Side-of-Body Separation

The prediction of premature side of body separation, illustrated in Figure S-X-20 (repeated here for convenience as Figure S-XV-1), continues to plague some simulations. Premature side-of-body separation is not a simple issue. It is intimately coupled to the choice of solver, turbulence model, and gridding in ways not fully understood. It has been an issue in all of the workshops. At the design condition of $M = 0.85$, $C_L = 0.50$, this should no longer be an issue for the CRM. However, as angle of attack is increased, some solutions do exhibit excessive side-of-body separation as shown for DPW-VI entries in Figure S-X-22, -23 -24, and -31. Figures S-X-22–24 show pressure distributions for angles of attack of 3.0°, 3.5°, and 4.0°, respectively. Figure S-X-31 shows the lift break. Similar results exist for DPW-V. The wind tunnel data do not exhibit any evidence of flow separation on the inboard portion of the wing (i.e., the first row of pressures located at BL = 151, nor is there any indication of a lift break prior to between 3° and 4° angle of attack. It is deemed that any solutions that exhibit such evidence are in error. Curiously, evidence from the 2017 High-Lift Prediction Workshop is for CFD to predict too little side-of-body separation on the JAXA Standard Model configuration, which just reinforces the existing lack of understanding.

CRM Wing-Body Angle-of-Attack Sweep – Separation Bubble Eye Locations

DPW-VI **DPW-V**



For many of the solutions there is no evidence of flow separation with increasing angle-of-attack along the most inboard row of wing pressures

Figure S-XV-1. DPW-VI Side-of-Body Separation Bubble Comparison with DPW-V, M=0.85.

Both DPW-V and -VI requested an angle-of-attack sweep between 2.5° and 4.0° at 0.25-degree increments. Examining the submitted results from these two workshops has allowed a determination of which solutions suffered from premature side-of-body separation. These findings have been collated into four categories for each workshop, which are presented in Tables S-XV-1 and -2 and also in Appendix C. The categories are: **N**, no side-of-body separation detected; Y, side-of-body separation prior to 4° angle of attack; and O, deemed an outlier for other reason, i.e., drag level, excessive nonlinearity of lift or pitching moment; did not run angle-of-attack sweep, or insufficient information submitted to make determination.

From these findings, several observations are made about this configuration at these conditions, though it is not known how universal these might be:

1. Premature side-of-body separation is very sensitive to the combination of solver, turbulence model, and gridding details. In DPW-V, 26 solutions, which did not show premature side-of-body separation, were based on either SA or SST turbulence models. Of these, 18 were based on the common grids provided by the DPW committee. These grids, whether structured multiblock or unstructured, were all derived from a common point-matched multiblock structured grid. Twenty-four solutions using either SA or SST turbulence models, some of which also used the committee-provided common grids suffered from premature side-of-body separation. However, all of these with one exception were based on different solvers from those that did not separate. The one exception were the TAU code solutions, which separated with the SA model but not with the SST both using the same grid. In DPW-VI, TAU using the SA model and a custom grid did not separate. Three other solvers using the SA model and custom grids also did not separate, while 11 did.
2. FOI's EDGE code has not shown a propensity for premature separation in any of the DPW workshops.
3. Some two-equation turbulence models, i.e., EARSM, Lag RST, k-kl-MEAH2015, RSM-ω, are more resistant to premature side-of-body separation. Others like Menter's k-ω SST model tended to have the same propensity to separation as does the one-equation SA variants.
4. Adding Spalart's QCR model [95,96] to either the SA or SST turbulence model seemed to eliminate the problem.

The good news is that adding (and using) the QCR model in either SA or SST pretty much eliminates the problem of premature side-of-body separation for these cases, as do some of the other two-equation turbulence models. However, this does not explain why the sensitivity to solver and grid occurs, or the implications this might have for other geometries, and/or, flow conditions. This type of 3D corner flow separation still needs more attention in turbulence model development and CFD application. The NASA Juncture Flow Model test will further contribute to understanding and dealing with this issue.

Table S-XV-1. DPW-V: Detailed Side-of-Body Separation by Participant.

ID	SYM	SYM	Name	Organization	Code	Algorithm	Grid Generator	Grid	Turbulence Model	SOB Sep
2			Hashimoto	JAXA	FaSTAR	Upwind, cell-centered	Custom Hex Hexabri oct-	Custom (Hex)	SA-noft2-R	N
5			Olson	NASA Ames	overflow2.2e_LRS	Full NS Matrix, cell-centered	Common Grid	Overset	Lag RST	N
7			Park	NASA Langley	CFL3D v6.6	Full NS, finite volume, cell centered	Common Grid	Multiblock Structured	SA	N
9			Hue	ONERA	elsA	Full NS Central Diff, cell-centered	Common Grid	Multiblock Structured	SA	N
d			Osusky	U. Toronto	Diablo	Newton-Krylov-Schur with SBP-SAT discretization, matrix diss	Common Grid	Multiblock Structured	SA	N
D			Sclafani	Boeing (Huntington)	OVERFLOW v2.2c	Full NS Central Diff, cell-centered	Custom Grid	Custom (Overset)	SA-Ia QCR	N
e			Levy	Cessna Aircraft Co.	NSU3D	TLNS Node-centered, central diff	Common Grid	Hybrid	SA	N
F			Sclafani	Boeing (Huntington)	OVERFLOW v2.2c	Full NS Central Diff, cell-centered	Custom Grid	Custom (Overset)	SA-Ia w/ RC QCR	N
h			Crippa	DLR	TAU	Node-centered, matrix	Common Grid	Hex	Menter k-w SST-V	N
H			Sclafani	Boeing (Huntington)	OVERFLOW v2.2c	Full NS Central Diff, cell-centered	Custom Grid	Custom (Overset)	SA-Ia w/ RC QCR	N
I			Chen	CADRC	MFlow	ROE scheme cell-centered upwind	Common Grid	Hex	SA	N
J			Chen	CADRC	MFlow	ROE scheme cell-centered upwind	Common Grid	Hybrid	SA	N
k			Moitra	CRL_INDIA	CFD++	Finite volume unstructured mixed-element cell-centered, upwind	Common Grid	Prism	SA-RC	N
λ	l		Brodersen	DLR	TAU	Node-centered, matrix diss 1	Custom2-hexa wake block	Custom (Hyb w/ Hex-Wake)	Menter k-w SST-V	N
m			Winkler	Boeing (St. Louis)	BCFD	cell-centered	Common Grid	Hex	SA	N
n			Winkler	Boeing (St. Louis)	BCFD	cell-centered	Common Grid	Hex	Menter k-w SST-V	N
π	p		Brodersen	DLR	TAU	Node-centered, matrix diss 1	Custom2-hexa wake block	Custom (Hyb w/ Hex-Wake)	Menter k-w SST-V	N
P			Scalabrin	Embraer	CFD++	Finite volume unstructured mixed-element cell-centered, upwind	Common Grid	Hybrid	Menter k-w SST	N
q			Winkler	Boeing (St. Louis)	BCFD	cell-centered	Common Grid	Hex	SA	N
r			Winkler	Boeing (St. Louis)	BCFD	cell-centered	Common Grid	Hex	Menter k-w SST-V	N
t			Temmerman	NUMECA	FINE/Open	Cell-centereed, scalar diss	Common Grid	Multiblock Structured	SA	N
U			Eliasson	FOI	EDGE	Unstructured node-centered, Finite-volume	Common Grid	Hex	EARSM Explicit Algebraic Reynolds	N
V			Eliasson	FOI	EDGE	Unstructured node-centered, Finite-volume	Common Grid	Hex	SA	N
W			Eliasson	FOI	EDGE	Unstructured node-centered, Finite-volume	Common Grid	Hex	Menter k-w SST	N
Ξ	X		Powell	Gulfstream	FUN3D	Node-centered UMUSCL	Custom Grid	Custom Hex)	SA	N
ψ	y		Powell	Gulfstream	USM3D		Custom Grid	Custom Hex)	SA	N
3			Yamamoto	JAXA	UPACS	Upwind, cell-vertex finite volume	Common Grid	Multiblock Structured	SA-noft2-R(Crot=1)	y
4			Yamamoto	JAXA	UPACS	Upwind, cell-vertex finite volume	Common Grid	Multiblock Structured	Menter k-w SST-V	Y
6			Park	NASA Langley	FUN3D v12.2	Node-centered UMUSCL	Common Grid	Hybrid	SA	Y
8			Cai	NPU China	ExStream	Full NS Upwind Diff, cell-centered	Common Grid	Overset	Menter k-w SST-V	y
α	a		Brodersen	DLR	TAU	Node-centered, matrix diss 1	Custom1-no hexa wake	Custom (Hybrid)	SA	y
a			Coder	Penn St. U	OVERFLOW 2.2c	Full NS Upwind Diff, cell-centered	Common Grid	Overset	SA-fv3	Y
β	b		Brodersen	DLR	TAU	Node-centered, matrix diss 1	Custom1-no hexa wake	Custom (Hybrid)	SA	y
b			Osusky	U. Toronto	Diablo	Newton-Krylov-Schur with SBP-SAT discretization, matrix diss	Common Grid	Multiblock Structured	SA	Y
C			Sclafani	Boeing (Huntington)	OVERFLOW v2.2c	Full NS Central Diff, cell-centered	Custom Grid	Custom (Overset)	SA-Ia	Y
δ	d		Brodersen	DLR	TAU	Node-centered, matrix diss 1	Custom2-hexa wake block	Custom (Hyb w/ Hex-Wake)	SA	Y
E			Sclafani	Boeing (Huntington)	OVERFLOW v2.2c	Full NS Central Diff, cell-centered	Custom Grid	Custom (Overset)	SA-Ia w/ RC	y
f			Levy	Cessna Aircraft Co.	FUN3D	Node-centered UMUSCL upwind	Common Grid	Hybrid	SA	Y
γ	g		Brodersen	DLR	TAU	Node-centered, matrix diss 1	Custom2-hexa wake block	Custom (Hyb w/ Hex-Wake)	SA	Y
g			Crippa	DLR	TAU	Node-centered, matrix	Common Grid	Hex	SA	y
G			Sclafani	Boeing (Huntington)	OVERFLOW v2.2c	Full NS Central Diff, cell-centered	Custom Grid	Custom (Overset)	SA-Ia w/ RC	Y
L			GariÈpy	EcolePolytech Montreal	Fluent V13	Density based solver, ROE scheme, cell-centered, upwind diff	Custom Grid	Custom (Hex)	SA	Y
N			Scalabrin	Embraer	CFD++	Finite volume unstructured mixed-element cell-centered, upwind	Common Grid	Hex	Menter k-w SST	y
R			Scalabrin	Embraer	CFD++	Finite volume unstructured mixed-element cell-centered, upwind	Common Grid	Prism	Menter k-w SST	y
σ	s		Yamamoto	JAXA	UPACS	Upwind, cell-vertex finite volume	Gridgen	Multiblock Structured	SA-noft2-R(Crot=1)	Y
T			Scalabrin	Embraer	CFD++	Finite volume unstructured mixed-element cell-centered, upwind	ICEM TGRID	Custom (Hybrid)	Menter k-w SST	y
ϖ	v		Yamamoto	JAXA	UPACS	Upwind, cell-vertex finite volume	Gridgen	Multiblock Structured	Menter k-w SST-V	Y
X			Powell	Gulfstream	FUN3D	Node-centered UMUSCL	Common Grid	Hybrid	SA	Y
Y			Balakrishnan	Indian Inst. Science	HiFUN	Upwind, cell-centered	Common Grid	Hex	SA	y
Z			Hashimoto	JAXA	FaSTAR	Upwind, cell-centered	Common Grid	Hex	SA-noft2-R	Y
M			Scalabrin	Embraer	CFD++	Finite volume unstructured mixed-element cell-centered, upwind	Common Grid	Hex	k-e-RT	O
O			Scalabrin	Embraer	CFD++	Finite volume unstructured mixed-element cell-centered, upwind	Common Grid	Hybrid	k-e-RT	O
Q			Scalabrin	Embraer	CFD++	Finite volume unstructured mixed-element cell-centered, upwind	Common Grid	Prism	k-e-RT	O
S			Scalabrin	Embraer	CFD++	Finite volume unstructured mixed-element cell-centered, upwind	ICEM TGRID	Custom (Hybrid)	k-e-RT	O
A			Sclafani	Boeing (Huntington)	OVERFLOW v2.2c	Full NS Central Diff, cell-centered	Common Grid	Overset	SA-Ia	-
B			Sclafani	Boeing (Huntington)	OVERFLOW v2.2c	Full NS Central Diff, cell-centered	Common Grid	Overset	SA-Ia w/ RC	-
K			GariÈpy	EcolePolytech Montreal	Fluent V13	Density based solver, ROE scheme, cell-centered, upwind diff	Common Grid	Prism	SA	-

N - No Side-of-Body Separation. Y - Side-of-Body Separation Prior to 4 deg, O - Other Outlier, - Insufficient Information Provided

Table S-XV-2. DPW-VI: Detailed Side-of-Body Separation by Participant.

ID	SYM	SYM	Name	Organization	Code	Algorithm	Grid Generator	Grid	Turbulence Model	SOB Sep
A2	a	a	Tony Sclafani	Boeing, BCA Advanced Concepts, Long Beach	Overflow v2.2k	Full NS Central Diff, cell-centered		Overset	SA-RC w/QCR on	N
B1	B	B	Khaled Abdol-Hamid	NASA Langley Research Center	FUN3D 12.8	Node-centered UMUSCL upwind		Unst-Geolab	-kL-MEAH2015 w/Limiter	N
B2	b	b	Khaled Abdol-Hamid	NASA Langley Research Center	FUN3D 12.8	Node-centered UMUSCL upwind		Unst-Geolab	-kL-MEAH2015 no-limiter	N
E1	E	E	Atsushi Hashimoto	JAXA, Ryoyu Systems	FaSTAR	Upwind, cell-centered		Unst-Geolab	SA-noft2-R w/QCR2000	N
H1	H	H	Ales Prachar/ Peter Eliasson	Aerospace Research and Test Establishment, CC	Edge	Unstructured node-centered, Finite-volume		Unst-Geolab	SA	N
H2	h	h	Ales Prachar/ Peter Eliasson	Aerospace Research and Test Establishment, CC	Edge	Unstructured node-centered, Finite-volume		Unst-Geolab	EARSM (Explicit Algebraic Reynolds	N
K3	γ	g	Taku Nagata	Kawasaki Heavy Industries	Cflow	Cell-centered, MUSCL	nternal Grid Gen	Custom Cart	SA-noft2	N
K4	Γ	G	Taku Nagata	Kawasaki Heavy Industries	Cflow	Cell-centered, MUSCL	nternal Grid Gen	Custom Cart	SA-noft2 w/QCR200	N
L1	L	L	Stefan Keye / Vamshi Togiti	DLR	TAU	Node-centered, matrix		Unst-custom	RSM-ω	N
L2	λ	l	Stefan Keye / Vamshi Togiti	DLR	TAU	Node-centered, matrix		Unst-custom	SA-neg	N
M2	m	m	Ryan S. Glasby	Tennessee, Pointwise, NASA Langley, NAVAIR, MIT, U Ala	COFFE/KCFD	Node-centered, Finite element	Pointwise Tets	Unst-custom	SA-neg w/QCR2000	N
O2	ϕ	f	David Hue	ONERA	elsA	Full NS Central Diff, cell-centered		Overset	SA-QCR2000	N
Q2	q	q	Gaetan Kenway	MDOlab, University of Michigan	ADflow	Full NS Central Diff, cell-centered		Cust-Overset	SA 1stOrder	N
Q3	θ	q	Gaetan Kenway	MDOlab, University of Michigan	ADflow	Full NS Central Diff, cell-centered		Embraer MB	SA-QCR2000	N
T1	T	T	Yuntao Wang	CARDC	TRIP	Upwind Roe cell-centered		CommonMB	Menter k-w SST-2003	N
U1	U	U	Jim Coder	Applied Research Lab, Penn State	Overflow 2.21 3rd Order WENO	Full NS Upwind Diff, cell-centered		Overset	SA-RC W/QCR2000	N
U2	u	u	Jim Coder	Applied Research Lab, Penn State	Overflow 2.21 5TH Order WENO	Full NS Upwind Diff, cell-centered		Overset	SA-RC W/QCR2000	N
Z1	Z	Z	Yasushi Ito	JAXA, Ryoyu Systems	TAS limiter K=1	Node-based		Unst-Geolab	SA-noft2-R w/QCR2000	N
Z2	ζ	z	Yasushi Ito	JAXA, Ryoyu Systems	TAS limiter K=5	Node-based		Unst-Geolab	SA-noft2-R w/QCR2000	N
Z3	Δ	D	Yasushi Ito	JAXA, Ryoyu Systems	TAS limiter K=10	Node-based		Unst-Geolab	SA-noft2-R w/QCR2000	N
B3	α	a	Khaled Abdol-Hamid	NASA Langley Research Center	FUN3D 12.8	Node-centered UMUSCL upwind		Unst-Geolab	SA no-limiter	Y
D1	D	D	Jiangtao Chen	CARDC	Mflow	ROE scheme cell-centered upwind		Unst-Geolab	SA	Y
D2	d	d	Jiangtao Chen	CARDC	Mflow	ROE scheme cell-centered upwind	nternal Grid Gen	Unst-custom	SA	Y
I1	I	I	Anna Rubekinak	Mentor Graphics	FloEFD	cell-centered	FloEFD Mesh	Custom Cart	efault k-e Lam-Bremhorst	Y
J1	J	J	Brian Edge	Metacomp	CFD++	cell-centered, upwind		Unst-Boeing	SA	Y
J2	ϑ	J	Brian Edge	Metacomp	CFD++	cell-centered, upwind		Unst-Boeing	Menter k-w SST-V	Y
K1	K	K	Taku Nagata	Kawasaki Heavy Industries	Cflow	Cell-centered, MUSCL		Unst-Boeing	SA-noft2	Y
K2	k	k	Taku Nagata	Kawasaki Heavy Industries	Cflow	Cell-centered, MUSCL		Unst-Boeing	SA-noft2 w/QCR200	Y
M1	M	M	Ryan S. Glasby	Tennessee, Pointwise, NASA Langley, NAVAIR, MIT, U Ala	COFFE/KCFD	Node-centered, Finite element	Pointwise Tets	Unst-custom	SA-neg	Y
N1	N	N	N. Balakrishnan	CAd Lab, Indian Institute of Sci	HiFun	Upwind, cell-centered	nternal Grid Gen	Unst-custom	SA	Y
O1	O	O	David Hue	ONERA	elsA	Full NS Central Diff, cell-centered		Overset	SA	Y
P1	P	P	Todd Michal	Boeing, St. Louis	BCFD	cell-centered		Unst-Boeing	SA-RC	Y
Q1	Q	Q	Gaetan Kenway	MDOlab, University of Michigan	ADflow	Full NS Central Diff, cell-centered		Embraer MB	SA 1stOrder	Y
S1	S	S	Kelly Laflin	Textron Aviation (Cessna)	FUN3D	Node-centered UMUSCL upwind		Unst-Geolab	SA-RC	Y
V1	V	V	odrigo Felix de Souza	Embraer S/A	CFD++	Nodel-centered, upwind		Unst-Geolab	Menter k-w SST-V	Y
V2	ς	V	odrigo Felix de Souza	Embraer S/A	CFD++	Nodel-centered, upwind		Embraer MB	Menter k-w SST-V	Y
V3	Ξ	X	odrigo Felix de Souza	Embraer S/A	CFD++	Nodel-centered, upwind		Unst-custom-A	Menter k-w SST-V	Y
V4	Ψ	Y	odrigo Felix de Souza	Embraer S/A	CFD++	Nodel-centered, upwind		Unst-custom-I	Menter k-w SST-V	Y
F1	F	F	Krishna Zore	Ansys	Fluent	Density based solver, ROE scheme, cell-centered, upwind diff	nternal Grid Gen	Unst-custom	Menter k-w SST-V	O
G1	G	G	Benedikt König	EXA Powerflow	PowerFLOW	LBM	nternal Grid Gen	Custom Cart	LBM-VLES	O
I2	β	b	Anna Rubekinak	Mentor Graphics	FloEFD	cell-centered	FloEFD Mesh	Custom Cart	bgrid k-e Lam-Bremhorst	O
A1	A	A	Tony Sclafani	Boeing, BCA Advanced Concepts, Long Beach	Overflow v2.2k	Full NS Central Diff, cell-centered		Overset	SA-RC	-
I3	χ	c	Anna Rubekinak	Mentor Graphics	FloEFD	cell-centered	FloEFD Mesh	Custom Cart-B	efault k-e Lam-Bremhorst	-
J3	φ	j	Brian Edge	Metacomp	CFD++	cell-centered, upwind		Unst-Geolab	SA	-
J4	Ω	W	Brian Edge	Metacomp	CFD++	cell-centered, upwind	nternal Grid Gen	Unst-custom	Realizable k-epsilon	-
P2	π	p	Todd Michal	Boeing, St. Louis	GGNS	Node-centered, Finite element		All Tets	SA-RC	-
R1	R	R	Andrei Cimpoeru	CFMS, Zenotech, ARA	ZCFD			Unst-custom	Menter k-w SST-V	-
V5			Rodrigo Felix de Souza	Embraer S/A	CMS AERO-F			Unst-custom	SA-QCR2013	-
W1	W	W	Dominic Chandar	Institute of High Performance	μSICS	Node-based	Internal Grid Gen	Unst-custom	SA	-
X1	X	X	Patrick Hanley	Hanley Innovations	Stallion3D			Custom Cart	k-e	-
Y1	Y	Y	Neil Ashton	University of Oxford, ESI Group, BETA CAE Systems	OpenFOAM	Pressure, Density based solver, cell-centered	SnappyHexMesh	Unst-custom	SA	-
Z4	ε	e	Yasushi Ito	JAXA, Ryoyu Systems	TAS limiter K=10	Node-based	nternal Grid Gen	Unst-custom	SA-noft2-R w/QCR2000	-
Z5	η	h	Yasushi Ito	JAXA, Ryoyu Systems	TAS limiter K=5	Node-based		Unst-Geolab	SA-noft2-R	-
Z6	Π	P	Yasushi Ito	JAXA, Ryoyu Systems	TAS limiter K=5	Node-based		Unst-Boeing	SA-noft2-R	-
Z7	ϒ	U	Yasushi Ito	JAXA, Ryoyu Systems	TAS limiter K=5	Node-based		Unst-Boeing	SA-noft2-R w/QCR2000	-

N - No Side-of-Body Separation. Y - Side-of-Body Separation Prior to 4 deg, O - Other Outlier, - Insufficient Information Provided

B. Excessive Aft-Loading

Close examination of the CFD pressure distributions around the wing trailing edge (x/c = 0.7 to 1.0) compared to the test, shown in Figure S-XV-2, reveals an excessive "aft-loading." The computational results are all from the finest grid solutions submitted for the M = 0.85, C_L = 0.50 condition. The pressure coefficient values on the upper surface of the wing are consistently lower (more negative) than those of the test data. The difference between the upper and lower surface represents lift and contributes to negative section pitching moment and flap/aileron hinge moment. A simpler way to look at "aft-loading" is to compare the C_p difference between upper and lower surface pressures at a chord fraction of 85%. Either way, the predicted "aft-loading" is greater than what is being measured. These differences become more aggregative the further outboard on the wing. This is illustrated in Figure S-IX-8, which shows the computed and measured delta C_p across the span for two Reynolds numbers. The difference (loading) peaks at around 80% span. Reynolds number trends and excessive "aft loading" on the CRM are also discussed in Section IX.

As long as the flow is attached, these "aft" pressure distributions vary little over the range of angles of attack of interest. This is shown in Figure S-XV-3 for one solver (for clarity) for angles of attack from 2.5° to 4.0°. Note only at η (span fraction) stations 0.502 and 0.603 is there any noticeable change in the pressure distribution with angle of attack. Here there is significant flow separation above 3.50° angle of attack. The effect of this increasing "aft loading" is clearly seen in the section lift (normal force) and pitching moment on the outboard part of the wing shown in Figure S-XV-4. A more complete spanwise distribution of these section coefficients was previously shown on Figures S-X-26 and -27. These show the computed results much closer to experiment on the inboard part of the wing consistent with the trend shown in Figure S-IX-8. This excessive "aft loading" is seen from every turbulence model, gridding scheme, and solver type presented in the DPW workshops.

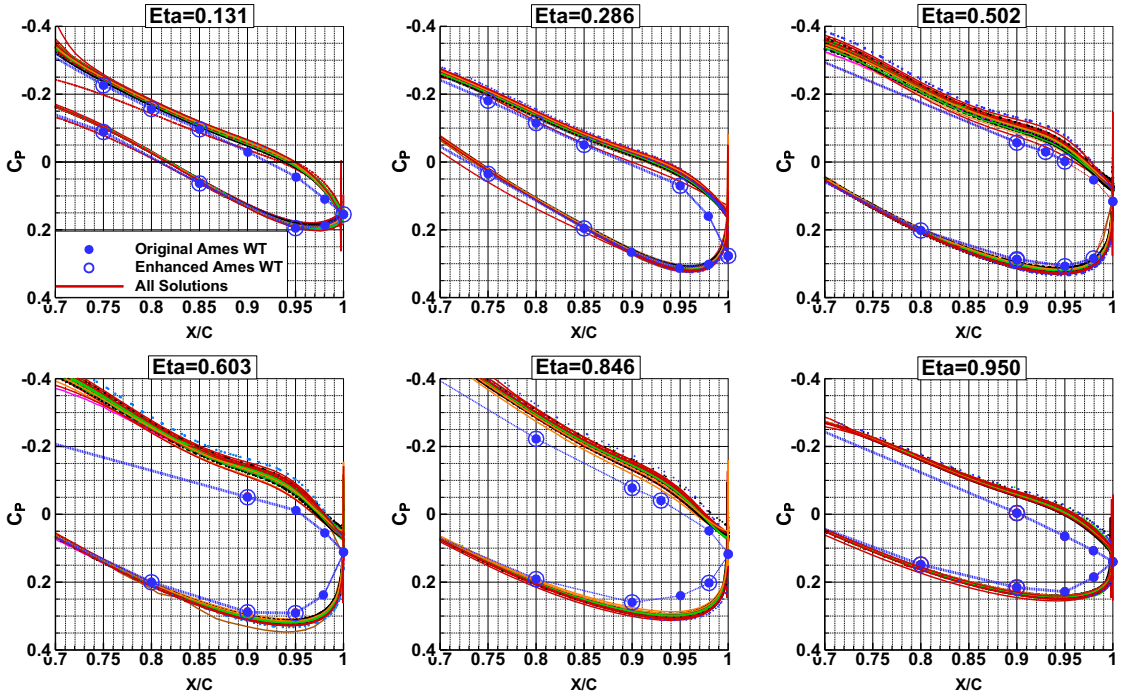


Figure S-XV-2. DPW-VI: WB (Aeroelastic) Wing Trailing Edge Pressures; All solutions; C_L = 0.50, M=0.85.

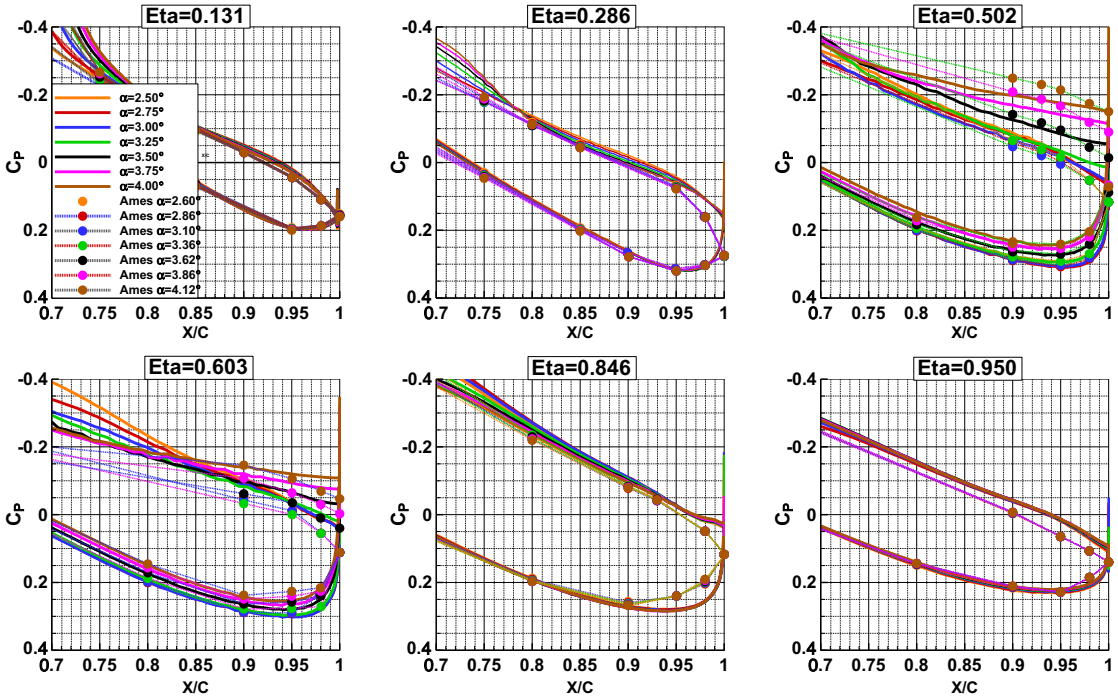


Figure S-XV-3. DPW-VI: WB (Aeroelastic) Wing Trailing Edge Pressures; AOA = 2.5° to 4.0°, M=0.85.

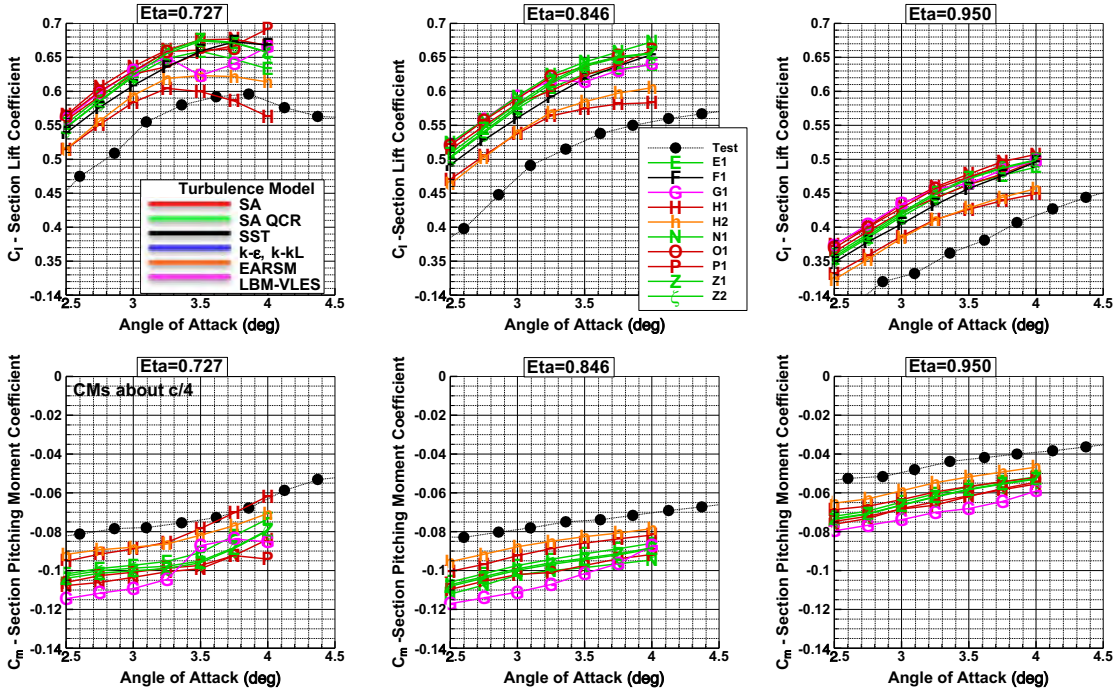


Figure S-XV-4. DPW-VI: WB (Aeroelastic) Wing Section Lift and Pitching Moment; Outboard Wing, M=0.85.

It is highly unlikely that this excessive "aft loading" is due to experimental issues. This same trend was seen over a range of Reynolds numbers on a 777-200 configuration [94] and has also been seen on other wind tunnel models with significant aft camber on the wing. The CRM computational results of pressure distribution, and forces and moments, are self-consistent. In the wind tunnel test, the instrumentation is completely independent. The geometry of the CRM wind tunnel model has been validated. The nearly solid nature of the wing minimizes any chordwise aeroelastic effects. Pressure distributions from the DPW-VI Case 5 aerostructural aeroelastic computations are included in Figure S-XV-2.

A potential source of difference between the predicted and measured "aft-loading," at least at low Reynolds numbers, could be the lack of a transition or "trip" model in the CFD analysis for the Workshop. "Trip strips" are routinely used on wind tunnel models tested at low Reynolds numbers to ensure the turbulent boundary layer flow expected on the full-scale vehicle in flight. An effect of the "trip" will be to increase the downstream boundary layer thickness [112]. This could have a "decambering" effect and will increase drag, reduce lift, and make pitching moment less negative. Even at higher Reynolds numbers, the flow will likely have some laminar run before becoming fully turbulent boundary layer flow. These flow differences tend to be magnified when going through a shock wave in transonic flow. While the lack of a "trip" or transition model might not explain the differences at higher Reynolds number, it still represents a feature not modeled here. These differences between CFD and the "real" flow could be important in some circumstances.

The excessive "aft loading" will contribute to higher total lift and more negative pitching moment. Estimates (based on the WBT [87]) of the magnitude of these effects are not sufficient to close the gap between CFD and experiment shown in Figure S-X-32. However, the excessive "aft loading" may be of sufficient magnitude to affect the sectional loads, in particular the pitching moment loads. The impact on aileron hinge moments would be of particular note. The magnitude of the hinge moment directly affects the actuator size. Too high a prediction leads to oversized and overweight components. Aileron hinge moments also are very difficult to measure accurately in the wind tunnel adding to the need for accurate CFD predictions. Dependable and accurate CFD prediction of aileron hinge moments would be very beneficial to the airplane design process. While progress has been made with the premature SOB separation, the question of the excessive "aft loading" remains an open issue.

C. Solution Spread

Another ongoing issue can be seen in Figure S-X-32 for total WB lift and pitching moment. These are the 20 solutions remaining after the elimination of outliers from the original 41 submitted for the angle-of-attack sweep in DPW-VI. The solutions show a lift that is higher and a pitching moment that is more negative than the experiment. The experimental force and moment data suffer from the lack of corrections for the presence of USS support to the wind tunnel model. As was pointed out in Section III, the necessary "tare and interference" tests were not carried out for the CRM in any of the wind tunnel campaigns, which is not unusual considering their complexity and cost. Computational studies [87] on the impact of the mounting system, the WBT $iH = 0$ model show that its effect reduces lift and the nose-down (negative) pitching moment. These studies were based on the CRM model with the horizontal tail and, therefore, cannot be directly applied to the WB configuration. However, estimates of the nominal impact of the mounting system (USS) based on those studies were made and are discussed in Section III. How "good" these corrections are is not known. These "corrections" for lift, drag, and pitching moment on the WB, WBT, and WBNP are tabulated in Table S-III-1. The corrections for the WB were applied to the computational data shown in Figure S-X-32. While the corrections move the computational data in the right direction, there is still a substantial gap with the test data.

More importantly, Figure S-X-32 shows the spread in lift at a given angle of attack and the spread in the pitching moment at a given lift coefficient between the various solutions. This "spread" increases with increasing angle of attack and lift coefficient, respectively. This "spread" is in addition to the level changes caused by the excessive "aft loading." Since the "aft loading" is almost identical for all the solutions, it might contribute to a level difference to the test data, but not to the "spread" between solutions. Looking at the wing pressure distributions at the outboard most three wing stations shown in Figures S-X-35–37 provides a clue for the increasing spread. These show pressure distributions for increasing angles of attack. As the angle of attack increases, so does the spread of shock location at the outboard stations. Figure S-X-37 shows pressure distributions at 4° angle of attack only from the solutions

remaining after all the outliers have been eliminated. Note that the large variation of shock location from these solutions still exists and is of the order of 20% chord. Compare this to the tight spread of shock locations shown in Figure S-X-34 from all solutions at $C_L = 0.50$, which corresponds to an angle of attack between 2.50° and 2.75°. Each one of the solutions, shown in Figures S-X-32–37, on its own is a valid solution, yet as angle of attack increases, so does the spread of shock location on the outboard portion of the wing.

These solutions can be parsed in terms of turbulence models in hopes of getting a better understanding of the quality of the solutions. Figures S-XV-5–7 show configuration lift and pitching moment, and the corresponding wing pressures at two outboard wing stations for $C_L = 0.50$ and 4.0° angle of attack. Figure S-XV-5 shows the results for the solutions using the SA turbulence model. Each solution used a different grid: H1 used a Geolab unstructured grid; K3 used a Cartesian grid; L2 used a custom unstructured grid; and O2 used an overset grid. This group of solutions exhibited the widest spread of lift and pitching moment and the widest range of shock location. Figure S-XV-6 shows the results for the solutions using the SA-QCR turbulence model. This is the biggest grouping of solutions. These were bounded by the extremes of the SA solutions, and mostly fell into two grid type groups. Solutions E1, Z1, Z2, and Z3 were based on the Geolab unstructured grid (green lines). Solutions A2, O2, U1, and U2 were based on overset grids (black lines). Note that pressure distributions were not available for solutions U1 and U2. Of the other three solutions, M2 was based on a custom unstructured grid (red), Q3 was based on a structured multiblock grid (blue), and K4 based on a Cartesian grid. Note that the solutions tend to group into the unstructured grid group and the overset grid group. Figure S-XV-7 shows the results for the solutions using non-SA type two-equation turbulence models. Solutions B1 and B2 used the k-kL-MEAH2015 model with and without a limiter, solution H2 used an EARSM model, L1 used an RSM-ω model, and T1 used Menter's k-ω SST-2003 model. These tended to fall into the lower end of the spread (in terms of lift), and with the exception of solution H2 did not show much variation of shock location.

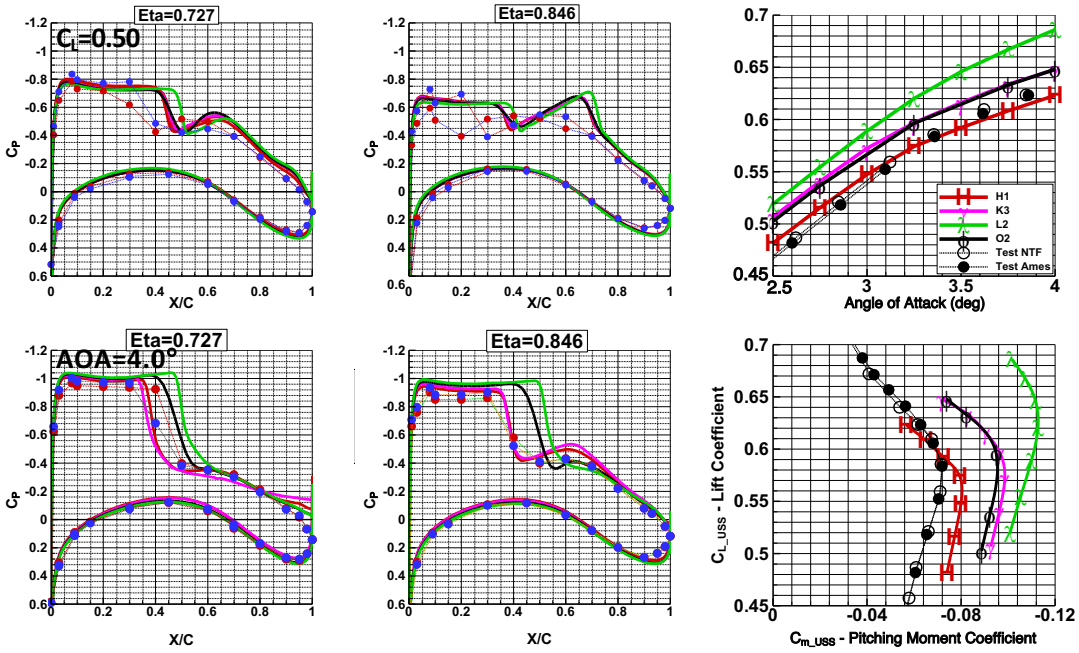


Figure S-XV-5. DPW-VI: WB (Aeroelastic) Lift, Pitching Moment, and Pressure Distributions; SA Turbulence Model, M=0.85.

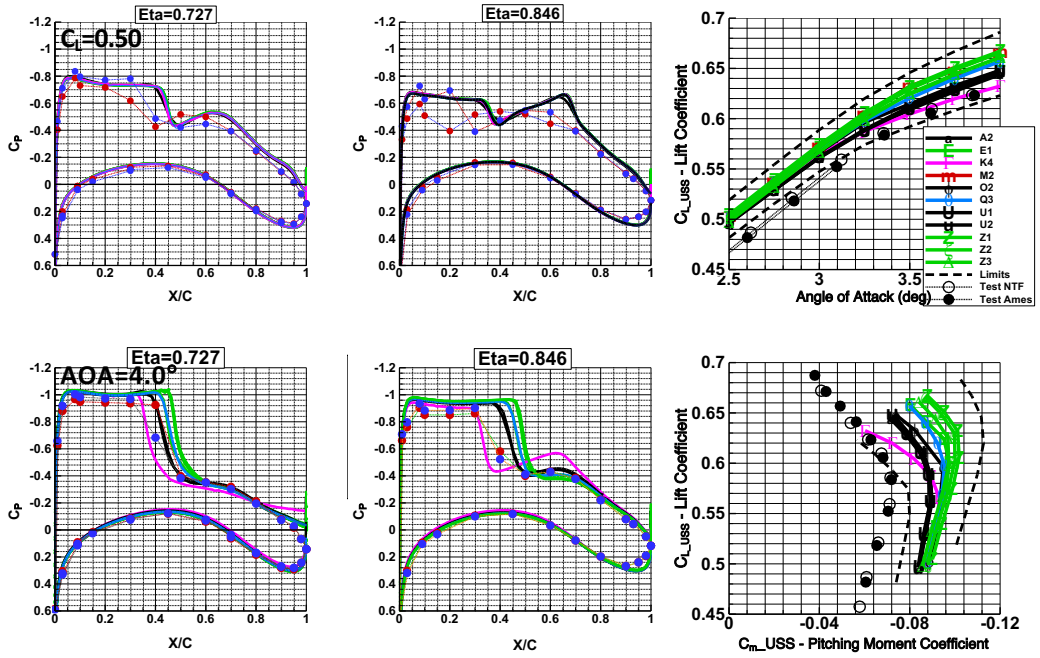


Figure S-XV-6. DPW-VI: WB (Aeroelastic) Lift, Pitching Moment, and Pressure Distributions; SA-QCR Turbulence Model.

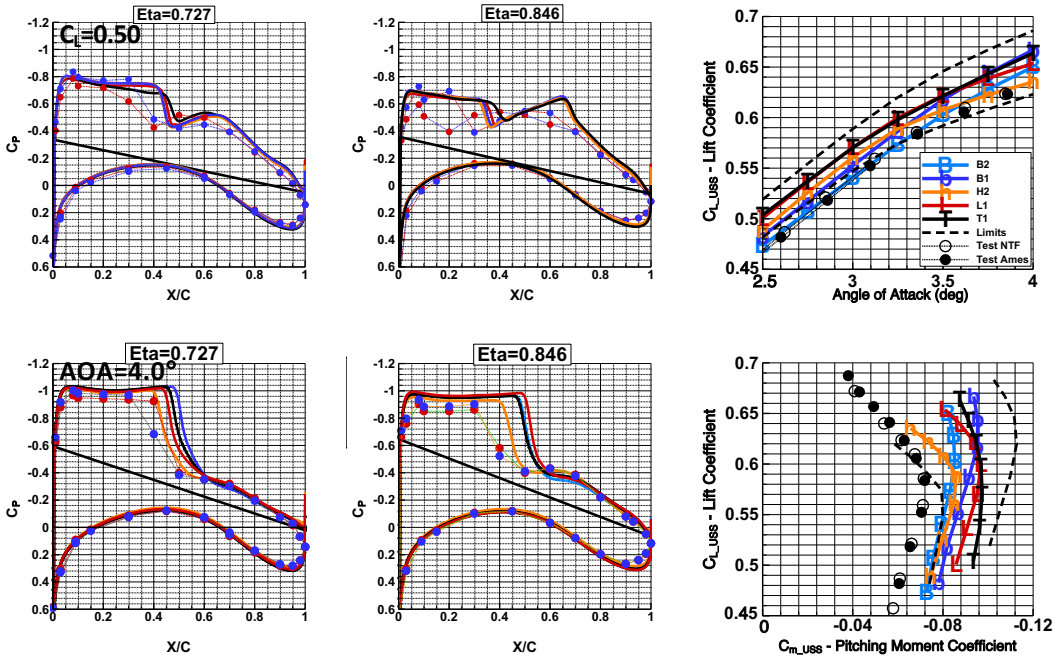


Figure S-XV-7. DPW-VI: WB (Aeroelastic) Lift, Pitching Moment, and Pressure Distributions; Non-SA Turbulence Models.

These last three figures appear very similar considering the spread of lift, pitching moment, and shock location. The only indication as to which solutions might be closer to the experimental data is given by the shock location. A deeper approach must be taken in trying to assess if any combination of solver, grid, and turbulence model might yield closer agreement with the experimental data recognizing that the experimental data itself has flaws. While knowing

that the absolute levels of lift and pitching moment may not be known with precision, we can have some confidence of their variation with angle of attack (Section III). By adding a constant value (different for each solution) to angle of attack and pitching moment to each solution to match the values of the average of NTF and 11-Foot test data at a $C_L = 0.53$, the CFD solutions can be collapsed around the experimental data as shown in Figure S-XV-8. The value of $C_L = 0.53$ was chosen to encompass all the submitted solutions. This figure shows that the solution spread starts at around $C_L = 0.58$ or between 3.0° and 3.5° angle of attack. At 4.0° angle of attack, the spread in lift and pitching moment is large. While this approach is somewhat unorthodox, the end result must be consistent and still make sense in terms of forces, moments, and pressure distributions.

Eliminating (pruning) solutions that deviate from the test data at the higher lift coefficients leaves six solutions, shown in Figure S-XV-9. Four of these solutions (A2, O2, U1, and U2) used overset grids and a variation of the SA with QCR turbulence model (3 with SA-RC, 1 identified just as SA). H2 used the Geolab unstructured grid and the EARSM turbulence model. K3, whose solution is beginning to look a little suspect at 4.0°, used a custom Cartesian grid and the SA-noft2 turbulence model. The same code and grid (K4) with the SA-noft2-QCR turbulence model deviated significantly from the test data at the higher lift values. The dashed lines shown in the figure represent the limits of the submitted solution minus the outliers. A significant characteristic of the pitching moment curve is the existence and location of the "pitch break" and the subsequent "pitch-up" shown in Figure S-XV-9. These characteristics can lead to exceeding the safe structural loads on the airplane and are subject to government certification rules. Adverse pitch characteristics (if not too severe) can be alleviated by a sophisticated computerized flight control system, and/or passive devices such as vortilons and wing vortex generators. It is important for CFD to accurately model these pitch characteristics.

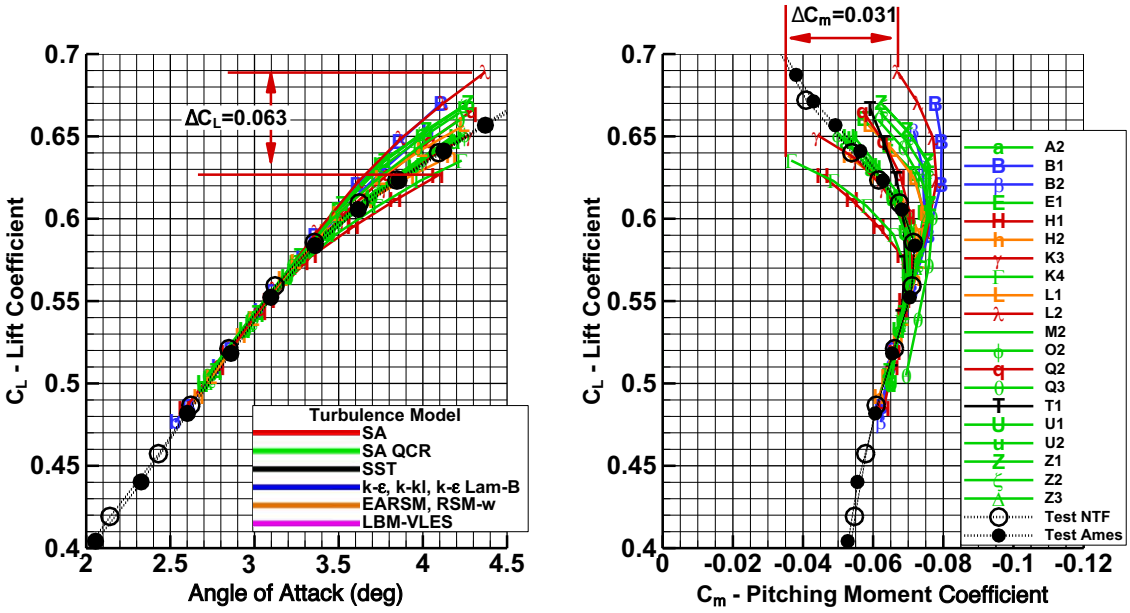


Figure S-XV-8. DPW-VI: WB (Aeroelastic) Lift and Pitching Moment Shifted to Match Experiment at $C_L = 0.53$.

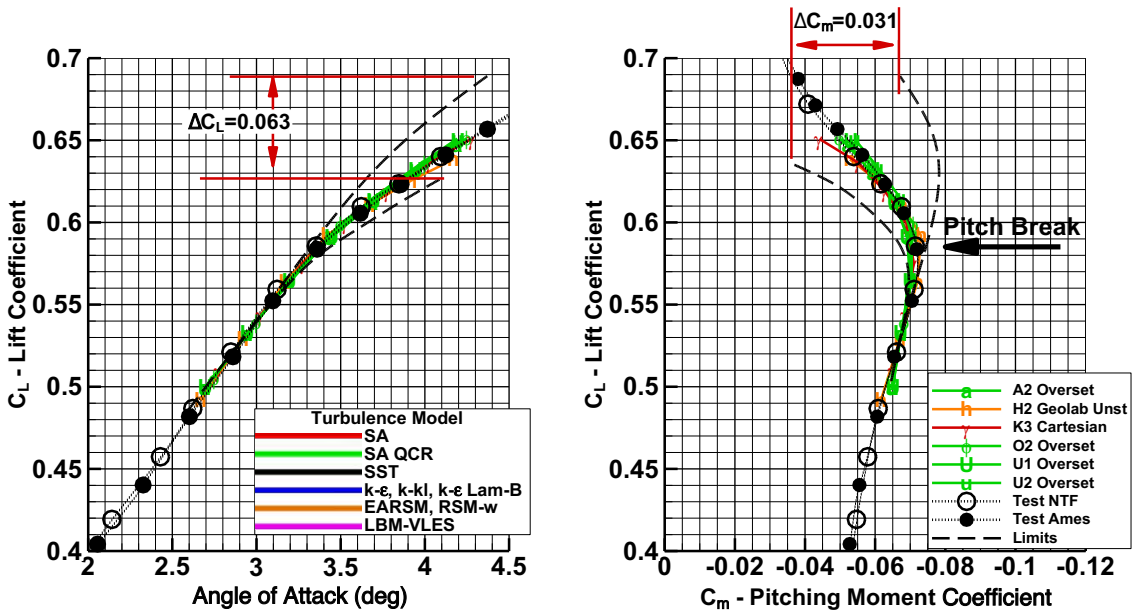


Figure S-XV-9. DPW-VI: WB (Aeroelastic) "Selected" Lift and Pitching Moment Solutions; Shifted to Match Experiment at C_L = 0.53.

Pressure distributions from these "Selected" solutions are shown in Figures S-XIV-10 to -13 for angles of attack of 3.0°, 3.5°, 3.75°, and 4.0°, respectively. As before, pressure distributions are not available for solutions U1 and U2. Solution O2 pressure distributions were also not available for angles of attack of 3.0° and 3.5°. There was little difference between the solutions at angles of attack of 3.5°, 3.75°, and 4.0°, except for K3 at 4.0°. Examination of the pressure distributions at all spanwise stations at 4.0° reveal excessive flow separation midspan ($\eta = 0.603$ in particular) for solution K3. This solution will now be deemed an outlier from this pruning on that basis. All of these solutions feature shocks that are further aft than the experiment, which is consistent with the "unshifted" lift and pitching moment data shown in Figure S-XV-14. The effect of the boundary layer trip is to move the shock forward and increase the boundary layer thickness in the experimental data, which might explain why the computational shocks (no trip modeling) are further aft. The further aft shock location of the CFD solutions leads to greater lift and more negative pitching moment. The comparisons make sense. These solutions all show the same behavior with increasing angle of attack as the test data, but there is still a spread of lift and pitching moment between the solutions. The spread of lift and pitching moment is due in most part to the wing. There is very little difference among the fuselage contributions. The spread appears to be entirely due to the small differences in shock location on the wing.

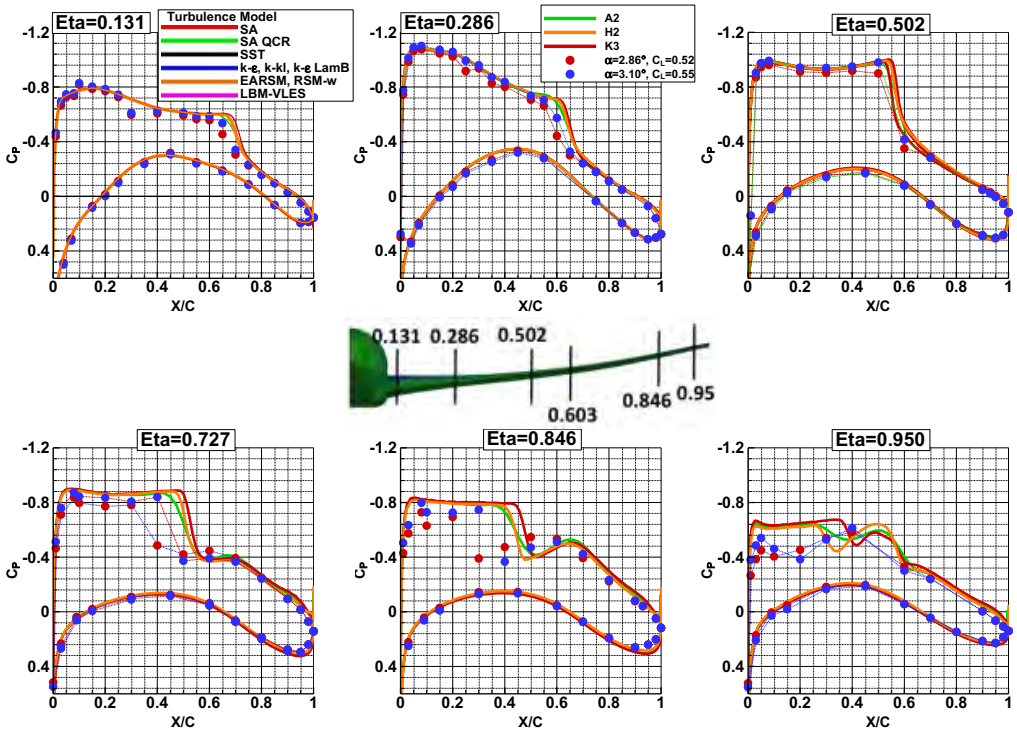


Figure S-XV-10. DPW-VI: WB (Aeroelastic) Wing Pressure Distributions: "Selected" Solutions; AOA = 3.0°.

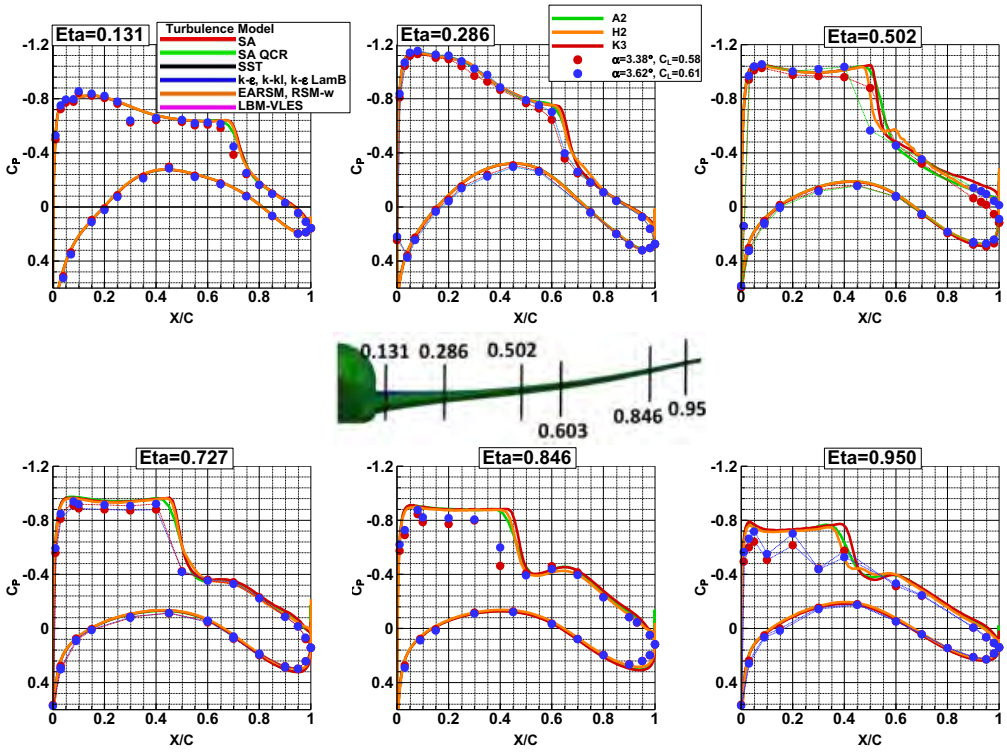


Figure S-XV-11. DPW-VI: WB (Aeroelastic) Wing Pressure Distributions: "Selected" Solutions; AOA = 3.5°.

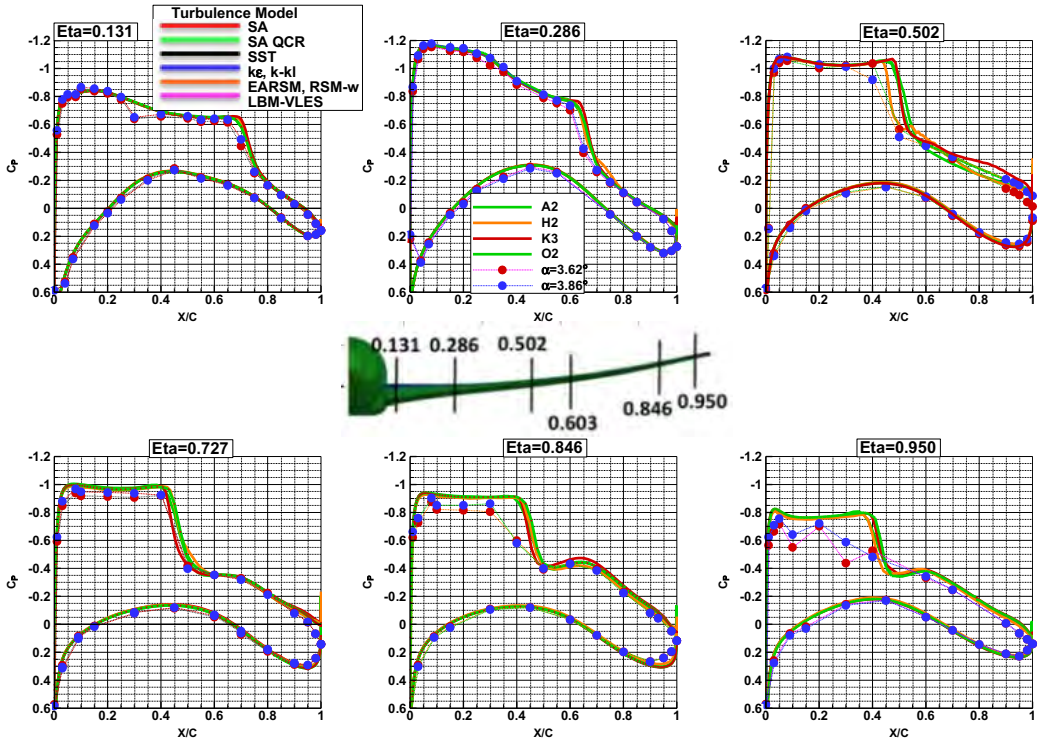


Figure S-XV-12. DPW-VI: WB (Aeroelastic) Wing Pressure Distributions: "Selected" Solutions; AOA = 3.75°.

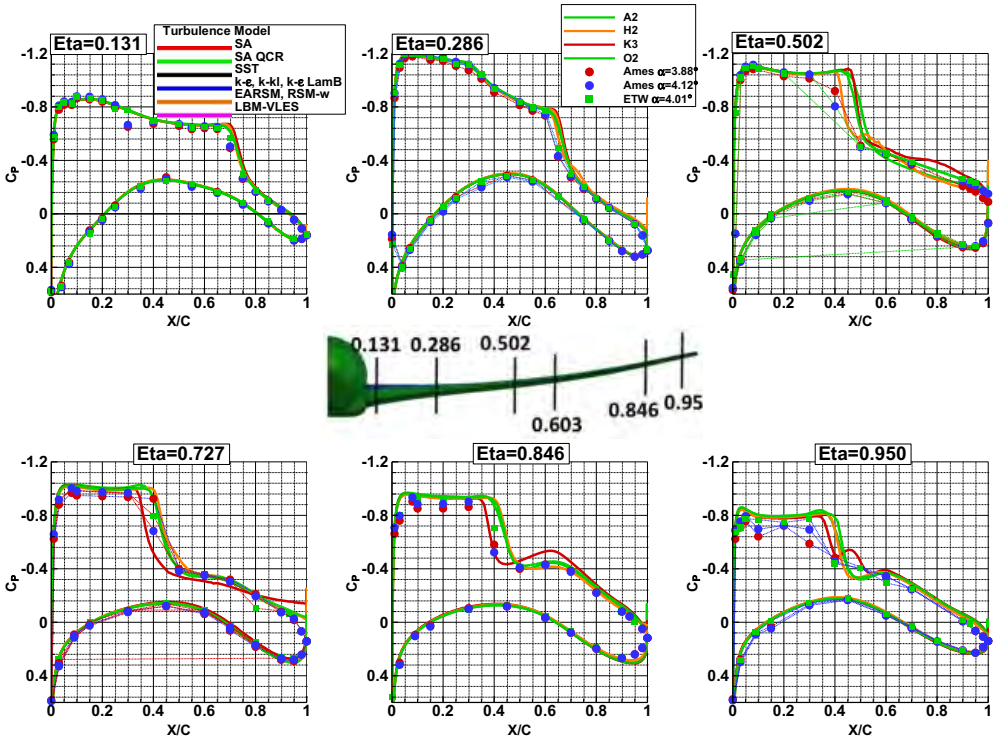


Figure S-XV-13. DPW-VI: WB (Aeroelastic) Wing Pressure Distributions: "Selected" Solutions; AOA = 4.0°.

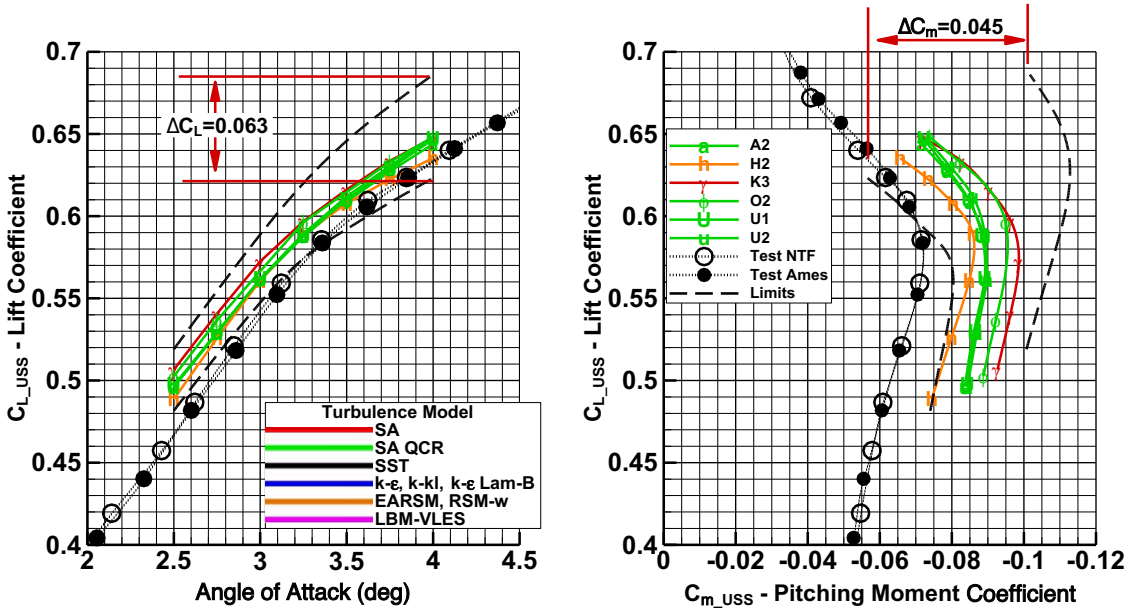


Figure S-XV-14. DPW-VI: WB (Aeroelastic) "Selected" Lift and Pitching Moment Solutions: USS Corrections Only.

The purpose of the Drag Prediction Workshop series is not a competition between organizations but a learning experience for all. In this vein, we also need to look at the characteristics of the solutions that did not agree with the test data trends. Table S-XV-3 lists the DPW-VI data entries from Table S-XV-2 that were not deemed outliers (these tables can also be found in Appendix C). The list is divided up into for groups: (1) the "Selected" shifted solutions that matched the test data; (2) solutions based on the SA turbulence model that failed to match the data; (3) solutions based on the SA with QCR turbulence model that failed to match the data; and (4) solutions based on two-equation turbulence models that failed to match the data. Lift and pitching moment for the three shifted solutions using some variation of the SA model that did not match the test data are shown in Figure S-XV-15. (Remember K3 was deemed an outlier based on pressure distribution, not lift and drag characteristics.) Two of these solutions marked the extremes of the spread of lift and pitching moment of the solutions that were not deemed outliers. Pressure distributions for these three cases are among the group previously shown in Figure S-XV-6. The L2 solution using the SA-neg turbulence model featured the most aft shock location and the corresponding highest lift and most negative pitching moment. The pitching moment and lift break was delayed compared to the test data. At the other extreme was the H1 solution. It featured the earliest pitching moment and lift break. The turbulence model was just identified as SA, but the variant is uncertain.

Lift and pitching moment for the seven shifted solutions using some variation of the SA model with QCR that did not match the test data are shown in Figure S-XV-16. All of the solutions except for K4, based on a custom Cartesian grid, exhibited higher lift and more negative pitching moment than the test data. The pressure distributions at 4.0° angle of attack shown in Figure S-XV-7 for all the SA-QCR solutions minus the outliers confirm a further aft shock location compared to those that matched the test data (black lines for the overset grids) for these six solutions. Solution K4, which exhibited lower lift and less negative pitching moment, had a more forward shock location. Note that all four of the solutions using SA with QCR that matched the test data used overset grids. Three of these were based on SA Rotation/Curvature correction (RC) with QCR. The fourth solution might have also but was not specific as to which version of SA was used. Solutions based on SA-neg with or without QCR failed to match the test data, as did the SA-noft2 with QCR variants. These results suggest that some rethinking might be in order regarding which variant of the SA turbulent models to use.

Table S-XV-1. DPW-VI: Solutions Minus Outliers Comparison to Test Data.

ID	SYM	SYM	Name	Organization	Code	Algorithm	Grid	Turbulence Mode
"Selected" Solutions that Match Test data								
H2	h	h	Ales Prachar/ Peter Eliasson	Aerospace Research and Test Establishment, FOI	Edge	Unstructured node-centered, Finite-volume	Unst-Geolab	EARSM (Explicit Algebraic Reynolds Stress Model)
K3	γ	g	Taku Nagata	Kawasaki Heavy Industries	Cflow	Cell-centered, MUSCL	Custom Cart	SA-noft2
O2	ϕ	f	David Hue	ONERA	elsA	Full NS Central Diff, cell-centered	Overset	SA-QCR2000
A2	a	a	Tony Sclafani	Boeing, BCA Advanced Concepts, Long Beach CA	Overflow v2.2k	Full NS Central Diff, cell-centered	Overset	SA-RC W/QCR2000
U1	U	U	Jim Coder	Applied Research Lab, Penn State	Overflow 2.21 3rd Order WENO	Full NS Upwind Diff, cell-centered	Overset	SA-RC W/QCR2000
U2	u	u	Jim Coder	Applied Research Lab, Penn State	Overflow 2.21 5TH Order WENO	Full NS Upwind Diff, cell-centered	Overset	SA-RC W/QCR2000
SA Turbulence Model Solutions that Do Not Match Test Data								
H1	H	H	Ales Prachar/ Peter Eliasson	Aerospace Research and Test Establishment, FOI	Edge	Unstructured node-centered, Finite-volume	Unst-Geolab	SA
Q2	q	q	Gaetan Kenway	MDOlab, University of Michigan	ADflow	Full NS Central Diff, cell-centered	Cust-Overset	SA 1stOrder
L2	λ	l	Stefan Keye / Vamshi Togiti	DLR	TAU	Node-centered, matrix	Unst-custom	SA-neg
SA w/QCR2000 Turbulence Model Solutions that Do Not Match Test Data								
¥	m	m	Ryan S. Glasby	Tennessee, Pointwise, NASA Langley, NAVAIR, MIT, U Ala	COFFE/KCFD	Node-centered, Finite element	Unst-custom	SA-neg w/QCR2000
K4	Γ	G	Taku Nagata	Kawasaki Heavy Industries	Cflow	Cell-centered, MUSCL	Custom Cart	SA-noft2 w/QCR200
E1	E	E	Atsushi Hashimoto	JAXA, Ryoyu Systems	FaSTAR	Upwind, cell-centered	Unst-Geolab	SA-noft2-R w/QCR2000
Z1	Z	Z	Yasushi Ito	JAXA, Ryoyu Systems	TAS limiter K=1	Node-based	Unst-Geolab	SA-noft2-R w/QCR2000
Z3	Δ	D	Yasushi Ito	JAXA, Ryoyu Systems	TAS limiter K=10	Node-based	Unst-Geolab	SA-noft2-R w/QCR2000
Z2	ζ	z	Yasushi Ito	JAXA, Ryoyu Systems	TAS limiter K=5	Node-based	Unst-Geolab	SA-noft2-R w/QCR2000
Q3	θ	q	Gaetan Kenway	MDOlab, University of Michigan	ADflow	Full NS Central Diff, cell-centered	Embraer MB	SA-QCR2000
Two-Equation Turbulence Model Solutions that Do Not Match Test Data								
B2	b	b	Khaled Abdol-Hamid	NASA Langley Research Center	FUN3D 12.8	Node-centered UMUSCL upwind	Unst-Geolab	k-kL-MEAH2015 no-limiter
B1	B	B	Khaled Abdol-Hamid	NASA Langley Research Center	FUN3D 12.8	Node-centered UMUSCL upwind	Unst-Geolab	k-kL-MEAH2015 w/Limiter
T1	T	T	Yuntao Wang	CARDC	TRIP	Upwind Roe cell-centered	CommonMB	Menter k-w SST-2003
L1	L	L	Stefan Keye / Vamshi Togiti	DLR	TAU	Node-centered, matrix	Unst-custom	RSM-ω

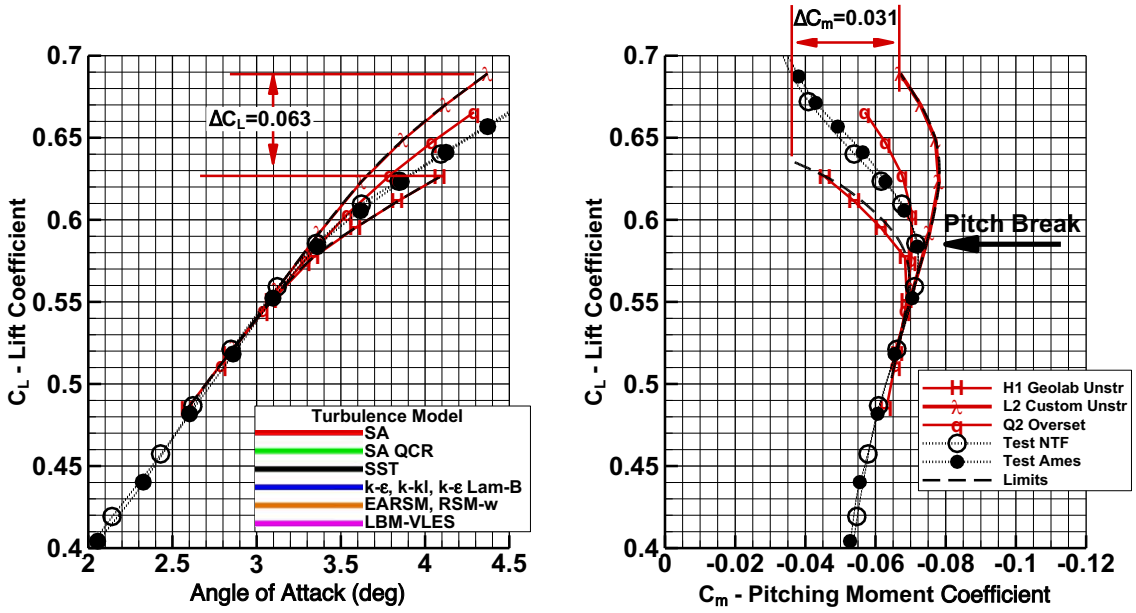


Figure S-XV-15. WB (Aeroelastic) Lift and Pitching Moment: SA Solution That Do Not Match Experiment.

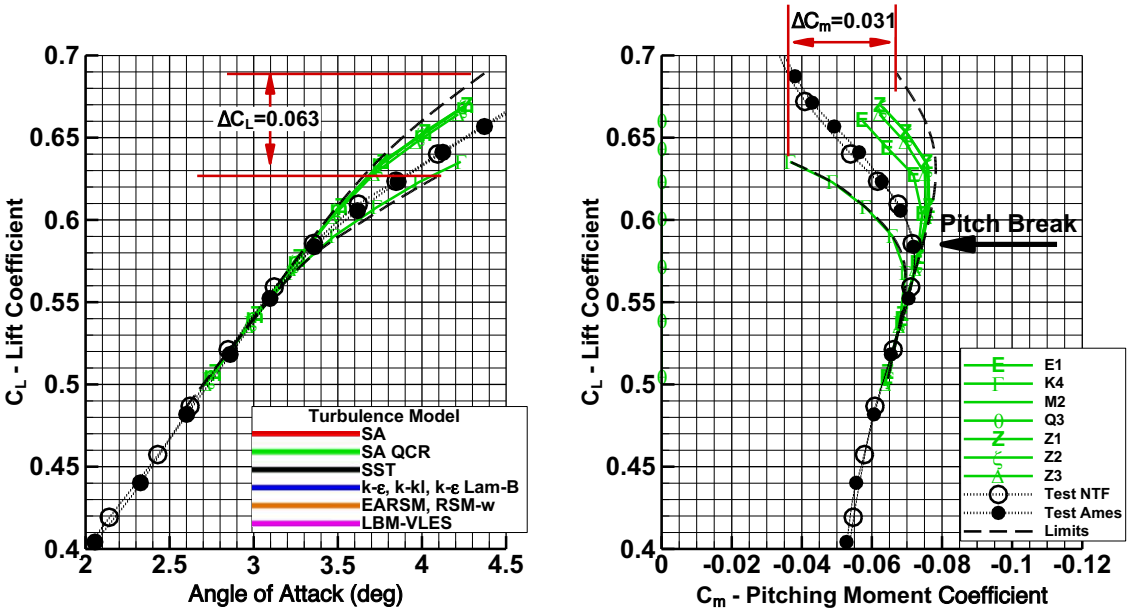


Figure S-XV-16. WB (Aeroelastic) Lift and Pitching Moment: SA-QCR Solution That Do Not Match Experiment.

Lift and pitching moment for the four shifted solutions using two-equation turbulence models that did not match the test data are shown in Figure S-XV-17. Solutions B1 and B2, show a higher pitch break and not as deep a pitch-up as the test data indicates. Solution L1 shows about the right amount of pitch-up but the break is at too high a lift coefficient. The pressure distributions at 4.0° angle of attack, shown in Figure S-XV-8 for all the two-equation

turbulent model solutions minus the outliers, confirm a further aft shock for these solutions compared to H2 (orange line), which matched the test data.

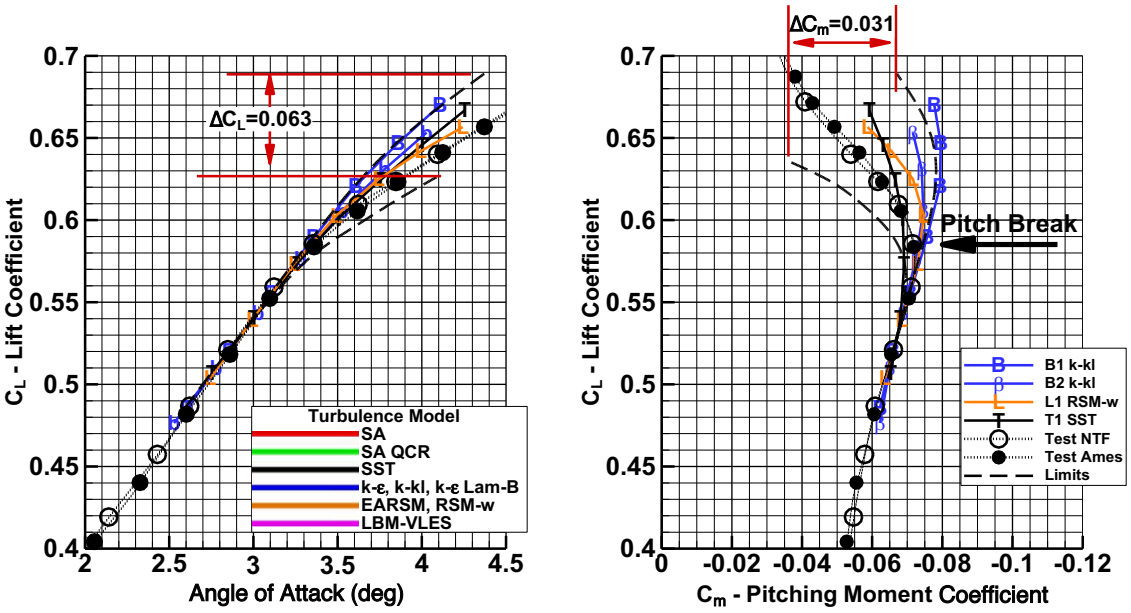


Figure S-XV-17. WB (Aeroelastic) Lift and Pitching Moment: 2-Eq. TM Solutions That Do Not Match Experiment.

D. Inadequate Test Data

RANS is doing well in the attached flow regime of the flight envelope as evidenced by the nacelle-pylon drag increment in DPW-VI, the reasonable prediction of stabilizer effectiveness in DPW-IV, and the reduction of premature side-of-body separation. However, the high-speed cruise OML development consists of less than 25% of the total aerodynamics-related airplane development effort. To be able to expand the use of CFD over the entire flight envelope, considerable progress in algorithm and hardware technology is still necessary. Many flight conditions are characterized by large regions of separated flows. Such conditions are encountered by transports at low speed with deployed high lift devices, at their structural design loads conditions, or subjected to in-flight upsets that expose them to speed and/or angle-of-attack conditions outside the envelope of normal flight conditions, to name a few. The focus of the High Lift Workshop, the Aeroelastic Prediction Workshop, etc., series intersect many of these areas, as did the angle-of-attack sweep cases of the Drag Prediction Workshop series. As demonstrated in DPW-VI, some success has been achieved in predicting flows with significant flow separation from 5 out of 42 data sets submitted, but clearly, this is not a mature CFD prediction area.

Over half of the solutions submitted in both DPW-V and -VI were deemed outliers. This was largely due to premature side-of-body flow separation. We do not know the reason for the sensitivity of premature side-of-body separation to solver, turbulence model, and grid, nor the implications this might have for other geometries, and/or, flow conditions. This type of 3D corner flow separation continues to need more attention in turbulence model development and CFD application. The NASA Juncture Flow Model test [113] will contribute to further understanding and dealing with this issue.

Pitch-up behavior after the initial break is very dependent on the progression of flow separation across the wing as angle of attack is increased. Pressure distributions based on physical pressure taps cannot adequately define these separated areas. Perhaps a fast response pressure sensitive paint or other flow visualization technique could.

The chaotic situation at these high angles of attack may be physical as well as computational. At 4° angle-of-attack, the wind tunnel model experiences a large amount of buffet. The force and moment data are heavily filtered, and the pressure transducers are incapable of responding to high frequency variations. To what extent the flow is unsteady at these conditions can be critical in the stability and control arena. One must ask if steady RANS is adequate for modeling this flow regime. Will Unsteady Reynolds Averaged Navier-Stokes be any better, or must one go to an eddy-resolving method such as Detached Eddy Simulation to accurately simulate this flow regime? Is LBM-VLES the wave of the future? Without adequate test data, how will we know? Without detailed experimental measurements that adequately capture the details of the flow separation and unsteadiness on these types of configurations, recommendations as to the level of "unsteady" modeling necessary to adequately model these flows cannot be made.

The Reynolds number increment case in DPW-IV revealed (at least to this author) an inconsistency between the NTF and ETW data. More research should be done to better understand the consistency and accuracy of the experimental data, as well as the computational predictions.

CFD development is stagnating when it comes to dealing with separated, unsteady flows. Better algorithms, turbulence models, etc., are needed to deal with this flow regime. Moore's Law will not solve the problem by itself. Without better, more detailed experimental data to characterize separated, unsteady flows, and to provide the details necessary to develop better turbulence models, CFD progress will come to a standstill. Without the detailed experimental data, it will be impossible to know if the CFD is good enough.

Section XVI: Observations, Recommendations, and Concluding Remarks

The six Drag Prediction Workshops have drawn a total of 125 participants submitting 225 data entries. Over half of these occurred in the last three workshops dealing with the NASA CRM. Participants have ranged from North America, Europe, Asia, and South America, representing Government, Industry, Academia, and Commercial/Vendors. A continuous improvement of the results as measured by the reduction of the spread of drag predictions for the specified "nominal" cruise point, accuracy of drag increment prediction, and the angle-of-attack sweep behavior has been noted [114]. The experiences and recommendations presented here are consistent with those espoused in the "CFD Vision 2030 Study: A Path to Revolutionary Computational Aerosciences," [115].

A. Observations

1. Single Point Solutions

With the increasing grid sizes between DPW-IV and -VI there has been a reduction of the spread of total drag among the solutions. In general, there has been a smaller spread of results with structured grid solutions compared to those using unstructured grids. Results from grid convergence studies are clearly dependent on the combination of solver, grid, turbulence model, etc. Using the same solver and turbulence model on different grid families shows different grid convergent rates, dCDT/dGRIDFAC, and force and moment values in the continuum (infinite grid size). Using the same solver and grid but different turbulence model can also show very different grid convergence rates, and values in the continuum. The bigger (absolute value) the grid convergence rate, the greater the difference between the drag evaluated at the continuum in a grid convergence study, and that calculated at some finite grid size. Convergence characteristics, using the same solver, grid family, and turbulence model between the Wing-Body and the Wing-Body-Nacelle-Pylon configurations are very similar. No determination can be made as to which combination of solver, grid, and turbulence model produces the "best" drag because there is no measure of what the "best" drag is. The experiment does not yield absolute drag.

Of significant importance to industry design processes is the prediction of the drag increment between the two configurations. A well-crafted wind tunnel campaign can yield very accurate drag increments. CFD also does a very credible job at calculating drag increments if done carefully. The CFD drag increment predictions between the Wing-Body and the Wing-Body-Nacelle-Pylon configurations were within or very close to the experimental values for many cases. Most (24 out of 36) solution pairs yielded drag increments calculated in the continuum within the experimental 1-sigma tolerance. Only 8 out of 36 solution pairs yielded increments within the experimental 1-sigma tolerance by

just differencing the medium grid results. Those 8 solution pairs were all characterized by a low drag/grid convergence (dCDT/dGRIDFAC) rate; that is a small change in drag over a range of grid sizes.

There was very little difference in the predicted wing or nacelle pressure distributions due to grid size from the DPW-VI solutions at the nominal $C_L = 0.50$ "cruise" condition. This is an indication that even the smallest grids were already quite adequate for predictions of pressure distributions at this condition. These solutions, based on the aeroelastically deflected geometry, were in good agreement with the experimental wing pressure distributions.

Close examination of the CFD pressure distributions around the wing trailing edge compared to test, reveals an excessive "aft-loading." The difference between the upper and lower surface represents lift and contributes to negative section pitching moment and flap/aileron hinge moment. These differences become more aggregative the further outboard on the wing. This excessive "aft loading" is seen from every turbulence model, gridding scheme, and solver type presented in the DPW workshops. It is highly unlikely that this excessive "aft loading" is due to geometric issues. The wind tunnel model geometry was validated. Measured spanwise aeroelastic wing twist at the test conditions was included in the model definition and was calculated in the coupled aerostructural simulations. Excessive "aft-loading" has also been seen on other wind tunnel models with significant aft camber on the wing and is not limited just to the CRM. One speculation is that the lack of modeling the transition trip present on the wing of the wind tunnel model combined with the significant aft camber contributes to the excessive "aft-loading." Turbulence modeling is also a suspect. The question of the excessive "aft loading" remains an open issue.

2. *Angle-of-Attack Sweep/Buffet Study*

DPW-V and -VI requested solutions at seven angles of attack specified between 2.5° and 4.0° at 0.25° increments to investigate the CFD predictions in an angle-of-attack range where significant flow separation is expected. Experimental data for the variation with angle of attack of lift and pitching moment show a nonlinearity in lift and a break in pitching moment slope beginning at about $C_L = 0.58$. CFD results from DPW-IV and -V showed very significant offsets from the data deemed to be due to the lack of accounting for the aeroelastic deflection the model undergoes over the angle-of-attack range, and for the presence of the USS mounting system. DPW-VI included the aeroelastic deflection in the computational model, and an estimate for the USS narrowed the gap between CFD and test. However, even after eliminating solution outliers, a significant spread of lift and pitching moment remain.

Over half of the solutions submitted in both DPW-V and -VI were deemed outliers. This was largely due to premature side-of-body flow separation. Spalart's QCR model, which was used in some entries with SA or SST turbulence models, appears to eliminate the tendency to predict a side-of-body separation that is early and too large. Some two-equation turbulence models, i.e., EARSM, Lag RST, k-kl-MEAH2015, RSM-ω, are also more resistant to premature side-of-body separation. We do not know why the sensitivity of premature side-of-body separation to solver, turbulence model, and grid exists, nor the implications this might have for other geometries, and/or, flow conditions. This type of 3D corner flow separation continues to need more attention in turbulence model development and CFD application.

The pressure distributions of the solutions minus the outliers show very little variation between solutions at $C_L = 0.50$. However, as the angle of attack is increased, there is an increasing variation of the shock location across the span of the wing. At 4° angle of attack, the shock location varies by as much as 20% chord. This variation of shock location is consistent with and is the primary source of the increasing spread of lift and moment with angle of attack. There is negligible spread among the fuselage contributions.

Close examination of the 20 DPW-VI solutions (out of 41 submitted) not deemed outliers revealed that only 5 of those could adequately match the variation of lift with angle of attack, and pitching moment with lift, and adequately match the wing pressure distributions at high angles of attack. Four of these solutions used overset grids and a variation of the SA with QCR (3 with SA-RC, 1 identified just as SA) turbulence model. One used the Geolab unstructured grid and the EARSM turbulence model. Turbulence models appeared to be the biggest discriminator between these five solutions and the other 15 that did not match the test data as well. These results suggest that some rethinking might be in order regarding turbulence models, and which variant of the SA turbulent model to use if using SA.

3. *One-of-a-Kind Studies*

A Mach sweep or drag rise study was included in DPW-IV. Solutions at fixed C_L's of 0.40, 0.45, and 0.50 were requested for a range of Mach numbers from 0.70 to 0.87 at a Reynolds number of 5 million. After adjusting for drag level differences (drag polar shape) between CFD and test data from both Ames 11-Foot and Langley NTF, the drag rise shapes were well predicted by the computational results at $C_L = 0.40$ and 0.45. The experimental drag rise at a $C_L = 0.50$ appeared slightly steeper above Mach = 0.83 than the CFD results.

Solutions were provided in DPW-IV for two Chord Reynolds numbers: 5 million and 20 million. CFD drag increments between the two Reynolds number solutions were within 5–6 percent (1–2 counts) of the experimental increment based on ETW data. Increments based on the SST turbulence model were on the high side, those based on the SA turbulence model were on the low side. The pitching moment increments were within an equivalent 0.1° of stabilizer deflection.

Also, unique to DPW-IV was the downwash study. Here, four angle-of-attack sweeps of the CRM were performed, three on the WBT configuration at different horizontal-tail settings, and one without the tail on the WB configuration. The solutions were sufficient to calculate trimmed drag polars and to determine stabilizer effectiveness. No test data were available in DPW-IV for comparison. Recent analysis has shown the impact of aeroelastic twist and USS corrections to the original DPW-IV data in comparison to the now available test data. DPW-IV CFD data with aeroelastic twist and USS corrections applied were used to calculate stabilizer effectiveness. Most of the CFD predictions were within 5% of the "rigidized" experimental values.

DPW-VI requested grid adaptation solutions of the CRM WB configuration as an optional case. This consists of a series of fixed lift, $C_L = 0.50$, solutions using an adapted grid family provided by the participant. Three solutions demonstrated solid grid convergence. GGNS (solution P2) demonstrated the combination of a strong solver, solid residual convergence, and grid adaption resulting in a rapid convergence to the continuum drag value with a very low grid convergence (dCDT/dGRIDFAC) rate. The solutions demonstrated that without adaption some flow features may not be adequately captured with fixed grids.

DPW-VI also requested a coupled aerostructural simulation. A NASTRAN® finite element model was provided for structural analyses and coupling with an aerodynamic CFD flow solver for analysis of the CRM WB configuration at a fixed Mach and lift condition. Four solutions were submitted with very similar results in line with the fixed aeroelastic grid results. Twist and deflection were well predicted. The fact that only 4 out of 25 participants chose to perform the optional case in DPW-VI indicates that coupled static aeroelastic computations remain the exception rather than the norm in the current state of the practice.

4. *Emerging Technologies*

Finite element solvers feature strong solvers that facilitate machine precision residual convergence. Reliable convergence to machine accuracy removes one source error where solutions just stagnate, which is sometimes mistaken as meaning convergence. Reliable convergence is essential to solution adaptive methods. It is a technology that needs to be followed.

The promise that solution adaptive grids bring is that they should be able to deliver a consistent set of solutions for configurations, and/or conditions for which prior gridding experience may not be available. Much work remains to be done to bring this technology to a "production" capability for 3D RANS. It is expected that combining an output-based error-estimate that is optimized for the analysis along with adaptive meshing will provide significant advantages in grid convergence for future adaptive grid applications, in addition to the user and uncertainty benefits demonstrated to date. It is a technology that needs to be matured.

A solution based on the LBM that is totally different from the classical finite volume/finite element methods used to date was submitted to DPW-VI. Although the drag levels were high, the predicted pressure distributions were in

as good agreement with test as those of most other entries. The predicted drag increment (in the continuum) between the WBNP and WB configurations was within the experimental results. With LBM being inherently unsteady, it might be more efficient than other unsteady scale-resolving methods due to its explicit and local nature. The method might be well suited for buffet calculations that contain unsteady flow content. This technology needs to be followed.

5. Experimental Data

No wind tunnel mounting system "tare and interference" tests have been carried out for the CRM model. These effects are essential for a better understanding of the experimental data and comparisons with CFD. The high cost of these type of tests is understood. A CFD study of the aeroelastic and mounting system effects on the CRM WBT model was previously reported. A new CFD study of the mounting system effects is needed. This study should be based on the aeroelastically deflected geometries created for DPW-VI, and include the effects on the CRM WB, WBT, and WBNP configurations.

There is a certain stagnation of CFD development due to the lack of experimental data in the public domain (and maybe even privately held). CFD can do a very credible job in the attached flow regime as demonstrated in DPW. It is in the expansion of the flight envelope where significant flow separation is present that issues arise. Detailed experimental data, beyond simple force and moment, and pressure distribution, are needed to guide the further development of CFD technology.

Pitch-up behavior after the initial break is very dependent on the progression of flow separation across the wing as angle of attack is increased. Pressure distributions based on physical pressure taps cannot adequately define these separated areas. Perhaps a fast response pressure sensitive paint or other flow visualization technique could. These data need to be better published and made available. Without detailed experimental measurements that adequately capture the flow separation and unsteadiness on these types of configurations, recommendations as to the level of "unsteady" CFD modeling necessary to adequately model these flows cannot be made. CRM data from the various wind tunnel campaigns may exist and needs to be better published and made available.

Premature side-of-body separation is very sensitive to the combination of solver, turbulence model, and gridding details. This type of 3D corner flow separation continues to need more attention in turbulence model development and CFD application. The NASA Juncture Flow Model test [113] will contribute to this question.

The Reynolds number increment case in DPW-IV revealed (at least to this author) an inconsistency between the NTF and ETW data. The 20 million Reynolds number data from the NTF is significantly different from that from ETW and CFD. More research should be done to better understand the consistency and accuracy of both the computational and experimental data.

6. Workshops and CFD Validation

Although the Drag Prediction Workshop and similar workshop series are not strictly "CFD validation" efforts, they do in a practical sense serve that purpose. Effective CFD validation requires intimate knowledge of both the CFD and the experimental data being compared. CFD validation cannot consist of the comparison of the results of one code to those of one experiment. Rather, it is the agglomeration of comparisons at multiple conditions, code-to-code comparisons, an understanding of the wind tunnel corrections, etc., that leads to the understanding of the CFD uncertainty and validation of its use as an engineering tool.The question is not can CFD give a great answer for one or two test cases, but can the CFD "processes" give good answers for a range of cases when run by a competent engineer? The Drag Prediction Workshop has given us this view, affirming the practices of those who have done well, and hopefully a wake-up call for those practices that have not. This is what validation in the "real world" for an intended purpose is all about [116]. These open forum workshop efforts must continue.

The issues with CFD validation, turbulent flow separation prediction, and the grid generation difficulties presented here were also deemed important in the CFD Vision 2030 Study.

B. Specific Recommendations

1. A new CFD study of the CRM wind tunnel mounting system effects is needed. This study should be based on the aeroelastically deflected geometries created for DPW-VI and include the effects on the CRM Wing-Body, Wing-Body-Tail, and Wing-Body-Nacelle-Pylon configurations.

2. The 20 million Reynolds number data from the NTF are significantly different from that from ETW and CFD. More research should be done to better understand the consistency and accuracy of both the computational and experimental data.

3. CFD pressure distributions around the wing trailing edge with significant aft camber reveal an excessive "aft-loading" compared to test. This contributes to excessive lift and flap/aileron hinge moments. The lack of modeling the "trip strip" on the wind tunnel model is one suspect for the excess; turbulence modeling is also a possibility. Further CFD studies are needed to resolve this issue.

4. Premature side-of-body separation plagued many of the submitted solutions. While we now know of some "fixes", we do not know why the sensitivity of premature side-of-body separation to solver, turbulence model, and grid, nor the implications this might have for other geometries, and/or, flow conditions. This type of 3D corner flow separation continues to need more attention in turbulence model development and CFD application. The NASA Juncture Flow Model test will contribute to further understanding and dealing with this issue.

5. CFD solutions over a sweep of angle of attack show an increasing spread of lift and pitching moment. An examination of CFD results revealed only 5 solutions (two turbulence models) that matched the experimental variation with angle of attack. Further CFD studies are needed to better understand this trend, and its implications as to the validity of different turbulence models.

6. Solution adaptive grids will provide significant advantages in grid convergence and solution accuracy, while significantly reducing the expert human labor currently required for grid generation. Much work remains to be done to bring this technology to a "production" capability for 3D RANS. This is a technology that must be matured.

7. The Lattice-Boltzmann Method provides an alternative technology that might overcome many of the limitations of the current classical finite volume/finite element methods dealing with grid generation, separated, and unsteady flows. Initial results presented in DPW-VI were encouraging, but extensive verification/validation will be necessary to prove its worth. This is a technology that must be watched.

8. Further detailed experimental measurements that adequately capture the flow separation and unsteadiness on these types of configurations at "off-design" conditions are needed. NASA, DLR, ONERA, JAXA, and other organizations/groups have ongoing research programs that address fundamental questions related to turbulence models, unsteady flows, etc. The NASA Juncture Flow Model test is this type. A working group should be convened to define experimental needs, identify existing relevant data, ongoing research programs, and better openly disseminate this type of fundamental information.

9. DPW has highlighted CFD and experimental issues dealing with "off-design" conditions involving significant separation and unsteady flows. An open forum with an agglomeration of comparisons at multiple conditions, code-to-code comparisons, an understanding of the wind tunnel corrections, etc., leads to a better understanding of the CFD progress and needs. A new workshop addressing these needs must be organized.

C. Concluding Remarks

After six workshops spanning almost two decades, the DPW Series has generated a tremendous amount of CFD data, freely available in the public domain. Although it has been difficult separating out the parts and pieces that contribute to errors in CFD drag predictions, part of the improvements over the years can be attributed to grid resolution. The scatter in predicted drag in the continuum has been reduced dramatically from ±50 counts in DPW-I

to around ±5 counts for DPW-V and -VI. In the six workshops, the grid size has grown dramatically. The average size of the medium wing-body meshes in DPW-I through DPW-IV have been 3.2, 5.4, 7.8 and 10.9 million, respectively. This represents a growth rate of ~17% per year during the eight years between DPW-I and DPW-IV. For DPW-VI, this number has grown from 25 to 50 million points for the various families of grids available. The finest level grids have increased steadily, from just over 3 million mesh points in DPW-I to 225 million for the WBNP in DPW-VI.

The recurring theme of juncture-flow separations causing difficulties with CFD drag predictions has been the motivation for an ongoing effort to develop a Juncture-Flow Model [113]. The JFM campaign will gather off-body data in juncture-flow regions for attached flows, flows at incipient separation, and flows with moderately sized separation bubbles. The intent for these measurements is to provide the turbulence modeling community with high-quality, high-resolution databases to help advance the next generation turbulence models. Experimental studies must also focus on shock induced separation, which plagues the accuracy of CFD predictions at conditions where it is encountered.

The Drag Prediction Workshop series is coming to an end. The tremendous amount of CFD data collected (and available) coupled with the public domain wind tunnel data should spawn further studies beyond what has been covered in this report. It is hoped that this vast, openly available set of CFD and related experimental data can serve as a catalyst for further work. This should be of particular value to the academic community, which frequently has not had access to quality industry relevant data. The CFD and experimental issues highlighted by this workshop series are still in need of further resolution. This is particularly so for the "off-design" conditions involving significant separation and unsteady flows. Hopefully, a new Workshop addressing these needs will be organized.

Section XVII: Acknowledgments

I would like to thank the AIAA Applied Aerodynamics Technical Committee for sponsoring the Drag Prediction Workshop Series. The planning of these workshops throughout the duration of the series has been conducted by a substantial number of dedicated individuals. Members of the aggregate organizing committees over the past six Workshops (not all at the same time) include: myself (Ed Tinoco), Shreekant Agrawal, Simone Crippa, Bob Dowgwillo, Bernhard Eisfeld, Jean Luc Godard, Mike Hemsch, Steve Klausmeyer, Rick Matus, Dimitri Mavriplis, Bas Oskam, Shahyar Pirzadeh, Mark Rakowitz, Juergen Quest, Martin Gariepy, David Hue, Olaf Brodersen, Stefan Keye, Tom Zickuhr, Kelly Laflin, Dave Levy, Ed Feltrop, Mori Mani, Ben Rider, Rich Wahls, Joe Morrison, Mitsuhiro Murayama, Chris Roy, and John Vassberg. Melissa Rivers, NASA Langley Research Center, has had major responsibility for the Common Research Model, its manufacture, its testing, coordination with other organizations in their testing campaigns, and in disseminating the experimental results. Thank you, Melissa, we would have been lost without your help. I would also like to thank Dave Bogue, Boom Supersonic, for his counsel concerning the downwash study, and for providing the "rigidized" stabilizer effectiveness. Last, but not least, I would like to thank Tecplot. They have provided support throughout the Drag Prediction Workshop Series, as well to other similar CFD workshops. Without the support I received from Tecplot, this report would not have been possible.

Section XVIII: References

1. 1st AIAA CFD Drag Prediction Workshop, Anaheim, CA, June 2001, http://aiaa-dpw.larc.nasa.gov/Workshop1/workshop1.html, accessed 4 September 2017.
2. Redeker, G., "DLR-F4 Wing-Body Configuration," *A Selection of Experimental Test Cases for the Validation of CFD Codes*, number AR-303, pages B4.1–B4.21. AGARD, August 1994.
3. Levy, D. W., Vassberg, J. C., Wahls, R. A., Zickuhr, T., Agrawal, S., Pirzadeh, S., and Hemsch, M. J., "Summary of data from the first AIAA CFD Drag Prediction Workshop," *Journal of Aircraft*, 40(5):875–882, Sep–Oct 2003. doi:10.2514/2.6877
4. Hemsch, M. J., "Statistical Analysis of CFD Solutions from the Drag Prediction Workshop," AIAA paper 2002-0842, 40th AIAA Aerospace Sciences Meeting and Exhibit, Reno, NV, January 2002 and *Journal of Aircraft*, Vol 41, 2004.
5. Rakowitz, M., Eisfeld, B., Schwamborn, D., and Sutcliffe, M., "Structured and Unstructured Computations on the DLR-F4 Wing-Body Configuration," *Journal of Aircraft*, 40(2):256–264, 2003. doi:10.2514/2.3117
6. Mavriplis, D. J. and Levy, D. W., "Transonic Drag Predictions Using an Unstructured Multigrid Solver," *AIAA Journal of Aircraft*, 42(4):887–893, 2005. doi:10.2514/1.8233
7. Pirzadeh, S. Z. and Frink, N. T., "Assessment of the Unstructured Grid Software TetrUSS for Drag Prediction of the DLR-F4 Configuration," AIAA Paper 2002-0839, 40th AIAA Aerospace Sciences Meeting and Exhibit, Reno, NV, January 2002.
8. Vassberg, J. C., Buning, P. G., and Rumsey, C. L., "Drag Prediction for the DLR-F4 Wing/Body Using OVERFLOW and CFL3D on an Overset Mesh," AIAA Paper 2002-0840, 40th AIAA Aerospace Sciences Meeting and Exhibit, Reno, NV, January 2002.
9. 2nd AIAA CFD Drag Prediction Workshop, Orlando, FL, June 2003, http://aiaa-dpw.larc.nasa.gov/Workshop2/workshop2.html, accessed 4 September 2017.
10. Laflin, K. R., Vassberg, J. C., Wahls, R. A., Morrison, J. H., Brodersen, O., Rakowitz, M., Tinoco, E. N., and Godard, J., "Summary of Data from the Second AIAA CFD Drag Prediction Workshop," *Journal of Aircraft*, 42(5):1165–1178, 2005. doi:10.2514/1.10771
11. Hemsch, M. and Morrison, J., "Statistical analysis of CFD solutions from 2nd Drag Prediction Workshop," AIAA Paper 2004-0556, 42nd AIAA Aerospace Sciences Meeting and Exhibit, Reno, NV, January 2004.
12. Pfeiffer, N., "Reflections on the Second Drag Prediction Workshop," AIAA Paper 2004-0557, 42nd AIAA Aerospace Sciences Meeting and Exhibit, Reno, NV, January 2004.
13. Brodersen, O. P., Rakowitz, M., Amant, S., Larrieu, P., Destarac, D., and Suttcliffe, M., "Airbus, ONERA and DLR Results from the Second AIAA Drag Prediction Workshop," *Journal of Aircraft*, 42(4):932–940, 2005. doi:10.2514/1.8662
14. Langtry, R. B., Kuntz, M., and Menter, F., "Drag Prediction of Engine-Airframe Interference Effects with CFX-5," *Journal of Aircraft*, 42(6):1523–1529, 2005. doi:10.2514/1.12728
15. Sclafani, J., DeHaan, M. A., and Vassberg, J. C., "OVERFLOW Drag Predictions for the DLR-F6 Transport Configuration: A DPW-II Case study," AIAA Paper 2004-0393, 42nd AIAA Aerospace Sciences Meeting and Exhibit, Reno, NV, January 2004.
16. Rumsey, C., Rivers, M., and Morrison, J., "Study of CFD Variations on Transport Configurations from the 2nd AIAA Drag Prediction Workshop," AIAA Paper 2004-0394, 42nd AIAA Aerospace Sciences Meeting and Exhibit, Reno, NV, January 2004.
17. Wutzler, K., "Aircraft Drag Prediction using Cobalt," AIAA Paper 2004-0395, 42nd AIAA Aerospace Sciences Meeting and Exhibit, Reno, NV, January 2004.
18. May, G., Van derWeide, E., Jameson, A., and Shankaran, S., "Drag Prediction of the DLR-F6 Configuration," AIAA Paper 2004-0396, 42nd AIAA Aerospace Sciences Meeting and Exhibit, Reno, NV, January 2004.
19. Kim, Y., Park, S., and Kwon, J., "Drag Prediction of DLR-F6 Using the Turbulent Navier-Stokes Calculations with Multigrid," AIAA Paper 2004-0397, 42nd AIAA Aerospace Sciences Meeting and Exhibit, Reno, NV, January 2004.
20. Yamamoto, K., Ochi, A., Shima, E., and Takaki, R., "CFD Sensitivity to Drag prediction on DLR-F6 Configuration by Structured Method and Unstructured Method," AIAA Paper 2004-0398, 42nd AIAA Aerospace Sciences Meeting and Exhibit, Reno, NV, January 2004.
21. Tinoco, E. and Su, T., "Drag Prediction with the Zeus/CFL3D System," AIAA Paper 2004-0552, 42nd AIAA Aerospace Sciences Meeting and Exhibit, Reno, NV, January 2004.

22. 3rd AIAA CFD Drag Prediction Workshop, San Francisco, CA, June 2006, http://aiaa-dpw.larc.nasa.gov/Workshop3/workshop3.html, accessed 4 September 2017.
23. Vassberg, J. C., Sclafani, A. J., and DeHaan, M. A., "A Wing-Body Fairing Design for the DLR-F6 Model: A DPW-III Case Study," AIAA Paper 2005-4730, AIAA 23rd Applied Aerodynamics Conference, Toronto, Canada, June 2005.
24. Vassberg, J. C., Tinoco, E. N., Mani, M., Brodersen, O. P., Eisfeld, B., Wahls, R. A., Morrison, J. H., Zickuhr, T., Laflin, K. R., and Mavriplis, D. J., "Abridged Summary of the Third AIAA CFD Drag Prediction Workshop," *Journal of Aircraft*, 45(3):781–798, May–June 2008. doi:10.2514/1.30572
25. Vassberg, J. C., Tinoco, E. N., Mani, M., Brodersen, O. P., Eisfeld, B., Wahls, R. A., Morrison, J. H., Zickuhr, T., Laflin, K. R., and Mavriplis, D. J., "Summary of DLR-F6 Wing-Body Data from the Third AIAA CFD Drag Prediction Workshop," RTO AVT-147 Paper 57, RTO-MP-AVT-147 Symposium on Computational Uncertainty in Military Vehicle Design, , Athens, Greece, December 2007. doi:10.14339/RTO-MP-AVT-147
26. Morrison, J. H. and Hemsch, M. J., "Statistical Analysis of CFD Solutions from the Third AIAA Drag Prediction Workshop," AIAA Paper 2007-0254, 45th AIAA Aerospace Sciences Meeting and Exhibit, Reno, NV, January 2007.
27. Tinoco, E. N., Winkler, C., Mani, M., and Venkatakrishnan, V., "Structured and Unstructured Solvers for the 3rd CFD Drag Prediction Workshop," AIAA Paper 2007-0255, 45th AIAA Aerospace Sciences Meeting and Exhibit, Reno, NV, January 2007.
28. Mavriplis, D. J., "Results from the 3rd Drag Prediction Workshop Using the NSU3D Unstructured Mesh Solver," AIAA Paper 2007-0256, 45th AIAA Aerospace Sciences Meeting and Exhibit, Reno, NV, January 2007.
29. Sclafani, A. J., Vassberg, J. C., Harrison, N. A., DeHaan, M. A., Rumsey, C. L., Rivers, S. M., and Morrison, J. H., "Drag Predictions for the DLR-F6 Wing/Body and DPW Wings Using CFL3D and OVERFLOW on an Overset Mesh," AIAA Paper 2007-0257, 45th AIAA Aerospace Sciences Meeting and Exhibit, Reno, NV, January 2007.
30. Brodersen, O., Eisfeld, B., Raddatz, J., and Frohnapfel, P., "DLR Results from the Third AIAA CFD Drag Prediction Workshop," AIAA Paper 2007-0259, 45th AIAA Aerospace Sciences Meeting and Exhibit, Reno, NV, January 2007.
31. Tinoco, E. N., Venkatakrishnan, V., Winkler, C., and Mani M., "Structured and Unstructured Solvers for the Third AIAA CFD Drag Prediction Workshop," *Journal of Aircraft*, 45(3):738–749, May–June 2008. doi:10.2514/1.30593
32. Mavriplis, D. J., "Third Drag Prediction Workshop Results Using NSU3D Unstructured Mesh Solver," *Journal of Aircraft*, 45(3):750–761, May–June 2008. doi:10.2514/1.29828
33. Sclafani, A. J., Vassberg, J. C., Harrison, N. A., Rumsey, C. L., Rivers, S. M., and Morrison, J. H., "CFL3D / OVERFLOW Results for DLR-F6 Wing/Body and Drag Prediction Workshop Wing," *Journal of Aircraft*, 45(3):762–780, May–June 2008. doi:10.2514/1.30571
34. Murayama, M. and Yamamoto, K., "Comparison Study of Drag Prediction by Structured and Unstructured Mesh Method," *Journal of Aircraft*, 45(3):799–822, May–June 2008. doi:10.2514/1.31072
35. Brodersen, O., Eisfeld, B., Raddatz, J., and Frohnapfel, P., "DLR results from the third AIAA Computational Fluid Dynamics Drag Prediction Workshop," *Journal of Aircraft*, 45(3):823–836, May–June 2008. doi:10.2514/1.30628
36. Eliasson, P. and Peng, S.-H., "Drag Prediction for the DLR-F6 Wing-Body Configuration Using the Edge Solver," *Journal of Aircraft*, 45(3):837–847, May–June 2008. doi:10.2514/1.31252
37. Mavriplis, D. J., Vassberg, J. C., Tinoco, E. N., Mani, M., Brodersen, O. P., Eisfeld, B., Wahls, R. H., Morrison, J., Zickuhr, T., Levy, D., and Murayama, M., "Grid quality and Resolution Issues from the Drag Prediction Workshop Series," *Journal of Aircraft*, 46(3):935–950, 2009. doi:10.2514/1.39201
38. 4thAIAA CFD Drag Prediction Workshop, San Antonio, TX, June 2009, http://aiaa-dpw.larc.nasa.gov/Workshop4/workshop4.html, accessed 4 September 2017.
39. Vassberg, J. C., DeHaan, M. A., Rivers, S. M., and Wahls, R. A., "Development of a Common Research Model for Applied CFD Validation Studies," AIAA Paper 2008-6919, 26th AIAA Applied Aerodynamics Conference, Hawaii, HI, August 2008.
40. Vassberg, J., Tinoco, E., Mani, M., Rider, B., Zickuhr, T., Levy, D., Broderson, O., Eisfeld, B., Crippa, S., Wahls, R., Morrison, J., Mavriplis, D., Murayama, M., "Summary of the Fourth AIAA CFD Drag

Prediction Workshop," AIAA 2010-4547, 28th AIAA Applied Aerodynamics Conference, Chicago, IL, June 2010.
41. Morrison, J., "Statistical Analysis of CFD Solutions from the Fourth Drag Prediction Workshop," *Journal of Aircraft*, 2014, 51:4, 1070-1089. doi:10.2514/1.C032418
42. Sclafani, A. J., Vassberg, J. C., Rumsey, C., DeHaan, M. A., and Pulliam, T. H., "Drag Prediction for the NASA CRM Wing/Body/Tail Using CFL3D and OVERFLOW on an Overset Mesh," *Journal of Aircraft*, 2014, 51:4, 1101-1117. doi:10.2514/1.C032571
43. Hue, D., Gazaix, M., and Esquieu, S., "Computational Drag and Moment Prediction of the DPW4 Configuration with elsA," AIAA Paper 2010-4220, 28th AIAA Applied Aerodynamics Conference, Chicago, IL, June 2010.
44. Mani, M., Rider, B. J., Sclafani, A. J., Winkler, C., Vassberg, J. C., Dorgan, A. J., Cary, A., and Tinoco, E. N., "RANS Technology for Transonic Drag Prediction; a Boeing Perspective of the 4th Drag Prediction Workshop," *Journal of Aircraft*, 2014, 51:4, 1118-1134. doi:10.2514/1.C032717
45. Yamamoto, K., Tanaka, K., and Murayama, M., "Comparison Study of Drag Prediction for the 4th CFD Drag Prediction Workshop Using Structured and Unstructured Mesh Methods," AIAA Paper 2010-4222, 28th AIAA Applied Aerodynamics Conference, Chicago, IL, June 2010.
46. Brodersen, O., Crippa, S., Eisfeld, B., Keye, S., and Geisbauer, S., "DLR Results for the Fourth AIAA CFD Drag Prediction Workshop," *Journal of Aircraft,* 2014, 51:4, 1135-1148. doi:10.2514/1.C031533
47. Eliasson, P., Peng, S., and Tysell, L., "Computations from the 4th Drag Prediction Workshop Using the Edge Solver," AIAA Paper 2010-4548, 28th AIAA Applied Aerodynamics Conference, Chicago, IL, June 2010.
48. Li, G. and Zhou, Z., "Validation of a Multigrid-Based Navier-Stokes Solver for Transonic Flows," AIAA Paper 2010-4549, 28th AIAA Applied Aerodynamics Conference, Chicago, IL, June 2010.
49. Mavriplis, D. J. and Long, M., "NSU3D Results for the Fourth AIAA Drag Prediction Workshop," *Journal of Aircraft*, 2014, 51:4, 1161-1171. doi:10.2514/1.C032556
50. Lee-Rausch, E., Hammond, E., Nielsen, E., Pirzadeh, S., and Rumsey C., "Application of the FUN3D Unstructured-Grid Navier-Stokes Solver to the 4th AIAA Drag Prediction Workshop Cases," *Journal of Aircraft*, 2014, 51:4, 1149-1160. doi:10.2514/1.C032558
51. Vos, J., Sanchi, S., Gehri, A., and Stephani, P., "DPW4 Results Using Different Grids, Including Near-Field/Far-Field Drag Analysis," AIAA Paper 2010-4552, 28th AIAA Applied Aerodynamics Conference, Chicago, IL, June 2010.
52. Hashimoto, A., Lahur, P., Murakami, K., and Aoyama, T., "Validation of Fully Automatic Grid Generation Method on Aircraft Drag Prediction," AIAA Paper 2010-4669, 28th AIAA Applied Aerodynamics Conference, Chicago, IL, June 2010.
53. Hashimoto, Atsushi, Keiichi Murakami, Takashi Aoyama, Kazuomi Yamamoto, Mitsuhiro Murayama, and Paulus R. Lahur, "Drag Prediction on NASA Common Research Model Using Automatic Hexahedra Grid-Generation Method," *Journal of Aircraft*, 2014, 51:4, 1172-1182 doi:10.2514/1.C032641
54. Temmerman, L. and Hirsch, C., "Simulations of the CRM Configuration on Unstructured Hexahedral Grids: Lessons Learned from the DPW-4 Workshop," AIAA Paper 2010-4670, 28th AIAA Applied Aerodynamics Conference, Chicago, IL, June 2010.
55. Chaffin, M. and Levy, D., "Comparison of Viscous Grid Layer Growth Rate of Unstructured Grids on CFD Drag Prediction Workshop Results," AIAA Paper 2010-4671, 28th AIAA Applied Aerodynamics Conference, Chicago, IL, June 2010.
56. Crippa, S., "Application of Novel Hybrid Mesh Generation Methodologies for Improved Unstructured CFD Simulations," AIAA Paper 2010-4672, 28th AIAA Applied Aerodynamics Conference, Chicago, IL, June 2010.
57. 5th AIAA CFD Drag Prediction Workshop, http://aiaa-dpw.larc.nasa.gov/Workshop5/workshop5.html, accessed 4 September 2017.
58. Vassberg, J. C., "A Unified Baseline Grid about the Common Research Model Wing-Body for the Fifth AIAA CFD Drag Prediction Workshop," AIAA Paper 2011-3508, 29th AIAA Applied Aerodynamics Conference, Honolulu, HI, June 2011.
59. Rumsey, C., "Langley Research Center Turbulence Modeling Resource," http://turbmodels.larc.nasa.gov/, accessed 4 September 2017.
60. Levy, D. W., Laflin, K. R., Tinoco, E. N., Vassberg, J. C., Mani, M., Rider, B., Rumsey, C. L., Wahls, R. A., Morrison, J. H., Brodersen, O. P., Crippa, S., Mavriplis, D. J., and Murayama, M., "Summary of Data

from the Fifth Computational Fluid Dynamics Drag Prediction Workshop," *Journal of Aircraft*, 2014, 51:4, 1194-1213 doi:10.2514/1.C032389
61. Morrison, J. H., "Statistical Analysis of the Fifth Drag Prediction Workshop Computational Fluid Dynamics Solutions," *Journal of Aircraft,* 2014, 51:4, 1214-1222 doi:10.2514/1.C032736
62. Sclafani, A. J., Vassberg, J. C., Winkler, C., Dorgan, A. J., Mani, M., Olsen, M. E., and Coder, J. G., "Analysis of the Common Research Model Using Structured and Unstructured Meshes," *Journal of Aircraft,* 2014, 51:4, 1223-1243 doi:10.2514/1.C032411
63. Murayama, M., Yamamoto, K., Hashimoto, A., Ishida, T., Ueno, M., Tanaka, K., and Ito, Y., "Japan Aerospace Exploration Agency Studies for the Fifth AIAA Drag Prediction Workshop," *Journal of Aircraft,* 2014, 51:4, 1244-1267 doi:10.2514/1.C032647
64. Park, M. A., Laflin, K. R., Chaffin, M. S., Powell, N., and Levy, D. W., "CFL3D, FUN3D, and NSU3D Contributions to the Fifth Drag Prediction Workshop," *Journal of Aircraft,* 2014, 51:4, 1268-1283 doi:10.2514/1.C032613
65. Ceze, M. and Fidkowski, K. J., "Drag Prediction Using Adaptive Discontinuous Finite Elements," *Journal of Aircraft,* 2014, 51:4, 1284-1294 doi:10.2514/1.C032622
66. Hue, D., "Fifth Drag Prediction Workshop: Computational Fluid Dynamics Studies Carried Out at ONERA," *Journal of Aircraft,* 2014, 51:4, 1295-1310 doi:10.2514/1.C032054
67. Hue, D., "Fifth Drag Prediction Workshop: ONERA Investigations with Experimental Wing Twist and Laminarity," *Journal of Aircraft,* 2014 51:4, 1311-1322 doi:10.2514/1.C032438
68. Keye, S., Brodersen, O., and Rivers, M. B., "Investigation of Aeroelastic Effects on the NASA Common Research Model," *Journal of Aircraft,* 2014, 51:4, 1323-1330, doi:10.2514/1.C032598
69. Eberhardt, S., Benedict, K., Hedges, L., Robinson, A., and Tinoco, E. N.,"Inclusion of Aeroelastic Twist into the CFD Analysis of the Twin-Engine NASA Common Research Model," AIAA Paper 2014-0251, National Harbor, MD, January 2014.
70. Togiti, V., Eisfeld, B., and Brodersen, O., "Turbulence Model Study for the Flow Around the NASA Common Research Model," *Journal of Aircraft,* 2014, 51:4, 1331-1343 doi:10.2514/1.C032609
71. Special Section: Drag Prediction Workshops IV and V, *Journal of Aircraft*, Volume 51, Number 4, July-August 2014.
72. 6th AIAA CFD Drag Prediction Workshop, Washington DC, June 2016, http://aiaa-dpw.larc.nasa.gov, accessed 4 September 2017.
73. Roy, C. J., Rumsey, C., and Tinoco, E. N., "Summary of Data from the Sixth AIAA CFD Drag Prediction Workshop: Case 1 Code Verification," AIAA Paper 2017-1206, 55th AIAA Aerospace Sciences Meeting, AIAA Science and Technology Forum and Exposition 2017, Grapevine, TX, January 2017, also *Journal of Aircraft*, 55:4, 1338-1351 doi:10.2514/1.c034856, July-August 2018.
74. Tinoco, Edward N., Brodersen, Olaf P., Keye, Stefan, Laflin, Kelly R., Feltrop, Edward, Wahls, Richard A., Morrison, Joseph H., Vassberg, John C., Mani, Mori, Rider, Ben, Hue, David, Roy, Christopher J., Mavriplis, Dimitri J., and Murayama, Mitsuhiro, "Summary of Data from the Sixth AIAA CFD Drag Prediction Workshop: CRM Cases 2 to 5" AIAA Paper 2017-1208, 55th AIAA Aerospace Sciences Meeting, AIAA Science and Technology Forum and Exposition 2017, Grapevine, TX, January 2017, also *Journal of Aircraft*, 55:4, 1352-1379 doi:10.2514/1.c034409, July-August 2018.
75. Derlaga, J. M. and Morrison, J. H., "Statistical Analysis of CFD Solutions from the Sixth AIAA Drag Prediction Workshop," AIAA-2017-1209, 55th AIAA Aerospace Sciences Meeting, AIAA Science and Technology Forum and Exposition 2017, Grapevine, TX, January 2017, also *Journal of Aircraft*, 55:4, 1388-1400 doi:10.2514/1.c034938, July-August 2018.
76. Keye, S. and Mavriplis, D., "Summary of Data from the Sixth AIAA CFD Drag Prediction Workshop: Case 5 (Coupled Aero-StructuralSimulation)," AIAA Paper 2017-1207, 55th AIAA Aerospace Sciences Meeting, AIAA Science and Technology Forum and Exposition 2017, Grapevine, TX, January 2017, also *Journal of Aircraft*, 55:4, 1380-1379 doi:10.2514/1.c034427, July-August 2018.
77. Special Section: Drag Prediction Workshop VI, *Journal of Aircraft*, Volume 55, Number 4, July-August 2018.
78. Keye, S. and Gammon, M. R., "Development of Deformed CAD Geometries of NASA's Common Research Model for the 6th AIAA CFD Drag Prediction Workshop," AIAA Paper 2016-3431, 34th AIAA Applied Aerodynamics Conference, June 2016, also *Journal of Aircraft*, 55:4, 1401-1405 doi:10.2514/1.c034428, July-August 2018.
79. Rivers, M. and Dittberner, A., "Experimental Investigations of the NASA Common Research Model," AIAA Paper 2010-4218, 28th AIAA Applied Aerodynamics Conference, Chicago, IL, June 2010.

80. Rivers, M. and Dittberner, A., "Experimental Investigations of the NASA Common Research Model in the NASA Langley National Transonic Facility and NASA Ames 11-Ft Transonic Wind Tunnel (Invited)," AIAA Paper 2011-1126, presented at the 49th Aerospace Sciences Meeting, Orlando, FL, Jan 2011.
81. Common Research Model, http://commonresearchmodel.larc.nasa.gov/, accessed 4 September 2017.
82. European Commission (EU), "European Strategic Wind Tunnels Improved Research Potential," http://www.eswirp.aero/, accessed 4 September 2017.
83. ETW CRM wind tunnel test data, http://www.eswirp.eu/ETW-TNA-Dissemination.html, accessed 4 September 2017.
84. Cartieri A., Hue D., and Chanzy Q, "Experimental Investigations on the Common Research Model at ONERA-S1 – Comparison with DPW Numerical Results," AIAA Paper 2017-0964, 55th AIAA Aerospace Sciences Meeting, AIAA Science and Technology Forum and Exposition 2017, Grapevine, TX, January 2017, also *Journal of Aircraft*, to be published.
85. Ueno, M., Kohzai, T., and Koga, S., "Transonic Wind Tunnel Test of the NASA CRM (Volume 1)," JAXA-RM-13-01E, March 2013.
86. Rivers, M. and Hunter, C., "Support System Effects on the NASA Common Research Model," AIAA Paper 2012-707, January 2012.
87. Rivers, M., Hunter, C., and Campbell, R., "Further Investigation of the Support System Effects and Wing Twist on the NASA Common Research Model," AIAA Paper 2012-3209, June 2012.
88. Martineau, D., Stokes, S., Munday, S., Jackson, A., Gribben, B., and Verhoeven, N., "Anisotropic Hybrid Mesh Generation for Industrial RANS Applications," AIAA Paper 2006-0534, Jan. 2006.
89. König, B., and Fares, E., "Validation of a Transonic Lattice-Boltzmann Method on the NASA Common Research Model," AIAA 2016-2023, January 2016.
90. Venkatakrishnan, V., Allmaras, S.R., Kamenetskii, D., and Johnson, F.T., "Higher Order Schemes for the Compressible Navier-Stokes Equations," AIAA Paper 2003-3987, 16th AIAA Computational Fluid Dynamics Conference, June 23–26, 2003, Orlando, FL.
91. Glasby, R. S., Erwin, J. T., Stefanski, D. L., Allmaras, S. R., Galbraith, M. C., Anderson, W. K., and Nichols, R. H., "Introduction to COFFE: The Next-Generation HPCMP CREATETM-AV CFD Solver," AIAA Paper 2016-0567, 54th AIAA Aerospace Sciences Meeting, AIAA SciTech, January 2016.
92. Kutney, John T. and Piszkin, Stanley P., "Reduction of Drag Rise on the Convair 990 Airplane," *Journal of Aircraft, Vol 1. No. 1, 1964*.
93. Elsenaar, A, Binion, T.W. Jr., and Stanewsky, E. "Reynolds Number Effects in Transonic Flow," AGARDograph No. 303, December 1988.
94. Curtin, M.M, Bogue, D.R., Om D., Rivers, S.M.B., Pendergraft, O.C., and Wahls, R. A., "Investigation of Transonic Reynolds Number Scaling on a Twin-Engine Transport (Invited)," AIAA-2002-0420, January 2002.
95. Spalart, P.R., "Strategies for turbulence modelling and simulations," International Journal of Heat and Fluid Flow Vol. 21 (2000) pp.252-263.
96. Yamamoto, K., Tanaka, K, and Murayama, M., "Effect of a Nonlinear Constitutive Relation for Turbulence Modeling on Predicting Flow Separation at Wing-Body Juncture of Transonic Commercial Aircraft," AIAA-2012-2895, June 2012.
97. Diskin, B., Thomas, J., Rumsey, C., and Schwoppe, A., "Grid Convergence for Turbulent Flows," 53rd AIAA Aerospace Sciences Meeting, AIAA 2015-1746, Jan 2015.
98. Loseille, A., Dervieux, A., and Alauzet, F., "Fully Anisotropic Goal-Oriented Mesh Adaptation for 3D Steady Euler Equations," *Journal of Computational Physics, Vol. 229, No. 8. 2010, pp 2866-2897*.
99. Park, MN. A. and Darmofal, D. L., "Parallel Anisotropic Tetrahedral Adaptation," AIAA Paper 2008-917, 2008.
100. Michael, T., and Krakos, J., "Anisotropic Mesh Adaptation Through Edge Primitive Operations," AIAA Paper 2012-159, January 2012.
101. Buning, P. G. and Pulliam, T. H., "Near-Body Grid Adaption for Overset Grids," 46th AIAA Fluid Dynamics Conference, AIAA Paper 2016-3326, Washington, DC, June 2016.
102. Dmitry S. Kamenetskiy, John E. Bussoletti, Craig L. Hilmes, Venkat Venkatakrishnan, Laurence B. Wigton, Numerical Evidence of Multiple Solutions for the Reynolds-Averaged Navier–Stokes Equations, *AIAA Journal Vol. 52, No. 8 (2014), pp. 1686-1698*.

103. James G. Coder, James G., David Hue, Gaetan Kenway, Thomas H. Pulliam, and Anthony J. Sclafani, " Contributions to the 6th AIAA CFD Drag Prediction Workshop Using Structured, Overset Grid Methods" AIAA-2017-0960, January 2017.
104. Michal, Todd, Deric Babcock, Dmitry Kamenetskiy, Joshua Krakos, Mortaza Mani, Ryan Glasby, Taylor Erwin, and Douglas L. Stefanski, "Comparison of Fixed and Adaptive Unstructured Grid Results for Drag Prediction Workshop 6," AIAA-2017-0961, January 2017.
105. Keye, S. and Mavriplis, D., "Summary of Data from the Sixth AIAA CFD Drag Prediction Workshop: Case 5 (Coupled Aero-Structural Simulation)," AIAA Paper 2017-1207, 55th AIAA Aerospace Sciences Meeting, AIAA Science and Technology Forum and Exposition 2017, Grapevine, TX, January 2017, also *Journal of Aircraft*, to be published.
106. Glasby, Ryan S., Erwin, J. Taylor, Stefanski, Douglass L., Allmaras, Steven R., Galbraith, Marshall C., Anderson, W. Kyle, and Nichols, Robert H., "Introduction to COFFE: The Next-Generation HPCMP CREATETM- AV CFD Solver," AIAA-2016-0567, AIAA SciTech 2016.
107. Dmitry S. Kamenetskiy, John E. Bussoletti, Craig L. Hilmes, Venkat Venkatakrishnan, Laurence B. Wigton, Numerical Evidence of Multiple Solutions for the Reynolds-Averaged Navier–Stokes Equations, *AIAA Journal Vol. 52, No. 8 (2014), pp. 1686-1698.*
108. Fares, E., Wessels, M., Li, Y., Gopalakrishnan, P., Zhang, R., Sun, C., Gopalaswamy, N., Roberts, P., Hoch, J., and Chen, H., "Validation of a Lattice-Boltzmann Approach for Transonic and Supersonic Flow Simulations," *52nd Aerospace Sciences Meeting*, 2014, AIAA 2014-0952.
109. Ribeiro, A. F. P., Singh, D., König, B., Fares, E., Zhang, R., Gopalakrishnan, P., Li, Y., and Chen, H., "Buffet Simulations with a Lattice-Boltzmann based Transonic Solver," *AIAA SciTech 2017*, AIAA 2017-1438, January 2017.
110. König, B., Fares, E., Murayama, M., Ito, Y., Yokokawa, Y., Yamamoto, K., and Ishikawa, K., "Lattice-Boltzmann Simulations of the JAXA JSM High-Lift Configuration," *34th AIAA Applied Aerodynamics Conference*, 2016, AIAA 2016-3721, January 2016.
111. König, B., Ribeiro, A., and Fares, E., "Exa PowerFLOW Simulations for the Sixth AIAA Drag Prediction Workshop," *55Aerospace Sciences Meeting*, AIAA 2017-0963, January 2017.
112. Mejia, Kevin, Jeffrey D. Crouch, Kazu Kusunose, Robin Melvin, Vladimir S. Kosorygin, and Alexander D. Kosinov, "A Hybrid Methodology to Evaluate the Effects of Trip Disks on Transonic Wind Tunnel Models," AIAA-2004-2613, June 2004.
113. Rumsey, Christopher L. and Morrison, Joseph H., "Goals and Status of the NASA Juncture Flow Experiment," AVT-246 Progress and Challenges in Validation Testing for Computational Fluid Dynamics Avila, Spain 26-28 September 2016.
114. Vassberg, John C., "Challenges and Accomplishments of the AIAA CFD Drag Prediction Workshop Series," AVT-246 Progress and Challenges in Validation Testing for Computational Fluid Dynamics Avila, Spain 26-28 September 2016.
115. Slotnick, Jeffrey, Khodadodoust, Abdollah, Alonso, Juan, Gropp, William, Lurie, Elizabeth, and Mavriplis, Dimitri, "CFD Vision 2030 Study: A Path to Revolutionary Computational Aerosciences," NASA/CR-2014-218178, March 2014.
116. Tinoco, E.N., "Validation and Minimizing CFD Uncertainty for Commercial Aircraft Applications," AIAA-2008-6902, August 2008, also see RTO AVT-147 Paper 20, RTO-MP-AVT-147 Symposium on Computational Uncertainty in Military Vehicle Design, Athens, Greece, December 2007.

Appendix A. Enhanced Experimental Pressure Distributions

Limitations in the total number of pressure taps that can be built into the wind tunnel model and subsequent plugged and/or "slow" taps may result in inadequate definition of the experimental pressure distributions at the various span stations. This is particularly the case in defining the wing shock location in transonic flow and adequately defining the aft loading near the wing trailing edge. For attached flow conditions, there is very little change in the pressures near the wing trailing edge with angle-of-attack changes. In order to calculate section lift and moment characteristics, it was necessary to get a complete distribution from the trailing edge around the section cut back to the trailing edge. This was accomplished by "enhancing" the experimental pressure distributions as necessary. The "enhancement" to the pressures near the wing trailing edge was based on a combination of interpolation/extrapolation guided by experience with test data and CFD. At three midspan stations, missing or very "slow" taps required a further "enhancement." These "enhanced pressures" were based on pressure measurements from the JAXA 80 percent CRM model, which did not suffer the same pressure tap manufacturing deficiencies found in the original model. A complete set of the enhanced pressure distributions for all nine spanwise stations and covering the specified DPW conditions of C_L = 0.50, AoA = 2.75°, 3.00°, 3.25°, 3.50°, 3.75°, 4.00°, (Experimentl AoA = –3.00° to 6.64°) follows. The original pressure data are shown by the open symbols, the enhanced distributions, which include the original data points, are shown by the solid symbols.

Eta = 0.131, WBL = 151.074
Eta = 0.201, WBL = 232.444
Eta = 0.283, WBL = 327.074
Eta = 0.397, WBL = 549.370
Eta = 0.502, WBL = 581.148
Eta = 0.603, WBL = 697.333
Eta = 0.727, WBL = 840.704
Eta = 0.846, WBL = 978.148
Eta = 0.950, WBL = 1098.926

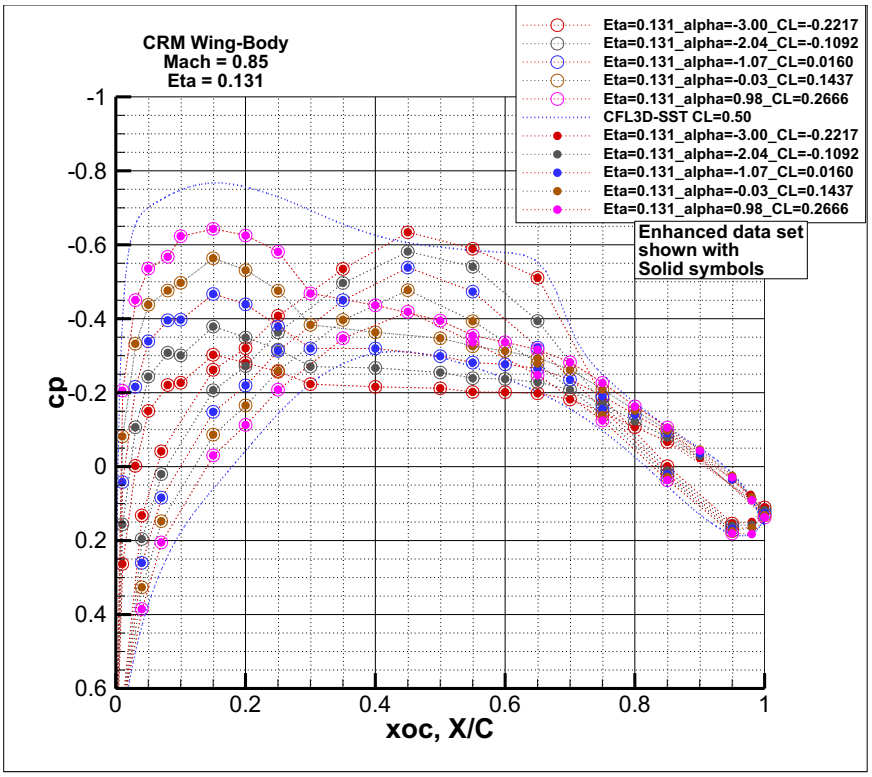


Figure A-A-1.Wing Pressure Distribution, Eta = 0.131, M = 0.85, AoA = –3.00° to 0.98°.

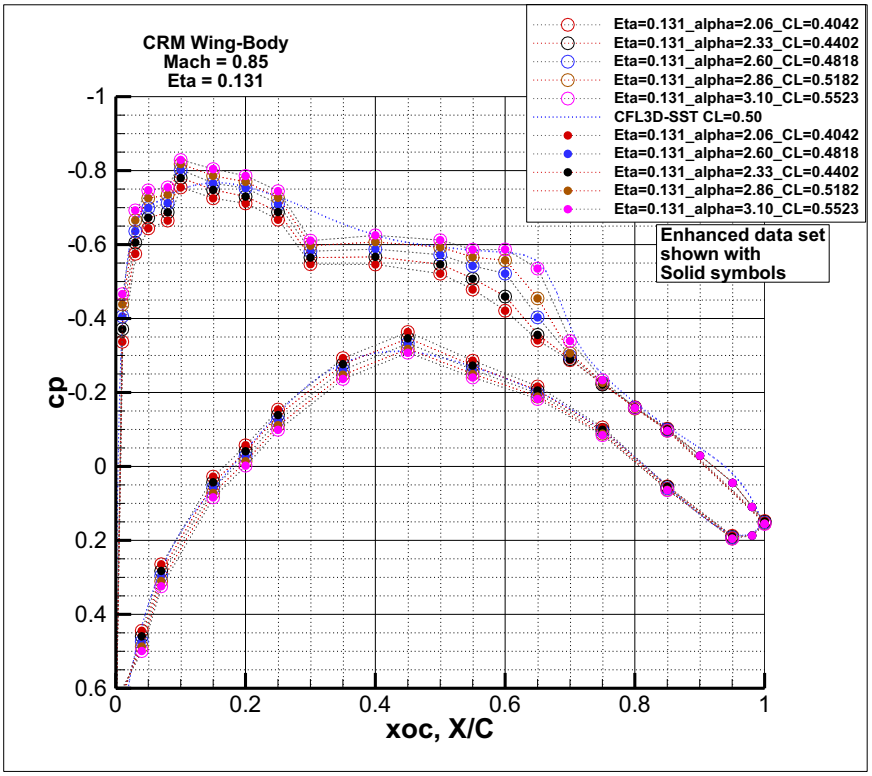


Figure A-A-2. Wing Pressure Distribution, Eta = 0.131, M = 0.85, AoA = 2.06° to 3.10°.

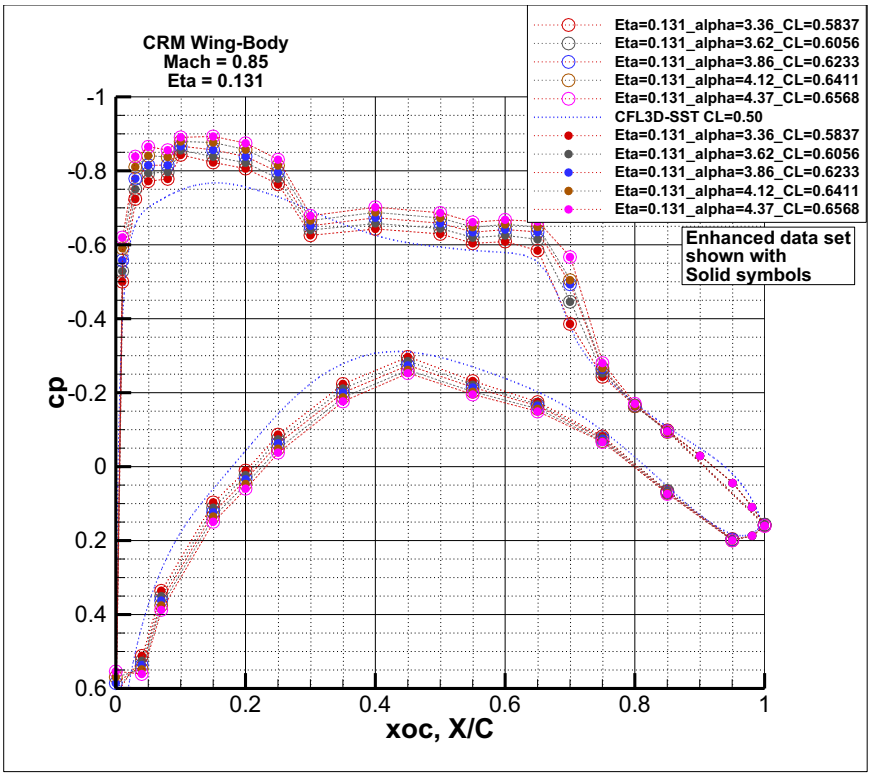


Figure A-A-3. Wing Pressure Distribution, Eta = 0.131, M = 0.85, AoA = 3.36° to 4.37°.

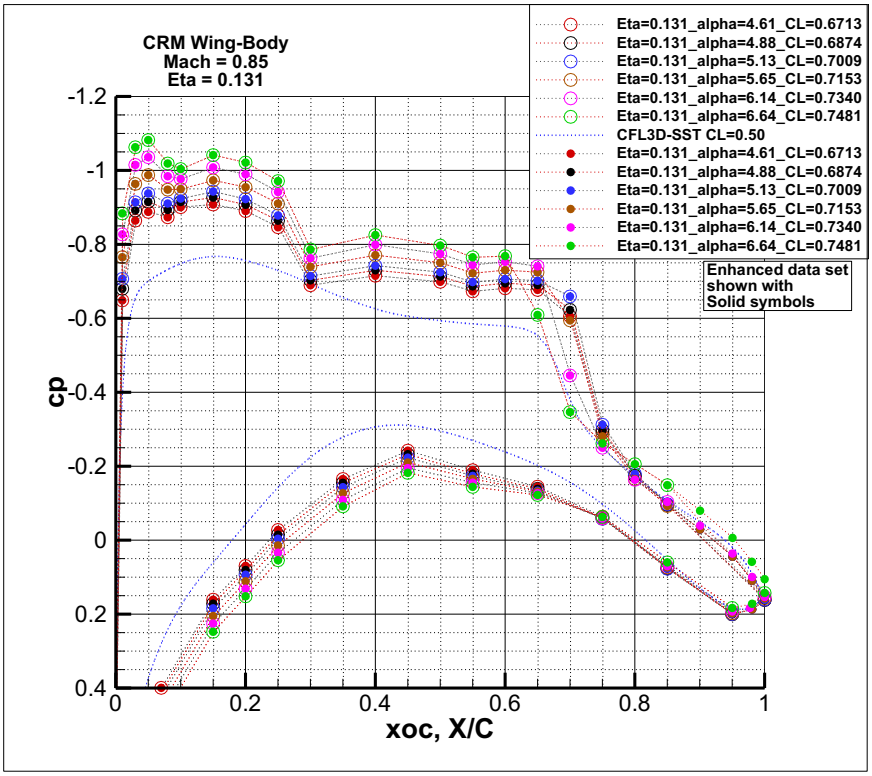


Figure A-A-4. Wing Pressure Distribution, Eta = 0.131, M = 0.85, AoA = 4.61° to 6.64°.

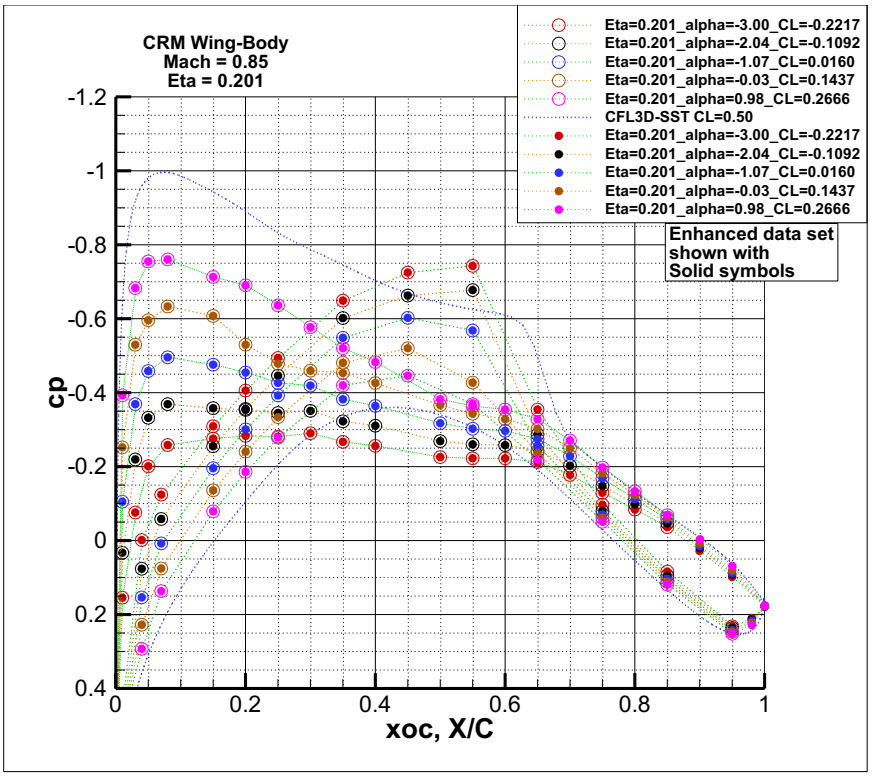


Figure A-A-5. Wing Pressure Distribution, Eta = 0.201, M = 0.85, AoA = –3.00° to 0.98°.

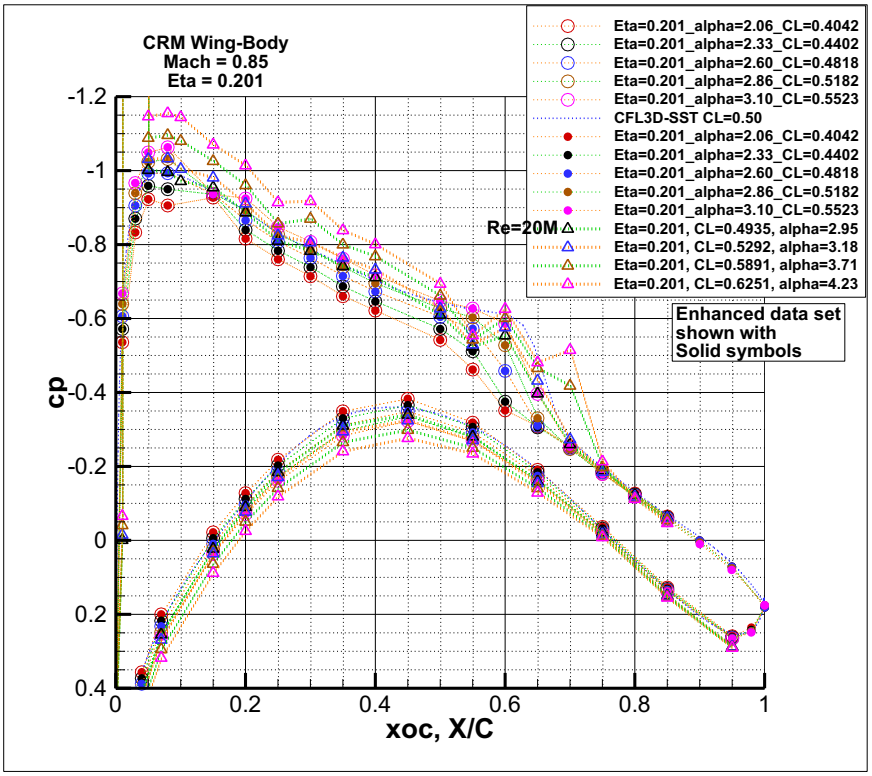


Figure A-A-6. Wing Pressure Distribution, Eta = 0.201, M = 0.85, AoA = 2.06° to 3.10°.

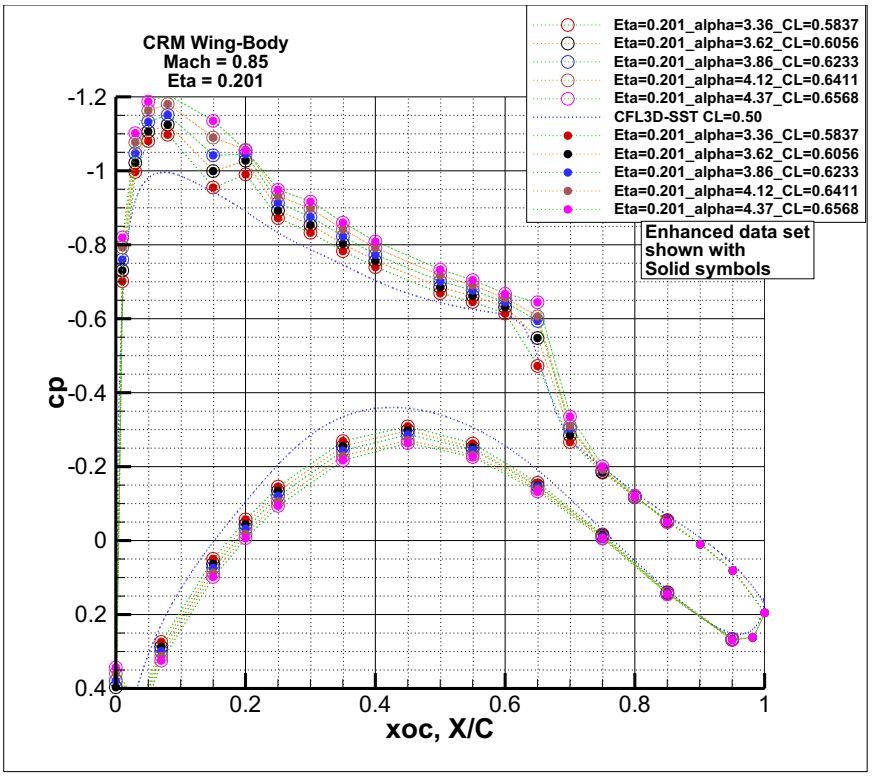


Figure A-A-7. Wing Pressure Distribution, Eta = 0.201, M = 0.85, AoA = 3.36° to 4.37°.

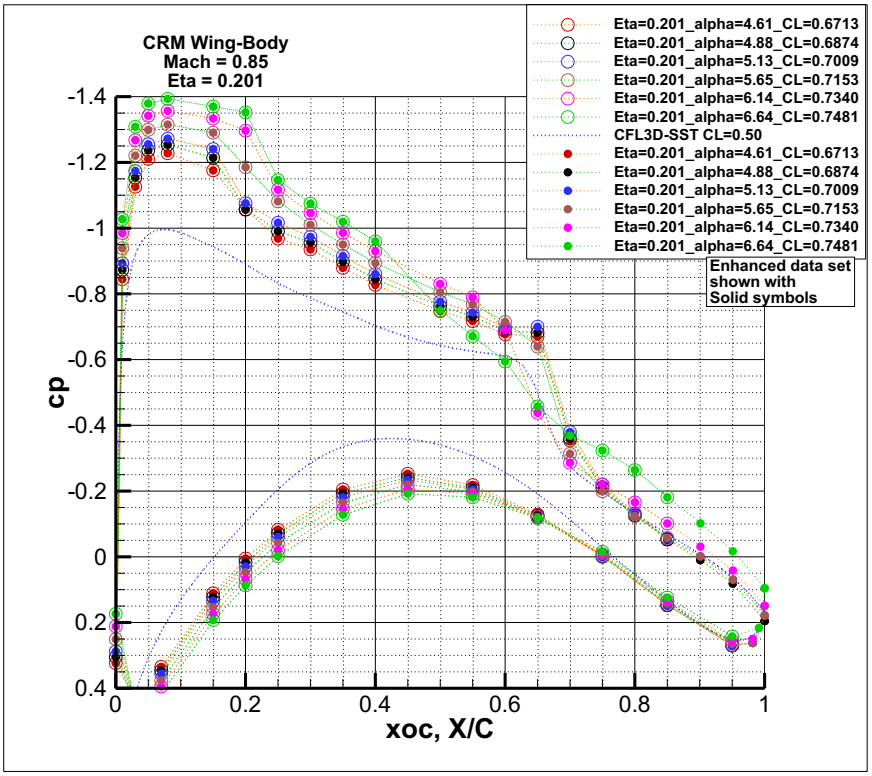


Figure A-A-8. Wing Pressure Distribution, Eta = 0.201, M = 0.85, AoA = 4.61° to 6.64°.

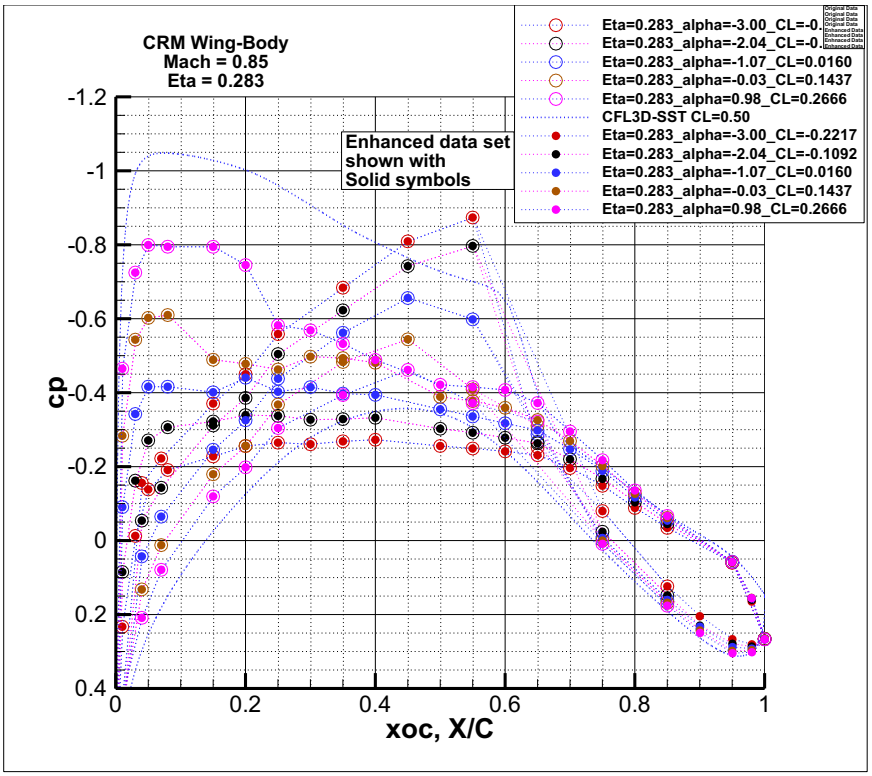


Figure A-A-9. Wing Pressure Distribution, Eta = 0.283, M = 0.85, AoA = –3.00° to 0.98°.

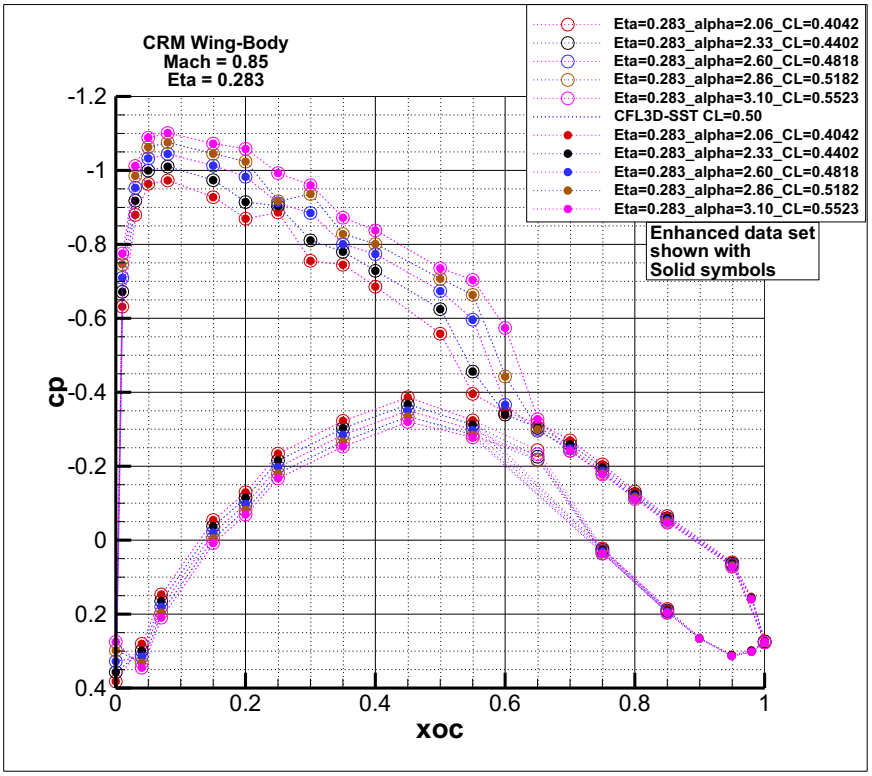


Figure A-A-10. Wing Pressure Distribution, Eta = 0.283, M = 0.85, AoA = 2.06° to 3.10°.

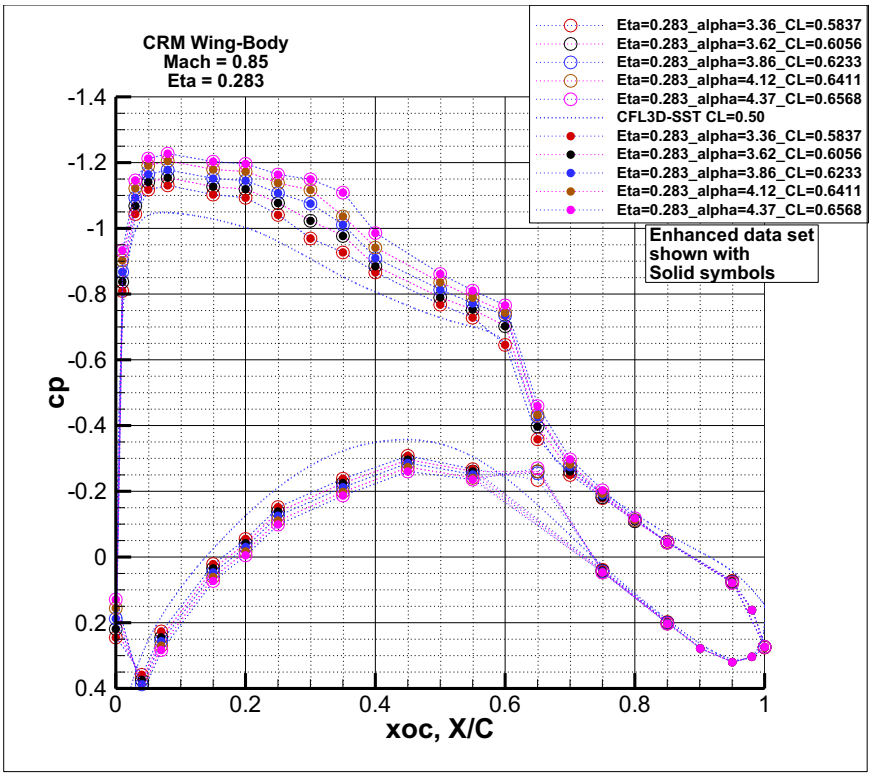


Figure A-A-11. Wing Pressure Distribution, Eta = 0.283, M = 0.85, AoA = 3.36° to 4.37°.

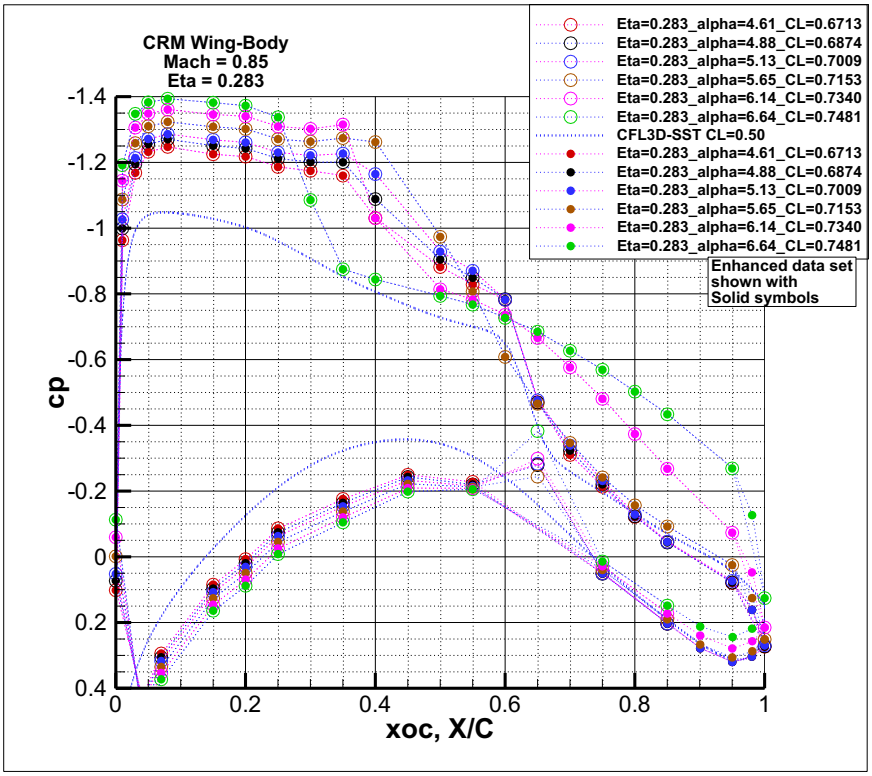


Figure A-A-12. Wing Pressure Distribution, Eta = 0.283, M = 0.85, AoA = 4.61° to 6.64°.

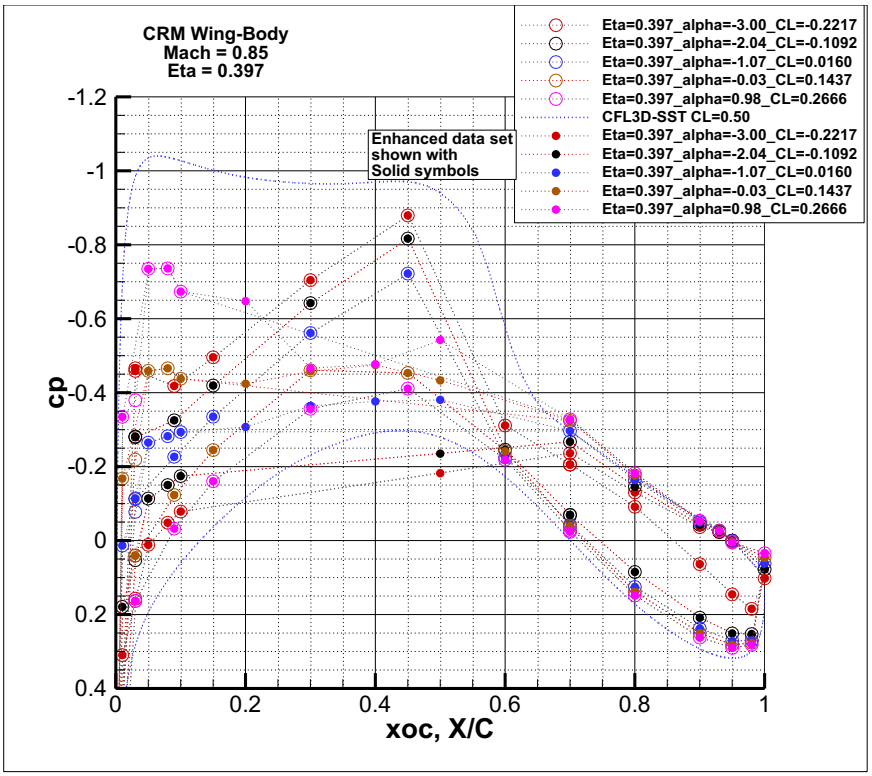


Figure A-A-13 Wing Pressure Distribution, Eta = 0.397, M = 0.85, AoA = –3.00° to 0.98°.

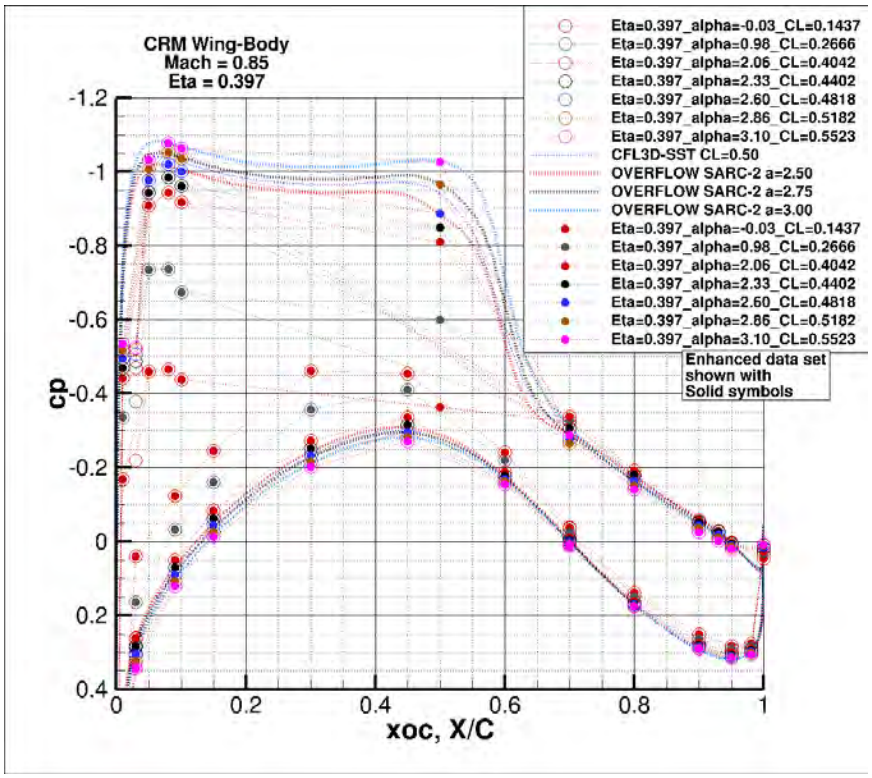


Figure A-A-14. Wing Pressure Distribution, Eta = 0. 397, M = 0.85, AoA = 2.06° to 3.10°.

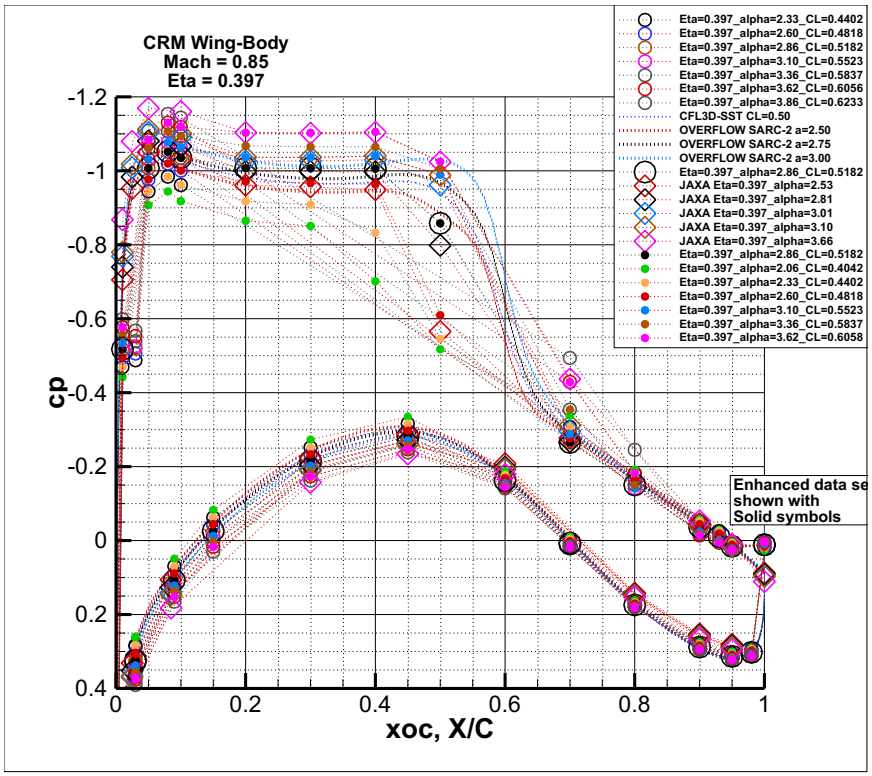


Figure A-A-15. Wing Pressure Distribution, Eta = 0. 397, M = 0.85, AoA = 3.36° to 4.37°.

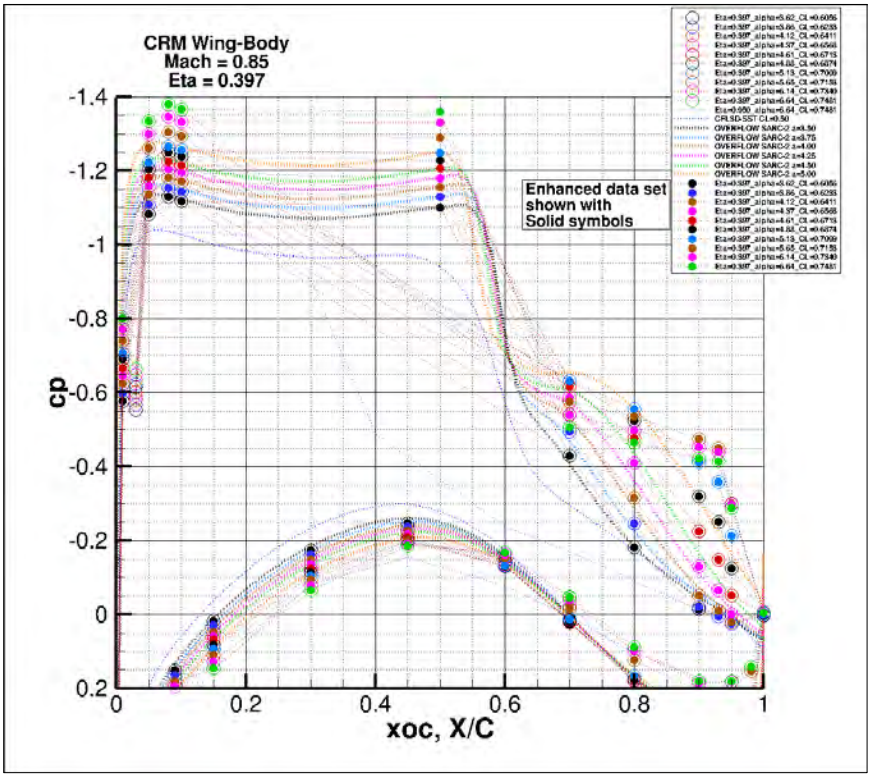


Figure A-A-16. Wing Pressure Distribution, Eta = 0. 397, M = 0.85, AoA = 4.61° to 6.64°.

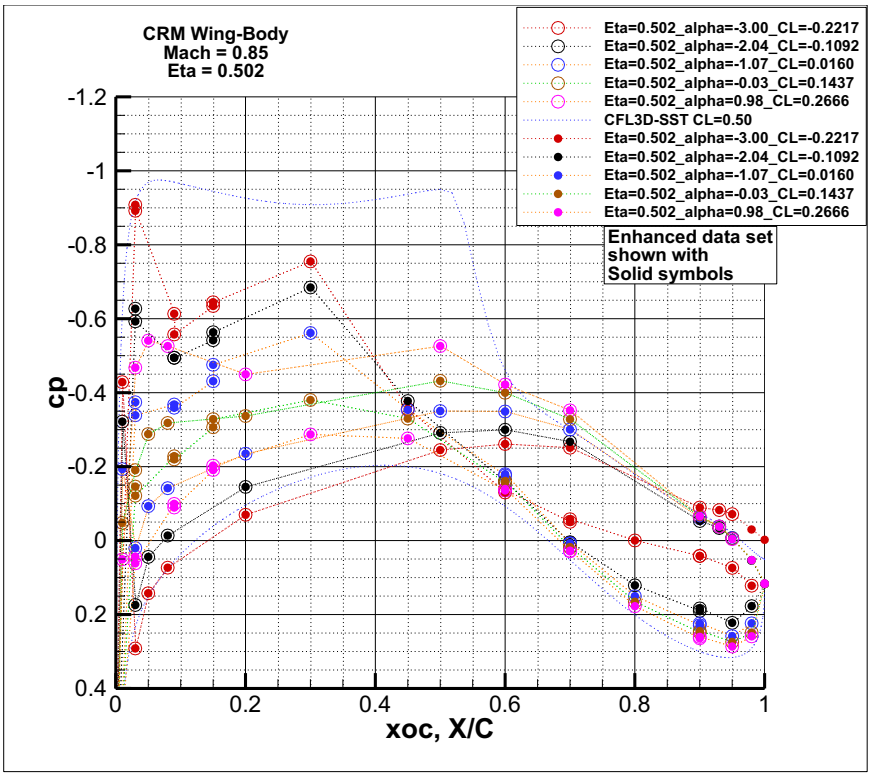


Figure A-A-17. Wing Pressure Distribution, Eta = 0.502, M = 0.85, AoA = –3.00° to 0.98°.

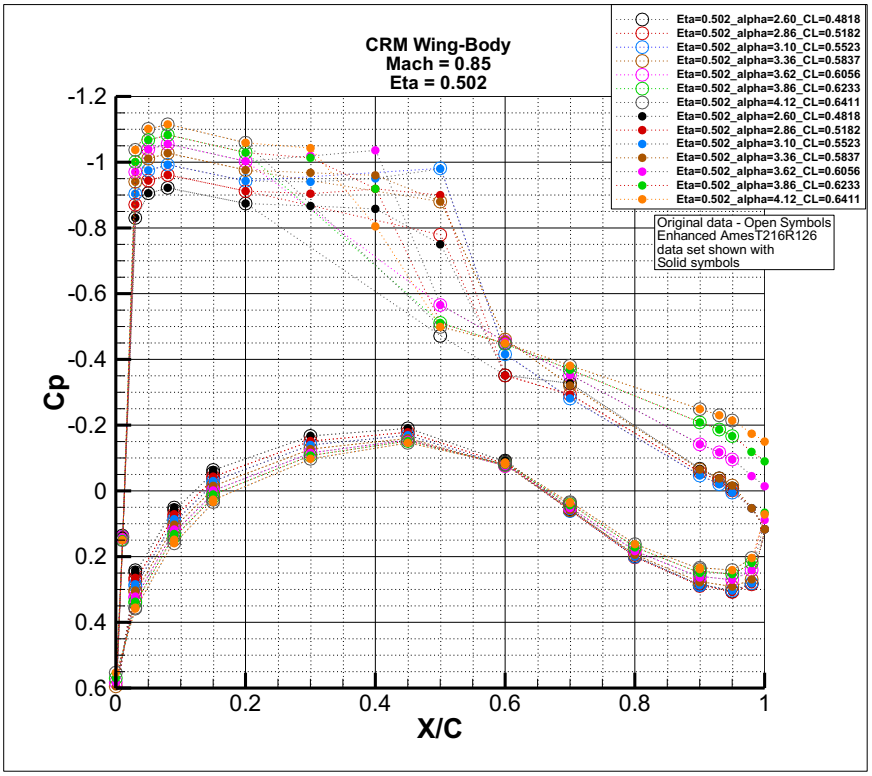


Figure A-A-18. Wing Pressure Distribution, Eta = 0. 502, M = 0.85, AoA = 2.06° to 3.10°.

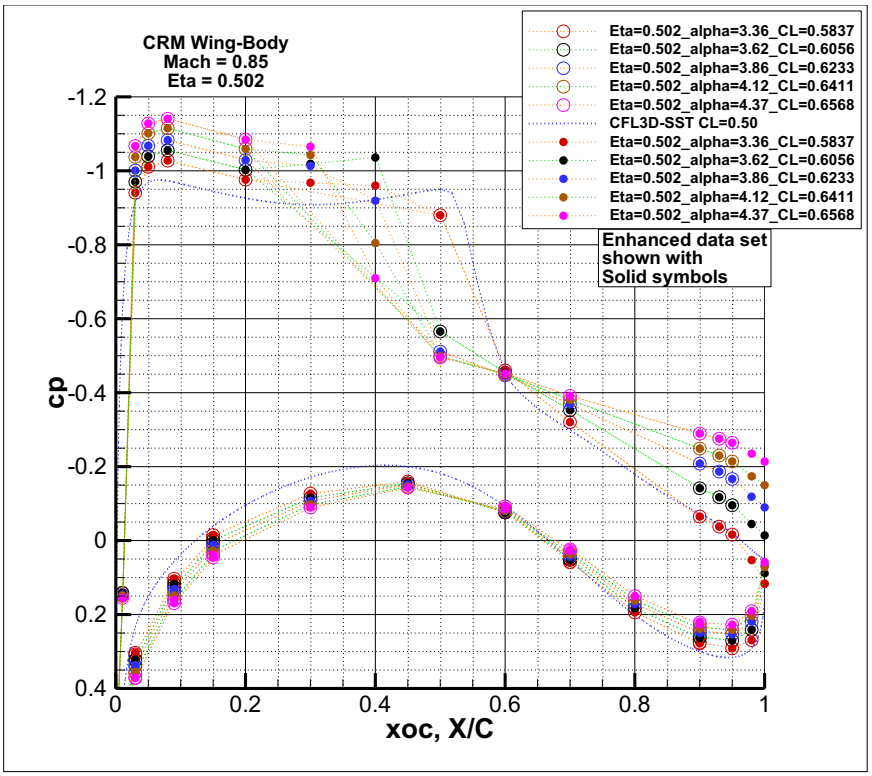


Figure A-A-19. Wing Pressure Distribution, Eta = 0. 502, M= 0 .85, AoA = 3.36° to 4.37°.

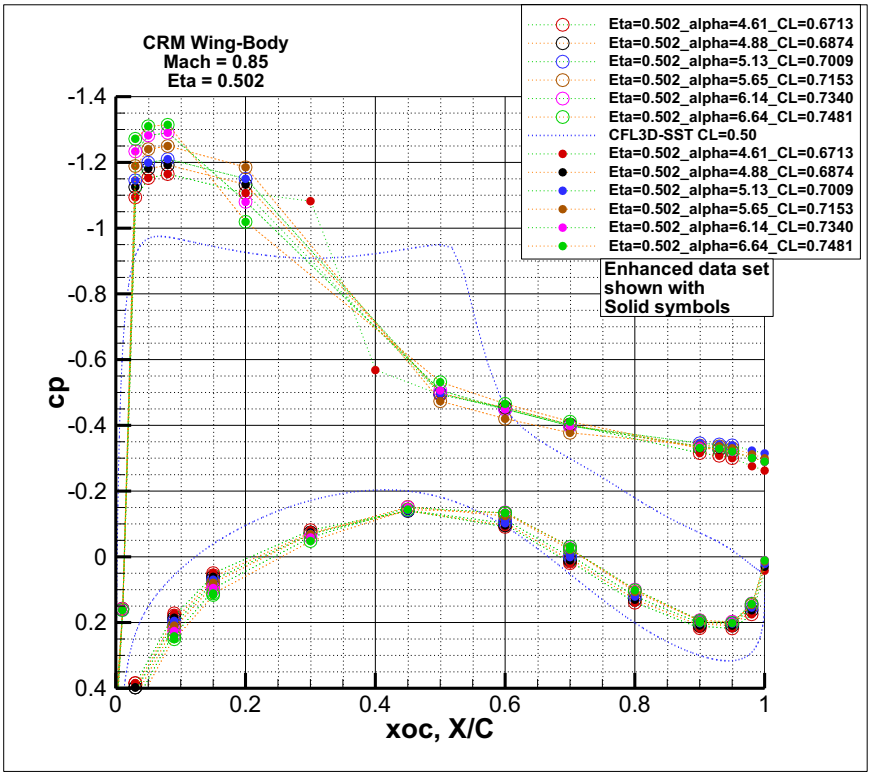


Figure A-A-20. Wing Pressure Distribution, Eta = 0. 502, M = 0.85, AoA = 4.61° to 6.64°.

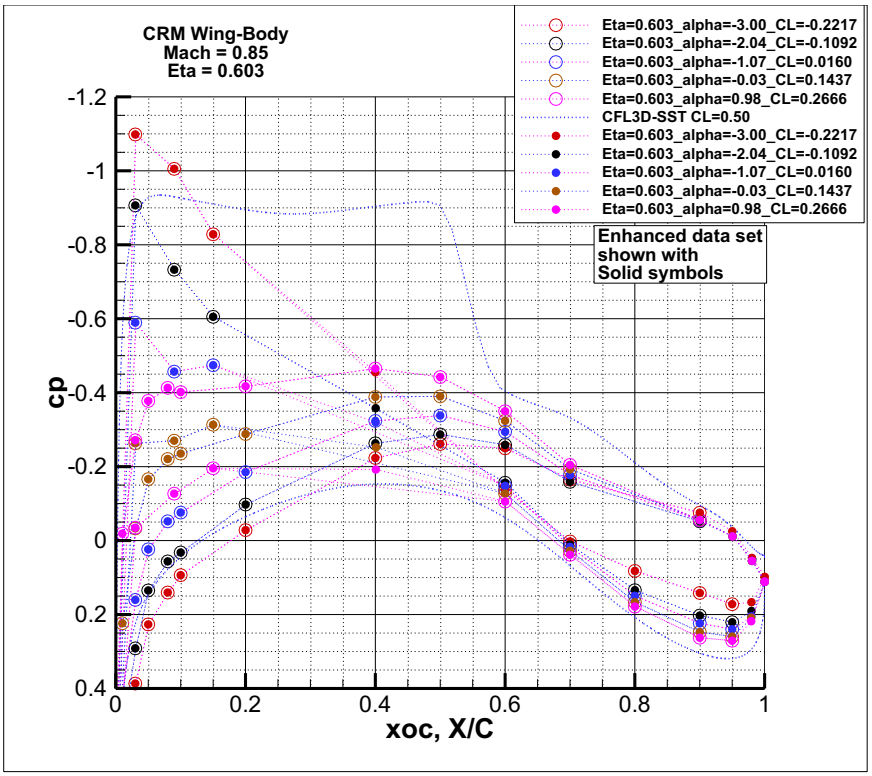


Figure A-A-21. Wing Pressure Distribution, Eta = 0.603, M = 0.85, AoA = –3.00° to 0.98°.

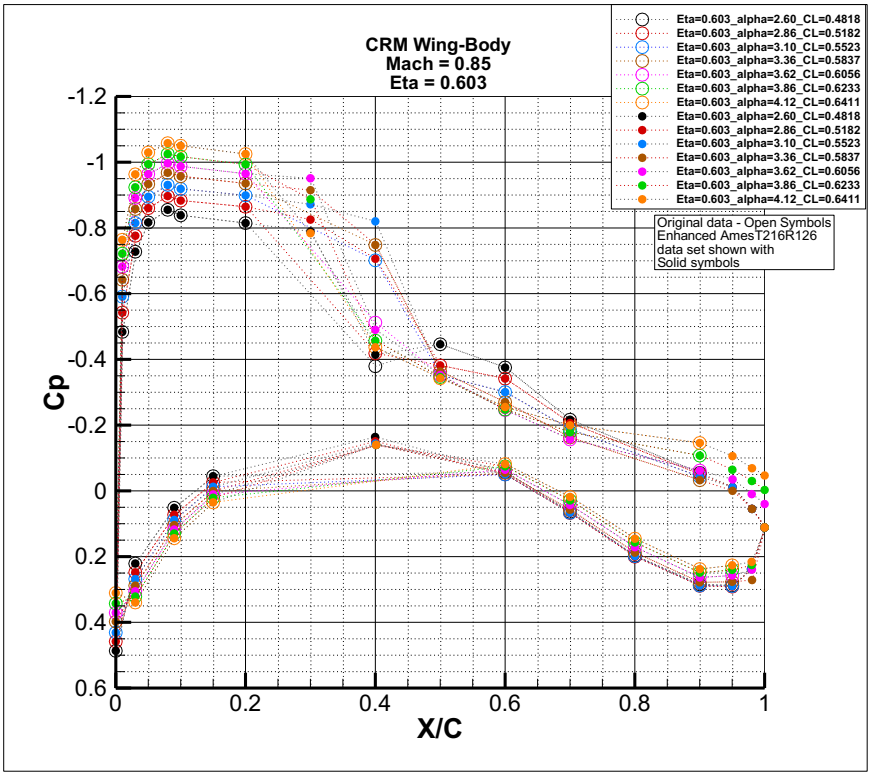


Figure A-A-22. Wing Pressure Distribution, Eta = 0. 603, M = 0.85, AoA = 2.06° to 3.10°.

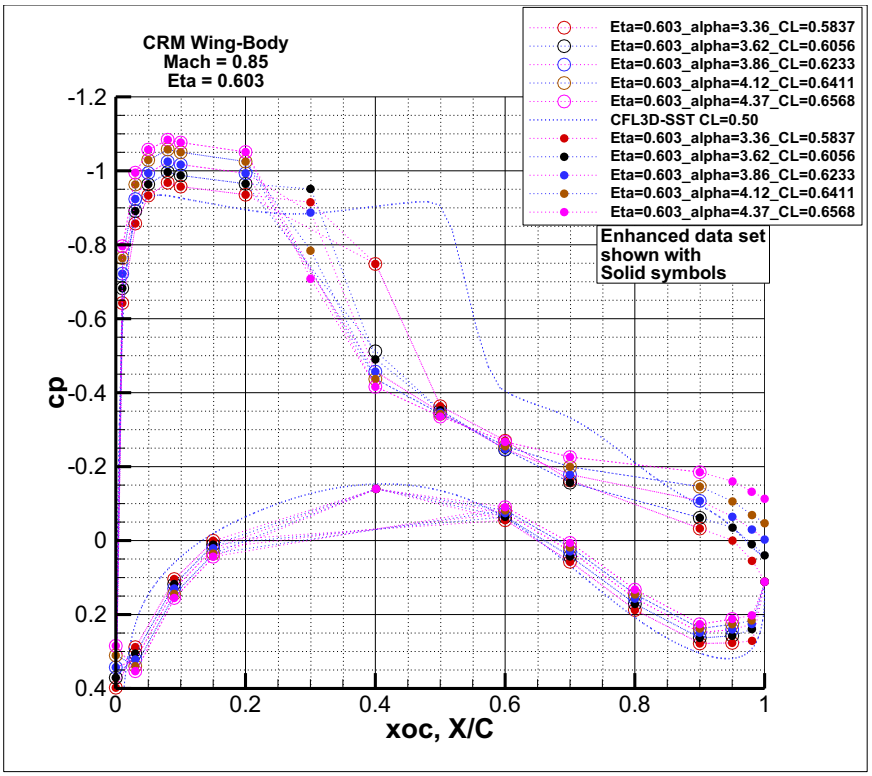


Figure A-A-23. Wing Pressure Distribution, Eta = 0. 603, M = 0.85, AoA = 3.36° to 4.37°.

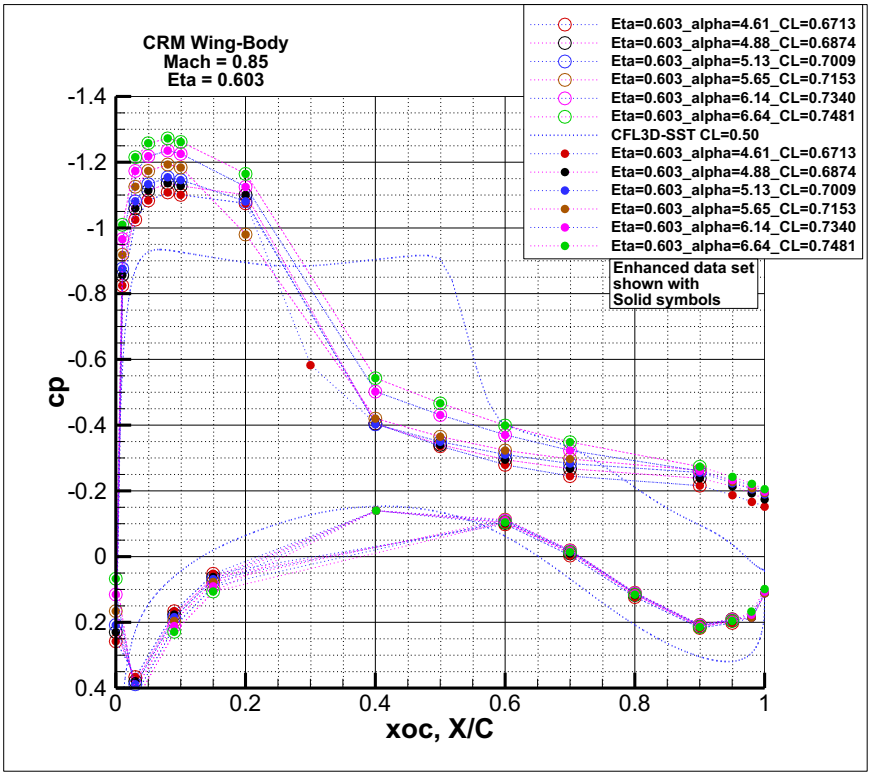


Figure A-A-24. Wing Pressure Distribution, Eta = 0. 603, M = 0.85, AoA = 4.61° to 6.64°.

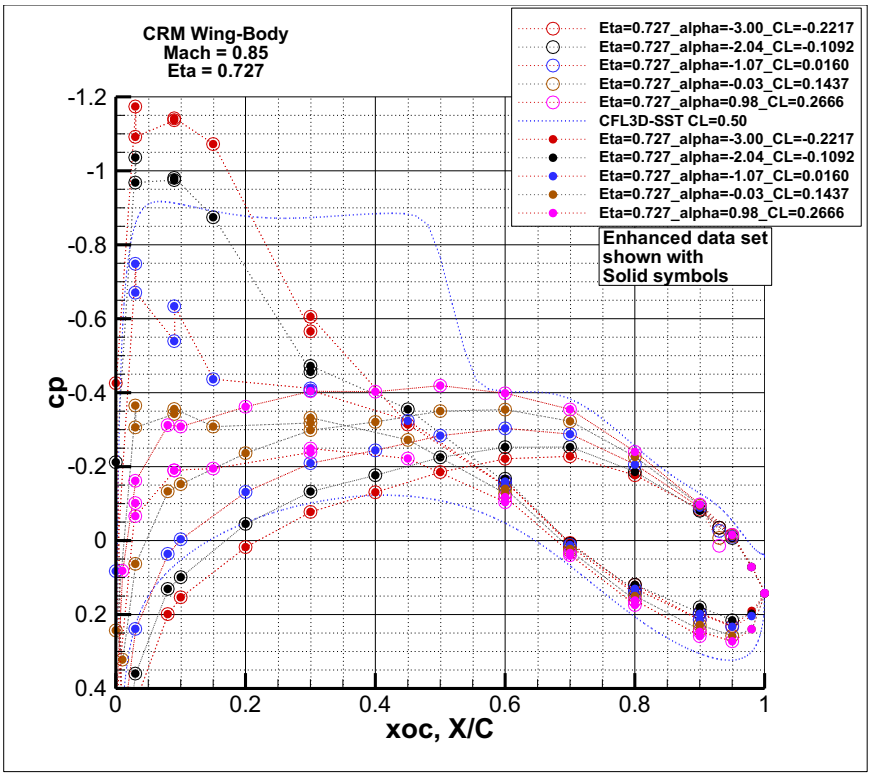


Figure A-A-25. Wing Pressure Distribution, Eta = 0.727, M = 0.85, AoA = –3.00° to 0.98°.

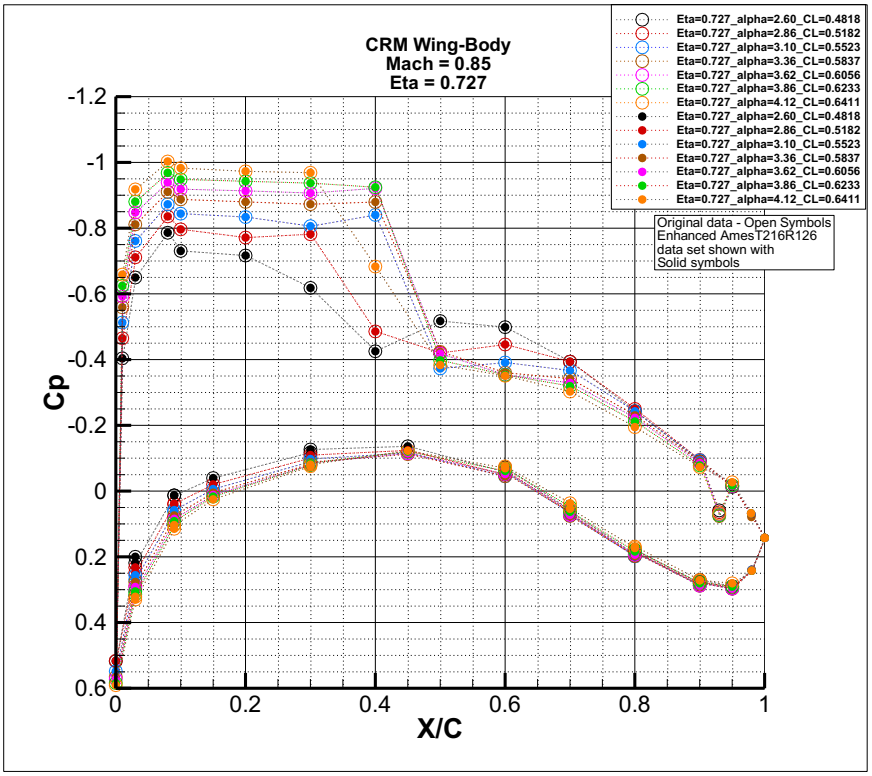


Figure A-A-26. Wing Pressure Distribution, Eta = 0. 727, M = 0.85, AoA = 2.06° to 3.10°.

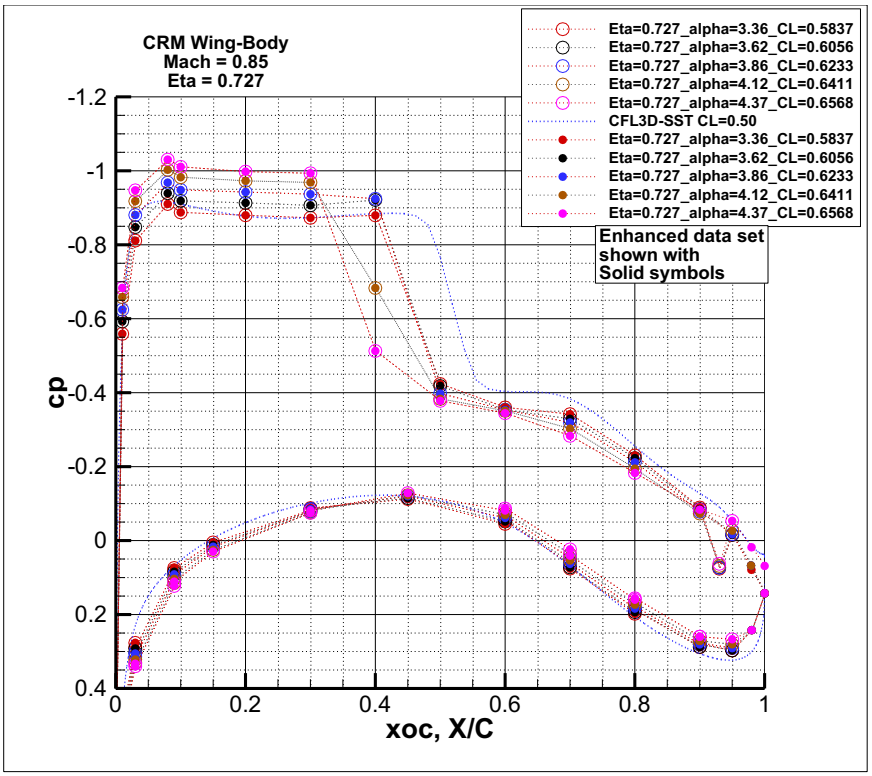


Figure A-A-27. Wing Pressure Distribution, Eta = 0. 727, M = 0.85, AoA = 3.36° to 4.37°.

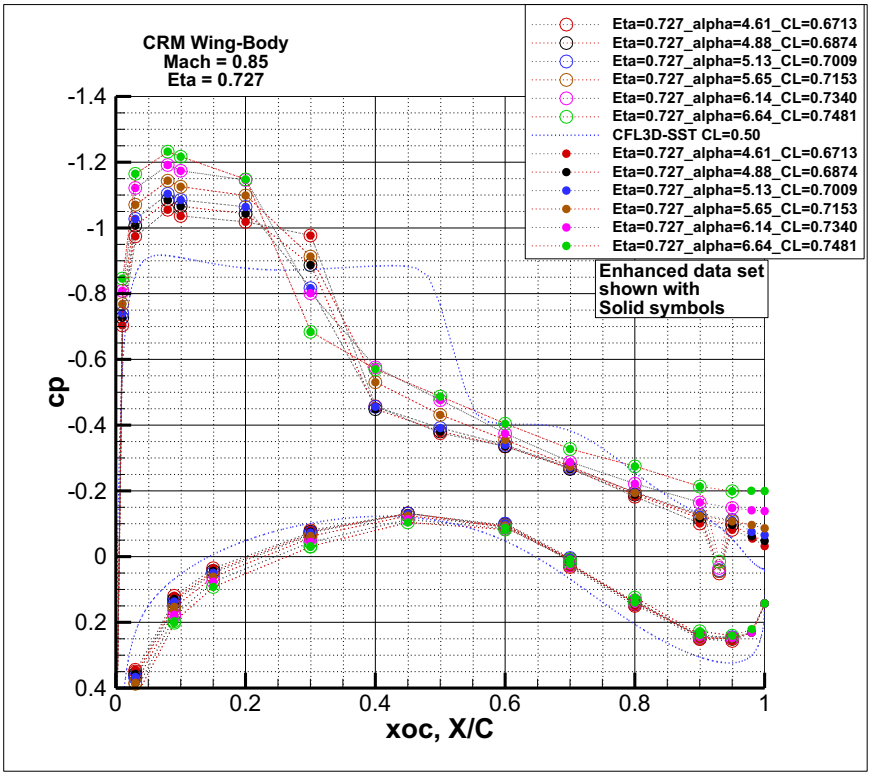


Figure A-A-28. Wing Pressure Distribution, Eta = 0. 727, M = 0.85, AoA = 4.61° to 6.64°.

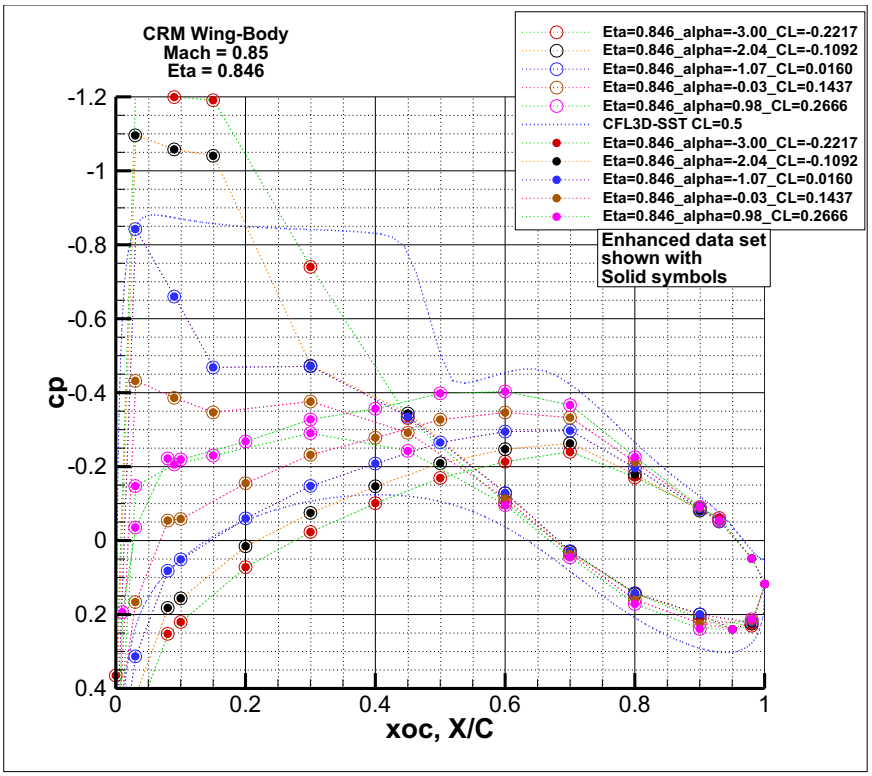


Figure A-A-29. Wing Pressure Distribution, Eta = 0.846, M = 0.85, AoA = –3.00° to 0.98°.

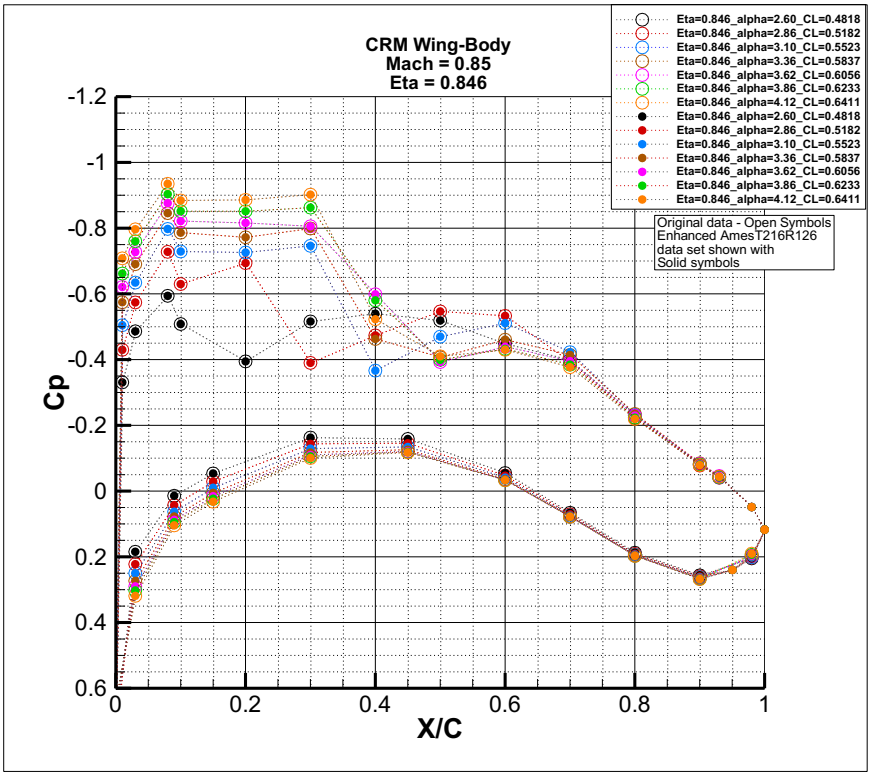


Figure A-A-30. Wing Pressure Distribution, Eta = 0. 846, M = 0.85, AoA = 2.06° to 3.10°.

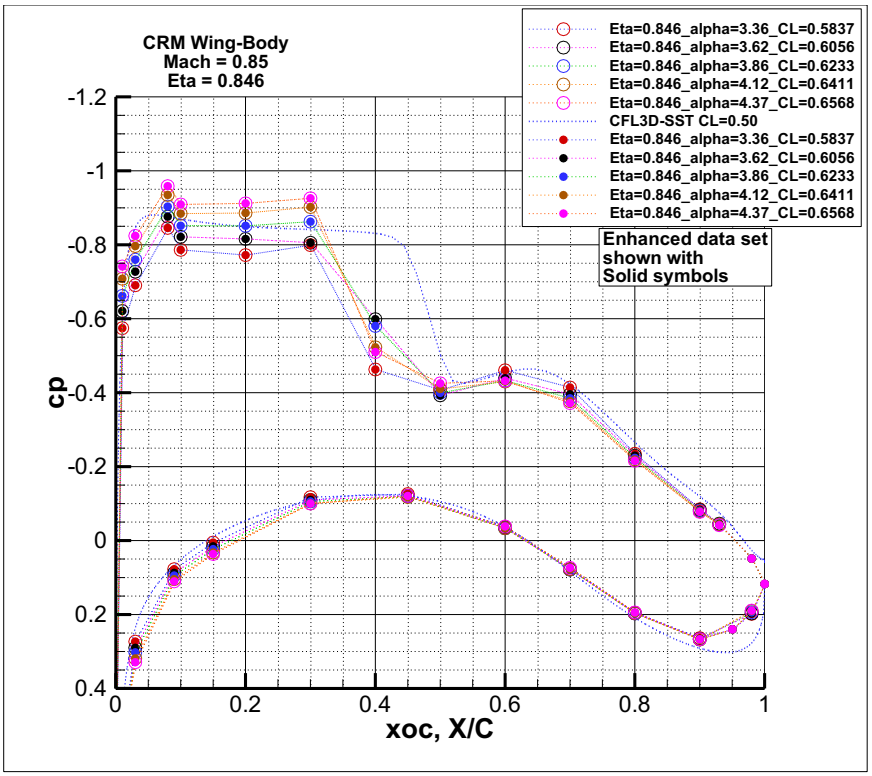


Figure A-A-31. Wing Pressure Distribution, Eta = 0. 846, M = 0.85, AoA = 3.36° to 4.37°.

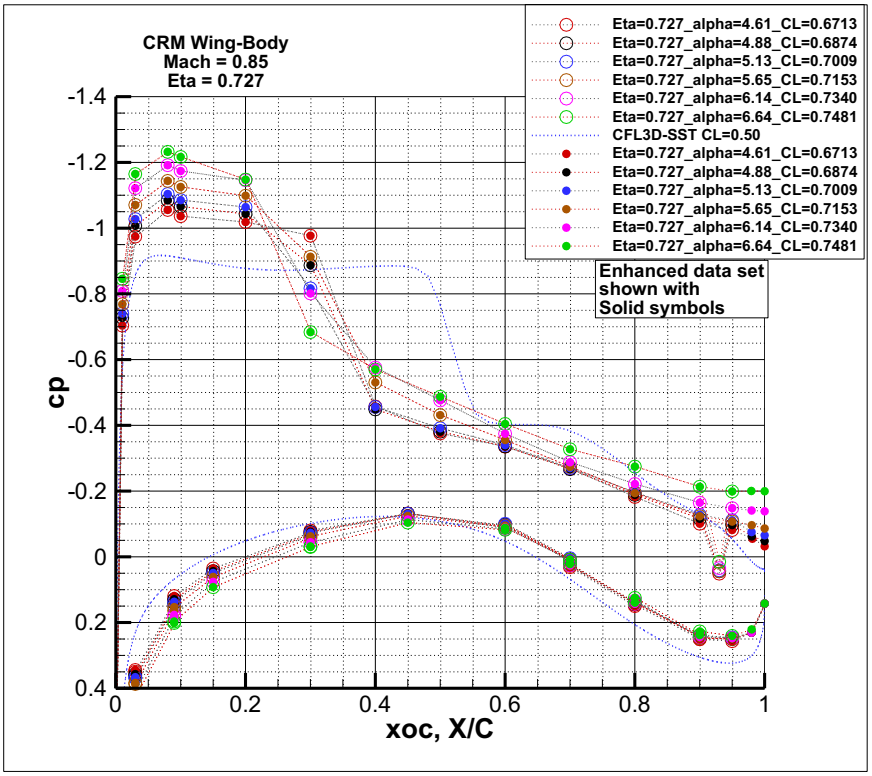


Figure A-A-32. Wing Pressure Distribution, Eta = 0. 846, M = 0.85, AoA = 4.61° to 6.64°.

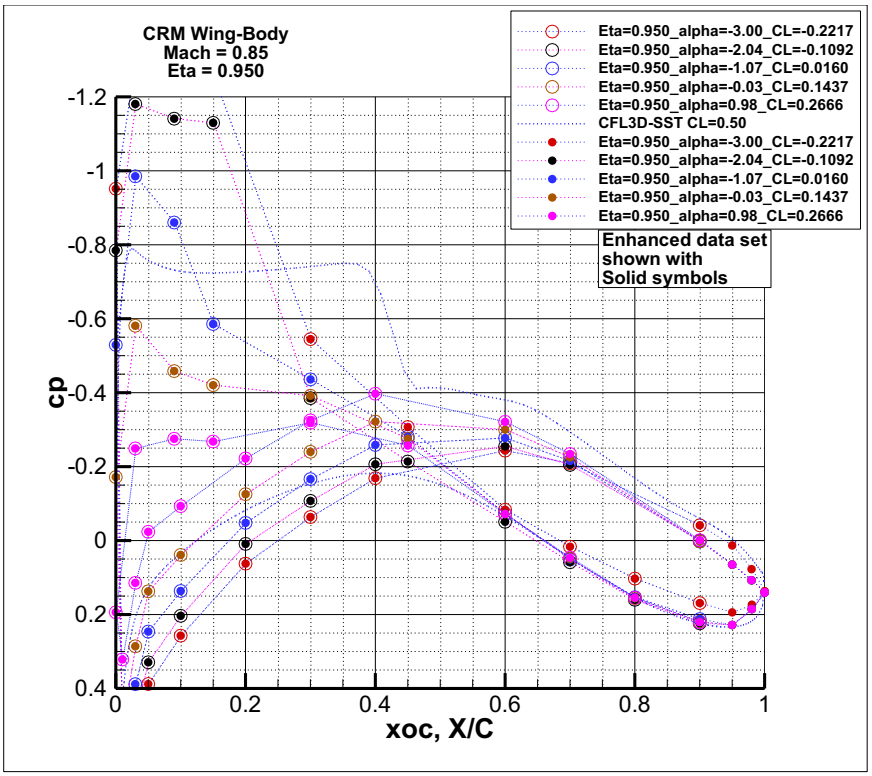


Figure A-A-33. Wing Pressure Distribution, Eta = 0. 846, M = 0.85, AoA = –3.00° to 0.98°.

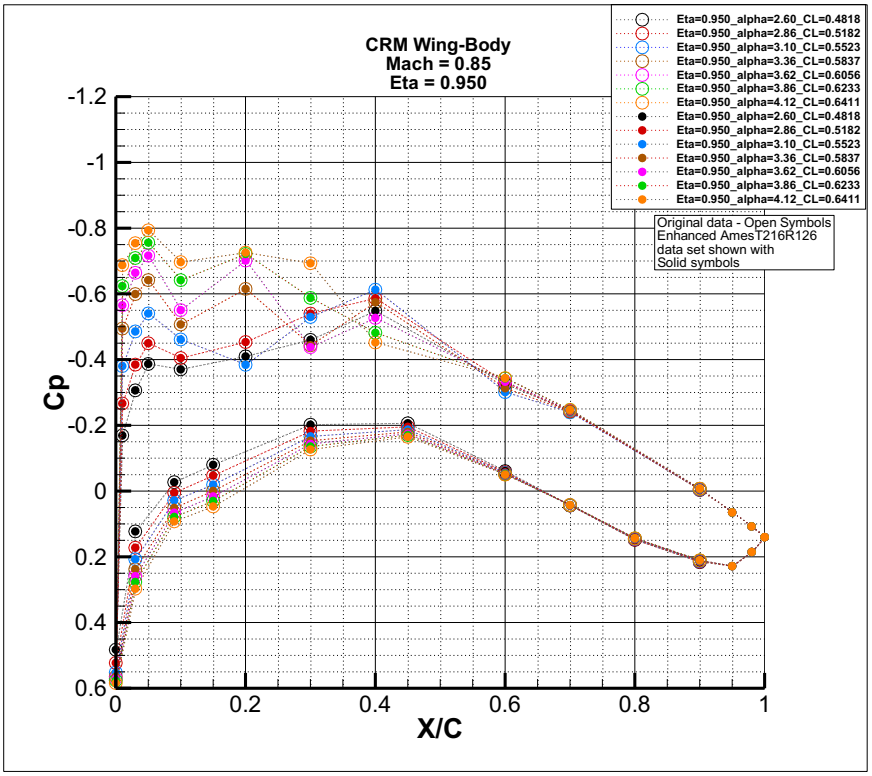


Figure A-A-34. Wing Pressure Distribution, Eta = 0.950, M = 0.85, AoA = 2.06° to 3.10°.

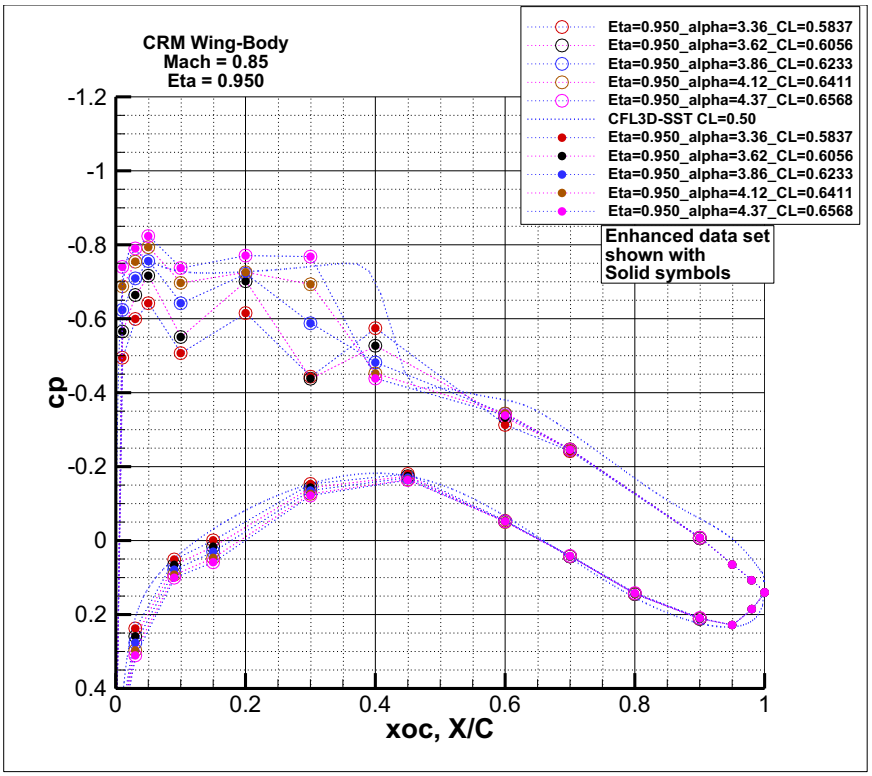


Figure A-A-35. Wing Pressure Distribution, Eta = 0.950, M = 0.85, AoA = 3.36° to 4.37°.

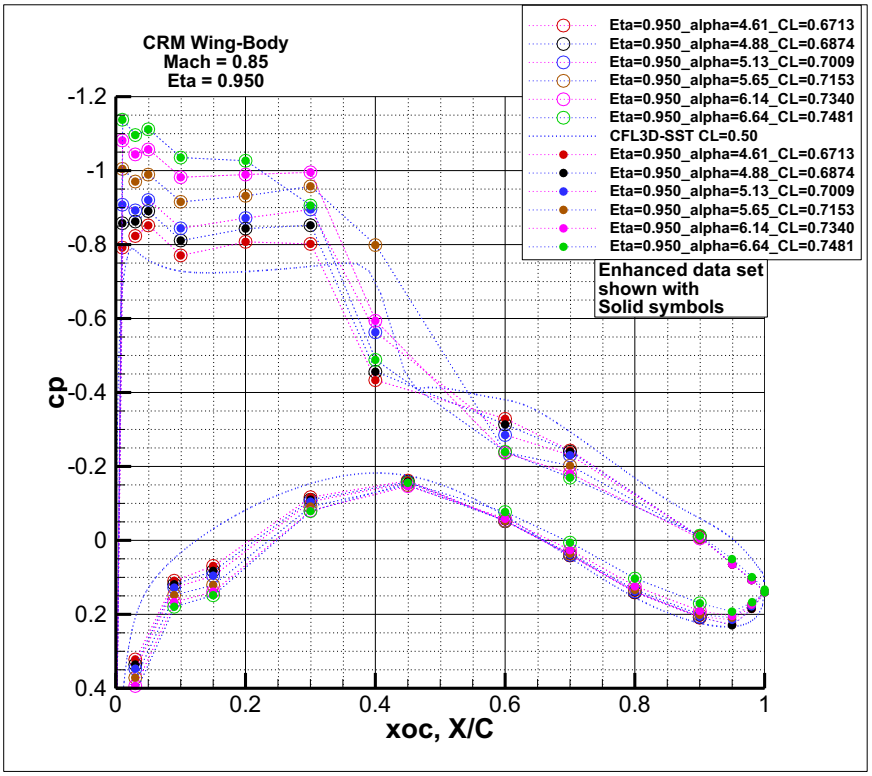


Figure A-A-36. Wing Pressure Distribution, Eta = 0. 950, M = 0.85, AoA = 4.61° to 6.64°.

Appendix B. Grids

B-A. Expanded Section IV: Description of Common Grids

This appendix provides a detailed description of the grids for the CRM configurations used in DPW-IV, -V, and -VI. This appendix will repeat some material found in the main report for completeness. A common theme and discussion topic in the DPW series has been the effect of the computational grid on the results. Gridding guidelines have been developed over the course of the DPW series and were little changed for the last three workshops except for the target sizes and as dictated by the geometries. The gridding guidelines were provided in an attempt to maintain some level of uniformity across all types of meshes. The gridding guidelines for DPW-IV and DPW-V are given in Table A-B-1, and those for DPW-VI in Table A-B-2.

Table A-B-1. Gridding guidelines for DPW-IV and DPW-V.

1) Initial spacing normal to all viscous walls (RE Based on c_{ref}= 275.80"):
   a) coarse: $y^+ \sim 1.0$ $\Delta y_1 = 0.001478$ (RE= 5M)
   b) medium: $y^+ \sim 2/3$ $\Delta y_1 = 0.000985$ (RE= 5M), $\Delta y_1 = 0.000273$ (RE= 20M)
   c) fine: $y^+ \sim 4/9$ $\Delta y_1 = 0.000657$ (RE= 5M)
   d) extra-fine: $y^+ \sim 8/27$ $\Delta y_1 = 0.000438$ (RE= 5M)
2) Recommended: generate grids with 2 cell layers of constant spacing normal to viscous walls
3) Total grid size to grow ~3X between each grid level for grid convergence cases
4) For structured meshes, this growth is ~1.5X in each coordinate direction
5) Grid convergence cases must maintain the same grid family between grid levels, i.e., maintain the same stretching factors, same topology, etc.
6) Growth rate of cell sizes in the viscous layer should be < 1.25.
7) Far field located at ~100c_{ref} for all grid levels.
8) For the Medium Baseline Grids:
   a) Chordwise spacing for wing and tail leading edge (LE) and trailing edge (TE) ~0.1% local chord.
   b) Wing and tail Spanwise spacing at root ~0.1% local semispan.
   c) Wing and tail Spanwise spacing at tip ~0.1% local semispan.
   d) Cell size near fuselage nose and after-body ~2.0% c_{ref}.
9) For the Coarse and Fine Baseline Grids, the above values should be scaled accordingly.
10) Wing and Tail Trailing Edge Base:
   a) Minimum of 8 cells across TE base for the coarse mesh
   b) Minimum of 12 cells across TE base for the medium mesh
   c) Minimum of 16 cells across TE base for the fine mesh
   d) Minimum of 24 cells across TE base for the extra-fine mesh
11) Be multigrid friendly
12) For unstructured grids designed for vertex-based solvers, the spacings refer to internodal spacings and the resulting grid sizes are expected to be similar to the structured grid sizes above. For unstructured grids for cell-centered solvers, the spacings refer to spacings between cell centers (or surface face centers), which corresponds approximately to a factor of 2 reduction in the overall number of surface points compared to the nodal solver case, for a triangular surface grid (this is based on triangle centroid separation distance of 2/3h). For tetrahedral cell-centered-solver meshes, the total number of grid points will be approximately 1/3 of the numbers listed above.

Table A-B-2. Gridding Guidelines for DPW-VI.

- **Grid Family Names: Tiny, Coarse, Medium, Fine, Extra-fine, Ultra-fine**
- **Tiny Grid**
  - Viscous Wall Spacing: $y^+ \sim 1.0 \rightarrow \Delta y_1 = 0.001478$”
  - At Least 2 Constantly-Spaced Cells at Viscous Walls, $\Delta y_2 = \Delta y_1$
  - Growth Rates < 1.2X Normal to Viscous Walls
  - Wing Spanwise Spacing < 0.1%*Semispan at Root, Engine & Tip
  - WNP Chordwise Spacing < 0.1%*c (local chord) at LE & TE
  - Wing & Nacelle TE Base >> 8 Cells [Pylon TE is Sharp]
  - Spacing Near Fuselage Nose & Afterbody < 1%*C_{ref}
- **Grow Next-Finer Grid in Family by ~ 1.5X in Size**
  - Scale Dimensions in All Three Computational Directions by ~ 1.15X
  - Grid Spacings Reduce by 0.87=(1/1.15) per Mesh Level
    - 0.1% in Tiny → [T,C,M,F,X,U] = [0.100, 0.087, 0.076, 0.066, 0.057, 0.050]%
- **WB Grids Consistent with Those within WBNP Systems**
  - Helps Minimize Deltas due to Grid → Better NP-Deltas
- **WBNP Grid Sizes ~ 1.3X-1.5X WB Grid Sizes, with Medium WB Mesh ~ 45 M-DOFs**
  - Pick Factor, Then Keep Constant Throughout Grid Family
- **Farfield Boundary > 100*Semispans**
  - Note: This is Farther than before, which was 100*C_{refs}
- **Miscellaneous Notes:**
  - Try to be Multigrid Friendly on Structured Meshes
  - Store Grid Coordinates in 64-bit Precision
  - If Storing Grids in Plot3D Format, Keep Zones < 33M Nodes
  - Itemize Surface Elements by Components [W, B, N, P, Sym, Far]
  - Itemize Element Count for Unstructured Meshes
    - Volume: Tetrahedra, Prisms, Pyramids, Hexahedra
    - Surface: Triangles, Quads
- **WB Grids Consistent with Those within WBNP Systems**
  - Helps Minimize Deltas due to Grid → Better NP-Deltas
- **WBNP Grid Sizes ~ 1.3X-1.5X WB Grid Sizes**
  - Pick Factor, Then Keep Constant Throughout Grid Family
- **Farfield Boundary > 100*Semispans**
  - Note: This is Farther than before, which was 100*C_{refs}
- **Miscellaneous Notes:**
  - Try to be Multigrid Friendly on Structured Meshes
  - Store Grid Coordinates in 64-bit Precision
  - If Storing Grids in Plot3D Format, Keep Zones < 33M Nodes
  - Itemize Surface Elements by Components [W, B, N, P, Sym, Far]
  - Itemize Element Count for Unstructured Meshes
    - Volume: Tetrahedra, Prisms, Pyramids, Hexahedra
    - Surface: Triangles, Quads

B-B. DPW-IV Grids

An overview of the baseline DPW-IV grids is provided in this section. However, the details of these grids are not included herein. For more information regarding these grids, refer to the companion papers [42–56] associated with this summary document. Because of the variation of grid types needed, a set of gridding guidelines, listed in Table A-B-1, is established to help facilitate the creation of these grids. The gridding guidelines are provided to persons responsible for generating baseline grids in an attempt to maintain some level of uniformity across all types of meshes. Note that each grid family is required to include coarse (C), medium (M), and fine (F) grids; adding an optional extra-fine (X) grid is also encouraged. Further, the organizing committee decided that the medium mesh should be representative of current engineering applications of CFD being used to estimate absolute drag levels on similar configurations. For unstructured meshes, the size of the medium mesh is also a function of the intended flow solver. For example, a cell-centered scheme has about 5.5 times the numbers of unknowns as that of a nodal scheme for a given unstructured tetrahedral mesh, with the ratio being closer to 3.5 for typical hybrid meshes.

Table A-B-3 provides the grid size for each grid family, configuration, and resolution for the grid convergence study (Case 1). The types of meshes include multiblock (MB), overset (OS), and unstructured (UN). This table also indicates whether the associated flow solver is based on a nodal (N) or cell (C) centered scheme. These grids range in size from 2.8–189.4 million. The average medium grid sizes for the WBH and WB configurations are 13.3 million and 10.9 million, respectively. This table also includes a mapping of the participants who used each grid. The usage key (tag) identifies the participant/data set listed in Table A-C-1 in Appendix C**.** For example, the Solar grid family (Type UN/N) is comprised of unstructured meshes, appropriately developed for node-based solvers, does not have an extra-fine mesh in its family, and is used by participants C, D, S, and T. Note that the average usage of each grid is by 1.6 participants. This low ratio is indicative of the fact that participants have realized that in order to obtain accurate solutions, they prefer to develop grids tailored to their flow solvers.

Table A-B-3. DPW-IV CRM Grids: Size in Millions.

		WBH ($i_H = 0$)				WB	
Family	Type	Extra-Fine	Fine	Medium	Coarse	Medium	Usage*
CFSE ICEM Hexa	MB/C	-	36.0	11.3	3.8	11.0	A
Centaur	UN/N	-	-	13.3	-	-	B
Solar	UN/N	-	34.1	11.7	4.1	8.6	C,D,S,T
Gambit/Tgrid	UN/C	-	58.1	21.3	6.2	5.4	E
MEGG3D	UN/N	-	31.3	13.5	5.9	9.8	F
HexaGrid	UN/N	-	36.6	11.1	3.2	9.2	G
GRIDGEN	MB/C	-	30.4	9.0	2.8	8.6	H
VGRID LaRC	UN/N	105.7	36.0	10.3	3.7	8.2	I,K,Z
VGRID Cessna	UN/N	-	35.2	9.9	3.5	8.5	J
Boeing Seattle	MB/C	81.7	47.2	11.0	4.8	10.9	L-O,Y
Boeing HB	OS/N	189.4	56.5	16.9	7.2	12.3	P
ANSYS ICEM Hexa	MB/C	104.3	35.8	10.8	3.5	8.6	R
GRIDZ	MB/C	-	-	15.4	4.4	-	U
Airbus ICEM Hexa	MB/C	104.7	36.7	12.6	4.5	8.8	V
MIME	UN/C	33.9	28.6	16.6	11.5	17.0	W,X
Boeing StL	UN/C	109.4	55.5	22.3	7.1	32.8	2,3
NUMECA	UN/C	-	27.3	14.3	5.2	9.7	4
TriTet	UN/N	-	32.1	10.2	3.2	5.7	5
Average	-	99.7	37.4	13.3	5.0	10.9	1.6

*Usage refers to the user key of the grid denoted in **Table A-B-1** in **Appendix C.**

B-C. DPW-V Grids

A substantial effort was made in DPW-IV to address the effect of computational grid on the results, yet there was still significant variation in the results among the different grid types. The DPW Organizing Committee recognized that for DPW-V a relatively simple multiblock structured grid could be created for the CRM wing-body geometry that conformed to the desired gridding guidelines. From this baseline grid, the remaining grid types could be generated, thereby guaranteeing a high degree of commonality. The grid topology for the baseline MB grid is shown in Fig. A-B-1. Starting with the finest grid (L6), the smaller grids were derived by combining cells, keeping even the smallest grid (L1) "multigrid friendly" for up to three levels. Once the MB series was developed, then a set of unified grids for other types were derived. These included overset and three types of unstructured grids: hexahedral (hex), prismatic, and hybrid tetrahedral (prismatic in the boundary layer and tetrahedral in the field). Details of the individual grid families can be found in reference 58 and are discussed below.

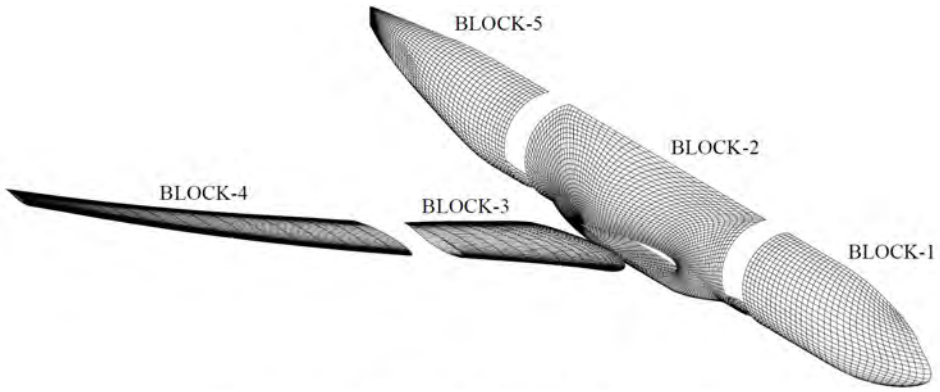


Figure A-B-1. Block Topology for the CRM Wing-Body Multiblock (MB) Grid Family (Figure-S-IV-1).

The finest grid (L6) was generated first and sized to extend well into the asymptotic range of grid convergence, while the coarsest grid (L1) would still be "multigrid friendly" for up to three levels. The next coarsest level (L5) was obtained by replacing every three cells in each of the I, J, and K directions with two cells. The L4 grid was created from L6 by removing every other point in each of the I, J, and K directions, and L3 by doing the same starting from the L5 grid. The process was repeated with the L4 and L3 grids to complete the sequence at L2 and L1. By interleaving the even and odd levels, a complete family of six grids was constructed. See Vassberg [58] for detailed information.

Once the MB series was developed, a set of unified grids for other types were derived. The overset series was created by extending each block using data from neighboring blocks to define four patch grids to bridge each block. The patch grids overlap each block by three cells, as shown in Fig. A-B-2, and are point matched to minimize interpolation errors. One issue was found on the K = 1 plane for the midbody block, where the J line has mixed symmetry plane and block boundary conditions. This issue caused difficulty for some participants using overset grids.

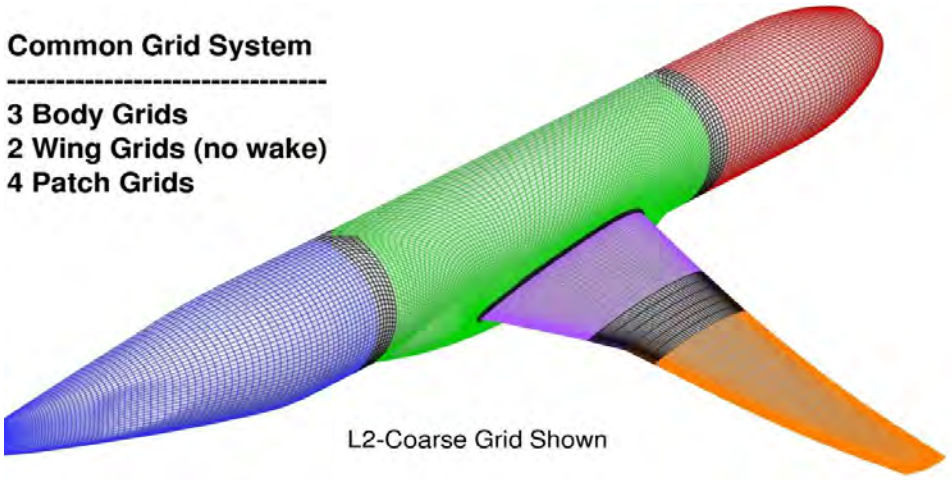
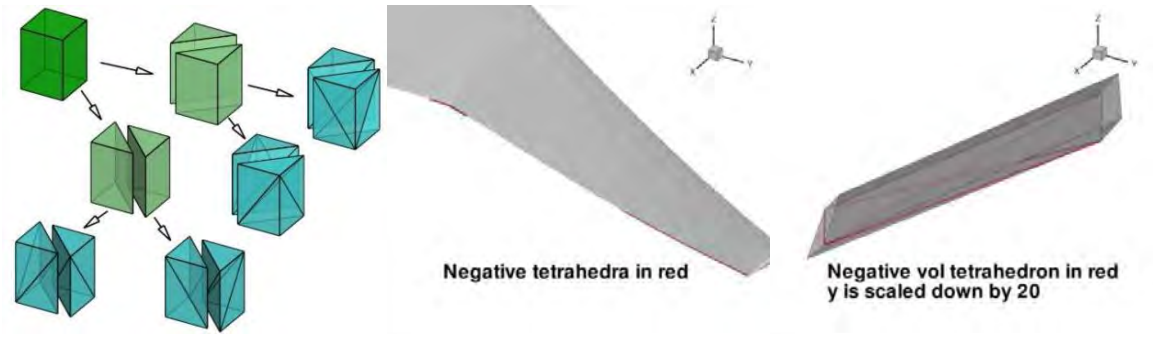


Figure A-B-2. Overset Patch Grids Derived from the Multiblock Structured Grid.

Three types of unstructured grids were created from the MB grids: hexahedral, prismatic, and hybrid tetrahedral (prismatic in the boundary layer and tetrahedral in the field). The hexahedral format preserves the structure of each individual cell of the MB grids but converts the file into finite element form with no IJK structure. Subdivision of hexahedral elements into prismatic and tetrahedral elements follows the sequence shown in Fig. A-B-3a. Each hex cell subdivides into two prism cells, and then each prism is split into three tetrahedra. A usable, fully tetrahedral grid could not be created due to issues at the trailing edge of the wing. Groups of cells inside the boundary layer grid were distorted such that a negative volume would result when subdivided into tetrahedra (Fig. A-B-3b). The prisms did not have this issue, so only the hybrid grids were created. Negative volumes were also encountered for the prism subdivision on the super fine (L6) grid, so only hex meshes are available at that level.



a) Hex to prisms and tetrahedra. **b) Issues with distorted high aspect ratio cells**

Figure A-B-3. Unstructured Grids Derived from Multiblock Structured Grid.

A summary comparison of the grid sizes for all levels and types is listed in Table A-B-4. Note that suitable grid refinement sequences are available for unstructured cell- or node-based schemes.

Table A-B-4 DPW-V Metric Parameters for the Common Grids (Counts in Millions).

				Multiblock Structured		Overset	Unstr. Hex		Unstr. Prism		Unstr. Hybrid		
Level	**Name**	**Label**	**~y^+**	**Cells**	**Nodes**	**Points**	**Cells**	**Nodes**	**Cells**	**Nodes**	**Tets**	**Prism**	**Nodes**
1	Tiny	T	2.00	0.64	0.66	0.8	0.64	0.66	1.3	0.66	2.6	0.43	0.66
2	Coarse	C	1.33	2.2	2.2	2.5	2.2	2.2	4.3	2.2	8.6	1.4	2.2
3	**Medium**	**M**	**1.00**	**5.1**	**5.2**	**5.7**	**5.1**	**5.2**	**10.2**	**5.2**	**20.8**	**3.3**	**5.2**
4	Fine	F	0.67	17.3	17.4	18.6	17.3	17.4	34.5	17.4	69.7	11.3	17.4
5	Extra Fine	X	0.50	40.9	41.2	43.3	40.9	41.2	81.8	41.2	166.1	26.4	41.2
6	Super Fine	S	0.33	138.0	138.8	143.5	138.0	138.8	---	---	---	---	---

B-D. DPW-VI Grids

B-D-1. Baseline Overset Grid Families for DPW-VI

The baseline overset grid family was developed by Leonel Serrano and John Vassberg of Boeing, and reviewed by Tony Sclafani, Mark DeHaan, Gaetan Kenway, Jim Coder, and Tom Pulliam. This group also comprised the principal set of participants who used the baseline overset grid systems in DPW-VI.

The basic layout of the overset structured meshes began with an exercise in numerology that addressed the gridding guidelines on (a) family members being parametrically equivalent, (b) growth between family member sizes being about 1.5x, (c) grid blocks being multigrid friendly, (d) having at least two constantly-spaced cells at all viscous walls, and (e) retaining feature lines in all members of the grid family. In order to grow grid size by a factor of about 1.5x, the growth factor in each of the three computational directions should be about 1.15x, as $1.15^3 \sim 1.5$, whereas 1.15 is about 8/7, and we adopted this rational growth factor for our fine-to-extra fine mesh. Working backward and forward, this established the growth factor sequence of tiny $\times (5/4)^3$ = coarse $\times (6/5)^3$ = medium $\times (7/6)^3$ = fine x $(8/7)^3$ = extra-fine $\times (9/8)^3$ = ultra-fine. (Note: ultra-fine nomenclature in DPW-VI corresponds Super-fine in DPW-V). Hence, the grid sizes of this six-member grid family span just over an order-of-magnitude, or a factor of 11.4x = $(9/4)^3$. Also, by using a cell-count dimension that is evenly divisible by 4 on each pertinent segment of the tiny mesh, the span of the segments will be exactly maintained for each of the members of the grid family. For example, the

segments of the airfoil sections on the wing of the tiny mesh were dimensioned as 16 cells on the trailing-edge, 88 cells on the upper surface, and 88 cells on the lower surface, for a total of 192 cells around the airfoils. Hence, all members of the overset grid family retain the two trailing-edge lines as well as the leading-edge line in their surface grids. Applying this approach throughout the grid layout, the intersection lines of the wing-body, the wing-pylon, and the nacelle-pylon, as well as the wing planform break, and pylon and nacelle leading, and trailing edges were all consistently maintained across all grid-family members.

With a basic understanding of our strategy to grid dimensions, a template mesh and topology layout was developed for the wing-body-nacelle-pylon (WBNP) geometry. The WBNP grid layout was comprised of 25 blocks. This template mesh was used to generate a parametrically equivalent family of WBNP grids. To generate the wing-body (WB) grid family, the NP grids were simply removed from the WBNP grids, leaving eight blocks to define the WB overset grid systems. The gridding guidelines recommended a ratio of grid sizes between the WBNP and WB systems of 1.3x–1.5x, whereas this ratio for the overset grid systems was about 1.6x.

The topology of the near-field grid blocks about the WBNP with a focus on the NP group is shown in Fig. A-B-4. Here, the fuselage is fully defined by three grid blocks: a half O-mesh covering most of the fuselage, a warped block at the nose, and a collar grid at the wing-body juncture. The wing is represented by an O-mesh wrapping around the airfoil sections, the wing-body collar grid, and a wingtip grid. The nacelle is comprised of five surface-abutting blocks: clamp grids at the leading and trailing edges, a collar grid, and inner and outer O-meshes. The pylon has collar grids at the wing and nacelle juncture regions, as well as a number of patch grids. Finally, a global box grid encompasses all of the above and places the farfield boundary at about 100 semispans from the CRM configuration. The WBNP surface grids for each grid size were created using ICEM-CFD HEXA using the template blocking file developed for this topology and ICEM replay scripts. Then, the surface-abutting grid blocks were generated using the NASA Chimera Grid Tools, more specifically, using BUILDVOL and HYPGEN. Finally, the hole-cutting and block-stitching steps were performed with the BUILDPEG5i script. This complete process was repeated to develop the WBNP family of grid resolution and another WBNP family of aeroelastic deflection. The corresponding WB families were developed by dropping the NP grids and rerunning BUILDPEG5i. This process yielded WB grids without any orphan points and WBNP grids with at most five orphans. Table A-B-5 provides statistics for the grid family of increasing sizes. Note that for the tiny mesh, the viscous spacing was $y^+ \sim 1$, its maximum stretching through the boundary-layer region was about 1.235, and that 4 cells of constant spacing at the viscous walls were utilized. These characteristics adhere closely to the gridding guidelines provided above. Note that the grid sizes are given as a total number of grid points in the systems.

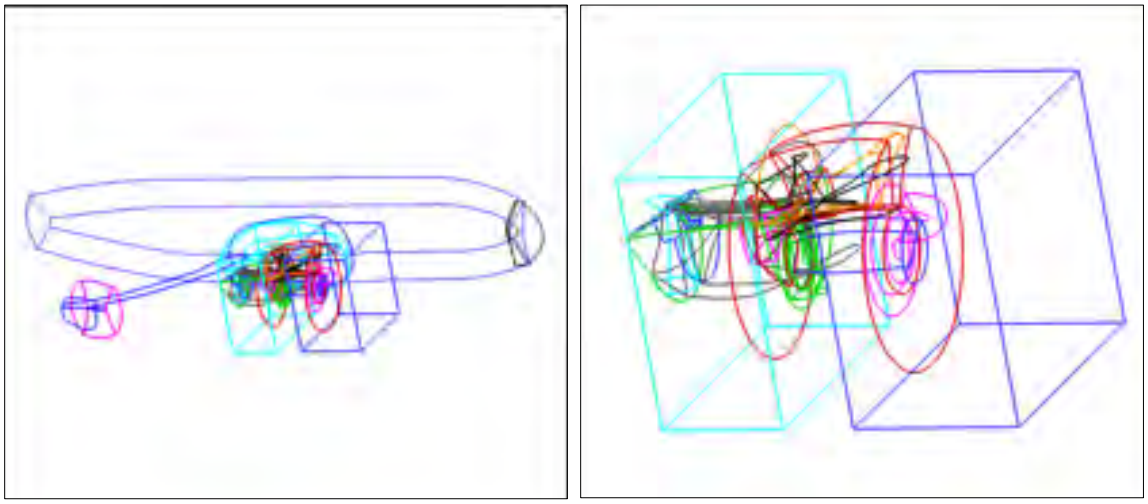
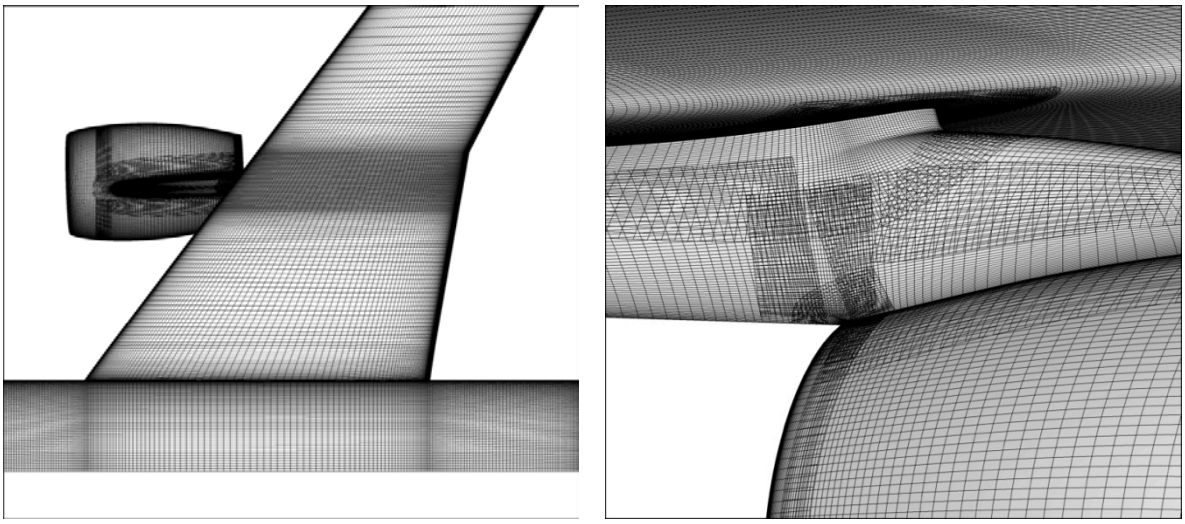


Figure A-B-4. Topology of Overset Near-Field Grid Blocks and Nacelle-Pylon Grid Blocks.

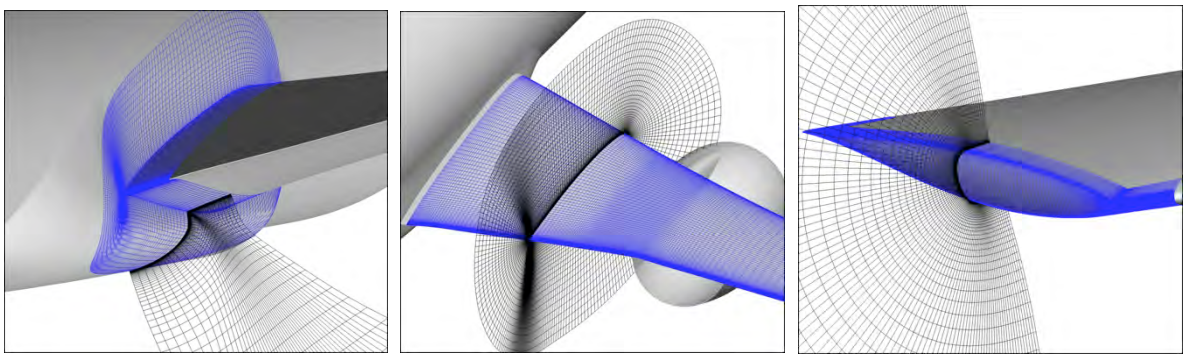
Figure A-B-5 provides close-up views of the WBNP surface grids for the medium mesh. Note that the spanwise clustering of the wing grid is established to capture gradients induced by the NP group. Retaining this clustering is somewhat of an overkill for WB simulations; however, it provides accurate results for the NP delta drag evaluations. Figure A-B-5b depicts a close-up of the nacelle-pylon surface grids that illustrate the wing-pylon and pylon-nacelle

collar grids, as well as numerous patch grids to complete the pylon surface. In addition to these body-conforming meshes, near-field box grids enclose the fuselage, the wing, and the nacelle inlet and nozzle openings. The WB collar grid, the O-mesh about the wing, and the wingtip clamp grid of the medium mesh are depicted in Figs. A-B-6a, -6b, and -6c, respectively.



a. WBNP Surface Grids **b. Nacelle/Pylon Surface Grids**

Figure A-B-5. Close-Up of WBNP Surface and Nacelle/Pylon Surface Grids for the Medium Overset Mesh.



a. WB Collar Grid **b. O-Mesh Abutting the Wing** **c. Wingtip Clamp Grid**

Figure A-B-6. Close-Up of Overset Features for Medium Overset Mesh.

The baseline overset grids can be downloaded from the DPW-VI website [72] and are located in the *overset_grids_Boeing_Serrano.REV00* directory. Included in this location is a *README.BoeingSerrano* file for additional information about these grid families. There are six WBNP grids and six WB grids about the *ae2p75* geometry that constitute the grid resolution families, and an additional seven WB grids at the Medium mesh density to fill out the aeroelastic family. All grids were built relative to the version v09 IGES geometry definitions of the CRM WBNPH configuration, also available for download at the DPW-VI website.

Table A-B-5. Overset Grid Family Statistics.

Grid	Viscous Spacing	~ y^+	Maximum Stretching	WB Size	WBNP Size
Tiny	0.001478	1.02	1.235	7,398,176	11,865,177
Coarse	0.001182	0.80	1.186	14,355,678	22,999,565
Medium	0.0009853	0.67	1.149	24,698,828	39,542,953
Fine	0.0008446	0.58	1.128	39,098,858	62,566,221
Extra-fine	0.0007390	0.50	1.112	58,227,000	93,176,522
Ultra-fine	0.0006569	0.45	1.099	82,754,486	132,381,764

B-D-2. Baseline NASA GeoLab Unstructured Meshes for DPW-VI

The baseline unstructured-mesh families for DPW-VI were developed by Norma Farr and Mike Wiese of NASA's GeoLab group. These grids can be downloaded from the DPW-VI website under the *unstructured_NASA_GeoLab.REV01* directory. Sample surface grids are shown in Fig. A-B-7. Statistics of the WB and WBNP grid-refinement families are given in Tables A-B-6 and -7, respectively, and for the WB aeroelastic family in Table A-B-8.

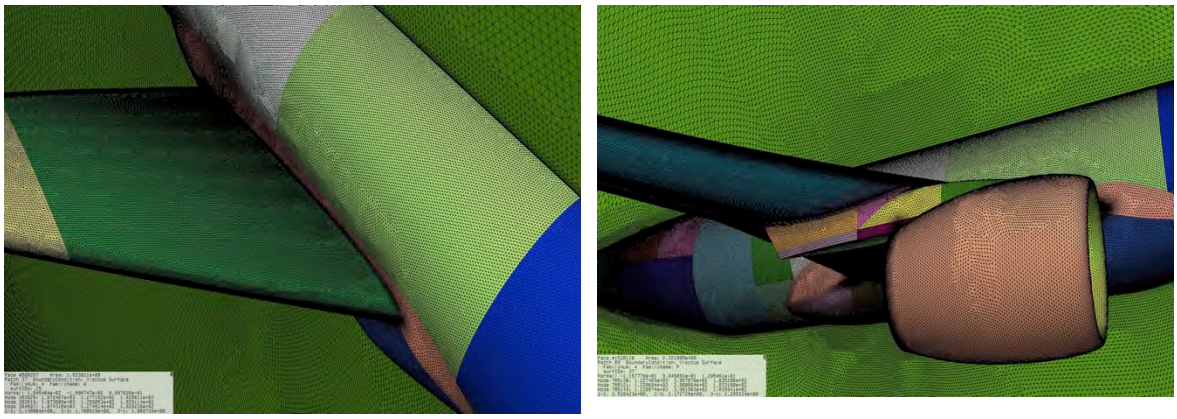


Figure A-B-7. Close-Up of NASA GeoLab Unstructured Surface Meshes.

Table A-B-6. NASA GeoLab Wing-Body Grid Refinement Family Statistics.

Wing Body Grid Refinement Study								
GRID LEVEL	1ST CELL SIZE	BL MAX GROWTH RATE	BOUNDARY NODES	BOUNDARY FACES	BL NODES	BL CELLS	TOTAL NODES	TOTAL CELLS
TINY	0.001478	1.15	655,339	1,310,674	10,775,077	60,647,514	20,419,925	119,554,125
COARSE	0.001285	1.15	860,282	1,720,560	15,384,236	87,036,885	29,851,330	174,999,801
MEDIUM	0.001118	1.15	1,127,127	2,254,250	22,397,227	127,458,345	44,162,574	259,261,343
FINE	0.000972	1.15	1,475,823	2,951,642	33,385,212	191,210,919	66,089,940	388,564,128
X-Fine	0.000845	1.15	1,938,196	3,876,388	52,391,237	302,286,426	100,550,619	592,197,654
U-Fine	0.000735	1.15	2,554,937	5,109,870	78,076,307	454,864,240	151,009,898	890,287,118

Table A-B-7. NASA GeoLab Wing-Body-Nacelle-Pylon Grid Refinement Family Statistics.

Wing Body Nacelle Pylon Grid Refinement Study								
GRID LEVEL	1ST CELL SIZE	BL MAX GROWTH RATE	BOUNDARY NODES	BOUNDARY FACES	BL NODES	BL CELLS	TOTAL NODES	TOTAL CELLS
TINY	0.001478	1.15	765,536	1,531,072	12,419,166	69,823,581	27,724,572	162,407,703
COARSE	0.001285	1.15	1,005,542	2,011,084	17,706,490	100,064,115	40,742,401	238,932,215
MEDIUM	0.001118	1.15	1,314,055	2,628,110	25,778,271	146,575,107	60,587,854	355,766,178
FINE	0.000972	1.15	1,724,835	3,449,670	38,458,890	220,091,481	91,001,054	535,012,345
X-Fine	0.000845	1.15	2,260,165	4,520,330	60,313,404	347,780,457	138,225,983	813,868,087
U-Fine	0.000735	1.15	2,984,841	5,969,682	89,895,562	520,670,697	208,476,294	1,228,538,520

Table A-B-8. NASA GeoLab Wing-Body Aeroelastic Sweep Grid Family Statistics.

Wing Body Aero-elastic Sweep								
AE DEG	1ST CELL SIZE	BL MAX GROWTH RATE	BOUNDARY NODES	BOUNDARY FACES	BL NODES	BL CELLS	TOTAL NODES	TOTAL CELLS
2.50	0.001118	1.15	1,125,555	2,251,106	22,400,868	127,488,333	44,158,719	259,240,907
3.00	0.001118	1.15	1,121,242	2,242,480	22,339,744	127,150,782	44,076,098	258,766,322
3.25	0.001118	1.15	1,123,880	2,247,756	22,348,358	127,185,981	44,077,100	258,758,138
3.50	0.001118	1.15	1,124,294	2,248,584	22,396,204	127,468,650	44,145,329	259,167,935
3.75	0.001118	1.15	1,124,810	2,249,616	22,382,789	127,386,228	44,132,000	259,084,730
4.00	0.001118	1.15	1,124,743	2,249,482	22,392,352	127,444,332	44,138,539	259,126,449

B-D-3. DLR SOLAR Unstructured Meshes for DPW-VI

Unstructured quadrilateral/hexahedral dominated grids were generated by Stefan Melber-Wilkending and Stefan Keye using the commercial, hybrid, quad-dominant grid generation package SOLAR, formerly developed by a consortium of ARA, BAE Systems, QinetiQ, and Airbus [87]. Four grid levels, tiny to fine, were successfully built on both configurations. Grid generation was started from the fine level, deriving the coarser grids through a linear scaling of meshing sources by a factor of $1/1.51^3 = 0.873$. All meshes are compliant to the DPW-VI gridding guidelines with two exceptions: (a) wing and nacelle trailing edge base spatial resolution was reduced from the required $\gg$ 8 cells to 2 cells inboard, increasing to 7 cells at the wing tip; (b) wing spanwise spacing was increased from $< 0.1\% \times$ semi-span at root and engine to ~0.34%. Table A-B-9 presents the data of the grids available. Figure A-B-8 shows the quadrilateral-dominated surface grid on the CRM with pylon and nacelle.

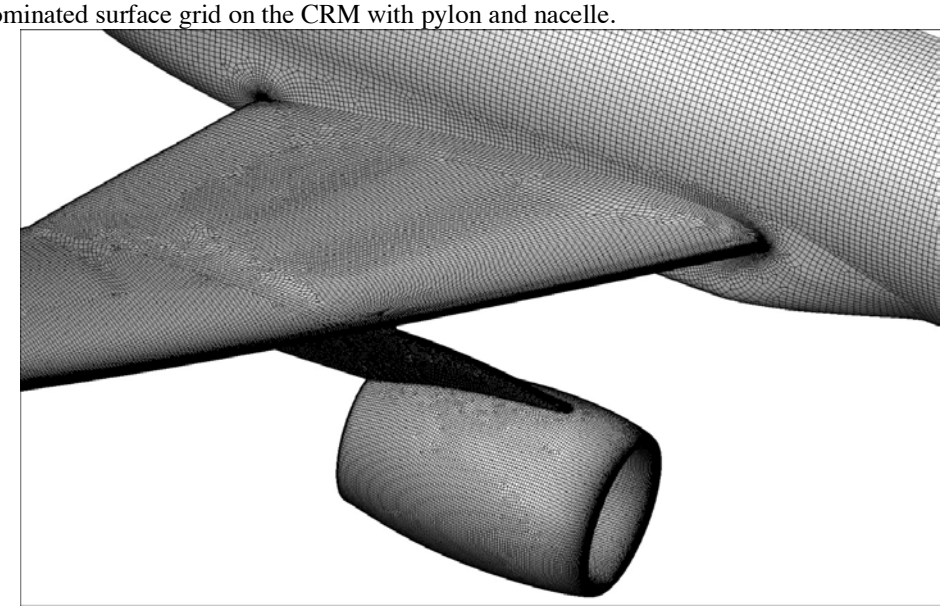


Figure A-B-8. Close-Up of DLR Solar Unstructured Surface Mesh.

Table A-B-9. Grid Resolution DLR Solar Grids (GG: Gridding Guidelines).

Name	WB GG	Solar	WBNP GG	Solar	Δy_1 [in]
Tiny (T)	20	7.15	25–30	11.8	0.001478
Coarse (C)	30	14.1	40–45	23.2	0.001285
Medium (M)	45	26.8	60–70	44.9	0.001118
Fine (F)	70	39.7	85–100	81.1	0.000972

B-D-4. Additional Available Meshes for DPW-VI

Several other grid families are available for download from the DPW-VI website. Mixed element and all-tet element unstructured grids can be found in the *Boeing_Babcock_Unstructured_CC.REV00* directory. The mixed element grids were generated using the MADCAP/AFLR toolset. A mesh sizing template was developed for the WBNP case and used to generate the 7 grid levels. The nacelle/pylon was removed, and the hole was filled for the WB cases. The mixed element grids were converted to generate the all-tet grid sets.

Another set of unstructured grids was made available by the China Aerodynamics Research and Development Center (CARDC). These unstructured grids were generated with Pointwsie (version 17.1 R4) by Dr. Zhang Yaobing. The grids are formatted with CGNS 2.54 and are best for cell-centered solvers. These are found in the *CARDC_ZhangYB_unstructured CC.REV00* directory.

Embraer and CFS Engineering created multiblock structured grids for the CRM. Embraer made a set of multiblock structured grids for the WB configuration available. These were generated by Marcello Areal Ferrari using Embraer's Automatic Mesh Generator (GMA) with Ansys ICEM. These grids are in CGNS format and are found in the *Embraer_Ferrari* directory.

Dominique Charbonnier from CFS Engineering used Ansys ICEM to generate the WBNP grids. These are also in CGNS format and are found in the *CFSE Charbonnier* directory on the DPW-VI website.

Further details on all the grid families can be found in the presentations in the DPW-VI website [72].

Appendix C. Participants

This appendix contains Participant Tables from Sections VI, XV, and Appendix D. They are placed here so as to have all of them available in one convenient location for reference.

C-A. Tables used in Section VI – Participant Descriptions

Table A-C-1. DPW-IV Submissions and Participant Data Key.

Team	ID	SYM	SYM	Name	Organization	Code	Algorithm	Grid Generator	Grid	Turbulence Model
1	A	A		Jan B. Vos	RUAG Aerospace	NSMB	4th order Central Scheme, LU-SGS time integration	ICEMCFD HEXA	Multiblock Structured	Menter k-w SST
2	B	B		O.Brodersen	DLR, Institute of Aerodynamics and Flow Technology	TAU	cell-vertex, finite volume, hybrid, unstructured mesh	Centaur 8.1	Hybrid	SA
	C	C					cell-vertex, finite volume, hybrid, unstructured mesh	SOLAR 13.0	Hybrid	SA
3	D	D		Peter Eliasson	FOI	EDGE	Unstructured node-centered, Finite-volume	SOLAR 13.0	Hybrid	EARSM (Explicit Algebraic Reynolds Stress
4	E	E		Prof N. Balakrishnan	Indian Inst. Science	HIFUN	Upwind, cell-centered	Gambit and Tgrid	Hybrid	SA
5	F	F		Kazuomi YAMAMOTO	JAXA	TAS_Flow code	Upwind, cell-vertex finite volume, Hybrid(Mixed Elm.) unstructured	TAS_Mesh code	hybrid	Spalart-Allmaras model with a modification (SA_mod)
	G	G					Upwind, cell-vertex finite volume, Hybrid(Mixed Elm.) unstructured	TAS_Mesh code	Hex	Spalart-Allmaras model with a modification (SA_mod)
5	H	H				UPACS Ver.2.0	Upwind, cell-centered finite volume, Multi-Block structured	Gridgen (V15.10)	Multiblock Structured	Spalart-Allmaras model with a modification (SA_mod)
6	I	I		Elizabeth Lee-Rausch & Christopher L.	NASA LaRC	FUN3D	Node-Based UMUSCL	VGrid-4.1	Unstructured_ Larc/NodeBase grids)	SA
7	J	J		Mark Chaffin	Cessna	NSU3D	TLNS Node-centered, central diff	VGRID 4.2	Unstructured, Cessna spacing	SA
	K	K					TLNS Node-centered, central diff	VGRID 4.2	Unstructured, Mods by	SA
8	L	L		Ben Rider	Boeing Commercial Airplanes, Seattle	CFL3D	Full NS, finite volume	BCA Zeus	Multiblock Structured	SA
	M	M					Full NS, finite volume	BCA Zeus	Multiblock Structured	Menter k-w SST
	N	N					thin-layer N-S, finite volume	BCA Zeus	Multiblock Structured	SA
	O	O					thin-layer N-S, finite volume	BCA Zeus	Multiblock Structured	Menter k-w SST
9	P	P		Tony Sclafani	Boeing (Huntington)	OVERFLOW	Thin-layer Overset Roe Upwind	MADCAP/ HYPGEN	Overset	SA
10	R	R		Marco Oswald	ANSYS	ANSYS	Density based, FDS Roe Upwind	ICEM Hexa	Multiblock Structured	Menter k-w SST
2	S	S		O.Brodersen	DLR, Institute of Aerodynamics and Flow Technology	TAU	cell-vertex, finite volume, hybrid, unstructured mesh	SOLAR 13.0	Hybrid	Reynolds stress SSG/LRR-omega
	T	T					cell-vertex, finite volume, hybrid, unstructured mesh	SOLAR 13.0	Hybrid	Menter k-w SST
11	U	U		Basant Kumar Gupta	Zeus Numerix Private Ltd.	HLLC	Explicit Time Marching	GridZ	Multiblock Structured	SA
12	V	V		Simon TRAPIER	Airbus	elsA	cell centered finite volume solver, Jameson type scheme	ICEM Hexa	Multiblock Structured	Menter k-w SST
13	W	W		Uriel Goldberg	Metacomp	CFD++	Finite volume unstructured mixed-element cell-based	MIME	Unstr/Hybrid	Realizable k-epsilon
	X	X					Finite volume unstructured mixed-element cell-based	MIME	Unstr/Hybrid	SA

Table A-C-1. (Cont.) DPW-IV Submissions and Participant Data Key.

14	Y	Y		Sebastien ESQUIEU	ONERA	elsA	cell centered finite volume solver, Jameson type	BCA Zeus	Multiblock Structured	SA
15	Z	Z		Dimitri Mavriplis and	U Wyoming	NSU3D	Unstructured, mixed elements, multigrid	VGRID	LaRC Node-Based	SA
	2	2		C. Winkler, A. Dorgan, A. Cary, and M. Mani	Boeing - St. Louis	BCFD	Unstructured, finite volume	AFLR3	mixed-element	SA
16	3	3					Unstructured, finite volume	AFLR3	mixed-element	Menter k-w SST
17	4	4		Lionel Temmerman	NUMECA International	FINE/ Open	Jameson-Schmidt-Turkel Scheme with scalar		Multiblock Structured	SA
3	5	5		Peter Eliasson	FOI	EDGE	Unstructured node-centered, Finite-volume	Tritet	Hybrid	EARSM (Explicit Algebraic Reynolds Stress

Table A-C-2. DPW-V Submissions and Participant Data Key.

Team	ID	SYM	SYM	Name	Organization	Code	Algorithm	Grid Generator	Grid	Turbulence Model
	A			Sclafani	Boeing (Huntington)	OVERFLOW v2.2c	Full NS Central Diff, cell-centered	Common Grid	Overset	SA-Ia
	B							Common Grid	Overset	SA-Ia w/ RC
	C								Custom (Overset)	SA-Ia
	D								Custom (Overset)	SA-Ia QCR
	E								Custom (Overset)	SA-Ia w/ RC
	F								Custom (Overset)	SA-Ia w/ RC QCR
	G								Custom (Overset)	SA-Ia w/ RC
1	H								Custom (Overset)	SA-Ia w/ RC QCR
2	I			Chen	CADRC	MFlow	ROE scheme cell-centered upwind	Common Grid	Hex	SA
	J							Common Grid	Hybrid	SA
3	K			GariÈpy	EcolePolytech Montreal	Fluent V13	Density based solver, ROE scheme, cell-centered, upwind diff	Common Grid	Prism	SA
	L								Custom (Hex)	SA
	M			Scalabrin	Embraer	CFD++	Finite volume unstructured mixed-element cell-centered, upwind	Common Grid	Hex	k-e-RT
	N							Common Grid	Hex	Menter k-w SST
	O							Common Grid	Hybrid	k-e-RT
	P							Common Grid	Hybrid	Menter k-w SST
	Q							Common Grid	Prism	k-e-RT
	R							Common Grid	Prism	Menter k-w SST
	S							ICEM TGRID	Custom (Hybrid)	k-e-RT
4	T							ICEM TGRID	Custom (Hybrid)	Menter k-w SST
	U			Eliasson	FOI	EDGE	Unstructured node-centered, Finite-volume	Common Grid	Hex	EARSM (Explicit Algebraic Reynolds Stress Model)
	V							Common Grid	Hex	SA
5	W							Common Grid	Hex	Menter k-w SST
6	X			Powell	Gulfstream	FUN3D	Node-centered UMUSCL	Common Grid	Hybrid	SA
7	Y			Balakrishnan	Indian Inst.	HiFUN	Upwind, cell-centered	Common Grid	Hex	SA
	Z			Hashimoto	JAXA	FaSTAR	Upwind, cell-centered	Common Grid	Hex	SA-noft2-R
8	2						Upwind, cell-centered	Custom Hex Hexabri oct-	Custom (Hex)	SA-noft2-R

Table A-C-2. (Cont.) DPW-V Submissions and Participant Data Key.

9	3			Yamamoto	JAXA	UPACS	Upwind, cell-vertex finite volume	Common Grid	Multiblock Structured	SA-noft2-R (Crot=1)
	4					UPACS		Common Grid	Multiblock Structured	Menter k-w SST-V
10	5			Olson	NASA Ames	overflow 2.2e_LRS	Full NS Matrix, cell-centered	Common Grid	Overset	Lag RST
11	6			Park	NASA Langley	FUN3D	Node-centered UMUSCL	Common Grid	Hybrid	SA
	7					CFL3D v6.6	Full NS, finite volume, cell centered	Common Grid	Multiblock Structured	SA
12	8			Cai	NPU China	ExStream	Full NS Upwind Diff, cell-centered	Common Grid	Overset	Menter k-w SST-V
13	9			Hue	ONERA	elsA	Full NS Central Diff, cell-centered	Common Grid	Multiblock Structured	SA
14	a			Coder	Penn St. U	OVERFLOW 2.2c	Full NS Upwind Diff, cell-centered	Common Grid	Overset	SA-fv3
15	b			Osusky	U. Toronto	Diablo	Newton-Krylov-Schur with SBP-SAT discretization, matrix diss	Common Grid	Multiblock Structured	SA
	d							Common Grid	Multiblock Structured	SA
16	e			Levy	Cessna Aircraft Co.	NSU3D	TLNS Node-centered, central diff	Common Grid	Hybrid	SA
	f					FUN3D	Node-centered UMUSCL upwind	Common Grid	Hybrid	SA
17	g			Crippa	DLR	TAU	Node-centered, matrix	Common Grid	Hex	SA
	h							Common Grid	Hex	Menter k-w SST-
18	k			Moitra	CRL_INDIA	CFD++	Finite volume unstructured mixed-element cell-centered, upwind	Common Grid	Prism	SA-RC
19	m			Winkler	Boeing (St. Louis)	BCFD	cell-centered	Common Grid	Hex	SA
	n							Common Grid	Hex	Menter k-w SST-
	q							Common Grid	Hex	SA
	r							Common Grid	Hex	Menter k-w SST-
20	t			Temmerman	NUMECA	FINE/	Cell-centereed, scalar diss	Common Grid	Multiblock	SA
21	α			Brodersen	DLR	TAU	Node-centered, matrix diss 1	Custom1-no hexa wake	Custom (Hybrid)	SA
	β							Custom1-no hexa wake	Custom (Hybrid)	SA
	δ							Custom2-hexa wake block	Custom (Hyb w/ Hex-Wake)	SA
	γ							Custom2-hexa wake block	Custom (Hyb w/ Hex-Wake)	SA
	λ							Custom2-hexa wake block	Custom (Hyb w/ Hex-Wake)	Menter k-w SST-V
	π							Custom2-hexa wake block	Custom (Hyb w/ Hex-Wake)	Menter k-w SST-V

Table A-C-3. DPW-VI Submissions and Participant Data Key.

Team	ID	SYM	SYM	Name	Organization	Code	Algorithm	Grid Generator	Grid	Turbulence Model
	A1	A	A		Boeing, BCA Advanced Concepts, Long Beach CA		Full NS Central Diff, cell-centered		Overset	SA-RC
1	A2	a	a	Tony Sclafani		Overflow v.			Overset	SA-RC w/QCR on
	B1	B	B		NASA Langley Research Center		Node-centered UMUSCL upwind		Unst-Geolab	MEAH2015 w/Lim
	B2	b	b						Unst-Geolab	MEAH2015 no-lin
2	B3	α	a	Khaled Abdol-H		FUN3D 12.8			Unst-Geolab	SA no-limiter
	D1	D	D				ROE scheme cell-centered upwind		Unst-Geolab	SA
3	D2	d	d	Jiangtao Chen	CARDC	Mflow			Unst-custom	SA

Table A-C-3. (Cont.) DPW-VI Submissions and Participant Data Key.

4	E1	E	E	Atsushi Hashim	JAXA, Ryoyu Syst	FaSTAR	Upwind, cell-centered		Unst-Geolab	-noft2-R w/QCR20
5	F1	F	F	Krishna Zore	Ansys	Fluent	Density based solver, ROE scheme, cell-centered, upwind diff		Unst-custom	Menter k-w SST-V
6	G1	G	G	Benedikt König	EXA Powerflow	PowerFLOW	LBM	Internal Grid Ger	Custom Cart	LBM-VLES
7	H1	H	H	Ales Prachar/ Peter Eliasson	Aerospace Research and Test Establishment,	Edge	Unstructured node-centered, Finite-volume		Unst-Geolab	SA
	H2	h	h						Unst-Geolab	EARSM (Explicit Algebraic
8	I1	I	I	Anna Rubekina	Mentor Graphics	FloEFD	cell-centered	FloEFD Mesh	Custom Cart	ult k-e Lam-Bremh
	I2	β	b					FloEFD Mesh	Custom Cart	rid k-e Lam-Bremh
	I3	χ	c					FloEFD Mesh	Custom Cart-B	ult k-e Lam-Bremh
9	J1	J	J	Brian Edge	Metacomp	CFD++	cell-centered, upwind		Unst-Boeing	SA
	J2	ϑ	J						Unst-Boeing	Menter k-w SST-
	J3	φ	j						Unst-Geolab	SA
	J4	Ω	W						Unst-custom	lealizable k-epsilo
10	K1	K	K	Taku Nagata	Kawasaki Heavy Industries	Cflow	Cell-centered, MUSCL		Unst-Boeing	SA-noft2
	K2	k	k						Unst-Boeing	A-noft2 w/QCR20
	K3	γ	g					Internal Grid Ger	Custom Cart	SA-noft2
	K4	Γ	G					Internal Grid Ger	Custom Cart	A-noft2 w/QCR20
11	L1	L	L	Stefan Keye / Vamshi Togiti	DLR	TAU	Node-centered, matrix		Unst-custom	RSM-ω
	L2	λ	l						Unst-custom	SA-neg
12	M1	M	M	Ryan S. Glasby	Tennessee, Pointwise, NASA Langley	COFFE/KCF	Node-centered, Finite eleme	Pointwise Tets	Unst-custom	SA-neg
	M2	m	m					Pointwise Tets	Unst-custom	SA-neg w/QCR200
13	N1	N	N	N. Balakrishnan	CAd Lab, Indian Institute of Sci	HiFun	Upwind, cell-centered		Unst-custom	SA
14	O1	O	O	David Hue	ONERA	elsA	Full NS Central Diff, cell-centered		Overset	SA
	O2	ϕ	f						Overset	SA-QCR2000
15	P1	P	P	Todd Michal	Boeing, St. Louis	BCFD	cell-centered		Unst-Boeing	SA-RC
	P2	π	p			GGNS	Node-centered, Finite element		All Tets	SA-RC
16	Q1	Q	Q	Gaetan Kenway	MDOlab, University of Michigan	ADflow	Full NS Central Diff, cell-centered		Embraer MB	SA 1stOrder
	Q2	q	q						Cust-Overset	SA 1stOrder
	Q3	θ	q						Embraer MB	SA-QCR2000
17	R1	R	R	Andrei Cimpoer	CFMS, Zenotech,	ZCFD			Unst-custom	Menter k-w SST-
18	S1	S	S	Kelly Laflin	Textron Aviation (Cessna)	FUN3D	Node-centered UMUSCL upwind		Unst-Geolab	SA-RC
19	T1	T	T	Yuntao Wang	CARDC	TRIP	Upwind Roe cell-centered		CommonMB	Menter k-w
20	U1	U	U	Jim Coder	Applied Research Lab, Penn State	Overflow 2.21 3rd	Full NS Upwind Diff, cell-centered		Overset	SA-RC W/QCF2000
	U2	u	u			Overflow 2.21 5TH	Full NS Upwind Diff, cell-centered		Overset	SA-RC W/QCF2000
21	V1	V	V	Rodrigo Felix de	Embraer S/A	CFD++	Nodel-centered, upwind		Unst-Geolab	Menter k-w SST-
	V2	ς	V						Embraer MB	Menter k-w SST-
	V3	Ξ	X						Unst-custom-A	Menter k-w SST-
	V4	Ψ	Y						Unst-custom-I	Menter k-w SST-
	V5					CMS AERO-F			Unst-custom	SA-QCR2013
22	W1	W	W	Dominic Chanda	Institute of High Performance	μSICS	Node-based	Internal Grid Gen	Unst-custom	SA
23	X1	X	X	Patrick Hanley	Hanley Innovatio	Stallion3D			Custom Cart	k-e
24	Y1	Y	Y	Neil Ashton	University of Oxford,	OpenFOAM	Pressure, Density based solver, cell-centered	SnappyHexMes h	Unst-custom	SA
25	Z1	Z	Z	Yasushi Ito	JAXA, Ryoyu Syst	TAS limiter	Node-based		Unst-Geolab	-noft2-R w/QCR20
	Z2	ζ	z			TAS limiter	Node-based		Unst-Geolab	-noft2-R w/QCR20
	Z3	Δ	D			TAS limiter	Node-based		Unst-Geolab	-noft2-R w/QCR20
	Z4	ε	e			TAS limiter	Node-based		Unst-custom	-noft2-R w/QCR20
	Z5	η	h			TAS limiter	Node-based		Unst-Geolab	SA-noft2-R
	Z6	Π	P			TAS limiter	Node-based		Unst-Boeing	SA-noft2-R
	Z7	Υ	U			TAS limiter	Node-based		Unst-Boeing	-noft2-R w/QCR20

C-B. Tables used in Appendix D - Grid Convergence

Table A-C-4. DPW-IV Participants and Data Set Characteristics-Convergence Slope and Drag in the Continuum: Wing-Body-Tail.

DPW-IV: CRM Wing-Body-Tail iH=0 deg									
Team	ID	SYM	SYM	Organization	Code	Grid	Turbulence Model	dCD/ dGRIDFAC	CD_TOT
1	A	A		RUAG Aerospace	NSMB	Multiblock Structured	Menter k-w SST	10.28	288.34
	C	C				Hybrid	SA	1.26	269.45
3	D	D		Aerospace Research and Test Establishment, FOI	EDGE	Hybrid	EARSM (Explicit Algebraic Reynolds Stress Model)	2.39	278.31
4	E	E		Indian Inst. Science	HiFun	Hybrid	SA	4.93	261.97
5	F	F		JAXA	TAS_Flow code	hybrid	SA model with a modification (SA_mod)	5.43	271.56
	G	G				Custom Cart	SA model with a modification (SA_mod)	5.97	267.36
5	H	H			UPACS Ver.2.0	Multiblock Structured	SA model with a modification (SA_mod)	1.86	269.17
6	I	I		NASA Langley Research Center	FUN3D	unstructured_Larc/ NodeBase grids)	SA	4.03	268.88
7	J	J		Cessna Aircraft Co.	NSU3D	Unstructured, Cessna spacing	SA	6.75	247.52
	K	K				Unstructured, Mods by Shahyar Pirzadeh	SA	5.75	265.21
8	L	L		Boeing Commercial Airplanes, Seattle	CFL3D	Multiblock Structured	SA	1.46	273.47
	M	M				Multiblock Structured	Menter k-w SST	0.80	272.33
	N	N				Multiblock Structured	SA	1.39	271.65
	O	O				Multiblock Structured	Menter k-w SST	0.77	270.98
9	P	P		Boeing (Huntington)	OVERFLOW 2.1	Overset	SA	4.42	264.34
10	R	R		ANSYS	ANSYS	Multiblock Structured	Menter k-w SST	0.57	268.32
2	S	S		DLR, Institute of Aerodynamics and Flow Technology	TAU	Hybrid	Reynolds stress SSG/LRR-omega	0.51	266.92
	T	T				Hybrid	Menter k-w SST	1.26	271.15
11	U	U		Zeus Numerix Private Ltd.	HLLC	Multiblock Structured	SA	4.14	399.40
12	V	V		Airbus	elsA	Multiblock Structured	Menter k-w SST	1.94	271.91
13	W	W		Metacomp	CFD++	Unstr/Hybrid	Realizable k-epsilon	3.95	257.69
	X	X				Unstr/Hybrid	SA	5.75	255.60
14	Y	Y		ONERA	elsA	Multiblock Structured	SA	1.33	272.10
15	Z	Z		U Wyoming	NSU3D	LaRC Node-Based Unstructured Grid Set	SA	1.87	268.65
16	2	2		Boeing - St. Louis	BCFD	mixed-element	SA	6.24	268.55
	3	3				mixed-element	Menter k-w SST	0.03	271.46
17	4	4		NUMECA International	FINE/Open	Multiblock Structured	SA	-16.23	274.13
3	5	5		Aerospace Research and Test Establishment, FOI	EDGE	Hybrid	EARSM (Explicit Algebraic Reynolds Stress Model)	6.13	280.41

Table A-C-5. DPW-V Participants and Data Set Characteristics-Convergence Slope and Drag in the Continuum: Wing-Body (As-Built).

DPW-V: CRM Wing-Body (As-Built)									
Team	ID	SYM	SYM	Organization	Code	Grid	Turbulence Model	dCD/ dGRIDFAC	CD_TOT
1	A			Boeing (Huntington)	OVERFLOW v2.2c	Overset	SA-Ia	2.60	249.17
	B					Overset	SA-Ia w/ RC	2.54	248.01
	E					Custom (Overset)	SA-Ia w/ RC	2.89	247.22
2	I			CADRC	MFlow	Hex	SA	0.83	249.42
	J					Hybrid	SA	5.37	254.60
3	K			EcolePolytech Montreal	Fluent V13	Prism	SA	1.79	249.60
	L					Custom (Hex)	SA	3.33	248.18
4	M			Embraer S/A	CFD++	Hex	k-e-RT	6.63	260.41
	N					Hex	Menter k-w SST	0.20	250.94
	O					Hybrid	k-e-RT	19.48	271.14
	P					Hybrid	Menter k-w SST	8.88	260.14
	Q					Prism	k-e-RT	9.59	259.84
	R					Prism	Menter k-w SST	0.83	250.07
	S					Custom (Hybrid)	k-e-RT	24.30	259.05
	T					Custom (Hybrid)	Menter k-w SST	22.40	243.28
5	U			Aerospace Research and Test Establishment, FOI	EDGE	Hex	EARSM (Explicit Algebraic Reynolds Stress Model)	-0.06	254.93
	V					Hex	SA	0.45	253.79
	W					Hex	Menter k-w SST	0.04	250.01
6	X			Gulfstream	FUN3D	Hybrid	SA	0.98	249.33
7	Y			Indian Inst. Science	HiFun	Hex	SA	0.86	250.55
8	Z			JAXA	FaSTAR	Hex	SA-noft2-R	0.94	248.77
	2					Custom Cart	SA-noft2-R	4.14	251.16
9	3			JAXA	UPACS	Multiblock Structured	SA-noft2-R (Crot=1)	0.83	248.97
	4				UPACS	Multiblock Structured	Menter k-w SST-V	-0.40	252.18
10	5			NASA Ames Research Center	overflow2.2e_LRS	Overset	Lag RST	1.41	252.77
11	6			NASA Langley Research Center	FUN3D v12.2	Hybrid	SA	1.77	248.11
	7				CFL3D v6.6	Multiblock Structured	SA	0.98	249.27
12	8			NPU China	ExStream	Overset	Menter k-w SST-V	2.02	256.83
13	9			ONERA	elsA	Multiblock Structured	SA	0.61	249.29
14	a			Penn St. U	OVERFLOW 2.2c	Overset	SA-fv3	1.35	246.91
15	b			U. Toronto	Diablo	Multiblock Structured	SA	1.47	248.99
	d					Multiblock Structured	SA	0.66	249.38
16	e			Cessna Aircraft Co.	NSU3D	Hybrid	SA	1.89	239.84
	f				FUN3D	Hybrid	SA	0.92	249.59
17	g			DLR, Institute of Aerodynamics and	TAU	Hex	SA	0.19	249.71
	h					Hex	Menter k-w SST-V	-0.33	250.95
18	k			CRL_INDIA	CFD++	Prism	SA-RC	2.98	249.30
19	m			Boeing - St. Louis	BCFD	Hex	SA	1.71	249.23
	n					Hex	Menter k-w SST-V	0.61	251.08
	q					Hex	SA	1.37	248.62
	r					Hex	Menter k-w SST-V	0.24	250.60
20	t			NUMECA	FINE/Open	Multiblock Structured	SA	1.71	258.12

Table A-C-6. DPW-VI Participants and Data Set Characteristics-Convergence Slope and Drag in the Continuum: Wing-Body (Aeroelastic).

DPW-VI: CRM Wing-Body (Aeroelastic)									
Team	ID	SYM	SYM	Organization	Code	Grid	Turbulence Model	dCD/ dGRIDFAC	CD_TOT
1	A1	A	A	Boeing, BCA Advanced Concepts, Long Beach CA	Overflow v2.2k	Overset	SA-RC	2.69	252.25
	A2	a	a			Overset	SA-RC w/QCR on	2.77	254.07
2	B1	B	B	NASA Langley Research Center	FUN3D 12.8	Unst-Geolab	k-kL-MEAH2015 w/Limiter	0.91	257.42
	B2	b	b			Unst-Geolab	k-kL-MEAH2015 no-limiter	2.67	256.32
	B3	α	a			Unst-Geolab	SA no-limiter		
3	D1	D	D	CARDC	Mflow	Unst-Geolab	SA	3.90	254.88
	D2	d	d			Unst-custom	SA	4.81	255.39
4	E1	E	E	JAXA, Ryoyu Systems	FaSTAR	Unst-Geolab	SA-noft2-R w/QCR2000	-1.11	256.06
5	F1	F	F	ANSYS	Fluent	Unst-custom	Menter k-w SST-V	23.54	262.43
6	G1	G	G	EXA Powerflow	PowerFLOW	Custom Cart	LBM-VLES	53.28	283.44
7	H1	H	H	Aerospace Research and Test Establishment, FOI	EDGE	Unst-Geolab	SA	3.37	255.29
	H2	h	h			Unst-Geolab	EARSM (Explicit Algebraic Reynolds Stress Model)	-7.20	261.29
8	I1	I	I	Mentor Graphics	FloEFD	Custom Cart	Default k-e Lam-Bremhorst	3.58	280.67
	I2	β	b			Custom Cart	Subgrid k-e Lam-Bremhorst	3.11	322.37
	I3	χ	c			Custom Cart-B	Default k-e Lam-Bremhorst	6.40	295.98
9	J1	J	J	Metacomp	CFD++	Unst-Boeing	SA	3.89	256.86
	J2	θ	J			Unst-Boeing	Menter k-w SST-V	6.13	257.91
	J3	φ	j			Unst-Geolab	SA	5.62	255.13
10	K1	K	K	Kawasaki Heavy Industries	Cflow	Unst-Boeing	SA-noft2	4.43	259.71
	K2	k	k			Unst-Boeing	SA-noft2 w/QCR200	4.88	260.86
	K3	γ	g			Custom Cart	SA-noft2	4.71	253.36
	K4	Γ	G			Custom Cart	SA-noft2 w/QCR200	4.71	253.36
11	L1	L	L	DLR, Institute of Aerodynamics and Flow	TAU	Unst-custom	RSM-ω	1.65	257.86
	L2	λ	l			Unst-custom	SA-neg	1.84	255.00
12	M1	M	M	Tennessee, Pointwise, NASA Langley, NAVAIR, MIT, U Ala	COFFE/KCFD	Unst-custom	SA-neg	0.45	255.54
13	N1	N	N	CAd Lab, Indian Institute of Sci	HiFun	Unst-custom	SA	-0.21	251.58
14	O1	O	O	ONERA	elsA	Overset	SA	0.28	253.01
15	P1	P	P	Boeing - St. Louis	BCFD	Unst-Boeing	SA-RC	1.98	254.49
	P2	π	p		GGNS	All Tets	SA-RC	1.54	256.00
16	Q1	Q	Q	MDOlab, University of Michigan	ADflow	Embraer MB	SA 1stOrder	4.00	253.34
	Q2	q	q			Cust-Overset	SA 1stOrder	1.52	253.80
	Q3	θ	q			Embraer MB	SA-QCR2000	4.07	255.03
18	S1	S	S	Textron Aviation (Cessna)	FUN3D	Unst-Geolab	SA-RC	9.70	250.60
19	T1	T	T	CARDC	TRIP	CommonMB	Menter k-w SST-2003	3.42	254.76
20	U1	U	U	Applied Research Lab, Penn State	Overflow 2.21 3rd Order WENO	Overset	SA-RC W/QCF2000	0.91	254.69
	U2	u	u		Overflow 2.21 5TH Order WENO	Overset	SA-RC W/QCF2000	0.97	254.17
21	V1	V	V	Embraer S/A	CFD++	Unst-Geolab	Menter k-w SST-V	0.18	253.91
	V2	ς	V			Embraer MB	Menter k-w SST-V	0.93	255.55
	V3	Ξ	X			Unst-custom-A	Menter k-w SST-V	0.83	254.35
	V4	Ψ	Y			Unst-custom-I	Menter k-w SST-V	0.83	255.35
25	Z1	Z	Z	JAXA, Ryoyu Systems	TAS limiter K=1	Unst-Geolab	SA-noft2-R w/QCR2000	-0.04	260.02
	Z2	ζ	z		TAS limiter K=5	Unst-Geolab	SA-noft2-R w/QCR2000	-0.33	259.68
	Z3	Δ	D		TAS limiter K=10	Unst-Geolab	SA-noft2-R w/QCR2000	0.32	258.83
	Z4	ε	e		TAS limiter K=10	Unst-custom	SA-noft2-R w/QCR2000	1.19	259.56
	Z5	η	h		TAS limiter K=5	Unst-Geolab	SA-noft2-R	0.88	253.32
	Z6	Π	P		TAS limiter K=5	Unst-Boeing	SA-noft2-R	5.45	258.15
	Z7	Υ	U		TAS limiter K=5	Unst-Boeing	SA-noft2-R w/QCR2000	5.99	263.16

Table A-C-7. DPW6 Participants and Data Set Characteristics-Convergence Slope and Drag in the Continuum: Wing-Body-Nacelle-Pylon (Aeroelastic).

DPW-VI: CRM Wing-Body-Nacelle-Pylon (Aeroelastic)									
Team	ID	SYM	SYM	Organization	Code	Grid	Turbulence Model	dCD/ dGRIDFAC	CD_TOT
1	A1	A	A	Boeing, BCA Advanced Concepts, Long Beach CA	Overflow v2.2k	Overset	SA-RC	4.51	273.91
	A2	a	a			Overset	SA-RC w/QCR on	4.57	275.60
2	B1	B	B	NASA Langley Research Center	FUN3D 12.8	Unst-Geolab	k-kL-MEAH2015 w/Limiter	1.97	279.87
	B2	b	b			Unst-Geolab	k-kL-MEAH2015 no-limiter	2.81	278.59
3	D1	D	D	CARDC	Mflow	Unst-Geolab	SA	16.79	279.15
	D2	d	d			Unst-custom	SA	7.58	277.18
4	E1	E	E	JAXA, Ryoyu Systems	FaSTAR	Unst-Geolab	SA-noft2-R w/QCR2000	-0.65	277.48
5	F1	F	F	ANSYS	Fluent	Unst-custom	Menter k-w SST-V	32.90	286.22
6	G1	G	G	EXA Powerflow	PowerFLOW	Custom Cart	LBM-VLES	78.02	305.93
7	H1	H	H	Aerospace Research and Test Establishment, FOI	EDGE	Unst-Geolab	SA	3.76	276.95
	H2	h	h			Unst-Geolab	EARSM (Explicit Algebraic Reynolds Stress Model)	-7.85	282.02
8	I1	I	I	Mentor Graphics	FloEFD	Custom Cart	Default k-e Lam-Bremhorst	4.30	300.23
	I2	β	b			Custom Cart	Subgrid k-e Lam-Bremhorst	3.70	341.68
9	J1	J	J	Metacomp	CFD++	Unst-Boeing	SA	2.36	284.11
	J2	ϑ	J			Unst-Boeing	Menter k-w SST-V	4.97	284.37
	J3	φ	j			Unst-Geolab	SA	7.71	277.58
10	K1	K	K	Kawasaki Heavy Industries	Cflow	Unst-Boeing	SA-noft2	3.94	285.44
	K2	k	k			Unst-Boeing	SA-noft2 w/QCR200	4.27	286.59
	K3	γ	g			Custom Cart	SA-noft2	8.15	275.03
	K4	Γ	G			Custom Cart	SA-noft2 w/QCR200	8.15	275.03
11	L1	L	L	DLR, Institute of Aerodynamics and Flow	TAU	Unst-custom	RSM-ω	3.74	278.82
	L2	λ	l			Unst-custom	SA-neg	3.72	277.24
12	M1	M	M	Tennessee, Pointwise, NASA Langley, NAVAIR, MIT, U Ala	COFFE/KCFD	Unst-custom	SA-neg	0.52	279.93
13	N1	N	N	CAd Lab, Indian Institute of Sci	HiFun	Unst-custom	SA	0.90	274.12
14	O1	O	O	ONERA	elsA	Overset	SA	0.71	274.43
15	P1	P	P	Boeing - St. Louis	BCFD	Unst-Boeing	SA-RC	4.39	276.23
16	Q1	Q	Q	MDOlab, University of Michigan	ADflow	Embraer MB	SA 1stOrder	6.89	276.82
	Q2	q	q			Cust-Overset	SA 1stOrder	2.75	276.03
18	S1	S	S	Textron Aviation (Cessna)	FUN3D	Unst-Geolab	SA-RC	177.47	232.85
19	T1	T	T	CARDC	TRIP	CommonMB	Menter k-w SST-2003	4.76	277.47
20	U1	U	U	Applied Research Lab, Penn State	Overflow 2.21 3rd Order WENO	Overset	SA-RC W/QCF2000	1.30	276.02
	U2	u	u		Overflow 2.21 5TH Order WENO	Overset	SA-RC W/QCF2000	0.99	275.61
21	V1	V	V	Embraer S/A	CFD++	Unst-Geolab	Menter k-w SST-V	0.06	275.77
	V3	Ξ	X			Unst-custom-A	Menter k-w SST-V	1.79	275.63
	V4	Ψ	Y			Unst-custom-I	Menter k-w SST-V	1.24	279.59
25	Z1	Z	Z	JAXA, Ryoyu Systems	TAS limiter K=1	Unst-Geolab	SA-noft2-R w/QCR2000	1.09	282.04
	Z2	ζ	z		TAS limiter K=5	Unst-Geolab	SA-noft2-R w/QCR2000	0.42	281.67
	Z3	Δ	D		TAS limiter K=10	Unst-Geolab	SA-noft2-R w/QCR2000	0.69	280.83
	Z4	ε	e		TAS limiter K=10	Unst-custom	SA-noft2-R w/QCR2000	1.55	282.87

Table A-C-8. DPW5: Participants Detail on Side-of-Body Separation.

ID	SYM	SYM	Name	Organization	Code	Algorithm	Grid Generator	Grid	Turbulence Model	SOB Sep
2			Hashimoto	JAXA	FaSTAR	Upwind, cell-centered	Custom Hex Hexabri oct-	Custom (Hex)	SA-noft2-R	N
5			Olson	NASA Ames	overflow2.2e_LRS	Full NS Matrix, cell-centered	Common Grid	Overset	Lag RST	N
7			Park	NASA Langley	CFL3D v6.6	Full NS, finite volume, cell centered	Common Grid	Multiblock Structured	SA	N
9			Hue	ONERA	elsA	Full NS Central Diff, cell-centered	Common Grid	Multiblock Structured	SA	N
d			Osusky	U. Toronto	Diablo	Newton-Krylov-Schur with SBP-SAT discretization, matrix diss	Common Grid	Multiblock Structured	SA	N
D			Sclafani	Boeing (Huntington)	OVERFLOW v2.2c	Full NS Central Diff, cell-centered	Custom Grid	Custom (Overset)	SA-Ia QCR	N
e			Levy	Cessna Aircraft Co.	NSU3D	TLNS Node-centered, central diff	Common Grid	Hybrid	SA	N
F			Sclafani	Boeing (Huntington)	OVERFLOW v2.2c	Full NS Central Diff, cell-centered	Custom Grid	Custom (Overset)	SA-Ia w/ RC QCR	N
h			Crippa	DLR	TAU	Node-centered, matrix	Common Grid	Hex	Menter k-w SST-V	N
H			Sclafani	Boeing (Huntington)	OVERFLOW v2.2c	Full NS Central Diff, cell-centered	Custom Grid	Custom (Overset)	SA-Ia w/ RC QCR	N
I			Chen	CADRC	MFlow	ROE scheme cell-centered upwind	Common Grid	Hex	SA	N
J			Chen	CADRC	MFlow	ROE scheme cell-centered upwind	Common Grid	Hybrid	SA	N
k			Moitra	CRL_INDIA	CFD++	Finite volume unstructured mixed-element cell-centered, upwind	Common Grid	Prism	SA-RC	N
λ	l		Brodersen	DLR	TAU	Node-centered, matrix diss 1	Custom2-hexa wake block	Custom (Hyb w/ Hex-Wake)	Menter k-w SST-V	N
m			Winkler	Boeing (St. Louis)	BCFD	cell-centered	Common Grid	Hex	SA	N
n			Winkler	Boeing (St. Louis)	BCFD	cell-centered	Common Grid	Hex	Menter k-w SST-V	N
π	p		Brodersen	DLR	TAU	Node-centered, matrix diss 1	Custom2-hexa wake block	Custom (Hyb w/ Hex-Wake)	Menter k-w SST-V	N
P			Scalabrin	Embraer	CFD++	Finite volume unstructured mixed-element cell-centered, upwind	Common Grid	Hybrid	Menter k-w SST	N
q			Winkler	Boeing (St. Louis)	BCFD	cell-centered	Common Grid	Hex	SA	N
r			Winkler	Boeing (St. Louis)	BCFD	cell-centered	Common Grid	Hex	Menter k-w SST-V	N
t			Temmerman	NUMECA	FINE/Open	Cell-centereed, scalar diss	Common Grid	Multiblock Structured	SA	N
U			Eliasson	FOI	EDGE	Unstructured node-centered, Finite-volume	Common Grid	Hex	EARSM (Explicit Algebraic Reynolds	N
V			Eliasson	FOI	EDGE	Unstructured node-centered, Finite-volume	Common Grid	Hex	SA	N
W			Eliasson	FOI	EDGE	Unstructured node-centered, Finite-volume	Common Grid	Hex	Menter k-w SST	N
Ξ	X		Powell	Gulfstream	FUN3D	Node-centered UMUSCL	Custom Grid	Custom Hex)	SA	N
ψ	y		Powell	Gulfstream	USM3D		Custom Grid	Custom Hex)	SA	N
3			Yamamoto	JAXA	UPACS	Upwind, cell-vertex finite volume	Common Grid	Multiblock Structured	SA-noft2-R(Crot=1)	y
4			Yamamoto	JAXA	UPACS	Upwind, cell-vertex finite volume	Common Grid	Multiblock Structured	Menter k-w SST-V	Y
6			Park	NASA Langley	FUN3D v12.2	Node-centered UMUSCL	Common Grid	Hybrid	SA	Y
8			Cai	NPU China	ExStream	Full NS Upwind Diff, cell-centered	Common Grid	Overset	Menter k-w SST-V	y
α	a		Brodersen	DLR	TAU	Node-centered, matrix diss 1	Custom1-no hexa wake	Custom (Hybrid)	SA	y
a			Coder	Penn St. U	OVERFLOW 2.2c	Full NS Upwind Diff, cell-centered	Common Grid	Overset	SA-fv3	Y
β	b		Brodersen	DLR	TAU	Node-centered, matrix diss 1	Custom1-no hexa wake	Custom (Hybrid)	SA	y
b			Osusky	U. Toronto	Diablo	Newton-Krylov-Schur with SBP-SAT discretization, matrix diss	Common Grid	Multiblock Structured	SA	Y
C			Sclafani	Boeing (Huntington)	OVERFLOW v2.2c	Full NS Central Diff, cell-centered	Custom Grid	Custom (Overset)	SA-Ia	Y
δ	d		Brodersen	DLR	TAU	Node-centered, matrix diss 1	Custom2-hexa wake block	Custom (Hyb w/ Hex-Wake)	SA	Y
E			Sclafani	Boeing (Huntington)	OVERFLOW v2.2c	Full NS Central Diff, cell-centered	Custom Grid	Custom (Overset)	SA-Ia w/ RC	y
f			Levy	Cessna Aircraft Co.	FUN3D	Node-centered UMUSCL upwind	Common Grid	Hybrid	SA	Y
γ	g		Brodersen	DLR	TAU	Node-centered, matrix diss 1	Custom2-hexa wake block	Custom (Hyb w/ Hex-Wake)	SA	Y
g			Crippa	DLR	TAU	Node-centered, matrix	Common Grid	Hex	SA	y
G			Sclafani	Boeing (Huntington)	OVERFLOW v2.2c	Full NS Central Diff, cell-centered	Custom Grid	Custom (Overset)	SA-Ia w/ RC	Y
L			GariÈpy	EcolePolytech Montreal	Fluent V13	Density based solver, ROE scheme, cell-centered, upwind diff	Custom Grid	Custom (Hex)	SA	Y
N			Scalabrin	Embraer	CFD++	Finite volume unstructured mixed-element cell-centered, upwind	Common Grid	Hex	Menter k-w SST	y
R			Scalabrin	Embraer	CFD++	Finite volume unstructured mixed-element cell-centered, upwind	Common Grid	Prism	Menter k-w SST	y
σ	s		Yamamoto	JAXA	UPACS	Upwind, cell-vertex finite volume	Gridgen	Multiblock Structured	SA-noft2-R(Crot=1)	Y
T			Scalabrin	Embraer	CFD++	Finite volume unstructured mixed-element cell-centered, upwind	ICEM TGRID	Custom (Hybrid)	Menter k-w SST	y
ϖ	v		Yamamoto	JAXA	UPACS	Upwind, cell-vertex finite volume	Gridgen	Multiblock Structured	Menter k-w SST-V	Y
X			Powell	Gulfstream	FUN3D	Node-centered UMUSCL	Common Grid	Hybrid	SA	Y
Y			Balakrishnan	Indian Inst. Science	HiFUN	Upwind, cell-centered	Common Grid	Hex	SA	y
Z			Hashimoto	JAXA	FaSTAR	Upwind, cell-centered	Common Grid	Hex	SA-noft2-R	Y
M			Scalabrin	Embraer	CFD++	Finite volume unstructured mixed-element cell-centered, upwind	Common Grid	Hex	k-e-RT	O
O			Scalabrin	Embraer	CFD++	Finite volume unstructured mixed-element cell-centered, upwind	Common Grid	Hybrid	k-e-RT	O
Q			Scalabrin	Embraer	CFD++	Finite volume unstructured mixed-element cell-centered, upwind	Common Grid	Prism	k-e-RT	O
S			Scalabrin	Embraer	CFD++	Finite volume unstructured mixed-element cell-centered, upwind	ICEM TGRID	Custom (Hybrid)	k-e-RT	O
A			Sclafani	Boeing (Huntington)	OVERFLOW v2.2c	Full NS Central Diff, cell-centered	Common Grid	Overset	SA-Ia	-
B			Sclafani	Boeing (Huntington)	OVERFLOW v2.2c	Full NS Central Diff, cell-centered	Common Grid	Overset	SA-Ia w/ RC	-
K			GariÈpy	EcolePolytech Montreal	Fluent V13	Density based solver, ROE scheme, cell-centered, upwind diff	Common Grid	Prism	SA	-

N - No Side-of-Body Separation. Y - Side-of-Body Separation Prior to 4 deg, O - Other Outlier, - Insufficient Information Provided

Table A-C-9. DPW6: Participants Detail on Side-of-Body Separation.

ID	SYM	SYM	Name	Organization	Code	Algorithm	Grid Generator	Grid	Turbulence Model	SOB Sep
A2	a	a	Tony Sclafani	Boeing, BCA Advanced Concepts, Long Beach	Overflow v2.2k	Full NS Central Diff, cell-centered		Overset	SA-RC w/QCR on	N
B1	B	B	Khaled Abdol-Hamid	NASA Langley Research Center	FUN3D 12.8	Node-centered UMUSCL upwind		Unst-Geolab	kL-MEAH2015 w/Limiter	N
B2	b	b	Khaled Abdol-Hamid	NASA Langley Research Center	FUN3D 12.8	Node-centered UMUSCL upwind		Unst-Geolab	kL-MEAH2015 no-limiter	N
E1	E	E	Atsushi Hashimoto	JAXA, Ryoyu Systems	FaSTAR	Upwind, cell-centered		Unst-Geolab	SA-noft2-R w/QCR2000	N
H1	H	H	Ales Prachar/ Peter Eliasson	Aerospace Research and Test	Edge	Unstructured node-centered, Finite-volume		Unst-Geolab	SA	N
H2	h	h	Ales Prachar/ Peter Eliasson	Aerospace Research and Test	Edge	Unstructured node-centered, Finite-volume		Unst-Geolab	EARSM (Explicit Algebraic Reynolds	N
K3	γ	g	Taku Nagata	Kawasaki Heavy Industries	Cflow	Cell-centered, MUSCL	nternal Grid Gen	Custom Cart	SA-noft2	N
K4	Γ	G	Taku Nagata	Kawasaki Heavy Industries	Cflow	Cell-centered, MUSCL	nternal Grid Gen	Custom Cart	SA-noft2 w/QCR200	N
L1	L	L	Stefan Keye / Vamshi Togiti	DLR	TAU	Node-centered, matrix		Unst-custom	RSM-ω	N
L2	λ	l	Stefan Keye / Vamshi Togiti	DLR	TAU	Node-centered, matrix		Unst-custom	SA-neg	N
M2	m	m	Ryan S. Glasby	Tennessee, Pointwise, NASA Langley, NAVAIR, MIT, U Ala	COFFE/KCFD	Node-centered, Finite element	Pointwise Tets	Unst-custom	SA-neg w/QCR2000	N
O2	ϕ	f	David Hue	ONERA	elsA	Full NS Central Diff, cell-centered		Overset	SA-QCR2000	N
Q2	q	q	Gaetan Kenway	MDOlab, University of Michigan	ADflow	Full NS Central Diff, cell-centered		Cust-Overset	SA 1stOrder	N
Q3	θ	q	Gaetan Kenway	MDOlab, University of Michigan	ADflow	Full NS Central Diff, cell-centered		Embraer MB	SA-QCR2000	N
T1	T	T	Yuntao Wang	CARDC	TRIP	Upwind Roe cell-centered		CommonMB	Menter k-w SST-2003	N
U1	U	U	Jim Coder	Applied Research Lab, Penn State	Overflow 2.21 3rd Order WENO	Full NS Upwind Diff, cell-centered		Overset	SA-RC W/QCR2000	N
U2	u	u	Jim Coder	Applied Research Lab, Penn State	Overflow 2.21 5TH Order WENO	Full NS Upwind Diff, cell-centered		Overset	SA-RC W/QCR2000	N
Z1	Z	Z	Yasushi Ito	JAXA, Ryoyu Systems	TAS limiter K=1	Node-based		Unst-Geolab	SA-noft2-R w/QCR2000	N
Z2	ζ	z	Yasushi Ito	JAXA, Ryoyu Systems	TAS limiter K=5	Node-based		Unst-Geolab	SA-noft2-R w/QCR2000	N
Z3	Δ	D	Yasushi Ito	JAXA, Ryoyu Systems	TAS limiter K=10	Node-based		Unst-Geolab	SA-noft2-R w/QCR2000	N
B3	α	a	Khaled Abdol-Hamid	NASA Langley Research Center	FUN3D 12.8	Node-centered UMUSCL upwind		Unst-Geolab	SA no-limiter	Y
D1	D	D	Jiangtao Chen	CARDC	Mflow	ROE scheme cell-centered upwind		Unst-Geolab	SA	Y
D2	d	d	Jiangtao Chen	CARDC	Mflow	ROE scheme cell-centered upwind	nternal Grid Gen	Unst-custom	SA	Y
I1	I	I	Anna Rubekinak	Mentor Graphics	FloEFD	cell-centered	FloEFD Mesh	Custom Cart	efault k-e Lam-Bremhorst	Y
J1	J	J	Brian Edge	Metacomp	CFD++	cell-centered, upwind		Unst-Boeing	SA	Y
J2	ϑ	J	Brian Edge	Metacomp	CFD++	cell-centered, upwind		Unst-Boeing	Menter k-w SST-V	Y
K1	K	K	Taku Nagata	Kawasaki Heavy Industries	Cflow	Cell-centered, MUSCL		Unst-Boeing	SA-noft2	Y
K2	k	k	Taku Nagata	Kawasaki Heavy Industries	Cflow	Cell-centered, MUSCL		Unst-Boeing	SA-noft2 w/QCR200	Y
M1	M	M	Ryan S. Glasby	Tennessee, Pointwise, NASA Langley, NAVAIR, MIT, U Ala	COFFE/KCFD	Node-centered, Finite element	Pointwise Tets	Unst-custom	SA-neg	Y
N1	N	N	N. Balakrishnan	CAd Lab, Indian Institute of Sci	HiFun	Upwind, cell-centered	nternal Grid Gen	Unst-custom	SA	Y
O1	O	O	David Hue	ONERA	elsA	Full NS Central Diff, cell-centered		Overset	SA	Y
P1	P	P	Todd Michal	Boeing, St. Louis	BCFD	cell-centered		Unst-Boeing	SA-RC	Y
Q1	Q	Q	Gaetan Kenway	MDOlab, University of Michigan	ADflow	Full NS Central Diff, cell-centered		Embraer MB	SA 1stOrder	Y
S1	S	S	Kelly Laflin	Textron Aviation (Cessna)	FUN3D	Node-centered UMUSCL upwind		Unst-Geolab	SA-RC	Y
V1	V	V	odrigo Felix de Souza	Embraer S/A	CFD++	Nodel-centered, upwind		Unst-Geolab	Menter k-w SST-V	Y
V2	ς	V	odrigo Felix de Souza	Embraer S/A	CFD++	Nodel-centered, upwind		Embraer MB	Menter k-w SST-V	Y
V3	Ξ	X	odrigo Felix de Souza	Embraer S/A	CFD++	Nodel-centered, upwind		Unst-custom-A	Menter k-w SST-V	Y
V4	Ψ	Y	odrigo Felix de Souza	Embraer S/A	CFD++	Nodel-centered, upwind		Unst-custom-I	Menter k-w SST-V	Y
F1	F	F	Krishna Zore	Ansys	Fluent	Density based solver, ROE scheme, cell-centered, upwind diff	nternal Grid Gen	Unst-custom	Menter k-w SST-V	O
G1	G	G	Benedikt König	EXA Powerflow	PowerFLOW	LBM	nternal Grid Gen	Custom Cart	LBM-VLES	O
I2	β	b	Anna Rubekinak	Mentor Graphics	FloEFD	cell-centered	FloEFD Mesh	Custom Cart	bgrid k-e Lam-Bremhorst	O
A1	A	A	Tony Sclafani	Boeing, BCA Advanced Concepts, Long Beach	Overflow v2.2k	Full NS Central Diff, cell-centered		Overset	SA-RC	-
I3	χ	c	Anna Rubekinak	Mentor Graphics	FloEFD	cell-centered	FloEFD Mesh	Custom Cart-B	efault k-e Lam-Bremhorst	-
J3	φ	j	Brian Edge	Metacomp	CFD++	cell-centered, upwind		Unst-Geolab	SA	-
J4	Ω	W	Brian Edge	Metacomp	CFD++	cell-centered, upwind	nternal Grid Gen	Unst-custom	Realizable k-epsilon	-
P2	π	p	Todd Michal	Boeing, St. Louis	GGNS	Node-centered, Finite element		All Tets	SA-RC	-
R1	R	R	Andrei Cimpoeru	CFMS, Zenotech, ARA	ZCFD			Unst-custom	Menter k-w SST-V	-
V5			Rodrigo Felix de Souza	Embraer S/A	CMS AERO-F			Unst-custom	SA-QCR2013	-
W1	W	W	Dominic Chandar	Institute of High Performance	μSICS	Node-based	Internal Grid Gen	Unst-custom	SA	-
X1	X	X	Patrick Hanley	Hanley Innovations	Stallion3D			Custom Cart	k-e	-
Y1	Y	Y	Neil Ashton	University of Oxford, ESI Group, BETA CAE Systems	OpenFOAM	Pressure, Density based solver, cell-centered	SnappyHexMesh	Unst-custom	SA	-
Z4	ε	e	Yasushi Ito	JAXA, Ryoyu Systems	TAS limiter K=10	Node-based	nternal Grid Gen	Unst-custom	SA-noft2-R w/QCR2000	-
Z5	η	h	Yasushi Ito	JAXA, Ryoyu Systems	TAS limiter K=5	Node-based		Unst-Geolab	SA-noft2-R	-
Z6	Π	P	Yasushi Ito	JAXA, Ryoyu Systems	TAS limiter K=5	Node-based		Unst-Boeing	SA-noft2-R	-
Z7	Υ	U	Yasushi Ito	JAXA, Ryoyu Systems	TAS limiter K=5	Node-based		Unst-Boeing	SA-noft2-R w/QCR2000	-

N - No Side-of-Body Separation. Y - Side-of-Body Separation Prior to 4 deg, O - Other Outlier, - Insufficient Information Provided

Table A-C-10. DPW6: Solutions minus Outliers Comparison to Test Data.

ID	SYM	SYM	Name	Organization	Code	Algorithm	Grid	Turbulence Mode
"Selected" Solutions that Match Test data								
H2	h	h	Ales Prachar/ Peter Eliasson	Aerospace Research and Test Establishment, FOI	Edge	Unstructured node-centered, Finite-volume	Unst-Geolab	EARSM (Explicit Algebraic Reynolds Stress Model)
K3	γ	g	Taku Nagata	Kawasaki Heavy Industries	Cflow	Cell-centered, MUSCL	Custom Cart	SA-noft2
O2	ϕ	f	David Hue	ONERA	elsA	Full NS Central Diff, cell-centered	Overset	SA-QCR2000
A2	a	a	Tony Sclafani	Boeing, BCA Advanced Concepts, Long Beach CA	Overflow v2.2k	Full NS Central Diff, cell-centered	Overset	SA-RC W/QCR2000
U1	U	U	Jim Coder	Applied Research Lab, Penn State	Overflow 2.21 3rd Order WENO	Full NS Upwind Diff, cell-centered	Overset	SA-RC W/QCR2000
U2	u	u	Jim Coder	Applied Research Lab, Penn State	Overflow 2.21 5TH Order WENO	Full NS Upwind Diff, cell-centered	Overset	SA-RC W/QCR2000
SA Turbulence Model Solutions that Do Not Match Test Data								
H1	H	H	Ales Prachar/ Peter Eliasson	Aerospace Research and Test Establishment, FOI	Edge	Unstructured node-centered, Finite-volume	Unst-Geolab	SA
Q2	q	q	Gaetan Kenway	MDOlab, University of Michigan	ADflow	Full NS Central Diff, cell-centered	Cust-Overset	SA 1stOrder
L2	λ	l	Stefan Keye / Vamshi Togiti	DLR	TAU	Node-centered, matrix	Unst-custom	SA-neg
SA w/QCR2000 Turbulence Model Solutions that Do Not Match Test Data								
¥	m	m	Ryan S. Glasby	Tennessee, Pointwise, NASA Langley, NAVAIR, MIT, U Ala	COFFE/KCFD	Node-centered, Finite element	Unst-custom	SA-neg w/QCR2000
K4	Γ	G	Taku Nagata	Kawasaki Heavy Industries	Cflow	Cell-centered, MUSCL	Custom Cart	SA-noft2 w/QCR200
E1	E	E	Atsushi Hashimoto	JAXA, Ryoyu Systems	FaSTAR	Upwind, cell-centered	Unst-Geolab	SA-noft2-R w/QCR2000
Z1	Z	Z	Yasushi Ito	JAXA, Ryoyu Systems	TAS limiter K=1	Node-based	Unst-Geolab	SA-noft2-R w/QCR2000
Z3	Δ	D	Yasushi Ito	JAXA, Ryoyu Systems	TAS limiter K=10	Node-based	Unst-Geolab	SA-noft2-R w/QCR2000
Z2	ζ	z	Yasushi Ito	JAXA, Ryoyu Systems	TAS limiter K=5	Node-based	Unst-Geolab	SA-noft2-R w/QCR2000
Q3	θ	q	Gaetan Kenway	MDOlab, University of Michigan	ADflow	Full NS Central Diff, cell-centered	Embraer MB	SA-QCR2000
Two-Equation Turbulence Model Solutions that Do Not Match Test Data								
B2	b	b	Khaled Abdol-Hamid	NASA Langley Research Center	FUN3D 12.8	Node-centered UMUSCL upwind	Unst-Geolab	k-kL-MEAH2015 no-limiter
B1	B	B	Khaled Abdol-Hamid	NASA Langley Research Center	FUN3D 12.8	Node-centered UMUSCL upwind	Unst-Geolab	k-kL-MEAH2015 w/Limiter
T1	T	T	Yuntao Wang	CARDC	TRIP	Upwind Roe cell-centered	CommonMB	Menter k-w SST-2003
L1	L	L	Stefan Keye / Vamshi Togiti	DLR	TAU	Node-centered, matrix	Unst-custom	RSM-ω

Appendix D. Convergence

This appendix contains plots from Section VII – Grid Convergence Study with additional plots showing further parsing by grid and turbulence model. The participant data-set key for each Workshop is found in Appendix C.

D-A. Richardson Extrapolation

A recurring case in all of the Drag Prediction Workshops had been the grid convergence study. A standard technique in grid convergence studies is to use Richardson extrapolation [40]. Solutions are obtained on a parametric family of three-dimensional meshes that have been "uniformly" refined in all three coordinate directions. Computational results are plotted versus grid factor, $N^{-2/3}$ (called GRIDFAC in the figures), where N is the number of unknowns. For second order codes, a linear fit should be observed with decreasing error as long as the refinement is in the asymptotic region. The y-intercept then estimates the theoretical infinite resolution (continuum) result. An example is shown in Fig. A-D-1. The slope of the linear fit (dCDT/dGRIDFAC) denotes the change in drag for a change in the GRIDFAC parameter. This can be thought of as the sensitivity of the solver/grid/turbulence model to grid size as long as the grid is in the asymptotic region. As discussed in Section IV, Gridding Guidelines and Description of Common Grids and in Appendix B, Grids, the pragmatic approach to grid generation has been to define guidelines that result in grid families that feature some level of uniformity and consistency. Grid convergence sensitivity slope, dCDT/dGRIDFAC, and drag in the continuum (GRIDFAC = 0) are listed in the tables that follow.

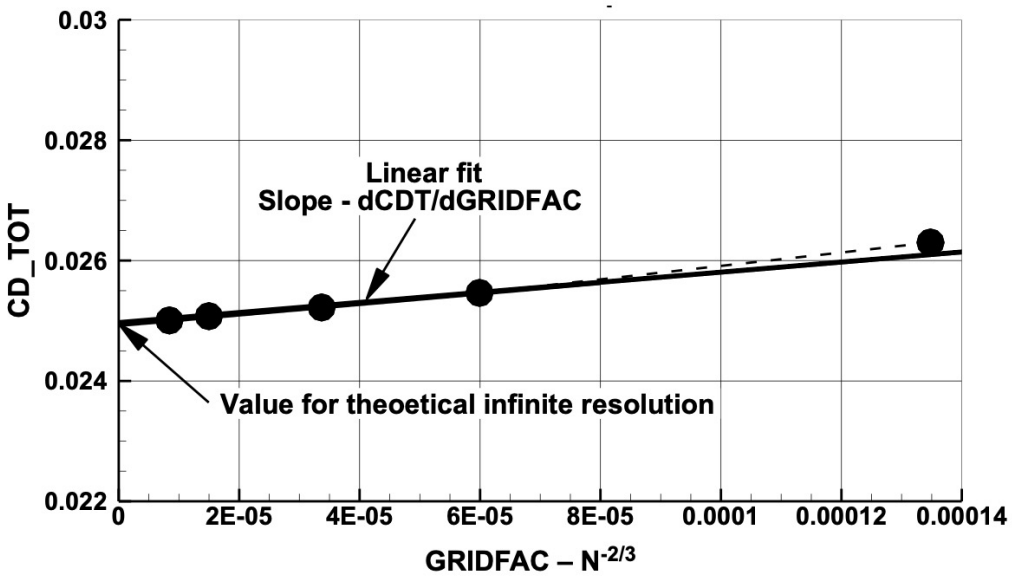


Figure A-D-1. Richardson Extrapolation Example; Drag (Figure S-VII-1 in Section VII).

D-B. DPW-IV Grid Convergence (WBT IH = 0°)

Table A-D-1. DPW-IV Participants and Data Set Characteristics; Wing-Body-Tail.

DPW-IV: CRM Wing-Body-Tail iH=0 deg									
Team	ID	SYM	SYM	Organization	Code	Grid	Turbulence Model	dCD/ dGRIDFAC	CD_TOT
1	A	A		RUAG Aerospace	NSMB	Multiblock Structured	Menter k-w SST	10.28	288.34
	C	C				Hybrid	SA	1.26	269.45
3	D	D		Aerospace Research and Test Establishment, FOI	EDGE	Hybrid	EARSM (Explicit Algebraic Reynolds Stress Model)	2.39	278.31
4	E	E		Indian Inst. Science	HiFun	Hybrid	SA	4.93	261.97
5	F	F		JAXA	TAS_Flow code	hybrid	SA model with a modification (SA_mod)	5.43	271.56
	G	G				Custom Cart	SA model with a modification (SA_mod)	5.97	267.36
5	H	H			UPACS Ver.2.0	Multiblock Structured	SA model with a modification (SA_mod)	1.86	269.17
6	I	I		NASA Langley Research Center	FUN3D	unstructured_Larc/ NodeBase grids)	SA	4.03	268.88
7	J	J		Cessna Aircraft Co.	NSU3D	Unstructured, Cessna spacing	SA	6.75	247.52
	K	K				Unstructured, Mods by Shahyar Pirzadeh	SA	5.75	265.21
8	L	L		Boeing Commercial Airplanes, Seattle	CFL3D	Multiblock Structured	SA	1.46	273.47
	M	M				Multiblock Structured	Menter k-w SST	0.80	272.33
	N	N				Multiblock Structured	SA	1.39	271.65
	O	O				Multiblock Structured	Menter k-w SST	0.77	270.98
9	P	P		Boeing (Huntington)	OVERFLOW 2.1	Overset	SA	4.42	264.34
10	R	R		ANSYS	ANSYS	Multiblock Structured	Menter k-w SST	0.57	268.32
2	S	S		DLR, Institute of Aerodynamics and Flow Technology	TAU	Hybrid	Reynolds stress SSG/LRR-omega	0.51	266.92
	T	T				Hybrid	Menter k-w SST	1.26	271.15
11	U	U		Zeus Numerix Private Ltd.	HLLC	Multiblock Structured	SA	4.14	399.40
12	V	V		Airbus	elsA	Multiblock Structured	Menter k-w SST	1.94	271.91
13	W	W		Metacomp	CFD++	Unstr/Hybrid	Realizable k-epsilon	3.95	257.69
	X	X				Unstr/Hybrid	SA	5.75	255.60
14	Y	Y		ONERA	elsA	Multiblock Structured	SA	1.33	272.10
15	Z	Z		U Wyoming	NSU3D	LaRC Node-Based Unstructured Grid Set	SA	1.87	268.65
16	2	2		Boeing - St. Louis	BCFD	mixed-element	SA	6.24	268.55
	3	3				mixed-element	Menter k-w SST	0.03	271.46
17	4	4		NUMECA International	FINE/Open	Multiblock Structured	SA	-16.23	274.13
3	5	5		Aerospace Research and Test Establishment, FOI	EDGE	Hybrid	EARSM (Explicit Algebraic Reynolds Stress Model)	6.13	280.41

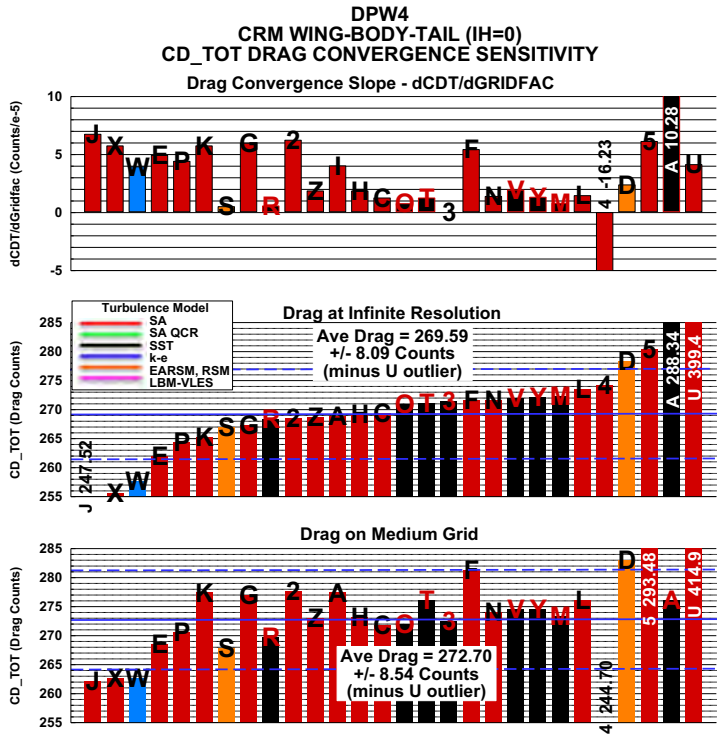


Figure A-D-2. DPW-IV: Total Drag Grid Convergence Sensitivity: Drag Ordered; TM (Figure S-VII-10).

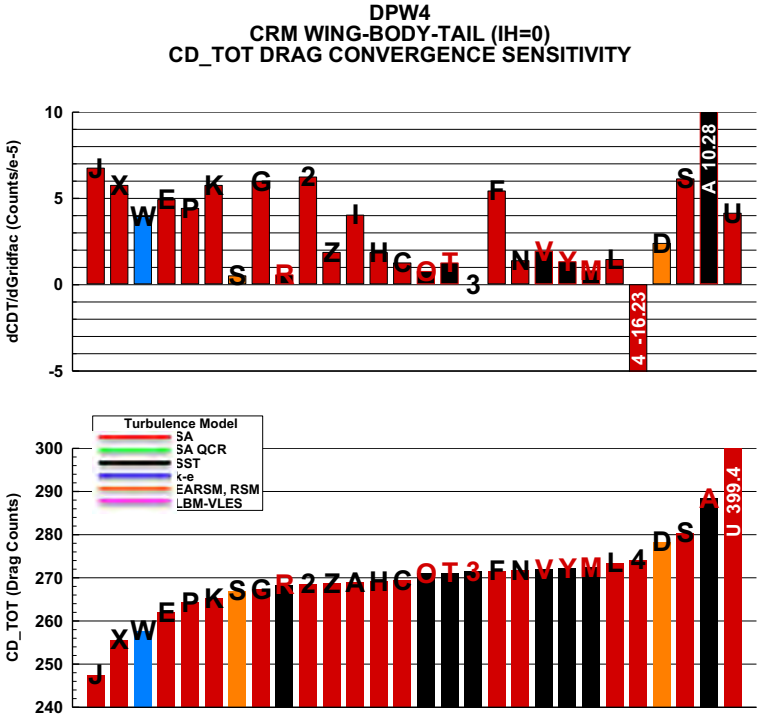


Figure A-D-3. DPW-IV: Total Drag Grid Convergence Sensitivity, M=0.85: Drag Ordered; TM.

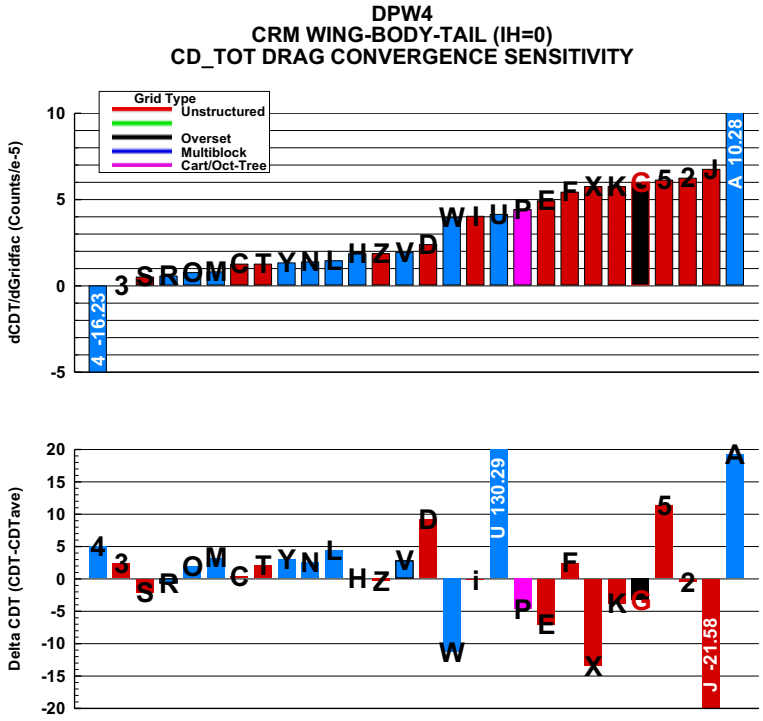


Figure A-D-4. DPW-IV: Total Drag Grid Convergence Sensitivity, M=0.85: Sensitivity Ordered; Grid.

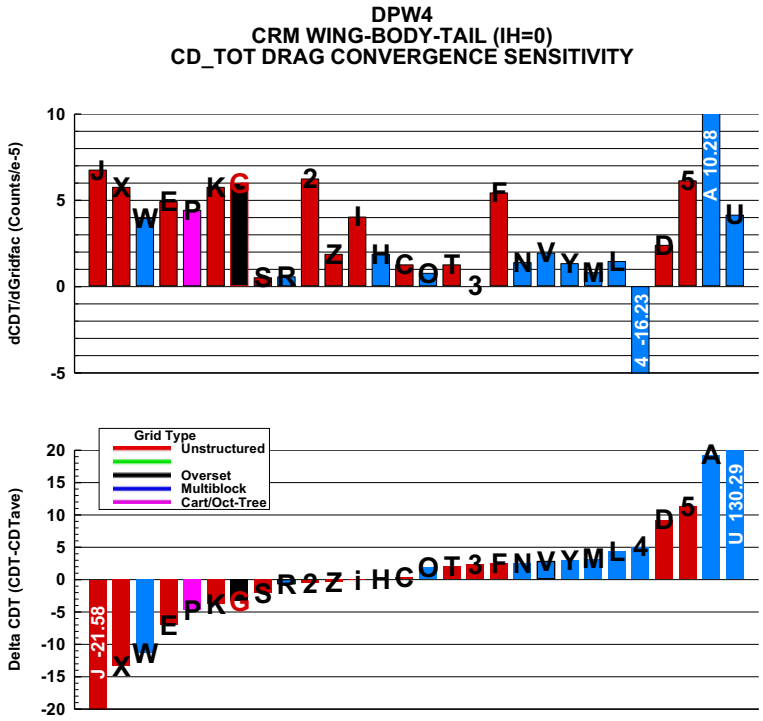


Figure A-D-5. DPW-IV: Total Drag Grid Convergence Sensitivity, M=0.85: Delta Drag Ordered; Grid.

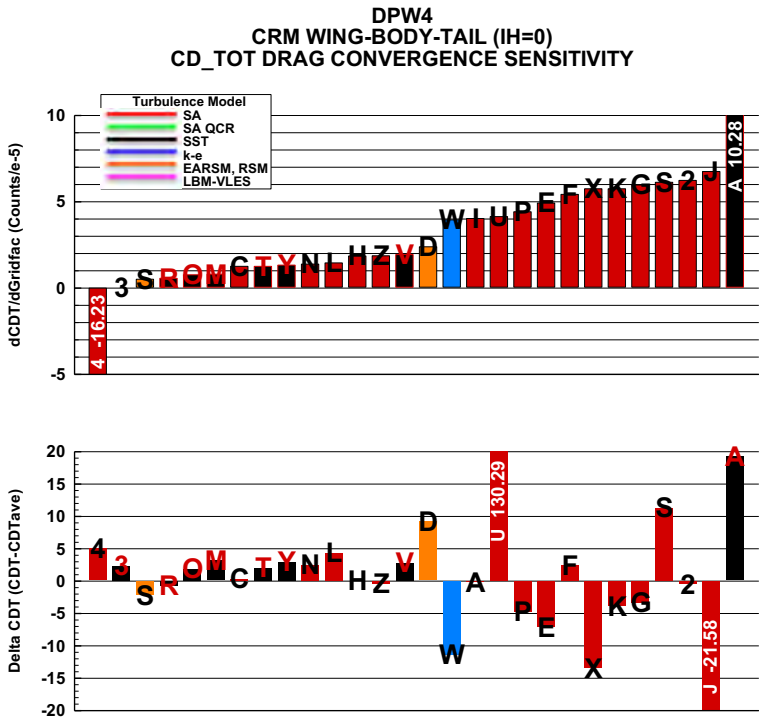


Figure A-D-6. DPW-IV: Total Drag Grid Convergence Sensitivity, M=0.85: Sensitivity Ordered; TM.

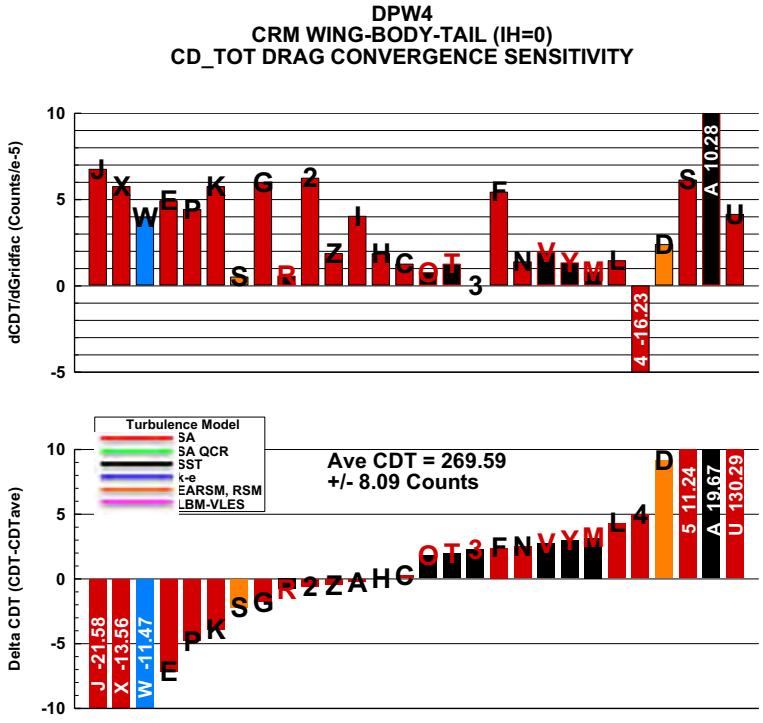


Figure A-D-7. DPW-IV: Total Drag Grid Convergence Sensitivity, M=0.85: Delta Drag Ordered; TM.

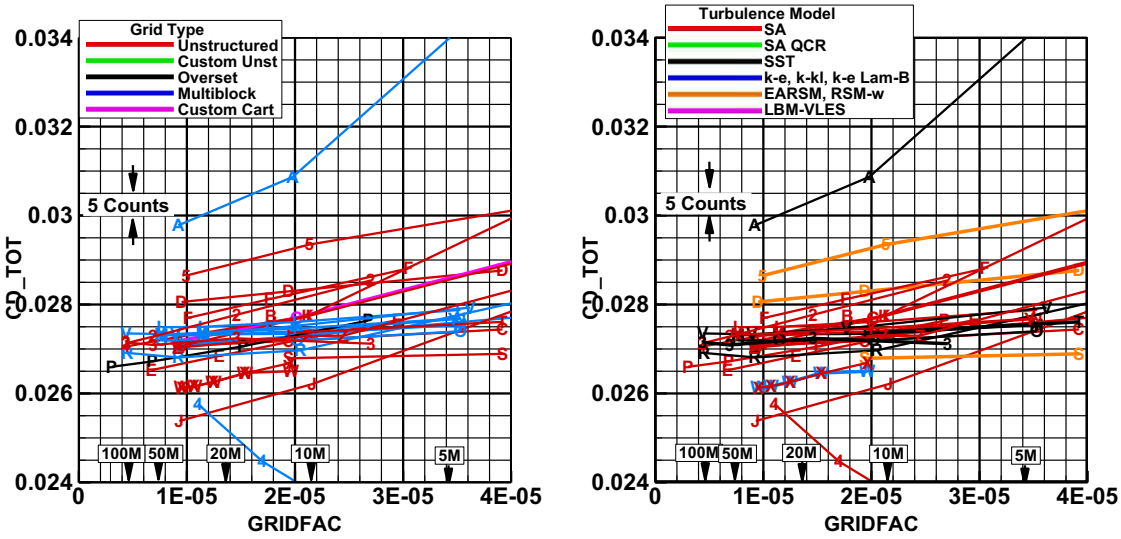


Figure A-D-8. DPW-IV: Grid Convergence; Total Drag C_{D_TOT}, M=0.85: All Solutions.

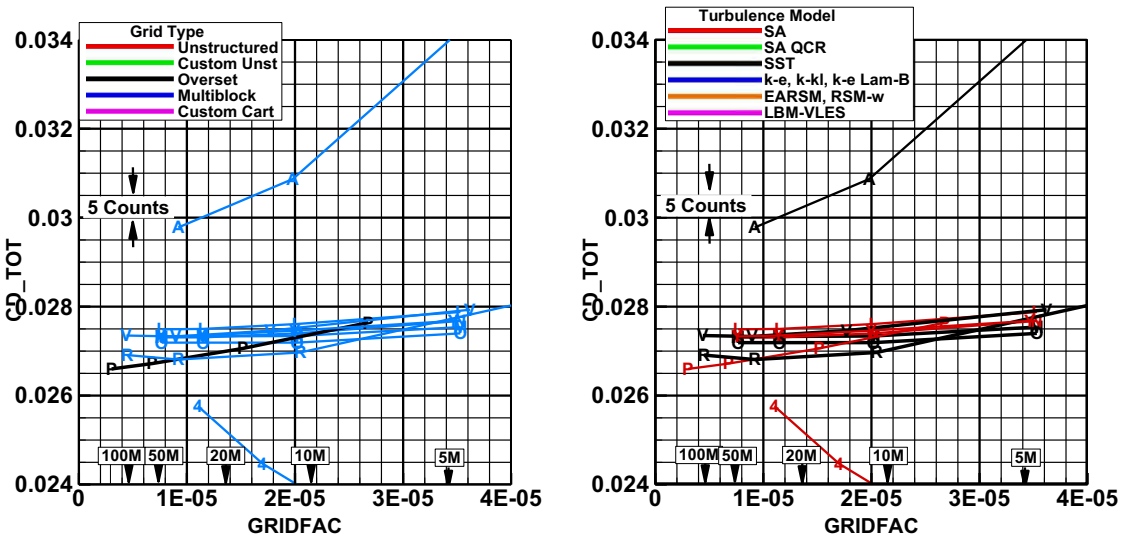


Figure A-D-9. DPW-IV: Grid Convergence; Total Drag C_{D_TOT}, M=0.85: Structured Grid Solutions.

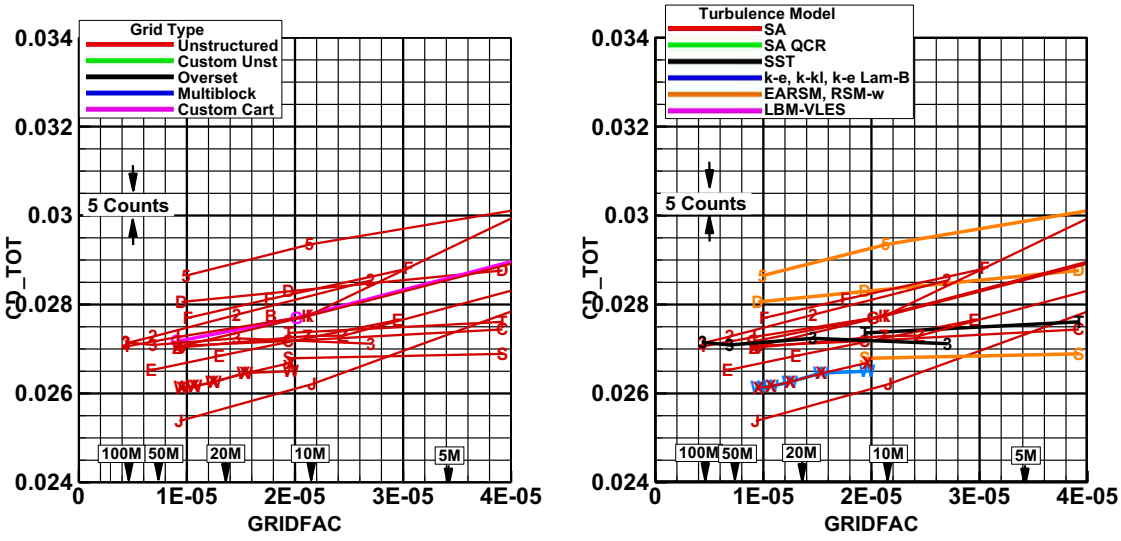


Figure A-D-10. DPW-IV: Grid Convergence; Total Drag C_{D_TOT}, M=0.85: Unstructured Grid Solutions.

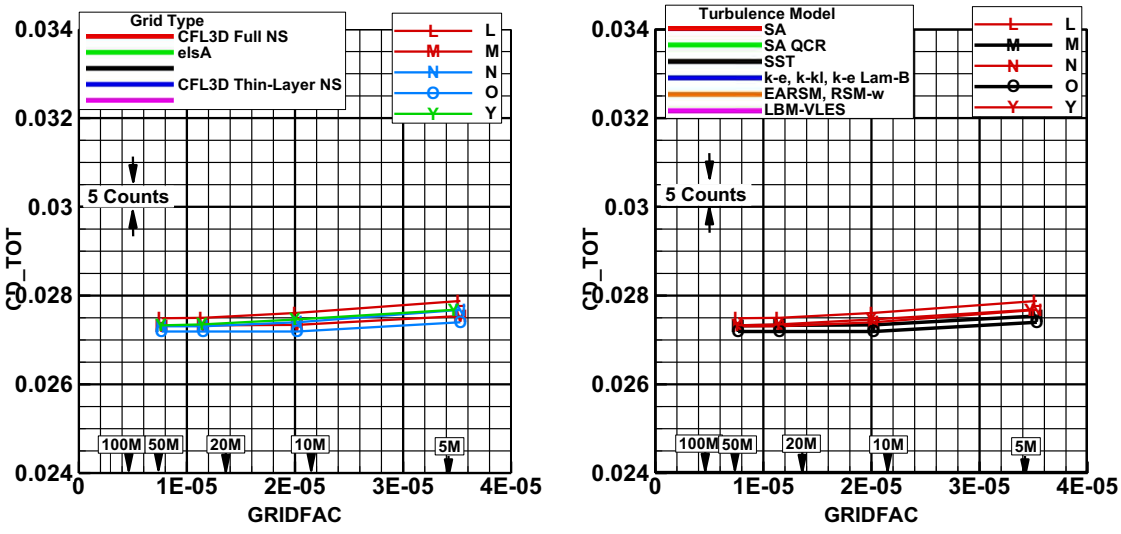


Figure A-D-11. DPW-IV: Grid Convergence; Total Drag C_{D_TOT}, M=0.85: BCA Zeus Structured Grid Solutions.

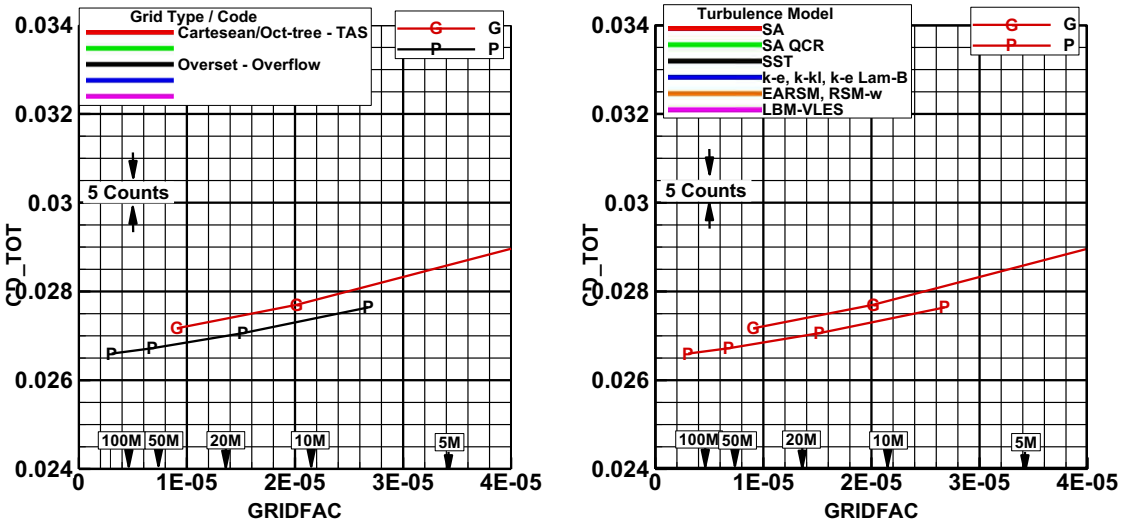


Figure A-D-12. DPW-IV: Grid Convergence; Total Drag C_{D_TOT}, M=0.85: Overflow and Cartesian/Oct-Tree Grid Solutions.

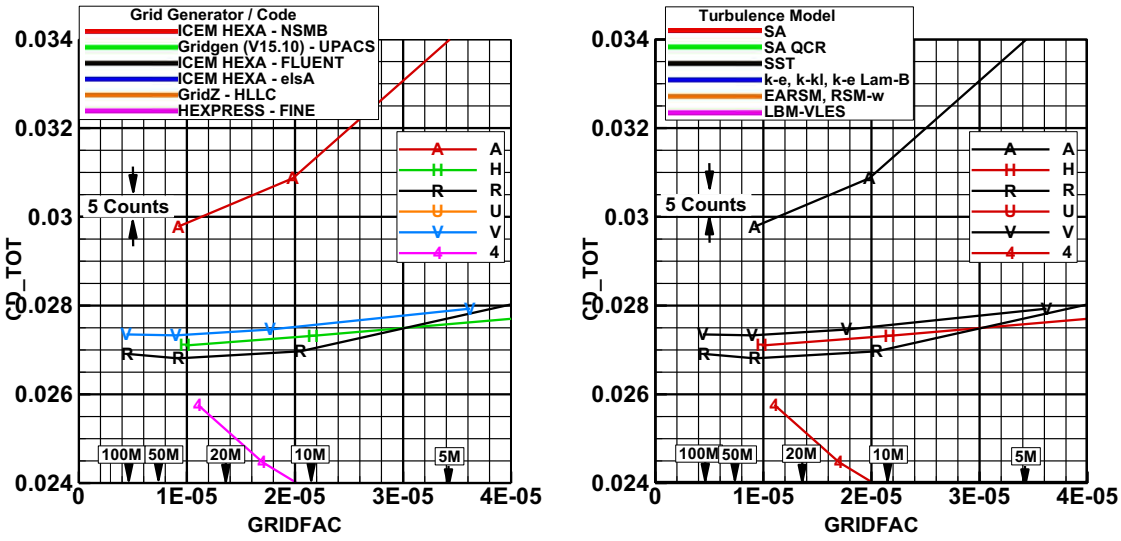


Figure A-D-13. DPW-IV: Grid Convergence; Total Drag C_{D_TOT}, M=0.85: Miscellaneous Structured Grid Solutions.

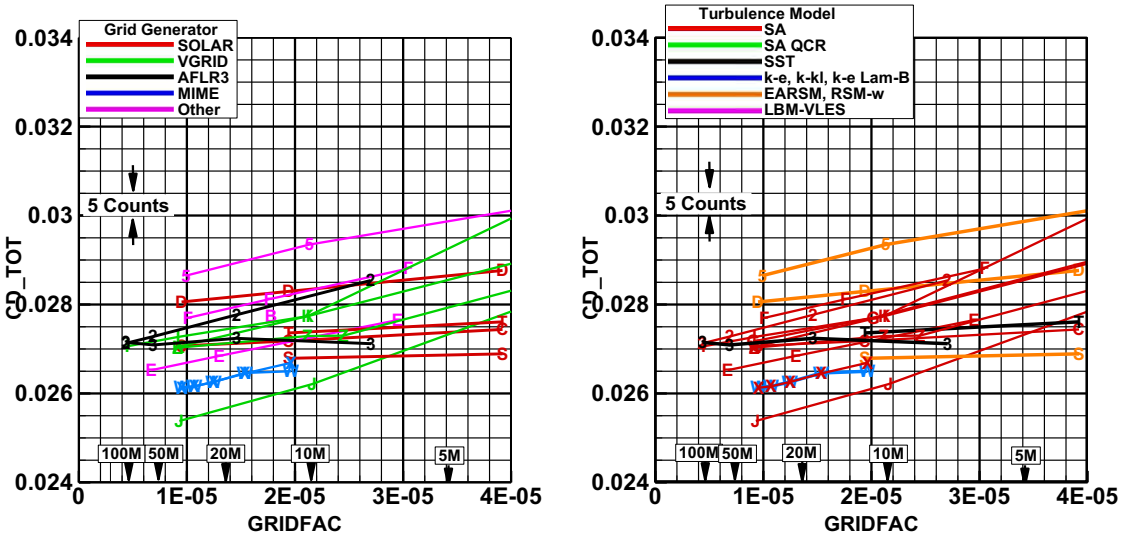


Figure A-D-14. DPW-IV: Grid Convergence; Total Drag $C_{D_{TOT}}$, M=0.85: All Unstructured Grid Solutions.

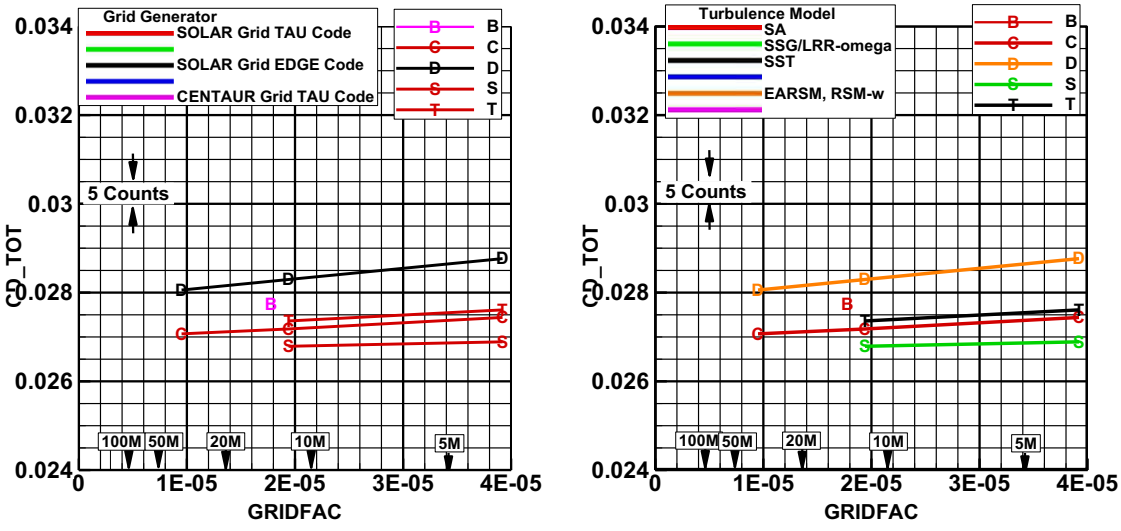


Figure A-D-15. DPW-IV: Grid Convergence; Total Drag $C_{D_{TOT}}$, M=0.85: SOLAR Unstructured Grid Solutions.

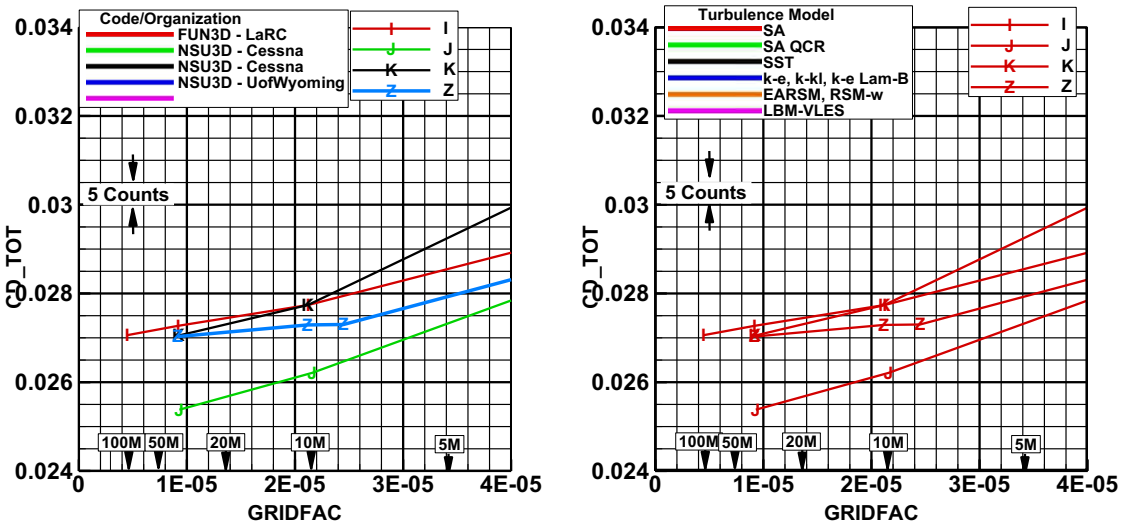


Figure A-D-16. DPW-IV: Grid Convergence; Total Drag C_{D_TOT}, M=0.85: VGRID Unstructured Grid Solutions.

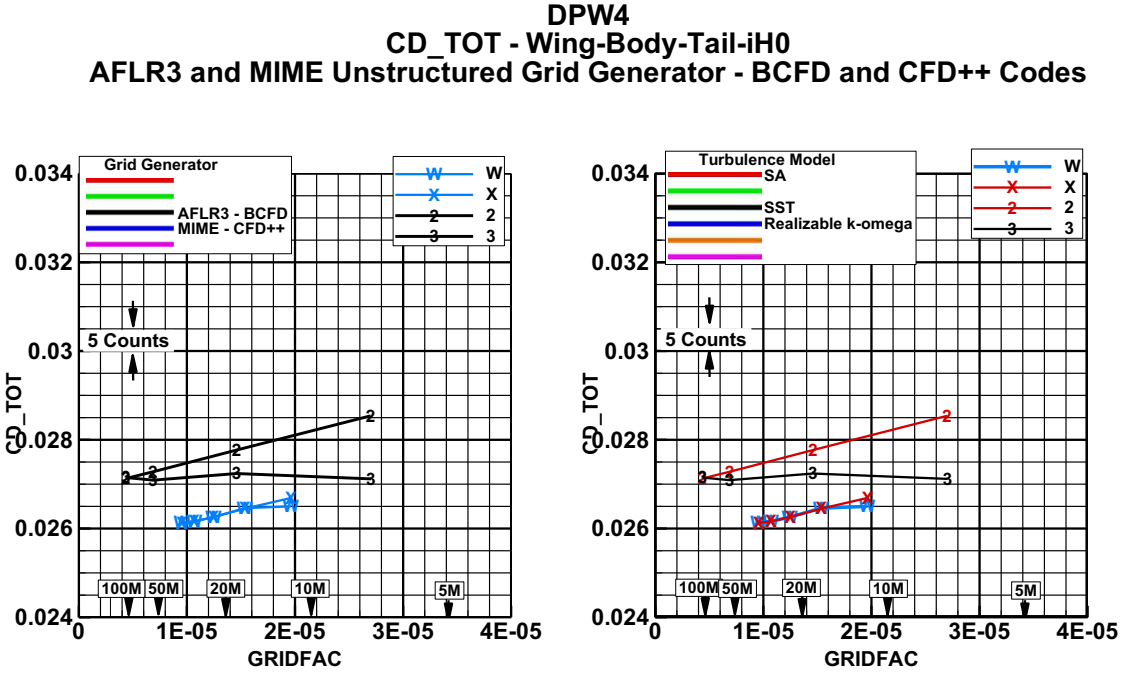


Figure A-D-17. DPW-IV: Grid Convergence; Total Drag C_{D_TOT}, M=0.85: AFLR3 and MIME Unstructured Grid Solutions.

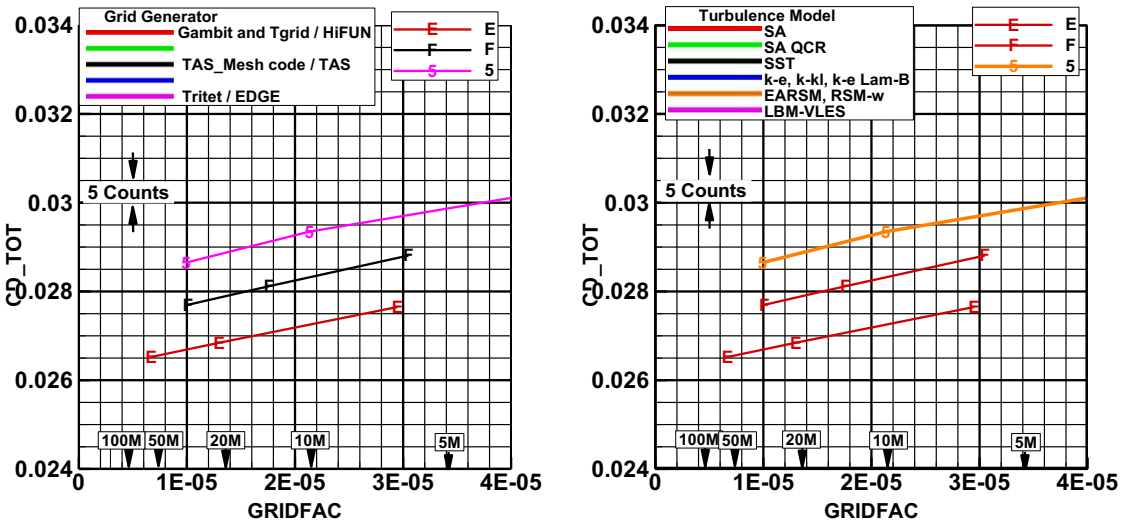


Figure A-D-18. DPW-IV: Grid Convergence; Total Drag C_{D_TOT}, M=0.85: Miscellaneous Unstructured Grid Solutions.

D-C. DPW-V Grid Convergence (WB "As -Built")

Table A-D-2. DPW-V Participants and Data Set Characteristics: Wing-Body (As-Built).

DPW-V: CRM Wing-Body (As-Built)									
Team	ID	SYM	SYM	Organization	Code	Grid	Turbulence Model	dCD/ dGRIDFAC	CD_TOT
1	A			Boeing (Huntington)	OVERFLOW v2.2c	Overset	SA-Ia	2.60	249.17
	B					Overset	SA-Ia w/ RC	2.54	248.01
	E					Custom (Overset)	SA-Ia w/ RC	2.89	247.22
2	I			CADRC	MFlow	Hex	SA	0.83	249.42
	J					Hybrid	SA	5.37	254.60
3	K			EcolePolytech Montreal	Fluent V13	Prism	SA	1.79	249.60
	L					Custom (Hex)	SA	3.33	248.18
4	M			Embraer S/A	CFD++	Hex	k-e-RT	6.63	260.41
	N					Hex	Menter k-w SST	0.20	250.94
	O					Hybrid	k-e-RT	19.48	271.14
	P					Hybrid	Menter k-w SST	8.88	260.14
	Q					Prism	k-e-RT	9.59	259.84
	R					Prism	Menter k-w SST	0.83	250.07
	S					Custom (Hybrid)	k-e-RT	24.30	259.05
	T					Custom (Hybrid)	Menter k-w SST	22.40	243.28
5	U			Aerospace Research and Test Establishment, FOI	EDGE	Hex	EARSM (Explicit Algebraic Reynolds Stress Model)	-0.06	254.93
	V					Hex	SA	0.45	253.79
	W					Hex	Menter k-w SST	0.04	250.01
6	X			Gulfstream	FUN3D	Hybrid	SA	0.98	249.33
7	Y			Indian Inst. Science	HiFun	Hex	SA	0.86	250.55
8	Z			JAXA	FaSTAR	Hex	SA-noft2-R	0.94	248.77
	2					Custom Cart	SA-noft2-R	4.14	251.16
9	3			JAXA	UPACS	Multiblock Structured	SA-noft2-R (Crot=1)	0.83	248.97
	4				UPACS	Multiblock Structured	Menter k-w SST-V	-0.40	252.18
10	5			NASA Ames Research Center	overflow2.2e_LRS	Overset	Lag RST	1.41	252.77
11	6			NASA Langley Research Center	FUN3D v12.2	Hybrid	SA	1.77	248.11
	7				CFL3D v6.6	Multiblock Structured	SA	0.98	249.27
12	8			NPU China	ExStream	Overset	Menter k-w SST-V	2.02	256.83
13	9			ONERA	elsA	Multiblock Structured	SA	0.61	249.29
14	a			Penn St. U	OVERFLOW 2.2c	Overset	SA-fv3	1.35	246.91
15	b			U. Toronto	Diablo	Multiblock Structured	SA	1.47	248.99
	d					Multiblock Structured	SA	0.66	249.38
16	e			Cessna Aircraft Co.	NSU3D	Hybrid	SA	1.89	239.84
	f				FUN3D	Hybrid	SA	0.92	249.59
17	g			DLR, Institute of Aerodynamics and	TAU	Hex	SA	0.19	249.71
	h					Hex	Menter k-w SST-V	-0.33	250.95
18	k			CRL_INDIA	CFD++	Prism	SA-RC	2.98	249.30
19	m			Boeing - St. Louis	BCFD	Hex	SA	1.71	249.23
	n					Hex	Menter k-w SST-V	0.61	251.08
	q					Hex	SA	1.37	248.62
	r					Hex	Menter k-w SST-V	0.24	250.60
20	t			NUMECA	FINE/Open	Multiblock Structured	SA	1.71	258.12

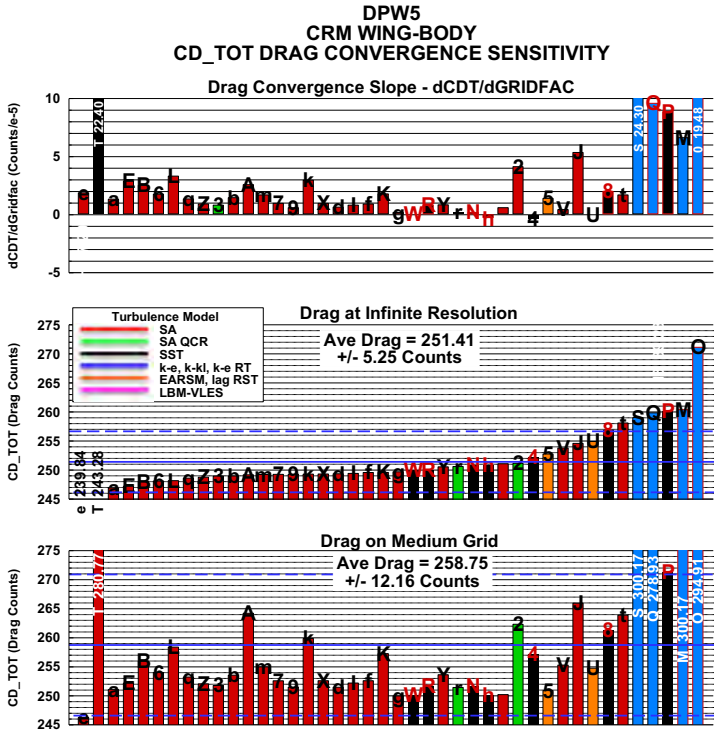


Figure A-D-19. DPW-V: Total Drag Grid Convergence Sensitivity, M=0.85: Drag Ordered; TM (Figure S-VII-11).

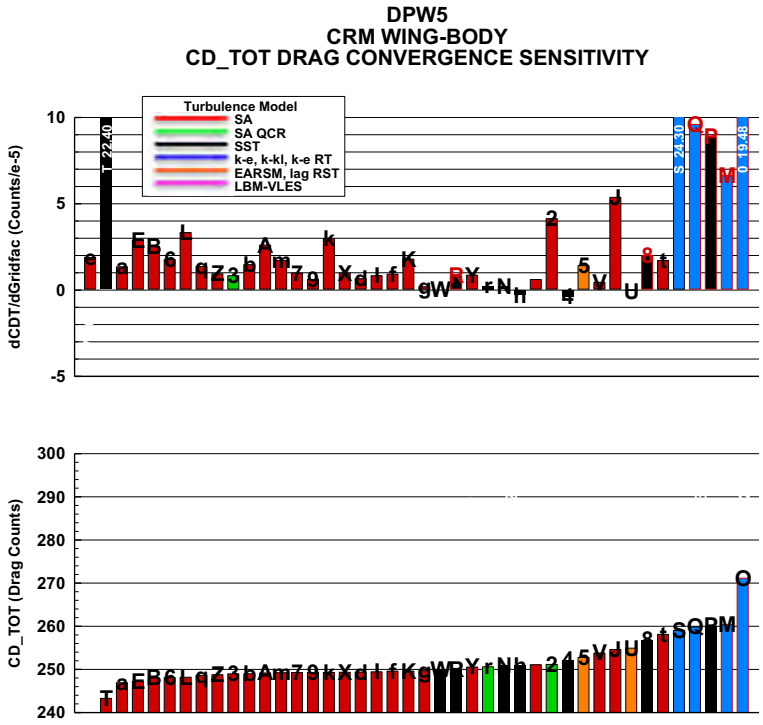


Figure A-D-20. DPW-V: Total Drag Grid Convergence Sensitivity, M=0.85: Drag Ordered; TM.

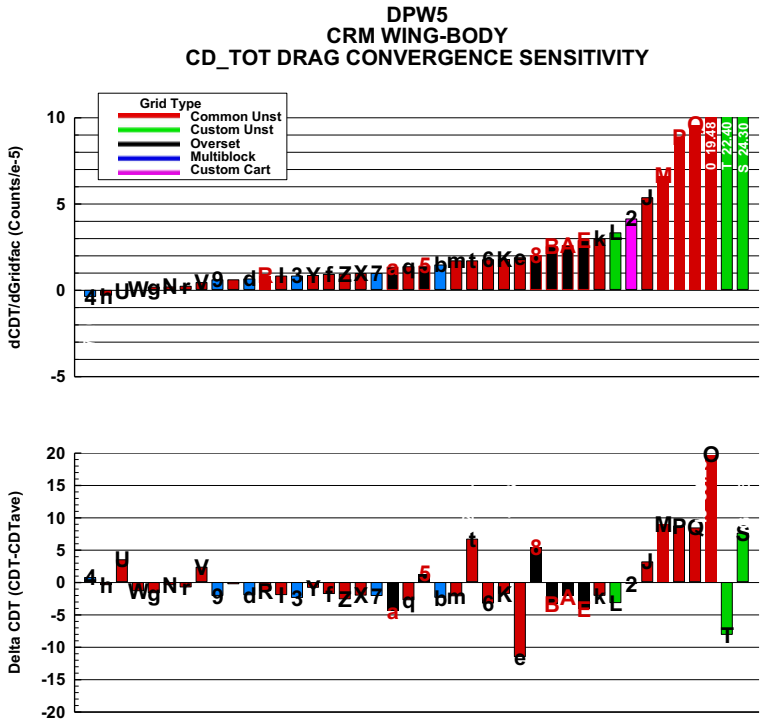


Figure A-D-21. DPW-V: Total Drag Grid Convergence Sensitivity, M=0.85: Sensitivity Ordered; Grid.

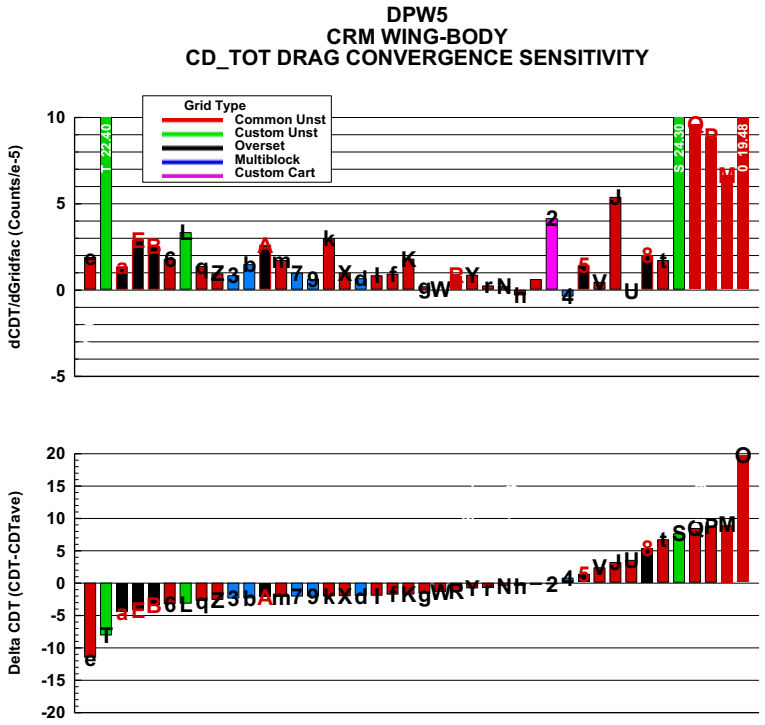


Figure A-D-22. DPW-V: Total Drag Grid Convergence Sensitivity, M=0.85: Delta Drag Ordered; Grid.

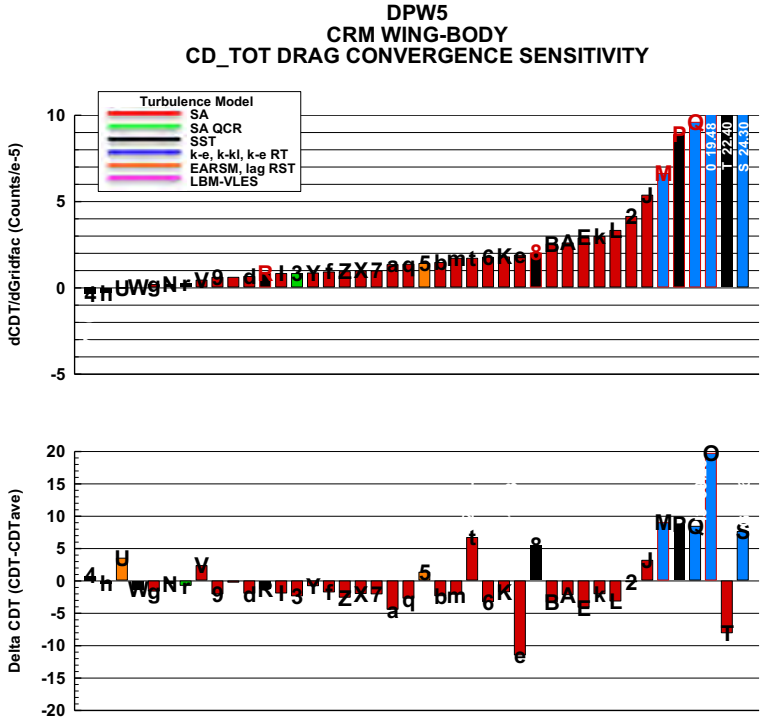


Figure A-D-23. DPW-V: Total Drag Grid Convergence Sensitivity, M=0.85: Sensitivity Ordered; TM.

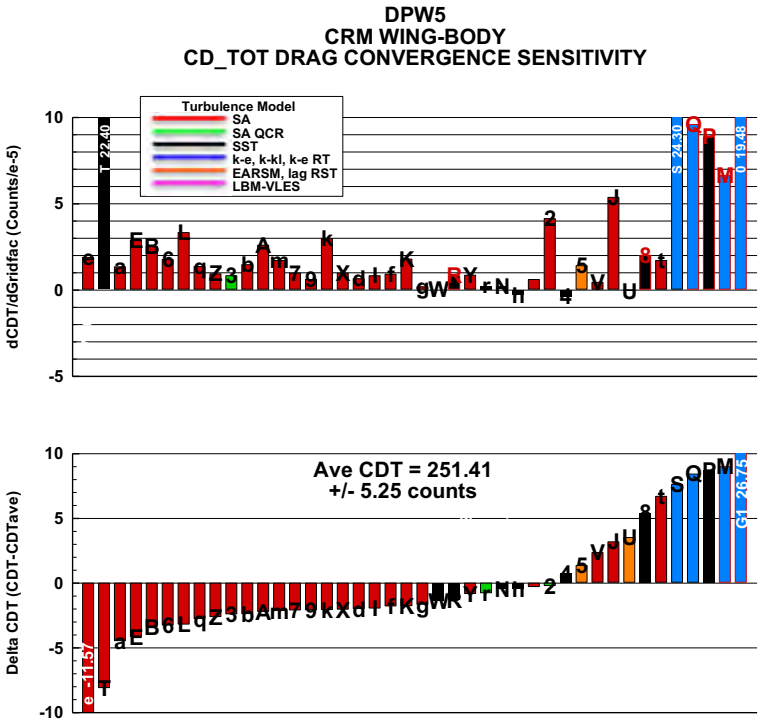


Figure A-D-24. DPW-V: Total Drag Grid Convergence Sensitivity, M=0.85: Delta Drag Ordered; Grid.

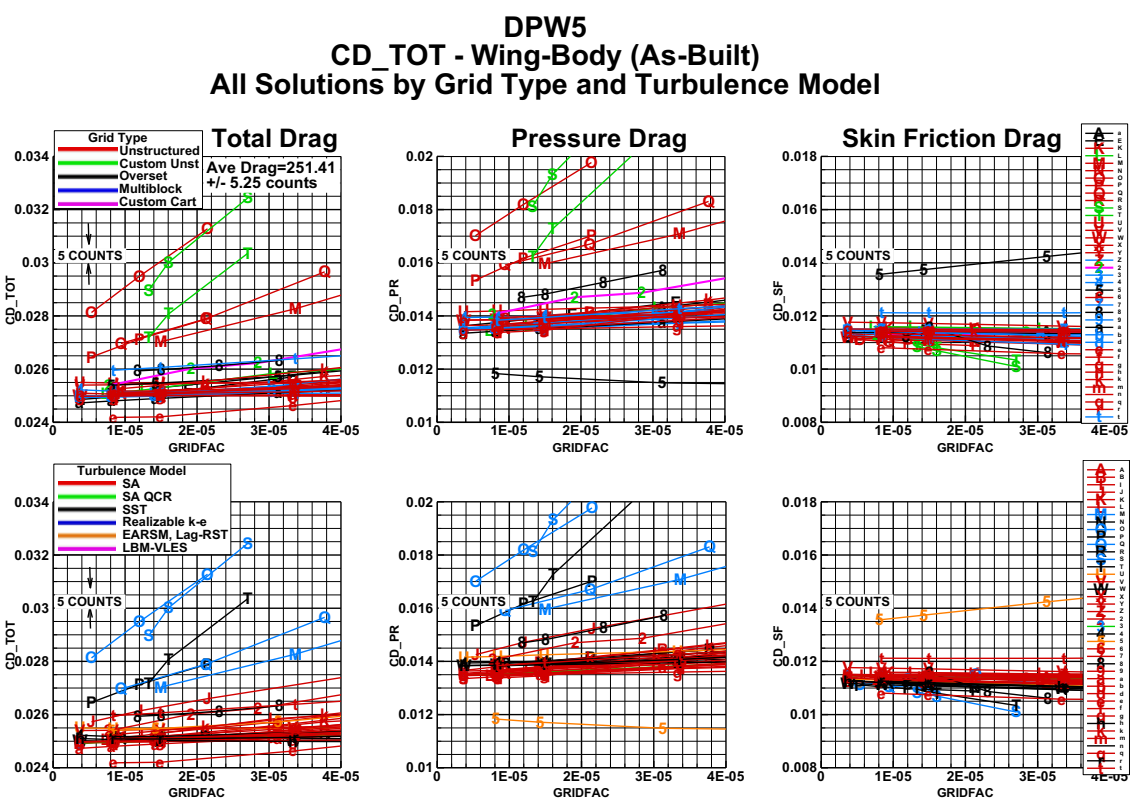


Figure A-D-25. DPW-V: Grid Convergence; Total, Pressure, and Skin Friction Drag, M=0.85: All Solutions.

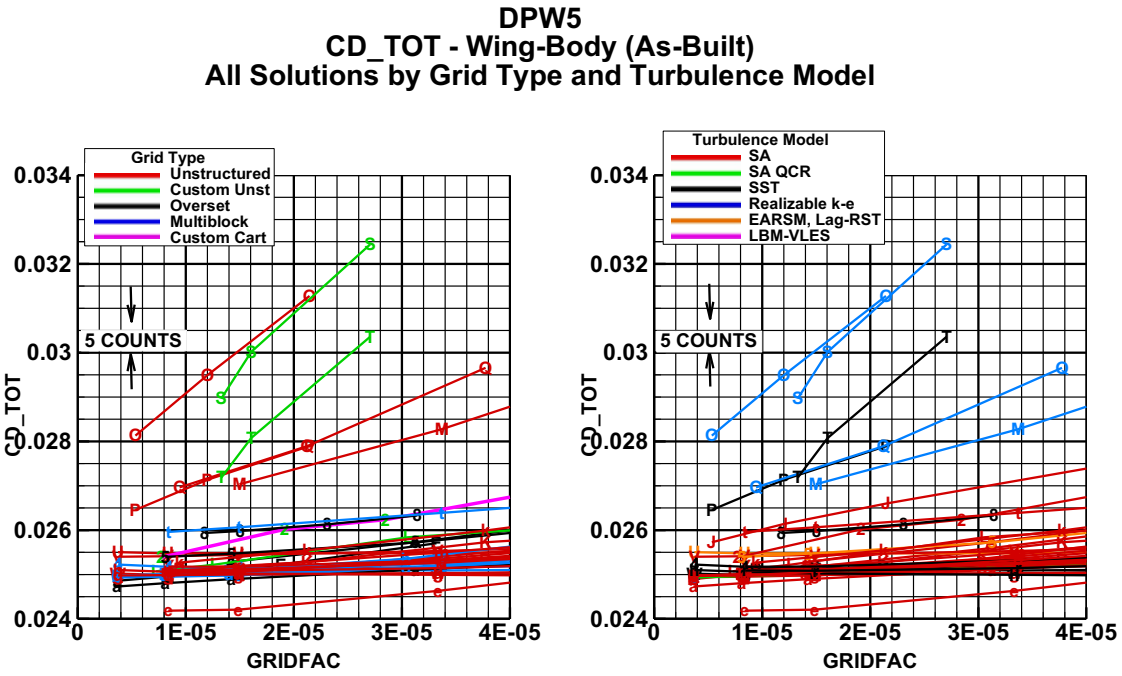


Figure A-D-26. DPW-V: Grid Convergence; Total Drag C_{D_TOT}, M=0.85: All Solutions.

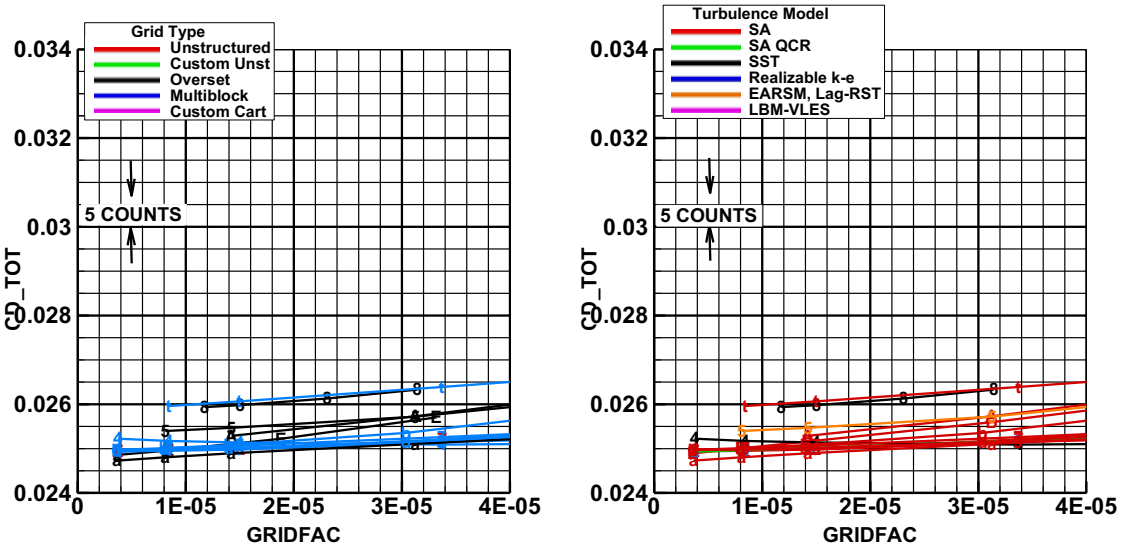


Figure A-D-27. DPW-V: Grid Convergence; Total Drag C_{D_TOT}, M=0.85: All Structured Grid Solutions.

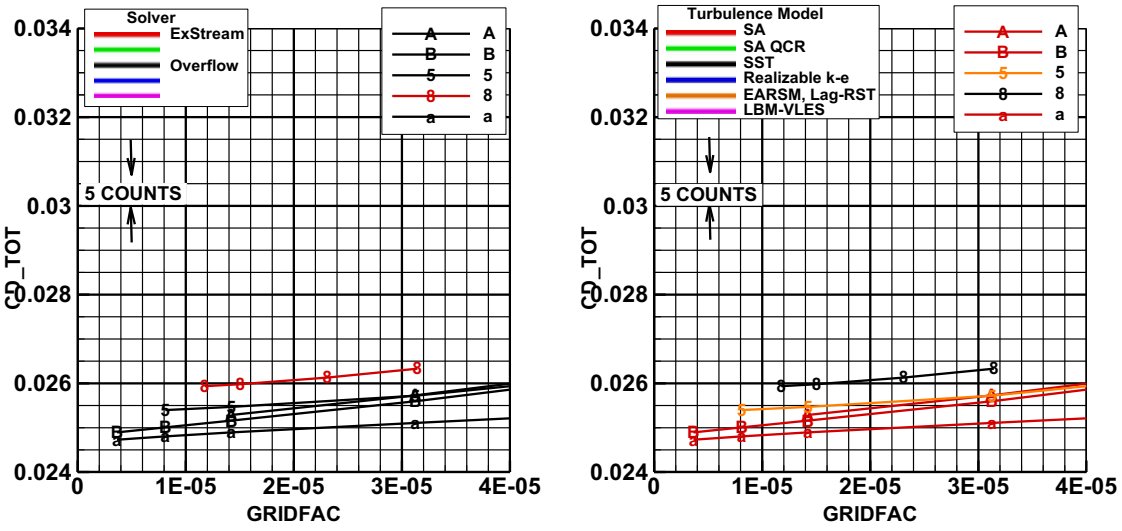


Figure A-D-28. DPW-V: Grid Convergence; Total Drag C_{D_TOT}, M=0.85: Common Overset Grid Solutions.

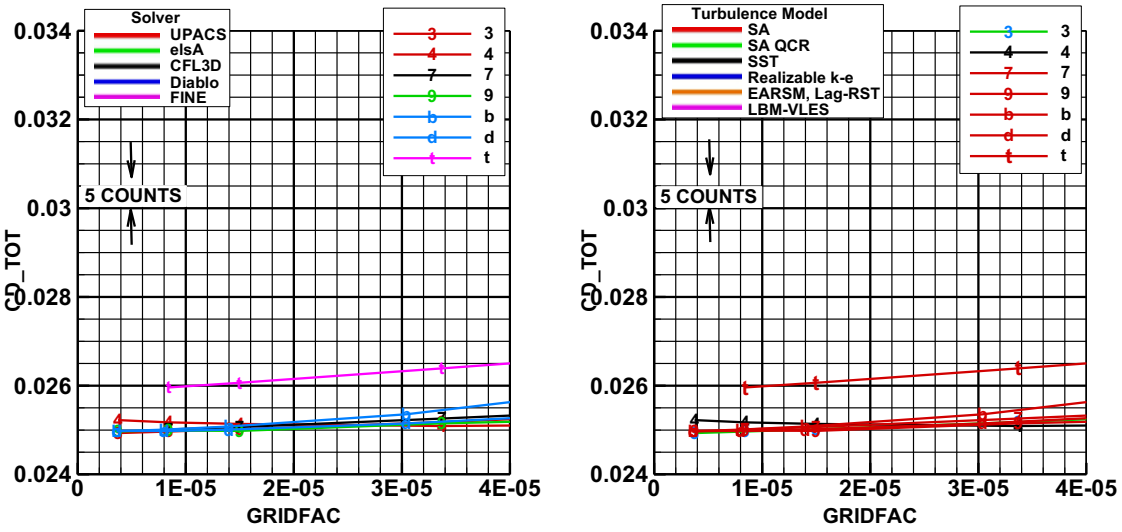


Figure A-D-29. DPW-V: Grid Convergence; Total Drag C_{D_TOT}, M=0.85: Common Mutliblock Grid Solutions.

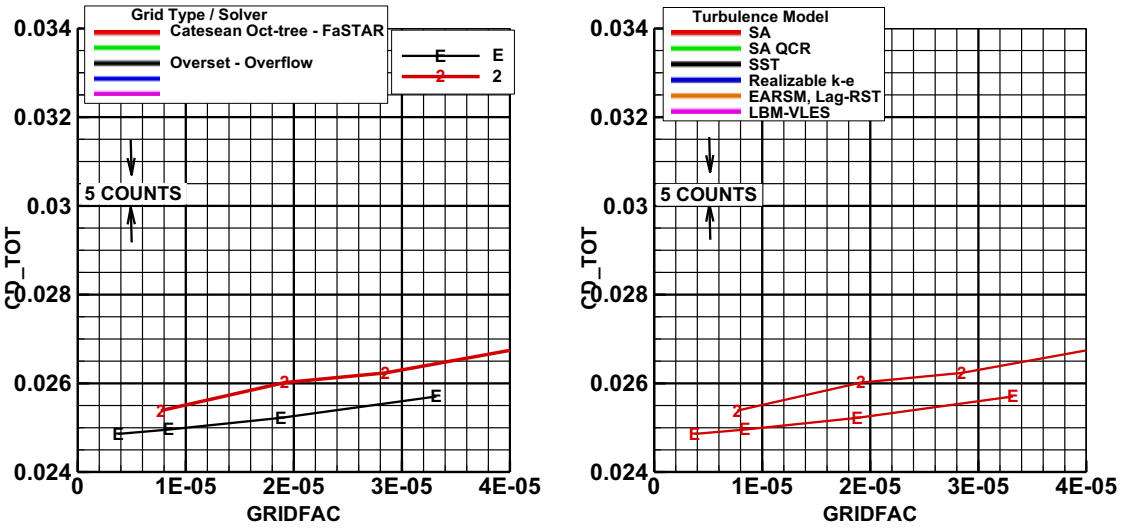


Figure A-D-30. DPW-V: Grid Convergence; Total Drag C_{D_TOT}, M=0.85Custom Structured Grid Solutions.

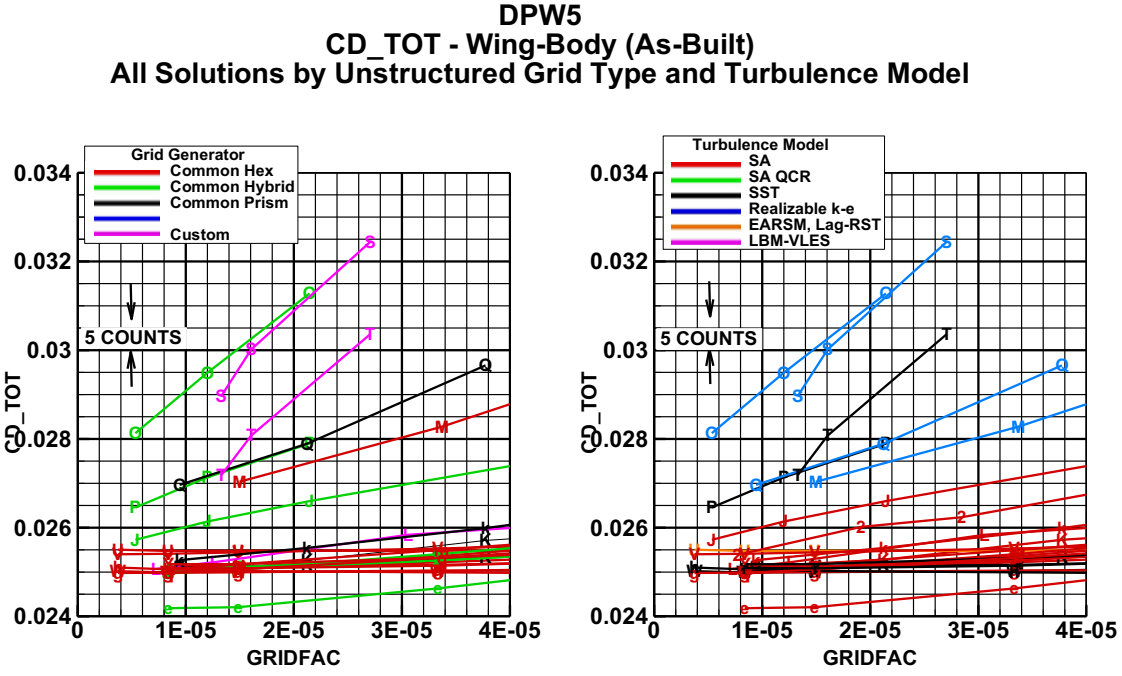


Figure A-D-31. DPW-V: Grid Convergence; Total Drag C_{D_TOT}, M=0.85: All Unstructured Grid Solutions.

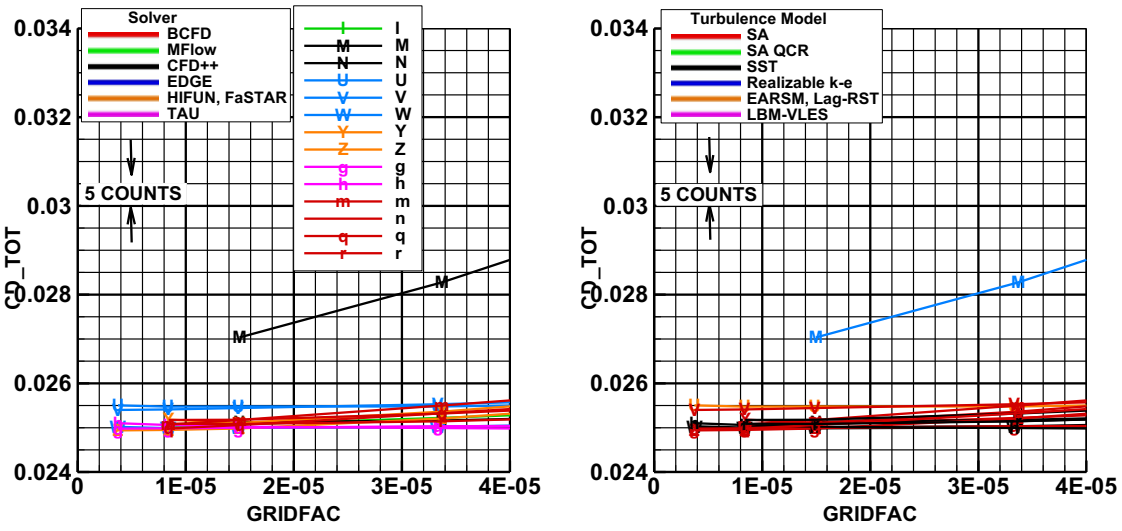


Figure A-D-32. DPW-V: Grid Convergence; Total Drag C_{D_TOT}, M=0.85: Common Hex Unstructured Grid Solutions.

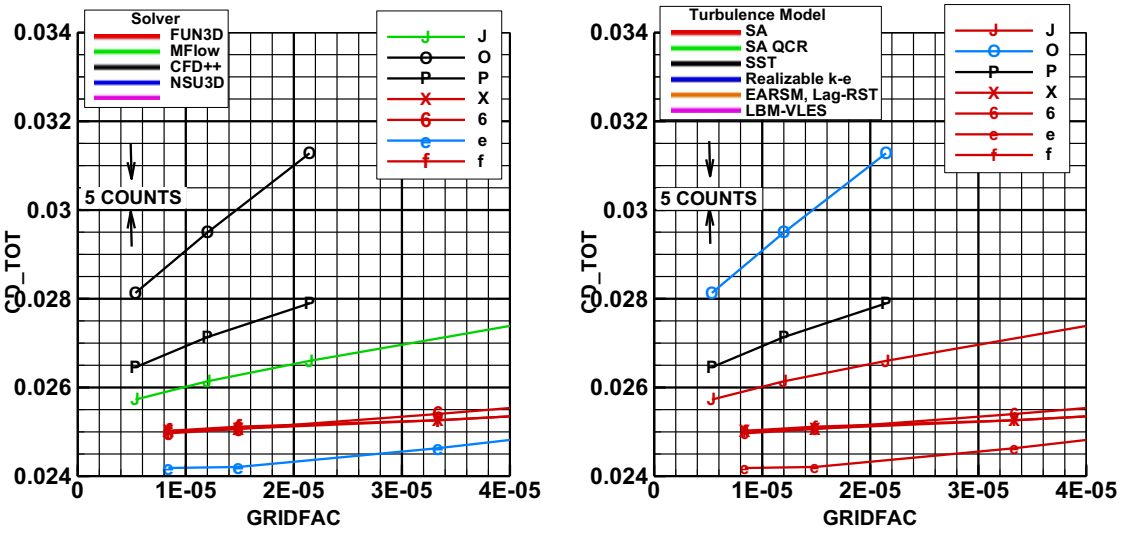


Figure A-D-33. DPW-V: Grid Convergence; Total Drag C_{D_TOT}, M=0.85: Common Hybrid Unstructured Grid Solutions.

DPW5
CD_TOT - Wing-Body (As-Built)
Common Prism Unstructured Grid Type and Turbulence Model

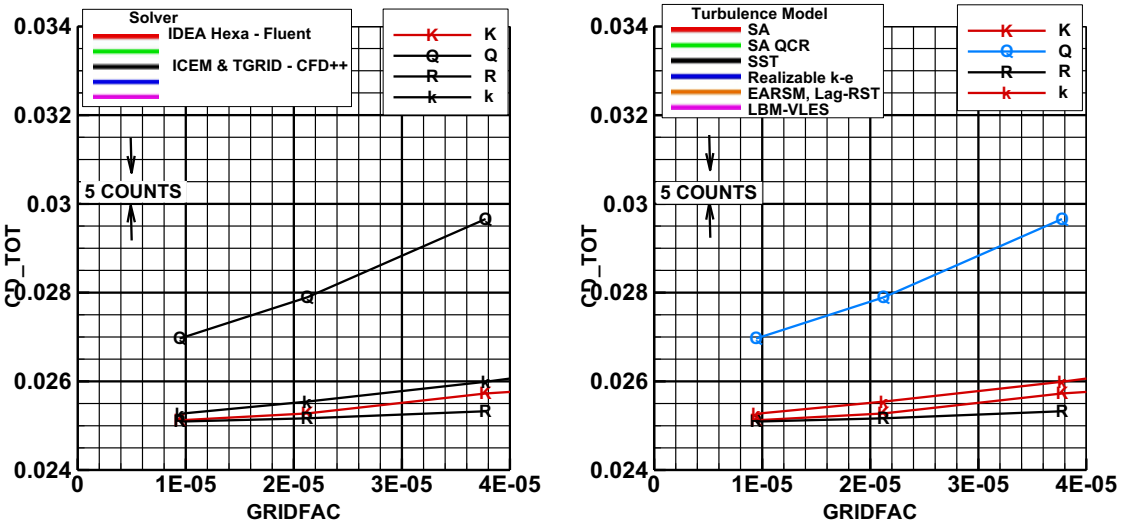


Figure A-D-34. DPW-V: Grid Convergence; Total Drag C_{D_TOT}, M=0.85: Common Prism Unstructured Grid Solutions.

DPW5
CD_TOT - Wing-Body (As-Built)
Custom Unstructured Grid Type and Turbulence Model

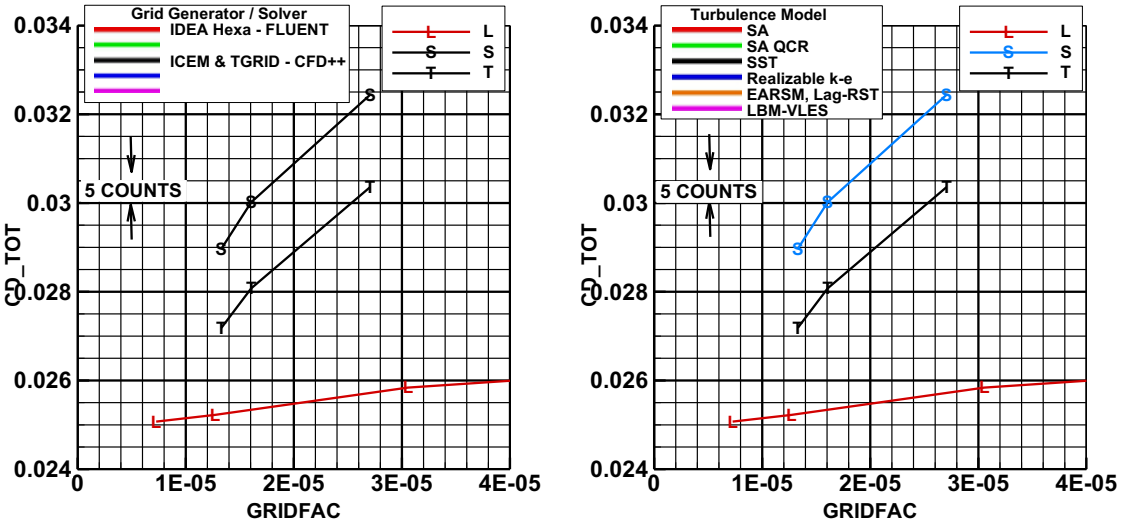


Figure A-D-35. DPW-V: Grid Convergence; Total Drag C_{D_TOT}, M=0.85: Custom Unstructured Grid Solutions.

D-D. DPW-VI Grid Convergence

D-D-1. DPW-VI Grid Convergence: Wing-Body (WB)

Table A-D-3. DPW-VI Participants and Data Set Characteristics: Wing-Body (Aeroelastic).

DPW-VI: CRM Wing-Body (Aeroelastic)									
Team	ID	SYM	SYM	Organization	Code	Grid	Turbulence Model	dCD/ dGRIDFAC	CD_TOT
1	A1	A	A	Boeing, BCA Advanced Concepts, Long Beach CA	Overflow v2.2k	Overset	SA-RC	2.69	252.25
	A2	a	a			Overset	SA-RC w/QCR on	2.77	254.07
2	B1	B	B	NASA Langley Research Center	FUN3D 12.8	Unst-Geolab	k-kL-MEAH2015 w/Limiter	0.91	257.42
	B2	b	b			Unst-Geolab	k-kL-MEAH2015 no-limiter	2.67	256.32
	B3	α	a			Unst-Geolab	SA no-limiter		
3	D1	D	D	CARDC	Mflow	Unst-Geolab	SA	3.90	254.88
	D2	d	d			Unst-custom	SA	4.81	255.39
4	E1	E	E	JAXA, Ryoyu Systems	FaSTAR	Unst-Geolab	SA-noft2-R w/QCR2000	-1.11	256.06
5	F1	F	F	ANSYS	Fluent	Unst-custom	Menter k-w SST-V	23.54	262.43
6	G1	G	G	EXA Powerflow	PowerFLOW	Custom Cart	LBM-VLES	53.28	283.44
7	H1	H	H	Aerospace Research and Test Establishment, FOI	EDGE	Unst-Geolab	SA	3.37	255.29
	H2	h	h			Unst-Geolab	EARSM (Explicit Algebraic Reynolds Stress Model)	-7.20	261.29
8	I1	I	I	Mentor Graphics	FloEFD	Custom Cart	Default k-e Lam-Bremhorst	3.58	280.67
	I2	β	b			Custom Cart	Subgrid k-e Lam-Bremhorst	3.11	322.37
	I3	χ	c			Custom Cart-B	Default k-e Lam-Bremhorst	6.40	295.98
9	J1	J	J	Metacomp	CFD++	Unst-Boeing	SA	3.89	256.86
	J2	ϑ	J			Unst-Boeing	Menter k-w SST-V	6.13	257.91
	J3	φ	j			Unst-Geolab	SA	5.62	255.13
10	K1	K	K	Kawasaki Heavy Industries	Cflow	Unst-Boeing	SA-noft2	4.43	259.71
	K2	k	k			Unst-Boeing	SA-noft2 w/QCR200	4.88	260.86
	K3	γ	g			Custom Cart	SA-noft2	4.71	253.36
	K4	Γ	G			Custom Cart	SA-noft2 w/QCR200	4.71	253.36
11	L1	L	L	DLR, Institute of Aerodynamics and Flow	TAU	Unst-custom	RSM-ω	1.65	257.86
	L2	λ	l			Unst-custom	SA-neg	1.84	255.00
12	M1	M	M	Tennessee, Pointwise, NASA Langley, NAVAIR, MIT, U Ala	COFFE/KCFD	Unst-custom	SA-neg	0.45	255.54
13	N1	N	N	CAd Lab, Indian Institute of Sci	HiFun	Unst-custom	SA	-0.21	251.58
14	O1	O	O	ONERA	elsA	Overset	SA	0.28	253.01
15	P1	P	P	Boeing - St. Louis	BCFD	Unst-Boeing	SA-RC	1.98	254.49
	P2	π	p		GGNS	All Tets	SA-RC	1.54	256.00
16	Q1	Q	Q	MDOlab, University of Michigan	ADflow	Embraer MB	SA 1stOrder	4.00	253.34
	Q2	q	q			Cust-Overset	SA 1stOrder	1.52	253.80
	Q3	θ	q			Embraer MB	SA-QCR2000	4.07	255.03
18	S1	S	S	Textron Aviation (Cessna)	FUN3D	Unst-Geolab	SA-RC	9.70	250.60
19	T1	T	T	CARDC	TRIP	CommonMB	Menter k-w SST-2003	3.42	254.76
20	U1	U	U	Applied Research Lab, Penn State	Overflow 2.21 3rd Order WENO	Overset	SA-RC W/QCF2000	0.91	254.69
	U2	u	u		Overflow 2.21 5TH Order WENO	Overset	SA-RC W/QCF2000	0.97	254.17
21	V1	V	V	Embraer S/A	CFD++	Unst-Geolab	Menter k-w SST-V	0.18	253.91
	V2	ς	V			Embraer MB	Menter k-w SST-V	0.93	255.55
	V3	Ξ	X			Unst-custom-A	Menter k-w SST-V	0.83	254.35
	V4	Ψ	Y			Unst-custom-I	Menter k-w SST-V	0.83	255.35
25	Z1	Z	Z	JAXA, Ryoyu Systems	TAS limiter K=1	Unst-Geolab	SA-noft2-R w/QCR2000	-0.04	260.02
	Z2	ζ	z		TAS limiter K=5	Unst-Geolab	SA-noft2-R w/QCR2000	-0.33	259.68
	Z3	Δ	D		TAS limiter K=10	Unst-Geolab	SA-noft2-R w/QCR2000	0.32	258.83
	Z4	ε	e		TAS limiter K=10	Unst-custom	SA-noft2-R w/QCR2000	1.19	259.56
	Z5	η	h		TAS limiter K=5	Unst-Geolab	SA-noft2-R	0.88	253.32
	Z6	Π	P		TAS limiter K=5	Unst-Boeing	SA-noft2-R	5.45	258.15
	Z7	Υ	U		TAS limiter K=5	Unst-Boeing	SA-noft2-R w/QCR2000	5.99	263.16

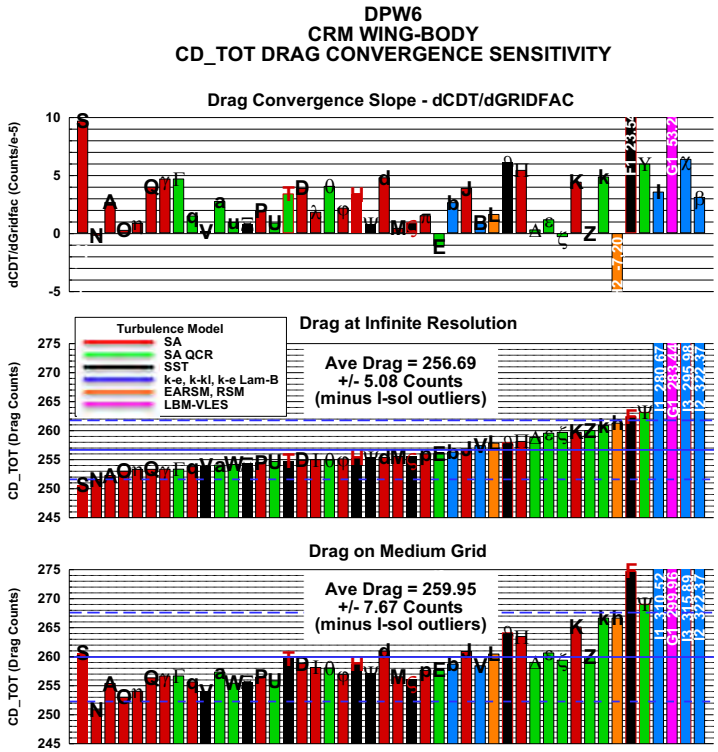


Figure A-D-36. DPW-VI: Total Drag Grid Convergence Sensitivity, M=0.85 (Figure S-VII-12).

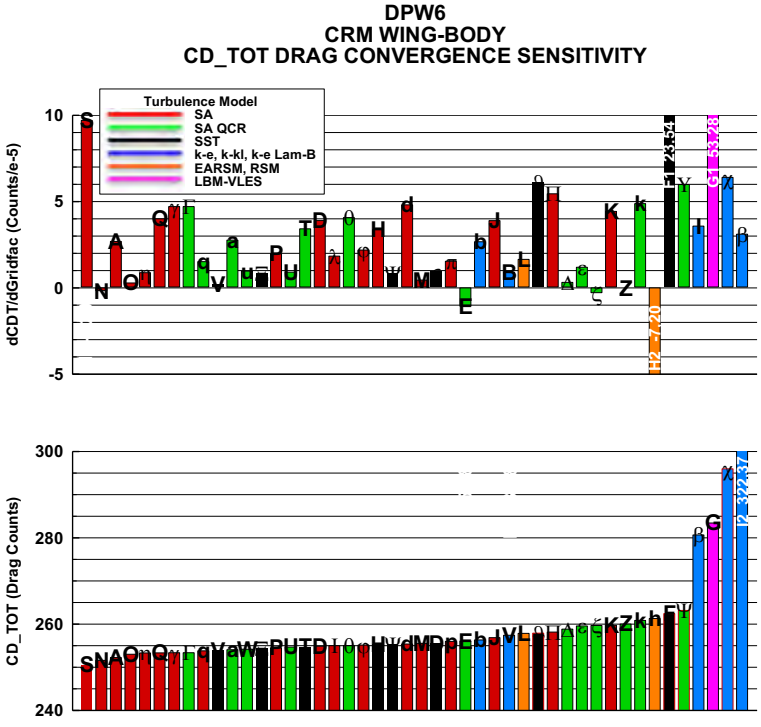


Figure A-D-37. DPW-VI: Total Drag Grid Convergence Sensitivity, M=0.85: Drag Ordered; TM.

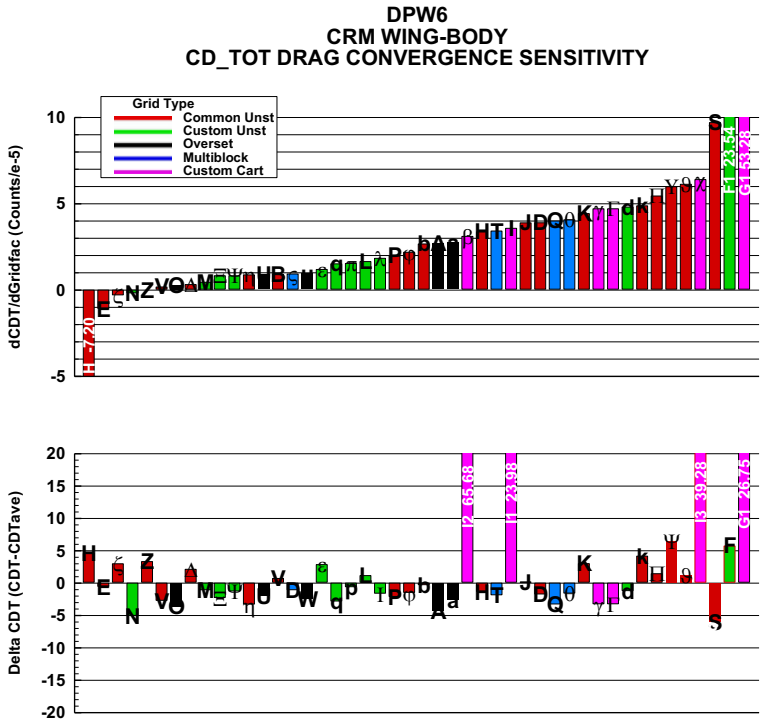


Figure A-D-38. DPW-VI: Total Drag Grid Convergence Sensitivity, M=0.85: Sensitivity Ordered; Grid.

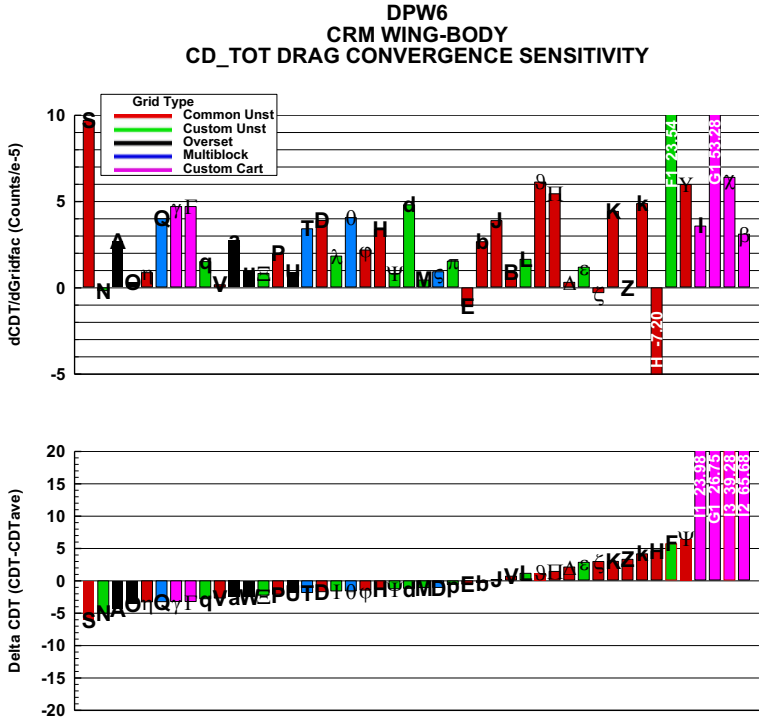


Figure A-D-39. DPW-VI: Total Drag Grid Convergence Sensitivity, M=0.85: Delta Drag Ordered; Grid.

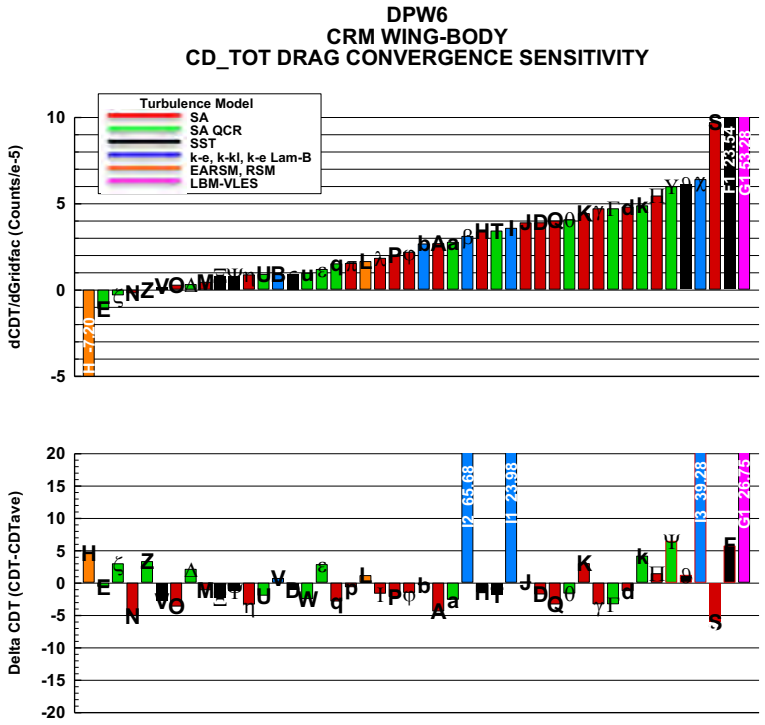


Figure A-D-40. DPW-VI: Total Drag Grid Convergence Sensitivity, M=0.85: Sensitivity Ordered; TM.

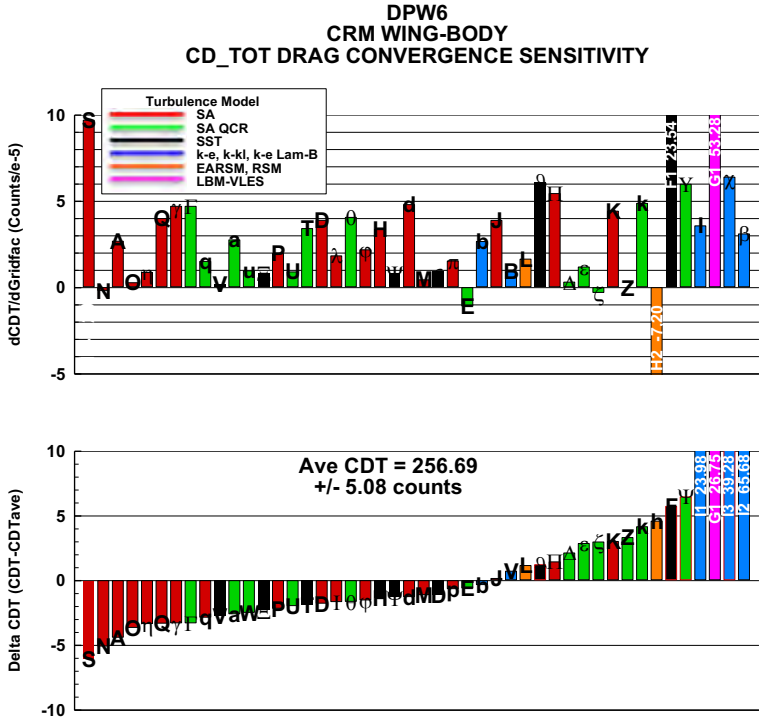


Figure A-D-41. DPW-VI: Total Drag Grid Convergence Sensitivity, M=0.85: Delta Drag Ordered; Grid.

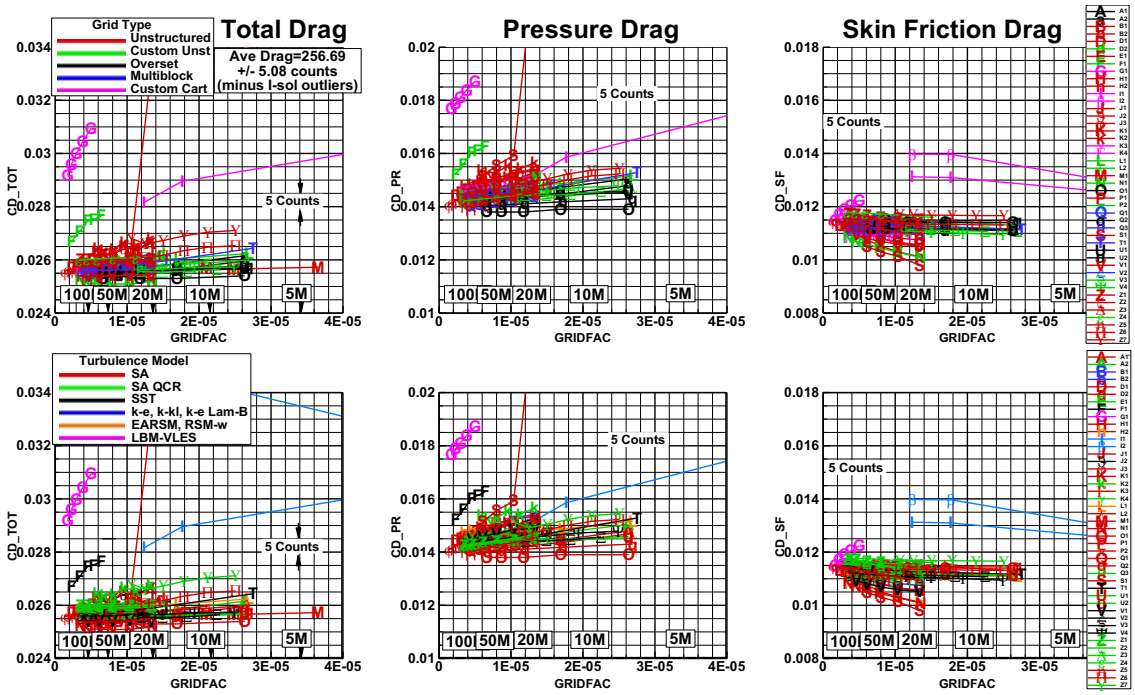


Figure A-D-42. DPW-VI: Grid Convergence; Total, Pressure, and Skin Friction Drag, M=0.85: All Solutions.

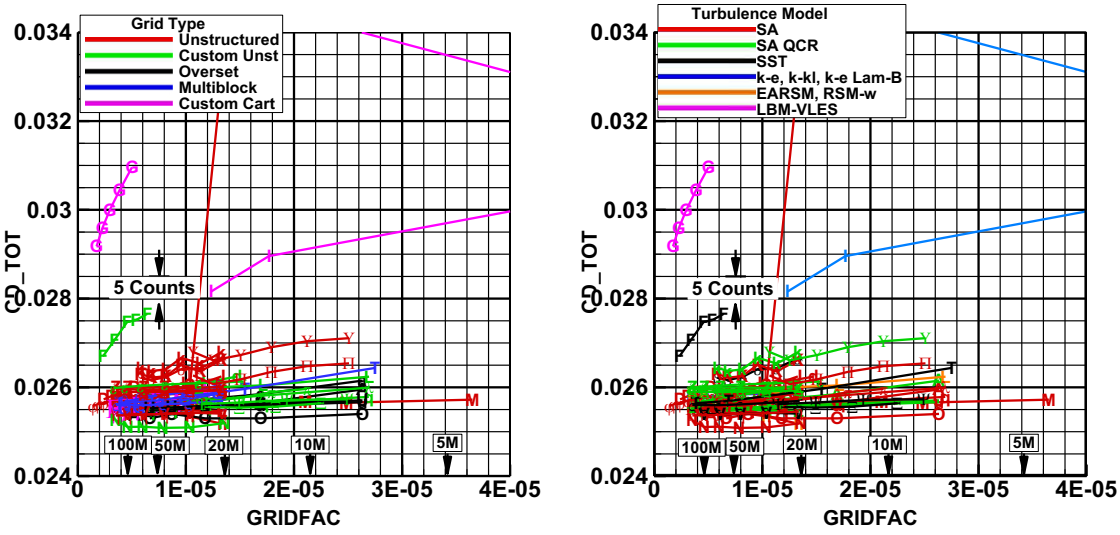
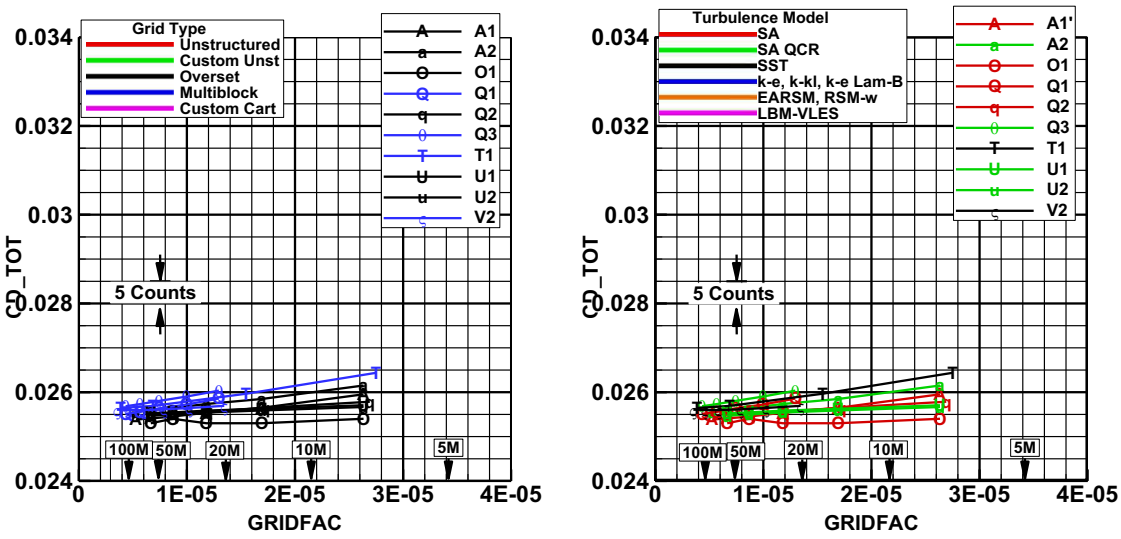


Figure A-D-43. DPW-VI: Grid Convergence; Total Drag C_{D_TOT}, M=0.85: All Solutions.



- **Figure A-D-44. DPW-VI: Grid Convergence; Total Drag $C_{D_{TOT}}$, M=0.85: All Structured Grid Solutions.**

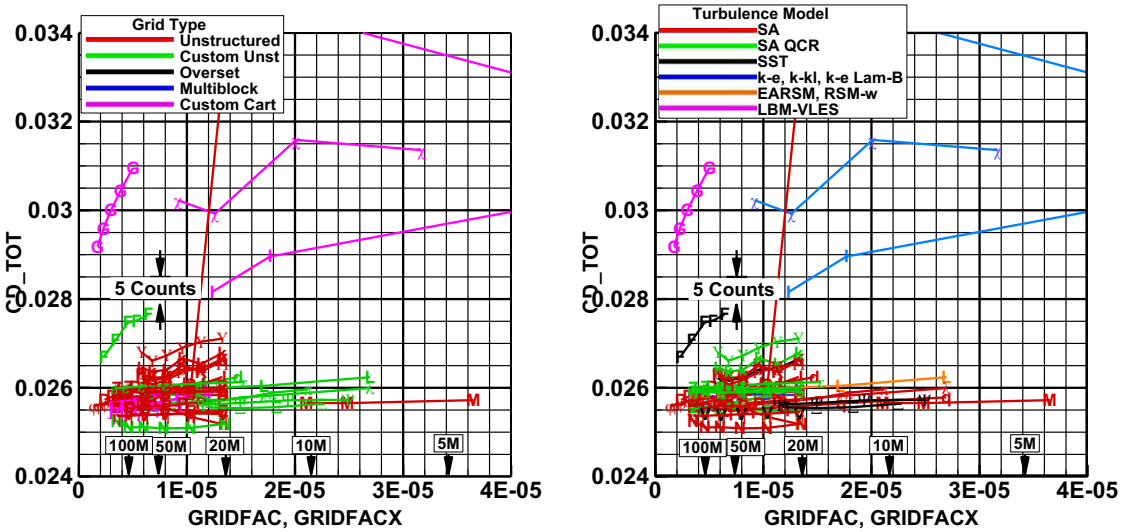


Figure A-D-45. DPW-VI: Grid Convergence; Total Drag $C_{D_{TOT}}$, M=0.85: All Unstructured Grid Solutions.

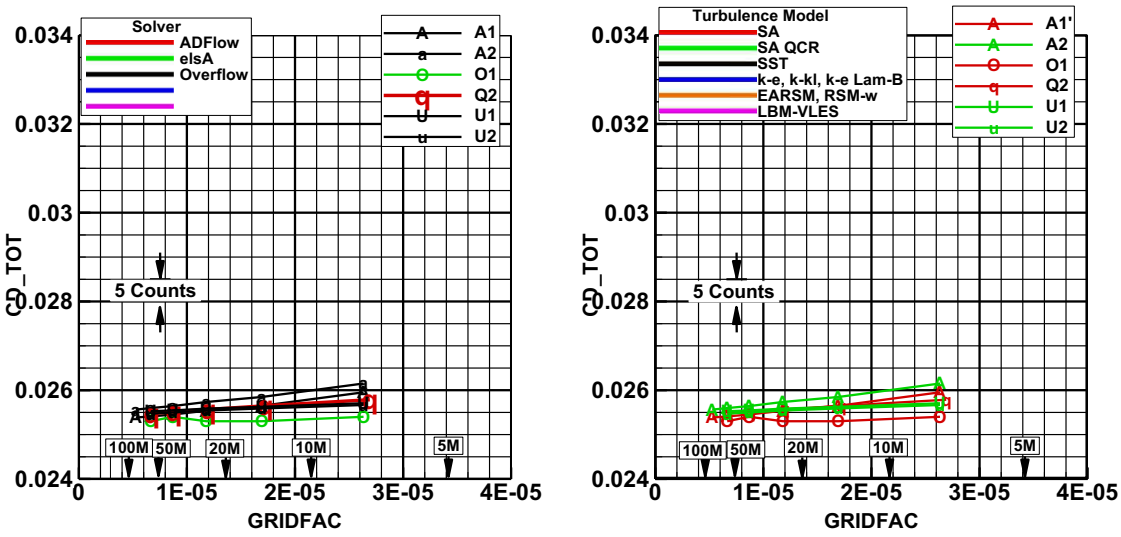


Figure A-D-46. DPW-VI: Grid Convergence; Total Drag C_{D_TOT}, M=0.85: Overflow Structured Grid Solutions.

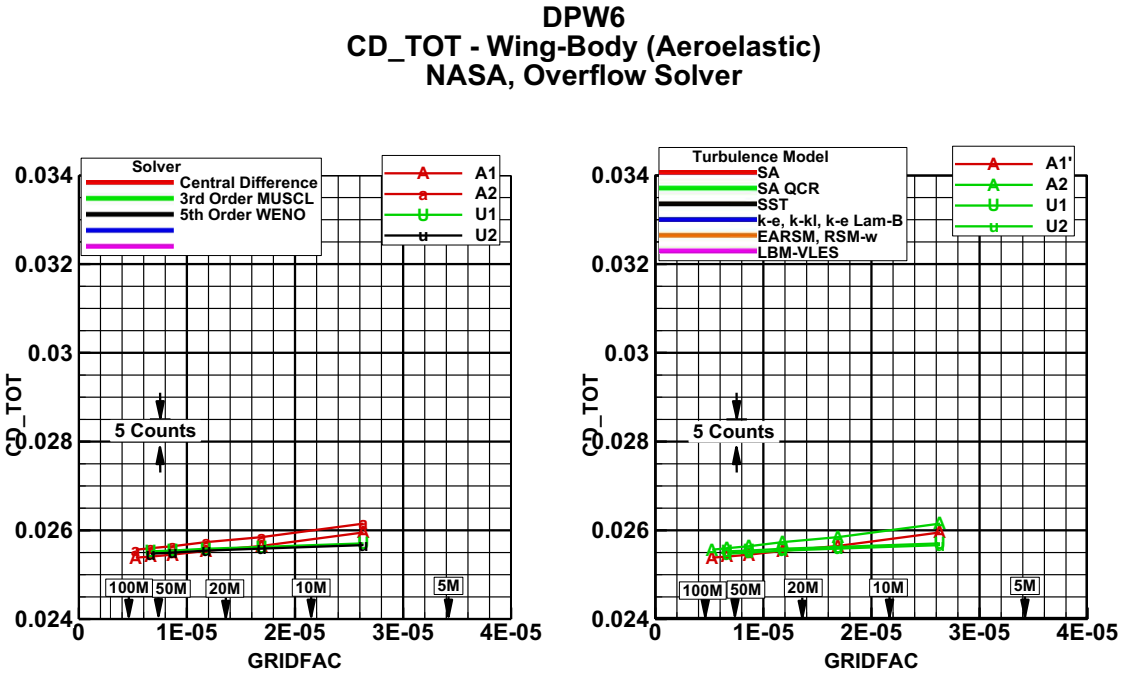


Figure A-D-47. DPW-VI: Grid Convergence; Total Drag C_{D_TOT}, M=0.85: NASA/Overflow Structured Grid Solutions.

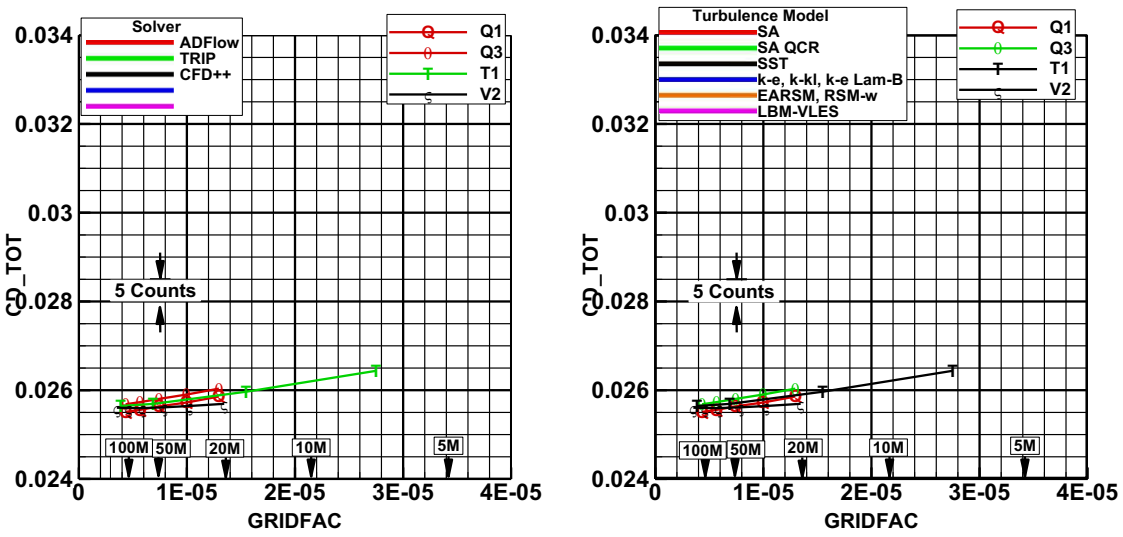


Figure A-D-48. DPW-VI: Grid Convergence; Total Drag C_{D_TOT}, M=0.85: Multiblock Structured Grid Solutions.

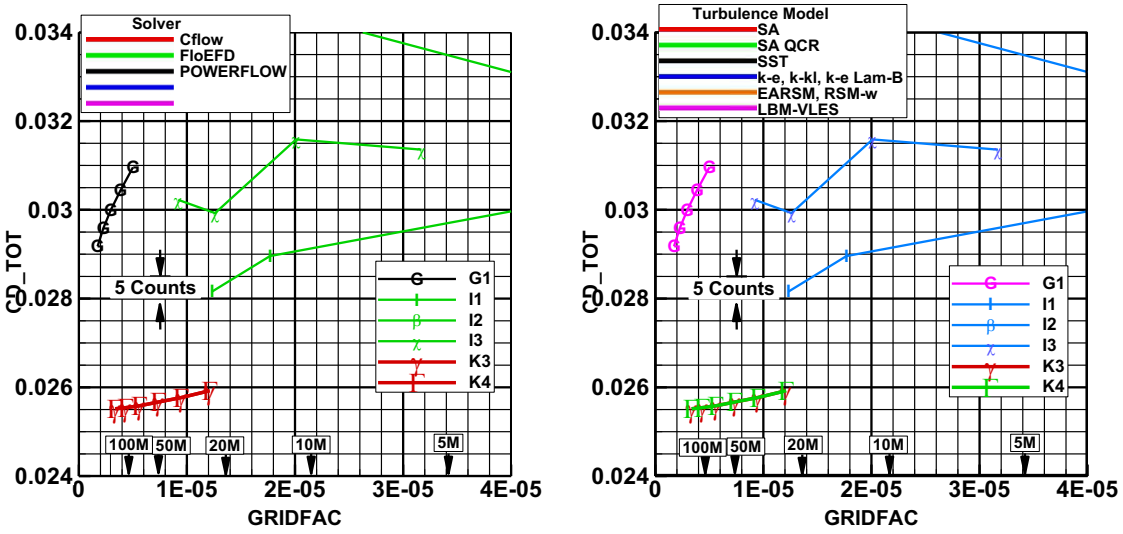


Figure A-D-49. DPW-VI: Grid Convergence; Total Drag C_{D_TOT}, M=0.85: Cartesian/Oct-Tree Grid Solutions.

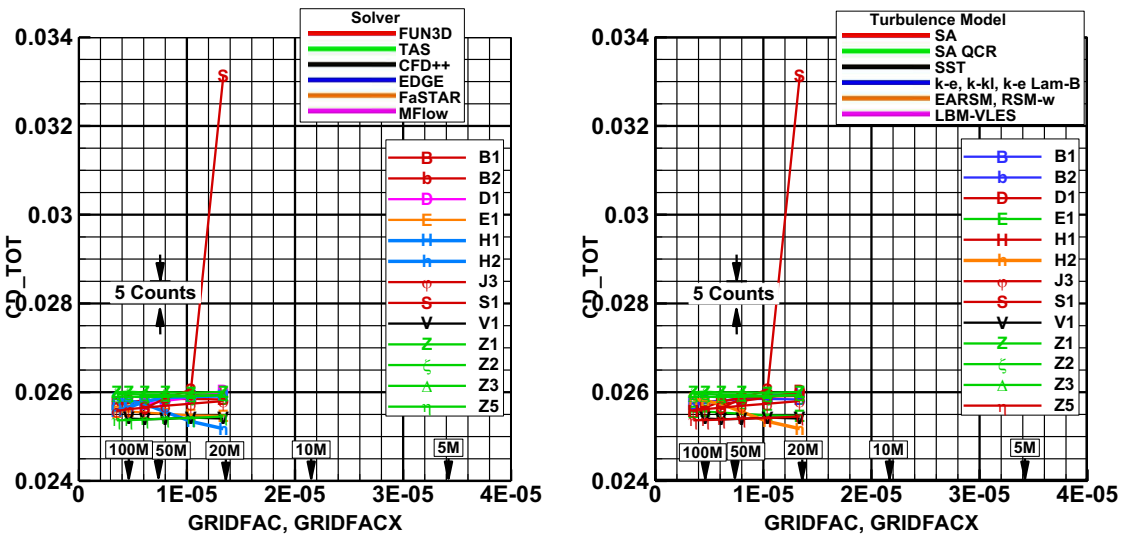


Figure A-D-50. DPW-VI: Grid Convergence; Total Drag C_{D_TOT}, M=0.85: Geolab Unstructured Grid Solutions.

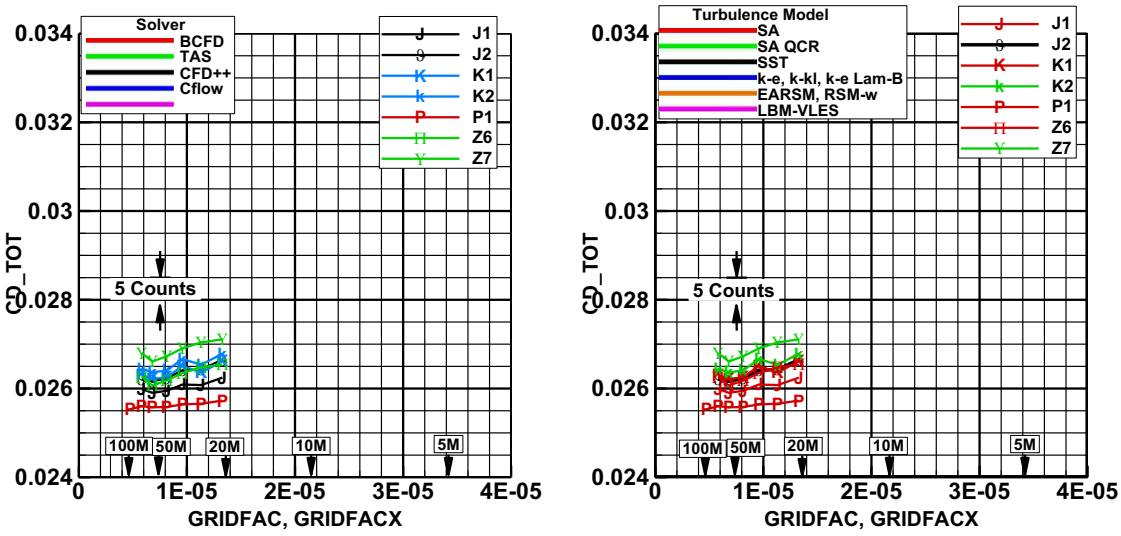


Figure A-D-51. DPW-VI: Grid Convergence; Total Drag C_{D_TOT}, M=0.85: Boeing Unstructured Grid Solutions.

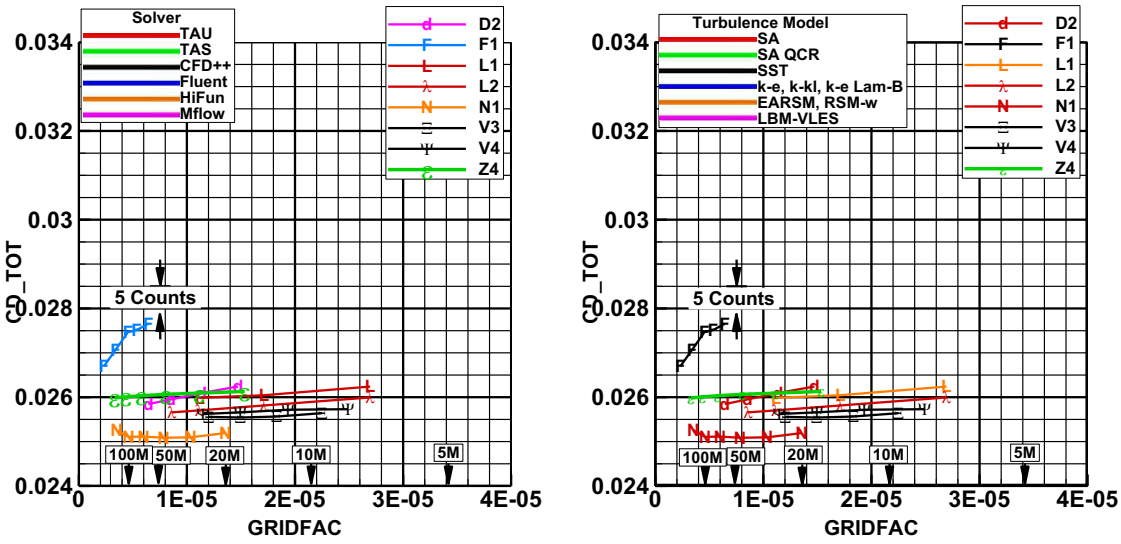


Figure A-D-52. DPW-VI: Grid Convergence; Total Drag $C_{D_{TOT}}$, M=0.85: Custom Unstructured Grid Solutions.

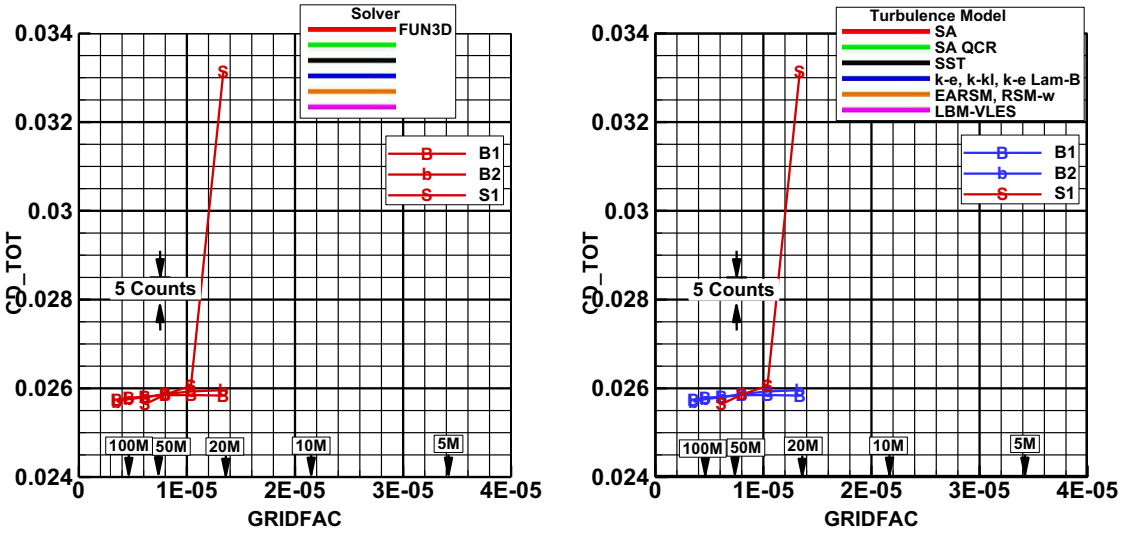


Figure A-D-53. DPW-VI: Grid Convergence; Total Drag $C_{D_{TOT}}$, M=0.85: FUN3D/Geolab Unstructured Grid Solutions.

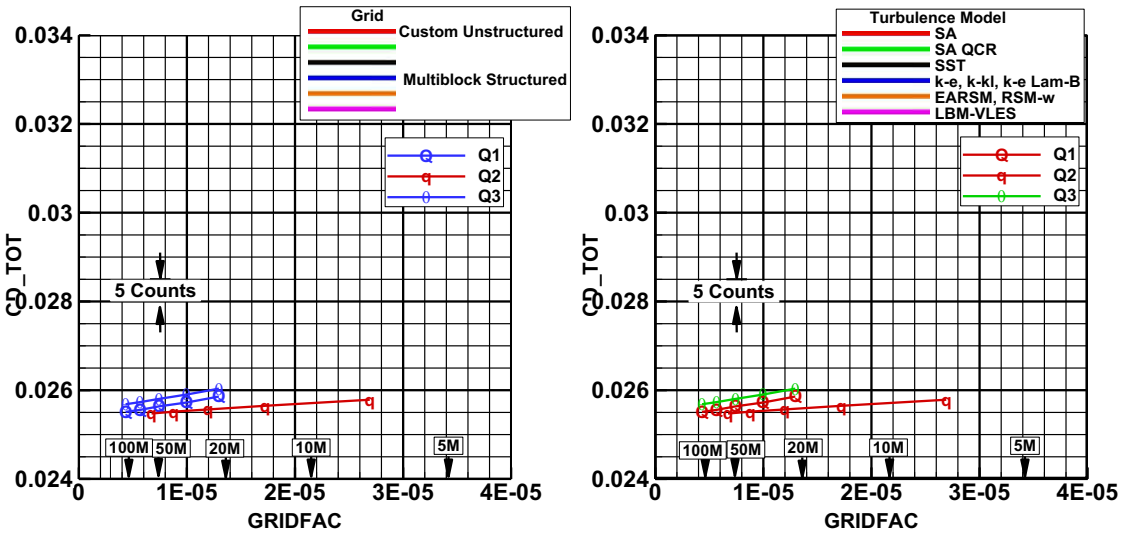


Figure A-D-54. DPW-VI: Grid Convergence; Total Drag C_{D_TOT}, M=0.85: MDOlab ADflow Solutions.

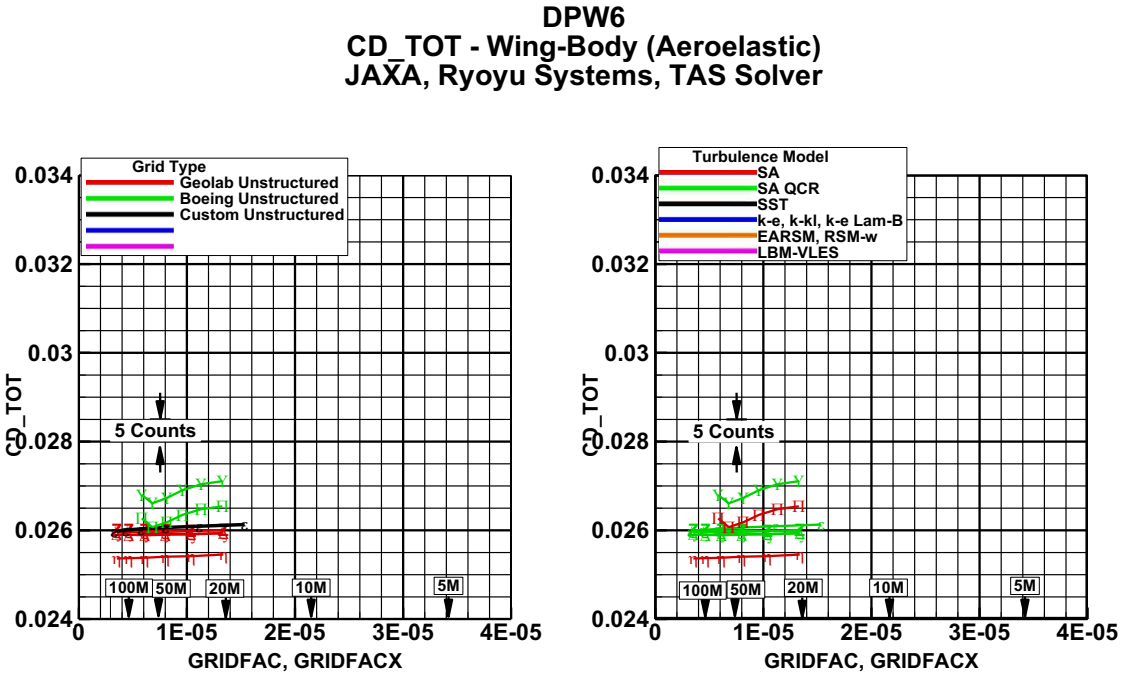


Figure A-D-55. DPW-VI: Grid Convergence; Total Drag C_{D_TOT}, M=0.85TAS Solver Solutions.

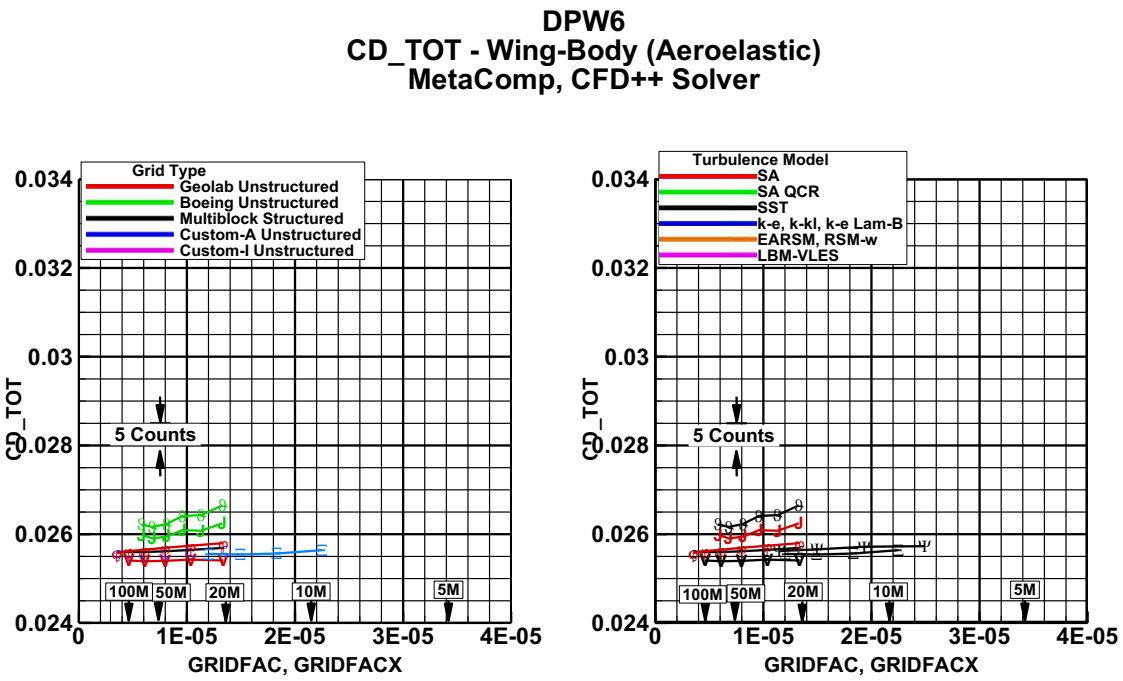


Figure A-D-56. DPW-VI: Grid Convergence; Total Drag C_{D_TOT}, M=0.85: CFD++ Solver Solutions.

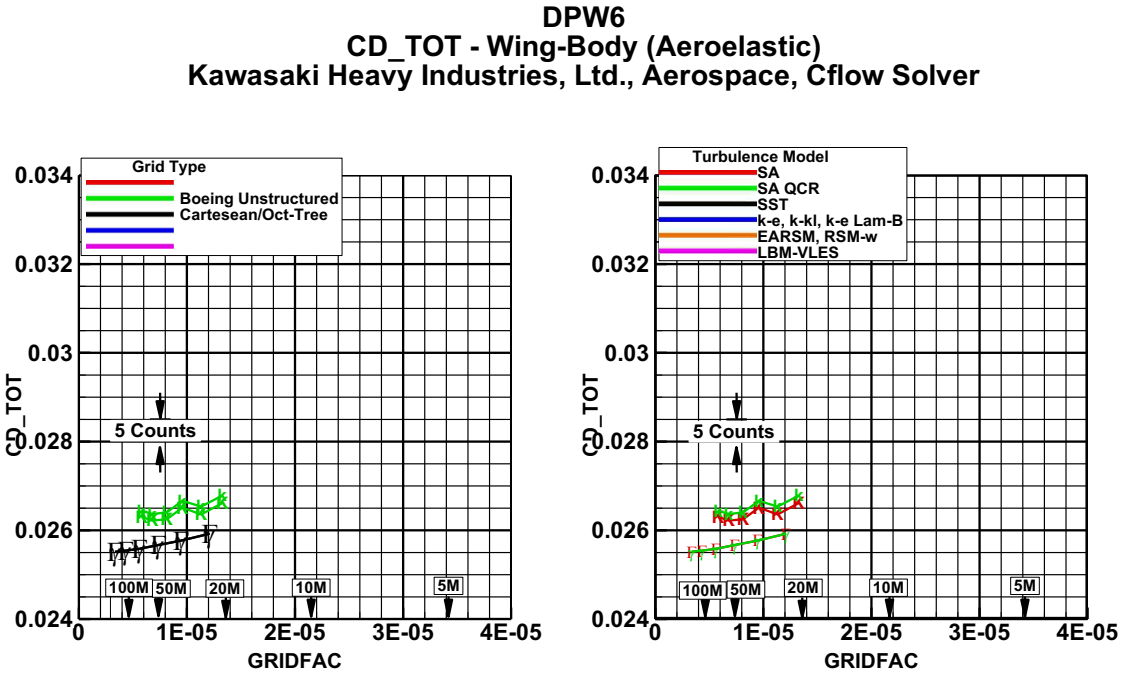


Figure A-D-57. DPW-VI: Grid Convergence; Total Drag C_{D_TOT}, M=0.85: Cflow Solver Solutions.

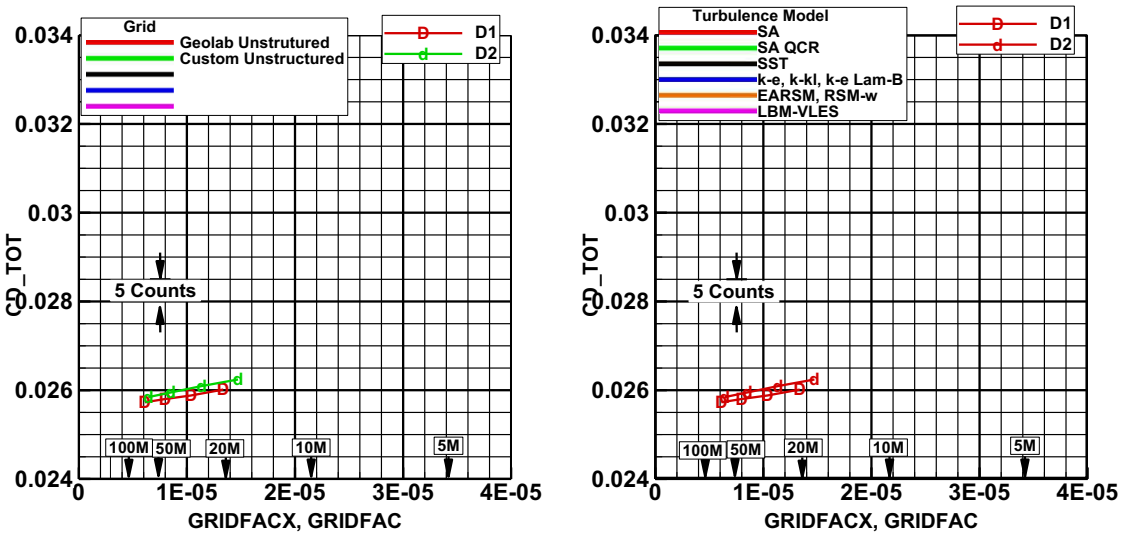


Figure A-D-58. DPW-VI: Grid Convergence; Total Drag C_{D_TOT}, M=0.85: CARDC, Mflow Solver Solutions.

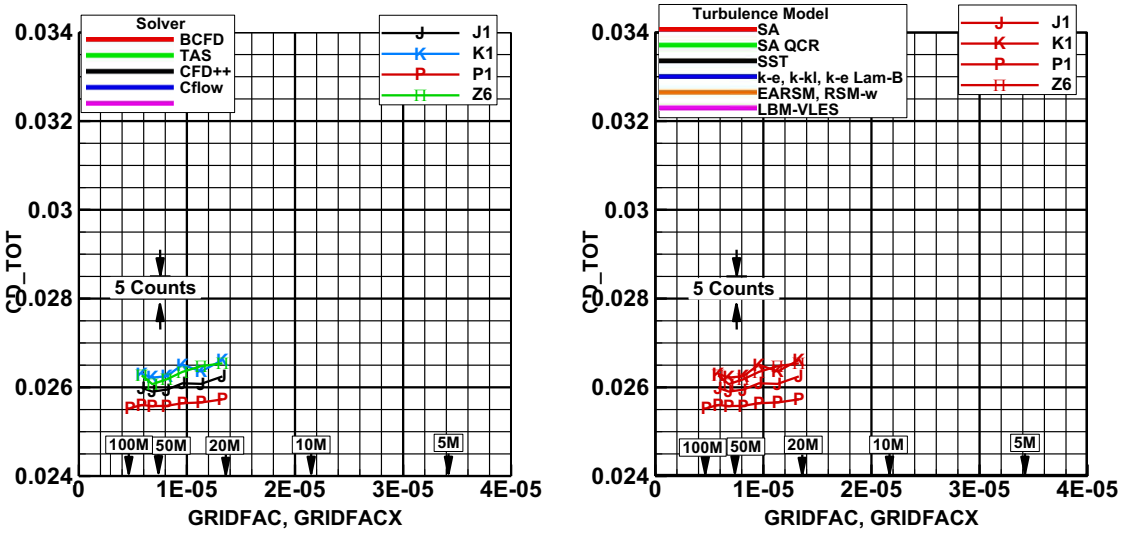


Figure A-D-59. DPW-VI: Grid Convergence; Total Drag C_{D_TOT}, M=0.85: Boeing Unstructured Grid Solutions with SA TM.

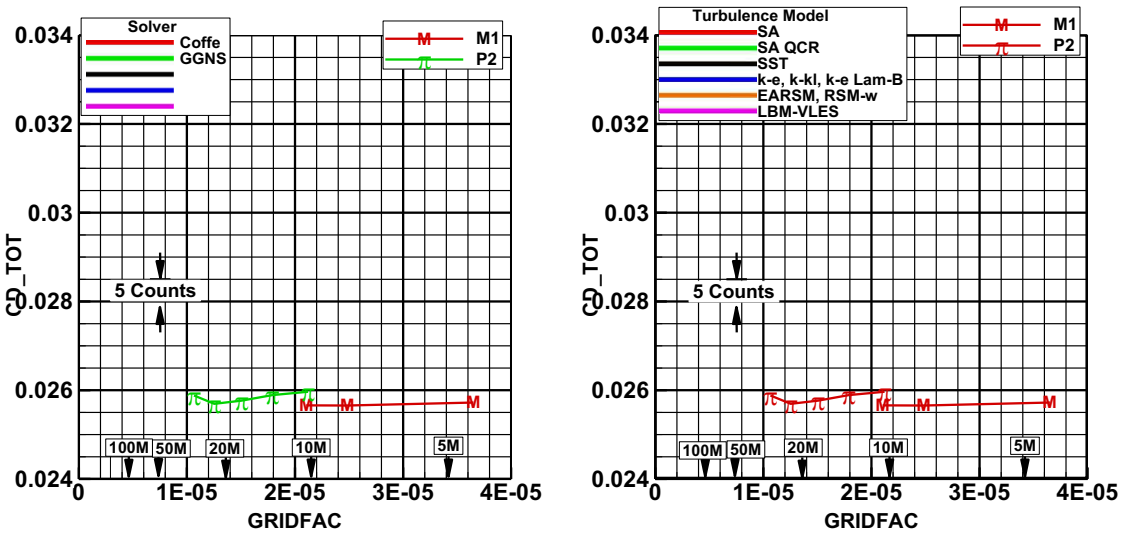


Figure A-D-60. DPW-VI: Grid Convergence; Total Drag $C_{D,TOT}$, M=0.85: All-Tests Unstructured Grid Solutions with Finite Element Solver.

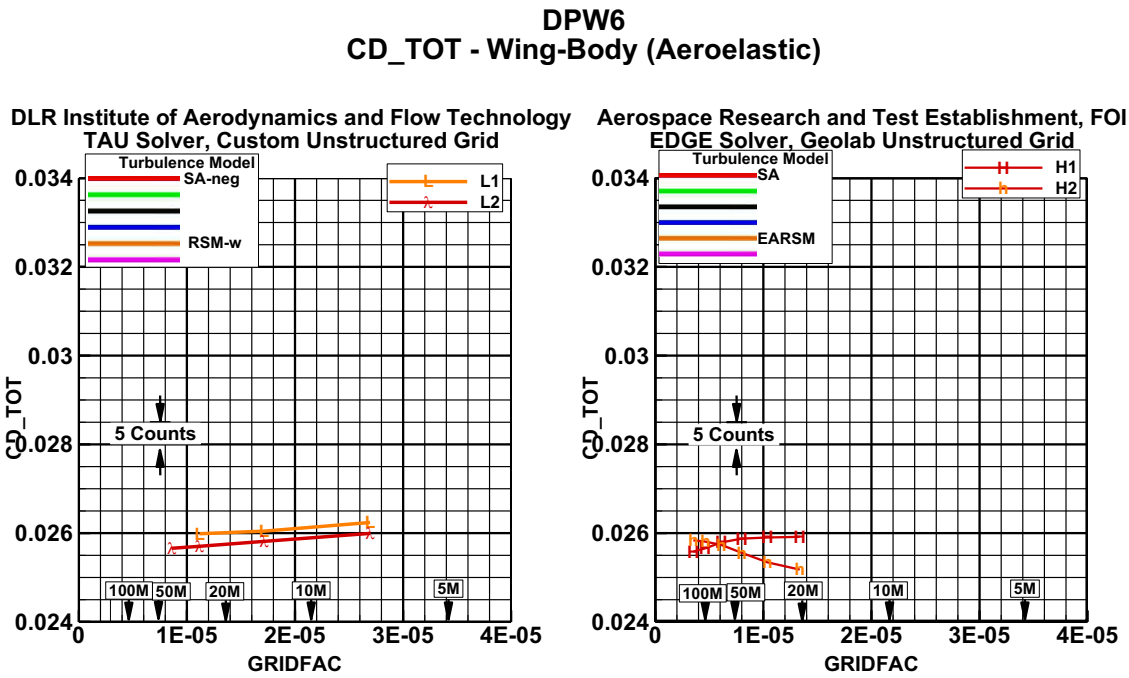


Figure A-D-61. DPW-VI: Grid Convergence; Total Drag $C_{D,TOT}$, M=0.85: Unstructured Grid Solutions with TAS and EDGE Solvers.

D-D-2. DPW-VI Grid Convergence: Wing-Body-Nacelle-Pylon (WBNP)

Table A-D-4. DPW6 Participants and Data Set Characteristics: Wing-Body-Nacelle-Pylon (Aeroelastic).

DPW-VI: CRM Wing-Body-Nacelle-Pylon (Aeroelastic)									
Team	ID	SYM	SYM	Organization	Code	Grid	Turbulence Model	dCD/ dGRIDFAC	CD_TOT
1	A1	A	A	Boeing, BCA Advanced Concepts, Long Beach CA	Overflow v2.2k	Overset	SA-RC	4.51	273.91
	A2	a	a			Overset	SA-RC w/QCR on	4.57	275.60
2	B1	B	B	NASA Langley Research Center	FUN3D 12.8	Unst-Geolab	k-kL-MEAH2015 w/Limiter	1.97	279.87
	B2	b	b			Unst-Geolab	k-kL-MEAH2015 no-limiter	2.81	278.59
3	D1	D	D	CARDC	Mflow	Unst-Geolab	SA	16.79	279.15
	D2	d	d			Unst-custom	SA	7.58	277.18
4	E1	E	E	JAXA, Ryoyu Systems	FaSTAR	Unst-Geolab	SA-noft2-R w/QCR2000	-0.65	277.48
5	F1	F	F	ANSYS	Fluent	Unst-custom	Menter k-w SST-V	32.90	286.22
6	G1	G	G	EXA Powerflow	PowerFLOW	Custom Cart	LBM-VLES	78.02	305.93
7	H1	H	H	Aerospace Research and Test Establishment, FOI	EDGE	Unst-Geolab	SA	3.76	276.95
	H2	h	h			Unst-Geolab	EARSM (Explicit Algebraic Reynolds Stress Model)	-7.85	282.02
8	I1	I	I	Mentor Graphics	FloEFD	Custom Cart	Default k-e Lam-Bremhorst	4.30	300.23
	I2	β	b			Custom Cart	Subgrid k-e Lam-Bremhorst	3.70	341.68
9	J1	J	J	Metacomp	CFD++	Unst-Boeing	SA	2.36	284.11
	J2	ϑ	J			Unst-Boeing	Menter k-w SST-V	4.97	284.37
	J3	φ	j			Unst-Geolab	SA	7.71	277.58
10	K1	K	K	Kawasaki Heavy Industries	Cflow	Unst-Boeing	SA-noft2	3.94	285.44
	K2	k	k			Unst-Boeing	SA-noft2 w/QCR200	4.27	286.59
	K3	γ	g			Custom Cart	SA-noft2	8.15	275.03
	K4	Γ	G			Custom Cart	SA-noft2 w/QCR200	8.15	275.03
11	L1	L	L	DLR, Institute of Aerodynamics and Flow	TAU	Unst-custom	RSM-ω	3.74	278.82
	L2	λ	l			Unst-custom	SA-neg	3.72	277.24
12	M1	M	M	Tennessee, Pointwise, NASA Langley, NAVAIR, MIT, U Ala	COFFE/KCFD	Unst-custom	SA-neg	0.52	279.93
13	N1	N	N	CAd Lab, Indian Institute of Sci	HiFun	Unst-custom	SA	0.90	274.12
14	O1	O	O	ONERA	elsA	Overset	SA	0.71	274.43
15	P1	P	P	Boeing - St. Louis	BCFD	Unst-Boeing	SA-RC	4.39	276.23
16	Q1	Q	Q	MDOlab, University of Michigan	ADflow	Embraer MB	SA 1stOrder	6.89	276.82
	Q2	q	q			Cust-Overset	SA 1stOrder	2.75	276.03
18	S1	S	S	Textron Aviation (Cessna)	FUN3D	Unst-Geolab	SA-RC	177.47	232.85
19	T1	T	T	CARDC	TRIP	CommonMB	Menter k-w SST-2003	4.76	277.47
20	U1	U	U	Applied Research Lab, Penn State	Overflow 2.21 3rd Order WENO	Overset	SA-RC W/QCF2000	1.30	276.02
	U2	u	u		Overflow 2.21 5TH Order WENO	Overset	SA-RC W/QCF2000	0.99	275.61
21	V1	V	V	Embraer S/A	CFD++	Unst-Geolab	Menter k-w SST-V	0.06	275.77
	V3	Ξ	X			Unst-custom-A	Menter k-w SST-V	1.79	275.63
	V4	Ψ	Y			Unst-custom-I	Menter k-w SST-V	1.24	279.59
25	Z1	Z	Z	JAXA, Ryoyu Systems	TAS limiter K=1	Unst-Geolab	SA-noft2-R w/QCR2000	1.09	282.04
	Z2	ζ	z		TAS limiter K=5	Unst-Geolab	SA-noft2-R w/QCR2000	0.42	281.67
	Z3	Δ	D		TAS limiter K=10	Unst-Geolab	SA-noft2-R w/QCR2000	0.69	280.83
	Z4	ε	e		TAS limiter K=10	Unst-custom	SA-noft2-R w/QCR2000	1.55	282.87

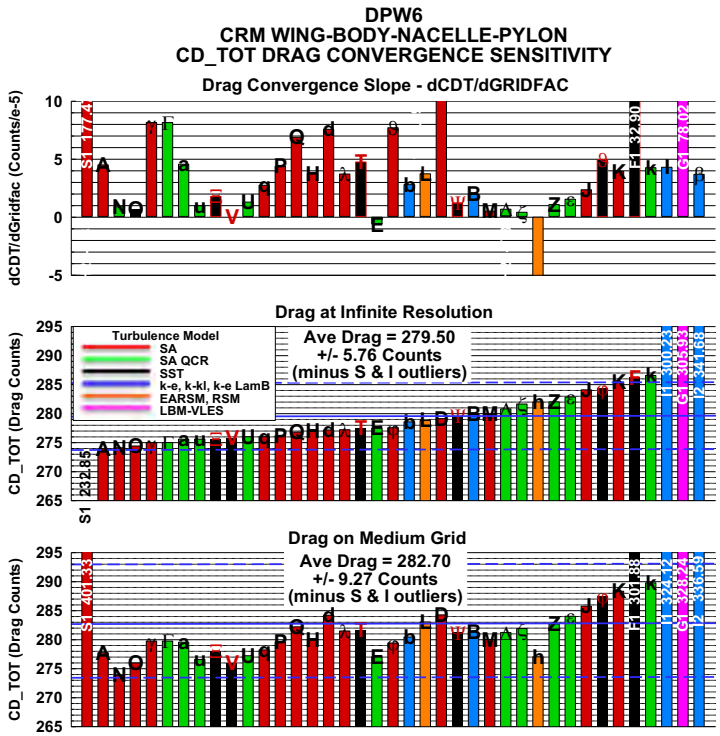


Figure A-D-62. DPW-VI WBNP Total Drag Grid Convergence Sensitivity, M=0.85 (Figure S-VII-15).

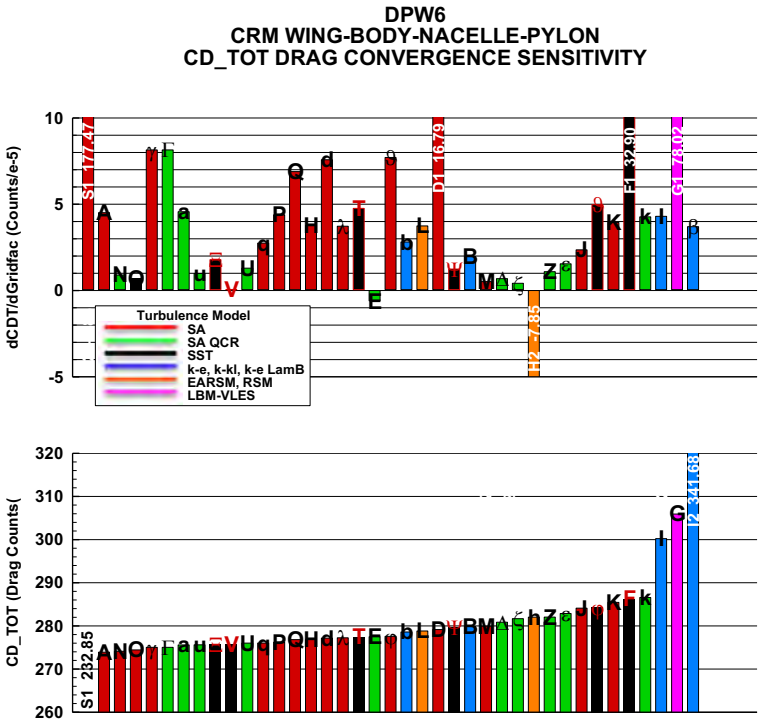


Figure A-D-63. DPW-VI: WBNP Total Drag Grid Convergence Sensitivity, M=0.85: TM.

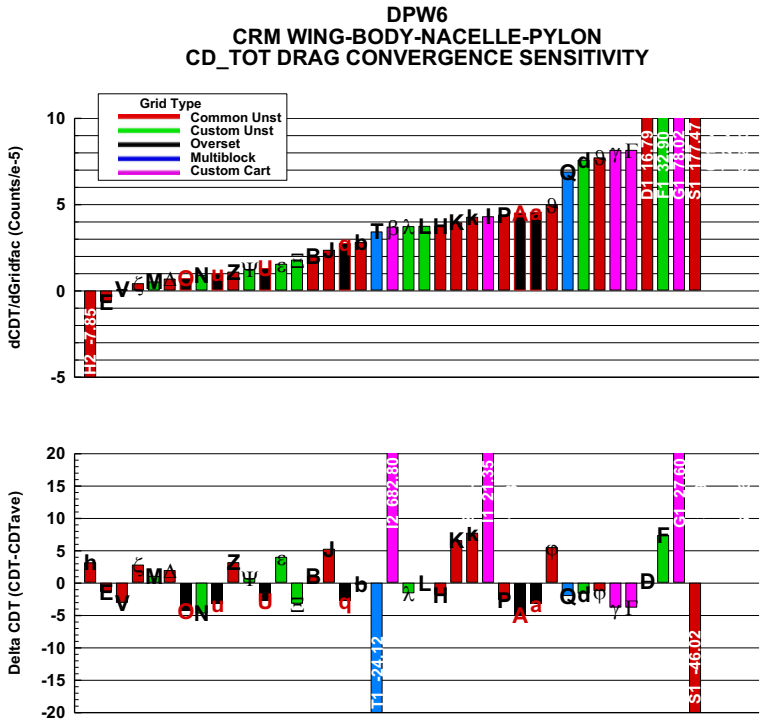


Figure A-D-64. DPW-VI: WBNP Total Drag Grid Convergence Sensitivity, M=0.85: Ordered by Sensitivity; Grid.

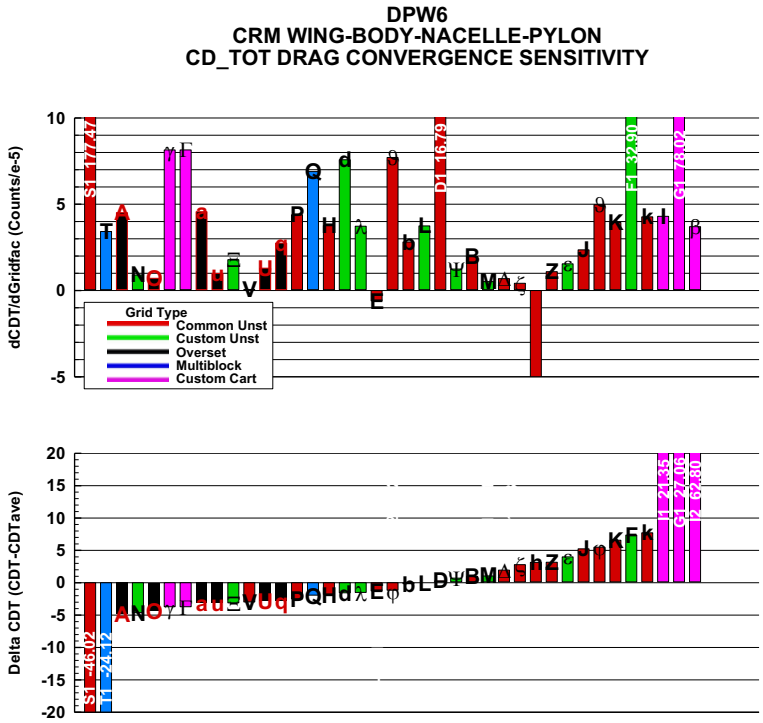


Figure A-D-65. DPW-VI: WBNP Total Drag Grid Convergence Sensitivity, M=0.85: Ordered by Delta Drag; Grid.

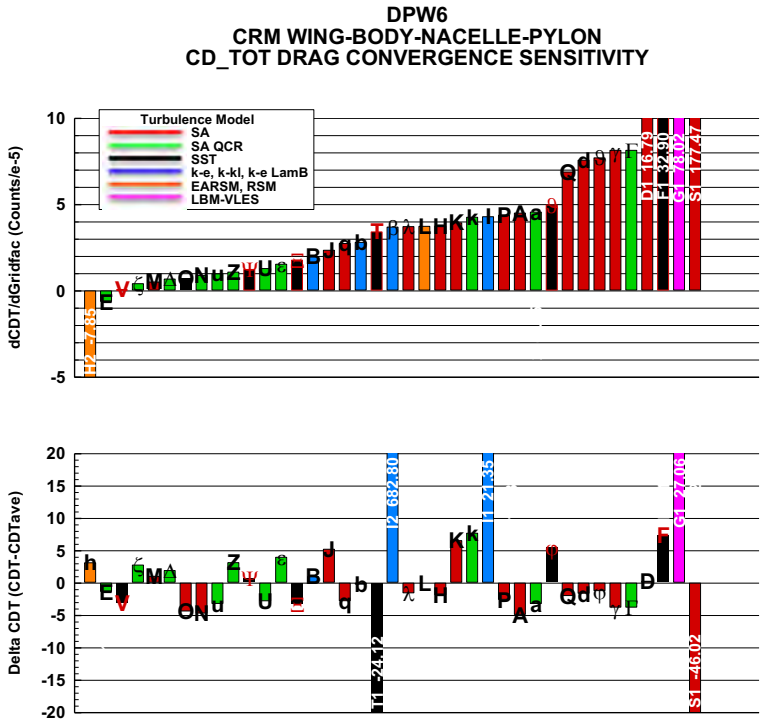


Figure A-D-66. DPW-VI: WBNP Total Drag Grid Convergence Sensitivity, M=0.85: Ordered by Sensitivity; TM.

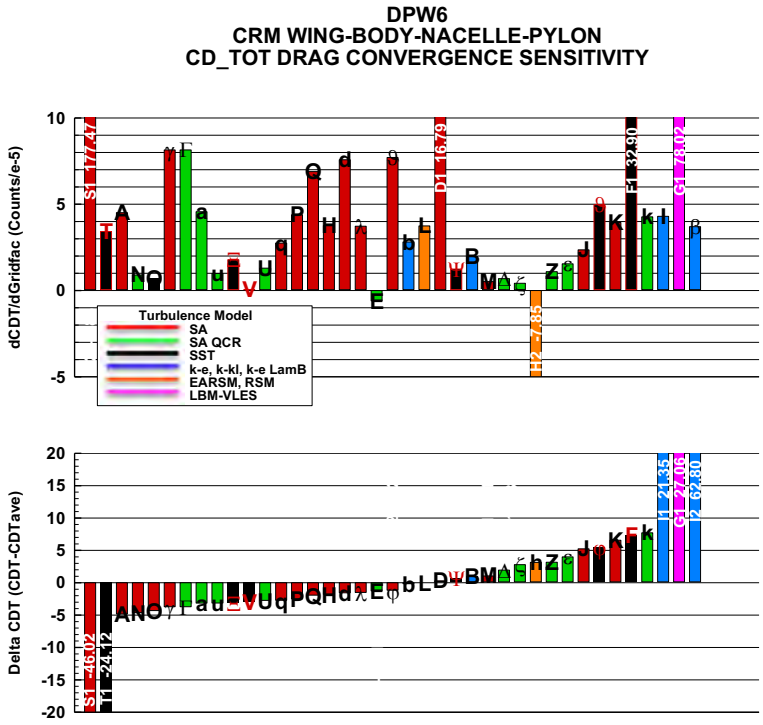


Figure A-D-67. DPW-VI: WBNP Total Drag Grid Convergence Sensitivity, M=0.85: Ordered by Delta Drag; TM.

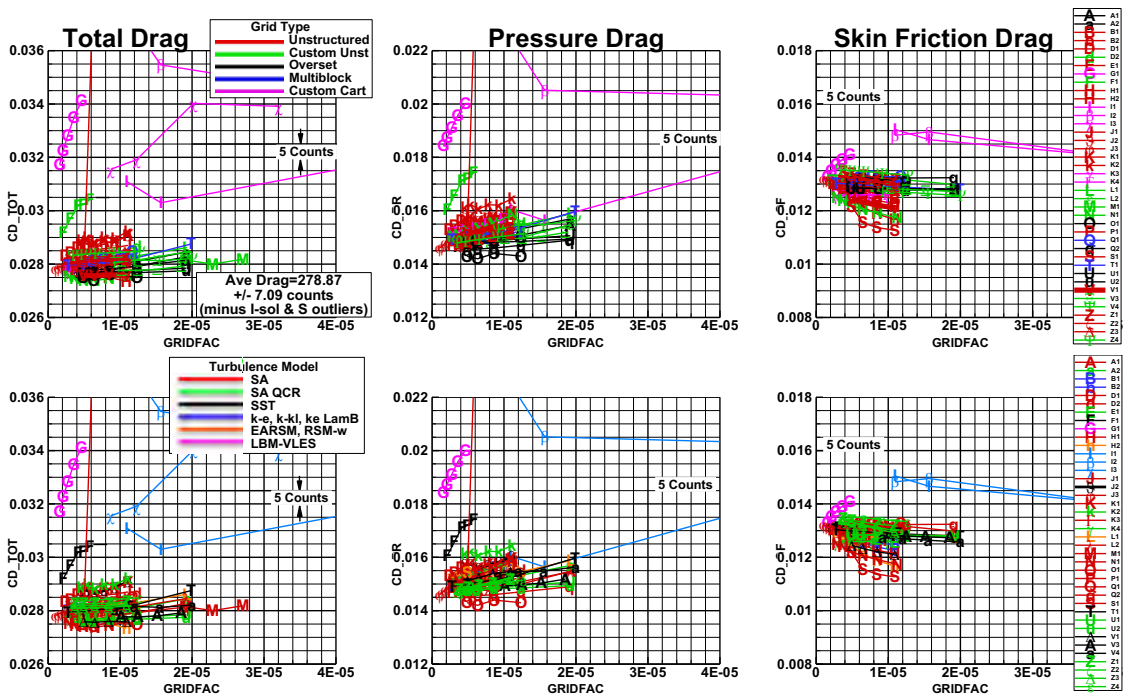


Figure A-D-68. DPW-VI: WBNP Grid Convergence; Total, Pressure, and Skin Friction Drag, M=0.85: All Solutions.

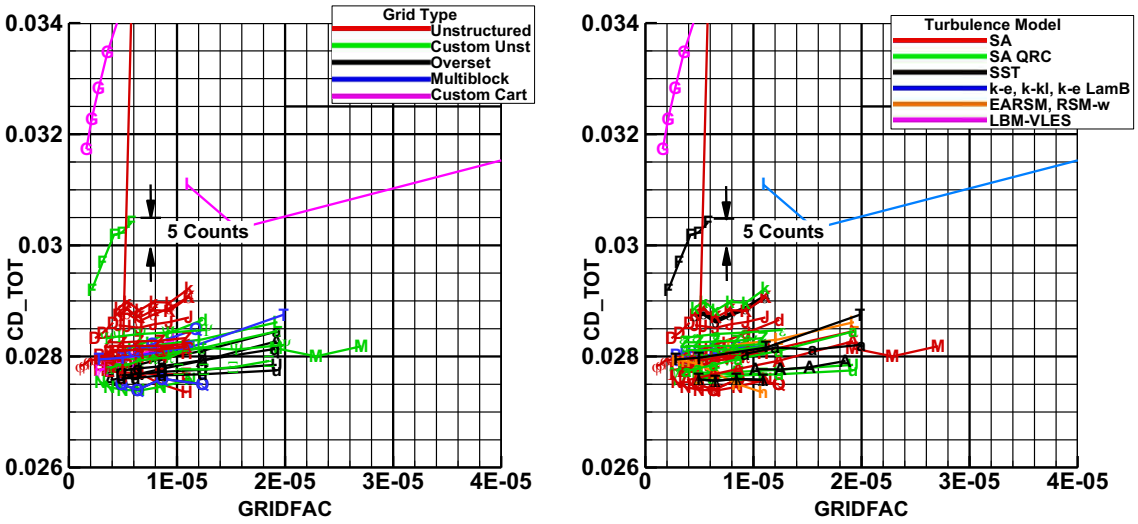


Figure A-D-69. DPW-VI: WBNP Grid Convergence; Total Drag, M=0.85: All Solutions.

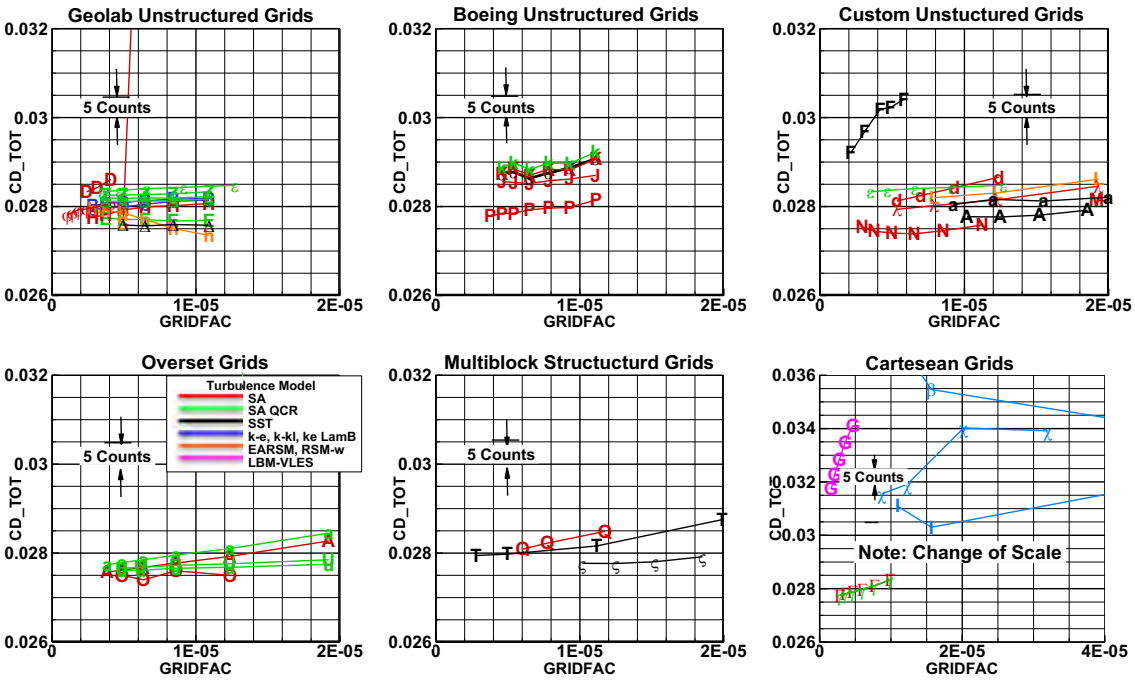


Figure A-D-70. DPW-VI: WBNP Grid Convergence; Total Drag, M=0.85: All Solutions Parsed by Grid Type and Turbulence Model.

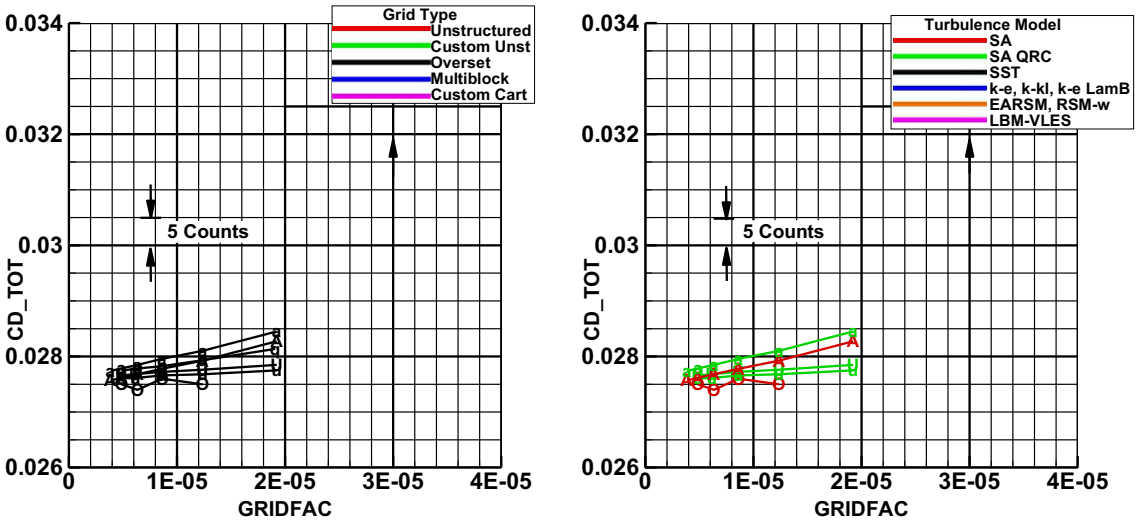


Figure A-D-71. DPW-VI: WBNP Grid Convergence; Total Drag, M=0.85: Overset Grid Solutions.

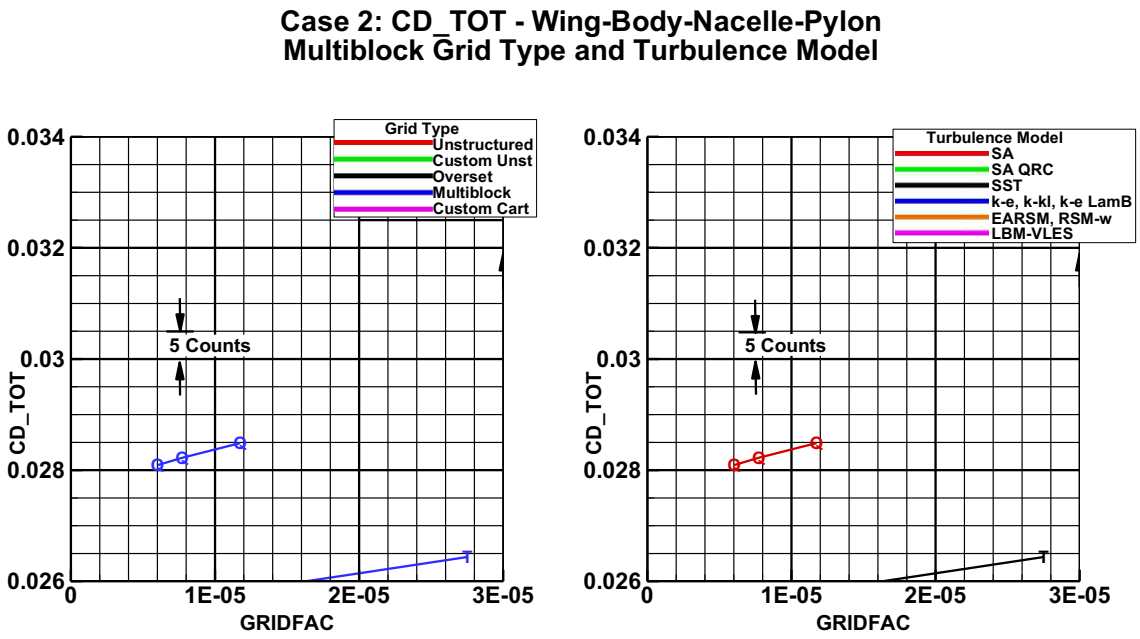


Figure A-D-72. DPW-VI: WBNP Grid Convergence; Total Drag, M=0.85: Multiblock Structured Grid Solutions.

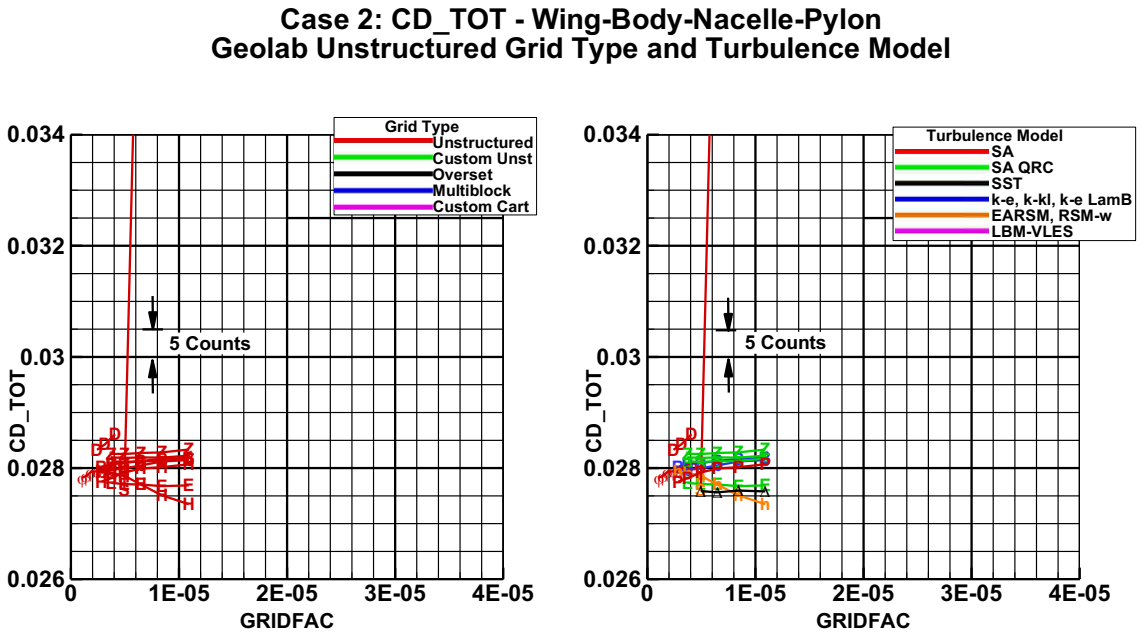


Figure A-D-73. DPW-VI: WBNP Grid Convergence; Total Drag, M=0.85: Geolab Unstructured Grid Solutions.

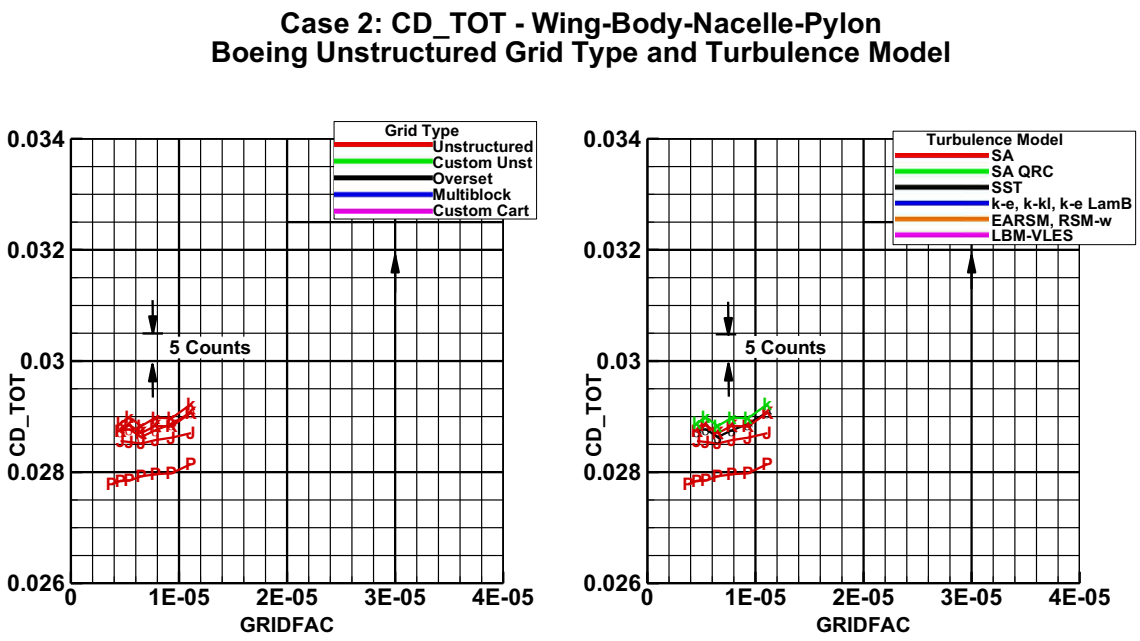


Figure A-D-74. DPW-VI: WBNP Grid Convergence; Total Drag, M=0.85: Boeing Unstructured Grid Solutions.

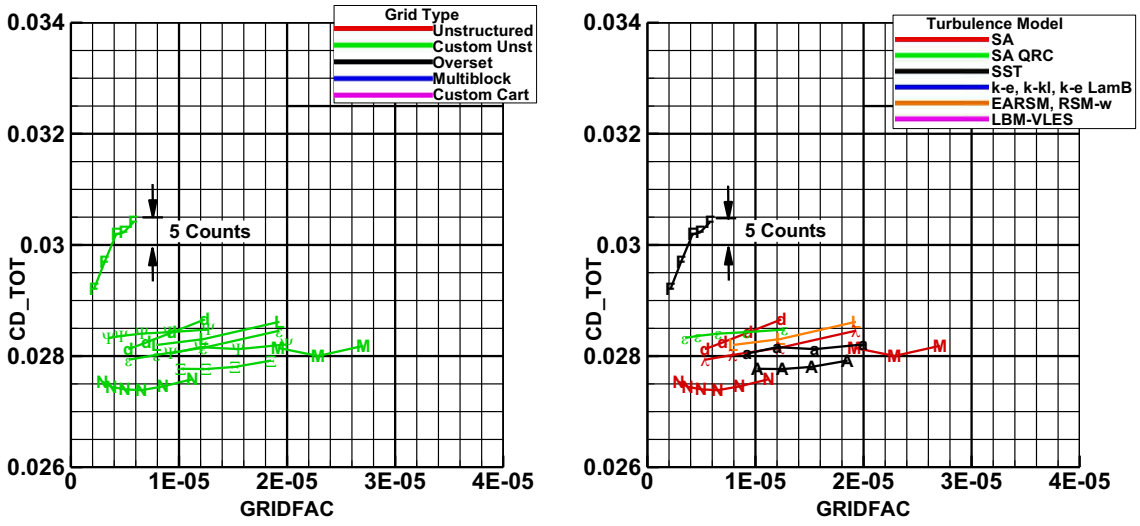


Figure A-D-75. DPW-VI: WBNP Grid Convergence; Total Drag, M=0.85: Custom Unstructured Grid Solutions.

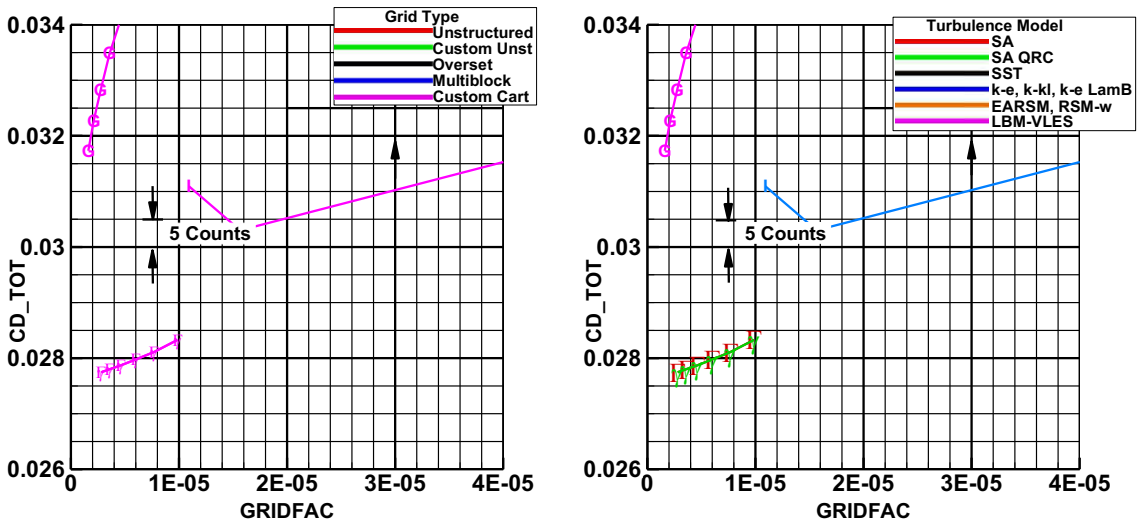


Figure A-D-76. DPW-VI: WBNP Grid Convergence; Total Drag, M=0.85: Cartesian/Oct-tree Grid Solutions.

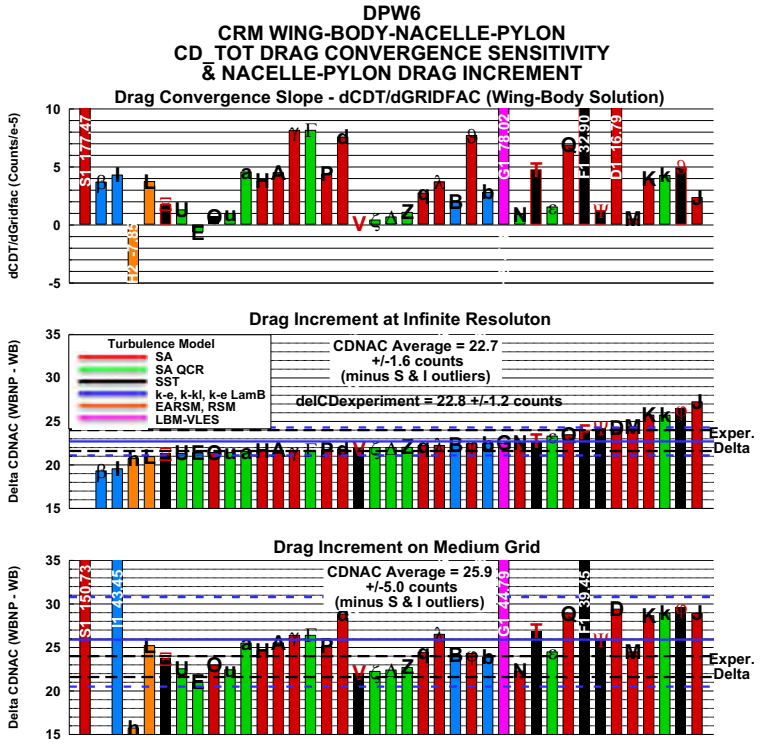


Figure A-D-77. DPW-VI: WBNP Drag Increment Grid Convergence Sensitivity, M=0.85. (Figure S-VII-18).

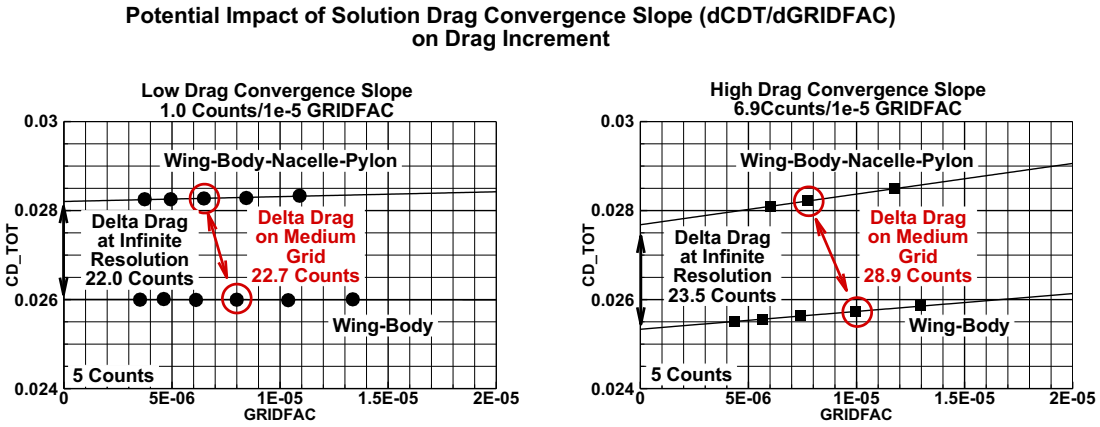


Figure A-D-78. DPW-VI: Impact of Grid Drag Convergence Slope on Drag Increment, M=0.85 (Figure S-VII-18).

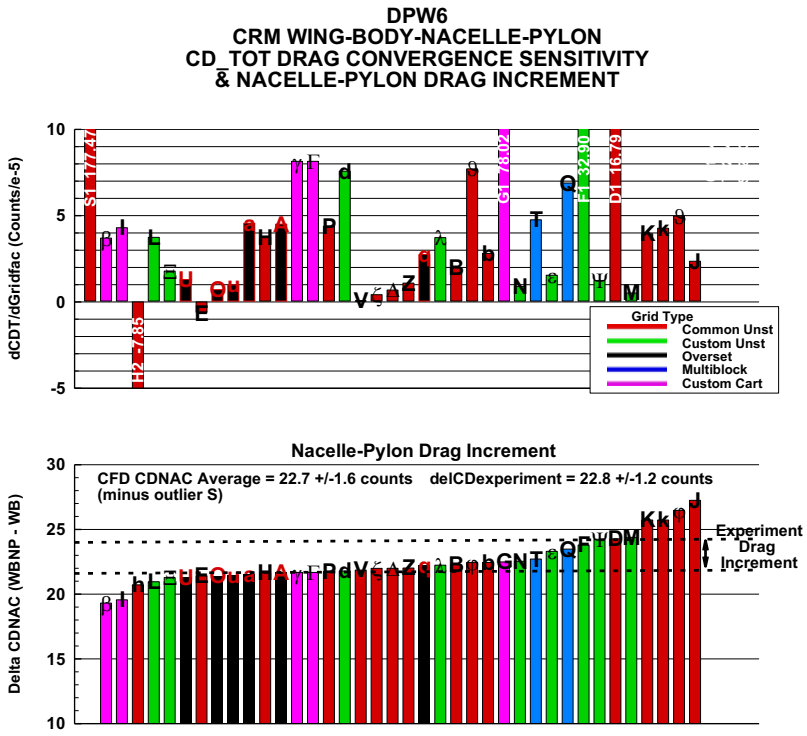


Figure A-D-79. DPW-VI: WBNP Drag Increment Grid Convergence Sensitivity, M=0.85: Ordered by Drag Increment.

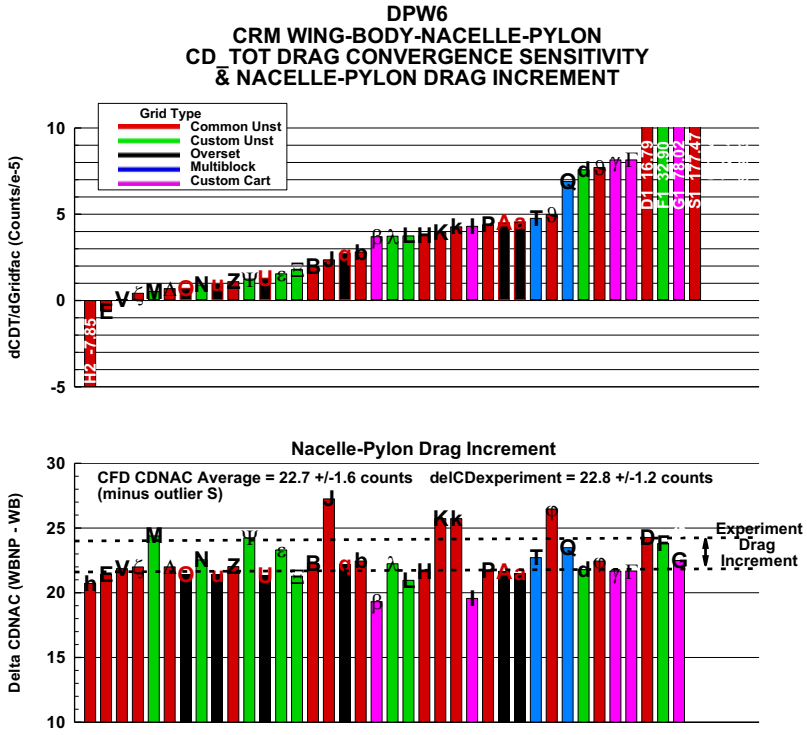


Figure A-D-80. DPW-VI: WBNP Drag Increment Grid Convergence Sensitivity, M=0.85: Ordered by Drag Sensitivity; Grid.

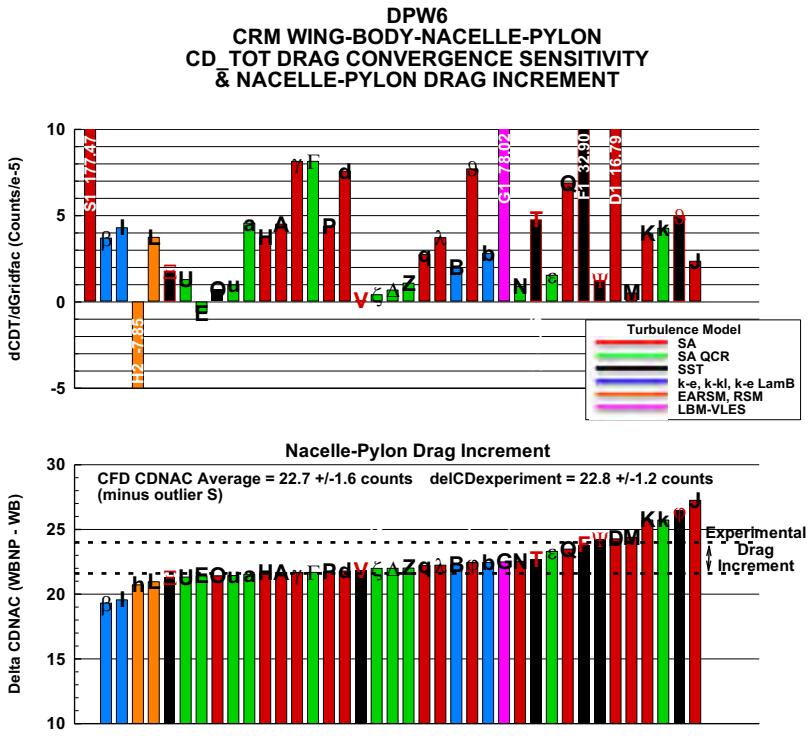


Figure A-D-81. DPW-VI: WBNP Drag Increment Grid Convergence Sensitivity, M=0.85: Ordered by Drag Increment; TM.

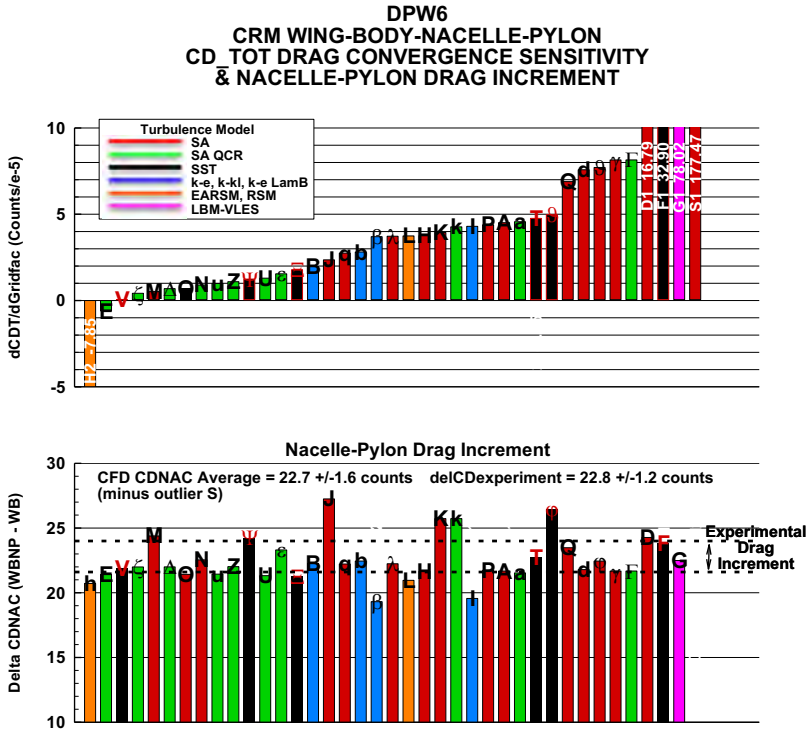


Figure A-D-82. DPW-VI: WBNP Drag Increment Grid Convergence Sensitivity, M=0.85: Ordered by Drag Sensitivity; TM.

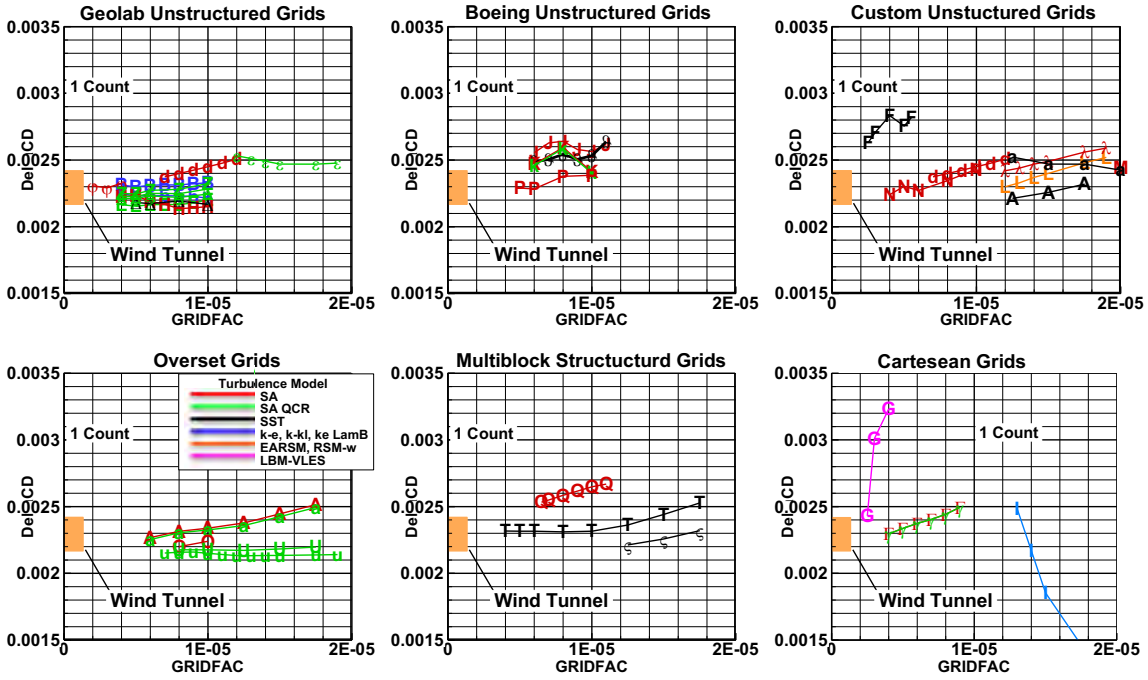


Figure A-D-83. DPW-VI: WBNP Grid Convergence; Drag Increment Compared to Test, M=0.85: All Solutions Parsed by Grid Type and Turbulence Model.

Appendix E. Angle-of-Attack Sweep Forces and Moments

An important recurring case in all the Drag Prediction Workshops has been the angle-of-attack sweep. This allows a look at the lift, drag, and pitching moment characteristics over a range of angle-of-attack of the computational results, and their comparison with experimental data as appropriate. Discussion of the CRM Wing-Body results from DPW-IV, -V, and -VI will be found in Section X – Angle-of-Attack Sweep/Buffet Study of this report. This appendix contains plots from Section X and additional plots showing total lift, drag, and pitching moment, wing sectional lift and pitching moment, and further parsing of forces and moments by grid and turbulence model. The participant data-set key for each Workshop is found in Appendix C.

E-A. DPW-IV: CRM Wing-Body (As-Built)

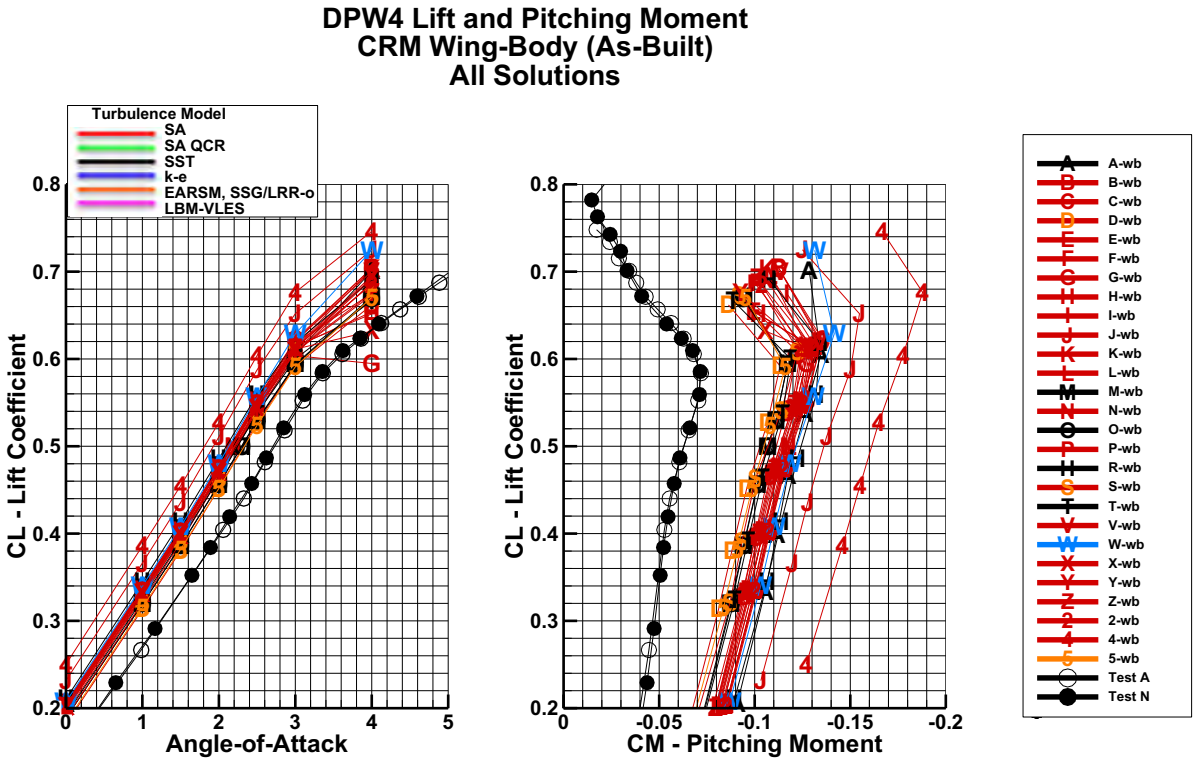


Figure A-E-1. DPW-IV: Lift and Pitching Moment, M=0.85; All Solutions.

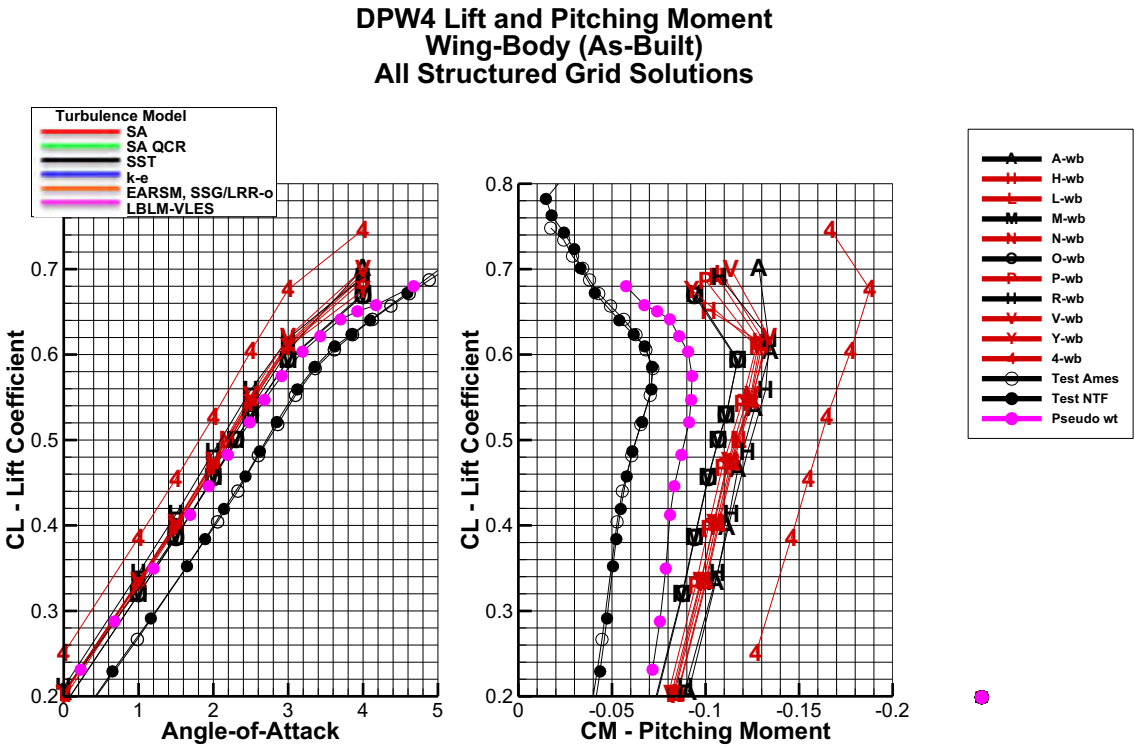


Figure A-E-2. DPW-IV: Lift and Pitching Moment; Structured Grid Solutions, M=0.85 (See Figure A-E-8 for Pseudo WT).

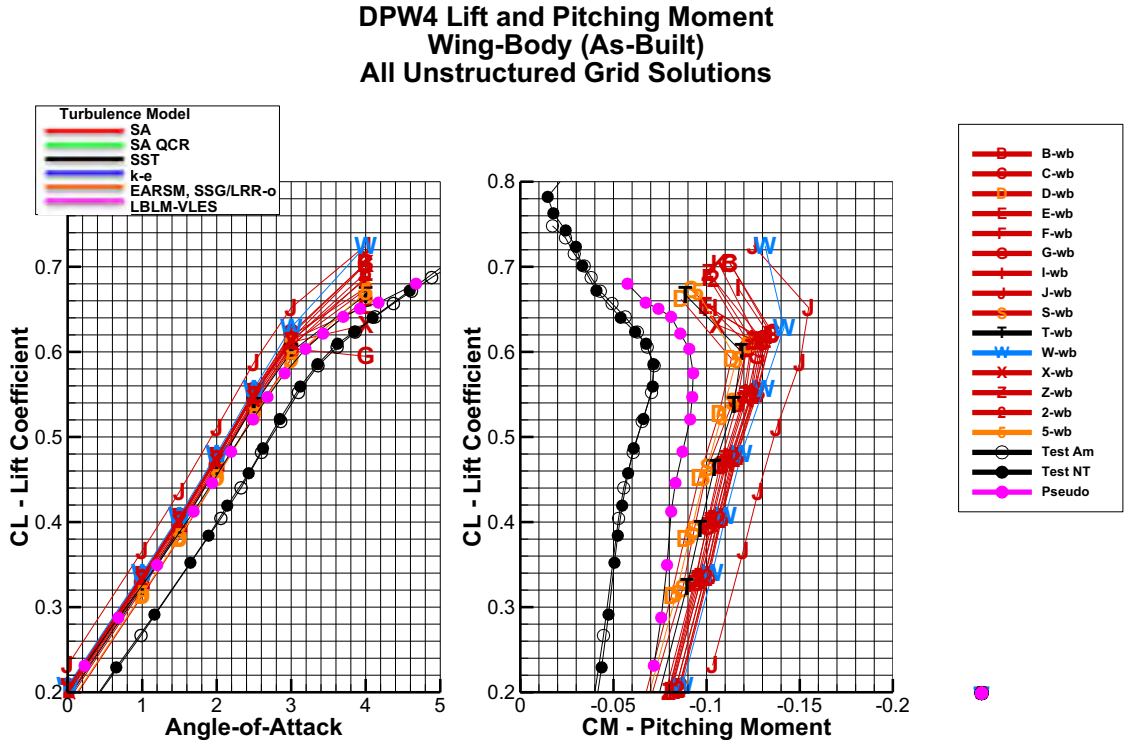


Figure A-E-3. DPW-IV: Lift and Pitching Moment; Unstructured Grid Solutions, M=0.85 (See Figure A-E-8 for Pseudo WT).

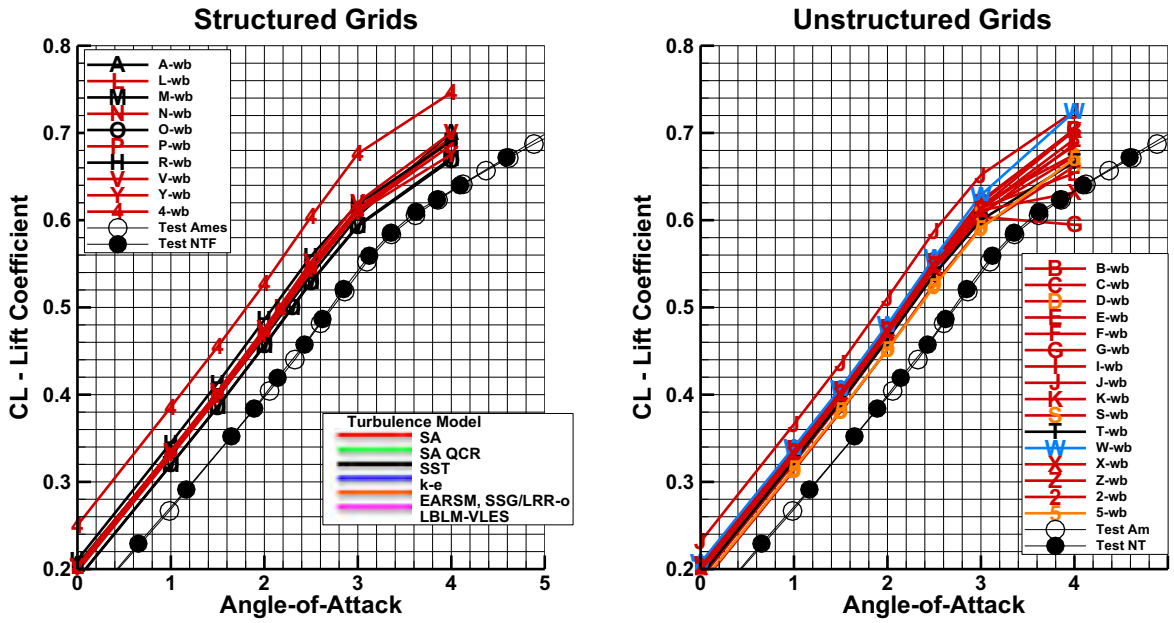


Figure A-E-4. DPW-IV: Lift; Structured and Unstructured Grid Solutions, M=0.85.

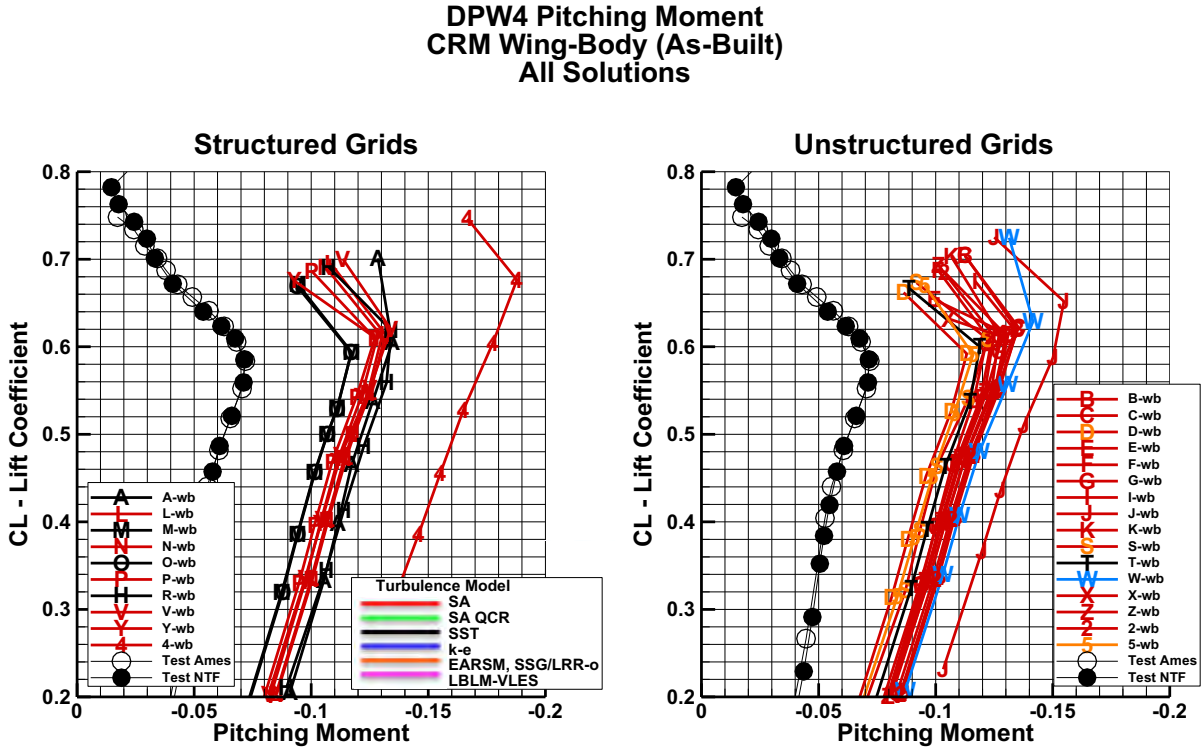


Figure A-E-5. DPW-IV: Pitching Moment; Structured and Unstructured Grid Solutions, M=0.85.

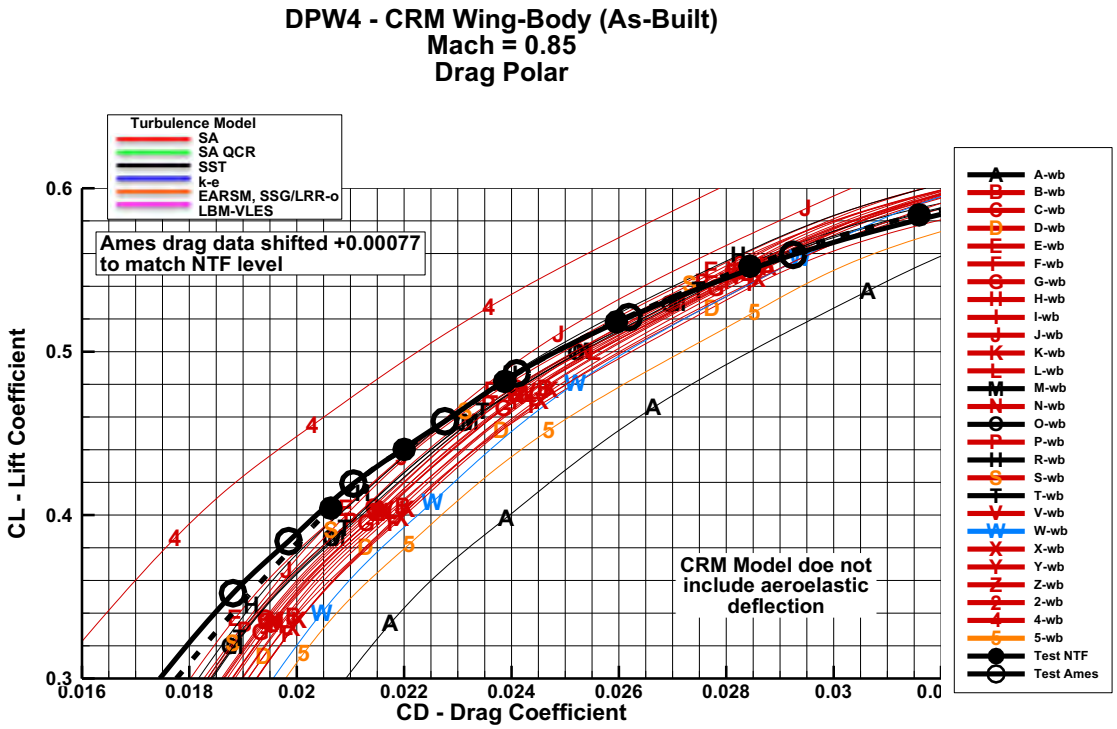


Figure A-E-6. DPW-IV: Drag Polar; All Solutions, M=0.85.

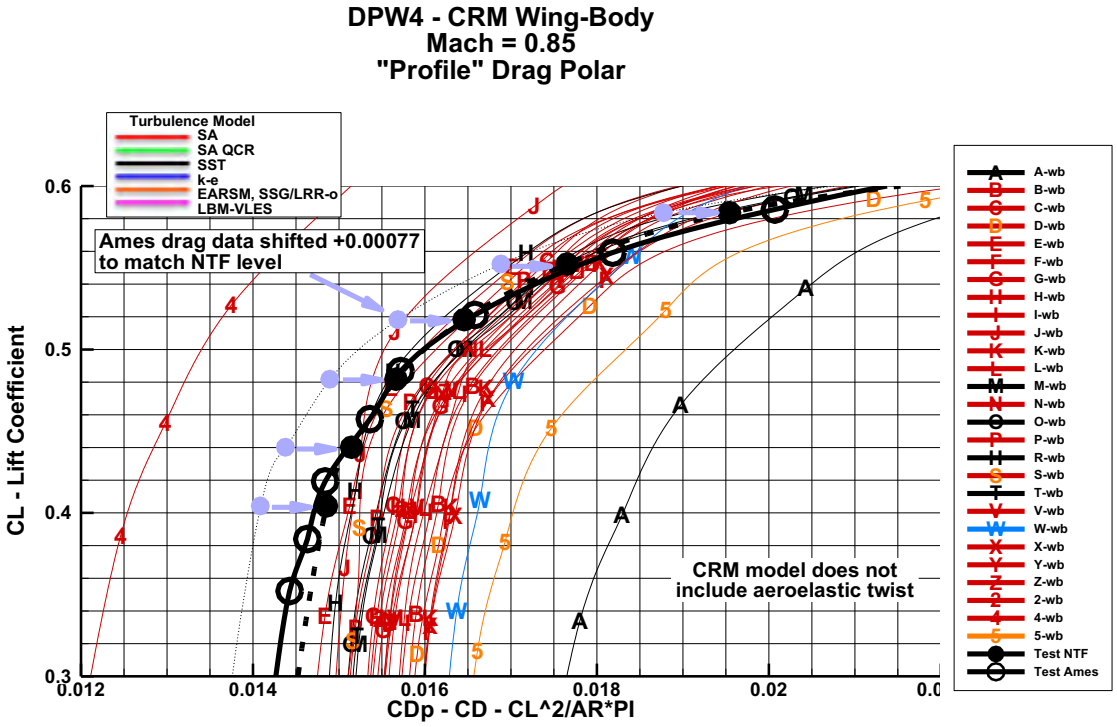
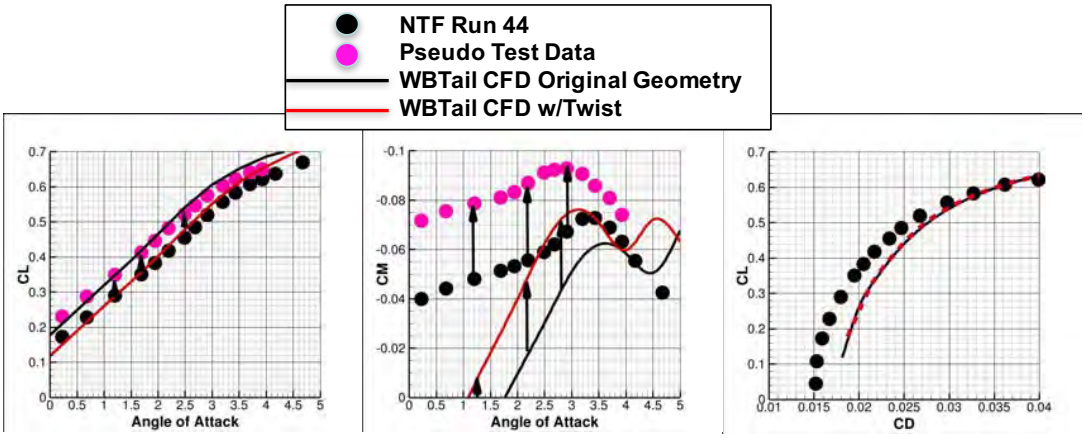


Figure A-E-7. DPW-IV: "Profile" Drag Polar; All Solutions, M=0.85.

CREATION OF "PSEUDO TEST DATA"

- The CRM geometry used for DPW5 was that of the wind tunnel model definition
- AIAA-2012-3209 details recent CFD analyses to account for the wing aeroelastic twist at Mach=0.85, C_L=0.50, and for additional wind tunnel mounting system effects.
- "Pseudo Test Data" were created from the NTF data and CFD analyses to reflect what the test data might look like for the wing without the "C_L=0.50 aeroelastic" twist.



- No corrections were applied to drag data

Figure A-E-8. DPW-V: "Pseudo" Wind Tunnel Test Data

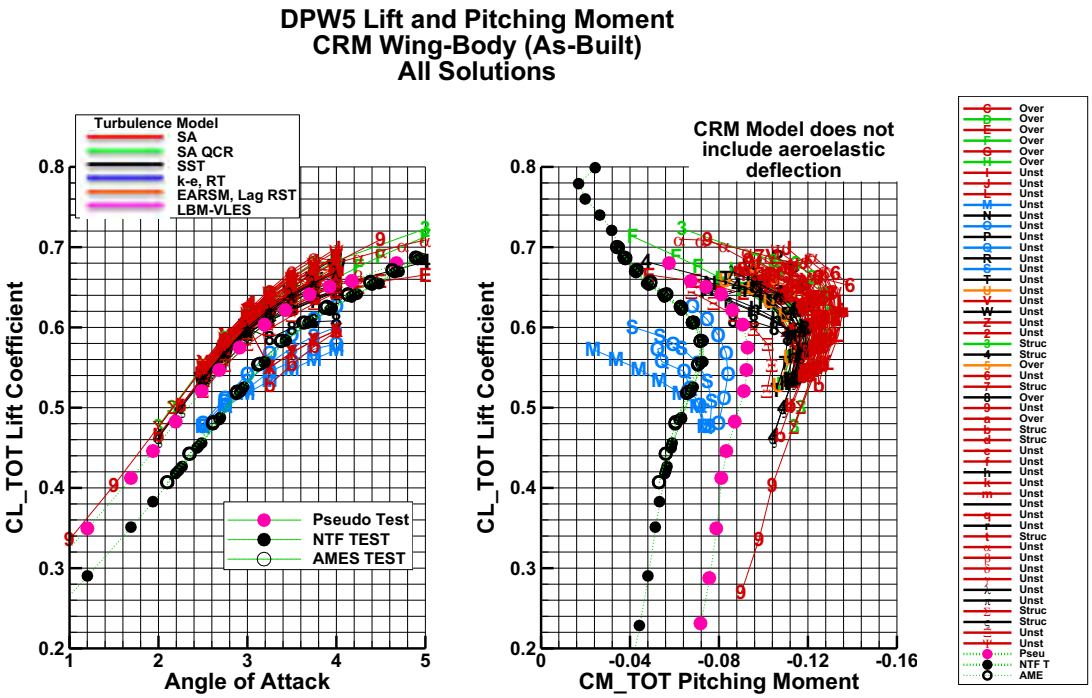


Figure A-E-9. DPW-V: Lift and Pitching Moment; All Solutions, M=0.85.

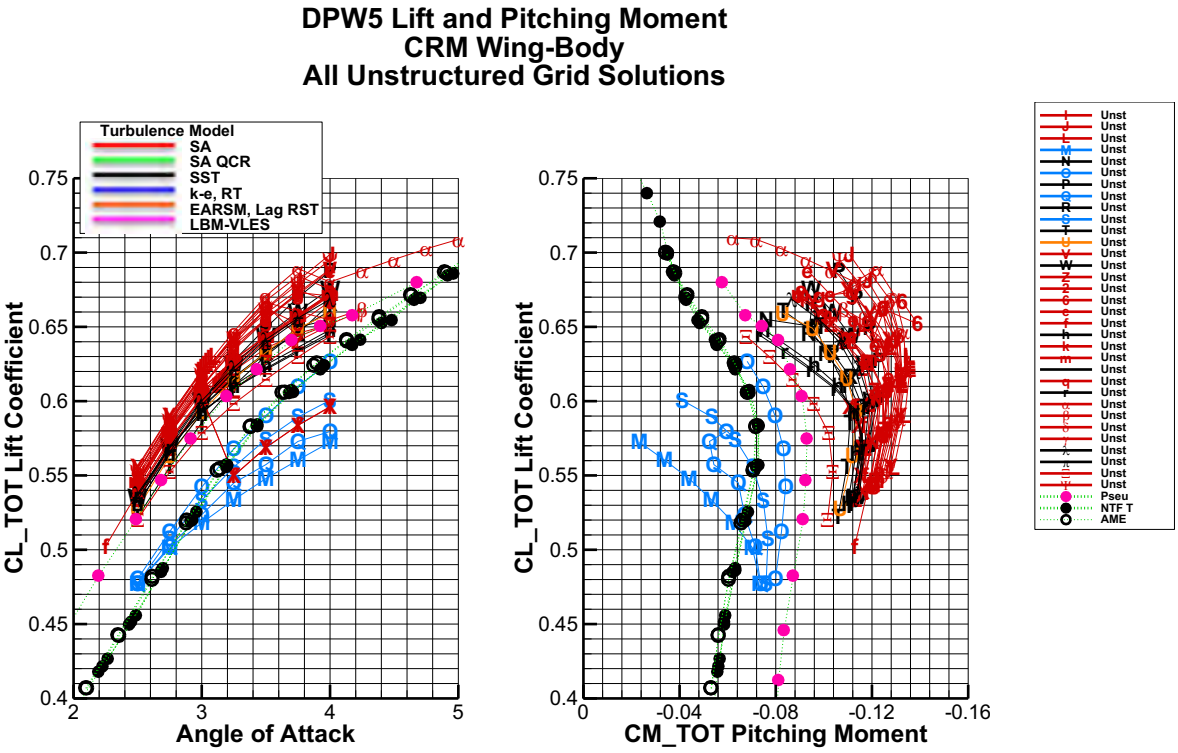


Figure A-E-10. DPW-V: Lift and Pitching Moment; All Unstructured Grid Solutions, M=0.85.

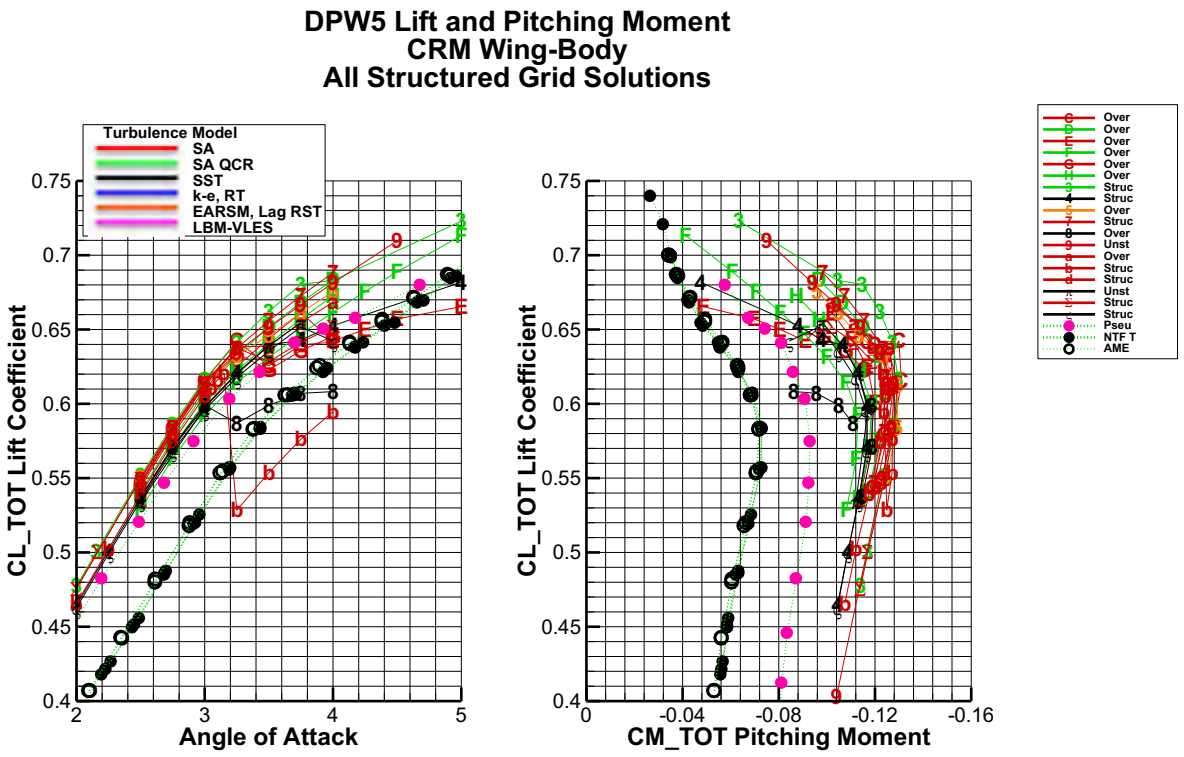


Figure A-E-11. DPW-V: Lift and Pitching Moment; All Structured Grid Solutions, M=0.85.

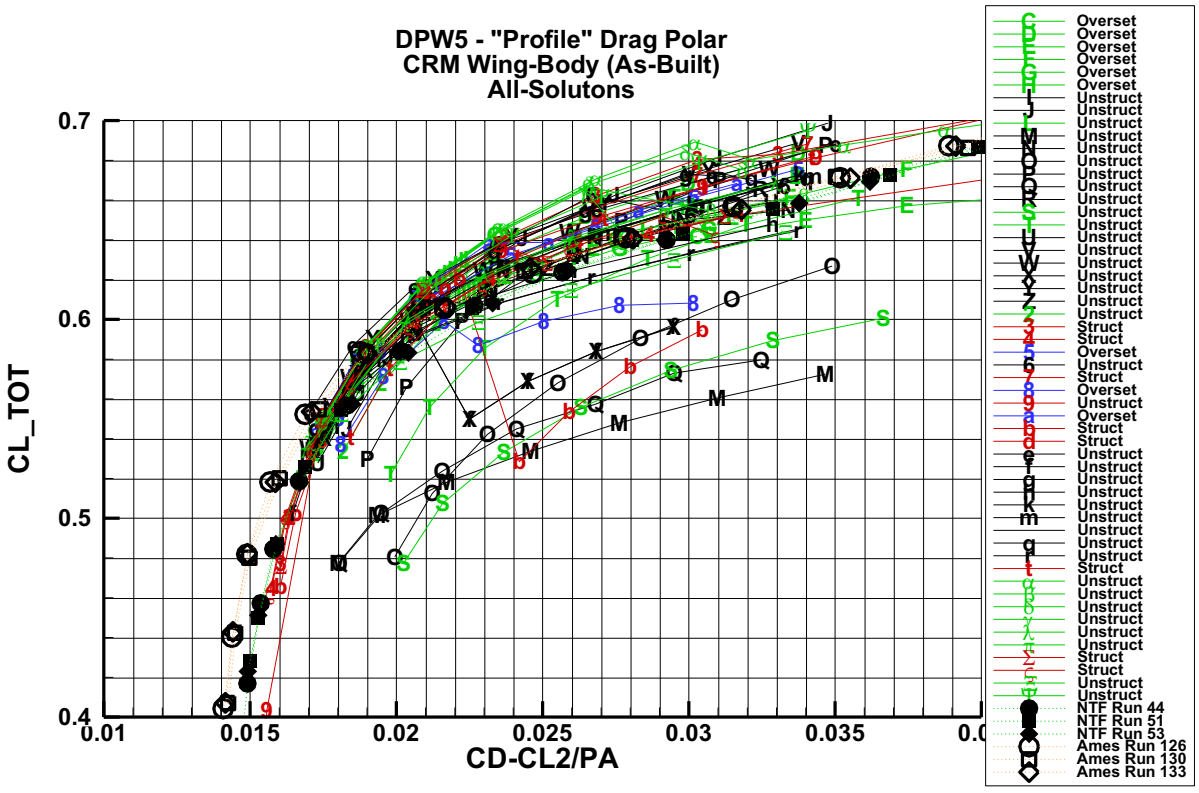
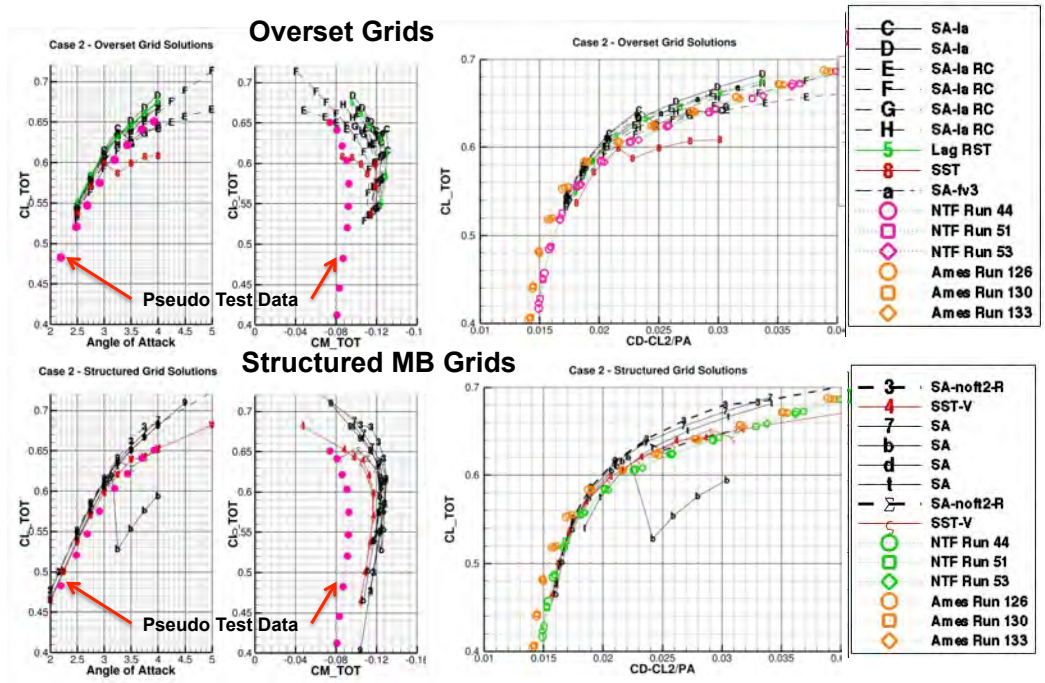
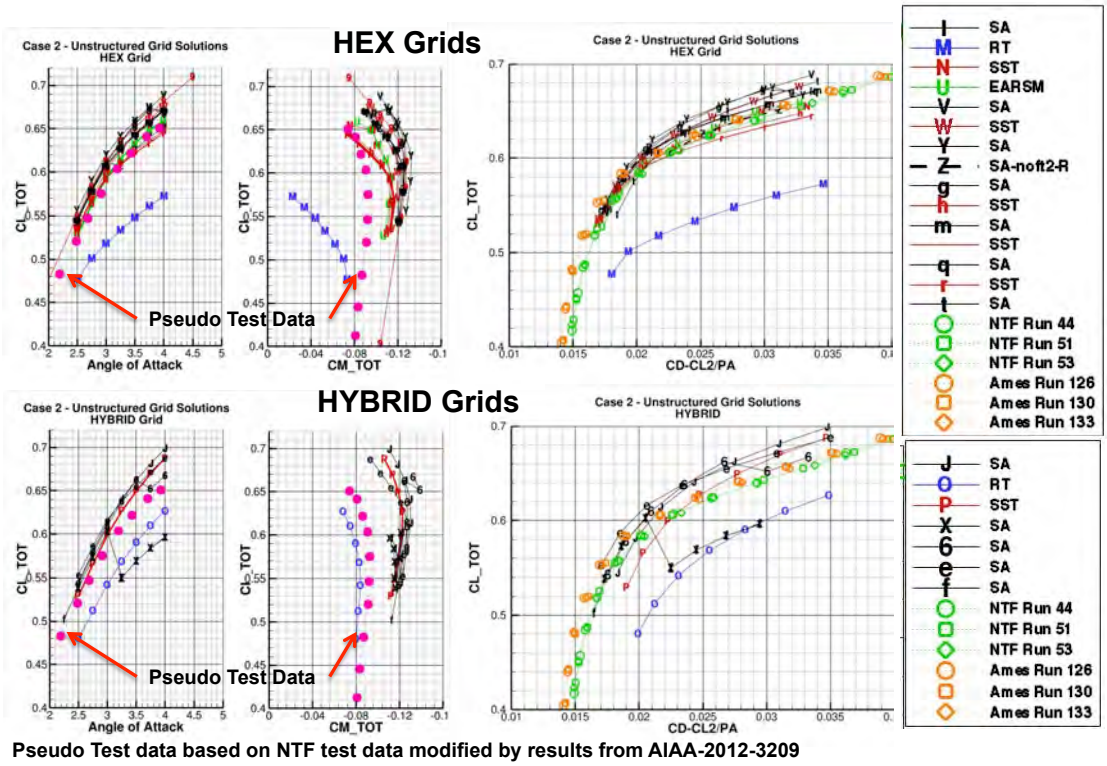


Figure A-E-12. DPW-V: "Profile" Drag Polar; All Solutions, M=0.85.



Pseudo Test data based on NTF test data modified by results from AIAA-2012-3209

Figure A-E-13. DPW-V: Overset and Multiblock Grid Solutions, M=0.85.



Pseudo Test data based on NTF test data modified by results from AIAA-2012-3209

Figure A-E-14. DPW-V: Hex and Hybrid Unstructured Grid Solutions, M=0.85.

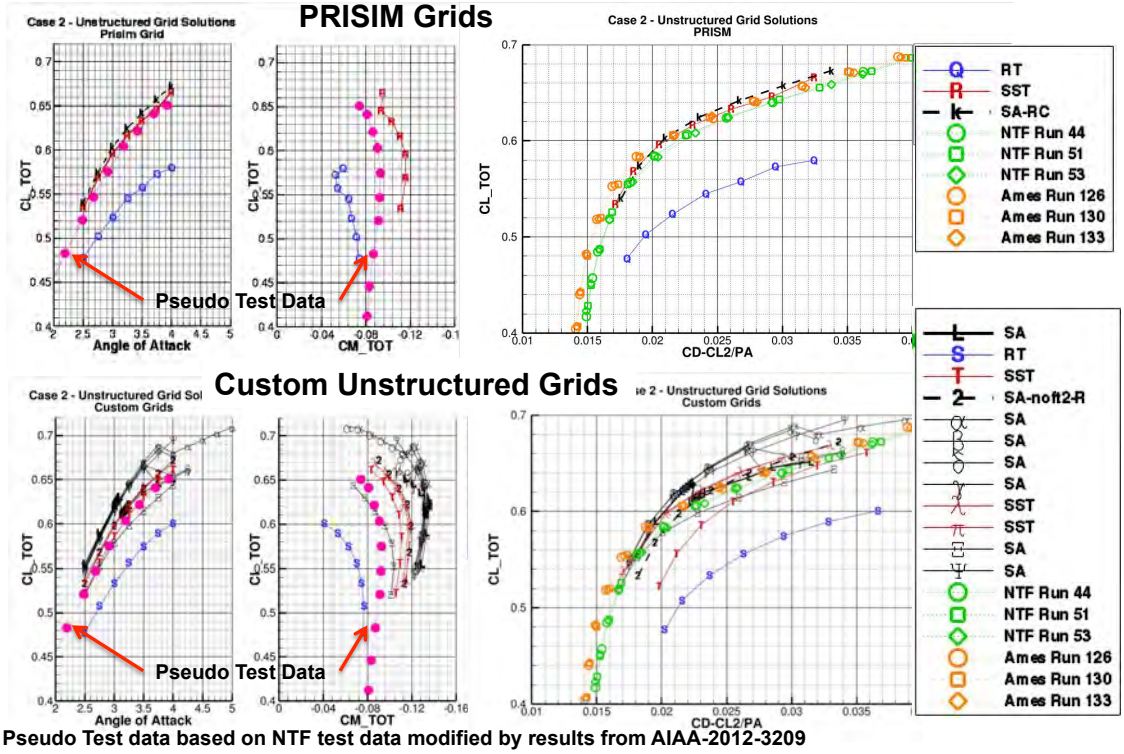


Figure A-E-15. DPW-V: Prism and Custom Unstructured Grid Solutions, M=0.85.

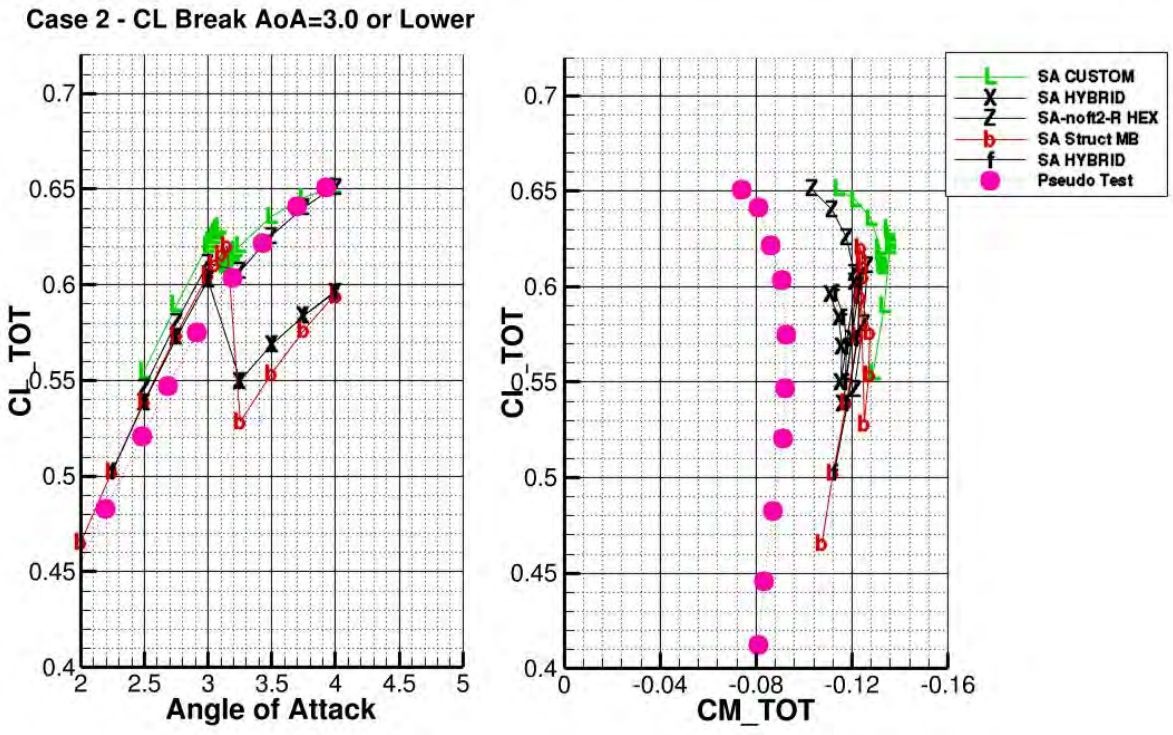


Figure A-E-16. DPW-V: Lift and Pitching Moment, M=0.85; Solutions with Lift Break AoA = 3.0° or Lower.

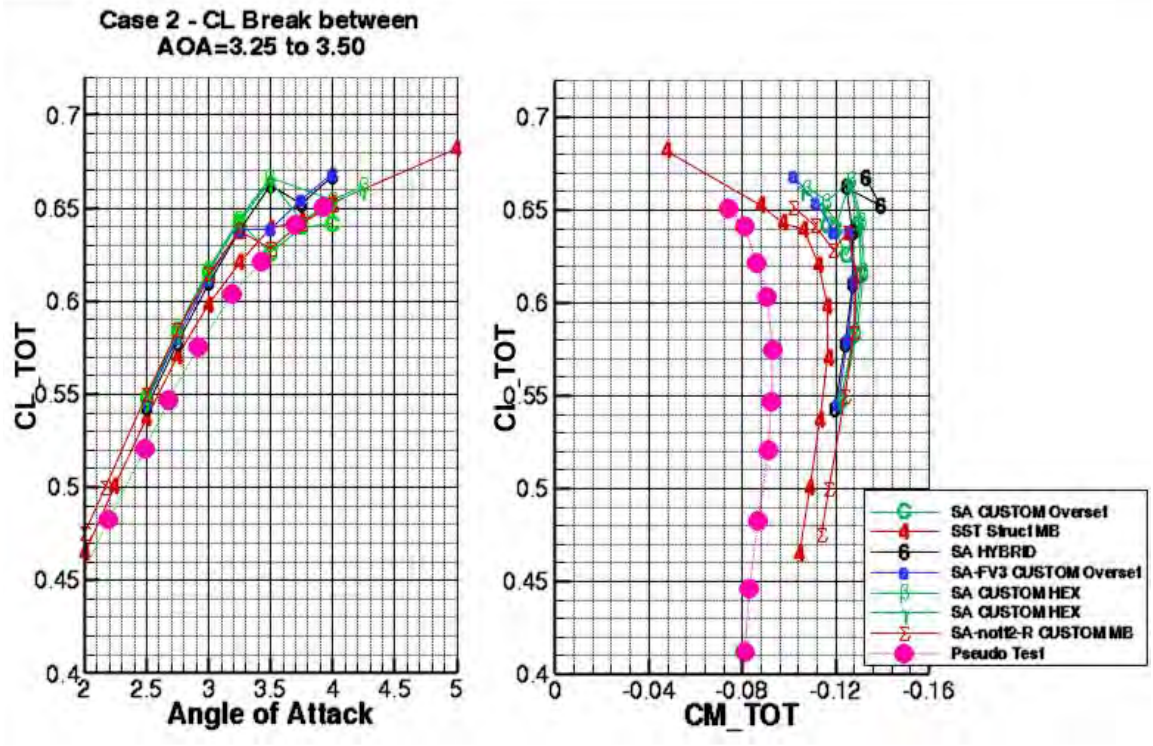


Figure A-E-17. DPW-V: Lift and Pitching Moment, M=0.85; Solutions with Lift Break between AoA = 3.25° to 3.50°.

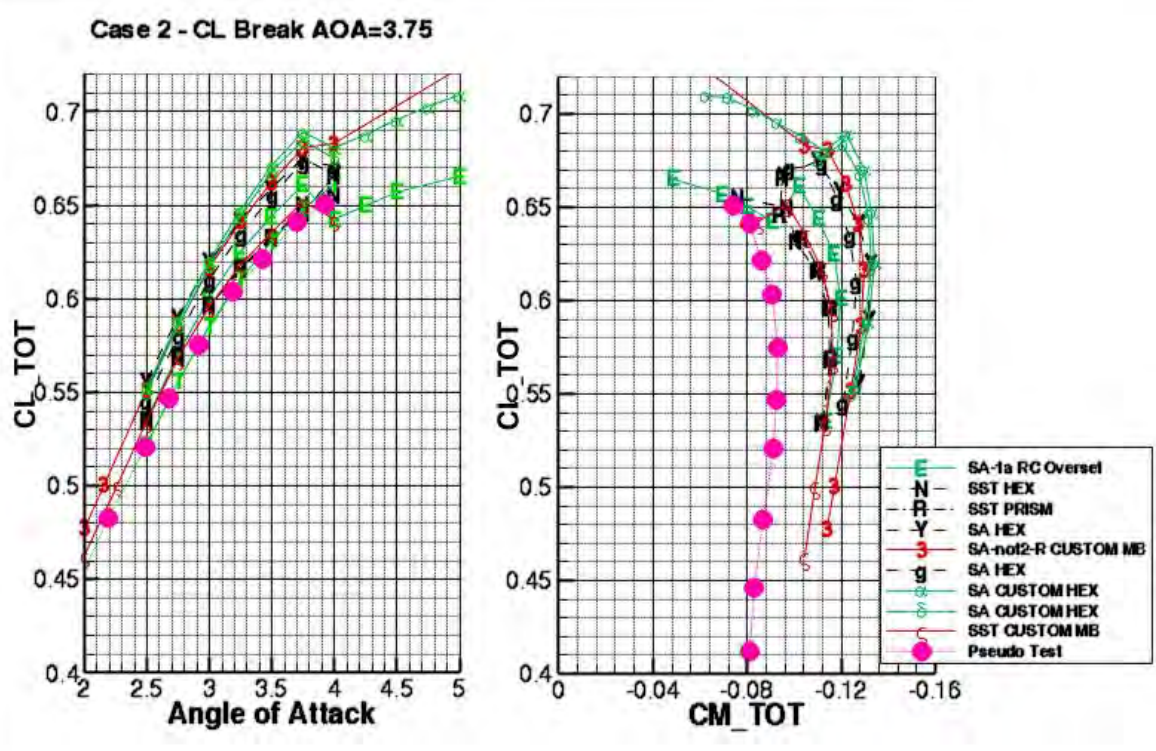


Figure A-E-18. DPW-V: Lift and Pitching Moment; Solutions with Lift Break, M=0.85, AoA = 3.75°.

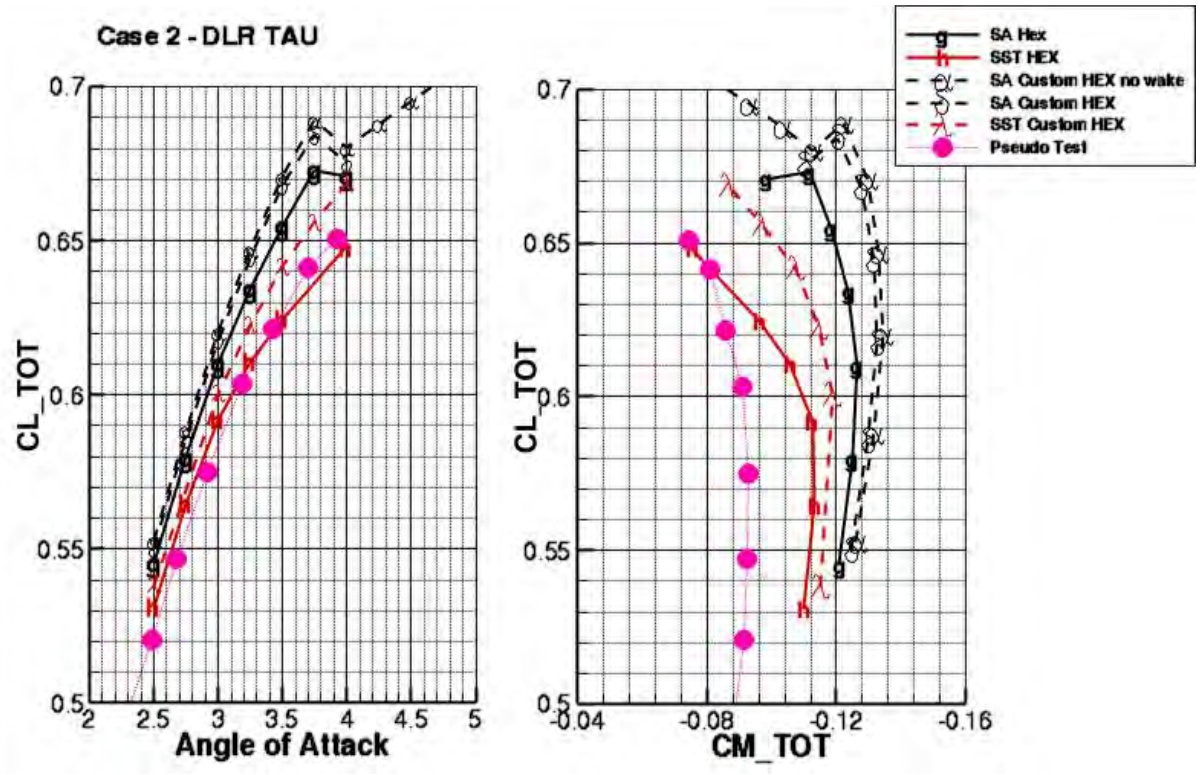


Figure A-E-19. DPW-V: Lift and Pitching Moment, M=0.85; DLR TAU Solver Results.

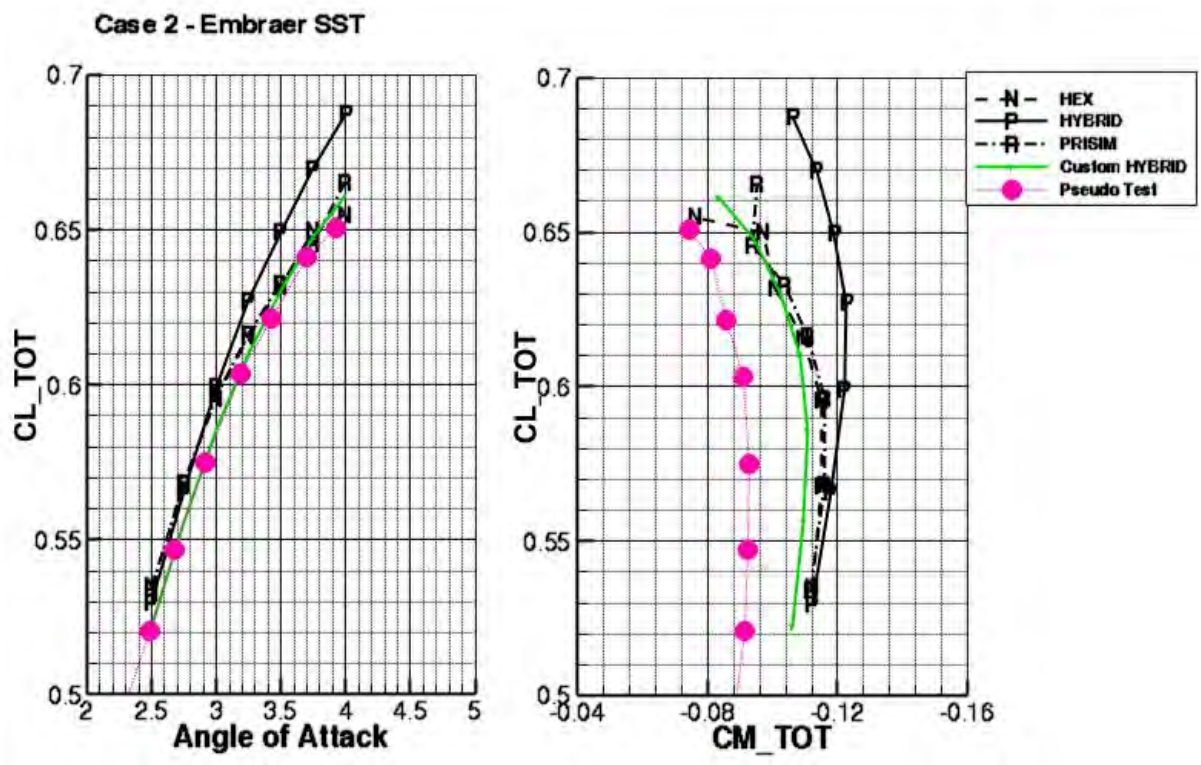


Figure A-E-20. DPW-V: Lift and Pitching Moment, M=0.85; Embraer CFD++ Solver with SST Results.

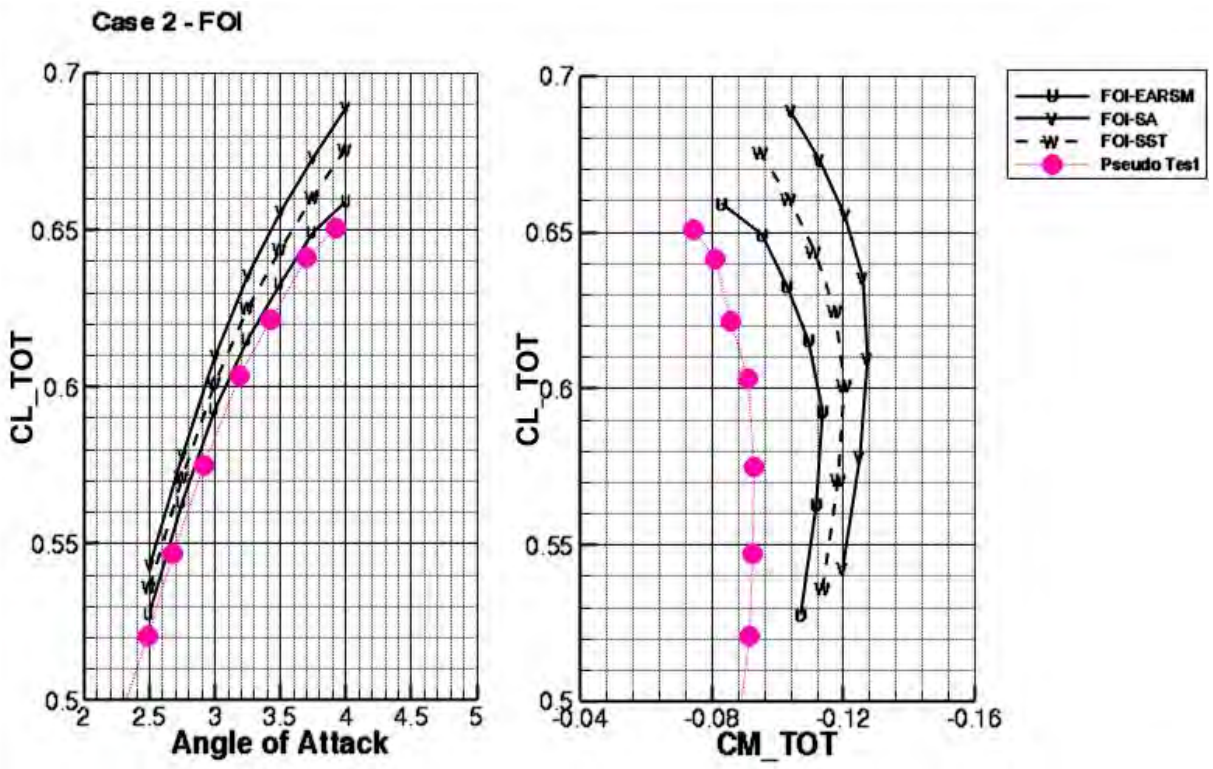


Figure A-E-20. DPW-V: Lift and Pitching Moment, M=0.85; FOI EDGE Solver Results.

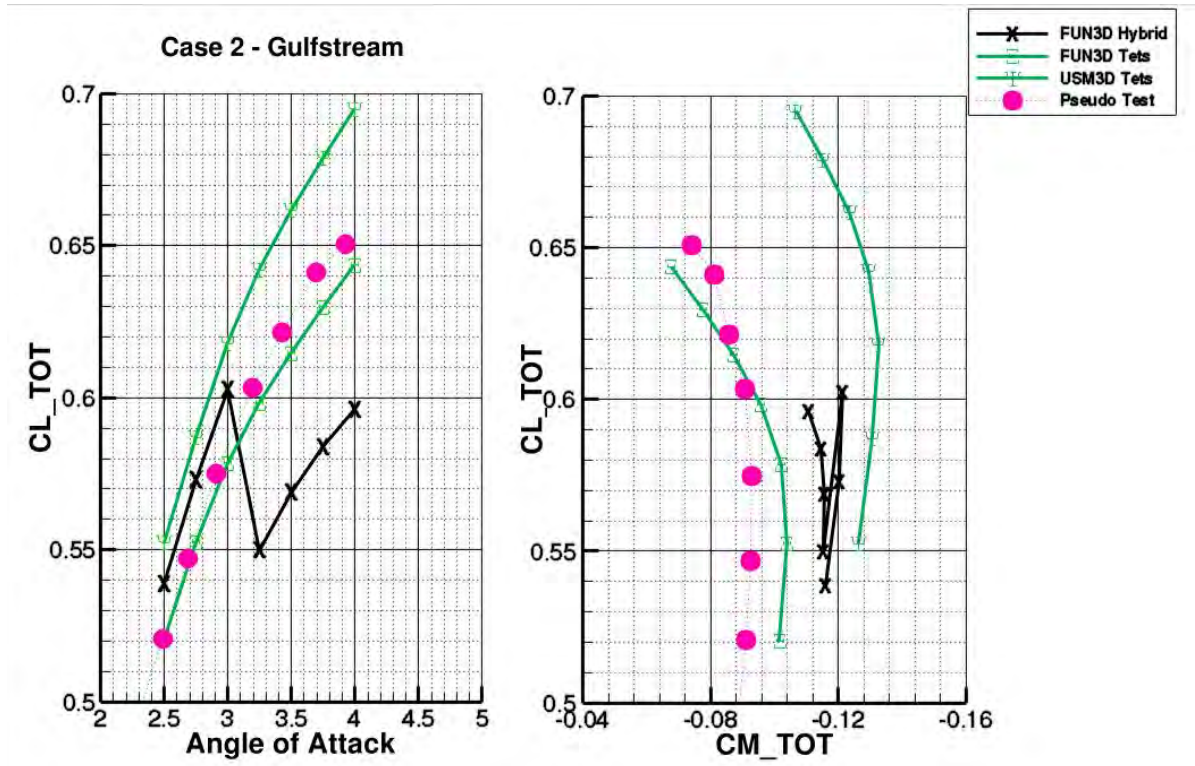


Figure A-E-21. DPW-V: Lift and Pitching Moment, M=0.85; Gulfstream FUN3D and USM3D Solver Results.

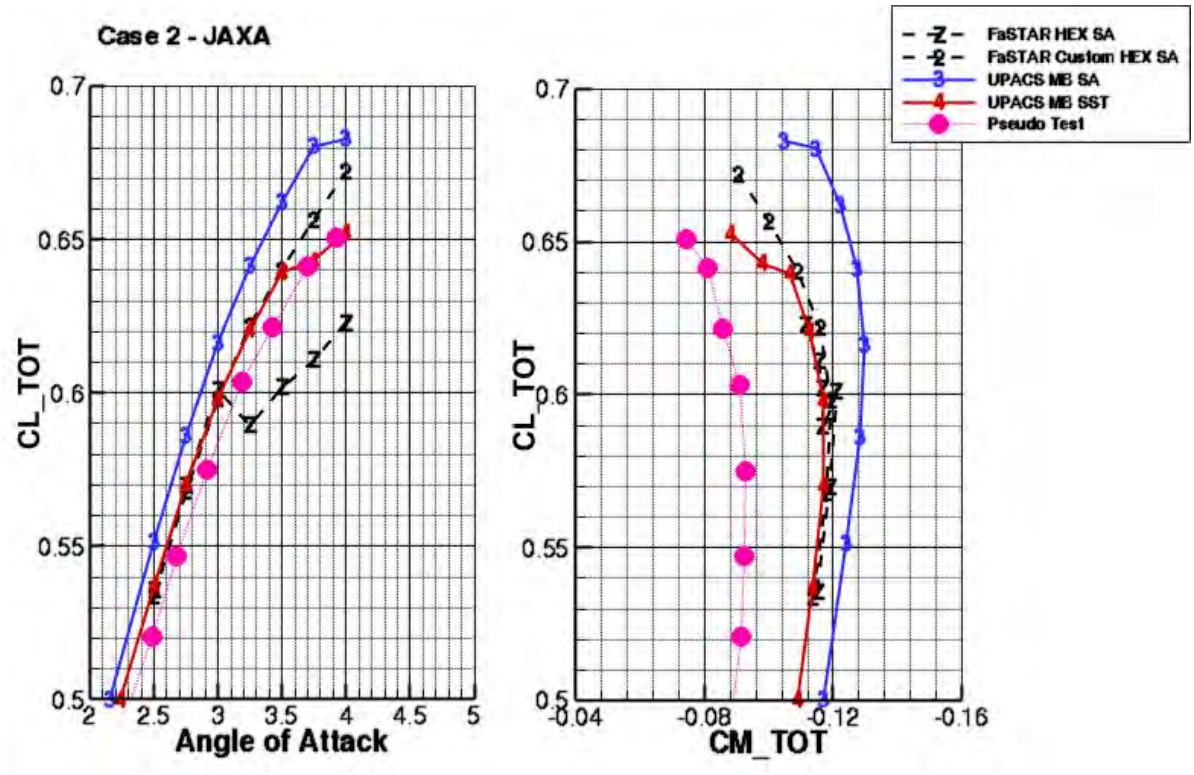


Figure A-E-22. DPW-V: Lift and Pitching Moment, M=0.85; JAXA FaSTAR and UPACS Solver Results.

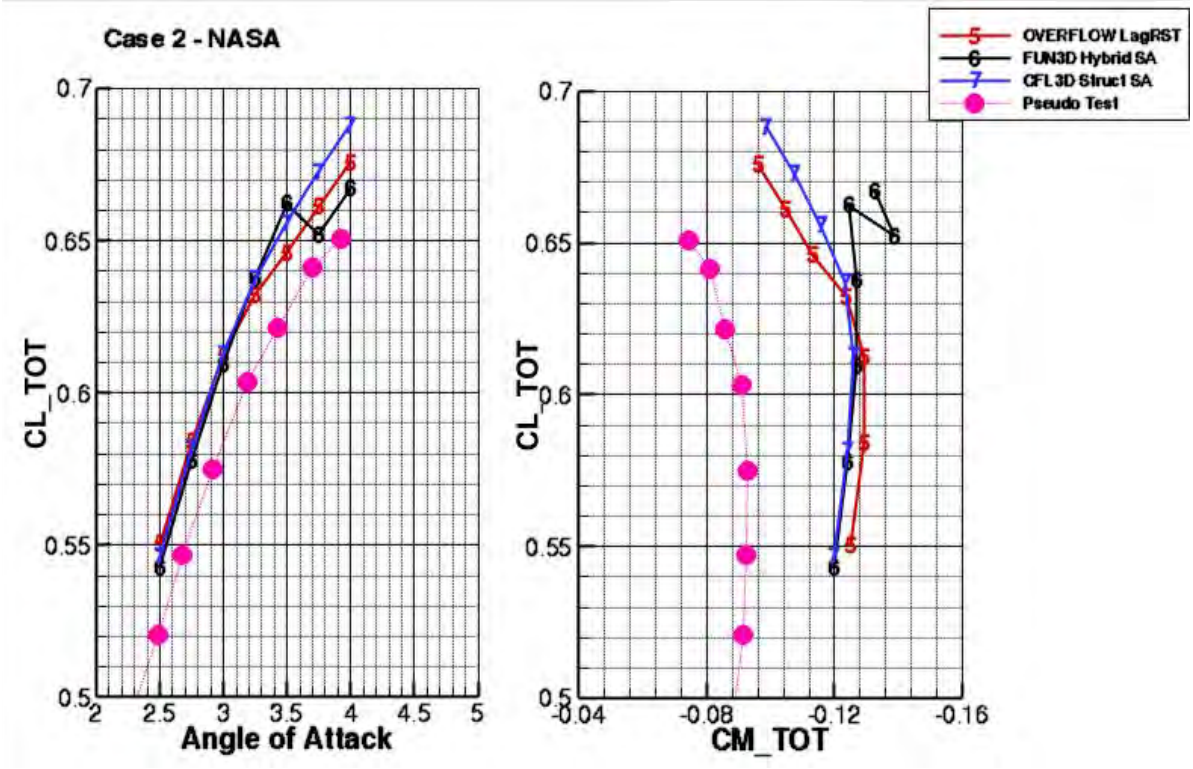


Figure A-E-23. DPW-V: Lift and Pitching Moment, M=0.85; NASA OVERFLOW, FUN3D, and CFL3D Solver Results.

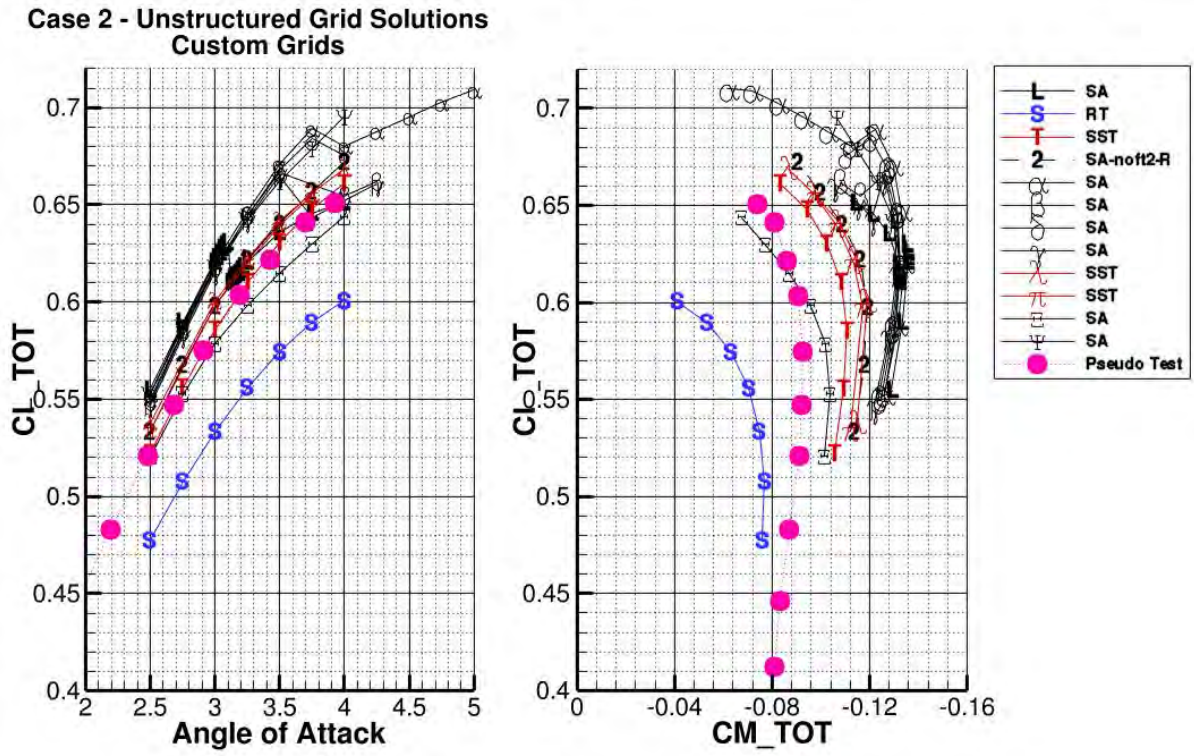


Figure A-E-24. DPW-V: Lift and Pitching Moment, M=0.85; Unstructured Custom Grid Solutions.

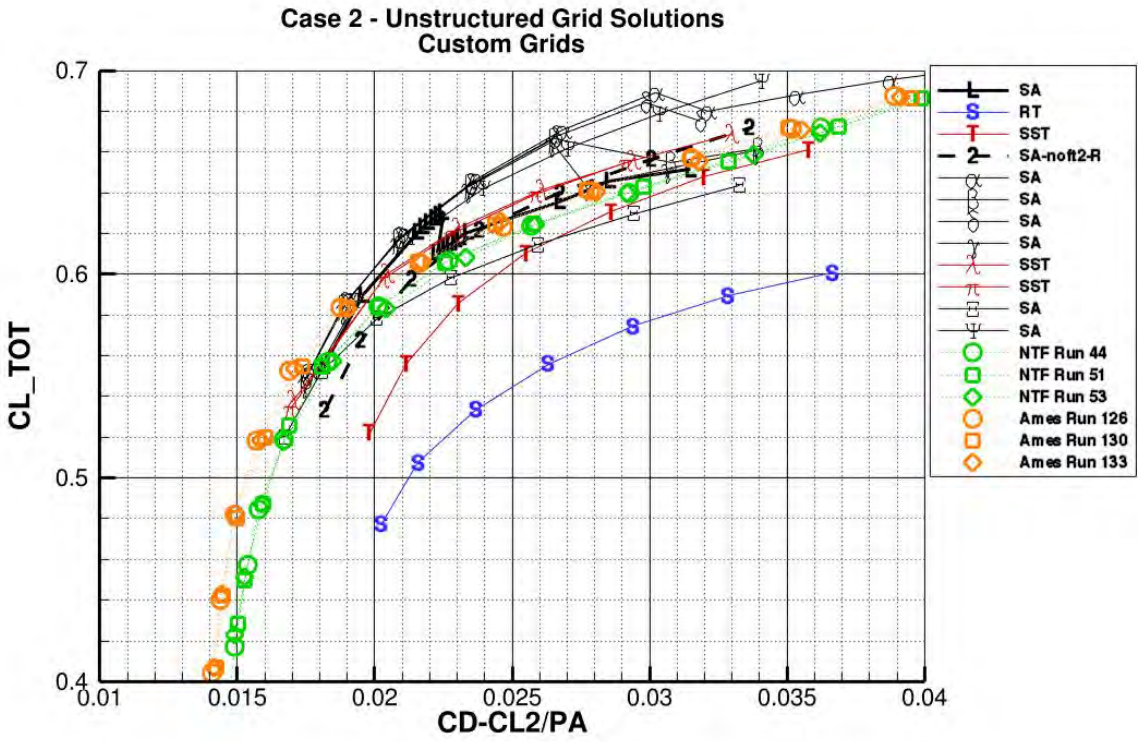


Figure A-E-25. DPW-V: "Profile" Drag Polar, M=0.85; Unstructured Custom Grid Solutions.

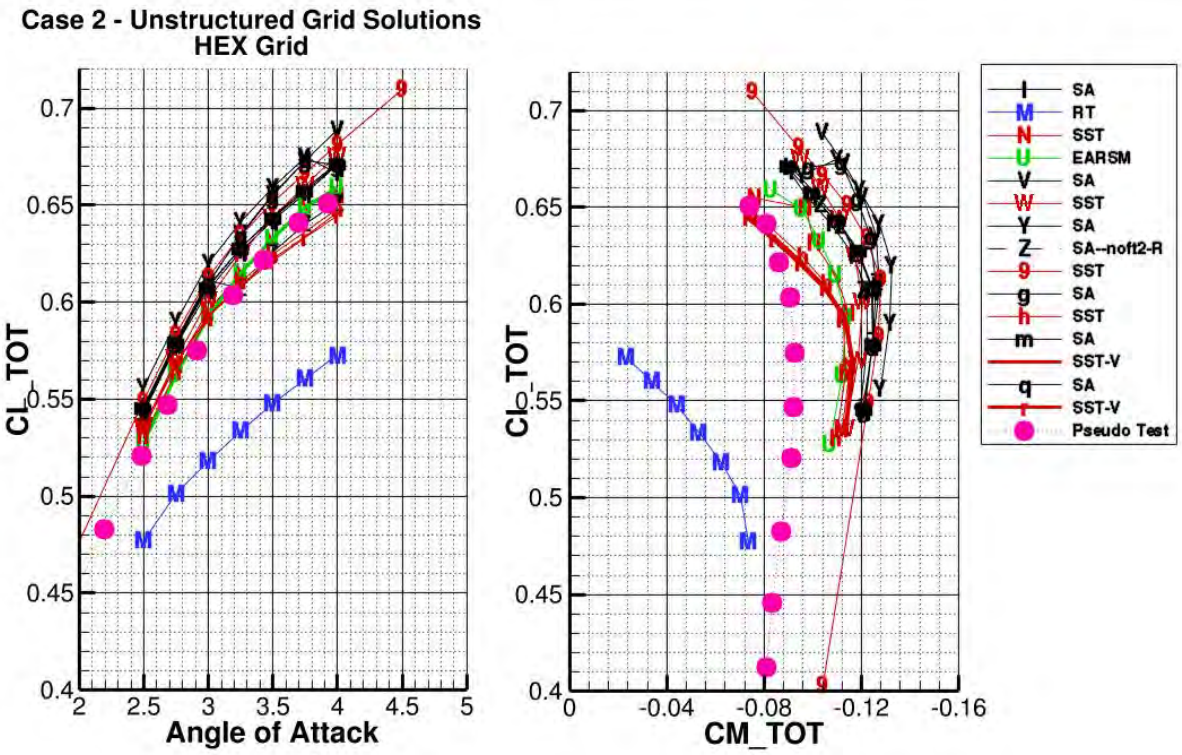


Figure A-E-26. DPW-V: Lift and Pitching Moment, M=0.85; Unstructured Hex Grid Solutions.

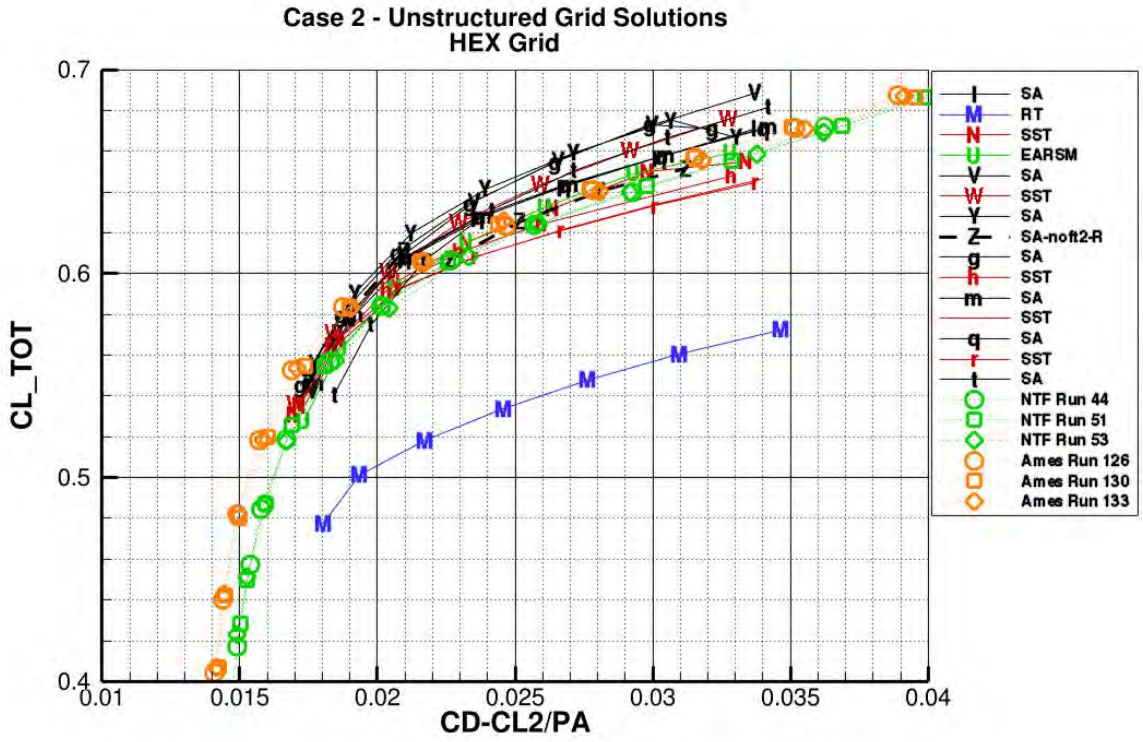


Figure A-E-27. DPW-V: "Profile" Drag Polar, M=0.85; Unstructured Hex Grid Solutions.

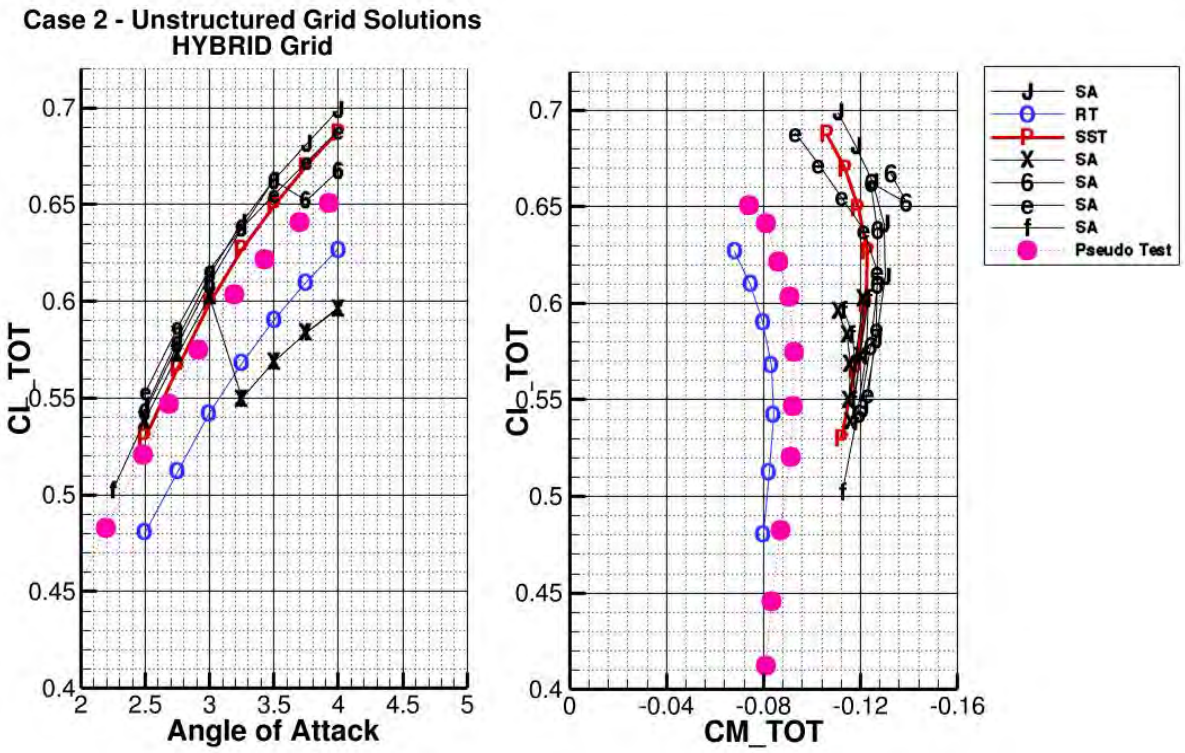


Figure A-E-28. DPW-V: Lift and Pitching Moment, M=0.85; Unstructured Hybrid Grid Solutions.

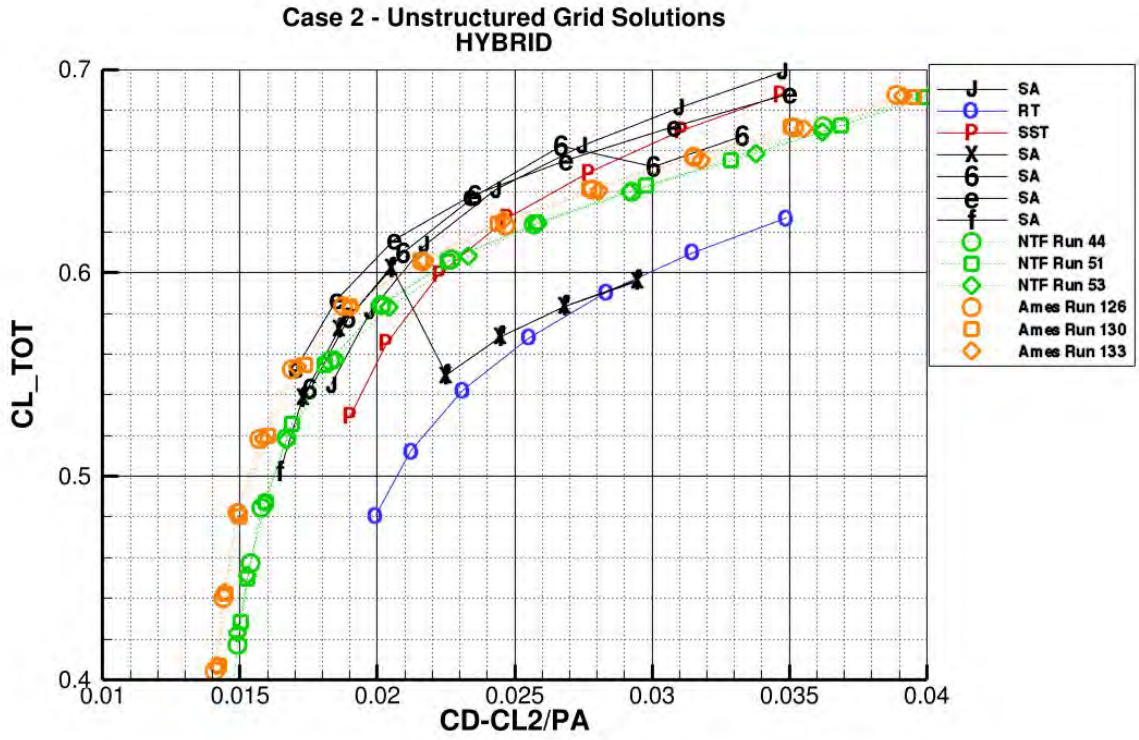


Figure A-E-29. DPW-V: "Profile" Drag Polar, M=0.85; Unstructured Hybrid Grid Solutions.

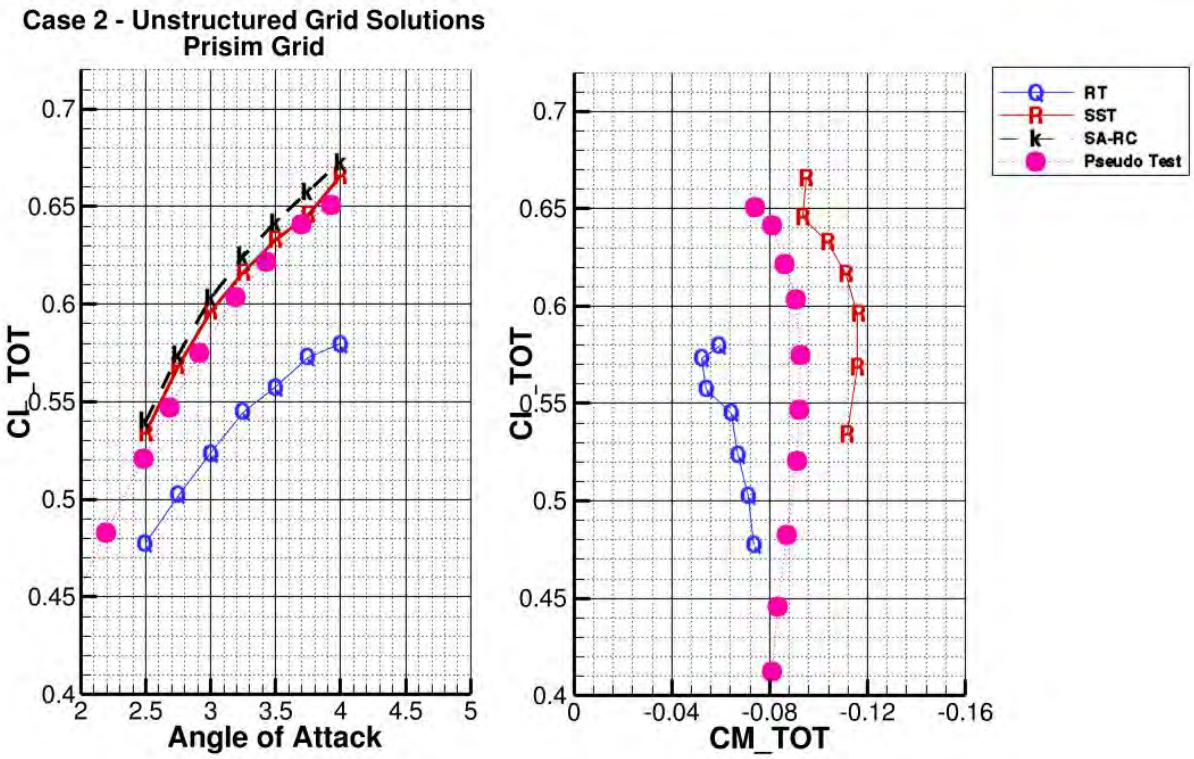


Figure A-E-30. DPW-V: Lift and Pitching Moment, M=0.85; Unstructured Prism Grid Solutions.

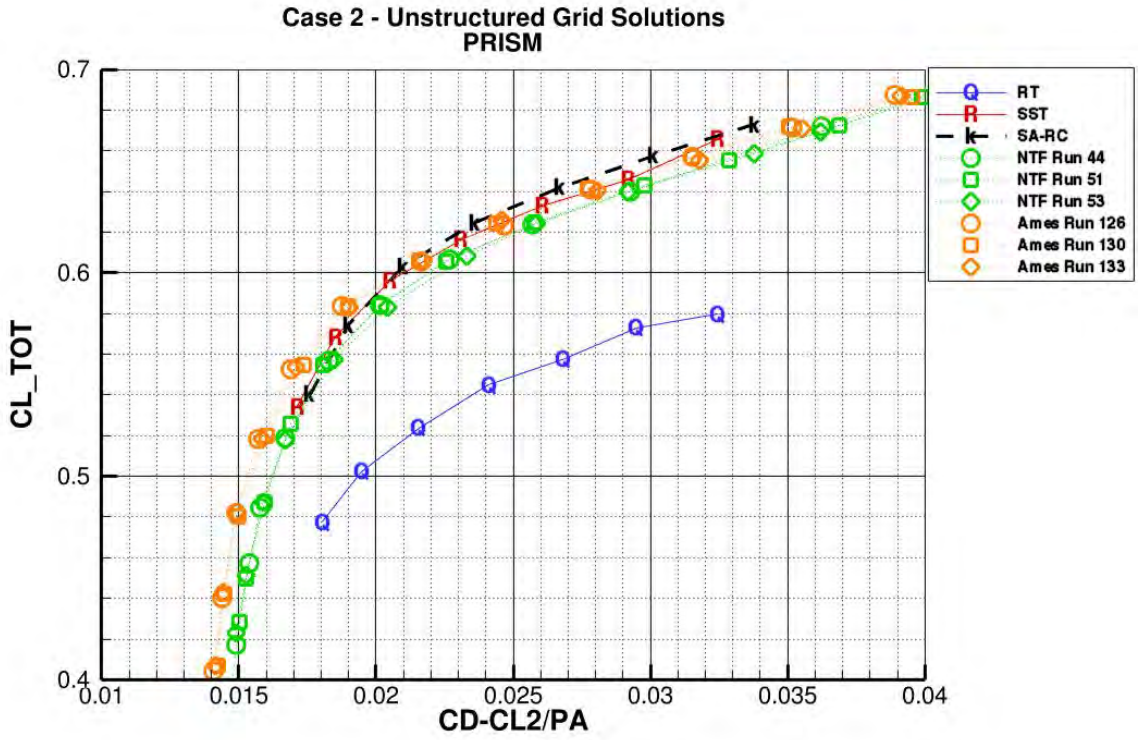


Figure A-E-31. DPW-V: "Profile" Drag Polar, M=0.85; Unstructured Prism Grid Solutions.

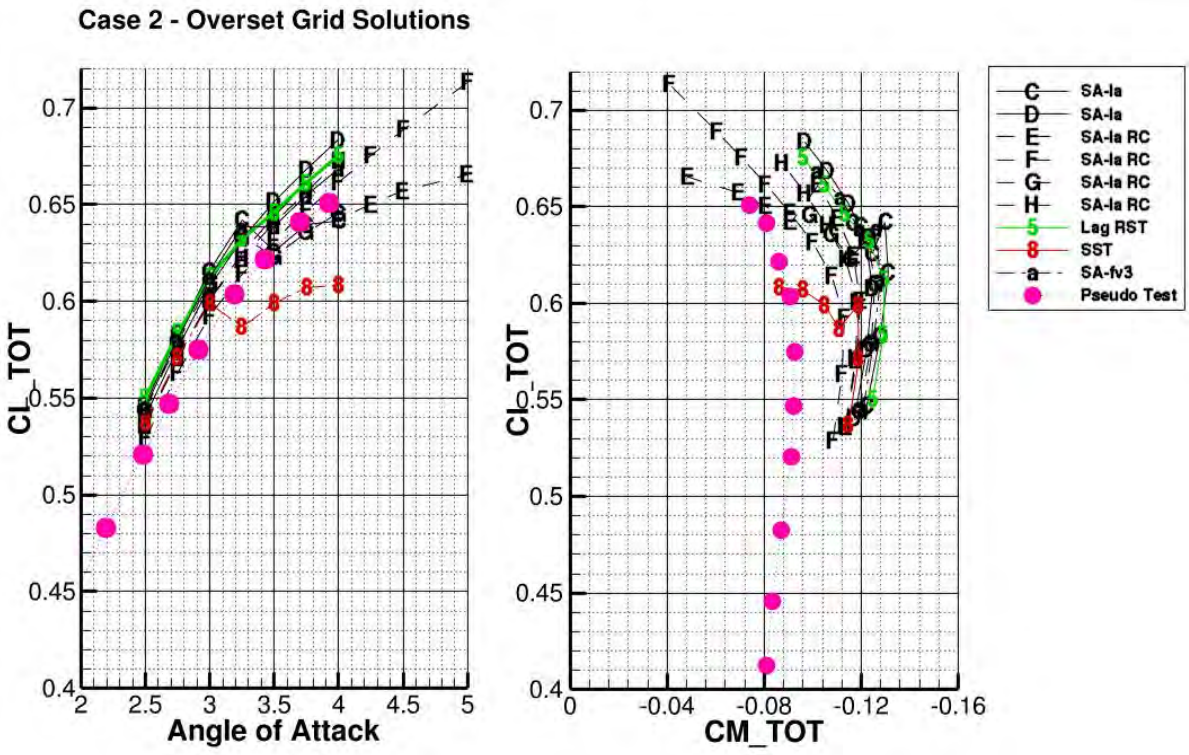


Figure A-E-32. DPW-V: Lift and Pitching Moment, M=0.85; Structured OVERFLOW Grid Solutions.

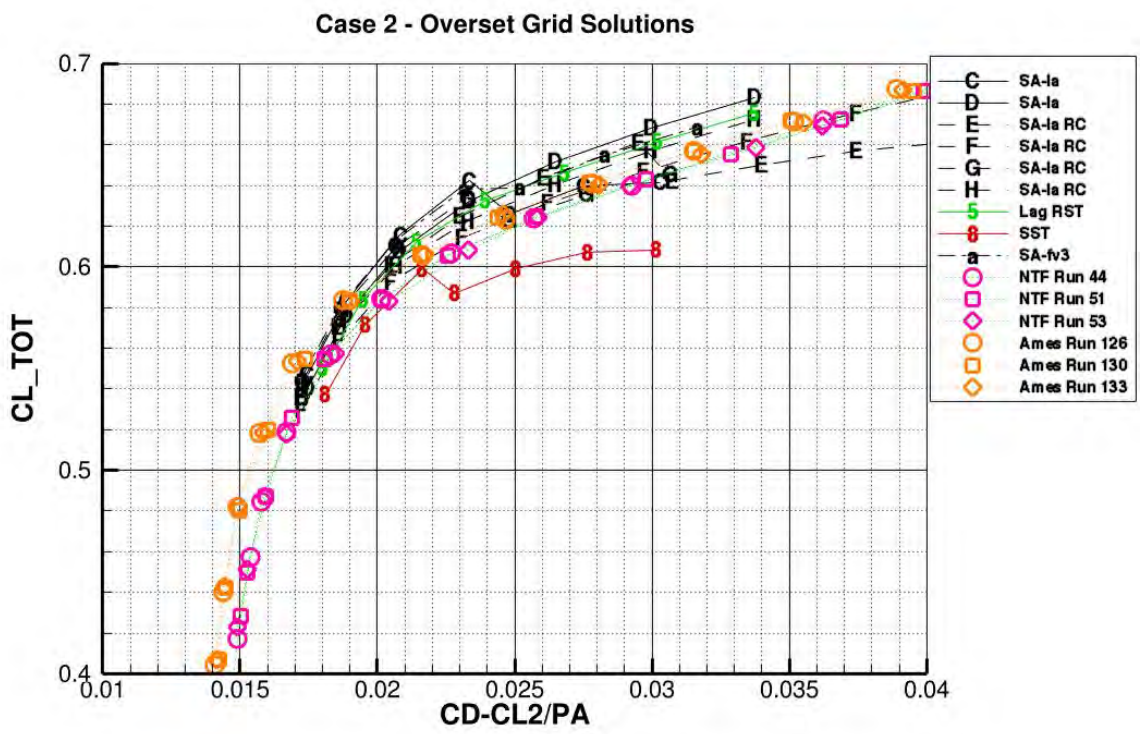


Figure A-E-33. DPW-V: "Profile" Drag Polar, M=0.85; Structured OVERFLOW Grid Solutions.

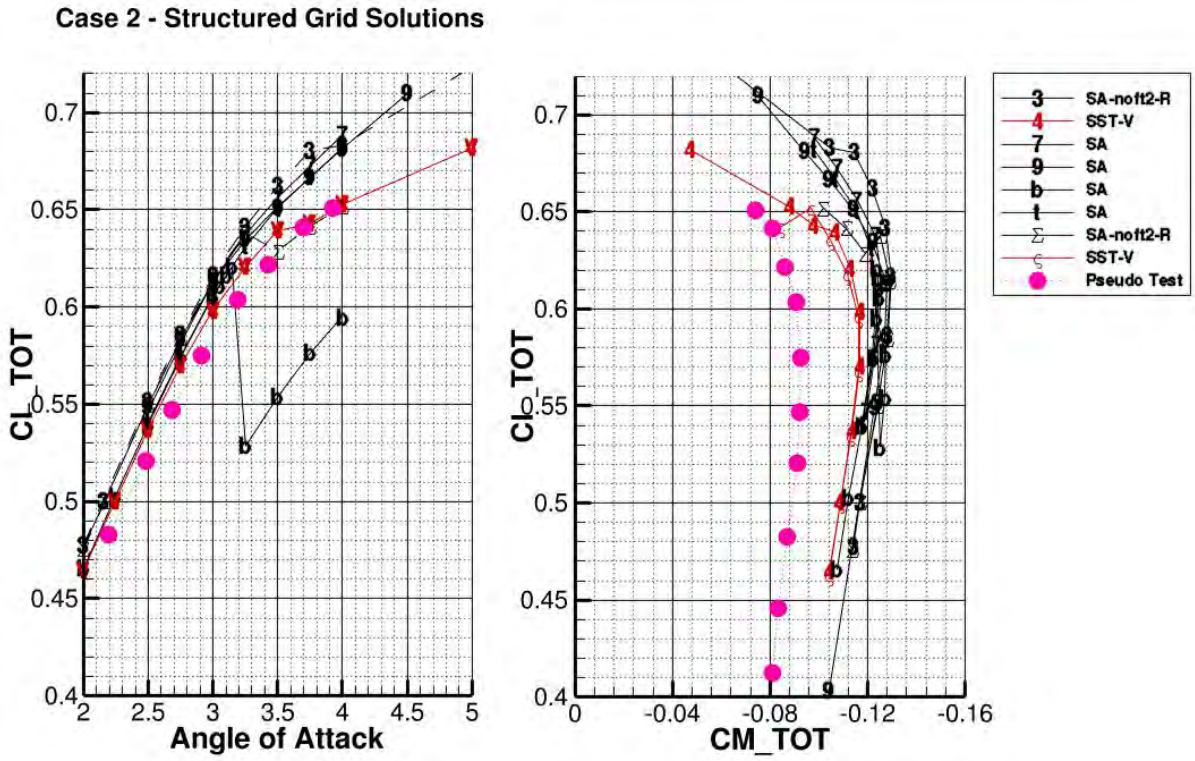


Figure A-E-34. DPW-V: Lift and Pitching Moment, M=0.85; Structured Multiblock Grid Solutions.

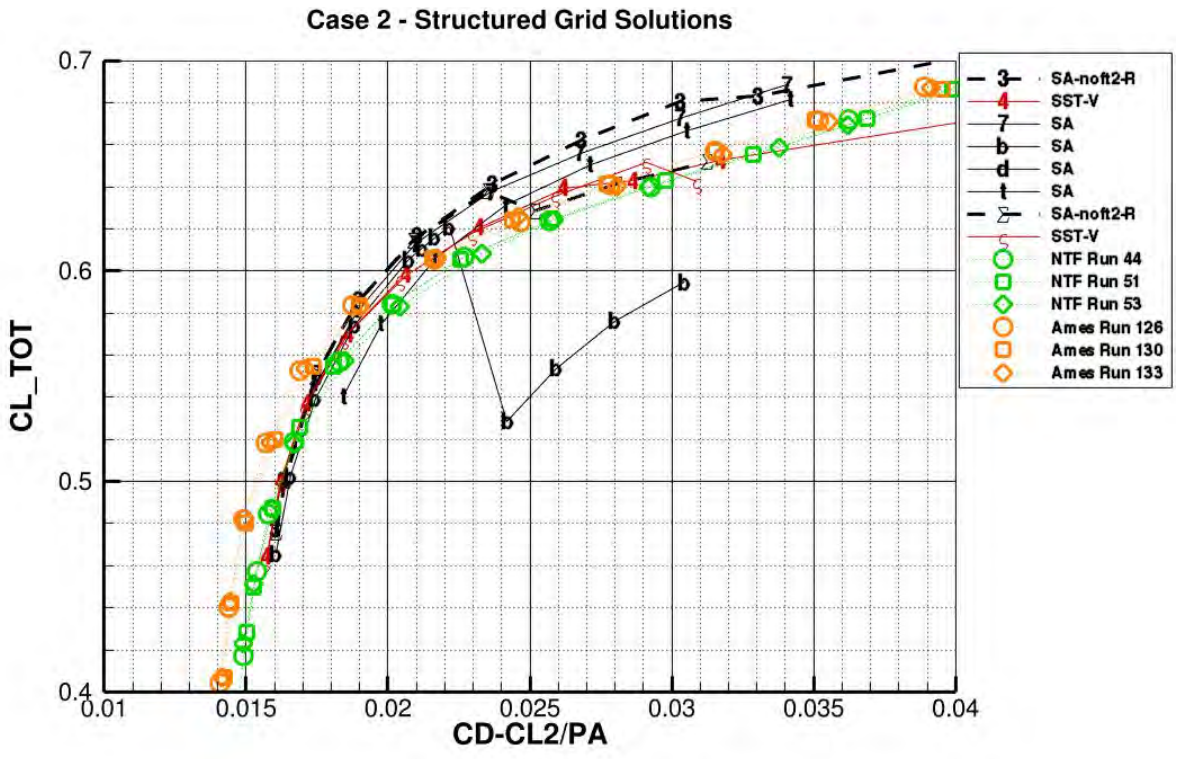


Figure A-E-35. DPW-V: "Profile" Drag Polar, M=0.85; Structured Multiblock Grid Solutions.

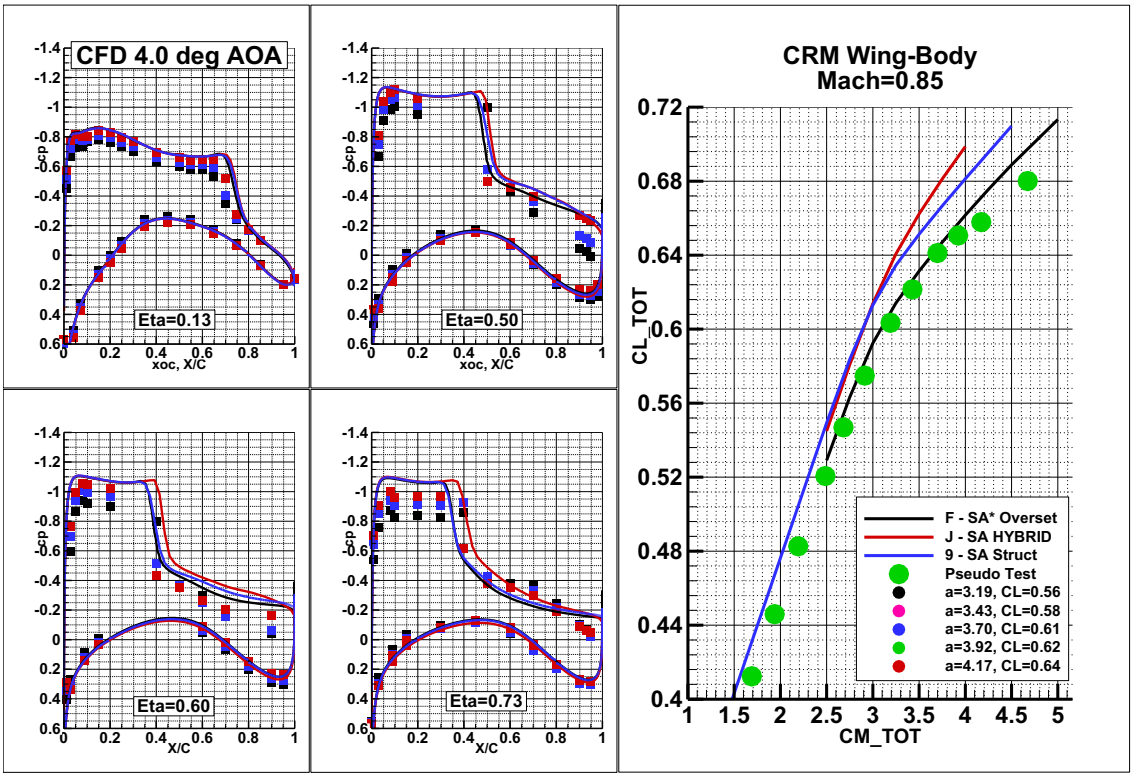


Figure A-E-36. DPW-V: Lift and Wing Pressure Distributions, M=0.85: Selected SA Turbulence Model Solutions AoA = 4.0°.

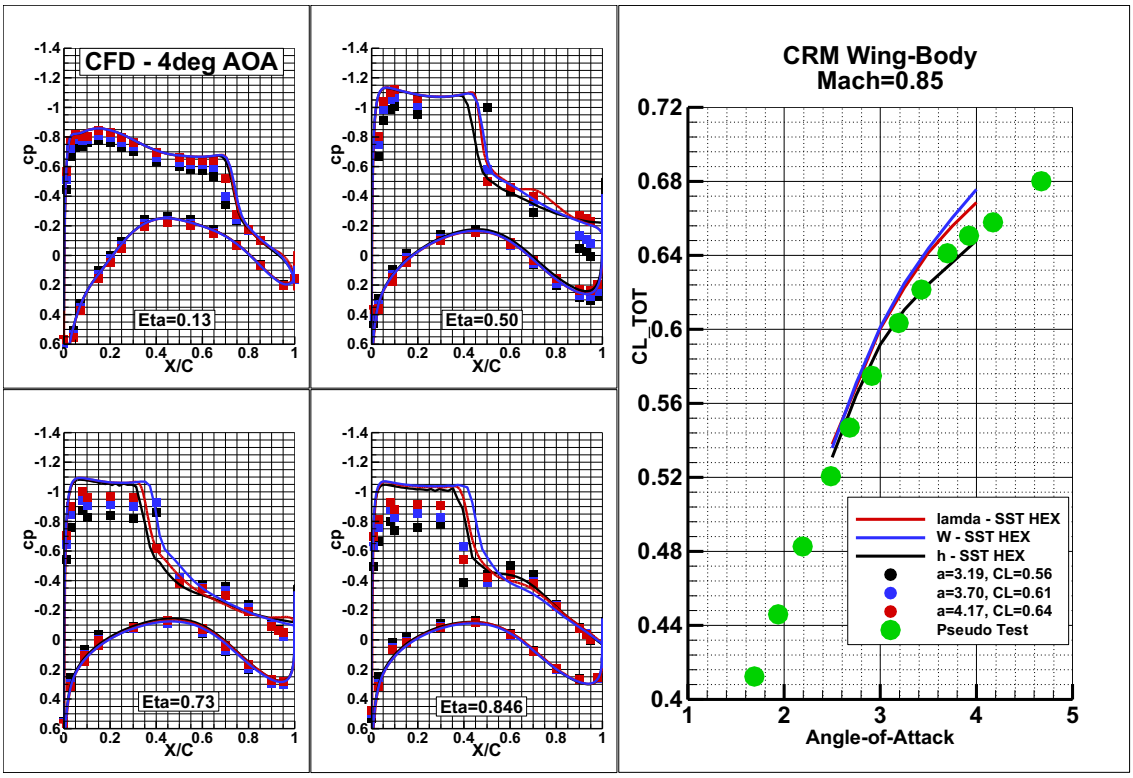


Figure A-E-37. DPW-V: Lift and Wing Pressure Distributions, M=0.85: Selected SST Turbulence Model Solutions AoA = 4.0°.

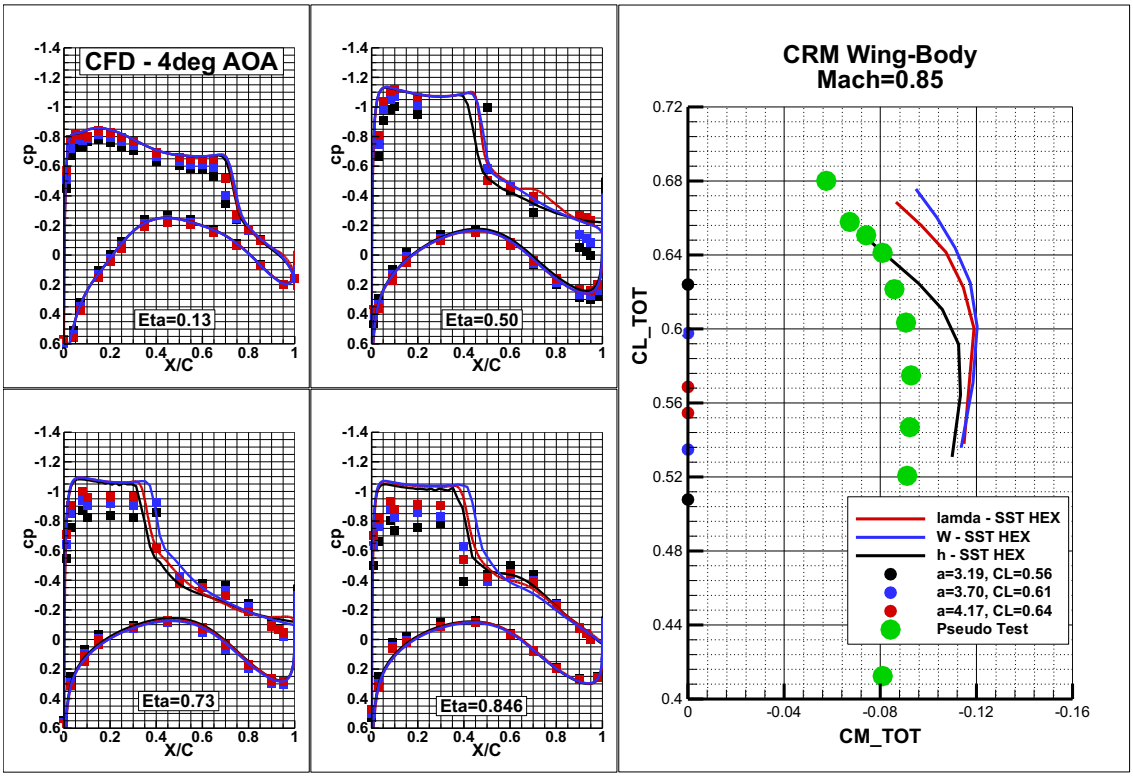


Figure A-E-38. DPW-V: Pitching Moment and Wing Pressure Distributions, M=0.85: Selected SST Turbulence Model Solutions AoA = 4.0°.

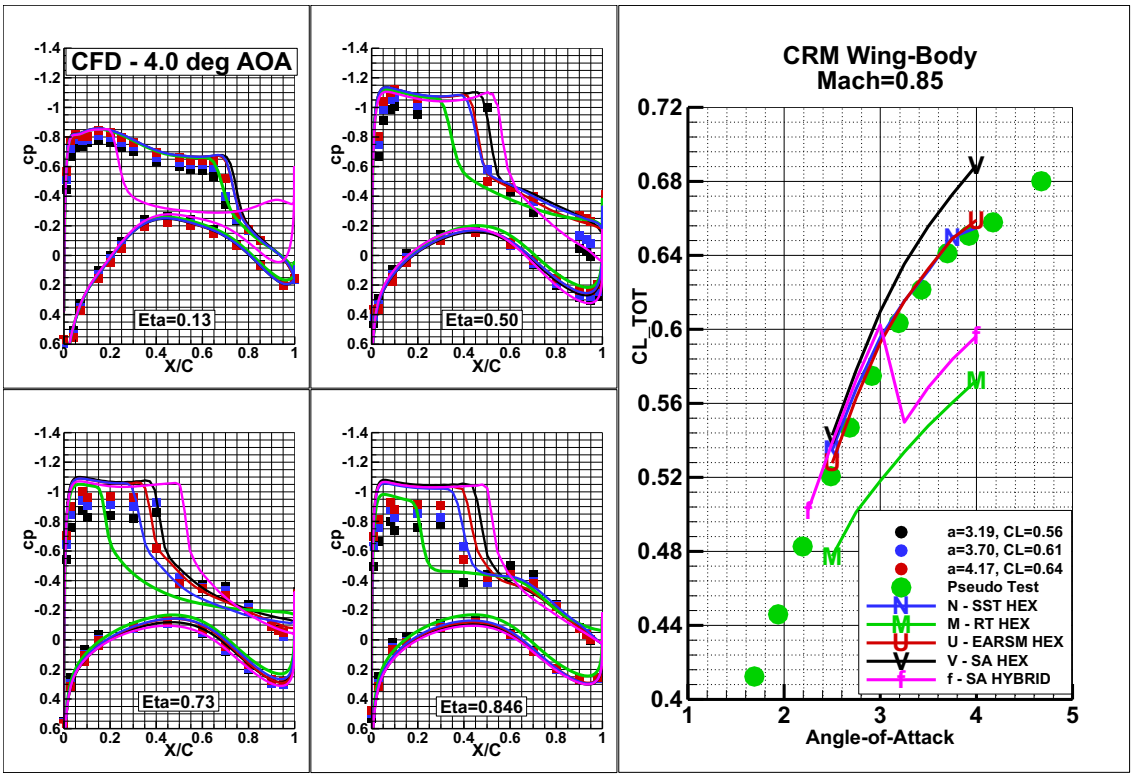


Figure A-E-39. DPW-V: Lift and Wing Pressure Distributions, M=0.85: Selected Turbulence Model Solutions: AoA = 4.0°.

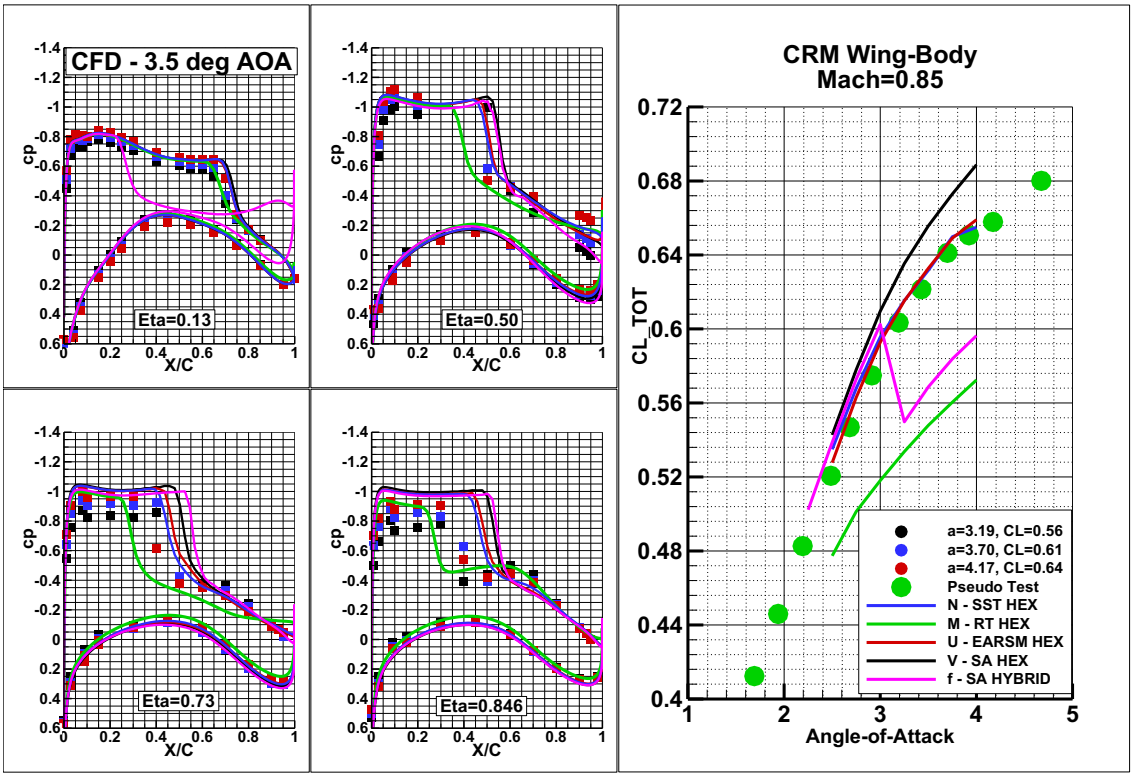


Figure A-E-40. DPW-V: Lift and Wing Pressure Distributions, M=0.85: Selected Turbulence Model Solutions: AoA = 3.5°.

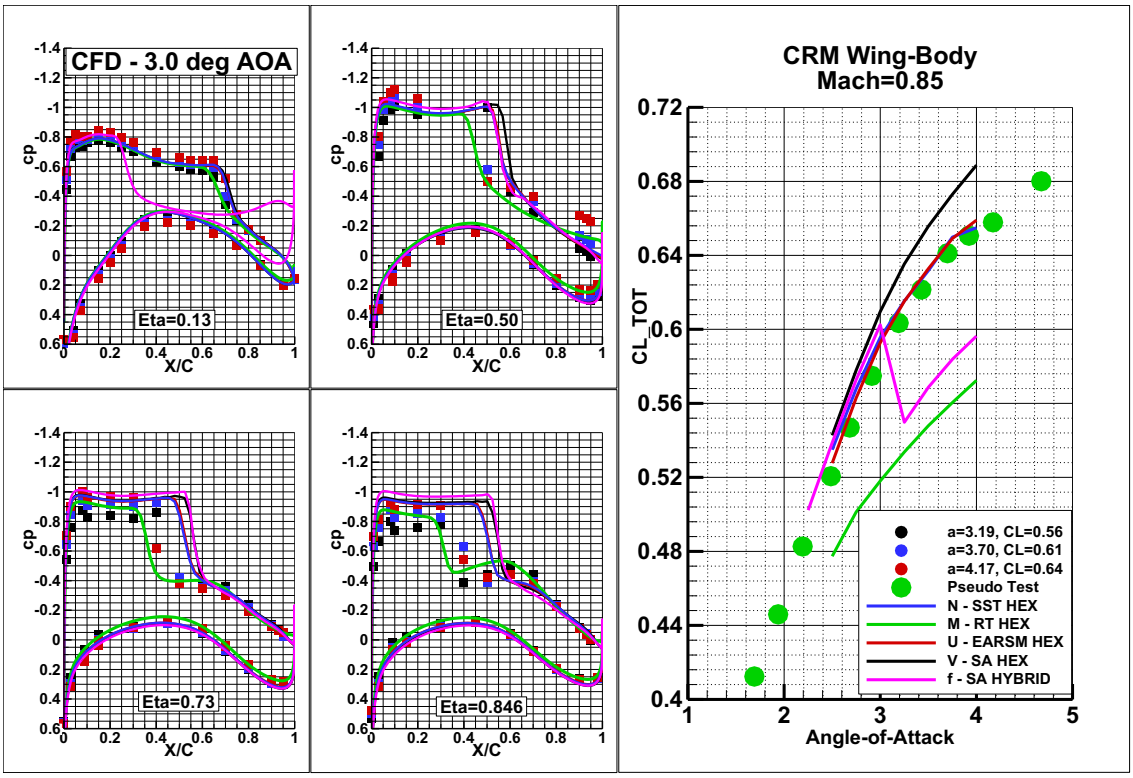


Figure A-E-41. DPW-V: Lift and Wing Pressure Distributions, M=0.85: Selected Turbulence Model Solutions: AoA = 3.0.

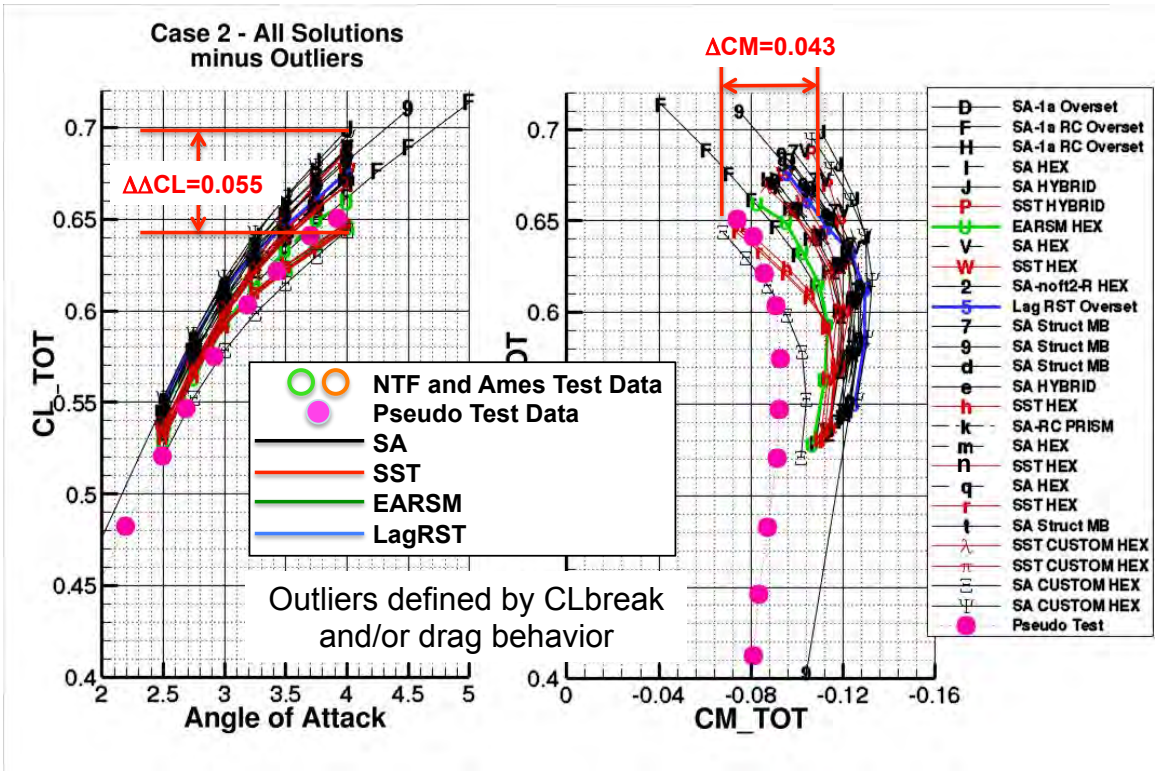


Figure A-E-42. DPW-V: Lift and Pitching Moment, M=0.85; All Solutions minus Outliers.

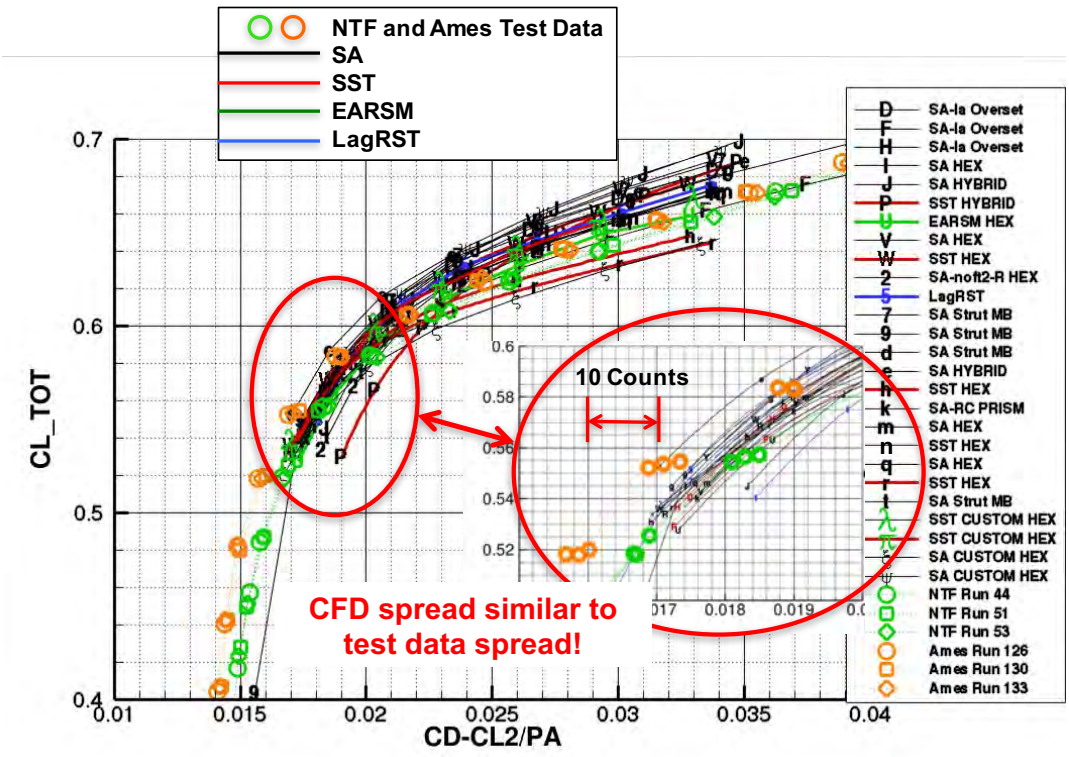


Figure A-E-43. DPW-V: "Profile" Drag Polar, M=0.85: All Solutions minus Outliers.

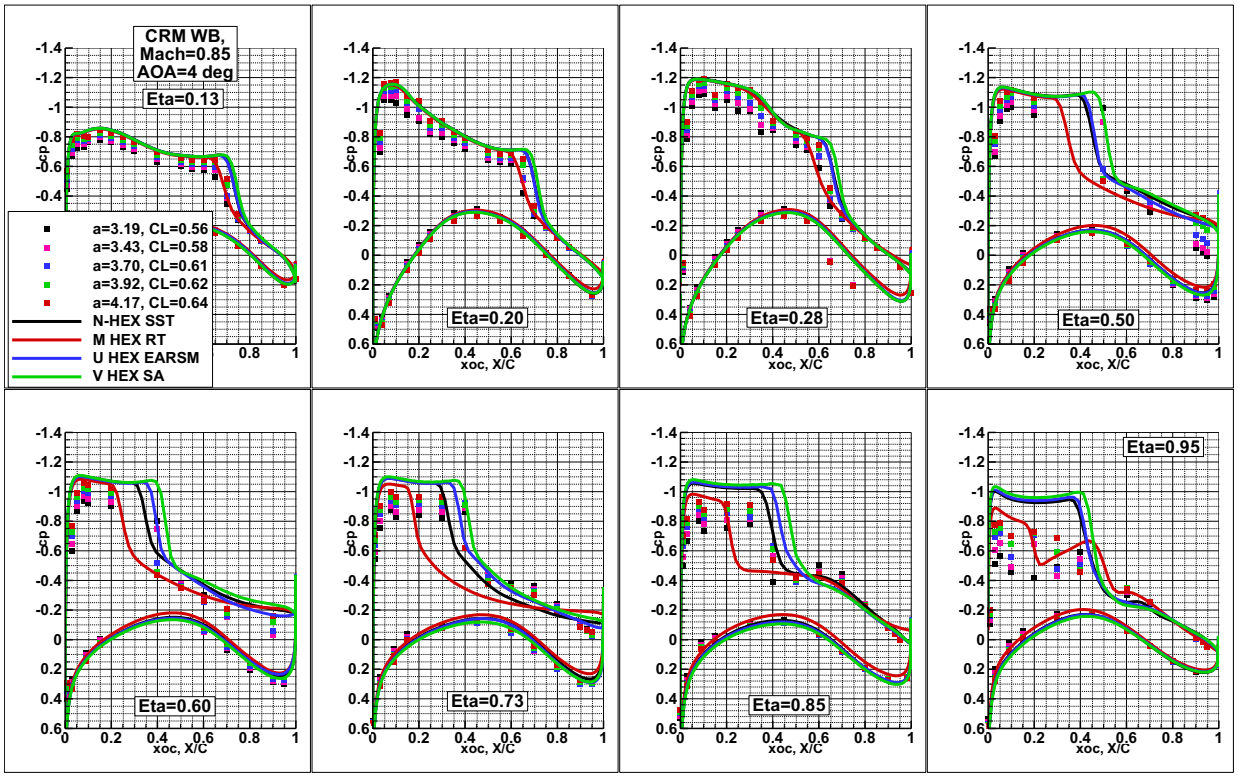


Figure A-E-44. DPW-V: Wing Pressure Distributions, M=0.85: Selected HEX Unstructured Grid Solutions: AoA = 4.0°.

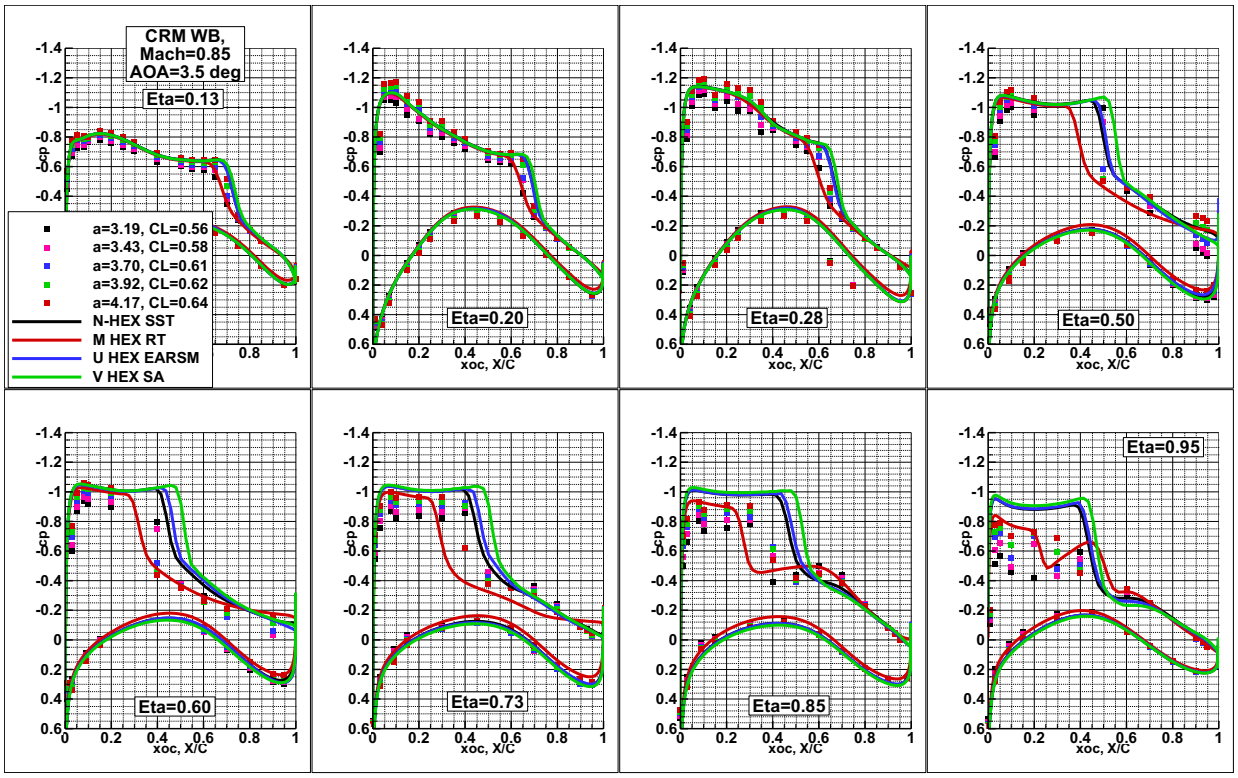


Figure A-E-45. DPW-V: Wing Pressure Distributions, M=0.85: Selected HEX Unstructured Grid Solutions: AoA = 3.5°.

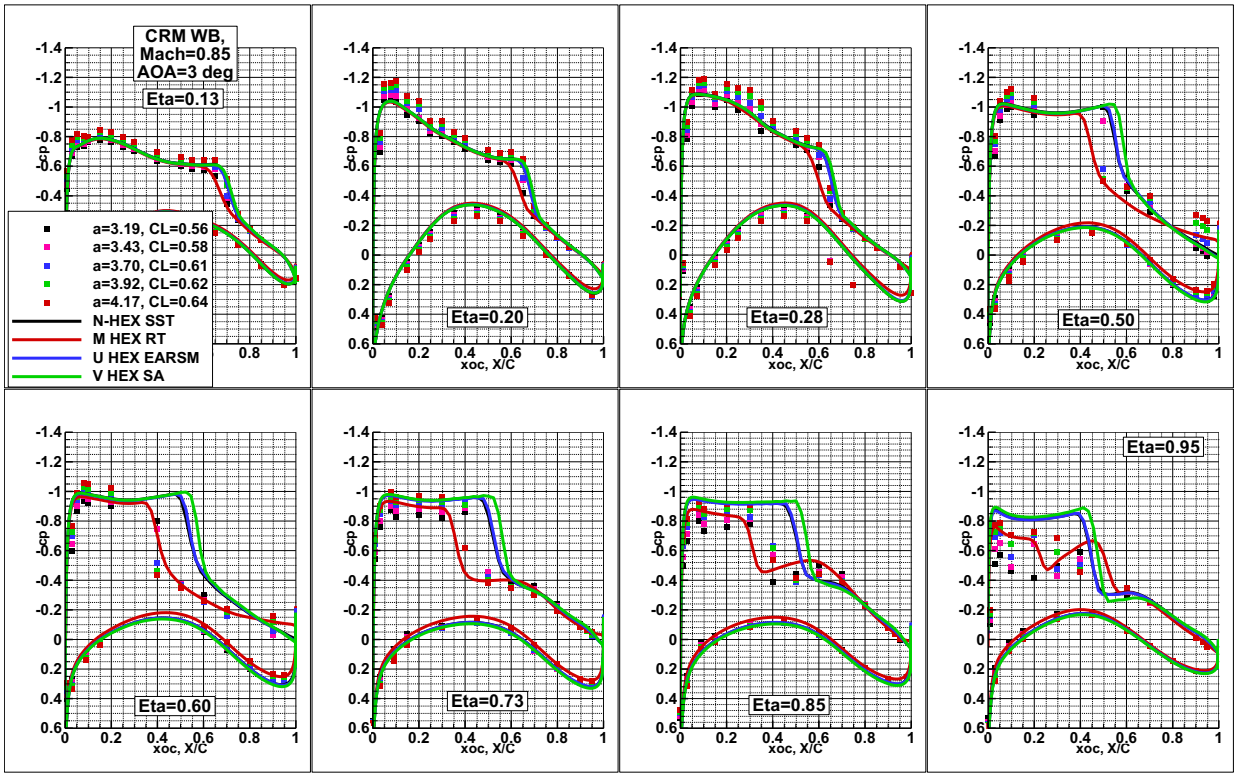


Figure A-E-46. DPW-V: Wing Pressure Distributions, M=0.85: Selected HEX Unstructured Grid Solutions: AoA = 3.0°.

E-C. DPW-VI: CRM Wing-Body (Aeroelastic)

The CRM wing geometry includes the measured aeroelastic deflection at each specified angle of attack.

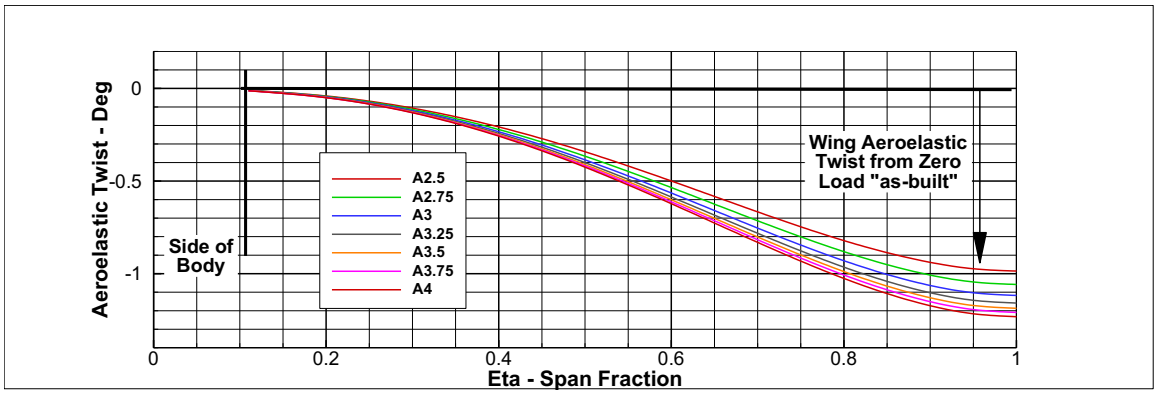


Figure A-E-47. Static Aeroelastic Twist Distribution Derived from Wind Tunnel Measurements, M=0.85.

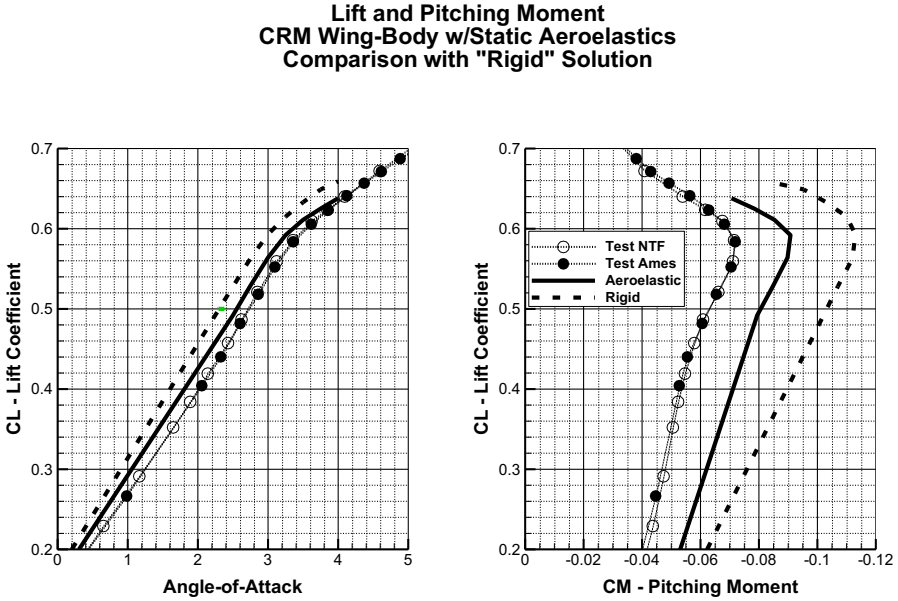


Figure A-E-48. Impact of Aeroelastic Deformation on Lift and Moment; M = 0.85, Re = 5 Million.

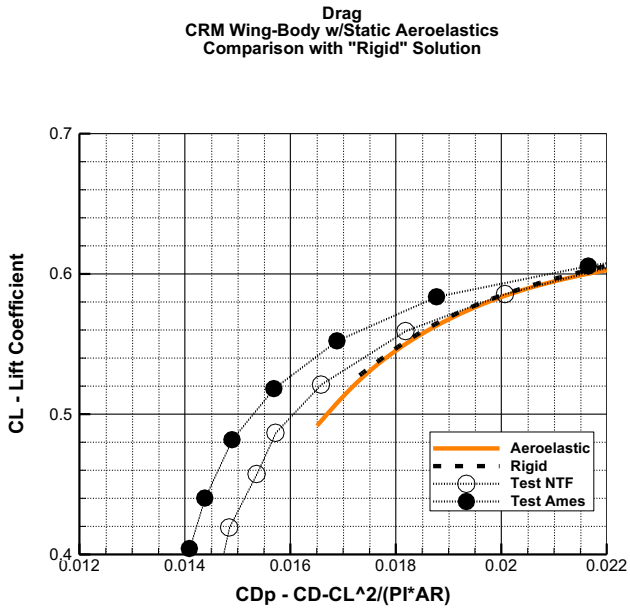


Figure A-E-49. Impact of Aeroelastic Deformation on "Profile" Drag Polar; M = 0.85, Re = 5 Million.

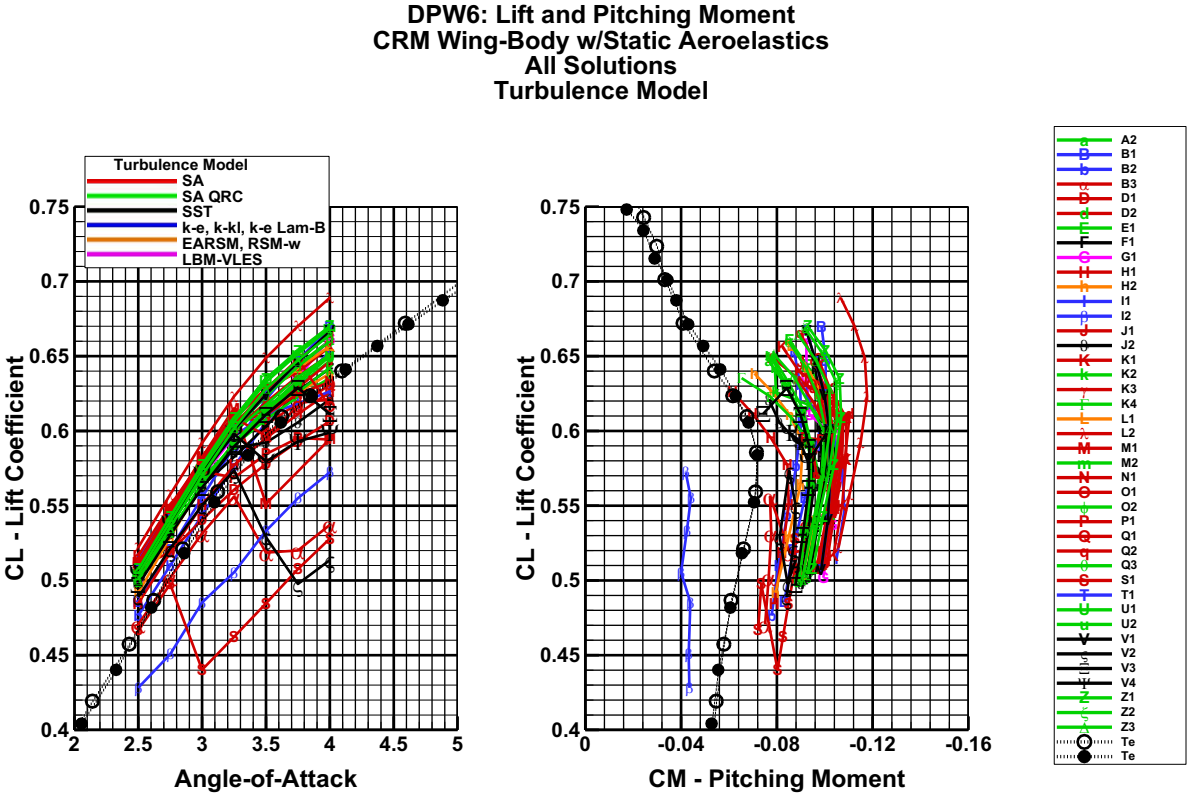


Figure A-E-50. DPW-VI: Lift and Pitching Moment, M=0.85; All Solutions.

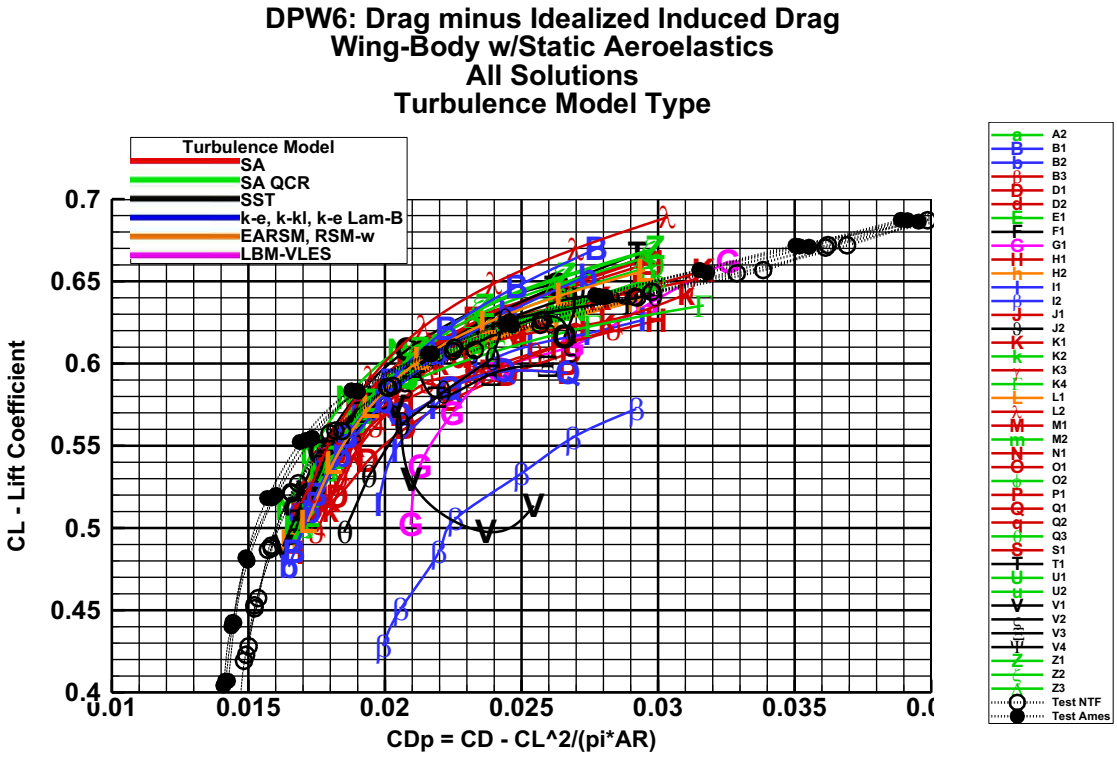


Figure A-E-51. DPW-VI: "Idealized Profile" Drag Polar, M=0.85; All Solutions.

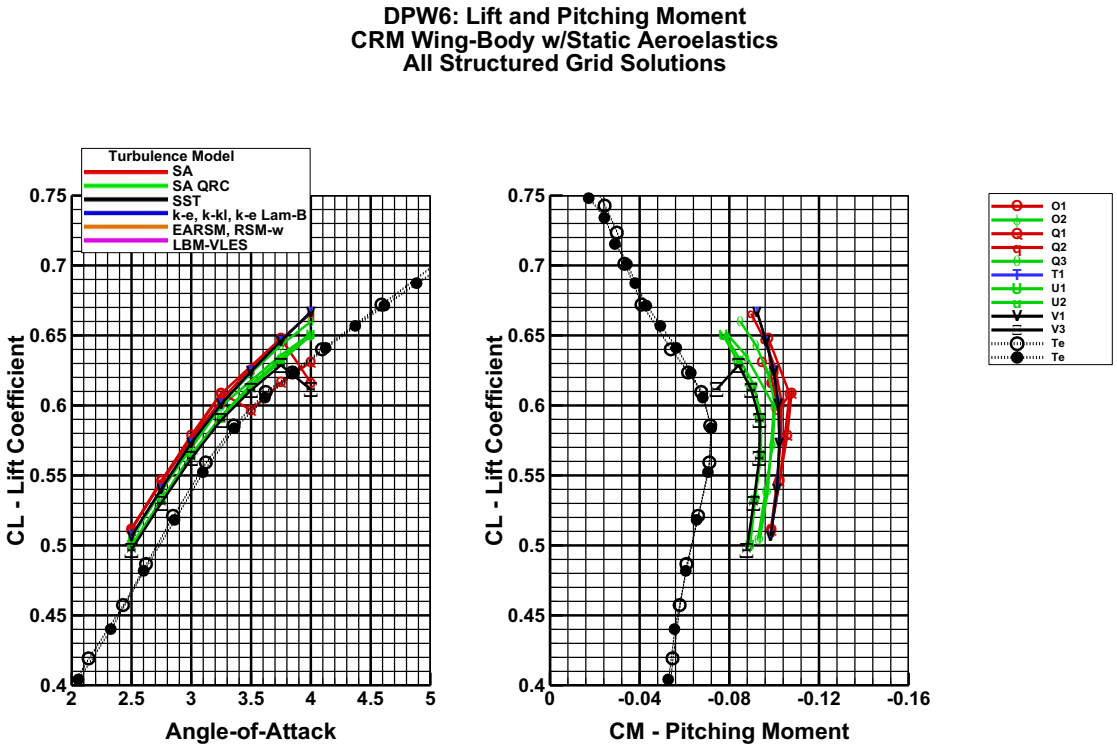


Figure A-E-52. DPW-VI: Lift and Pitching Moment, M=0.85; All Structured Grid Solutions.

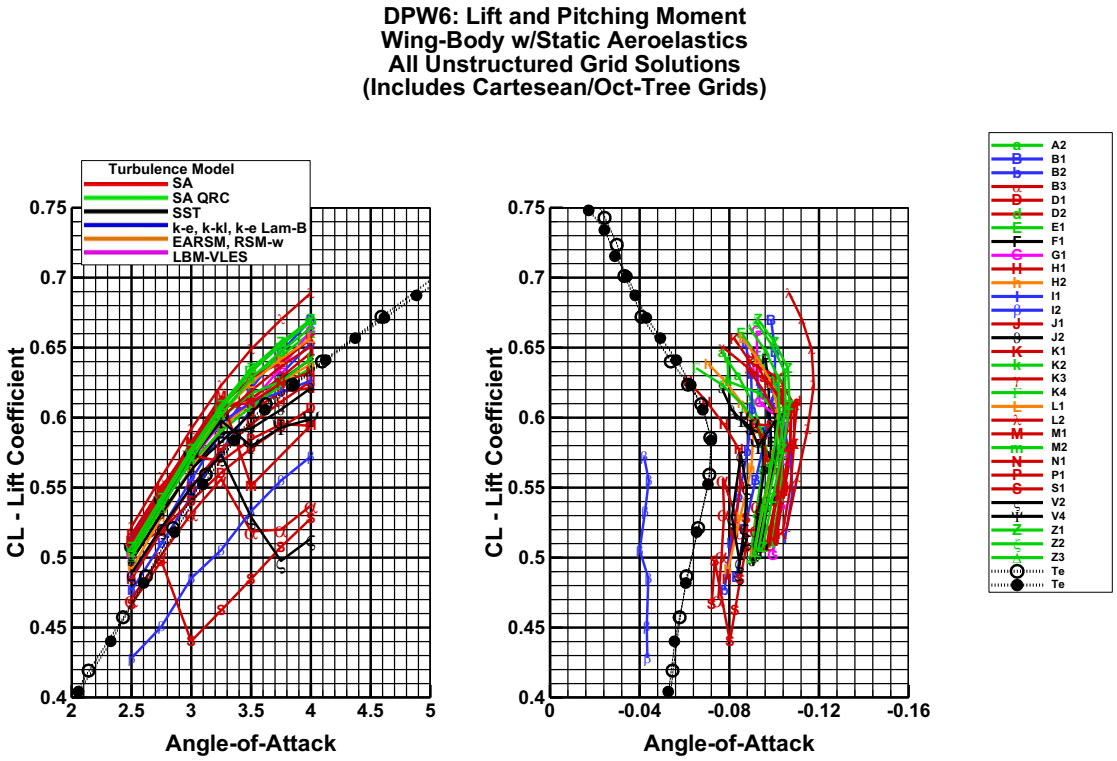


Figure A-E-53. DPW-VI: Lift and Pitching Moment, M=0.85; All Unstructured Grid Solutions.

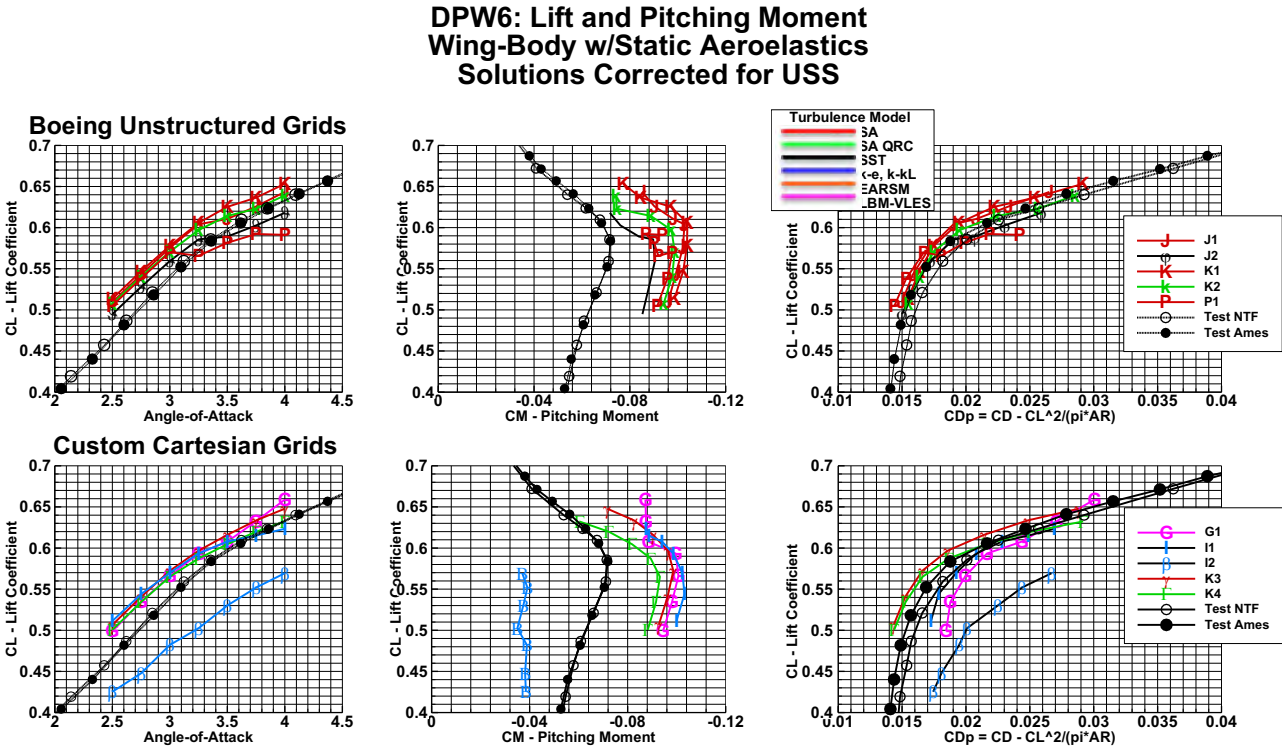


Figure A-E-54. DPW-VI: Forces and Moments, M=0.85; Boeing Unstructured and Custom Cartesian Grids.

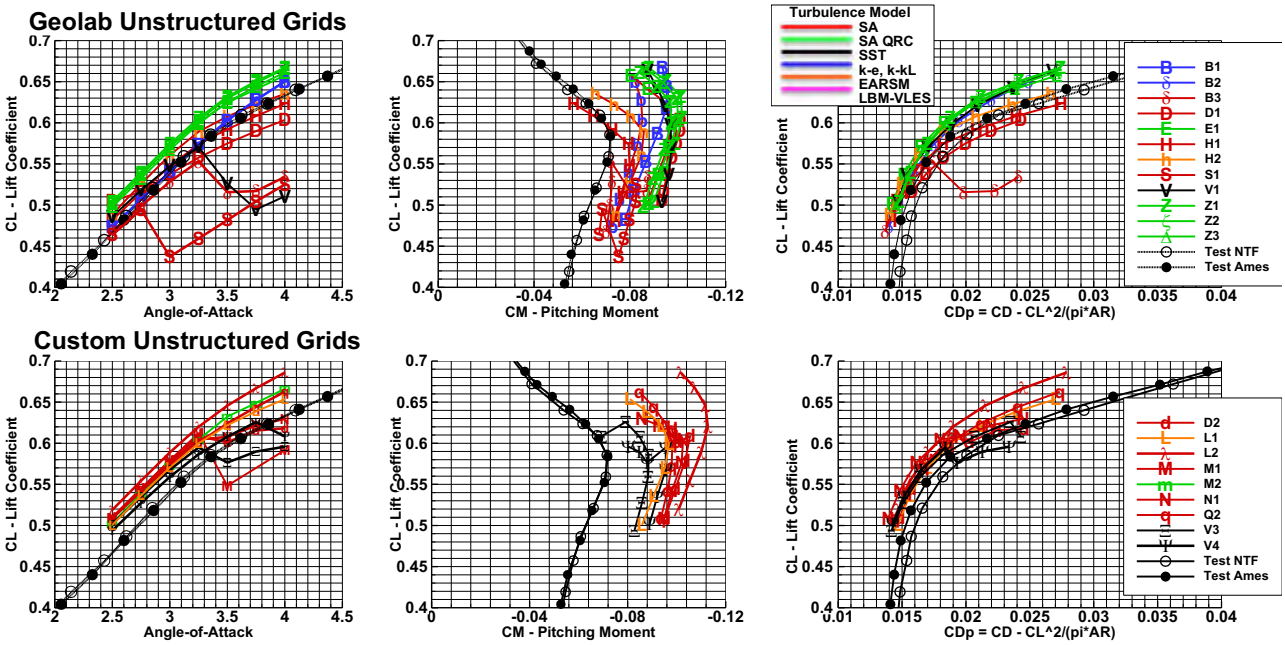


Figure A-E-55. DPW-VI: Forces and Moments, M=0.85; Geolab and Custom Unstructured Grids.

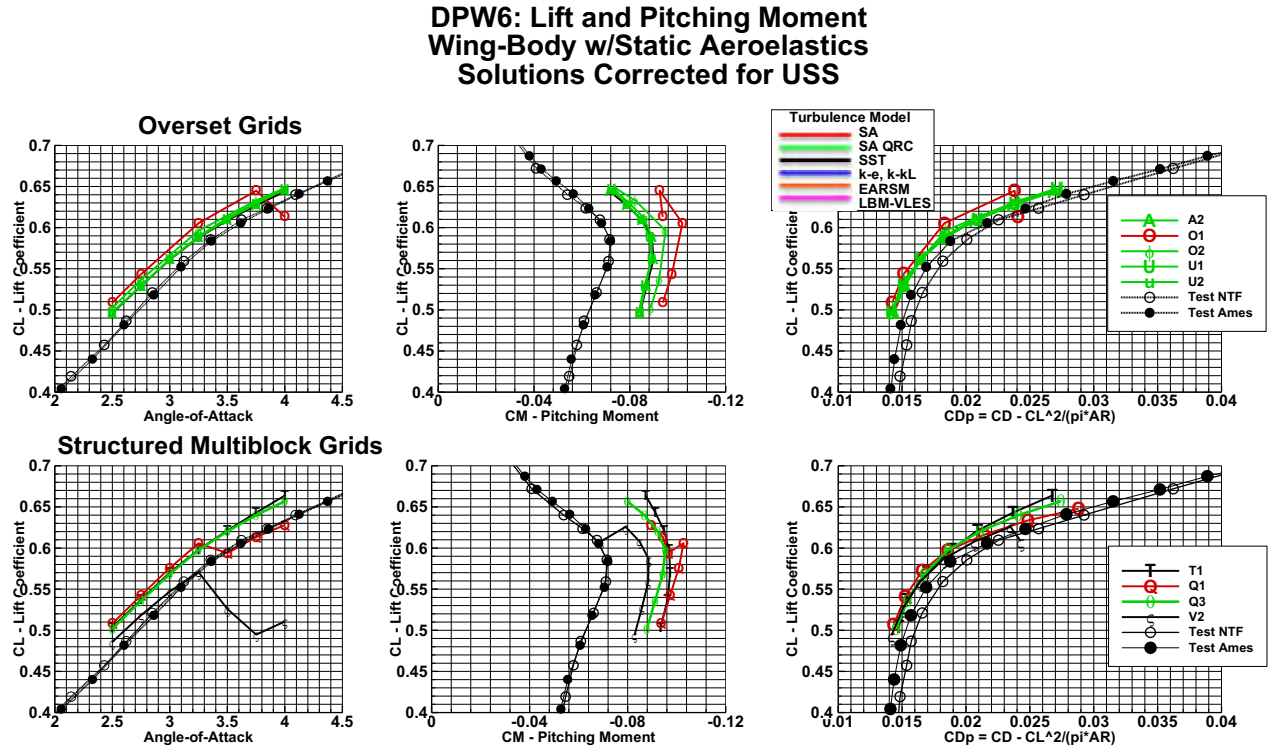


Figure A-E-56. DPW-VI: Forces and Moments, M=0.85; Overset and Multiblock Grids.

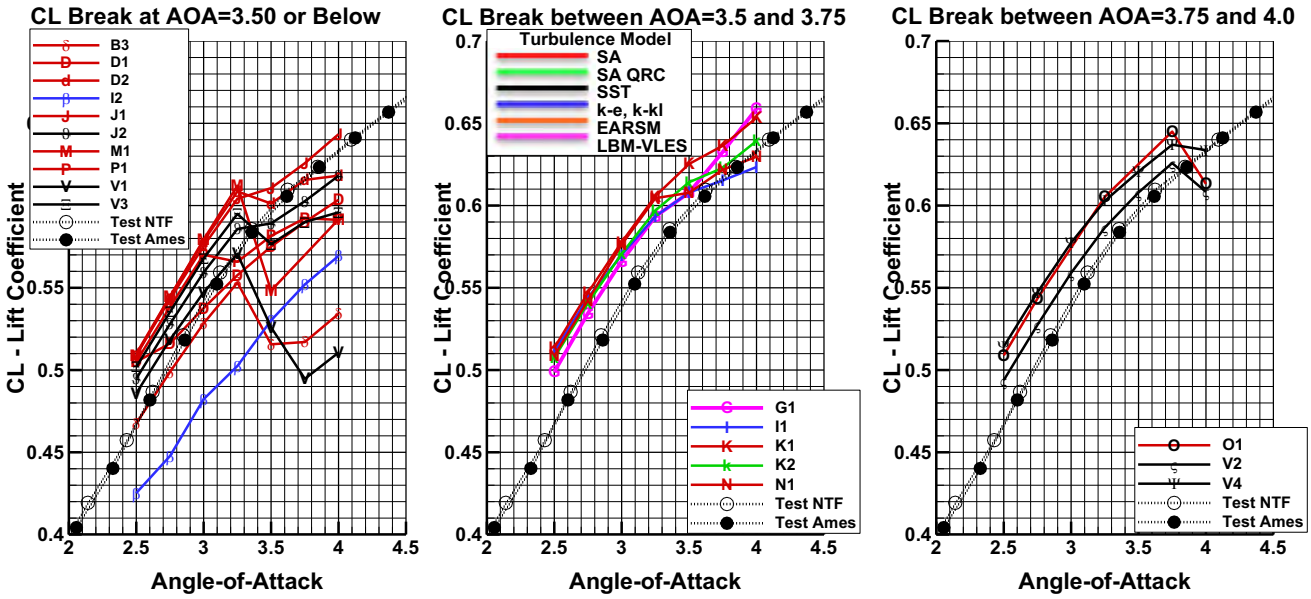


Figure A-E-57. DPW-VI: Solution Outliers, M=0.85.

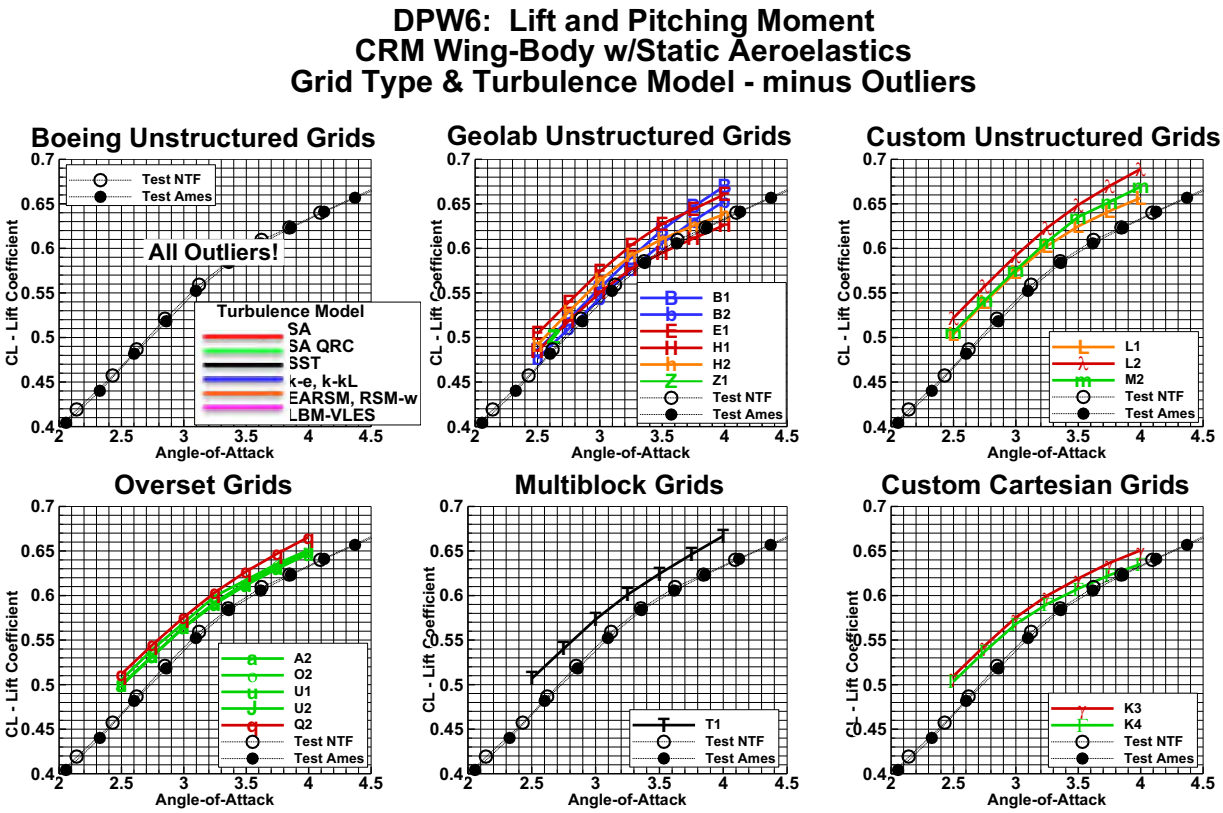


Figure A-E-58. DPW-VI: Solutions minus Outliers Parsed by Grid and Turbulence Model, M=0.85.

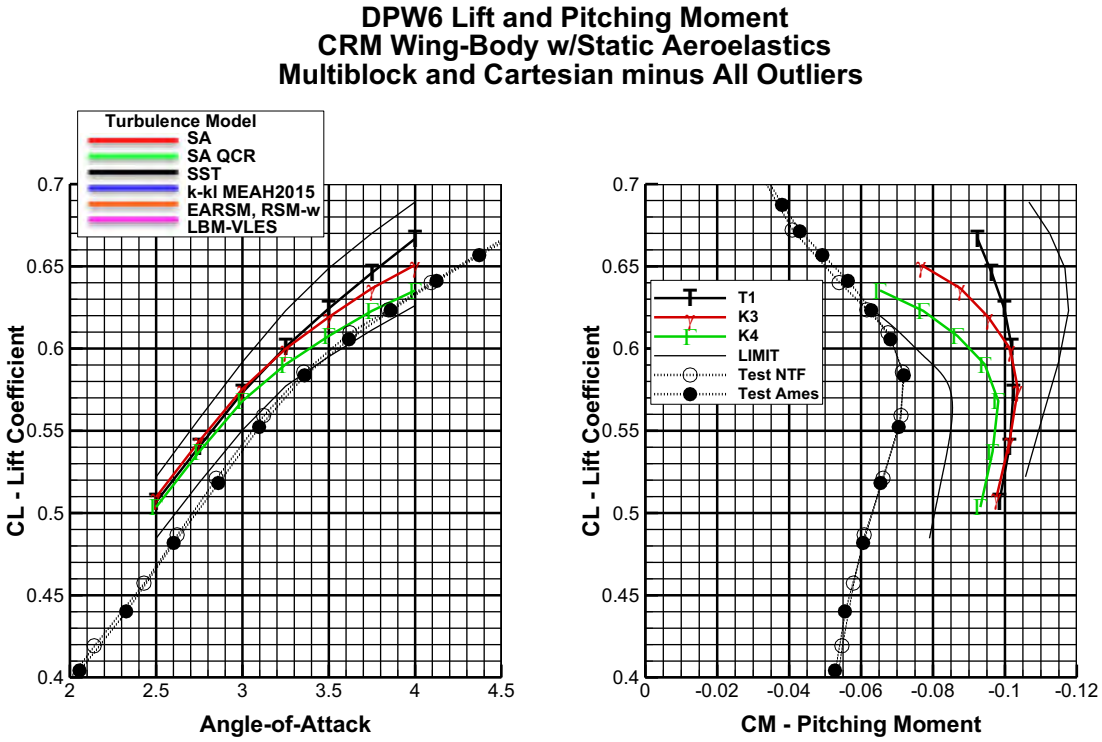


Figure A-E-59. DPW-VI: Multiblock and Cartesian Grid Solutions minus Outliers, M=0.85.

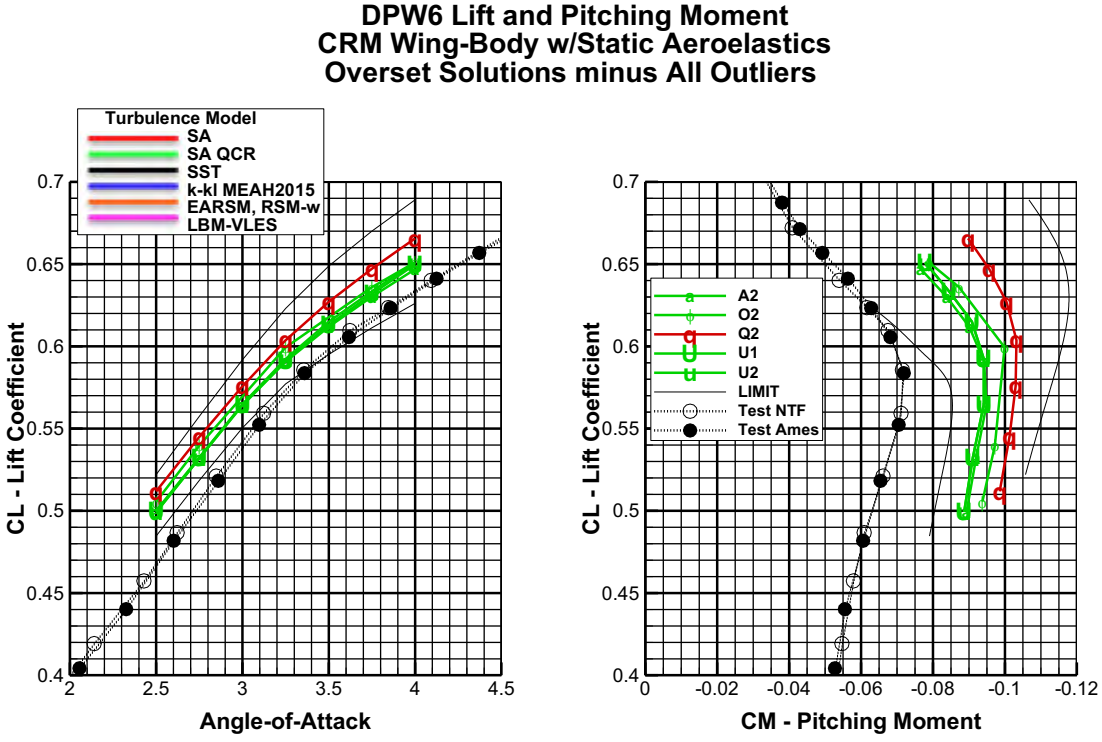


Figure A-E-60. DPW-VI: Overset Grid Solutions minus Outliers, M=0.85.

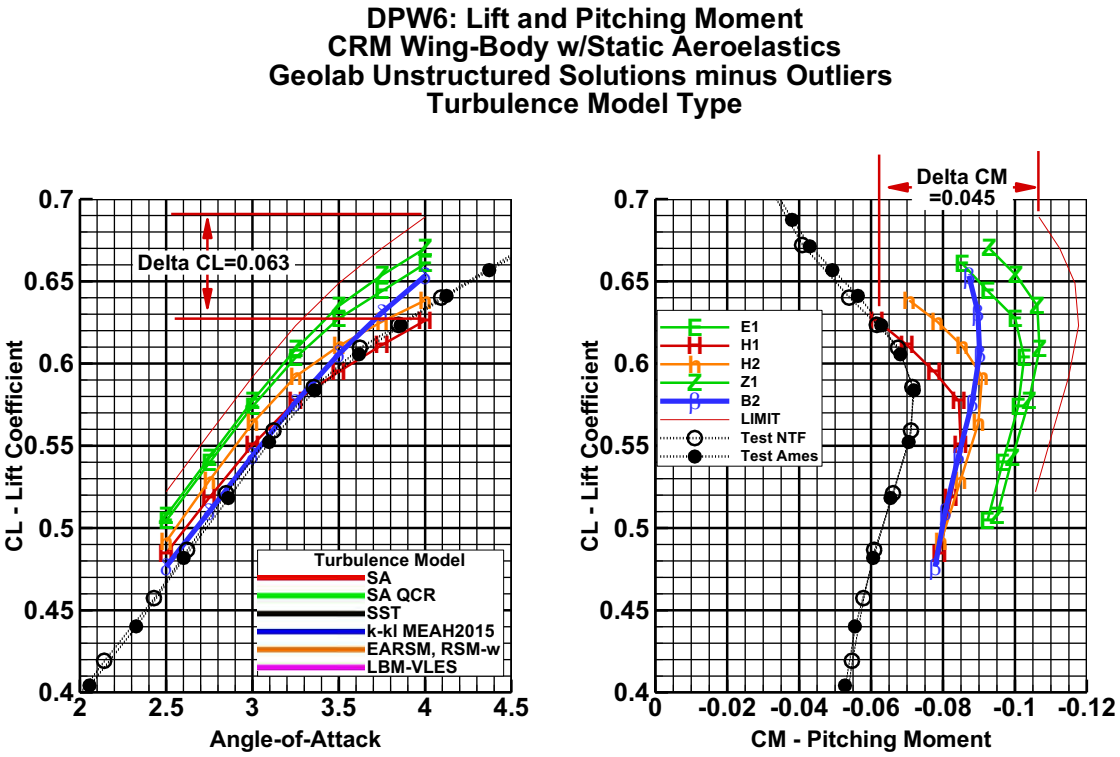


Figure A-E-61. DPW-VI: Geolab Unstructured Grid Solutions minus Outliers, M=0.85.

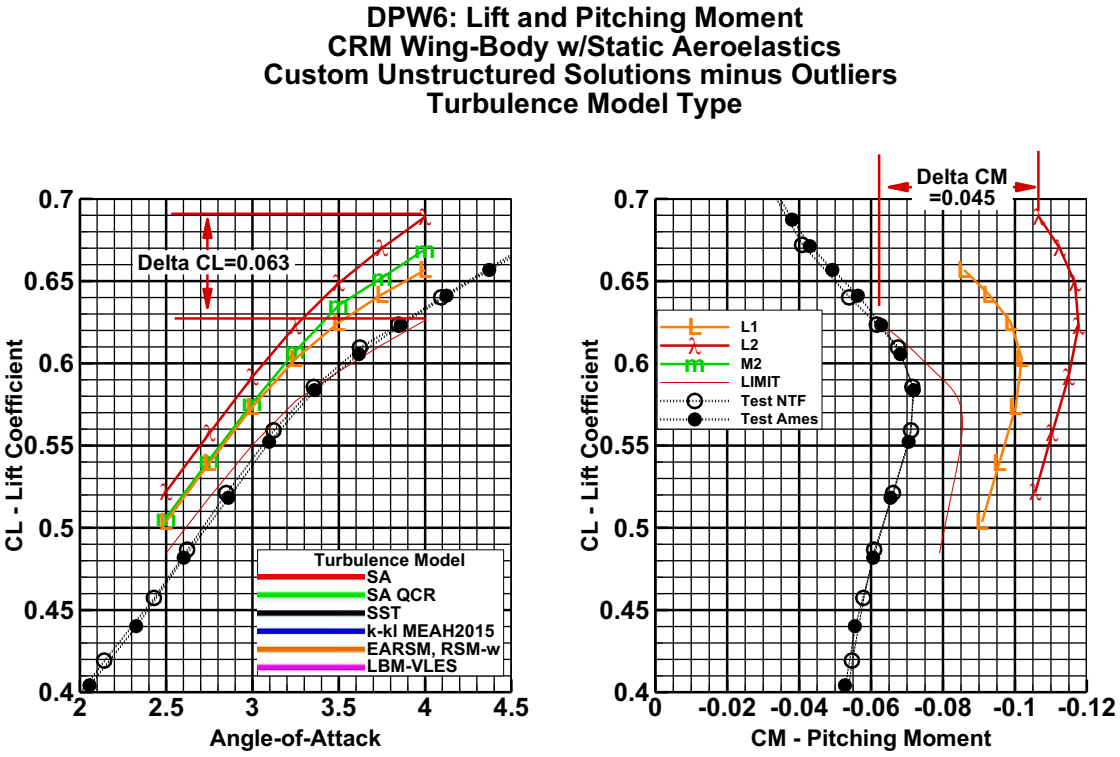


Figure A-E-62. DPW-VI: Custom Unstructured Grid Solutions minus Outliers, M=0.85.

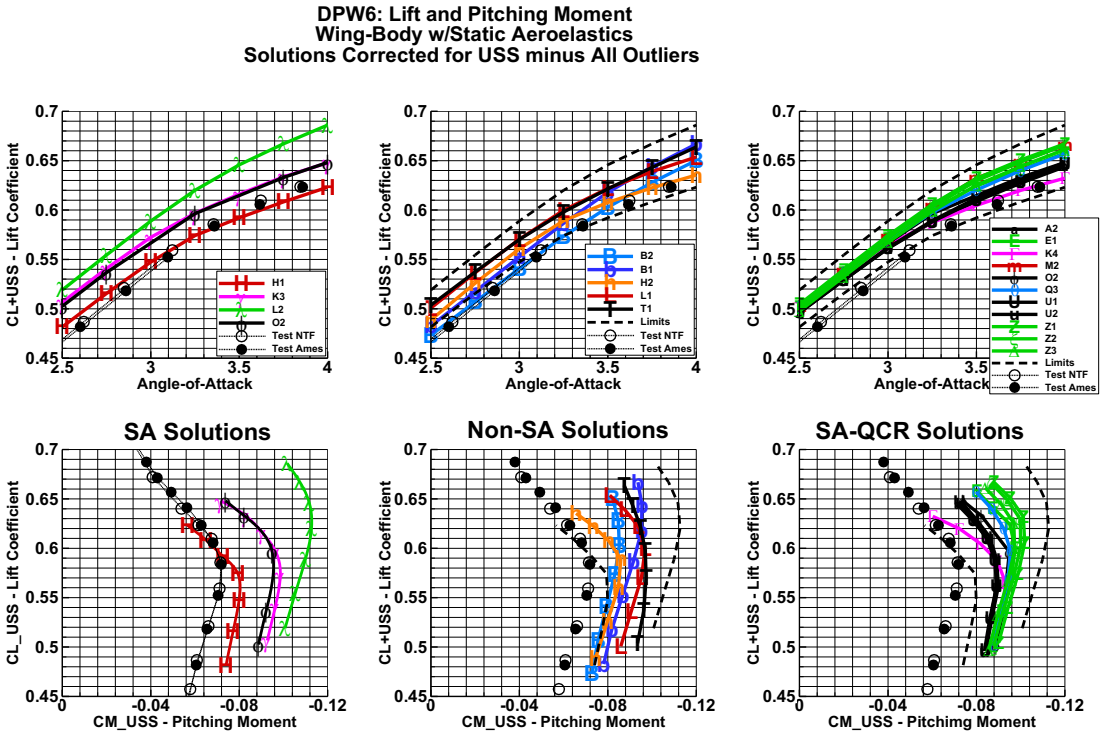


Figure A-E-63. DPW-VI: Parsed Lift and Pitching Moment Solutions Corrected for USS minus Outliers, M=0.85.

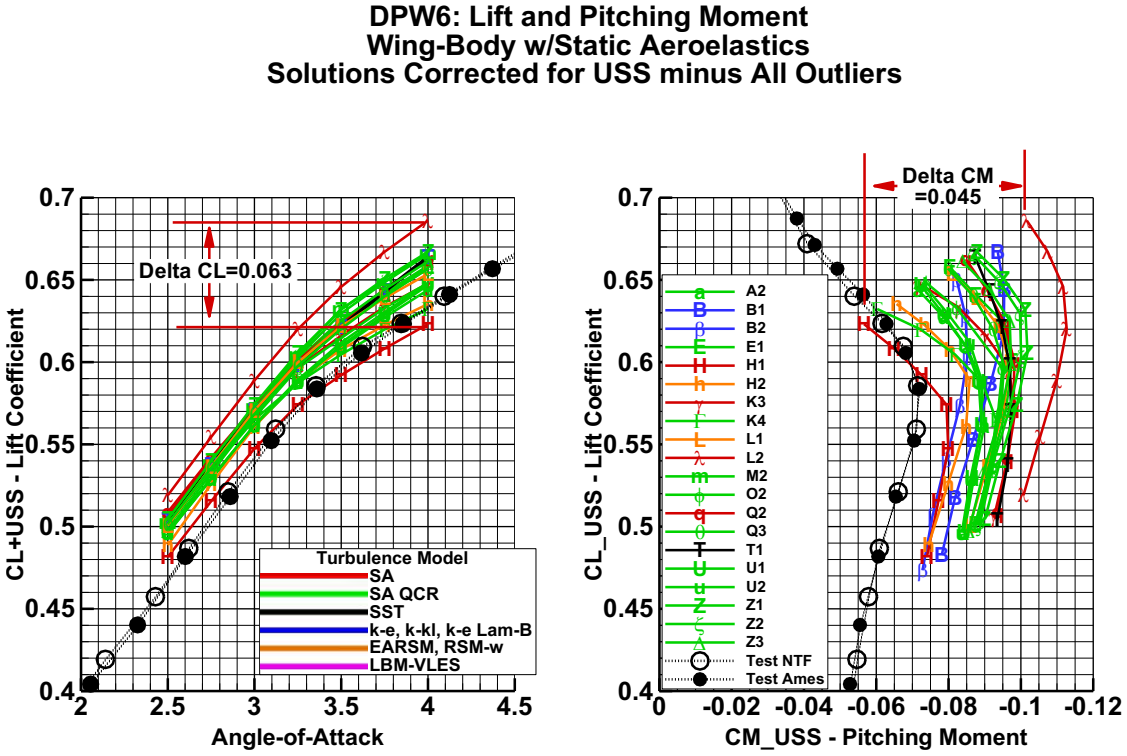


Figure A-E-64. DPW-VI: Lift and Pitching Moment Solutions Corrected for USS minus Outliers, M=0.85.

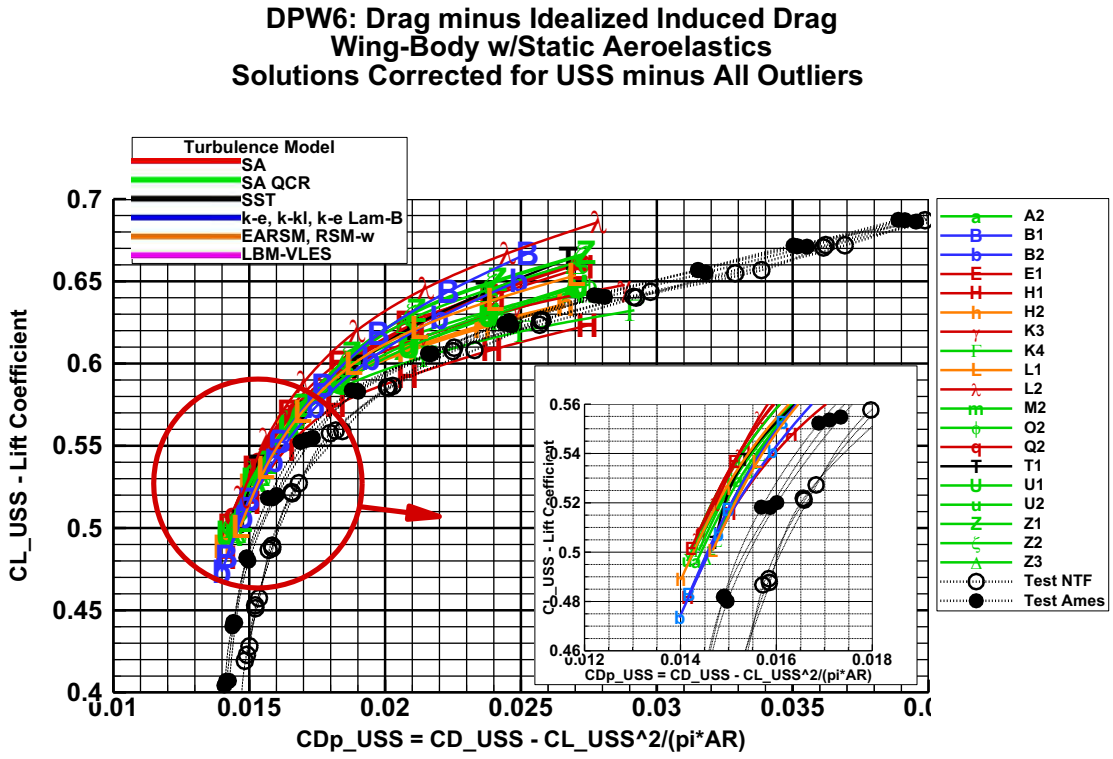


Figure A-E-65. DPW-VI: "Profile" Drag Solutions Corrected for USS minus Outliers, M=0.85.

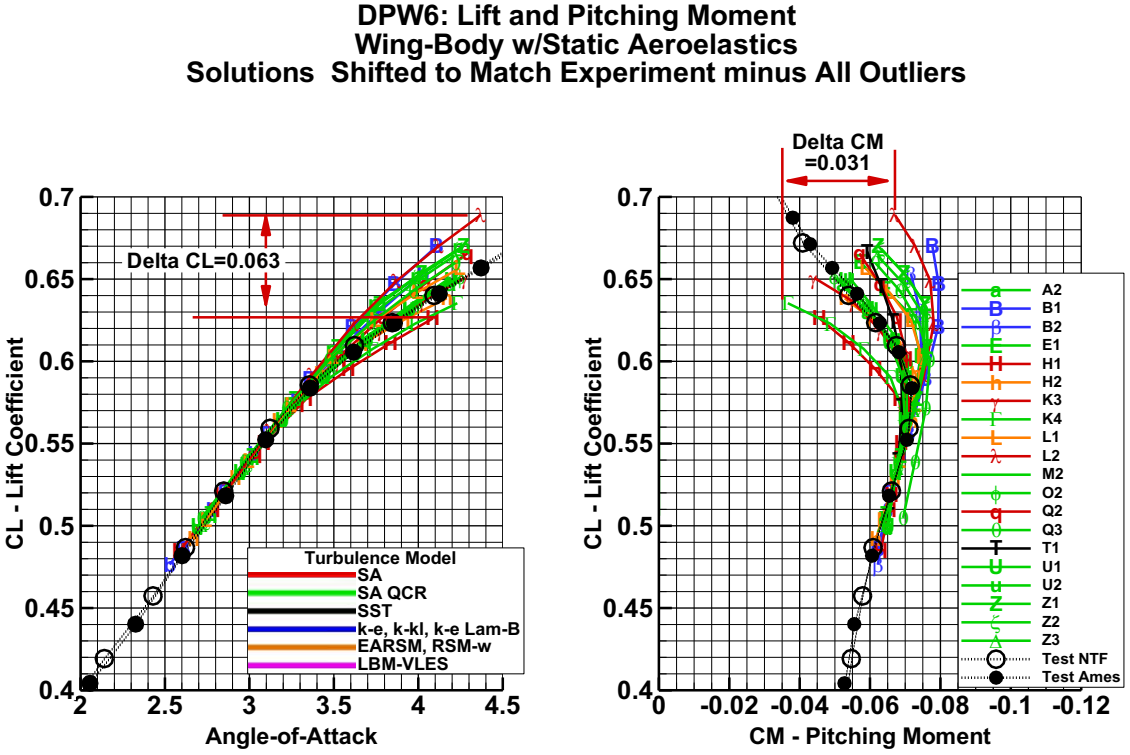


Figure A-E-66. DPW-VI: Shifted Lift and Pitching Moment Solutions minus Outliers, M=0.85.

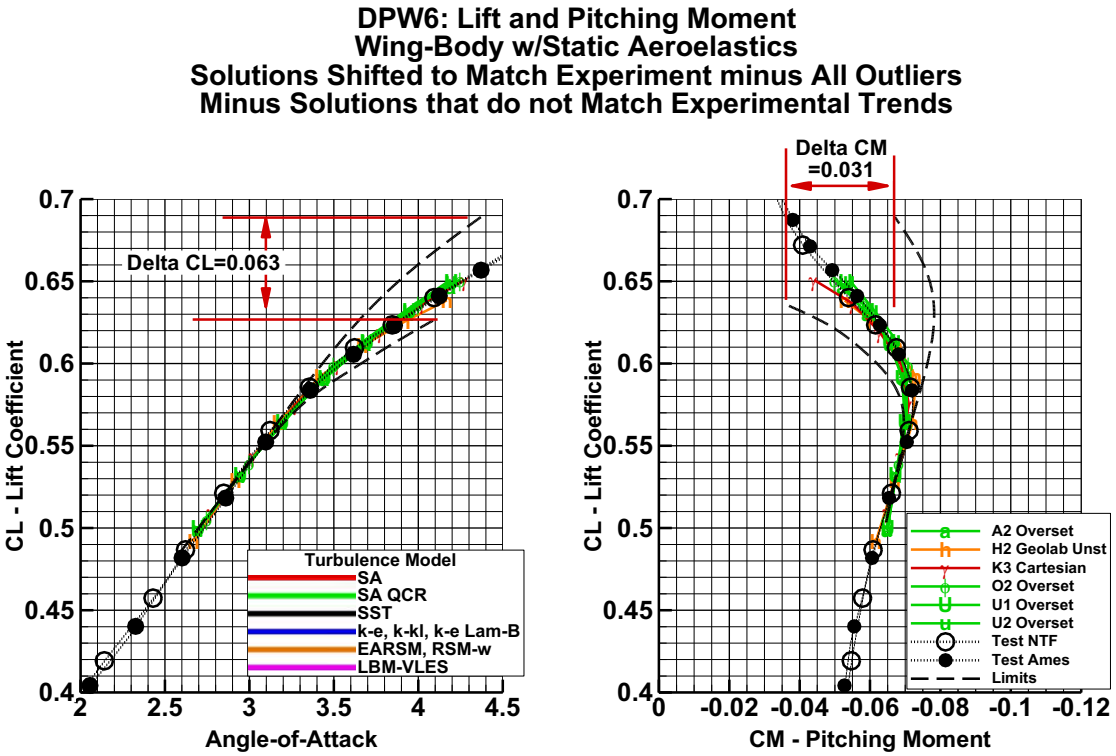


Figure A-E-67. DPW-VI: Shifted Lift and Pitching Moment Solutions minus Outliers minus Solutions that do not Match Experimental trends, M=0.85.

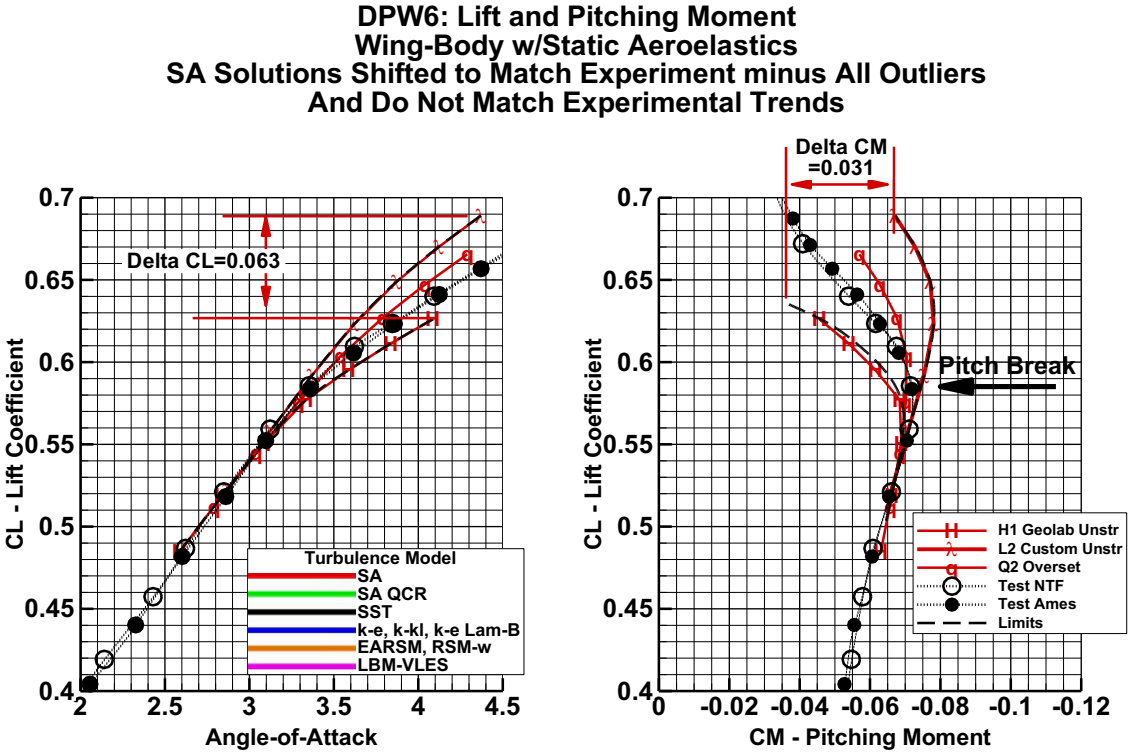


Figure A-E-68. DPW-VI: Shifted Lift and Pitching Moment SA Solutions minus Outliers, M=0.85.

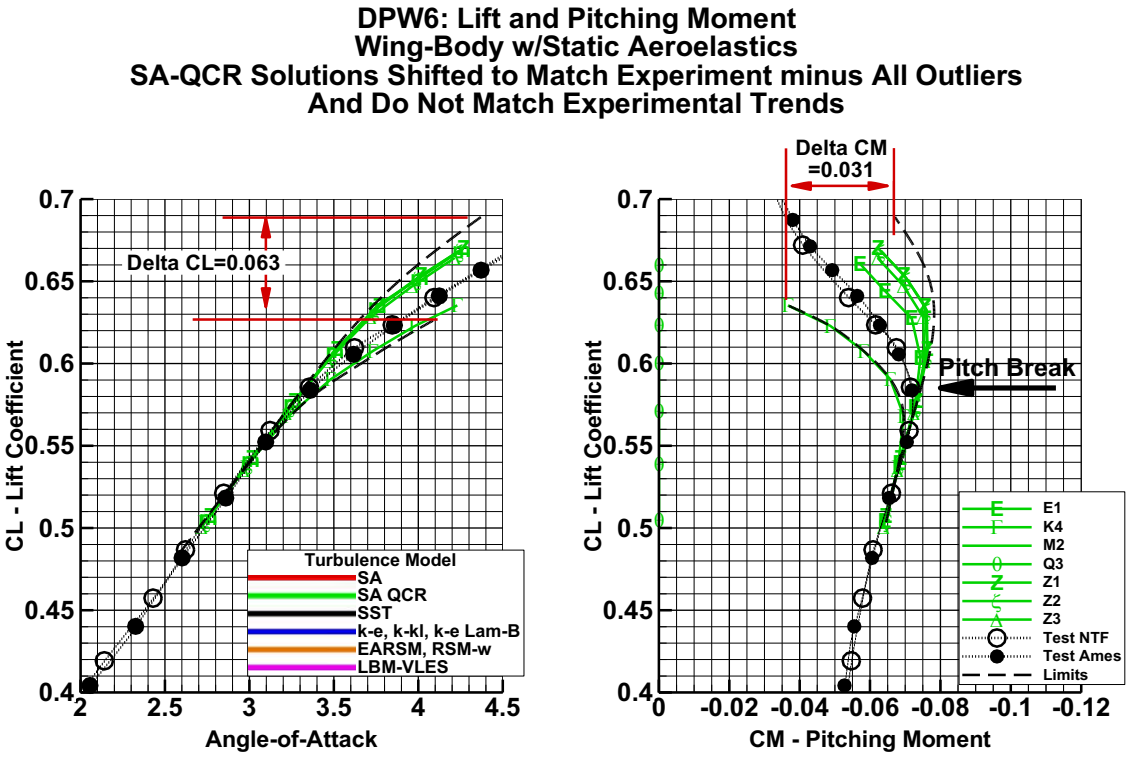


Figure A-E-69. DPW-VI: Shifted Lift and Pitching Moment SA-QCR Solutions minus Outliers, M=0.85.

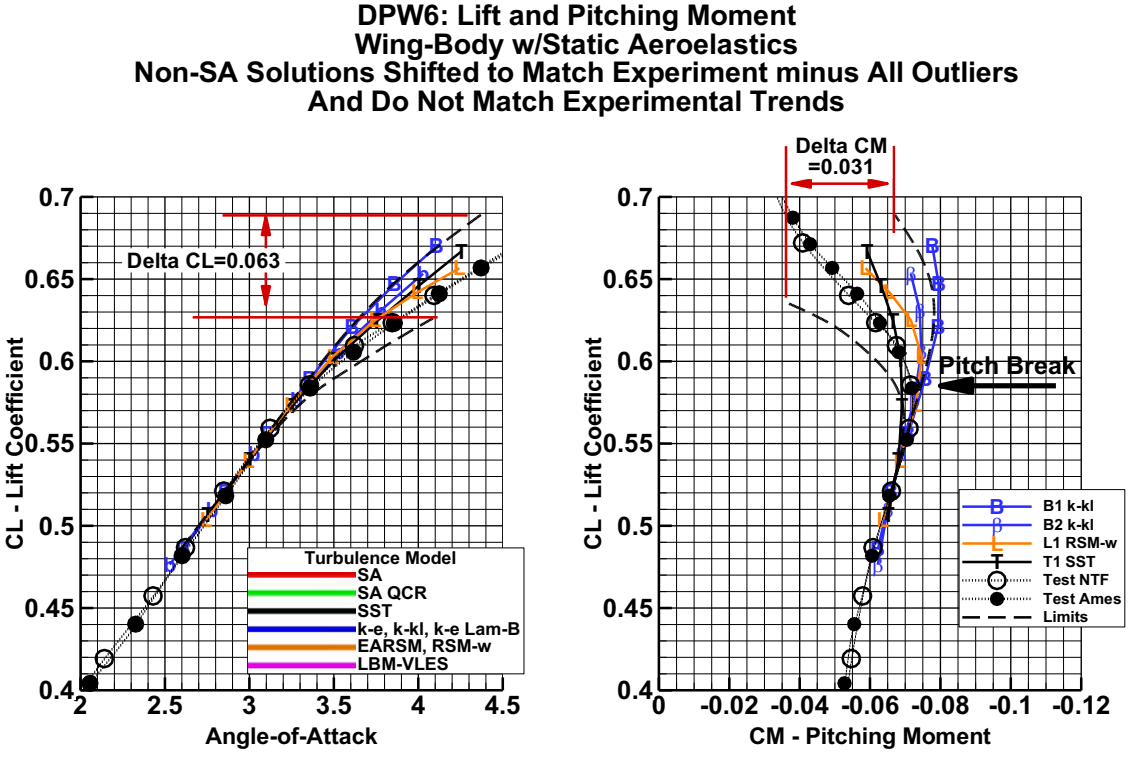


Figure A-E-70. DPW-VI: Shifted Lift and Pitching Moment Non-SA Solutions minus Outliers, M=0.85.

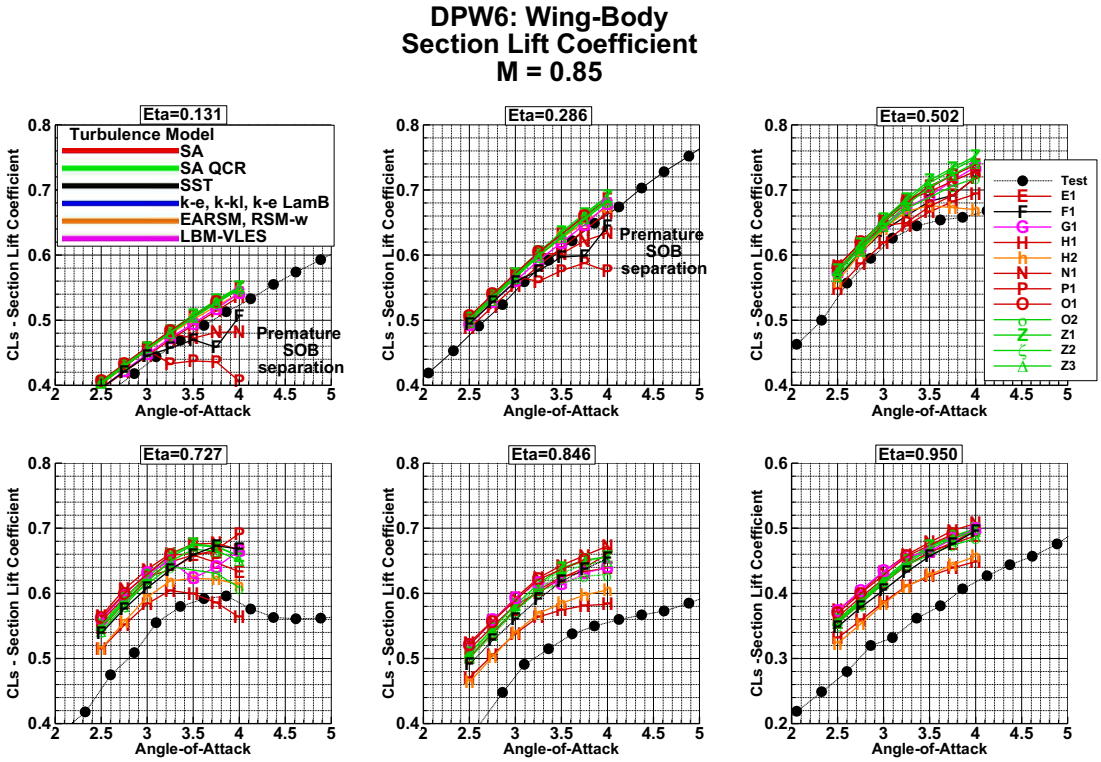


Figure A-E-71. DPW-VI: Wing Section Lift Coefficient; All Solutions, M=0.85.

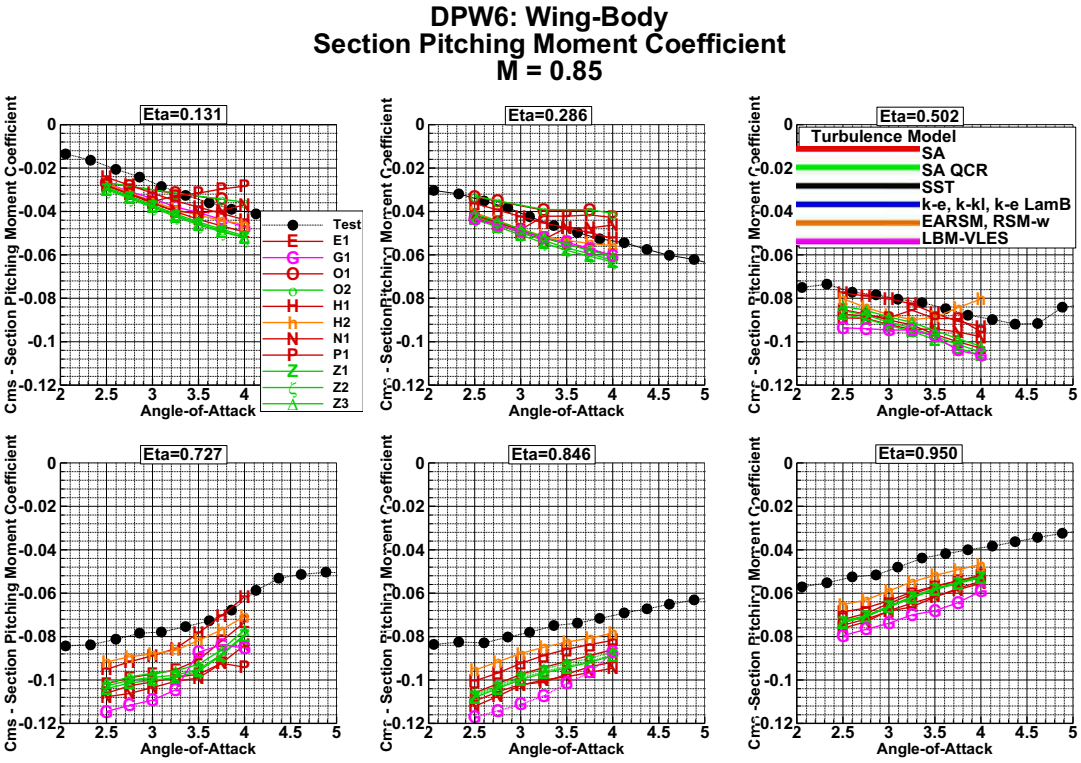


Figure A-E-72. DPW-VI: Wing Section Pitching Moment Coefficient; All Solutions, M=0.85.

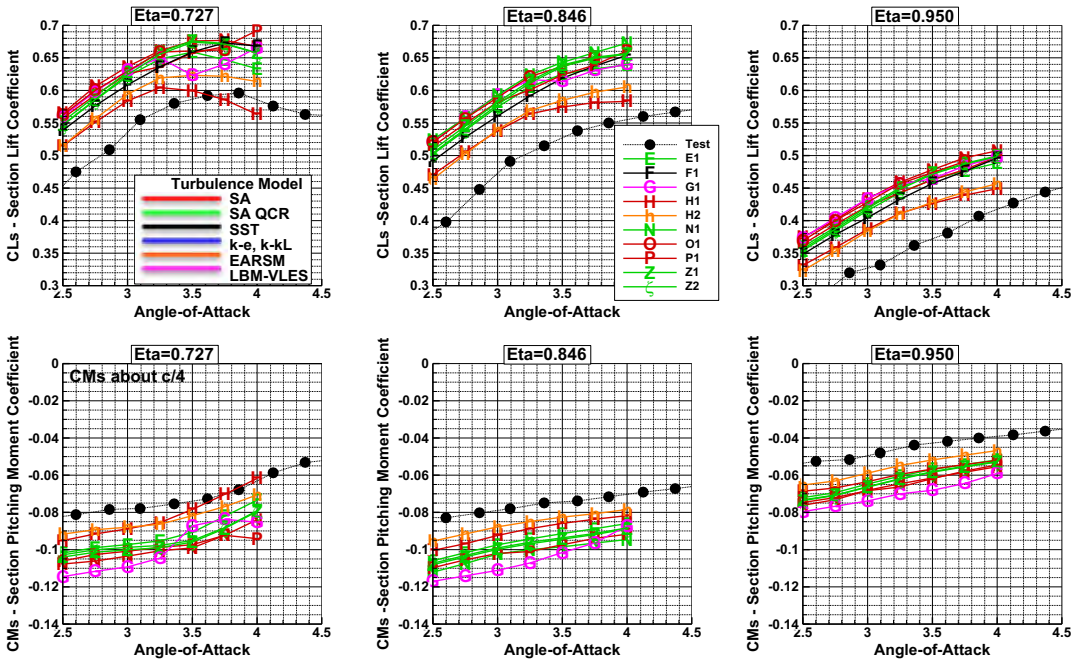


Figure A-E-73. DPW-VI: Wing Section Lift and Pitching Moment Coefficient on Outboard Wing, M=0.85; All Solutions.

Appendix F. Downwash Study

The downwash study was unique to DPW-IV. Here, four angle-of-attack sweeps of the CRM were performed, three on the Wing-Body-Tail configuration at different horizontal-tail settings, and one without the tail on the Wing-Body configuration. The tail settings were iH = [–2°,0°, +2°]. The three WBT polars provide sufficient information to reconstruct a trimmed drag polar, and trimmed lift curve, which was the stated purpose of this study. In addition, these computational results provide sufficient data to calculate stabilizer effectiveness. The data set identifiers for DPW-IV are found in Table S-VI-1 and in Appendix C. Discussion is in Section XI - Trim Drag and Stabilizer Effectiveness of this report.

A Microsoft Excel spreadsheet was provided in the DPW-IV website [38] to facilitate calculating the trimmed drag polars.

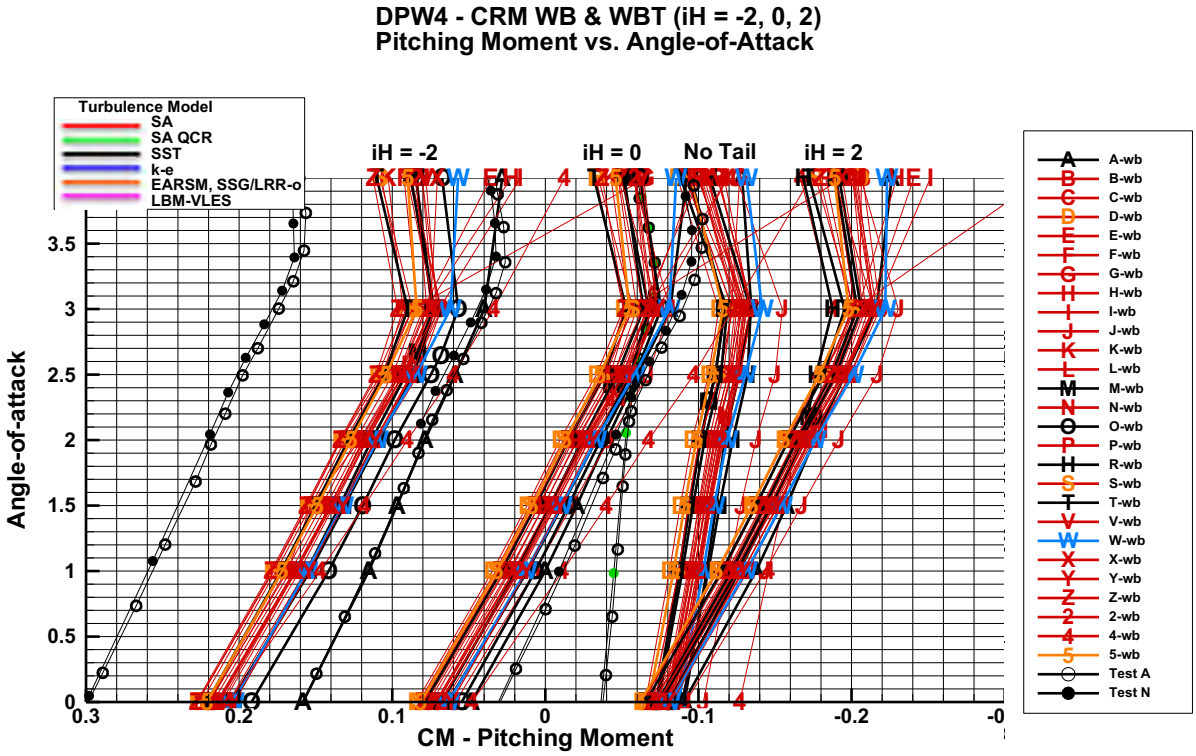


Figure A-F-1. DPW-IV: Pitching Moment, M=0.85: Wing-Body and Wing-Body-Tail iH = –2°, 0°, 2° (Figure S-XI-2).

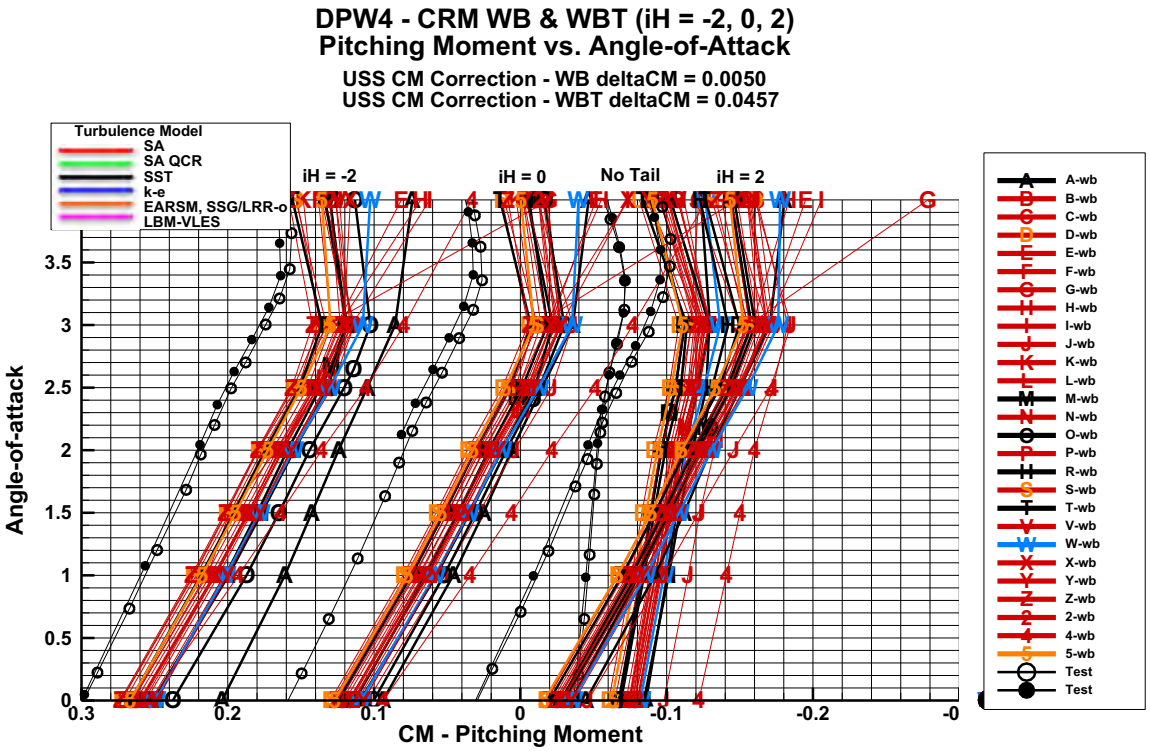


Figure A-F-2. DPW-IV: Pitching Moment Corrected for CFD based Mounting System USS, M=0.85: Wing-Body and Wing-Body-Tail iH = –2°, 0°, 2°.

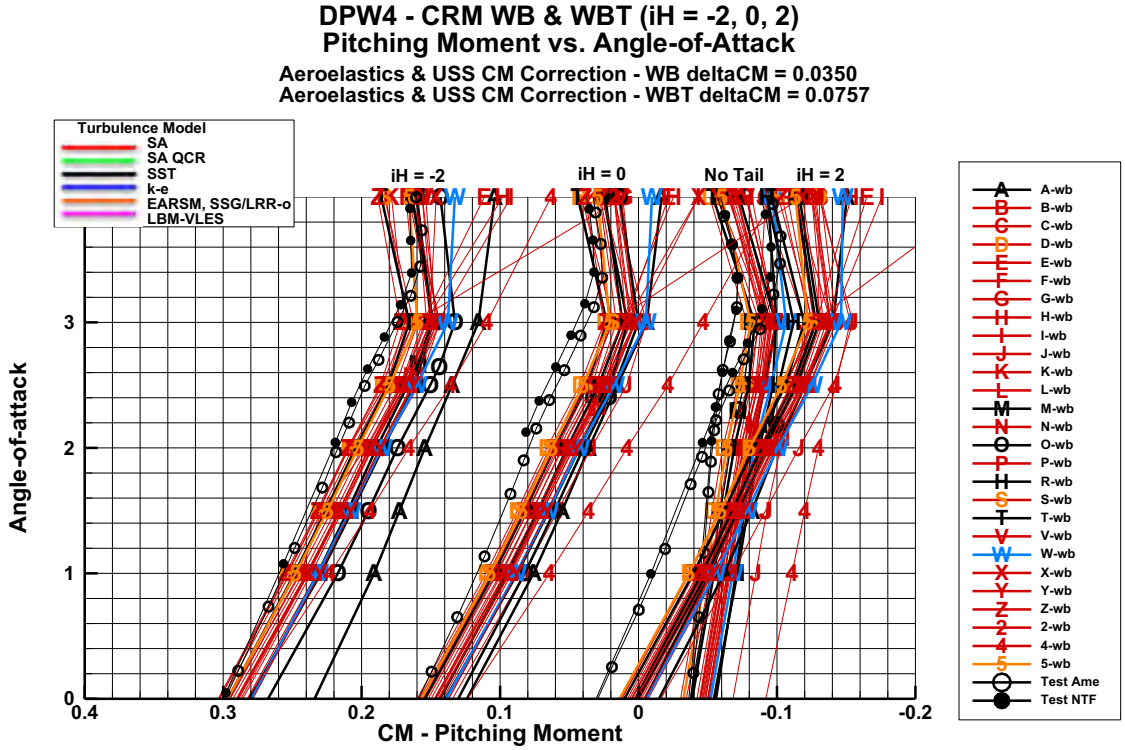


Figure A-F-3. DPW-IV: Pitching Moment Corrected for CFD based Mounting System USS and Aeroelastics, M=0.85: Wing-Body and Wing-Body-Tail iH = –2°, 0°, 2° (Figure S-XI-5).

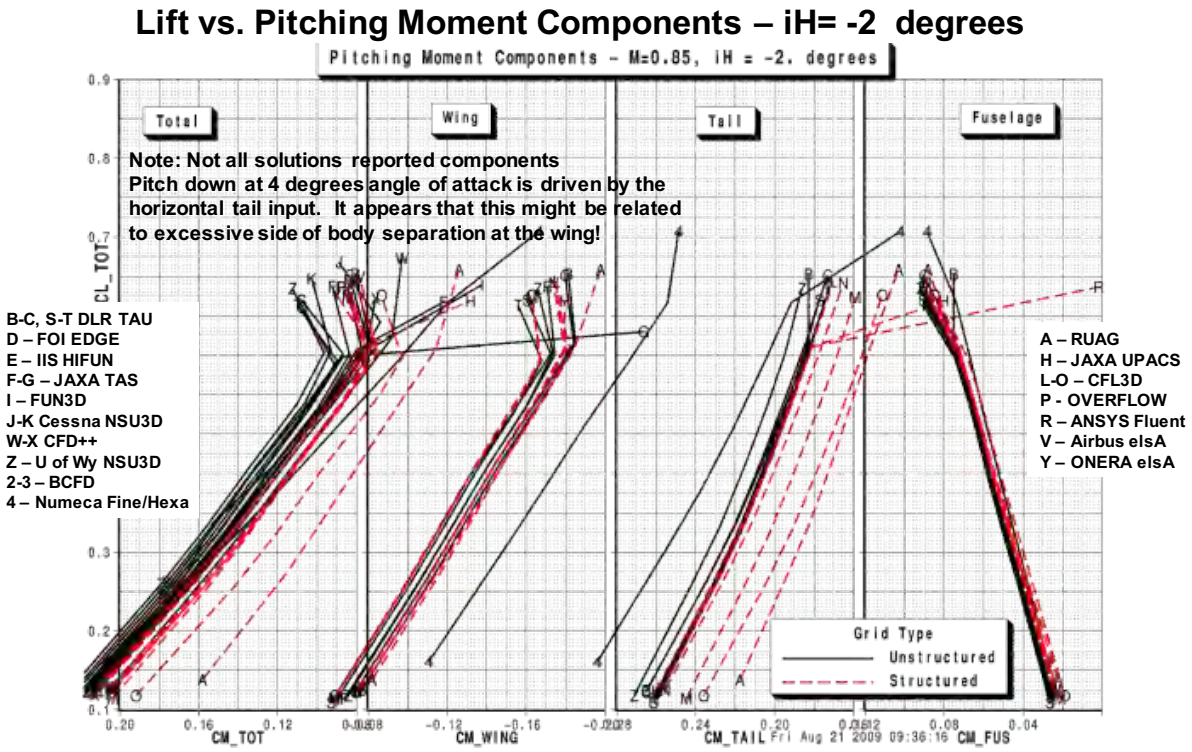


Figure A-F-4. DPW-IV: Pitching Moment Components, M=0.85; Wing-Body-Tail iH = –2° (Figure S-XI-3).

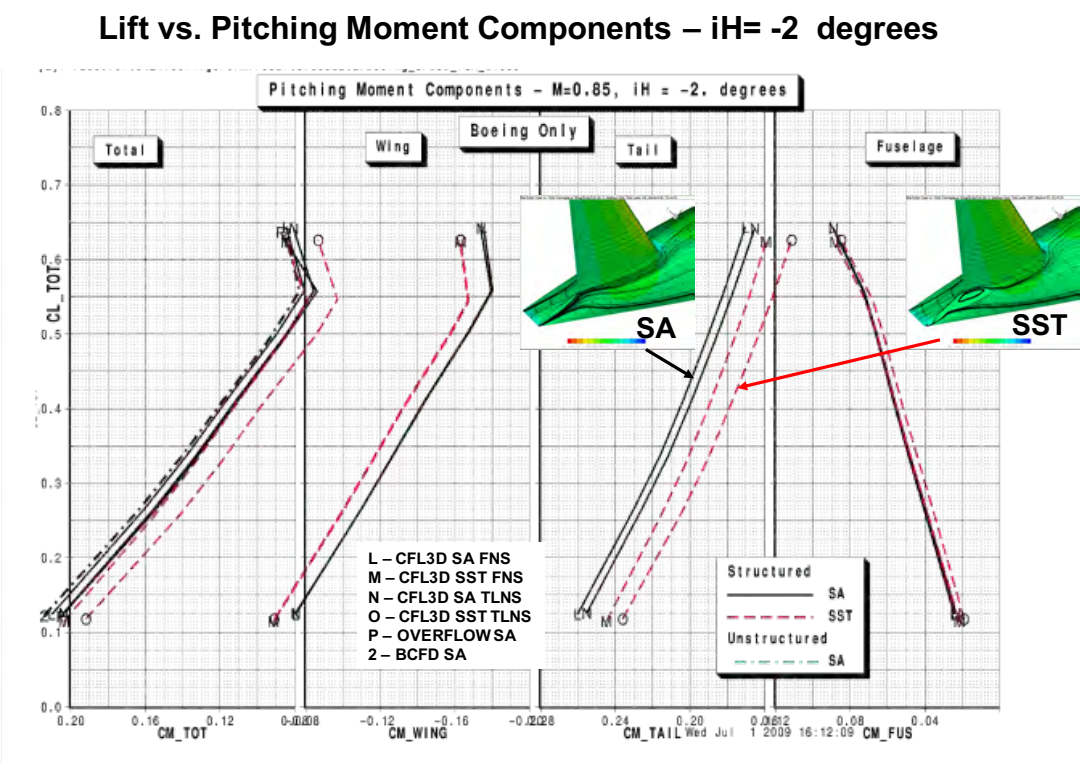


Figure A-F-5. DPW-IV: Pitching Moment Components: Boeing CFL3D Solver, M=0.85; Wing-Body-Tail iH = –2°.

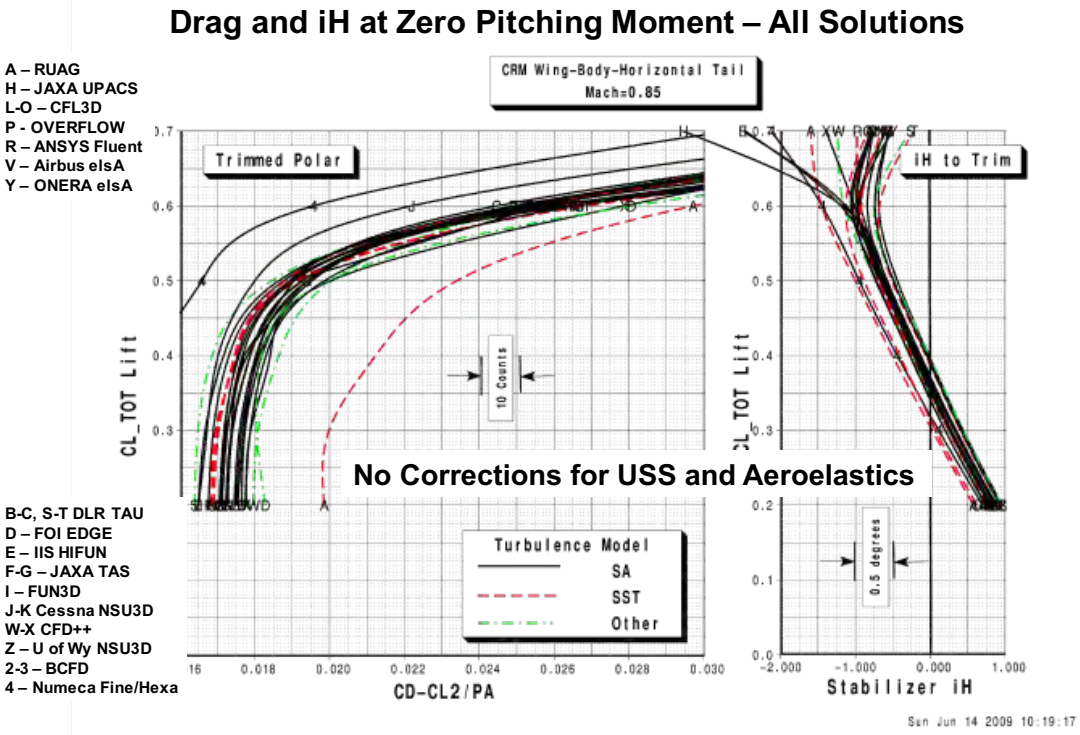


Figure A-F-6. DPW-IV: Trimmed Drag Polars and iH to Trim, M=0.85 (Figure S-XI-4).

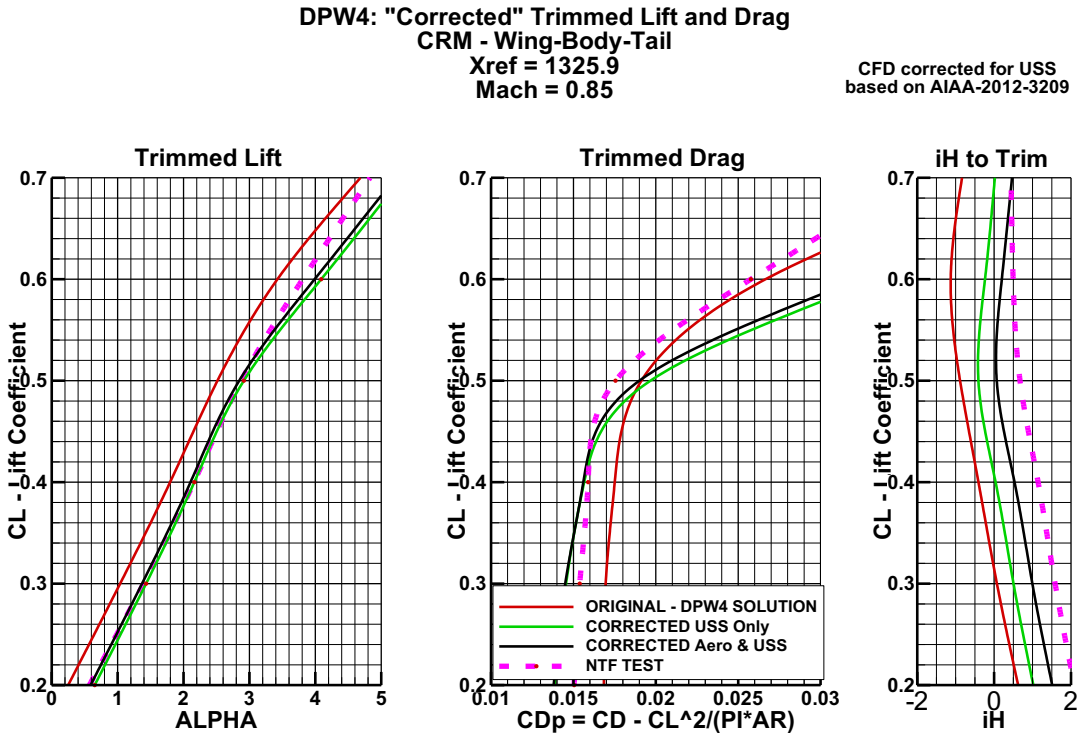


Figure A-F-7. DPW-IV: "Corrected" Trimmed Lift and Drag, M=0.85 (Figure S-XI-6).

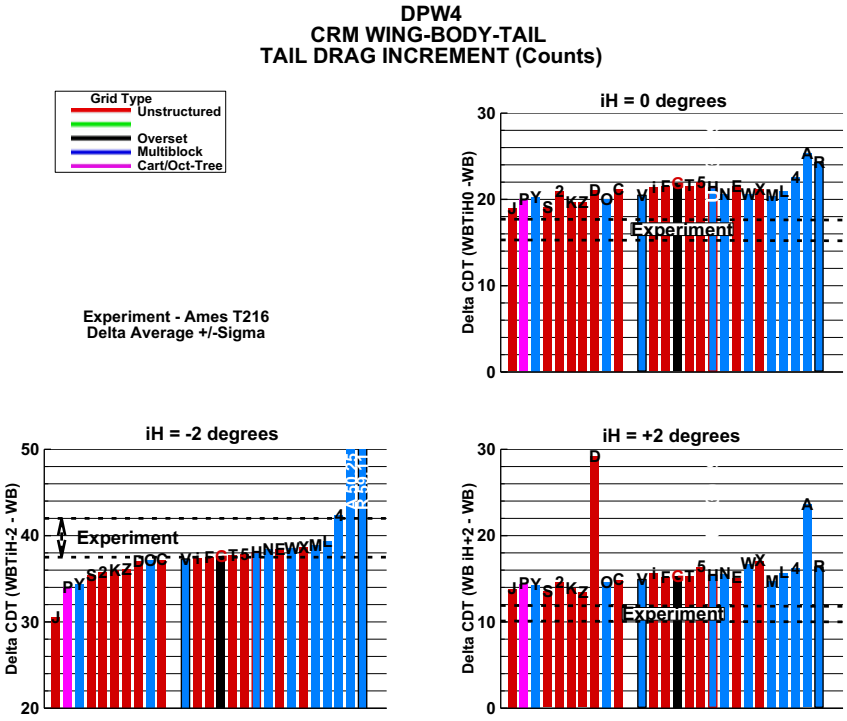


Figure A-F-8. DPW-IV: Tail Drag Increment shown by Grid Type, M=0.85: iH = –2°, 0°, 2°.

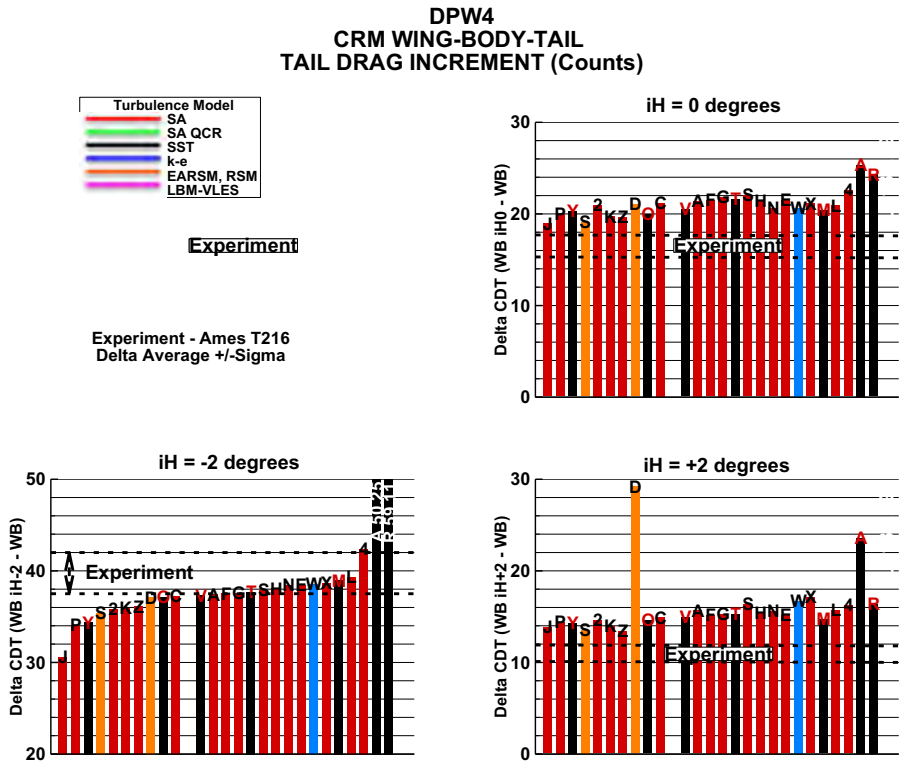


Figure A-F-9. DPW-IV: Tail Drag Increment shown by Turbulence Model, M=0.85: iH = –2°, 0°, 2°.

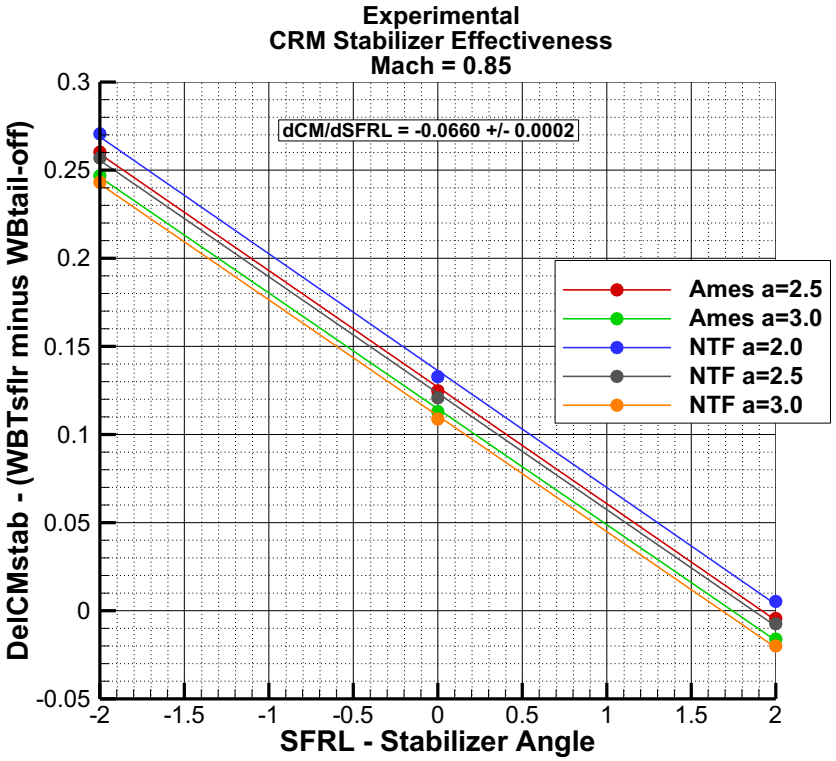


Figure A-F-10. DPW-IV: Experimental Stabilizer Effectiveness with CFD based Corrections for Mounting System USS, M=0.85.

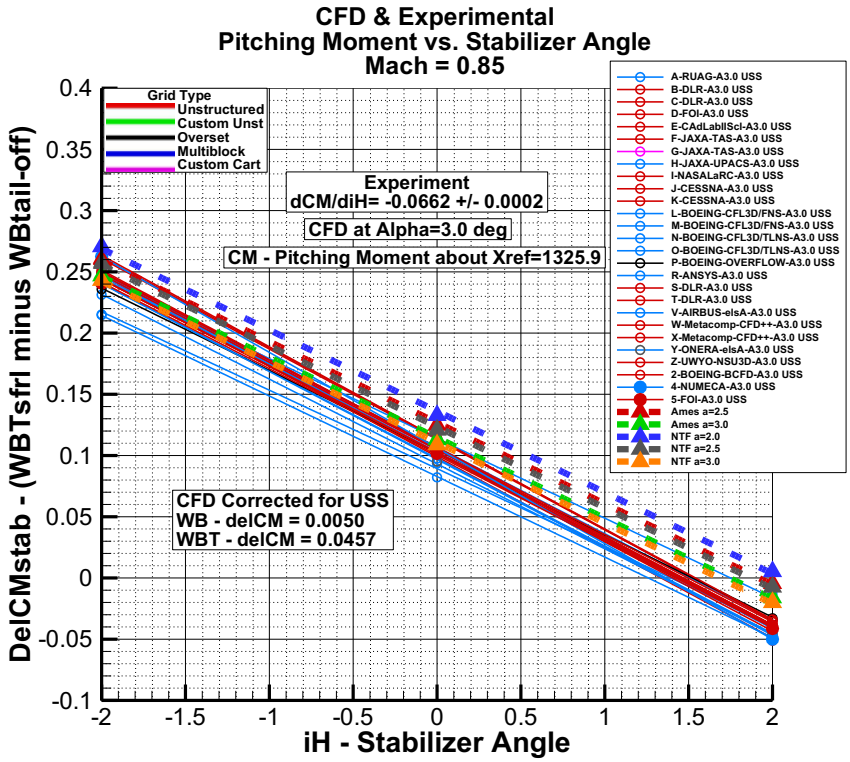


Figure A-F-11. DPW-IV: Experimental Pitching Moment vs. Stabilizer Angle with CFD based Corrections for Mounting System USS Compared to CFD, M=0.85 (Figure S-XI-7).

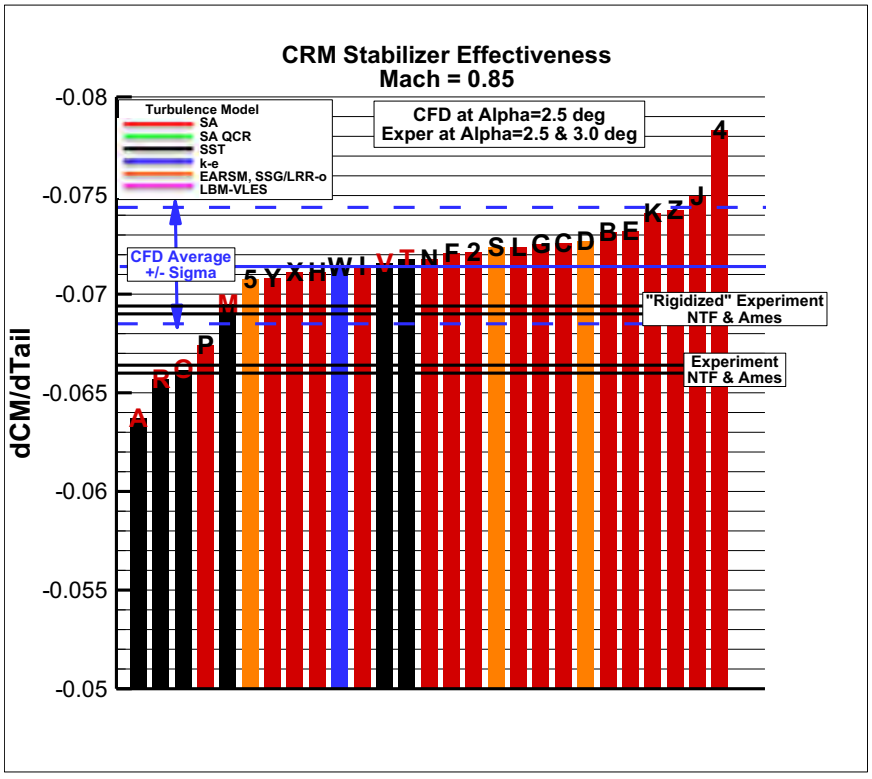


Figure A-F-12. DPW-IV: Corrected and Rigidized Experimental Stabilizer Effectiveness Compared to CFD at AoA = 2.5° shown by Turbulence Model, M=0.85.

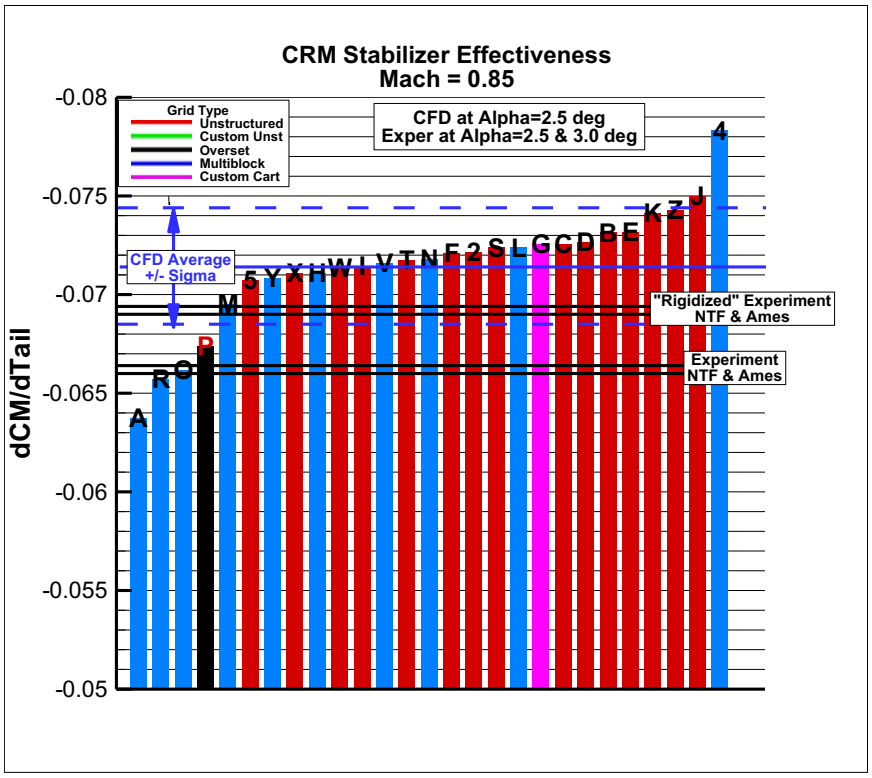


Figure A-F-13. DPW-IV: Corrected and Rigidized Experimental Stabilizer Effectiveness Compared to CFD at AoA = 2.5° shown by Grid Type, M=0.85.

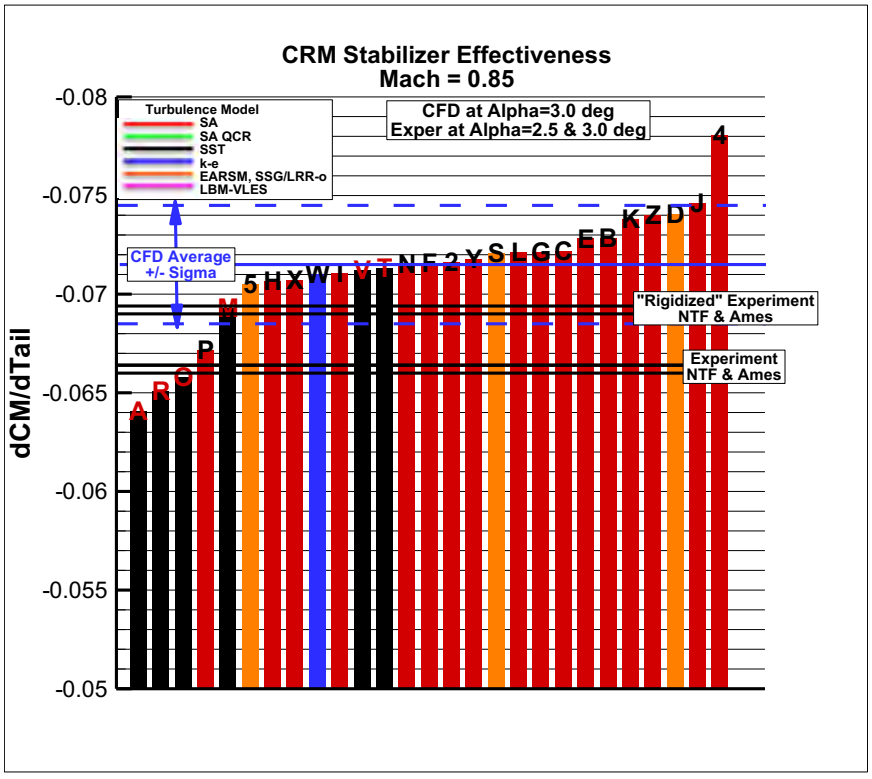


Figure A-F-14. DPW-IV: Corrected and Rigidized Experimental Stabilizer Effectiveness Compared to CFD at AoA = 3.0° shown by Turbulence Model, M=0.85 (Figure S-XI-9).

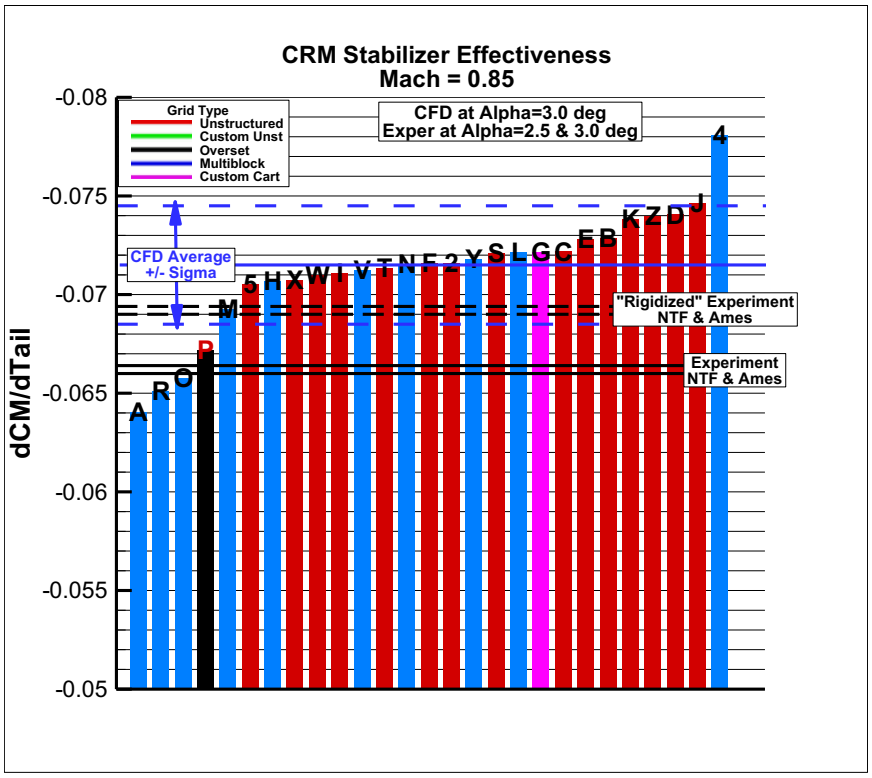


Figure A-F-15. DPW-IV: Corrected and Rigidized Experimental Stabilizer Effectiveness Compared to CFD at AoA = 3.0° shown by Grid Type, M=0.85 (Figure S-XI-8).

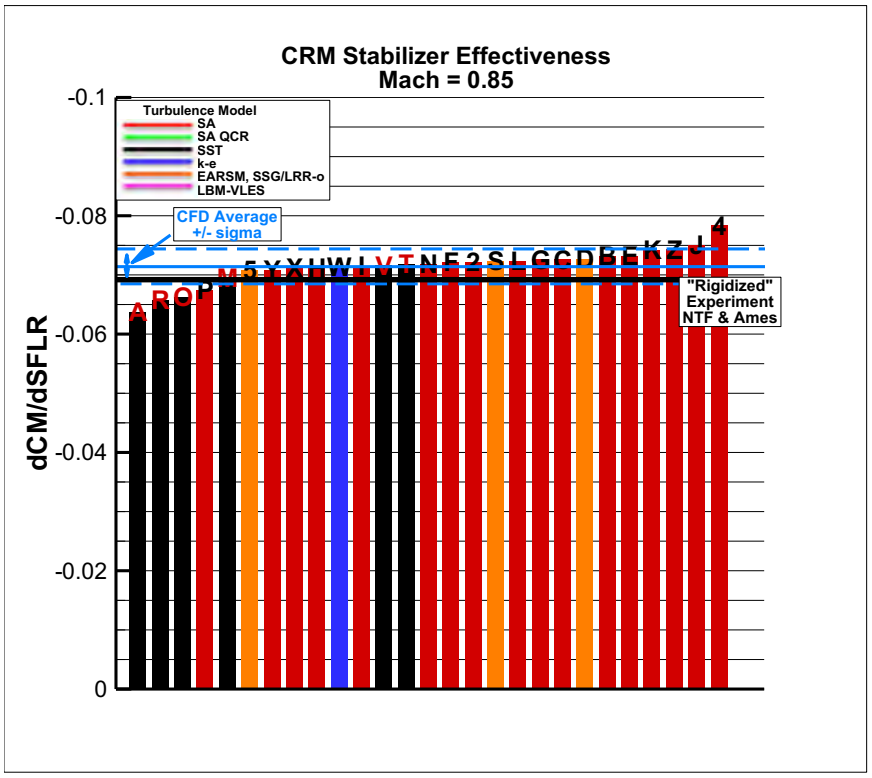


Figure A-F-16. DPW-IV: Corrected and Rigidized Experimental Stabilizer Effectiveness Compared to CFD at AoA = 2.5° shown by Turbulence Model, M=0.85 (Note origin set to zero).

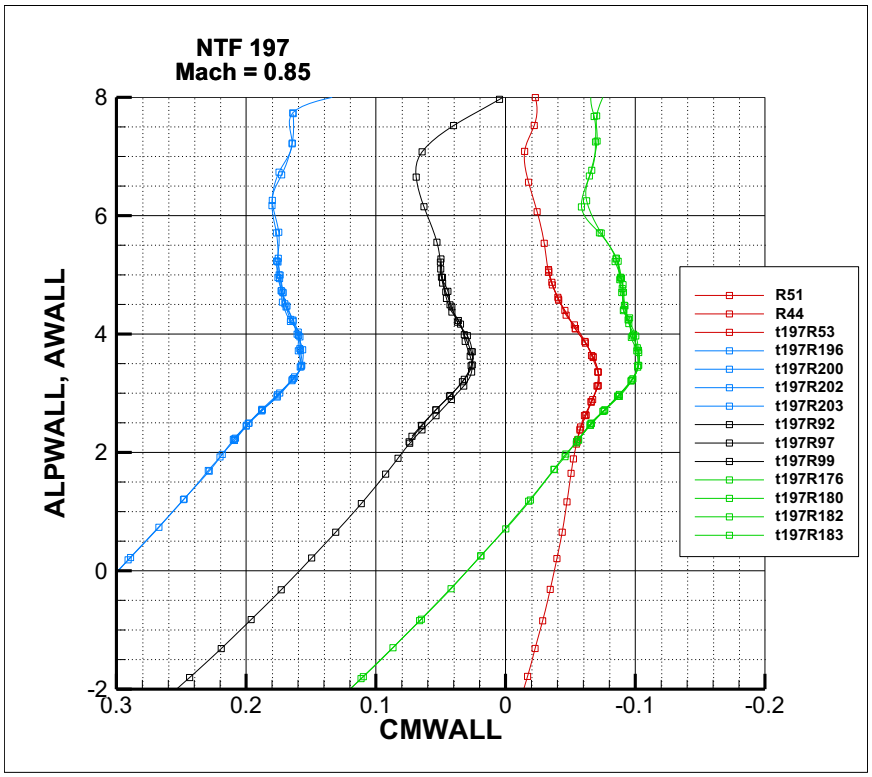


Figure A-F-17. NTF 197 Test Data for Wing-Body and Wing-Body-Tail iH = –2°, 0°, 2°, M = 0.85.

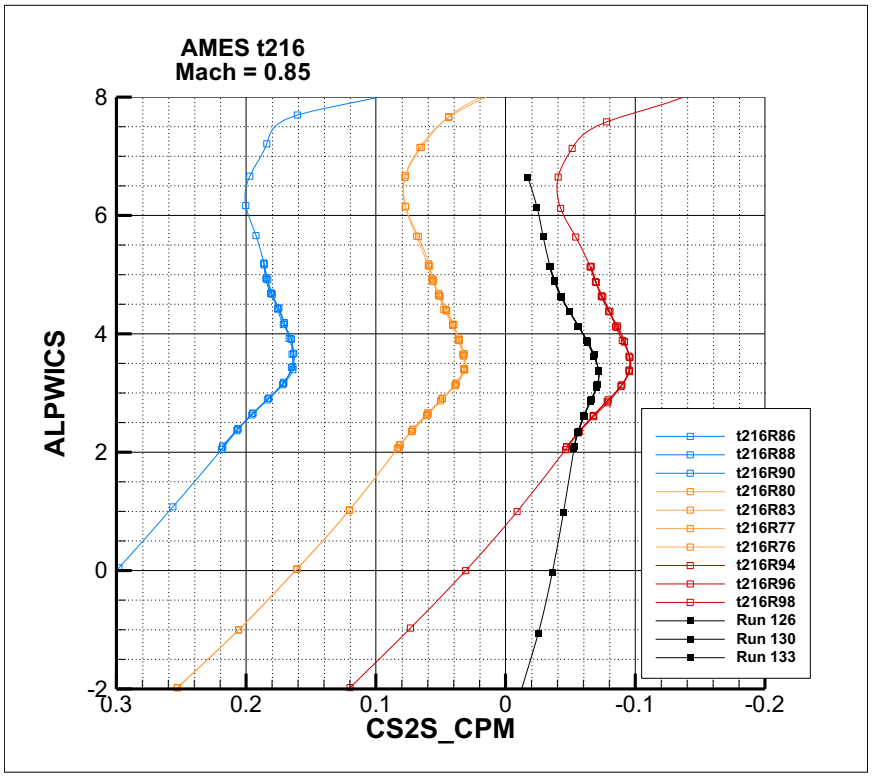


Figure A-F-18. Ames 11-Foot T216 Test Data for Wing-Body and Wing-Body-Tail iH = –2°, 0°, 2°, M = 0.85.

Appendix G. CFD Wing Pressure Distributions

Wing pressure distributions are presented in this appendix. This appendix contains plots from Sections VII, X, and XV. The participant data-set key for each Workshop is found in Appendix C. Only a limited number of solutions are shown for DPW-IV and DPW-V. These geometries were for the "as-built" zero wind shape and are not representative of the model under load at wind tunnel conditions. As such, those detailed pressure distribution comparisons are of limited value.

G-A DPW-VI Comparisons

Figures A-G-25 to -28: Matched "Selected" Solutions are those that matched experimental lift and pitching moment trends

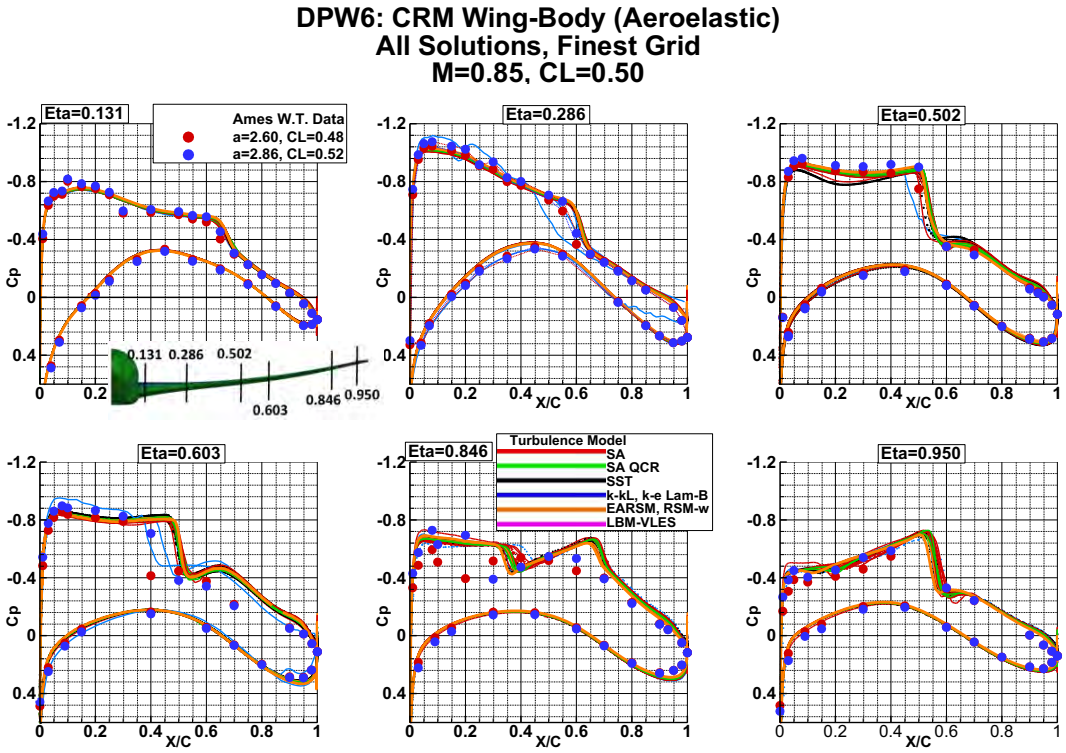


Figure A-G-1. DPW-VI: Wing Pressure Distribution; All Solutions; Finest Grid, C_L = 0.50, M = 0.85.

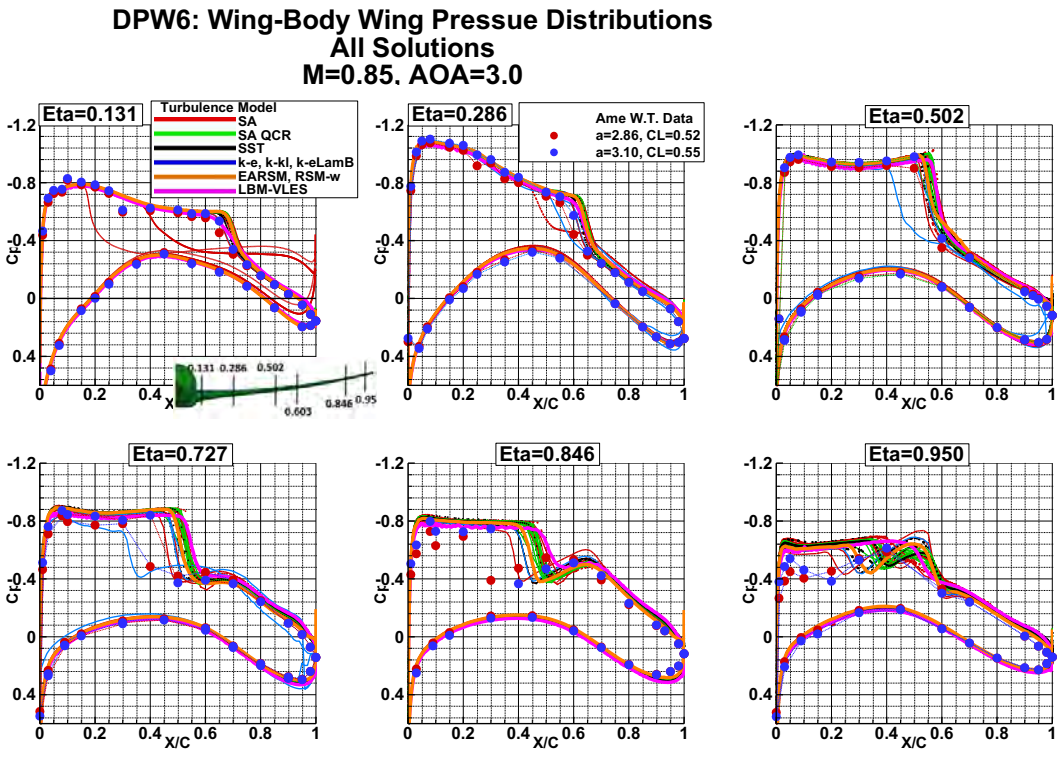


Figure A-G-2. DPW-VI: Wing Pressure Distribution; All Solutions, AoA = 3.0°, M = 0.85.

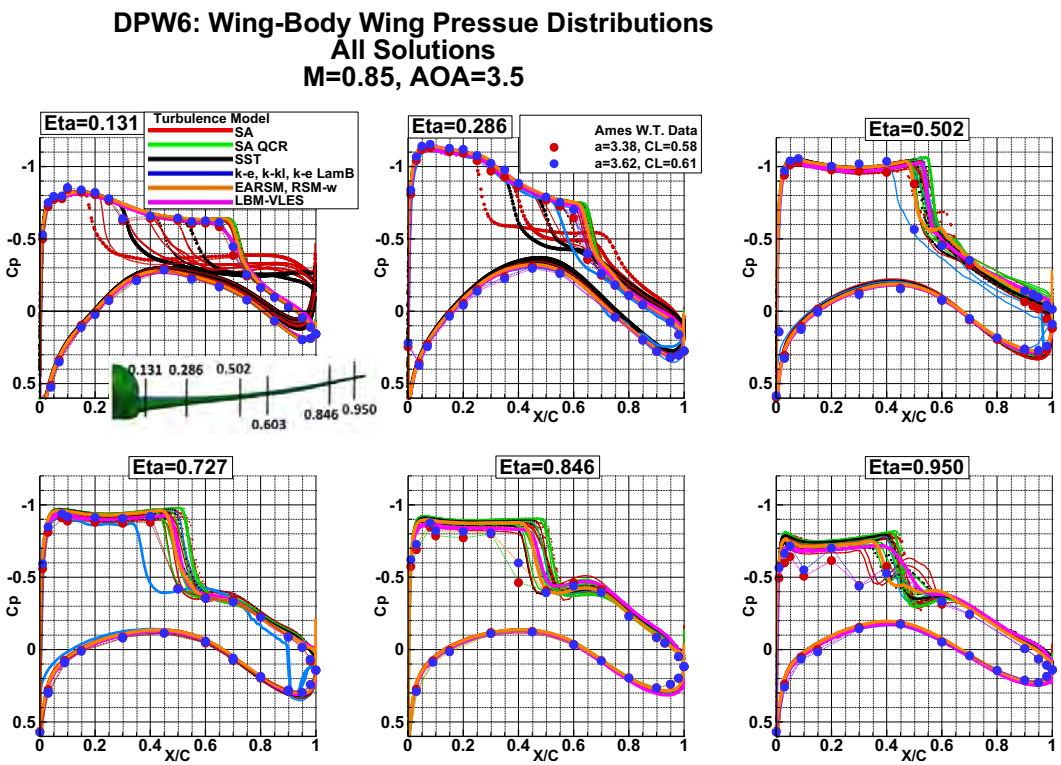


Figure A-G-3. DPW-VI: Wing Pressure Distribution; All Solutions, AoA = 3.5°, M = 0.85.

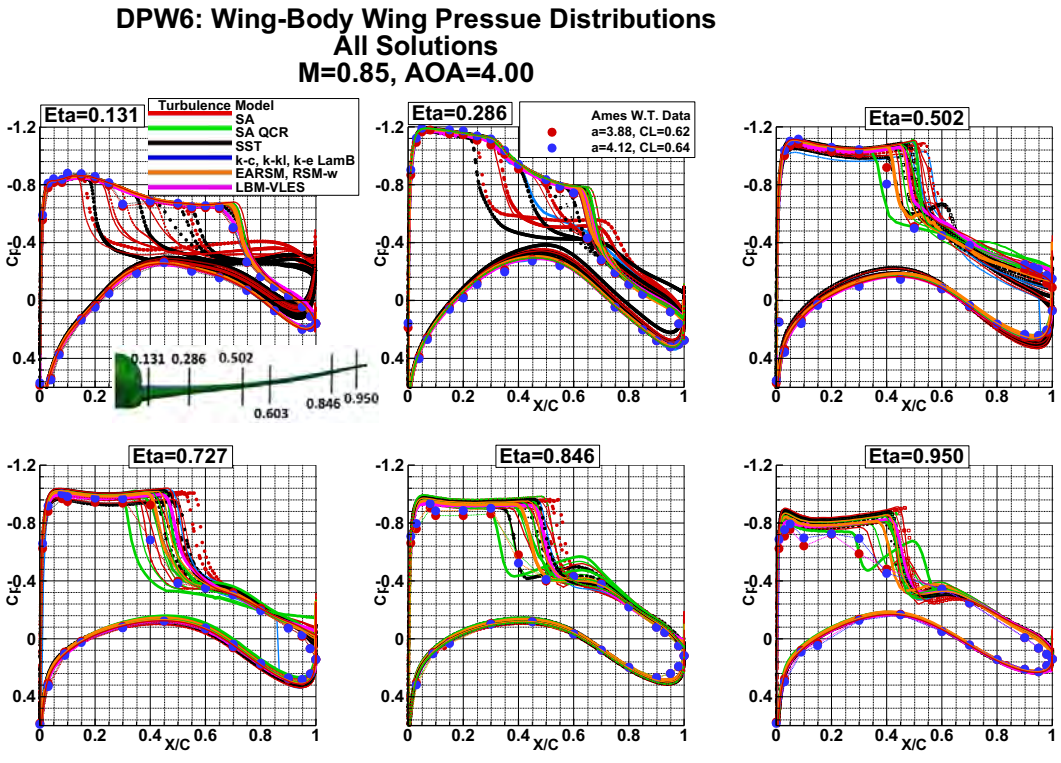


Figure A-G-4. DPW-VI: Wing Pressure Distribution; All Solutions, AoA = 4.0°, M = 0.85.

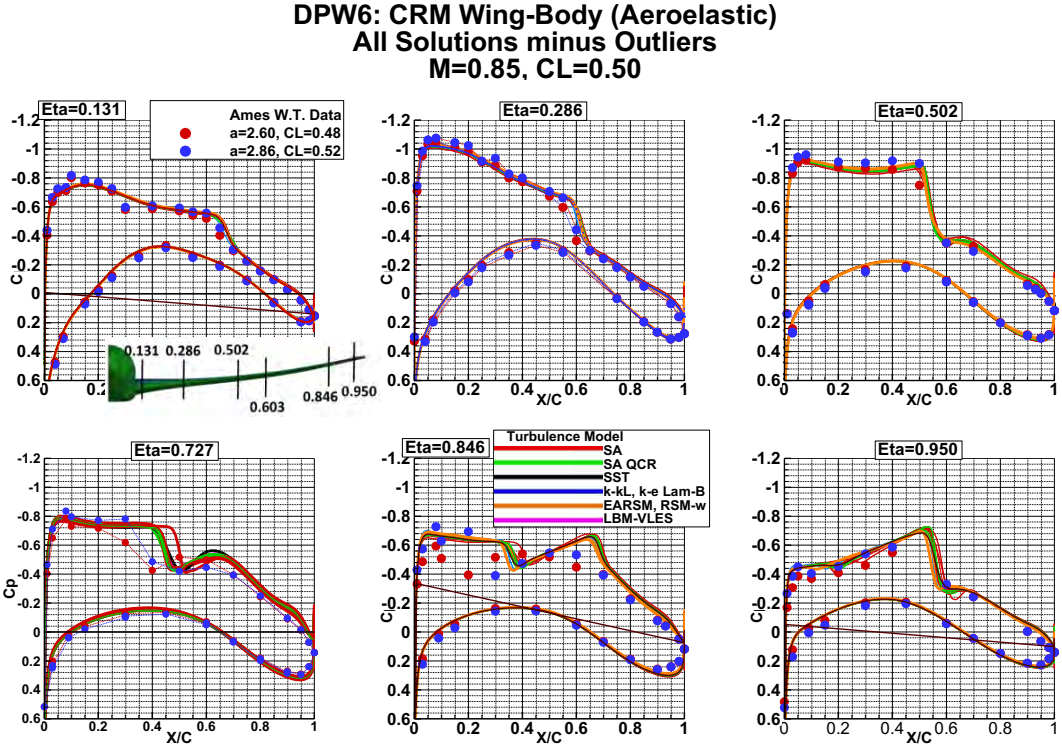


Figure A-G-5. DPW-VI: Wing Pressure Distribution; All Solutions minus Outliers, C_L = 0.50, M = 0.85.

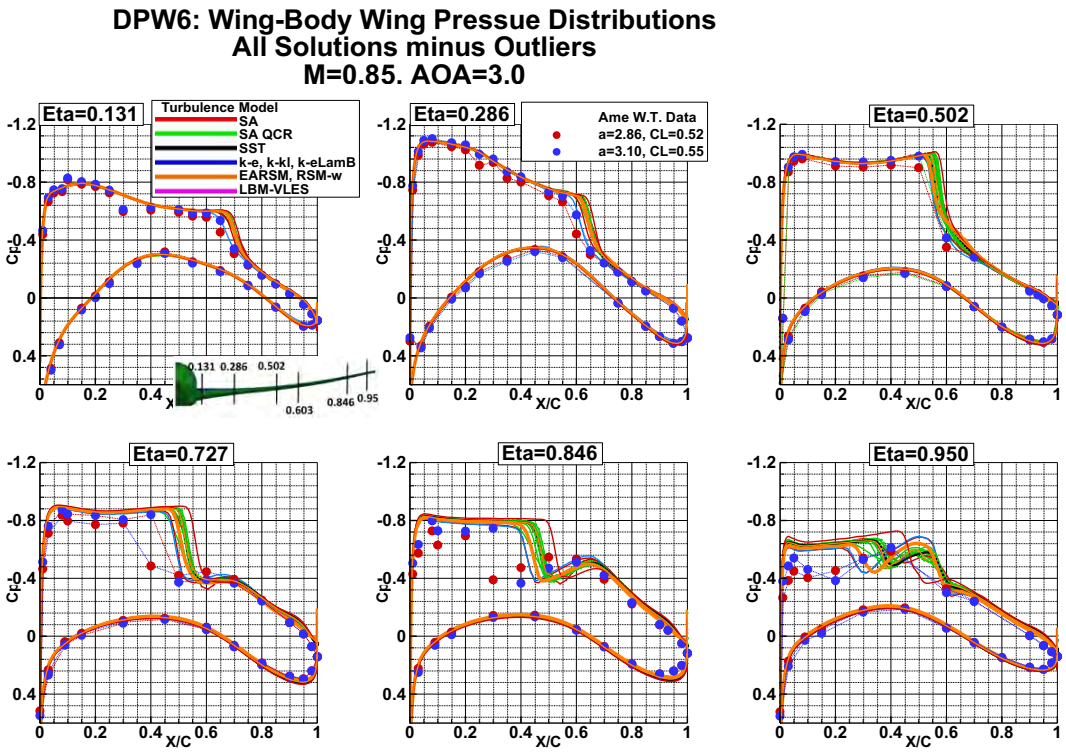


Figure A-G-6. DPW-VI: Wing Pressure Distribution; All Solutions minus Outliers, AoA = 3.0°, M = 0.85.

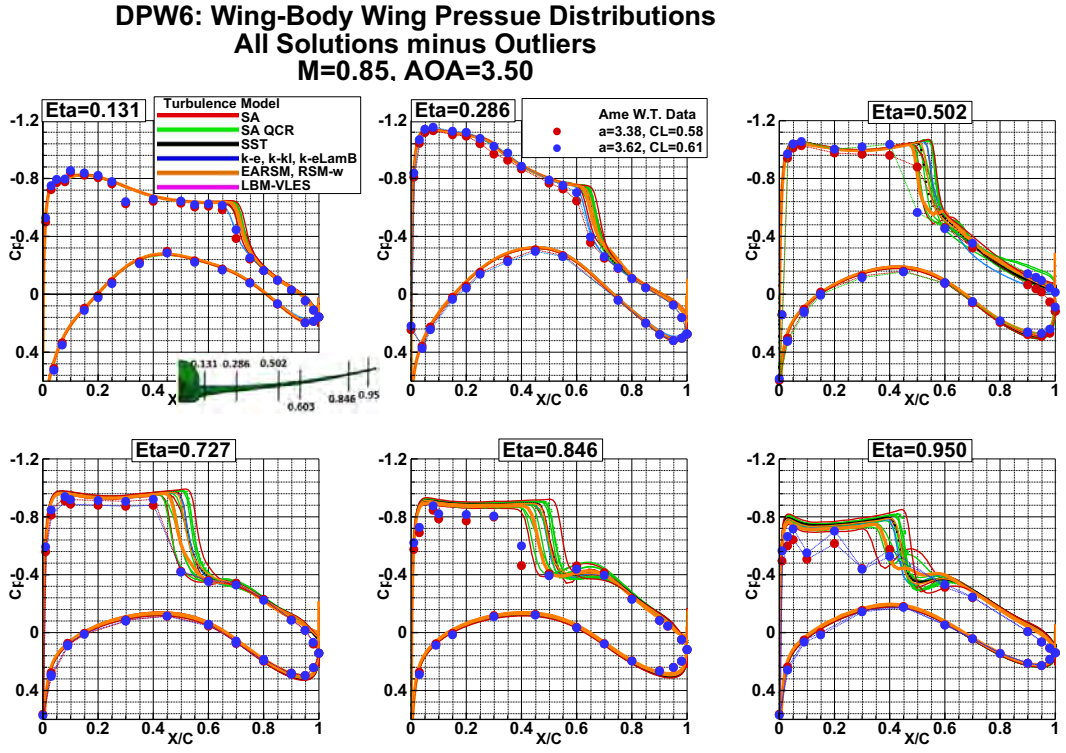


Figure A-G-7. DPW-VI: Wing Pressure Distribution; All Solutions minus Outliers, AoA = 3.5°, M = 0.85.

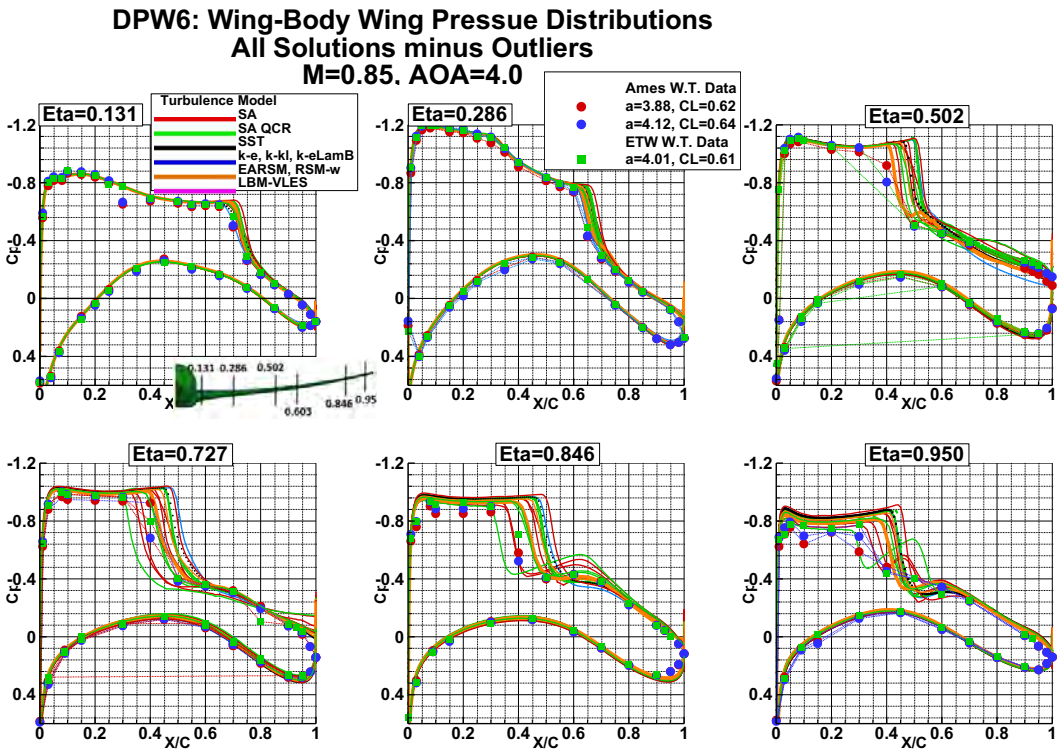


Figure A-G-8. DPW-VI: Wing Pressure Distribution; All Solutions minus Outliers, AoA = 4.0°, M = 0.85.

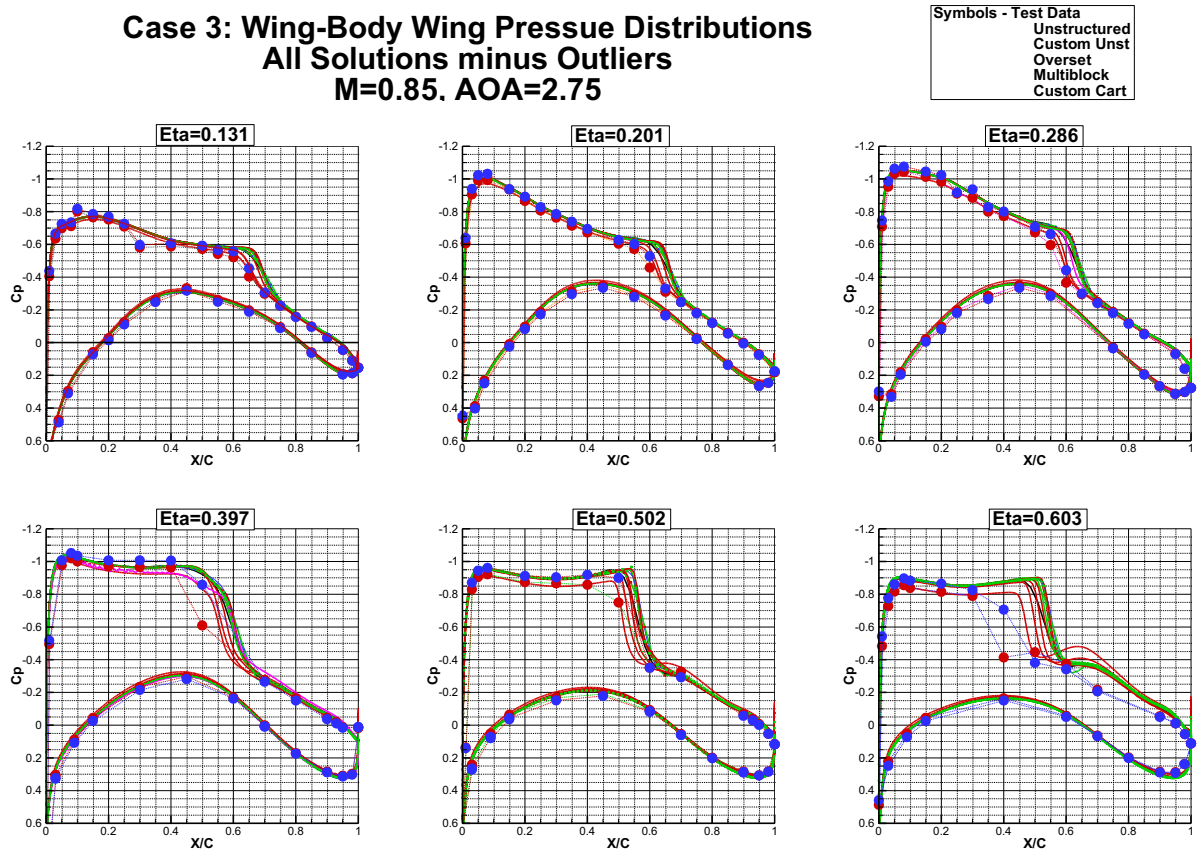


Figure A-G-9. DPW-VI: Wing Pressure Distribution; All Solutions minus Outliers, AoA = 2.75°, M = 0.85, Eta = 0.131 to 0.603.

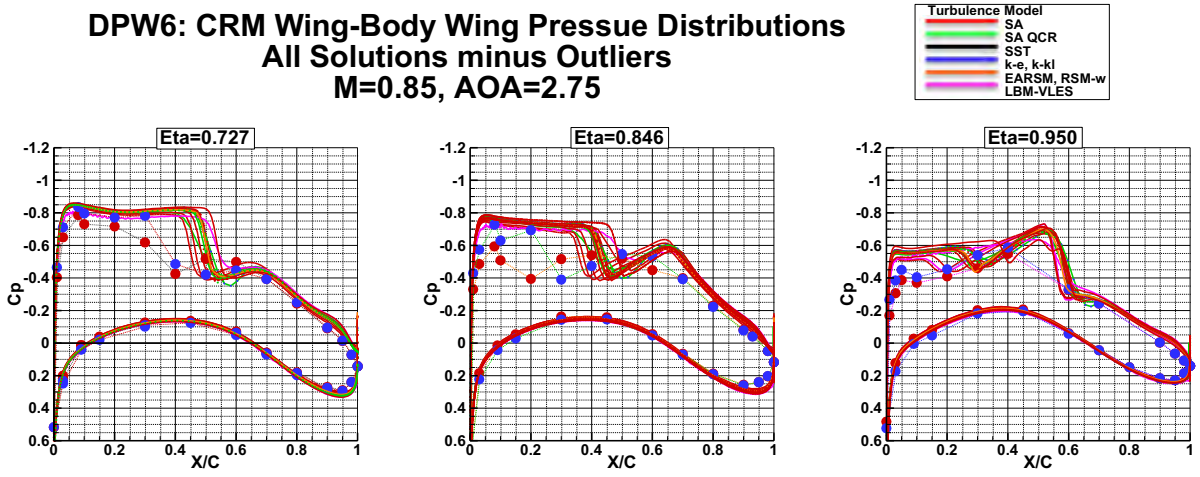


Figure A-G-10. DPW-VI: Wing Pressure Distribution; All Solutions minus Outliers, AoA = 2.75°, M = 0.85, Eta = 0.727 to 0.950.

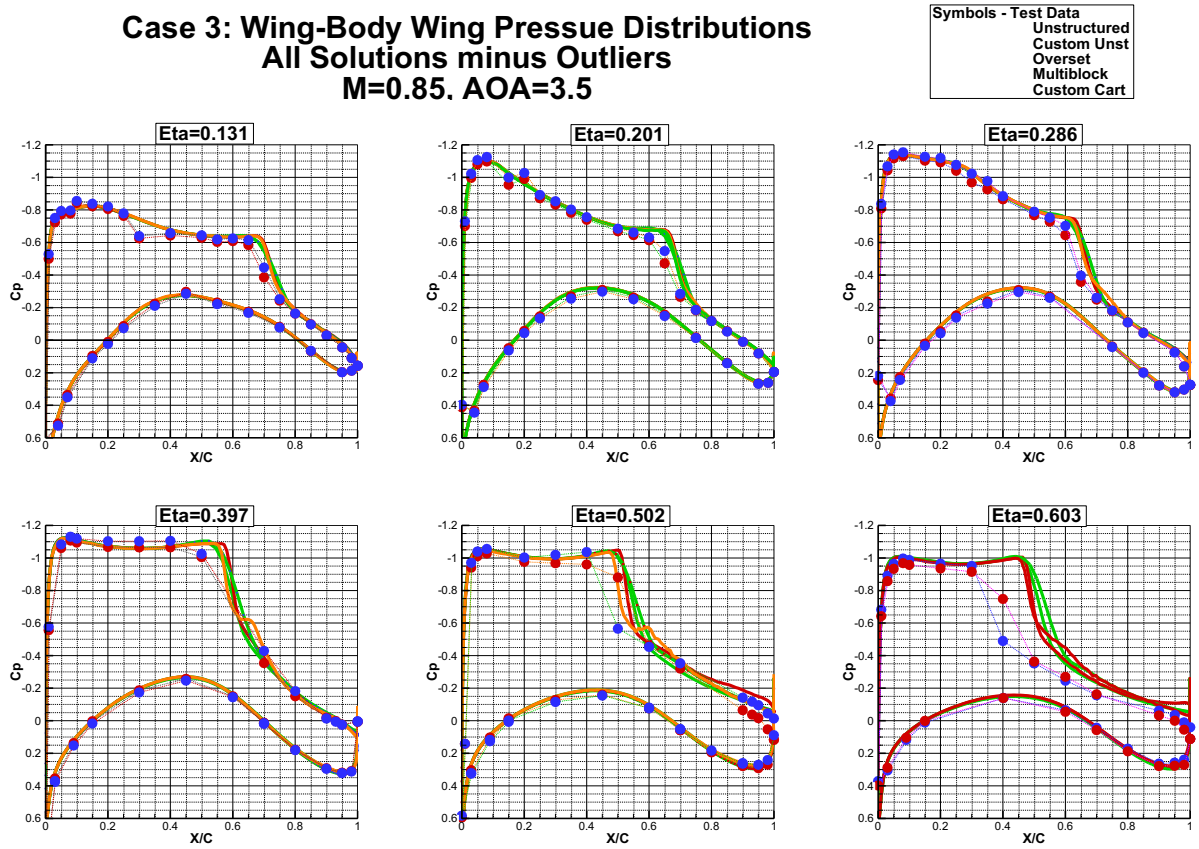


Figure A-G-11. DPW-VI: Wing Pressure Distribution; All Solutions minus Outliers, AoA = 3.50°, M = 0.85, Eta = 0.131 to 0.603.

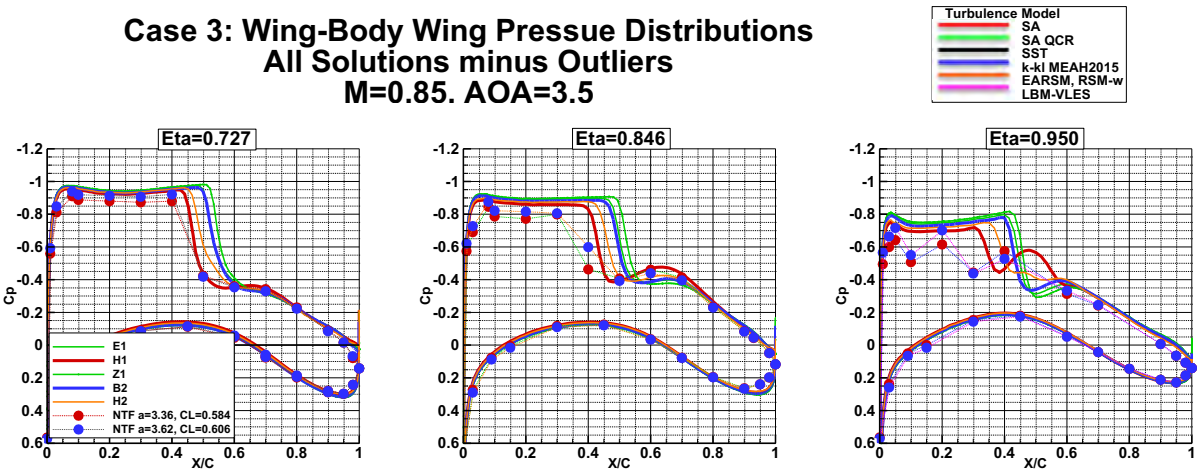


Figure A-G-12. DPW-VI: Wing Pressure Distribution; All Solutions minus Outliers, AoA = 3.50°, M = 0.85, Eta = 0.727 to 0.950.

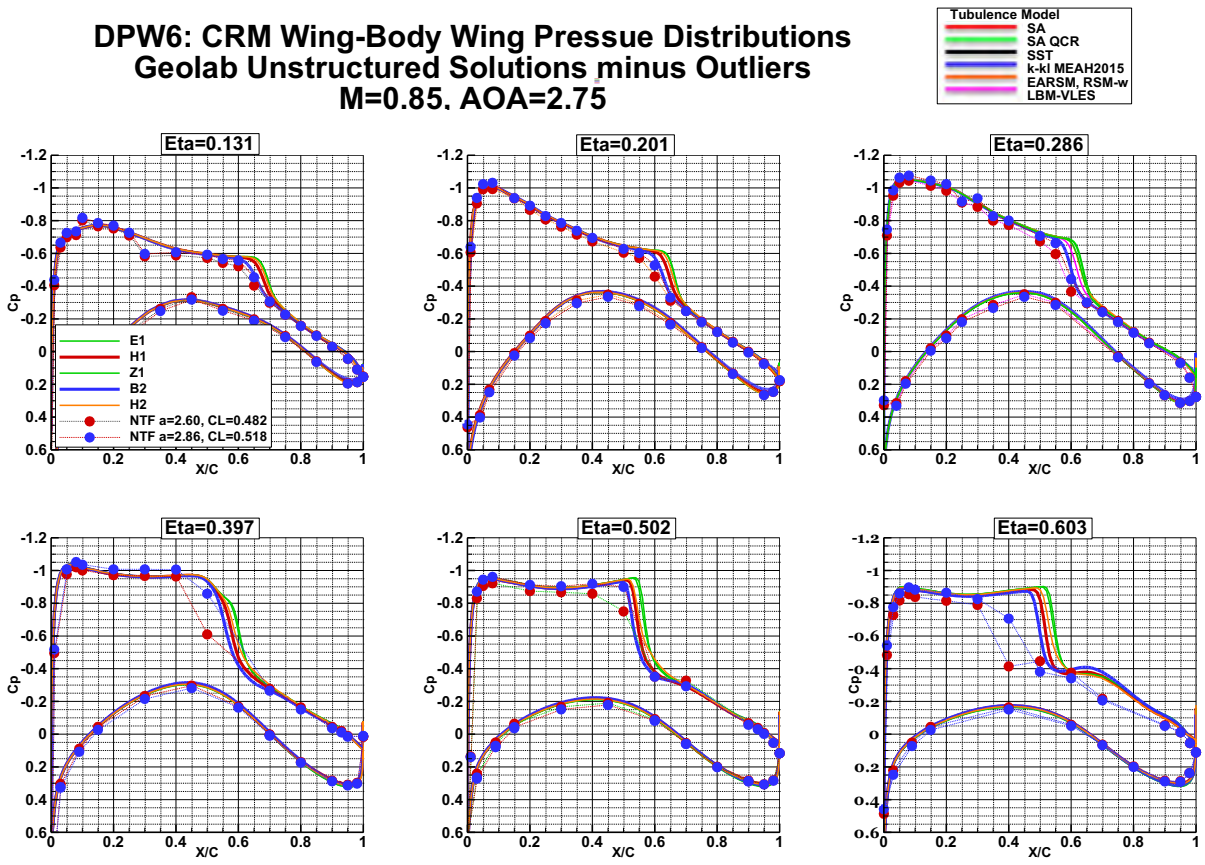


Figure A-G-13. DPW-VI: Wing Pressure Distribution; Geolab Unstructured Grid Solutions minus Outliers, AoA = 2.75°, M = 0.85, Eta = 0.131 to 0.603.

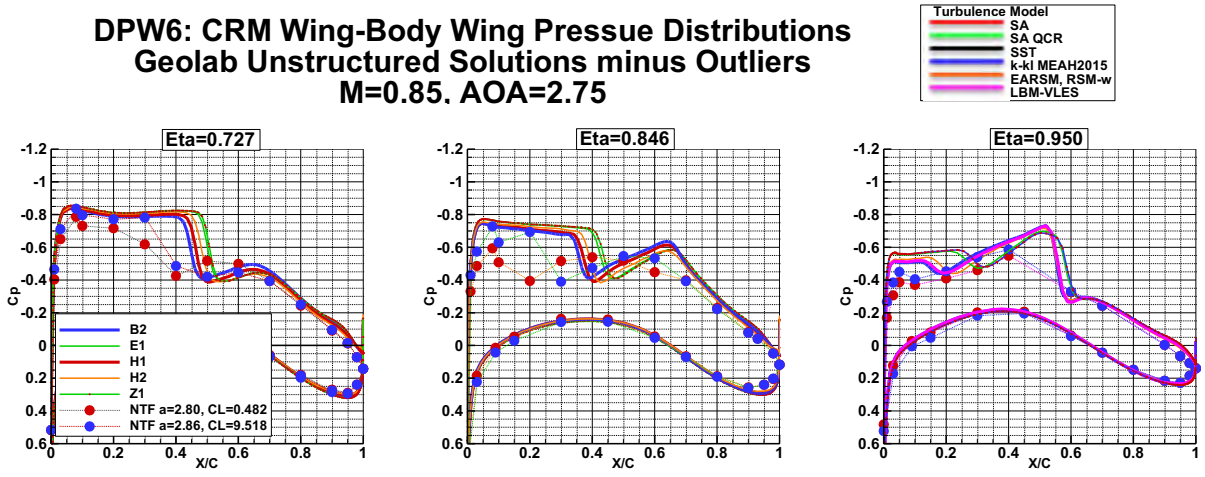


Figure A-G-14. DPW-VI: Wing Pressure Distribution; Geolab Unstructured Grid Solutions minus Outliers, AoA = 2.75°, M = 0.85, Eta = 0.727 to 0.950.

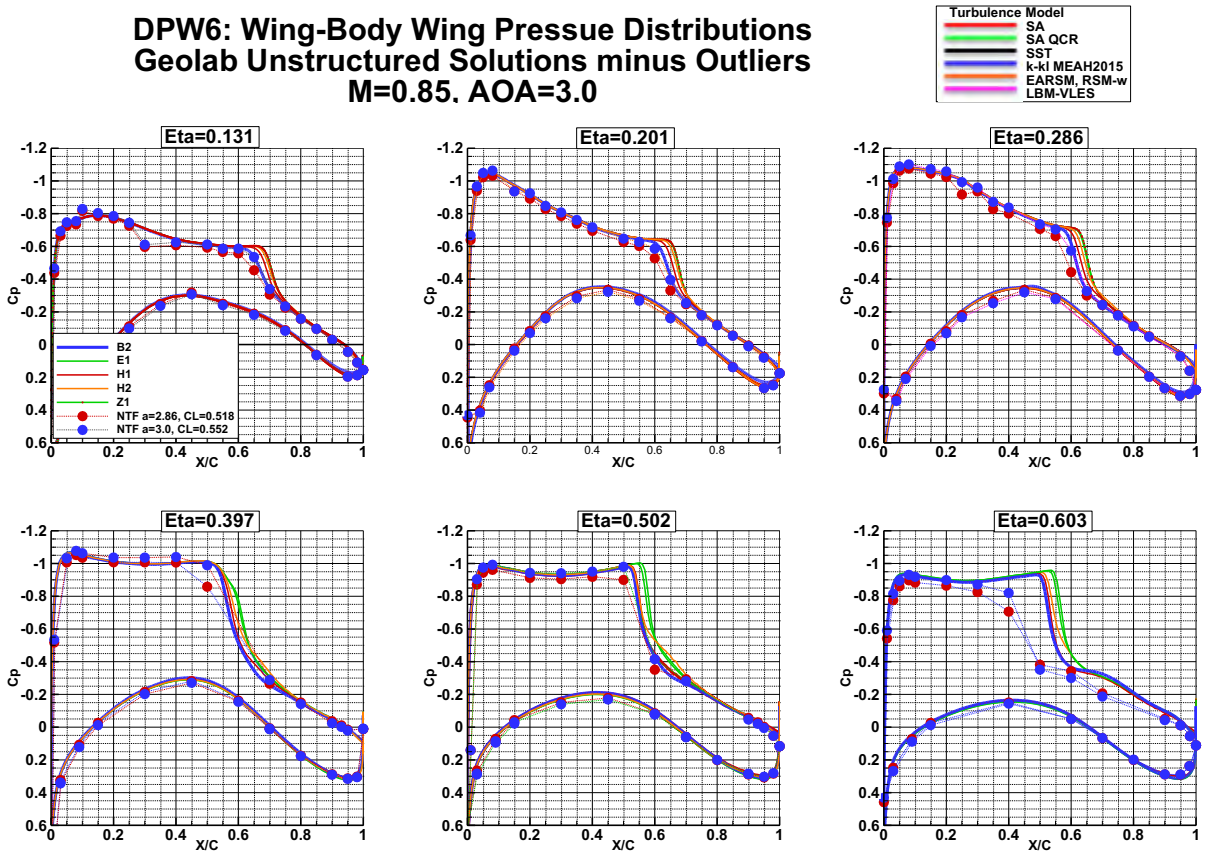


Figure A-G-15. DPW-VI: Wing Pressure Distribution; Geolab Unstructured Grid Solution minus Outliers, AoA = 3.0°, M = 0.85, Eta = 0.131 to 0.603.

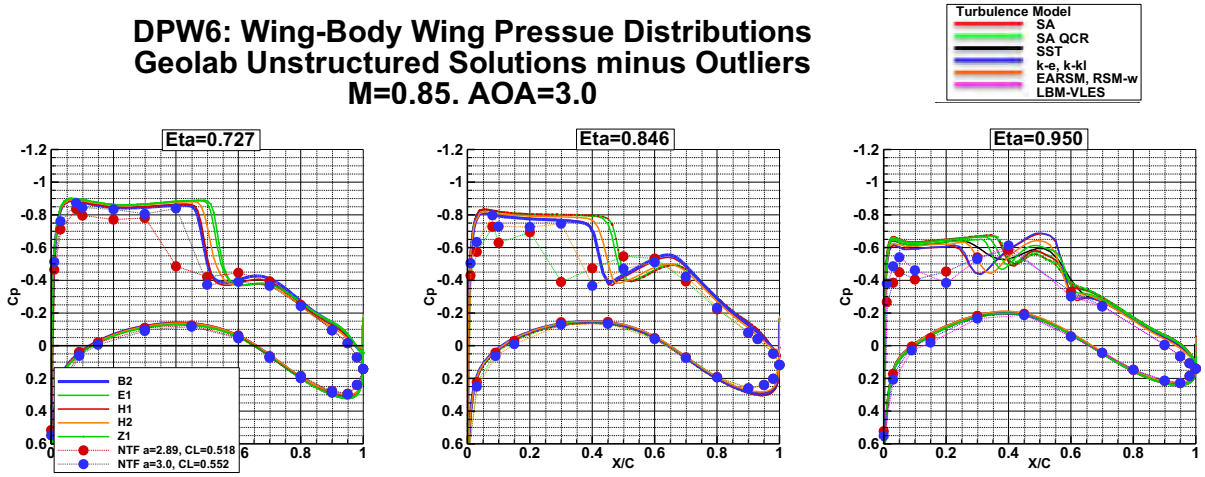


Figure A-G-16 DPW-VI: Wing Pressure Distribution; Geolab Unstructured Grid Solutions minus Outliers, AoA = 3.0°, M = 0.85, Eta = 0.727 to 0.950.

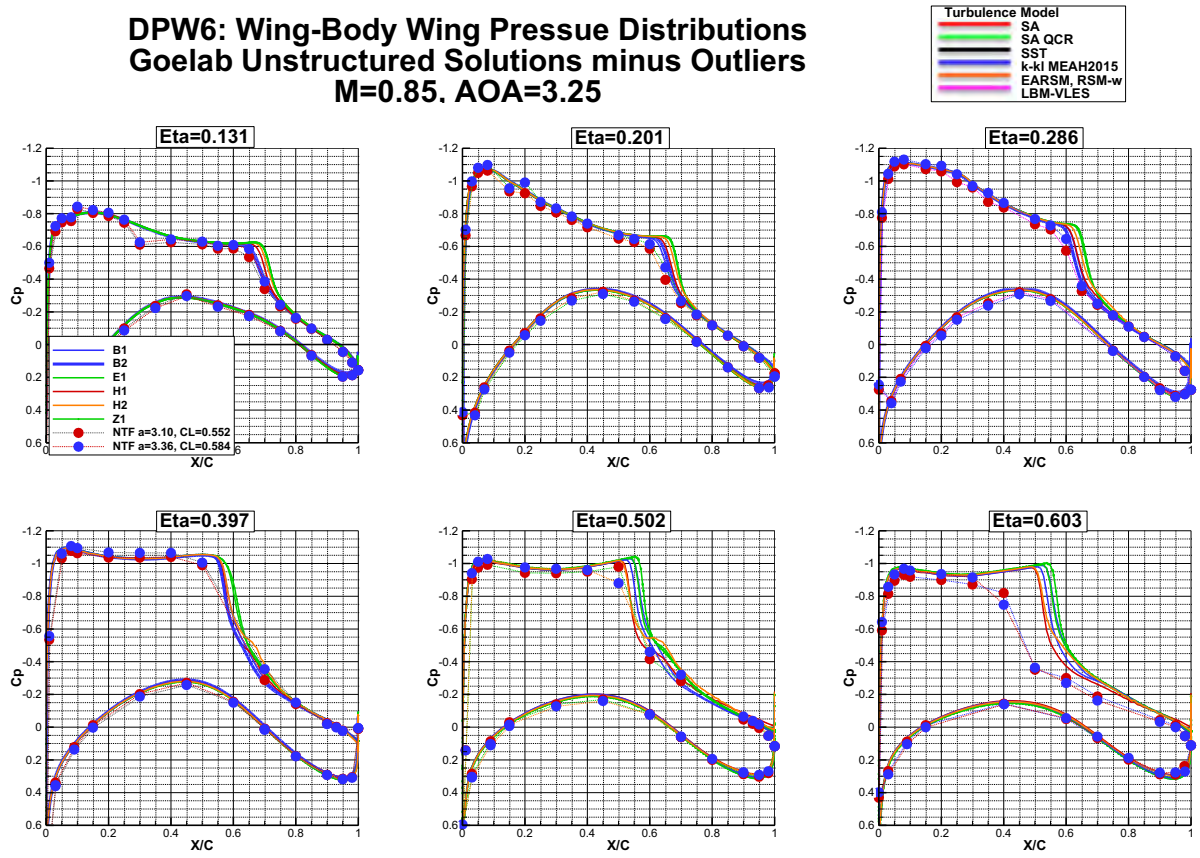


Figure A-G-17. DPW-VI: Wing Pressure Distribution; Geolab Unstructured Grid Solutions minus Outliers, AoA = 3.25°, M = 0.85, Eta = 0.131 to 0.603.

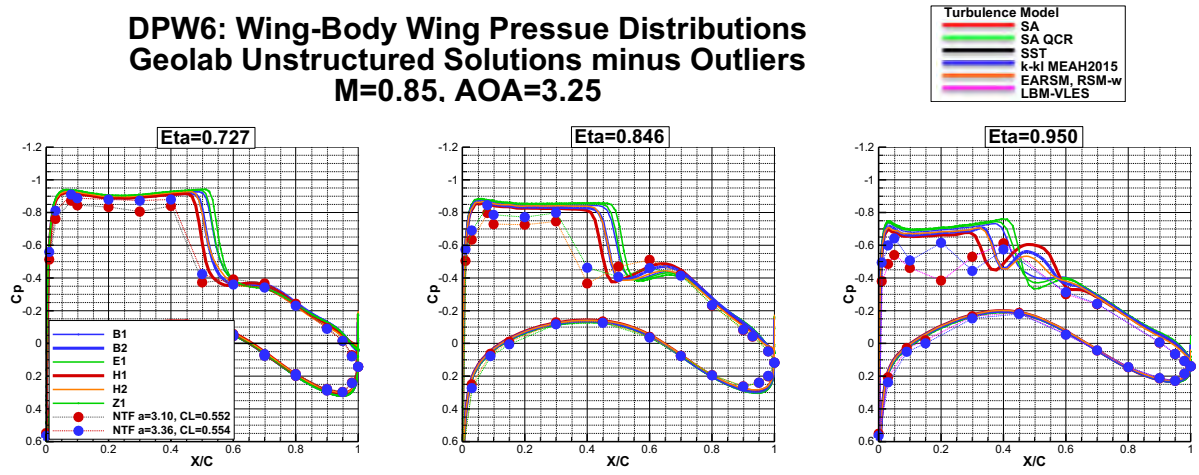


Figure A-G-18. DPW-VI: Wing Pressure Distribution; Geolab Unstructured Grid Solutions minus Outliers, AoA = 3.25°, M = 0.85, Eta = 0.727 to 0.950.

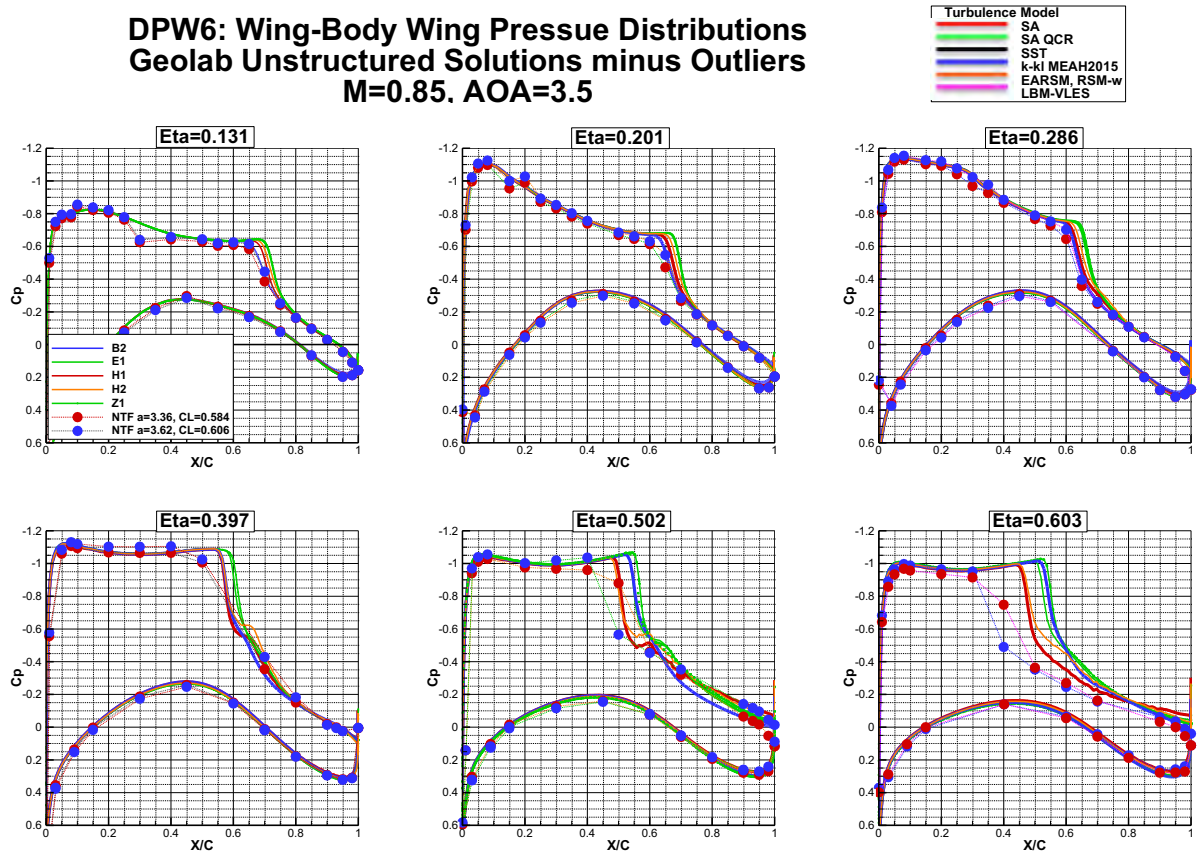


Figure A-G-19. DPW-VI: Wing Pressure Distribution; Geolab Unstructured Grid Solutions minus Outliers, AoA = 3.50°, M = 0.85, Eta = 0.131 to 0.603.

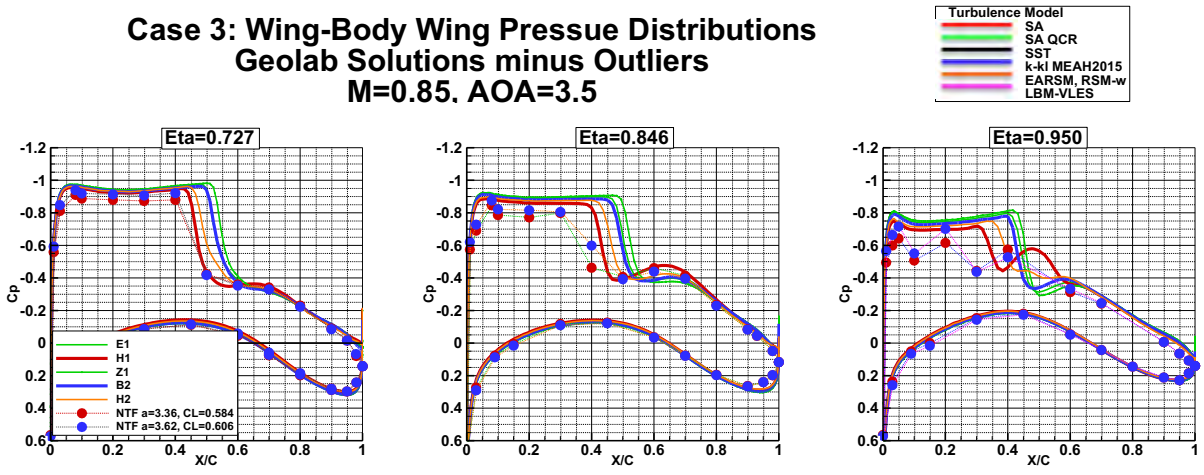


Figure A-G-20. DPW-VI: Wing Pressure Distribution; Geolab Unstructured Grid Solutions minus Outliers, AoA = 3.50°, M = 0.85, Eta = 0.727 to 0.950.

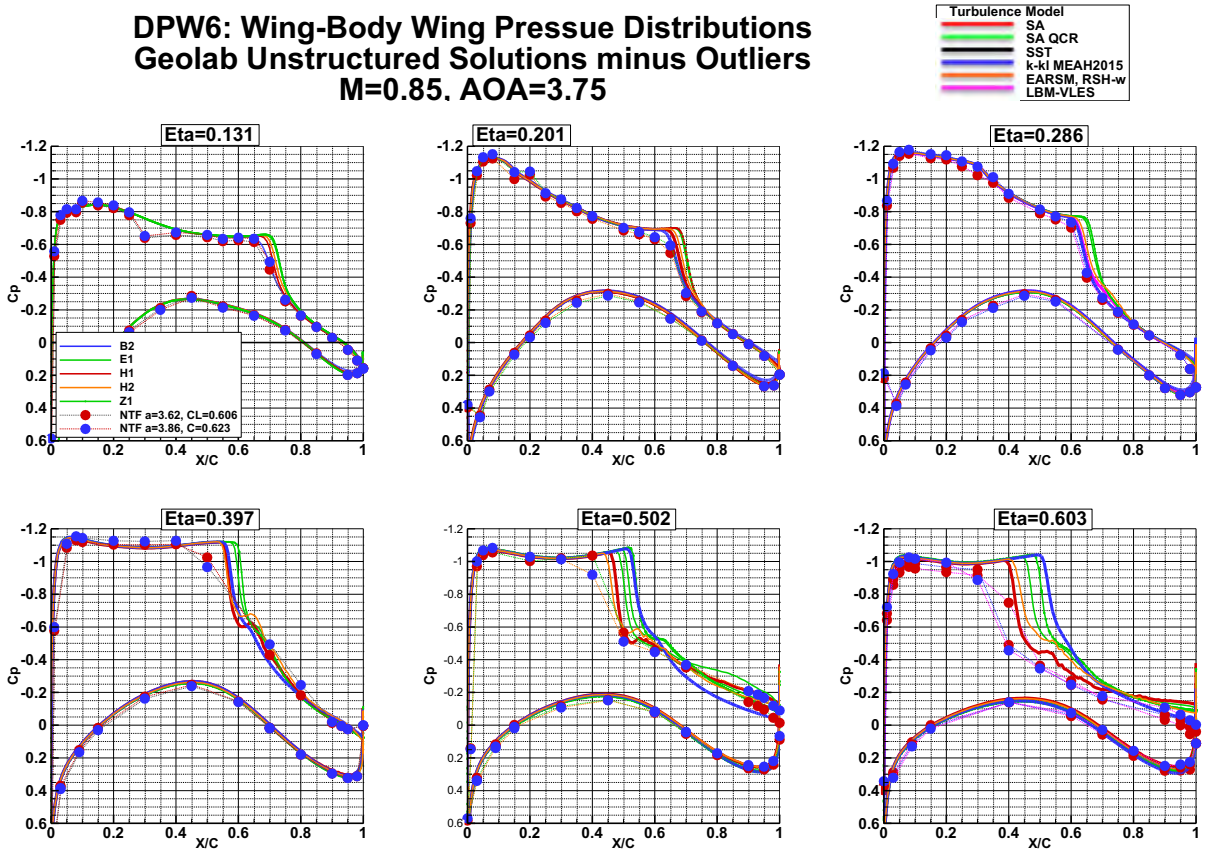


Figure A-G-21. DPW-VI: Wing Pressure Distribution; Geolab Unstructured Grid Solution minus Outliers, AoA = 3.75°, M = 0.85, Eta = 0.131 to 0.603.

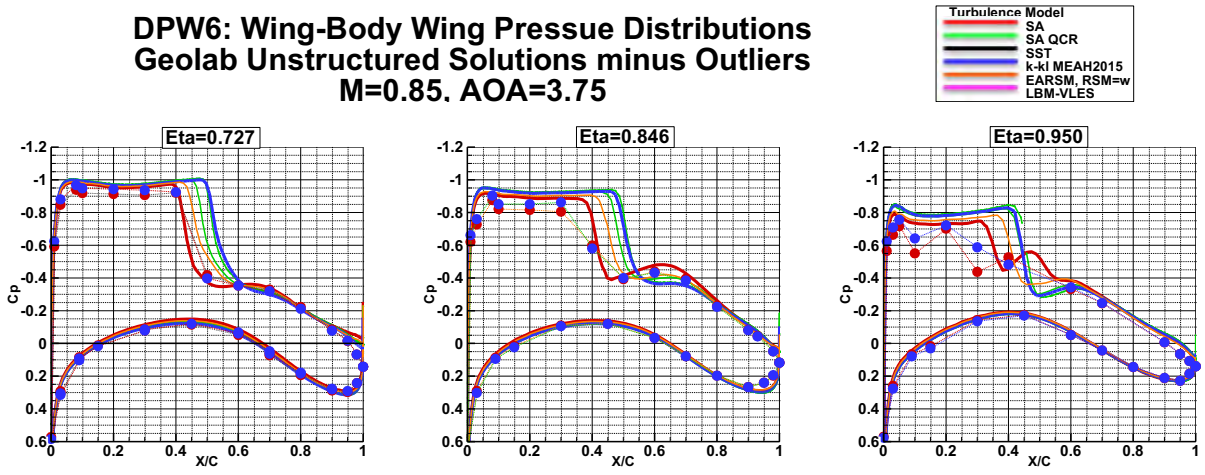


Figure A-G-22. DPW-VI: Wing Pressure Distribution; Geolab Unstructured Grid Solutions minus Outliers, AoA = 3.75°, M = 0.85, Eta = 0.727 to 0.950.

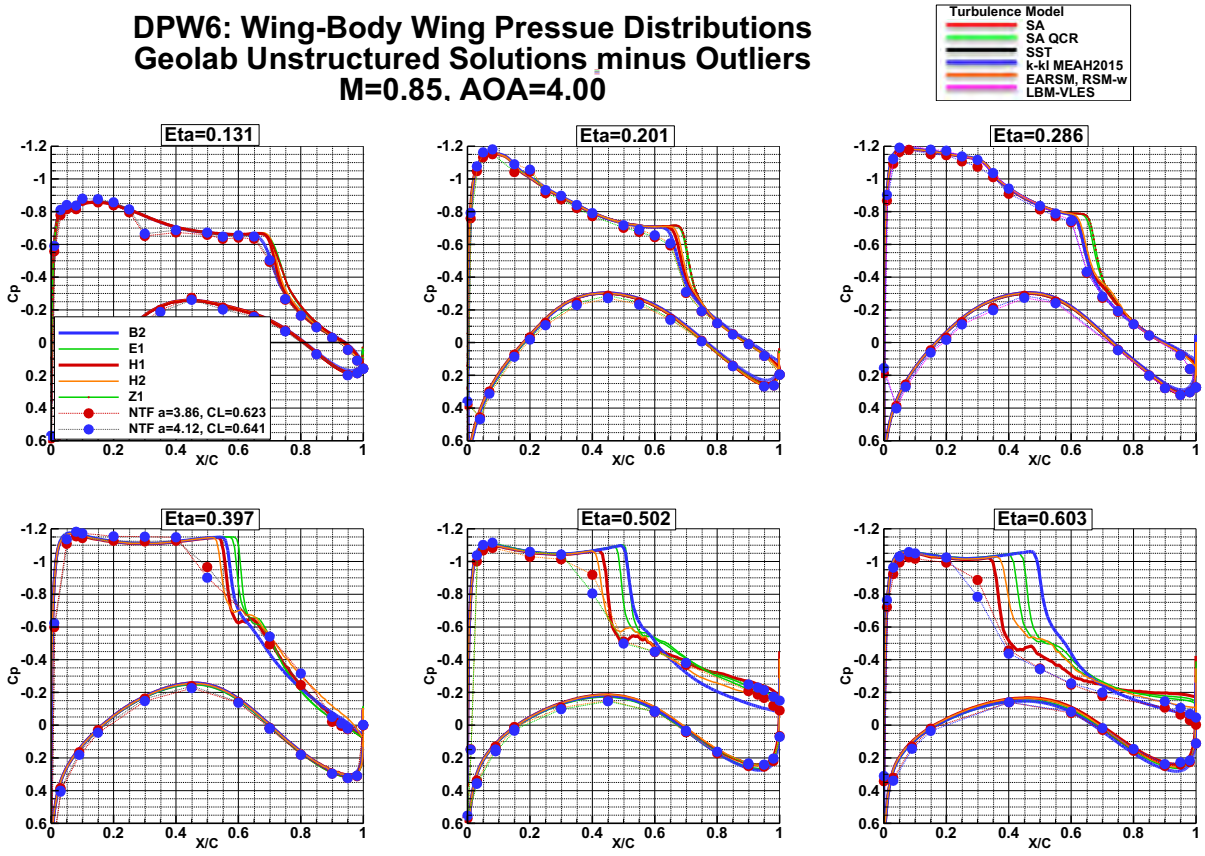


Figure A-G-23. DPW-VI: Wing Pressure Distribution; Geolab Unstructured Grid Solutions minus Outliers, AoA = 4.0°, M = 0.85, Eta = 0.131 to 0.603.

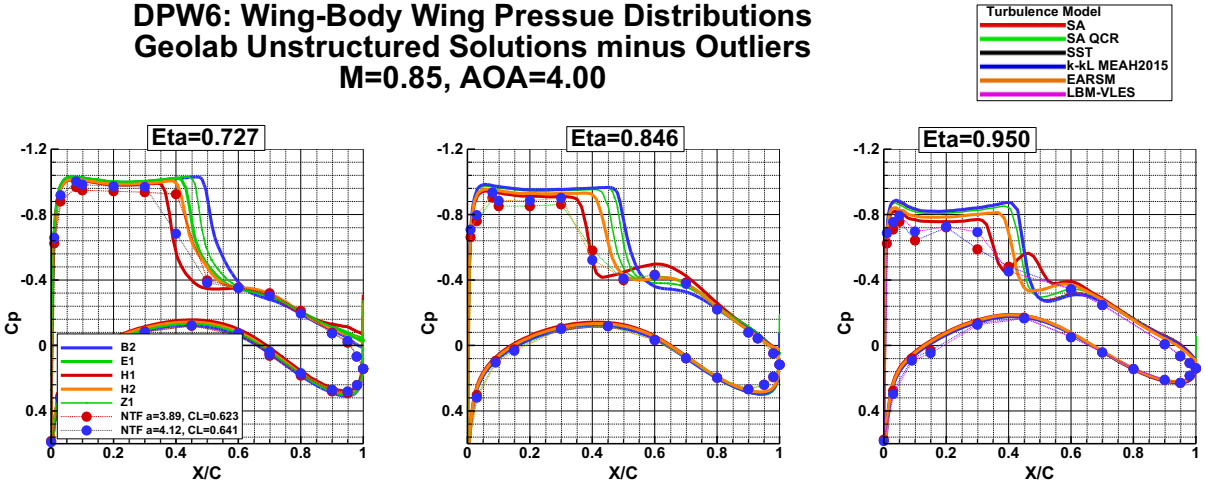


Figure A-G-24. DPW-VI: Wing Pressure Distribution; Geolab Unstructured Grid Solutions minus Outliers, AoA = 4.0°, M = 0.85, Eta = 0.727 to 0.950.

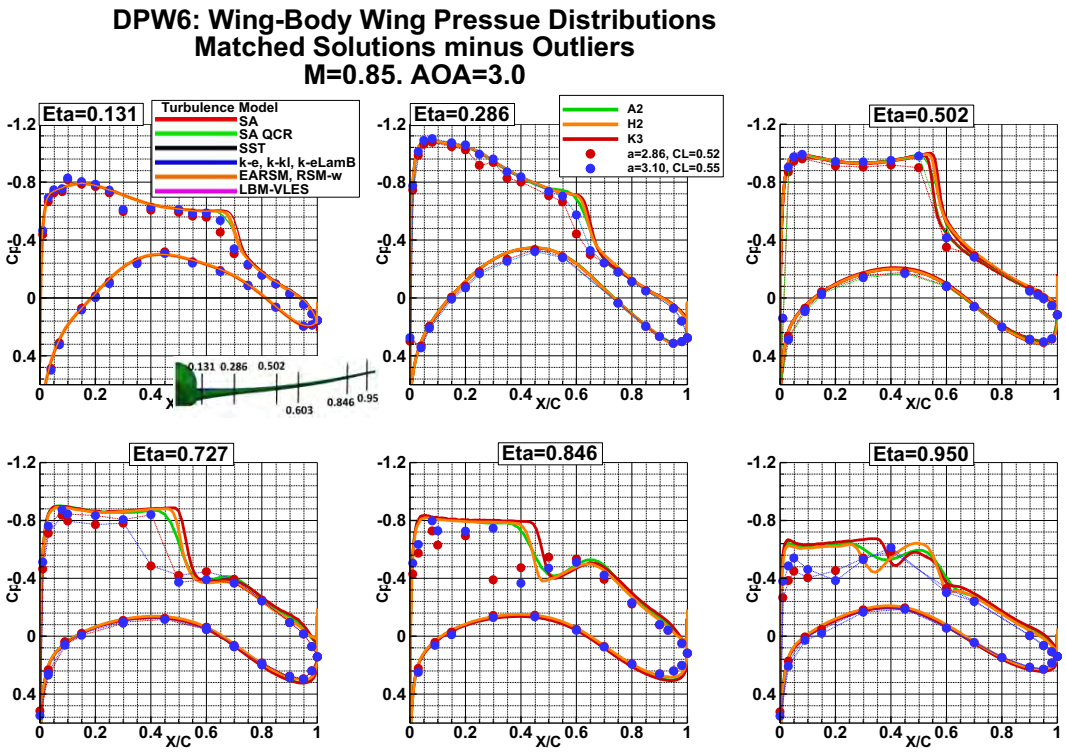


Figure A-G-25. DPW-VI: Wing Pressure Distribution; Matched "Selected" Solutions minus Outliers, AoA = 3.0°, M = 0.85.

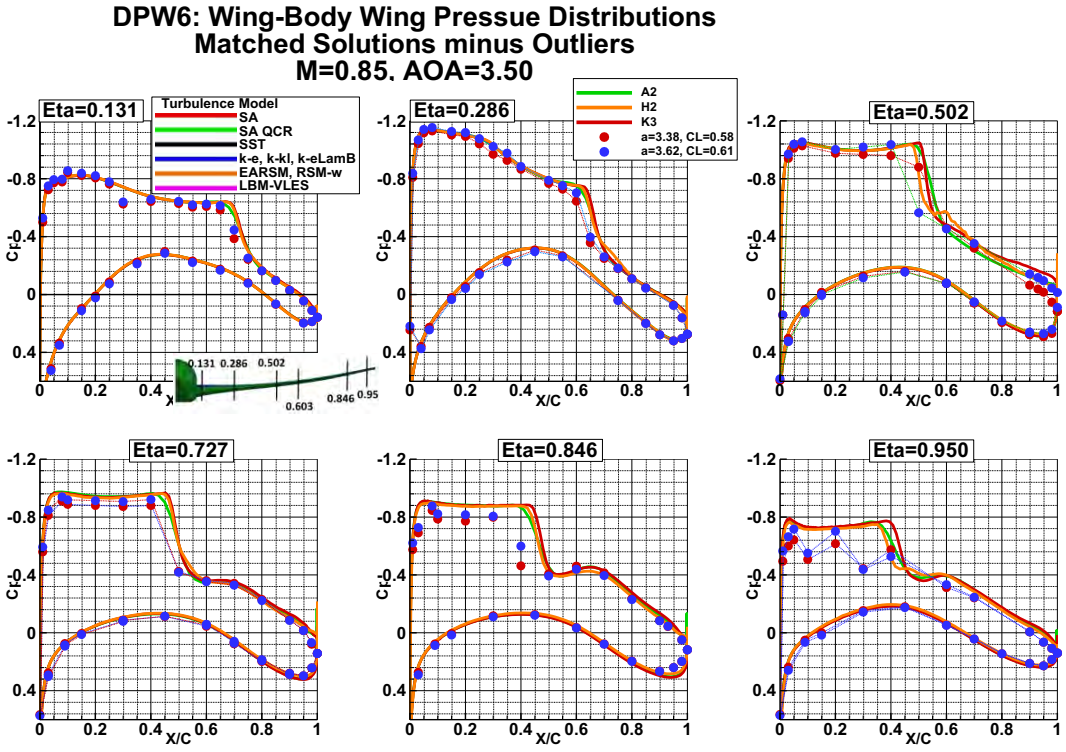


Figure A-G-26. DPW-VI: Wing Pressure Distribution; Matched "Selected" Solutions minus Outliers, AoA = 3.5°, M = 0.85.

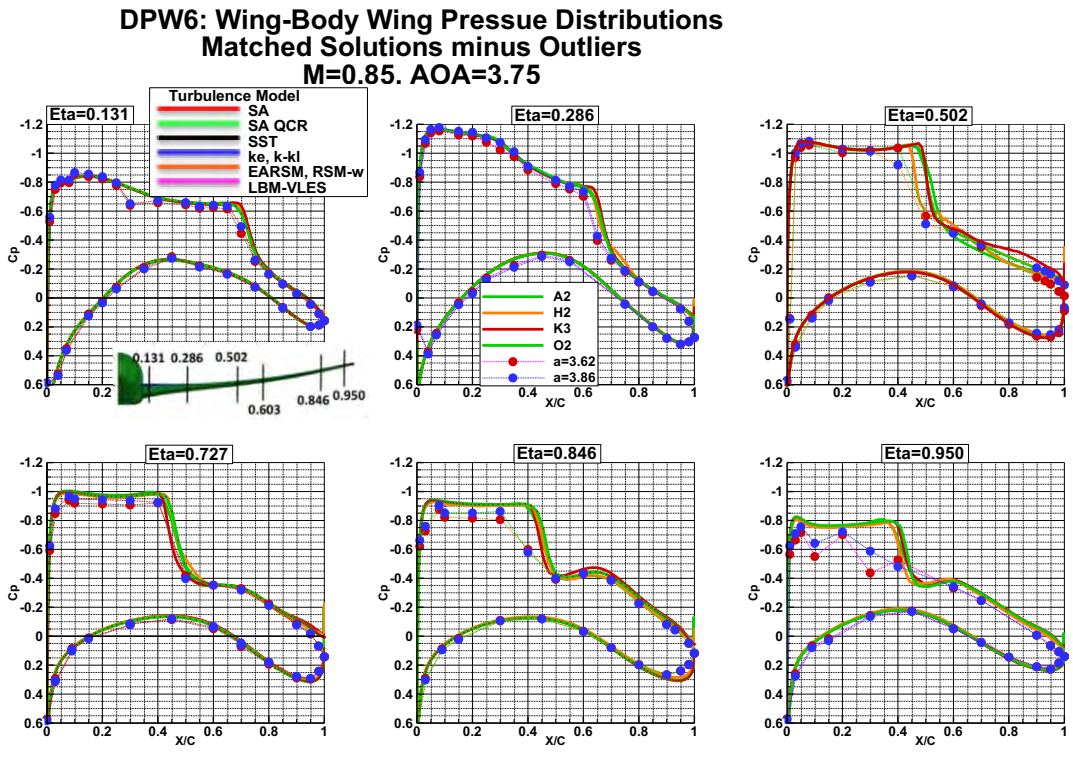


Figure A-G-27. DPW-VI: Wing Pressure Distribution; Matched "Selected" Solutions minus Outliers, AoA = 3.75°, M = 0.85.

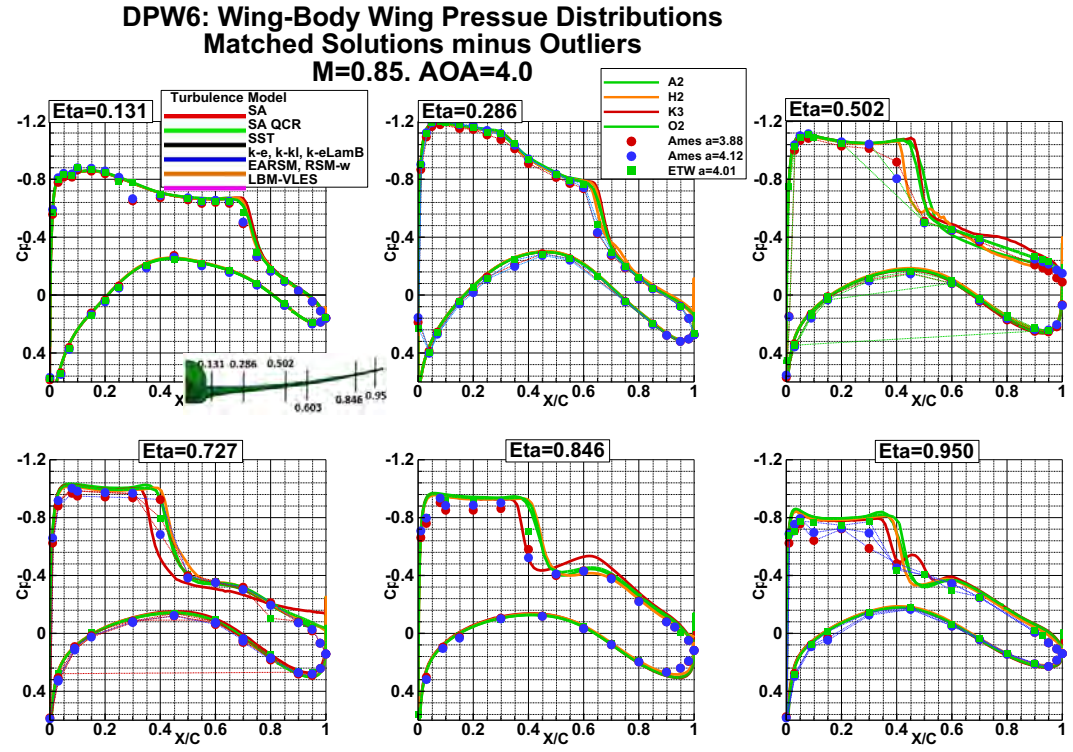


Figure A-G-28. DPW-VI: Wing Pressure Distribution; Matched "Selected" Solutions minus Outliers, AoA = 4.0°, M = 0.85.

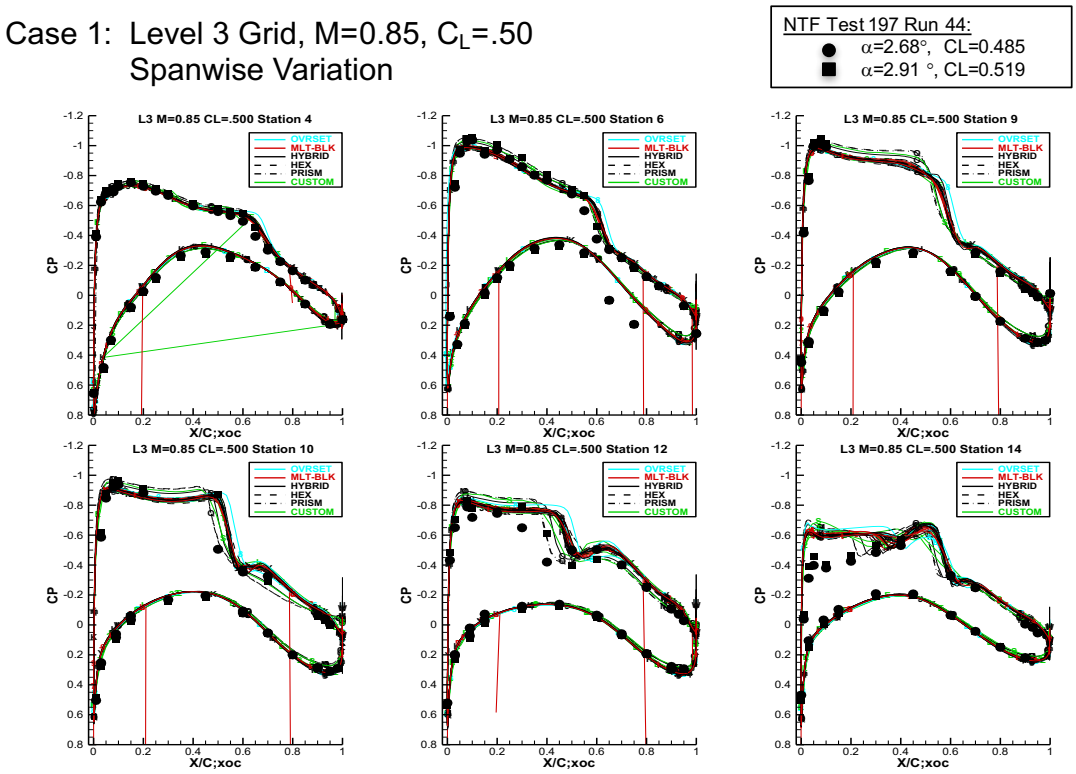


Figure A-G-29. DPW-V: Wing Pressure Distribution; All Solutions Medium Grid, C_L = 0.50, M = 0.85.

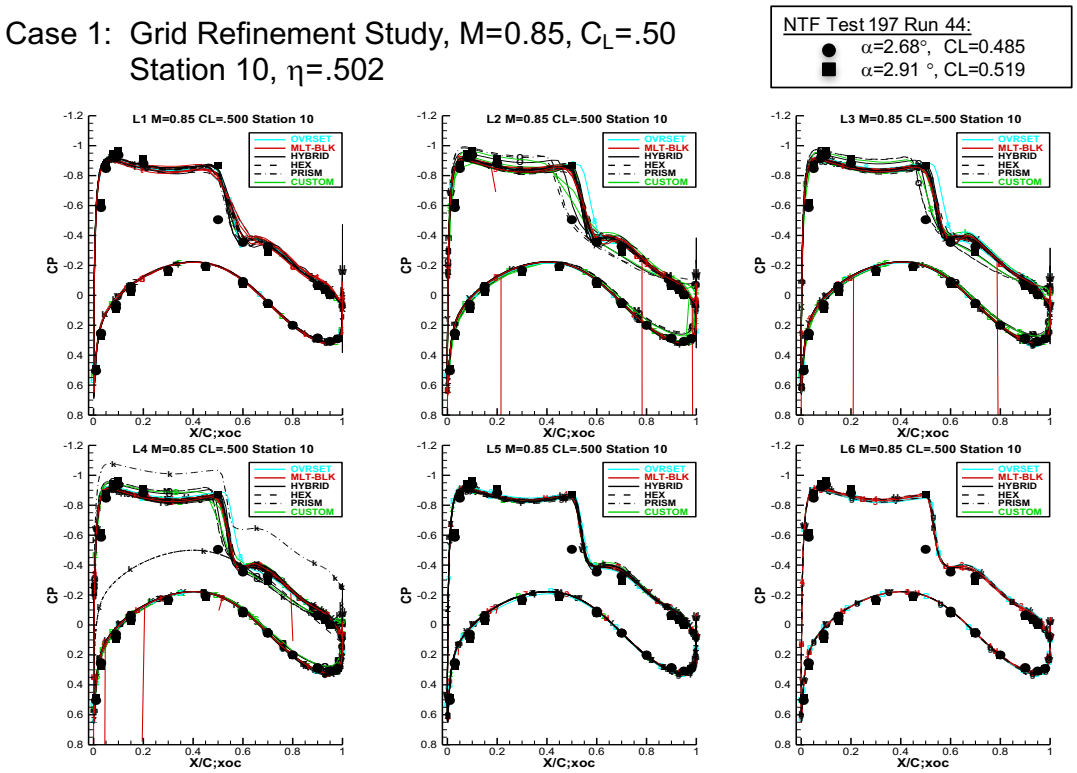


Figure A-G-30. DPW-V: Wing Pressure Distribution; All Solutions, Grid Refinement, Eta = 0.502, C_L = 0.50, M = 0.85.

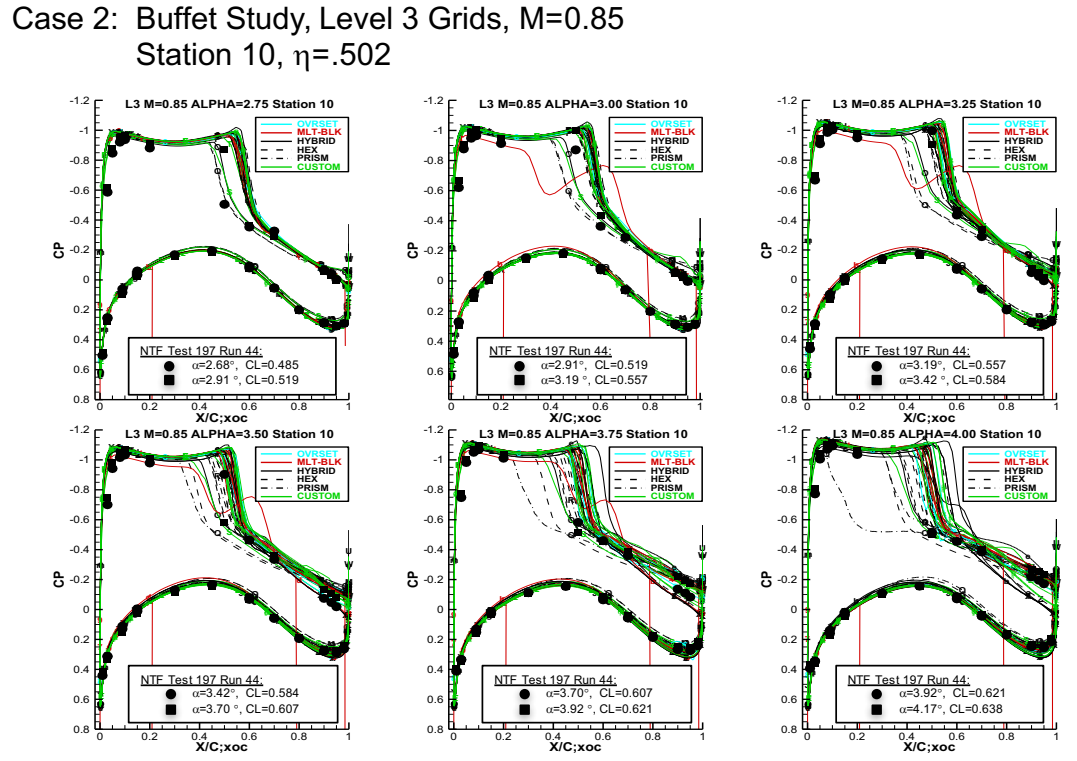


Figure A-G-31. DPW-V: Wing Pressure Distribution; All Solutions, Medium Grid, Eta = 0.502, AoA Sweep = 2.75° to 4.0°, M = 0.85.

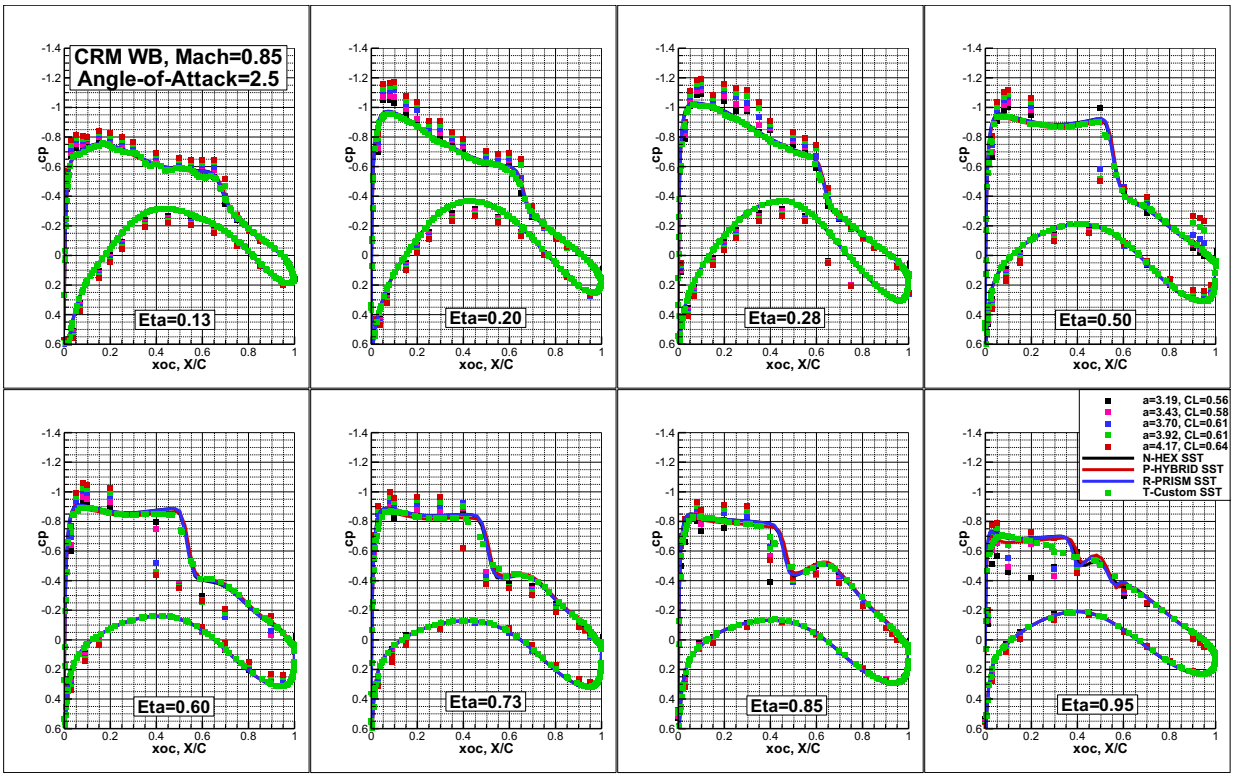


Figure A-G-32. DPW-V: Wing Pressure Distribution; Embraer Solutions with SST, AoA = 2.5° M = 0.85

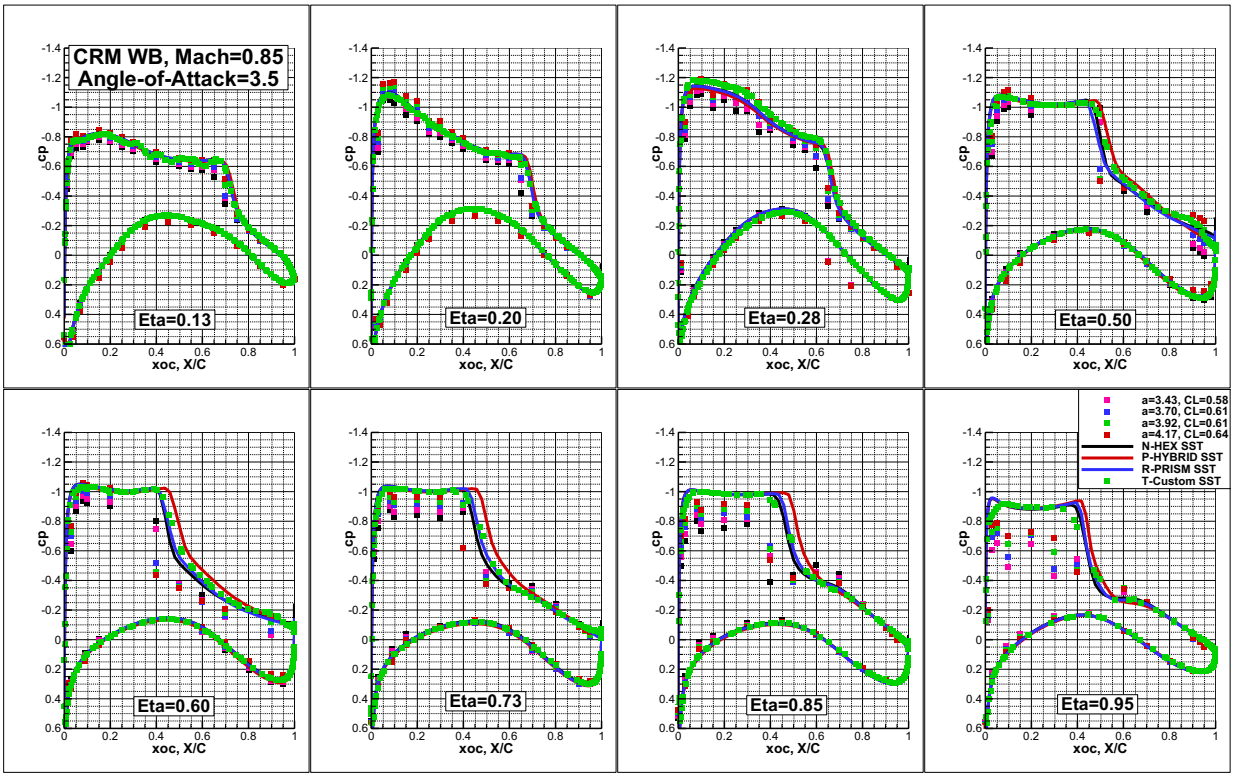


Figure A-G-33. DPW-V: Wing Pressure Distribution; Embraer Solutions with SST, AoA = 3.5°, M = 0.85.

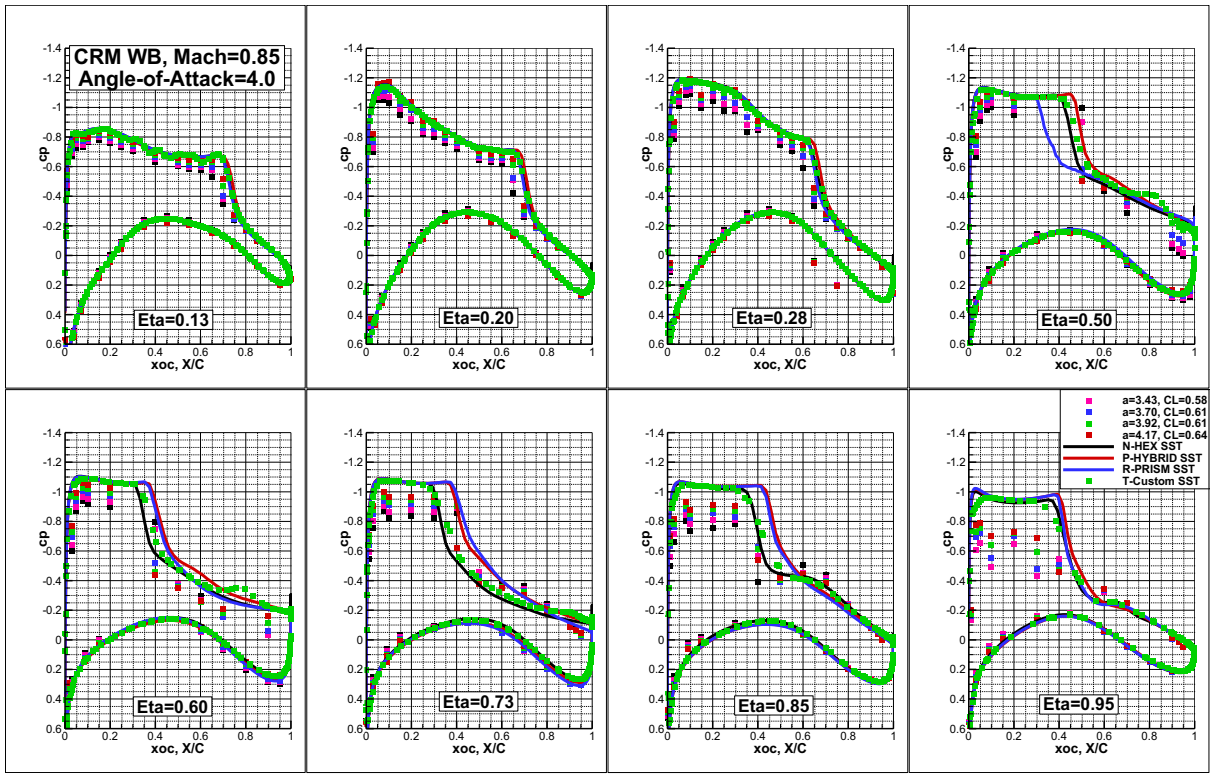


Figure A-G-34. DPW-V: Wing Pressure Distribution; Embraer Solutions with SST, AoA = 4.0°, M = 0.85.

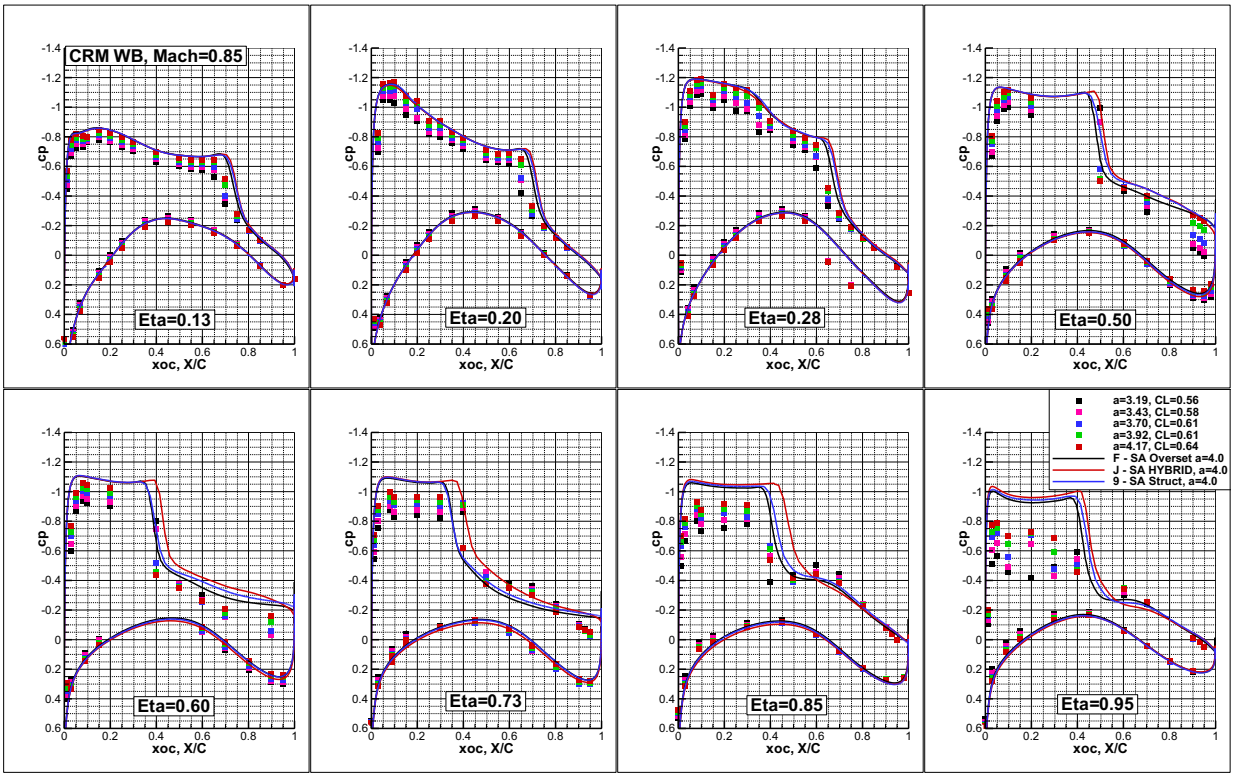


Figure A-G-35. DPW-V: Wing Pressure Distribution; 3 Solutions with SA, Different Grids, AoA = 4.0°, M = 0.85.

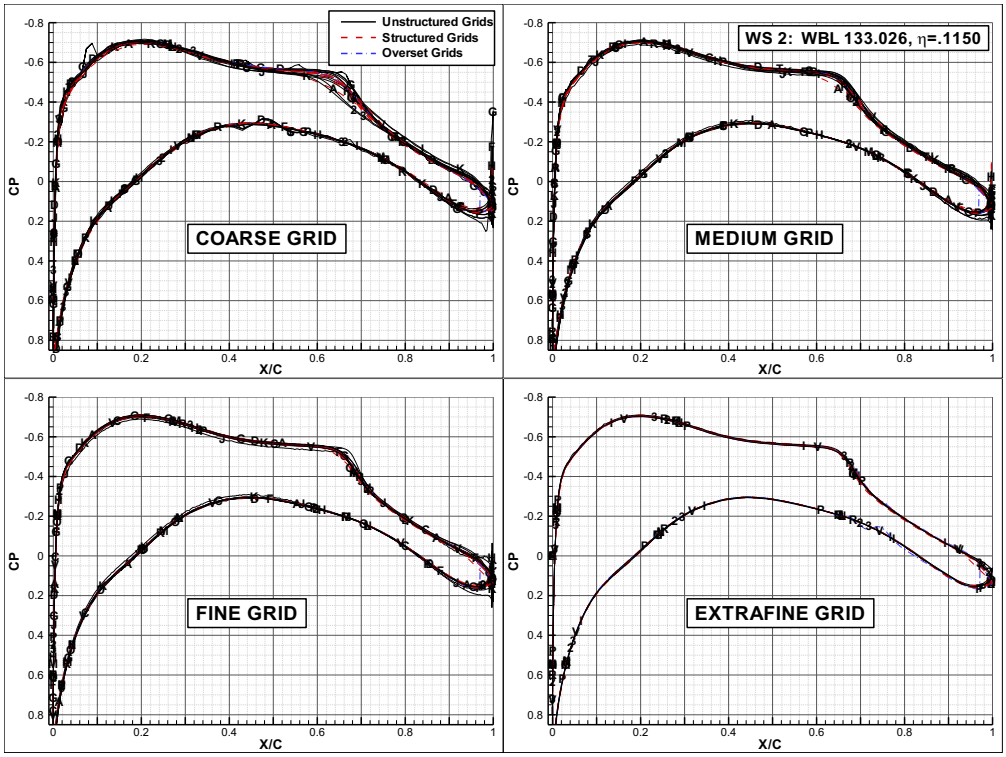


Figure A-G-36. DPW-IV: Wing Pressure Distribution; Grid Convergence, Eta=0.131, C_L=0.50, M = 0.85.

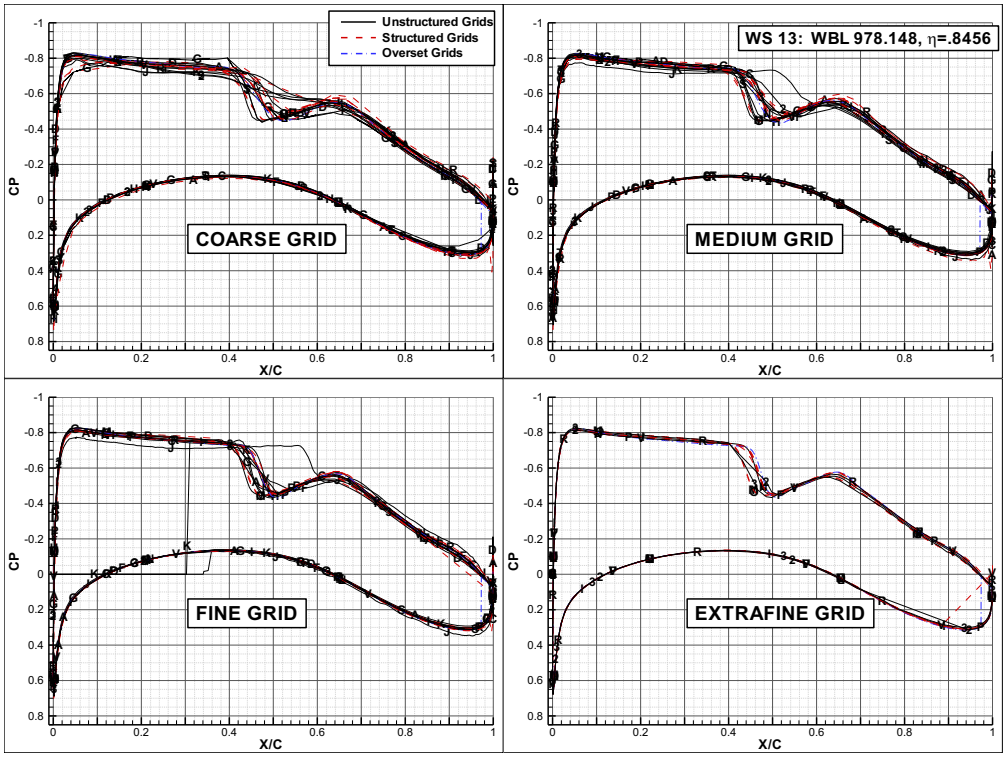


Figure A-G-37. DPW-IV: Wing Pressure Distribution; Grid Convergence, Eta=0.846, C_L =0.50, M = 0.85.

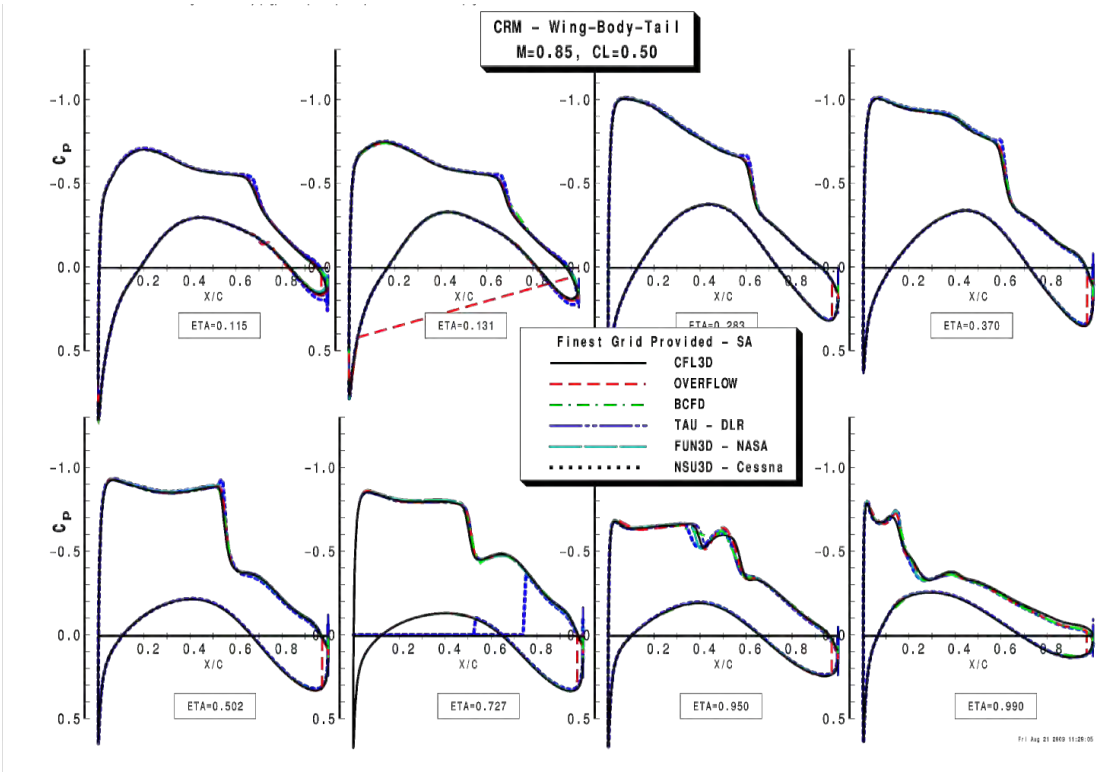


Figure A-G-38. DPW-IV: Wing Pressure Distribution; SA Turbulence Model, C_L =0.50, M = 0.85.

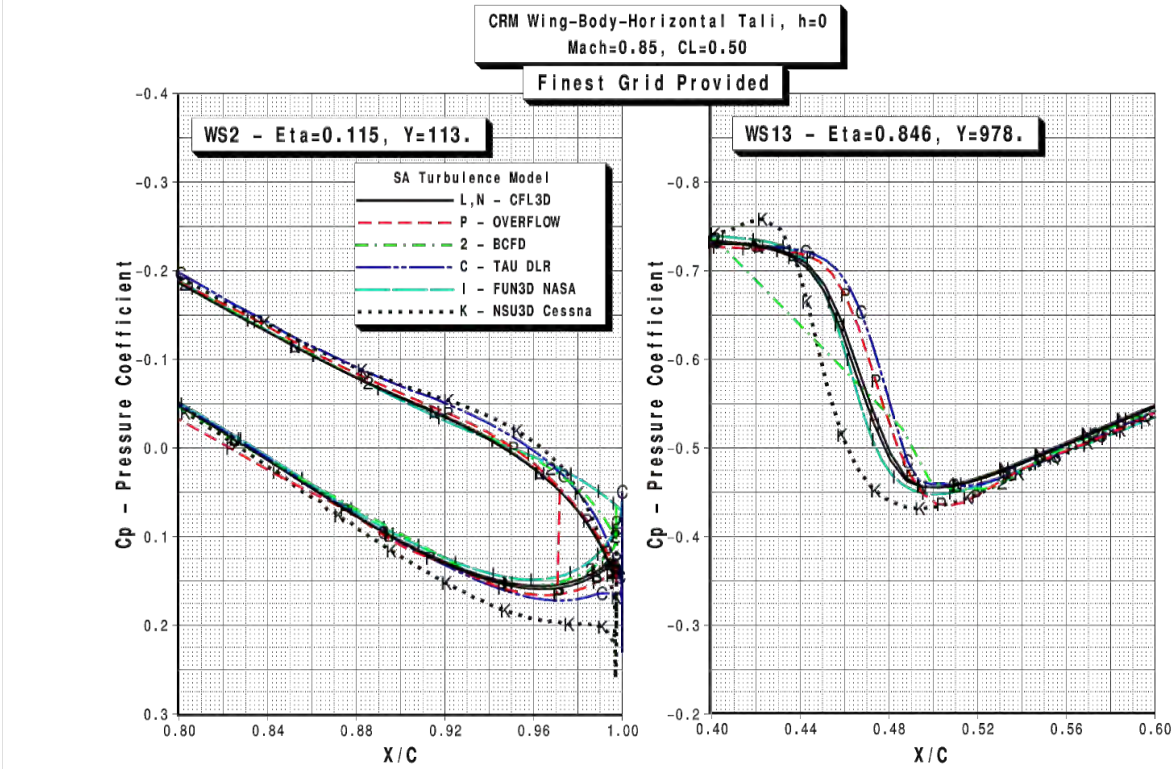


Figure A-G-39. DPW-IV: Wing Pressure Distribution; SA Turbulence Model, Aft loading at Eta=131, Shock location at Eta=0.846, C_L =0.50, M = 0.85.

REPORT DOCUMENTATION PAGE

Form Approved
OMB No. 0704–0188

The public reporting burden for this collection of information is estimated to average 1 hour per response, including the time for reviewing instructions, searching existing data sources, gathering and maintaining the data needed, and completing and reviewing the collection of information. Send comments regarding this burden estimate or any other aspect of this collection of information, including suggestions for reducing this burden, to Department of Defense, Washington Headquarters Services, Directorate for Information Operations and Reports (0704-0188), 1215 Jefferson Davis Highway, Suite 1204, Arlington, VA 22202-4302. Respondents should be aware that notwithstanding any other provision of law, no person shall be subject to any penalty for failing to comply with a collection of information if it does not display a currently valid OMB control number.
PLEASE DO NOT RETURN YOUR FORM TO THE ABOVE ADDRESS.

1. REPORT DATE *(DD-MM-YYYY)*	2. REPORT TYPE	3. DATES COVERED *(From - To)*
01-06-2019	Contractor Report	

4. TITLE AND SUBTITLE

An Evaluation and Recommendations for Further CFD Research Based on the NASA Common Research Model (CRM) Analysis from the AIAA Drag Prediction Workshop (DPW) Series

5a. CONTRACT NUMBER

5b. GRANT NUMBER

5c. PROGRAM ELEMENT NUMBER

6. AUTHOR(S)

Tinoco, Edward N.

5d. PROJECT NUMBER

5e. TASK NUMBER

NNL09AA00A

5f. WORK UNIT NUMBER

109492.02.07.01.01

7. PERFORMING ORGANIZATION NAME(S) AND ADDRESS(ES)

NASA Langley Research Center
Hampton, Virginia 23681-2199

8. PERFORMING ORGANIZATION REPORT NUMBER

9. SPONSORING/MONITORING AGENCY NAME(S) AND ADDRESS(ES)

National Aeronautics and Space Administration
Washington, DC 20546-0001

10. SPONSOR/MONITOR'S ACRONYM(S)

NASA

11. SPONSOR/MONITOR'S REPORT NUMBER(S)

NASA/CR-2019-220284

12. DISTRIBUTION/AVAILABILITY STATEMENT

Unclassified-
Subject Category 02
Availability: NASA STI Program (757) 864-9658

13. SUPPLEMENTARY NOTES

Langley Technical Monitor: Mujeeb R. Malik

14. ABSTRACT

This report provides a critical analysis of the six Drag Prediction Workshops (DPW) held under the auspices of AIAA during the time period 2001 to 2016. A total of 225 data entries were made by participants from North America, Europe, Asia, and South America, representing Government, Industry, Academia, and Commercial/Vendors. The DPW Series generated a tremendous amount of CFD data for various wing-body configurations, culminating with the analyses of the Common Research Model that included static aeroelastic effects. The submitted results showed that scatter in predicted drag was reduced dramatically from +/- 50 counts in DPW-I to around +/-5 counts for DPW-V and –VI. During this period, the finest level grids increased steadily, from just over 3 million solution points in DPW-I to 225 million in DPW-VI. While significant progress has been made, persistent problems with grid generation and separated flow prediction continue. Getting new CFD technology into the product development cycle is a long and arduous task. Additional development efforts are needed to deal with issues of adaptive grid generation, separated and unsteady flows, etc., as well as experimental validation of the computed results. Several recommendations are made to improve CFD prediction capability for problems of industrial interest.

15. SUBJECT TERMS

Aircraft; CFD; Drag; Performance; Prediction

16. SECURITY CLASSIFICATION OF:			17. LIMITATION OF ABSTRACT	18. NUMBER OF PAGES	19a. NAME OF RESPONSIBLE PERSON
a. REPORT	b. ABSTRACT	c. THIS PAGE			STI Help Desk (email: help@sti.nasa.gov)
U	U	U	UU	306	19b. TELEPHONE NUMBER *(Include area code)* (757) 864-9658